Mechanisms and Machine Science 54

João Carlos Mendes Carvalho
Daniel Martins
Roberto Simoni
Henrique Simas *Editors*

Multibody Mechatronic Systems

Proceedings of the MUSME Conference held in Florianópolis, Brazil, October 24–28, 2017

Springer

Mechanisms and Machine Science

Volume 54

Series editor

Marco Ceccarelli
LARM: Laboratory of Robotics and Mechatronics
DICeM: University of Cassino and South Latium
Via Di Biasio 43, 03043 Cassino (Fr), Italy
e-mail: ceccarelli@unicas.it

More information about this series at http://www.springer.com/series/8779

João Carlos Mendes Carvalho
Daniel Martins · Roberto Simoni
Henrique Simas
Editors

Multibody Mechatronic Systems

Proceedings of the MUSME Conference
held in Florianópolis, Brazil, October 24–28, 2017

Springer

Editors
João Carlos Mendes Carvalho
School of Mechanical Engineering
Federal University of Uberlândia
Uberlândia, Minas Gerais
Brazil

Roberto Simoni
Mobility Engineering Center
Federal University of Santa Catarina
Joinville, Santa Catarina
Brazil

Daniel Martins
Mechanical Engineering
Federal University of Santa Catarina
Florianópolis, Santa Catarina
Brazil

Henrique Simas
Mechanical Engineering
Federal University of Santa Catarina
Florianópolis, Santa Catarina
Brazil

ISSN 2211-0984 ISSN 2211-0992 (electronic)
Mechanisms and Machine Science
ISBN 978-3-319-67566-4 ISBN 978-3-319-67567-1 (eBook)
DOI 10.1007/978-3-319-67567-1

Library of Congress Control Number: 2017954901

Printed on acid-free paper

This Springer imprint is published by Springer Nature
The registered company is Springer International Publishing AG
The registered company address is: Gewerbestrasse 11, 6330 Cham, Switzerland

Preface

The MuSMe 2017, the International Symposium on Multibody Systems and Mechatronics, is the sixth event of a series that has been started in 2002 as joint activity of the FeIbIM Commission for Mechatronics and IFToMM Technical Committees for Multibody Dynamics, and Robotics and Mechatronics. The MuSMe International Symposium is a conference initiative to bring together researchers from the broad ranges of disciplines referring to Multibody Systems and Mechatronics.

Modern systems can be considered as integrated systems that can be properly studied, designed, and operated by using Mechatronics viewpoints, but even considering the multibody architecture. In particular, the aim of the MuSMe Symposium is to be a forum to exchange views, opinions, experiences, and stimulating integration between Mechatronics and Multibody Systems disciplines, a forum for facilitating contacts among research people and students.

These proceedings contain 52 papers by authors from all around the world, which cover several aspects of the wide field of Mechatronics. The contributions address mainly to kinematics, static and dynamic analysis, control of mechatronic systems, mechatronic systems for assistive technology, modeling and simulation, prototypes and experimental validations, synthesis of mechanisms and robots, and vehicle dynamics.

These proceedings can be considered to be of interest to researchers, graduate students, and engineers specializing or addressing attention to Mechatronics. We believe that a reader will take advantage of the papers in these proceedings with further satisfaction and motivation for her or his work, both in teaching and researching on mechatronic systems.

We would like to express grateful thanks to the members of the International Scientific Committee of the Symposium for cooperating enthusiastically for the success of the MuSMe initiative, in particular Prof. Marco Ceccarelli, President of IFToMM, and the authors who have contributed with very interesting papers in several subjects, covering many fields of Mechatronics and Multibody Systems. We are grateful to the reviewers for the time and effort they spent evaluating the papers.

The Organizing Committee would like to thank the Federal University of Santa Catarina (UFSC), Brazil, for supporting the MuSMe 2017 and hosting the event. We would like also to thank the auspices of ABCM—The Brazilian Society of Engineering and Mechanical Sciences, IFToMM—The International Federation for the Promotion of Mechanisms and Machine Science, FeIbIM—The Iberoamerican Federation of Mechanical Engineering, Springer, and the support of CNPq, CAPES, FAPESC, UFSC, for their financial help, recognizing that without their partnership it would not be possible to organize this meeting.

May 2017 The Editors

Contents

Kinematic Analysis

Static Analysis

Dynamic Analysis

Synthesis of Mechanisms and Robots

Synthesis of Precision Flexible Mechanisms Using Screw Theory with a Finite Elements Validation

Martín A. Pucheta(✉) and Alejandro G. Gallardo

Centro de Investigación en Informática para la Ingeniería (CIII)
and CONICET Facultad Regional Córdoba, Universidad Tecnológica Nacional,
Maestro M. López esq. Cruz Roja Argentina, X5016ZAA Córdoba, Argentina
{mpucheta,agallardo}@frc.utn.edu.ar

Abstract. The design of flexible parallel stages has recently been systematized for the three-dimensional space using Screw Theory. This methodology has shown to be practical for precision engineering applications where flexural elements, like beams and blades, are subjected to small displacements; therefore, the statics can be represented by using infinitesimal twists and wrenches. The relationships between the reciprocal twists and wrenches spaces can be related and manipulated by linear algebra. In this work, an analytical enumeration of twists and their associated wrenches for any degree of freedom with zero and infinite pitches is developed. Two synthesis problems are analytically calculated and validated using finite element analysis.

Keywords: Precision mechanisms · Screw Theory · Linear algebra · Finite element analysis

1 Introduction

Compliant mechanisms can transmit twists and/or wrenches on a point of interest of the mechanism by means of the deformation of their flexible members. Flexible parallel stages are used in precise positioning of measurement and scientific instruments, in biomedical devices, in industrial applications, among others [8].

Ball [1,9,12,13] identified the parallelism between first-order *instantaneous kinematics* (angular and linear velocity combined in the differential *Twist*) and the *static* (force and moment combined in the *Wrench*). Using screw algebra, it can also be expressed that the work is null if the differential twist and the wrench done over a body are reciprocal. Recently, Linear Algebra and Set Theory were used together to manipulate the screw algebra [14,15] complementing the use of graphical maps [6,7].

The synthesis methodologies for designing three-dimensional parallel flexures fall into four main categories [8]: (i) Rigid-body Replacement, (ii) Freedom, Actuation and Constraint Topologies, (iii) Building Blocks, (iv) Topology Optimization. The first category uses a kinematic and dynamic analysis based on

J.C.M. Carvalho et al. (eds.), *Multibody Mechatronic Systems*,
Mechanisms and Machine Science 54, DOI 10.1007/978-3-319-67567-1_1

rigid bodies and then, some sets of joints and links are replaced by flexure elements (notches, living hinges, beams). The second category known as Freedom, Actuation and Constraint Topologies (FACT) is based on Screw Theory [6,7] and linear static analysis, also expressed in algebraic form by Yu et al. [15]. A similar methodology combines several parallel flexures to eliminate parasitic motions [4]. Another approach, also based on Screw Theory, proposed by Su [10,16] combines a library of flexure elements with concentrated (notch hinges, small length flexure pivots) and distributed flexibility (beams, blades) as possible building blocks with given degree of constraints. This merges the idea of the first category (Rigid-body Replacement) and the second one. On the other hand, topology optimization is based on the iterative removal of material guided by an objective function; the most effective algorithms of this category are based on the topological derivative [11]. As unique disadvantage, it produces a solution for a unique load path, and the shapes are optimal but often complex to manufacture. Before resorting to these optimal design procedures it is a good practice to explore firstly more simple solutions based on Screw Theory, kinematics principles and static analysis.

In this work, the goal is to propose a methodology based on Screw Theory to design flexible mechanisms from the required twist system. All null-pitched twist systems and their complementary wrench systems are tabulated and used to design flexure stages by means of constraints composed only by flexure beam elements.

In Sect. 2 the necessary Screw Theory definitions used in this work are introduced. Section 3 presents the methodology to design parallel flexures from a given twist system using flexure elements. Section 4 shows the results for two 3-degrees-of-freedom flexure stages. Finally, a finite element validation is performed for each design to evaluate the accuracy of the synthesis procedure.

2 Screw Theory Background

The screw was introduced by Ball [1] as a geometric entity composed by a line $(\mathbf{s}, \mathbf{s}_0)$ and an associated real scalar quantity named pitch h, which is a ratio of linear and angular quantities. The line is expressed in Plücker coordinates, the moment of the line $\mathbf{s}_0 = \mathbf{r} \times \mathbf{s}$ is computed using any arbitrary vector $\mathbf{r}$ from the origin O to the line so that the vector components are orthogonal and satisfy the condition

$$\mathbf{s} \cdot \mathbf{s}_0 = 0 \tag{1}$$

and are normalized by the moment magnitude.

The primary or direction vector of the screw is $\mathbf{s}$. The secondary or moment vector of the screw $\mathbf{s}^0$ is the sum of the moment of the vector $\mathbf{s}_0$ defining the line axis plus h times the screw direction. Thus, the moment vector of the screw $\mathbf{s}^0$ can be decomposed into two directions: one parallel to $\mathbf{s}$, equal to $h\mathbf{s}$, and one perpendicular to the screw axis, $\mathbf{s}_0$, such that $\mathbf{s}^0 = \mathbf{s}_0 + h\mathbf{s}$ as shown in Fig. 1(a).

Given the screw $(\mathbf{s}, \mathbf{s}^0)$, the axis has coordinates

$$(\mathbf{s}, \mathbf{s}^0 - h\mathbf{s}) \tag{2}$$

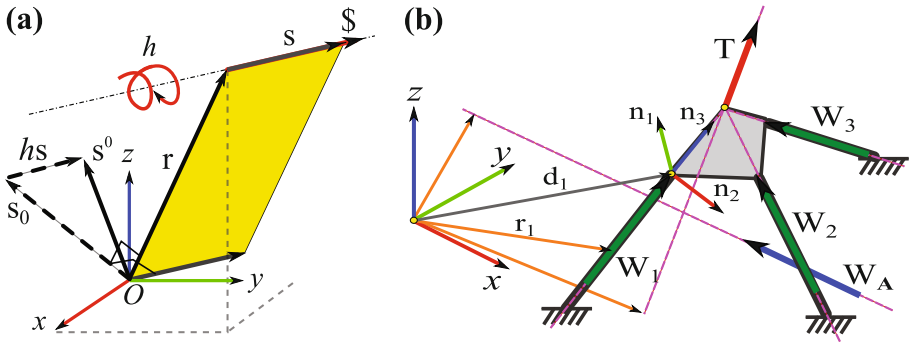

Fig. 1. Screw definition (a) and parallel flexure defined by screws (b)

where the moment of the line is $\mathbf{r}\times\mathbf{s} = \mathbf{s}^0 - h\mathbf{s}$. Then, the screw can be written as

$$\$ = (\mathbf{s}, \mathbf{s}^0) = (\mathbf{s}, \underbrace{\mathbf{s}^0 - h\mathbf{s}}_{\mathbf{s}_0} + h\mathbf{s}) = (\mathbf{s}, \underbrace{\mathbf{s}_0}_{\mathbf{r}\times\mathbf{s}} + h\mathbf{s}) = (\mathbf{s}, \mathbf{r}\times\mathbf{s} + h\mathbf{s}) \tag{3}$$

as function of the unit vector $\mathbf{s}$ of the screw axis, an arbitrary localization vector of the line $\mathbf{r}$, and the pitch h.

By applying the condition (1) to the screw axis (2) it is obtained

$$\mathbf{s}\cdot(\mathbf{s}^0 - h\mathbf{s}) = \mathbf{s}\cdot\mathbf{s}^0 - h\mathbf{s}\cdot\mathbf{s} = 0 \tag{4}$$

from which the pitch is computed as

$$h = \frac{\mathbf{s}\cdot\mathbf{s}^0}{\mathbf{s}\cdot\mathbf{s}} \tag{5}$$

where, the pitch is (i) null, $h = 0$, when the screw coincides with a line vector, (ii) infinite $h \to \infty$ when $\mathbf{s} \to \mathbf{0}$, $\mathbf{s}^0 \neq \mathbf{0}$ representing a line at infinity with direction $\mathbf{s}^0$, and (iii) finite and non-null, $h = h_\alpha$ when the secondary vector is not orthogonal to the screw axis $\mathbf{s}\cdot\mathbf{s}^0 \neq \mathbf{0}$, provided that $\mathbf{s}\cdot\mathbf{s}^0 = h\mathbf{s}\cdot\mathbf{s}$. The primary and secondary components of the screw cannot be simultaneously null. For screws representing displacements, the pitch leads to a classification of three kinds of motions (i) pure rotation $\$_0 = (\mathbf{s}, \mathbf{s}_0)$, (ii) pure translation $\$_\infty = (\mathbf{0}, \mathbf{s}^0)$, and (iii) combined or general motion, the finite screw $\$_h = (\mathbf{s}, \mathbf{s}^0)$.

The reciprocal product of two screws, $\$_1 = (\mathbf{u}, \mathbf{u}^0)$ and $\$_2 = (\mathbf{v}, \mathbf{v}^0)$, is defined as

$$\$_1 \circ \$_2 = (\mathbf{u}, \mathbf{u}^0) \circ (\mathbf{v}, \mathbf{v}^0) = \mathbf{u}\cdot\mathbf{v}^0 + \mathbf{v}\cdot\mathbf{u}^0 \tag{6}$$

The two screws are reciprocal if their reciprocal product is null, i.e., $\$_1 \circ \$_2 = 0$.

In the statics of flexure stages, two elements will be related: (i) The infinitesimal displacement screw or Twist

$$\mathbf{T} = \begin{bmatrix}\theta \\ \delta\end{bmatrix} = \begin{bmatrix}\theta \\ \mathbf{c}\times\theta + p\theta\end{bmatrix} \tag{7}$$

where, θ is a vector that coincides with the screw direction and collects rotational displacements, δ is the linear displacement, $\mathbf{c}$ is a location vector going from the origin to any point of the screw axis, and p is the pitch of the screw. (ii) The wrench screw

$$\mathbf{W} = \begin{bmatrix} \mathbf{f} \\ \mathbf{M} \end{bmatrix} = \begin{bmatrix} \mathbf{f} \\ \mathbf{r} \times \mathbf{f} + q\mathbf{f} \end{bmatrix} \tag{8}$$

where, $\mathbf{f}$ is a vector in the direction of the screw, $\mathbf{M}$ represents the moment around the screw axis, $\mathbf{r}$ is a location vector going from the origin to any point of the screw axis, and q is the pitch of screw. These screws will be used for designing flexure stages subjected to small displacements, so that screws are vector spaces and can be manipulated by linear algebra.

In order to operate with the reciprocal product in matrix form, the screws (twists (7) and wrenches (8)) are written as column vectors. The work obtained by the reciprocal product is computed by the dot product between the twist and the transpose of the wrench vector, inverted by blocks using a 6×6 exchange matrix

$$\mathbf{Q} = \begin{bmatrix} \mathbf{O}_3 & \mathbf{I}_3 \\ \mathbf{I}_3 & \mathbf{O}_3 \end{bmatrix} \tag{9}$$

composed of a 3×3 block of zeros $\mathbf{O}_3$ and a 3×3 identity matrix $\mathbf{I}_3$. Then, the matrix form of the reciprocal product expressing the infinitesimal work of wrenches is

$$\mathbf{T}^T \cdot \widehat{\mathbf{W}} = \mathbf{T}^T(\mathbf{Q}\mathbf{W}) = \mathbf{0} \tag{10}$$

2.1 Screw Systems and Complementary Screw Spaces

A set of n independent screws can be linearly combined to generate a space named n-screw system. Following Hopkins [5,15], a set of n independent twists generates a freedom space of rank n. In the three-dimensional space, the constraint space that allows a freedom space of rank n, has, by resorting to linear algebra theorems, a rank of $c = 6 - n$. The constraint space is generated by c independent wrenches. The freedom and constraint spaces are complementary. In terms of the reciprocal product, the twist system is reciprocal to the wrench system and the converse is also true. One of the most relevant contributions by Hopkins to the systematic design of flexure stages was the introduction of the actuation space as the set of screws that individually excite each independent twist without exciting parasitic motions. These screw systems can be represented in matrix form as:

Freedom space: generated by n unit basis screws

$$[\mathbf{T}] = [\mathbf{T}_1, \mathbf{T}_2, \ldots, \mathbf{T}_n]; \qquad n = \text{rank}([\mathbf{T}]). \tag{11}$$

Constraint space: generated by $6 - n$ basis screws computed as the complement of the freedom space, where $c = \text{rank}([\mathbf{W}]) = 6 - n$,

$$[\mathbf{W}] = [\mathbf{W}_1, \mathbf{W}_2, \ldots, \mathbf{W}_{6-n}]. \tag{12}$$

Actuation space: it has the same dimension as the freedom space [**T**] and consists of n pure force screws

$$[\mathbf{W}_A] = [\mathbf{W}_{A1}, \mathbf{W}_{A2}, \ldots, \mathbf{W}_{An}] \tag{13}$$

required to actuate the twist related to each degree of freedom by a desired magnitude of the associated displacement.

The computation of the reciprocal screw system [**W**] from a given screw system [**T**] can be done using a linear-algebra-based step: Use the transpose $[\mathbf{T}]^T$ to compute the null space (its complement) as

$$[\mathbf{T}^{\perp}] = \text{null}([\mathbf{T}]^T). \tag{14}$$

Then, use the exchange operator to determine a basis of unit screws for the constraint space

$$[\mathbf{W}] = \mathbf{Q}[\mathbf{T}^{\perp}]. \tag{15}$$

The reciprocal systems [**T**] and [**W**] can be computed one from the other. This leads to two possible design strategies. The synthetic strategy consists in the enumeration (design) of all the possible physical implementations of the wrench system [**W**] for a prescribed motion or screw system [**T**]. By physical implementations, the designer can choose between rigid or flexible mechanisms, and among the flexible ones, they can be parallel, serial, or hybrid stages. This work is limited to the use of parallel flexures with small displacements for potential use in precision engineering applications.

The main additional requirement in precision mechanisms is that the constrained motions, called parasitic motions, must be bounded below a given threshold or tolerance (as it is shown in the results, their magnitudes have from 3 to 5 orders less than the magnitudes of the desired motions). The main challenge is not only to design the proper constraints but also to choose the proper actuation that avoids exciting parasitic motions.

2.2 Linear Static and Constitutive Relationships of Flexures

When parallel flexures stages are conceived as a guided rigid body subjected to the reactions of flexure beams, as shown in Fig. 1(b), a linear constitutive relationship can be assumed between the resultant of the wrenches and the common twist. The forces and moments exerted by each individual beam can be added in a global frame of coordinates. The flexure elements (beams or blades) have one end fixed to the ground and the opposite end attached to the guided body.

The wrench at the end of the beam has a linear relationship with the twist through a symmetric Twist/Wrench stiffness matrix [5], which is the inverse of the compliance matrix

$$\mathbf{W} = \mathbf{K}_{TW}\mathbf{T} \tag{16}$$

As usually done for structural analysis and finite element analysis, this equation is established for a master element and changed of coordinates from a local (attached to the flexure element) to a global coordinate system.

The change of coordinates for screws corresponds to the adjoint transformation of the Lie group in SE(3) [14] and consists in multiplying the screw by the 6×6 matrix defined as

$$[\mathrm{Ad}] = \mathbf{N} = \begin{bmatrix} \mathbf{R} & \mathbf{O}_3 \\ \mathbf{DR} & \mathbf{R} \end{bmatrix} = \begin{bmatrix} \begin{bmatrix} \mathbf{n}_1 & \mathbf{n}_2 & \mathbf{n}_3 \end{bmatrix} & \begin{bmatrix} \mathbf{0} & \mathbf{0} & \mathbf{0} \end{bmatrix} \\ \begin{bmatrix} \mathbf{d} \times \mathbf{n}_1 & \mathbf{d} \times \mathbf{n}_2 & \mathbf{d} \times \mathbf{n}_3 \end{bmatrix} & \begin{bmatrix} \mathbf{n}_1 & \mathbf{n}_2 & \mathbf{n}_3 \end{bmatrix} \end{bmatrix} \tag{17}$$

where, $\mathbf{R}$ is a 3×3 proper orthogonal matrix of passive rotation, $\mathbf{O}_3$ is a 3×3 matrix of zeroes, $\mathbf{D}$ is the 3×3 skew-symmetric matrix associated to the displacement vector $\mathbf{d}$, such that $\mathbf{Dv} = \mathbf{d} \times \mathbf{v}$ for all $\mathbf{v} \in \mathbb{R}^3$. The transformation matrix can also be build, as shown at the right-hand side of Eq. (17), in terms of 4 vectors: a local frame defined by orthogonal unit vectors $\{\mathbf{n}_1, \mathbf{n}_2, \mathbf{n}_3\}$ attached to a point of interest (e.g., the end-tip of the flexure 1 in Fig. 1(b)) and the location vector $\mathbf{d}$, going from the global origin to the origin of that local frame. For instance, a beam with a square cross-section is attached to a guided stage in a global position $\mathbf{d}$, its longitudinal axis is oriented as the unit direction vector, $\mathbf{n}_3$, and has a vector $\mathbf{n}_2$ which is normal to its lateral face, thus defining a change of coordinates transformation matrix $\mathbf{N}(\mathbf{d}, \mathbf{n}_2 \times \mathbf{n}_3, \mathbf{n}_2, \mathbf{n}_3)$. Then, by using this matrix the twist and wrench screws transform their coordinates as $\mathbf{T}' = \mathbf{NT}$ and $\mathbf{W}' = \mathbf{NW}$.

In order to apply the constitutive relationship between screws and wrenches, the vector components of the wrench are exchanged as $\widehat{\mathbf{W}} = \mathbf{QW}$. Then, the linear relationship between screws can be expressed through the symmetric stiffness matrix $\mathbf{K}$. For instance, this relationship for a beam with a square cross-section can be of the form

$$\widehat{\mathbf{W}} = \mathbf{KT} \quad \rightarrow \begin{bmatrix} \mathbf{M} \\ \mathbf{f} \end{bmatrix} = \begin{bmatrix} 4EI/L & 0 & 0 & 0 & 6EI/L^2 & 0 \\ & 4EI/L & 0 & -6EI/L^2 & 0 & 0 \\ & & GJ/L & 0 & 0 & 0 \\ & & & 12EI/L^3 & 0 & 0 \\ & & & & 12EI/L^3 & 0 \\ \text{sym.} & & & & & AE/L \end{bmatrix} \begin{bmatrix} \theta \\ \delta \end{bmatrix} \tag{18}$$

where, the material properties are the Young modulus E and the torsional rigidity modulus G, A is the cross-sectional area, I is the area moment of inertia about a traversal axis, and J is the polar moment of inertia with respect to the longitudinal beam axis.

The global stiffness is computed in global coordinates. Therefore, the wrench in a master element has conveniently exchanged its vector components as $\widehat{\mathbf{W}} = \mathbf{QW}_{\text{master}}$. Then, it is changed to global coordinates using

$$\mathbf{W} = \mathbf{N}\widehat{\mathbf{W}} = \mathbf{NQW}_{\text{master}} \tag{19}$$

where, the twist at the master element can be expressed $\mathbf{T} = \mathbf{N}\mathbf{T}_{\text{master}}$, from which

$$\mathbf{T}_{\text{master}} = \mathbf{N}^{-1}\mathbf{T} \tag{20}$$

Then, the constitutive relationship can be applied to the master element as $\mathbf{W}_{\text{master}} = \mathbf{K}\mathbf{T}_{\text{master}}$, which is replaced in Eq. (19) to obtain the same relationship in global coordinates

$$\mathbf{W} = \mathbf{N}\mathbf{Q}\mathbf{K}\underbrace{\mathbf{T}_{\text{master}}}_{(20)} = \underbrace{\mathbf{N}\mathbf{Q}\mathbf{K}\mathbf{N}^{-1}}_{\mathbf{K}_{TW}}\mathbf{T} = \mathbf{K}_{TW}\mathbf{T}. \tag{21}$$

If several flexible constraints are applied in parallel over a rigid body subjected to a unique twist $\mathbf{T}$, the wrenches are additive

$$\mathbf{W} = \Sigma_{i=1}^{r}\mathbf{W}_i = \Sigma_{i=1}^{r}\left(\mathbf{K}_{TWi}\mathbf{T}\right) = \left(\Sigma_{i=1}^{r}\mathbf{K}_{TWi}\right)\mathbf{T} = \underbrace{\left(\Sigma_{i=1}^{r}\mathbf{N}_i\mathbf{Q}\mathbf{K}_i\mathbf{N}_i^{-1}\right)}_{\mathbf{K}_{\Sigma TW}}\mathbf{T} \tag{22}$$

and therefore, the stiffness $\mathbf{K}_{\Sigma TW} = \Sigma_{i=1}^{r}\mathbf{K}_{TWi} = \Sigma_{i=1}^{r}\mathbf{N}_i\mathbf{Q}\mathbf{K}_i\mathbf{N}_i^{-1}$ is additive.

3 Synthesis Method

The main goal is to design a system that is flexible and strong (working far from the material failure, e.g. with stress values far from the yield stress, using an adequate safety factor) in the desired motions but stiff in the constrained motions. These two objectives are encoded in the way that the flexure elements are arranged to configure the global stiffness $\mathbf{K}_{\Sigma TW}$ because the screw systems of the desired motions are related by $[\mathbf{W}_A] = \mathbf{K}_{\Sigma TW}[\mathbf{T}_d]$ and the constrained motions $[\mathbf{T}^R]$ with rank $6-n$ are related by $[\mathbf{T}^R] = \mathbf{K}_{\Sigma TW}^{-1}[\mathbf{W}]$; the magnitude of each twist in $[\mathbf{T}^R]$ subject to the unit wrenches $[\mathbf{W}]$ must tend to zero.

The semi-analytic methodology here proposed starts from the motion requirements

Step 1: Construct the Freedom system of the desired twists $[\mathbf{T}_d]$.
Step 2: Identify the normalized twist system $[\mathbf{T}]$.
Step 3: Compute the normalized wrench system $[\mathbf{W}]$ as the complement of the twist system.
Step 4: Select (in all possible forms) the type, number, and geometric arrangement of flexural elements to satisfy the wrench system.
Step 5: Compute the optimal actuation $[\mathbf{W}_A] = \mathbf{K}_{T\Sigma W}[\mathbf{T}_d]$.
Step 6: Verify the resultant motions using finite element analysis.

This methodology is based on FACT [5] but clearly uses a different order and does not require the use of graphical maps. In the following paragraphs, each step of the methodology is described.

Table 1. Combinations without repetitions of freedom and constraints expressed as systems

DOF	Case	Sub-case	**T**	**W**
1	R	(1) R_x	$(\theta_x, 0, 0; 0, 0, 0)$	$(f_x, f_y, f_z; 0, M_y, M_z)$
	T	(2) T_x	$(0, 0, 0; \delta_x, 0, 0)$	$(0, f_y, f_z; M_x, M_y, M_z)$
2	RR	(3) $R_x \cdot R_y$	$(\theta_x, \theta_y, 0; 0, 0, 0)$	$(f_x, f_y, f_z; 0, 0, M_z)$
	RT	(4) $R_x \cdot T_x$	$(\theta_x, 0, 0; \delta_x, 0, 0)$	$(0, f_y, f_z; 0, M_y, M_z)$
		(5) $R_x \cdot T_y$	$(\theta_x, 0, 0; 0, \delta_y, 0)$	$(f_x, 0, f_z; 0, M_y, M_z)$
	TT	(6) $T_x \cdot T_y$	$(0, 0, 0; \delta_x, \delta_y, 0)$	$(0, 0, f_z; M_x, M_y, M_z)$
3	RRR	(7) $R_x \cdot R_y \cdot R_z$	$(\theta_x, \theta_y, \theta_z; 0, 0, 0)$	$(f_x, f_y, f_z; 0, 0, 0)$
	RRT	(8) $R_x \cdot R_y \cdot T_x$	$(\theta_x, \theta_y, 0; \delta_x, 0, 0)$	$(0, f_y, f_z; 0, 0, M_z)$
		(9) $R_x \cdot R_y \cdot T_z$	$(\theta_x, \theta_y, 0; 0, 0, \delta_z)$	$(f_x, f_y, 0; 0, 0, M_z)$
	RTT	(10) $R_x \cdot T_x \cdot T_y$	$(\theta_x, 0, 0; \delta_x, \delta_y, 0)$	$(0, 0, f_z; 0, M_y, M_z)$
		(11) $R_x \cdot T_y \cdot T_z$	$(\theta_x, 0, 0; 0, \delta_y, \delta_z)$	$(f_x, 0, 0; 0, M_y, M_z)$
	TTT	(12) $T_x \cdot T_y \cdot T_z$	$(0, 0, 0; \delta_x, \delta_y, \delta_z)$	$(0, 0, 0; M_x, M_y, M_z)$
4	RRRT	(13) $R_x \cdot R_y \cdot R_z \cdot T_x$	$(\theta_x, \theta_y, \theta_z; \delta_x, 0, 0)$	$(0, f_y, f_z; 0, 0, 0)$
	RRTT	(14) $R_x \cdot R_y \cdot T_x \cdot T_y$	$(\theta_x, \theta_y, 0; \delta_x, \delta_y, 0)$	$(0, 0, f_z; 0, 0, M_z)$
		(15) $R_x \cdot R_y \cdot T_x \cdot T_z$	$(\theta_x, \theta_y, 0; \delta_x, 0, \delta_z)$	$(0, f_y, 0; 0, 0, M_z)$
	RTTT	(16) $R_x \cdot T_x \cdot T_y \cdot T_z$	$(\theta_x, 0, 0; \delta_x, \delta_y, \delta_z)$	$(0, 0, 0; 0, M_y, M_z)$
5	RRRTT	(17) $R_x \cdot R_y \cdot R_z \cdot T_x \cdot T_y$	$(\theta_x, \theta_y, \theta_z; \delta_x, \delta_y, 0)$	$(0, 0, f_z; 0, 0, 0)$

Step 1: The freedoms that a point of interest can have in the guided rigid-body form a subset of 6 possibilities: 3 pure rotation screws and 3 pure translation screws, respectively, around and along x, y, z orthogonal Cartesian axes (excluding the case where all the 6 screws are chosen)

$$\begin{aligned} &\mathbf{T}(\theta_x) = \theta_x[1,0,0;0,0,0]^T;\ \mathbf{T}(\theta_y) = \theta_y[0,1,0;0,0,0]^T;\ \mathbf{T}(\theta_z) = \theta_z[0,0,1;0,0,0]^T \\ &\mathbf{T}(\delta_x) = \delta_x[0,0,0;1,0,0]^T;\ \mathbf{T}(\delta_x) = \delta_y[0,0,0;0,1,0]^T;\ \mathbf{T}(\delta_x) = \delta_x[0,0,0;0,0,1]^T \end{aligned} \tag{23}$$

Step 2: The unit or normalized form of the twists can be obtained by factorizing the desired amplitude for each motion.

Step 3: The complement of the twist system can be constructed and computed off-line. In Table 1 the enumeration for all possible twists composed exclusively by zero and infinite pitch is shown [9]. In the last column, the reciprocal wrench is computed. Clearly and intuitively, the resultant wrench has null components in the allowed conjugated components of the twist, i.e., $M_i = 0$ if θ_i is a desired motion and $f_i = 0$ if δ_i is a desired motion, for $i \in \{x, y, z\}$. By using a 0–1 normal form of the screw and Boolean algebra, the linear components of the wrenches are the *negation* of those of the twist. The same is valid for rotational components.

Step 4: Choose the number and the type of flexure elements and arrange them geometrically to satisfy the wrench system, in all possible forms. This dif-

ficult step is neither fully automated nor systematic. Some rules known as *Exact constraint* [2,3] can be applied in the case that beam flexures are used, though it is combinatorially more complex if a more comprehensive library of flexures is considered. By knowing the freedom that a beam constraints and the hypotheses underlying in the associated stiffness matrix, the constrained translations can be tackled first by aligning the longitudinal beam axis in the direction of the constrained translation. The deformation mode must not stretch the neutral fiber of the beam. Then, if a rotation must be constrained, two coplanar and parallel beams can be connected to the guided rigid-body with the rotation axis being perpendicular to the beams plane. The motions can be constrained in sequence.

Step 5: The physical implementation of the actuation system $[\mathbf{W}_A]$ can be simplified if (push/pull) linear actuators are applied (Hopkins [5] identified 26 actuation systems). Conveniently, each twist $\mathbf{T}_i$ in $[\mathbf{T}_d]$ can be associated to one wrench $\mathbf{W}_{Ai}$ in $[\mathbf{W}_A]$ in an uncoupled way, such that the location of the actuation plane for each wrench of the form $(\mathbf{f} \cdot \mathbf{f}_0)$ can be analytically computed using the formula $\mathbf{r}_{min} = (\mathbf{f} \times \mathbf{f}_0)/(\mathbf{f} \cdot \mathbf{f})$.

Step 6: The resultant motions of the stage under the loading conditions computed in the *Step 5* are validated using a finite element analysis. The mesh of the structure is refined in the neighborhood of the attachment of the beam flexures. The geometry of the rigid moving platform also contains: (i) adequately chosen surfaces to locate and apply the actuation wrenches, and (ii) datum geometries to measure the rotation and translation components of the twist. All these elements are considered as flexible bodies in the finite element simulation.

4 Results

Two problems are solved using the methodology, (i) a benchmark proposed in the Hopkins thesis [5] consisting in an RRR flexure stage, and (ii) a here proposed test, a RTT flexure stage. The finite element results were obtained using SolidWorks Simulation®.

RRR test: The desired magnitude for each twist is 1°. Three beams of length 8.2 cm and square cross-section with a width of $w = 0.3$ cm are arranged on three orthogonal axes and attached to a distance of 10.2 cm from the origin coincident with the point to guide in the rigid platform. The material properties of the beams are $E = 68\text{e}9$ Pa and $G = 25\text{e}9$ Pa. The geometric properties, $\{A, I, J\}$, are computed from w. The opposite end-points are attached to the ground and form a triangle. This structure is rotated around the origin such that the ground triangle is aligned with the $x - y$ plane. The finite element analysis is shown in Fig. 2 and the measured results are shown in Table 2.

RTT test: The desired magnitude for the rotation twist is 1° and for the two translations is 0.1 mm. Four beams of length 15 cm and square cross-section with a width of 0.3 cm are arranged parallel to the x axis and attached to a

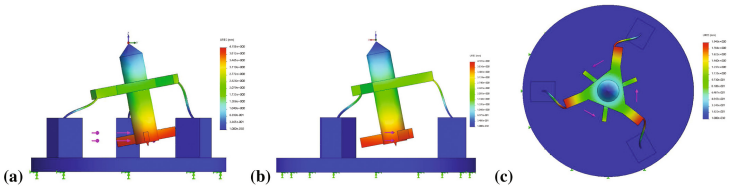

Fig. 2. FEA Static analysis RRR: rotation around (a) x axis, (b) y axis, and (c) z axis

Table 2. Twist component values (linear and angular displacements) obtained for the $R_x \cdot R_y \cdot R_z$ flexure stage. Desired motions are shown in bold font and the parasitic ones are in regular font.

	$\mathbf{T}_1$	$\mathbf{T}_2$	$\mathbf{T}_3$
	R_x	R_y	R_z
θ_x [°]	**1.083**	$1.55 \cdot 10^{-4}$	$-1.88 \cdot 10^{-5}$
θ_y [°]	$6.4 \cdot 10^{-5}$	**1.083**	$-1.11 \cdot 10^{-4}$
θ_z [°]	$5.979 \cdot 10^{-4}$	$5.037 \cdot 10^{-7}$	**1.085**
δ_x [mm]	$-3.46 \cdot 10^{-3}$	$2.83 \cdot 10^{-3}$	$-1.56 \cdot 10^{-5}$
δ_y [mm]	$-2.82 \cdot 10^{-3}$	$-3.459 \cdot 10^{-3}$	$8.78 \cdot 10^{-6}$
δ_z [mm]	$1.64 \cdot 10^{-5}$	$-5.607 \cdot 10^{-6}$	$-3.41 \cdot 10^{-3}$

square stage with half diagonals of length 7.07107 cm measured from the origin. Two beams are coplanar and parallel to the xy plane constraining the rotation around the z axis, and two beams do the same to constrain the rotation of the y axis, one beam is redundant and added to provide a symmetric behavior in displacements. The geometric and material properties are identical to the beams of the RRR test. The opposite end-points are attached to the ground and form a square parallel to the guided platform, and thus avoid the translation in the x direction. The finite element analysis is shown in Fig. 3 and the measured results are shown in Table 3.

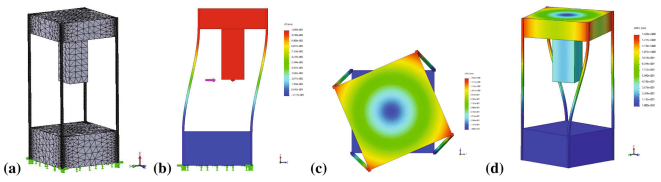

Fig. 3. FEA Static analysis RTT: (a) mesh (b) translation along z axis (results are identical to y axis), (c, d) rotation around x axis

Table 3. Twist component values (linear and angular displacements) obtained for the $R_x \cdot T_y \cdot T_z$ flexure stage. Desired motions are shown in bold font and the parasitic ones are in regular font.

	$\mathbf{T}_1$	$\mathbf{T}_2$	$\mathbf{T}_3$
	R_x	T_y	T_z
θ_x [°]	**1.1027**	$8.78564 \cdot 10^{-7}$	$8.78564 \cdot 10^{-7}$
θ_y [°]	$1.5914 \cdot 10^{-6}$	$1.22168 \cdot 10^{-7}$	$1.371 \cdot 10^{-3}$
θ_z [°]	$5.04 \cdot 10^{-4}$	$1.371 \cdot 10^{-3}$	$1.22168 \cdot 10^{-7}$
δ_x [mm]	$2.809 \cdot 10^{-6}$	$3.466 \cdot 10^{-7}$	$3.466 \cdot 10^{-7}$
δ_y [mm]	$-4.417 \cdot 10^{-2}$	**0.1072**	$9.719 \cdot 10^{-7}$
δ_z [mm]	$-4.705 \cdot 10^{-2}$	$9.719 \cdot 10^{-7}$	**0.1072**

The results are more accurate for the RRR test than for the RTT test. This means that the constraint of the translations using flexure beams is more effective than for constraining rotations. In future work, the database of motions and its complementary wrench spaces will be completed with the enumeration for twists with non-null finite pitches. Then, the design and control of the flexure stages for a desired workspace will be tackled.

5 Conclusions

A new synthetic approach to the design of parallel flexure stages was presented. A methodology based on constraining a guided platform with flexure beams arranged in parallel was introduced. Screw theory and linear algebra were used to enumerate an exhaustive list of 17 twists and their complementary constraint wrenches using exclusively zero and infinite pitch screws. In the procedure the unique non-systematic step is the arrangement of flexures to provide a given wrench system, which is based on exact constraint rules. This open-issue deserves further investigation to make it fully automatic. The analytical results were validated using finite element analysis.

Acknowledgements. The authors acknowledge the financial support from the *Universidad Tecnológica Nacional (UTN)* through project PID-UTN 3935, from the *Agencia Nacional de Promoción Científica y Tecnológica* PICT-2013-2894, and from *Consejo Nacional de Investigaciones Científicas y Técnicas* PIP 1105, all from Argentina. We gratefully acknowledge the joint work and friendly assistance of Juan A. Bernad from UTN-FRC, Córdoba, Argentina.

References

1. Ball, R.S.: A Treatise on the Theory of Screws, 2nd edn. Cambridge University Press, Cambridge (1900). (originally published in 1876 and revised by the author in 1900, now reprinted with an introduction)

2. Blanding, D.L.: Exact constraint: machine design using kinematic principles. ASME Press, New York (1999)
3. Hale, L.C.: Principles and techniques for designing precision machines. Ph.D. thesis, Massachusetts Institute of Technology, Massachusetts, U.S.A. (1999)
4. Hao, G., Kong, X.: A normalization-based approach to the mobility analysis of spatial compliant multi-beam modules. Mech. Mach. Theory **59**, 1–19 (2013)
5. Hopkins, J.: Design of flexure-based motion stages for mechatronic systems via Freedom, Actuation and Constraints Topologies (FACT). Ph.D. thesis, Massachusetts Institute of Technology, Massachusetts, U.S.A. (2010)
6. Hopkins, J., Culpepper, M.: Synthesis of multi-degree of freedom, parallel flexure system concepts via freedom and constraint topology (FACT) - part I: principles. Precis. Eng. **34**(2), 259–270 (2010)
7. Hopkins, J., Culpepper, M.: Synthesis of multi-degree of freedom, parallel flexure system concepts via freedom and constraint topology (FACT) - part II: practice. Precis. Eng. **34**(2), 271–278 (2010)
8. Howell, L.L., Magleby, S.P., Olsen, B.M.: Handbook of Compliant Mechanisms. Wiley, New York (2013)
9. Hunt, K.H.: Kinematic Geometry of Mechanisms. Oxford University Press, New York (1978)
10. Su, H.J., Zhou, L., Zhang, Y.: Mobility analysis and type synthesis with screw theory: from rigid body linkages to compliant mechanisms. In: Kumar, V., Schmiedeler, J., Sreenivasan, S., Su, H.J. (eds.) Advances in Mechanisms, Robotics and Design Education and Research. Mechanisms and Machine Science, vol. 14, pp. 55–66. Springer, Heidelberg (2013)
11. Novotny, A.A., Sokolowski, J.: Topological Derivatives in Shape Optimization. Interaction of Mechanics and Mathematics. Springer, Heidelberg (2013). 10.1007/978-3-642-35245-4
12. Phillips, J.: Freedom in Machinery: vol. 1. Introducing Screw Theory. Cambridge University Press, Cambridge (1984)
13. Phillips, J.: Freedom in Machinery: vol. 2. Screw Theory Exemplified. Cambridge University Press, Cambridge (1990)
14. Selig, J.: Geometric Fundamentals of Robotics, 2nd edn. Springer, New York (2006)
15. Yu, J.J., Li, S.Z., Su, H.J., Culpepper, M.L.: Screw theory based methodology for the deterministic type synthesis of flexure mechanisms. ASME J. Mech. Rob. **3**(3), 031,008-1–031,008-14 (2011)
16. Yue, C., Zhang, Y., Su, H.J., Kong, X.: Type synthesis of three-degree-of-freedom translational compliant parallel mechanisms. ASME J. Mech. Rob. **7**(3), 031,012 (2015). 8 pages

Enumeration of Kinematic Chains with Zero Variety for Epicyclic Gear Trains with One and Two Degrees of Freedom

Marina Baldissera de Souza(✉), Rodrigo de Souza Vieira, and Daniel Martins

Federal University of Santa Catarina, Florianópolis, Santa Catarina 88040-900, Brazil
marina.bs@posgrad.ufsc.br

Abstract. The enumeration of kinematic chains for epicyclic gear trains allows to obtain all the possible configurations from specified structural characteristics. However, the more complex becomes the desired structure, the greater the number of options to analyse in order to select the most suitable one, what makes necessary a criterion to reduce this range of choices. The concept of variety and the conditions when its value equals to zero can be used for this purpose. This paper enumerates the kinematic chains with zero variety for epicyclic gear trains with one and two degrees of freedom, and with up to four independent loops. It is presented afterward two examples of transmissions obtained from the chains enumerated. Finally, the advantages of using zero variety chains are discussed.

Keywords: Enumeration of kinematic chains · Number synthesis · Epicyclic gear trains · Variety · Minimal sets

1 Introduction

The enumeration of kinematic chains or number synthesis for epicyclic gear trains is a prolific field of study and it is an important stage of design of system's transmissions, enabling to obtain all the possible configurations from specified structural characteristics. It allows to identify existing gear sets and to generate new ones, thereby avoiding a possible patent infringement. However, the more complex the desired structure, the greater the number of options to analyse in order to select the most suitable one, what renders impractical the task for verifying individually each one, and makes necessary a criterion to reduce this range of choices. The concept of *variety* and the conditions to force that its value being equal to zero can be used for this purpose [6,11,12].

This paper aims to enumerate and to present the kinematic chains with zero variety and with up to four independent loops for epicyclic gear trains with one and two degrees of freedom. The remainder of this paper is structured as follows. Section 2 introduces the concept of mobility and how it can be calculated. Section 3 briefly reviews the definition of number synthesis and the main tools

J.C.M. Carvalho et al. (eds.), *Multibody Mechatronic Systems*,
Mechanisms and Machine Science 54, DOI 10.1007/978-3-319-67567-1_2

employed on it. Section 4 introduces the definition of variety, minimal sets and the advantage of selecting a variety zero kinematic chain. In Sect. 5, the results of the enumeration are presented and for each mobility, a possible application is shown. The results found are compared to the current status of enumeration of non-fractionated chains with the specified structural characteristics [10]. Finally, Sect. 6 presents the final considerations about the results achieved in this paper.

2 Mobility

The mobility M, or the number of degrees of freedom (DoF) of a kinematic chain, is the number of independent parameters needed to define completely its configuration in the space, with respect to a specified link chosen as reference [6,10]. The mobility is used to determine the number of necessary actuators to drive a mechanism and to verify its existence [10]. The mobility can be calculated by the Kutzbach-Chebyshev-Gruebler equation, formulated as:

$$M = \lambda(n - j - 1) + \sum_{i=1}^{j} f_i \tag{1}$$

Where λ is the order of screw system to which all joints of the kinematic chain belong, n is the number of links, j the number of joints and f_i are the degrees of relative motion allowed by the joint i.

Through the replacement of the joints with more than 1-DoF by a combination of single DoF joints, the Eq. 1 becomes:

$$M = \lambda(n - j - 1) + j \tag{2}$$

The number of independent loops ν of a kinematic chain can be expressed as a function of the number of links n and the number of joints j, as defined as:

$$\nu = j - n + 1 \tag{3}$$

The combination of Eqs. 2 and 3 yields:

$$M = j - \lambda\nu \tag{4}$$

Equation 4 is known as the loop mobility criterion [13] and it permits to quickly calculate the mobility of a kinematic chain, besides being the main parameter used in number synthesis process. The mobility criterion, Eq. 4, has some known limitations when applied to a few classical mechanisms and parallel robots, e.g. the Tripteron manipulator. Normally these discrepancies occur only with high values of λ, for example in the general spatial screw-system ($\lambda = 6$) [5]. Nevertheless, Eq. 4 has been proved suitable for lower values of λ such as $\lambda = 2$ and $\lambda = 3$, i.e. those applied to gear trains and the only systems considered in this paper.

3 Number Synthesis

The number synthesis or enumeration of kinematic chains consists of the generation of a complete list of kinematic chains that satisfy Eq. 2, excluding isomorphic and degenerated chains (kinematic chain where at least one subchain has mobility less than or equal to zero [10]). The main tools employed on the enumeration methodologies developed so far are: graph theory, group theory and matricial representation [9]. In this paper, only the first and second ones will be adopted, for further information about the number synthesis, see [9,10,13].

Kinematic chains can be represented in a univocal form by graphs, where the vertices correspond to the links and the edges correspond to the joints. Therefore, the number synthesis of kinematic chains is equivalent to the enumeration of graphs [9].

The McKay's algorithm and his graph generator [7,8] allow an isomorph-free enumeration of graphs/kinematic chains and the elimination of those which contain independent loops whose mobility is not desired. The graph generator will be used in Sect. 5 to achieve the purpose of this paper.

4 Variety

4.1 Definition

As defined by Tischler et al. [11], a kinematic chain is *variety* V if it does not contain any loop, or subset of loops, with a mobility less than $M - V$, but does contain at least one loop, or a subset of loops, which has a mobility of $M - V$. A kinematic chain is variety $V = 0$ if it contains no loop, or a subset of loops, with a mobility less than the mobility of the whole chain.

The concept of variety can be interpreted as a relationship between inputs and outputs of a kinematic chain, thus it must be considered in the selection of the joints that are going to be actuated [6]. In a kinematic chain of mobility M and variety V, $M - V$ joints may be selected at random for actuation, the other V actuated joints being selected so that not more than $M - V$ actuated joints belong to any subset of loops with mobility of $M - V$ [11].

For example, a variety $V = 1$ kinematic chain with mobility M contains a closed subset of one or more loops with mobility of $M - 1$, where only $M - 1$ actuated joints belonging to this subset are necessary to reduce its mobility to zero. Also, for this same kinematic chain, $M - 1$ joints can be randomly selected to be actuated, but the choice of the M^{th} actuated joint is restricted to the joints which do not belong to the subset with mobility $M - 1$.

Consequently, in a kinematic chain with j joints, mobility M and variety $V = 0$, M from those j joints must be selected and locked to decrease its mobility to zero. As $V = 0$, this selection of all the M actuated joints can be random. However, kinematic chains with lesser values of variety, like $V = 0$, are scarcer than those with higher values [12], what makes the use of the concept of null variety as a criterion to reduce the possible candidates of the enumeration process a very effective strategy, which may be employed in the synthesis of any parallel mechanism.

4.2 Minimal Sets

To understand the concept of minimal set, introduced in [11], consider the atlas of kinematic chains with $\lambda = 3$, $M = 0$ and $\nu = \{1, 2\}$, represented in Fig. 1. Note that all of them are variety $V = 0$. Visual inspection of kinematic chains in Fig. 1(b) and (d) shows that they contain at least one subset isomorphic to Fig. 1(a), therefore the chains in Fig. 1(a and c) compose the *minimal set* of kinematic chains for the case $\lambda = 3$, $M = 0$ and $\nu = \{1, 2\}$.

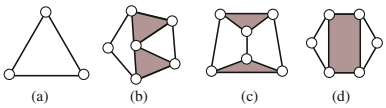

Fig. 1. Atlas of kinematic chains with $\lambda = 3$, $M = 0$ and $\nu \leq 2$

Chains with mobility $M > 0$ also have minimal sets, e.g., the elements of the minimal set of kinematic chains with $\lambda = 3$, $M = 1$ and $\nu \leq 3$ are presented in Fig. 2, again emphasizing that all are variety $V = 0$. There are no chains for the case $\nu = 2$.

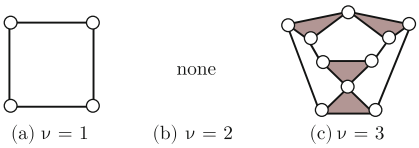

Fig. 2. Minimal set for the case $M = 1$, $\lambda = 3$ and $\nu \leq 3$

The relationship between minimal sets and variety is clear and unidirectional: it must be stressed that whilst all members of the minimal set have variety $V = 0$, not all kinematic chains with $V = 0$ belong to the minimal sets [6,11]. An example is the Watt's chain, shown in Fig. 3: it is variety $V = 0$ and it has mobility $M = 1$, but as it contains two subchains identical to the kinematic chain of Fig. 2(a), it cannot belong to the minimal set presented in Fig. 2.

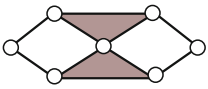

Fig. 3. Watt's chain ($\lambda = 3$, $M = 1$ and $\nu = 2$): despite of being variety $V = 0$, it does not belong to the minimal set for the case shown in Fig. 2

The variety of a kinematic chain is determined by searching for at least one subset which is member of the minimal set for the case of the chain's structural

characteristics. The subset which presents the smallest mobility, M', may be used to calculate the variety of the kinematic chain with M DoF, through the difference $V = M - M'$ [11].

5 Kinematic Chains with Zero Variety for Epicyclic Gear Trains

In an *epicyclic gear train* (EGT), some gears not only rotate about their own axes, but also revolve around some other gears. Depending on whether it is an internal or external gear, a gear that rotates about a central stationary axis is called *sun* or *ring* gear, and those whose axes revolve about the central axis are called *planet* gears. The *carrier* or *arm*, a supporting link, keeps the center distance between two meshing gears constant. EGTs can have multiple applications, such as vehicle transmissions, machine tool gear boxes, robot manipulators, and so on.

One of the first methods for enumeration of kinematic chains for EGTs was developed by Buchsbaum and Freudenstein [2]. Tsai [13] presented an atlas of bicolored graphs containing one to four independent loops for EGTs, considering the order of screw system $\lambda = 2$, as proposed by Davies [3,4].

The objective of this section is to enumerate the variety $V = 0$ kinematic chains for EGTs with one and two degrees of freedom, by employing the Eq. 4 to determine the number of joints, i.e., the number of edges of the graphs to be generated, and then the Eq. 2 to calculate the number of links/vertices, considering the cases $\lambda = 2$, $M = \{1, 2\}$ and $\nu = \{1, 2, 3, 4\}$. The values obtained are used into the McKay's graph generator [7,8] and it is demanded to disconsider graphs with independent loops with mobility equivalent to one or two when necessary.

Chains with $M \neq \{1, 2\}$ and higher number of independent loops are not included in the scope of this paper, neither are fractionated chains. The amount of $V = 0$ kinematic chains found is compared to the status of enumeration of non-fractionated chains for $\lambda = 2$ and $M = \{1, 2\}$ presented by Simoni et al. [10], shown in Table 1, to verify their proportion among the chains with the structural characteristics analysed.

Table 1. Current status of enumeration of non-fractionated chains for $\lambda = 2$, $M = \{1, 2\}$ and $\nu \leq 4$ (adapted from [10])

ν	$M = 1$	$M = 2$
1	1	1
2	1	2
3	3	9
4	13	49

5.1 Epicyclic Gear Trains with $M = 1$

In total, eighteen kinematic chains with $\lambda = 2$, $M = 1$ and $\nu \leq 4$ have variety $V = 0$, depicted in Figs. 4 and 5. By comparing the quantity of results that have been found to the values of Table 1, it can be concluded that all kinematic chains with $\nu \leq 4$ representing EGTs with one DoF have $V = 0$.

Regarding the minimal set, by visual inspection, it inferred that it is composed by exclusively two kinematic chains, those shown in Fig. 4(a) and in Fig. 5(n), as the latter is the only one that does not contain one subset isomorphic

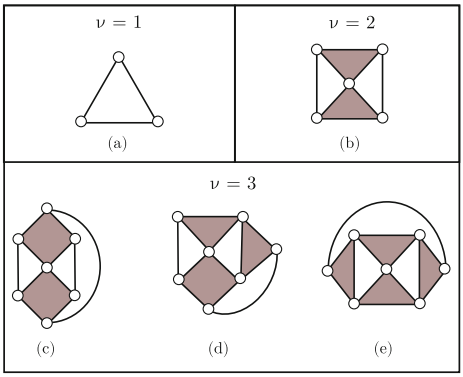

Fig. 4. Variety $V = 0$ kinematic chains with $\lambda = 2$, $M = 1$ and $\nu \leq 3$

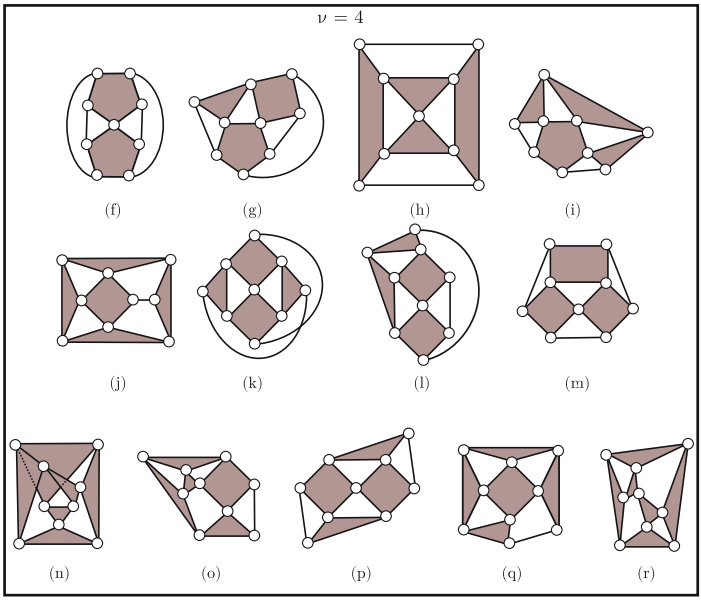

Fig. 5. Variety $V = 0$ kinematic chains with $\lambda = 2$, $M = 1$ and $\nu = 4$

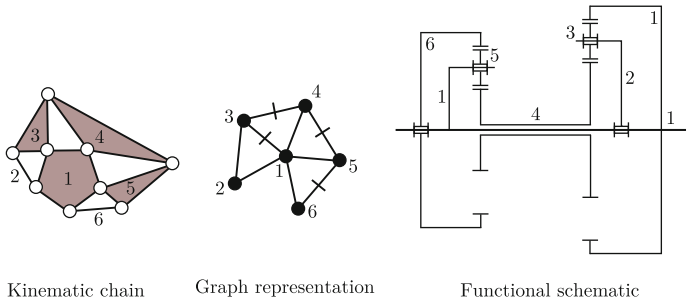

Fig. 6. Kinematic chain of Fig. 4(i), its graph representation (where the edges crossed by a perpendicular line stand for gear joints and the remaining ones, revolute joints) and the functional schematic of the Simpson gear set

to the former. It must be remarked that in the kinematic chain of Fig. 5(n), there are three ternary links that cross each other, what is represented by dashed lines.

Further development for a specific case is seen in Fig. 6, where the kinematic chain in Fig. 5(i) is shown with its graph representation, whose edges crossed by a perpendicular line stand for gear joints and the remaining ones, revolute joints. The links are enumerated from 1 to 6 in order to generate a functional schematic of a possible EGT configuration, known as Simpson gear set. It is a compound EGT consisting of two basic EGTs, each having a sun gear (link 4), a ring gear (links 1 and 6), a carrier (links 1 and 2) and four planets (links 3 and 5). The two sun gears are connected to each other by a common shaft (link 4), whereas the carrier of one EGT is connected to the ring gear of the other EGT by a spline shaft (link 1). The Simpson gear set is most used in three-speed automotive automatic transmissions [13]. As its respective kinematic chain is variety $V = 0$, any joint can be chosen for actuation without restriction, i.e., any link can be the system's input, respecting the EGT's configuration.

5.2 Epicyclic Gear Trains with $M = 2$

There are eight variety $V = 0$ kinematic chains with $\lambda = 2$, $M = 2$ and $\nu \leq 4$, as shown in Fig. 7, fewer than the number of chains enumerated in Table 1. In regards to the previous section, the number of results found for $M = 2$ are also lesser than the ones for $M = 1$. The minimal set is reduced by half with the increase of mobility as well, on this circumstance being composed exclusively by the chain represented by Fig. 7(a), as all the kinematic chains with $V = 0$ present an identical subset to this chain. Again, in Fig. 7(h), the crossing of some links is represented by dashed lines.

In Fig. 8, the chain of Fig. 7(b) has its links enumerated from 1 to 5 and it is shown with its graph representation, and a feasible EGT configuration, where the link 2 is chosen to be the ground link. EGTs with mobility $M = 2$, associated with a continuous variable unit (CVU), may compose an *infinitely variable transmission* (IVT), a transmission system which allows for step-less

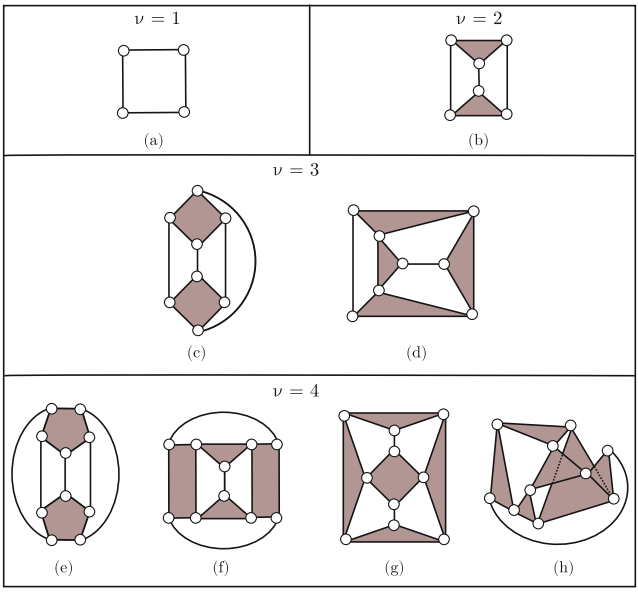

Fig. 7. Variety $V = 0$ kinematic chains with $\lambda = 2$, $M = 2$ and $\nu \leq 4$

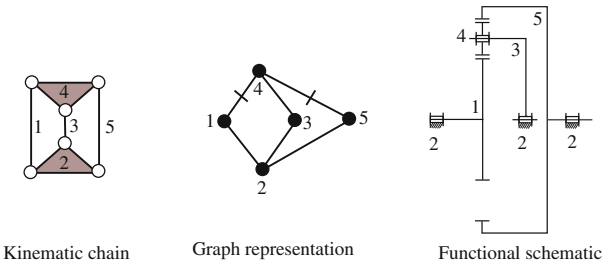

Fig. 8. The kinematic chain in Fig. 7(b), its graph representation (where the edges crossed by a perpendicular line stand for gear joints and the remaining ones, revolute joints) and a feasible EGT configuration

variability of speed ratio, including zero velocity ratio. It is used as the power train for exercising machines and agricultural tractors [1,14].

As the kinematic chain in Fig. 7(b) is variety $V = 0$, the choice of the two actuated joints can be randomly made, i.e., any links can be the inputs, although the EGT's configuration must be taken in consideration. By analysing the EGT's functional schematic in Fig. 8, it can be inferred that the two inputs may be chosen among three links: the sun gear (link 1), the ring gear (link 5) and the carrier (link 2), the one not selected as input being defined as the system's output. There are three alternatives for the inputs' choice: *sun gear/carrier*, *ring gear/carrier* and *sun gear/ring gear*. The last one is represented in Fig. 9,

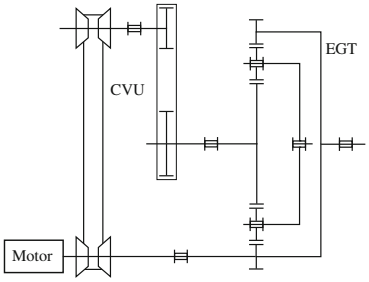

Fig. 9. Possible IVT configuration with the EGT of Fig. 8

where the links 1 and 5 are the two inputs of the two DoF EGT and the link 2 is the output.

6 Conclusion

The concept of variety is a good criterion to reduce the options' range of kinematic chains for a defined purpose. A kinematic chain with variety $V = 0$ erases a constraint in the selection of the actuated joints, allowing to choose them at random, what can be interesting depending on the aimed utilization, thus the importance of enumerating the chains which have this characteristic.

This paper presented the variety $V = 0$ kinematic chains for epicyclic gear trains with mobilities $M = 1$ and $M = 2$. A comparison between the number of results found and the current status of enumeration of non-fractionated chains for $\lambda = 2$, $M = \{1, 2\}$ and $\nu \leq 4$ is made to verify the proportion of chains among them whose actuated joints can be chosen randomly. It was corroborated that, as stated by Tischler et al. [12], the amount of kinematic chains decreases when lesser the variety's value: while all the 18 kinematic chains with $\lambda = 2$, $M = 1$ and $\nu \leq 4$ are variety $V = 0$, only 8 of the 61 kinematic chains with $\lambda = 2$, $M = 2$ and $\nu \leq 4$ have zero variety. It was also verified that the minimal sets for both cases are not large, the minimal set for the case $M = 1$ consisting of two chains and the one for the case $M = 2$ being composed only by one chain.

In spite of the variety $V = 0$ kinematic chains allowing to actuate any joint without restriction, the EGT's configuration must be taken into account when determining the system's inputs/outputs, as seen in Sect. 5.2. Nonetheless, by using only chains with zero variety, this selection can be made without hesitation.

References

1. Bottiglione, F., De Pinto, S., Mantriota, G.: Infinitely variable transmissions in neutral gear: torque ratio and power re-circulation. Mech. Mach. Theory **74**, 285–298 (2014)
2. Buchsbaum, F., Freudenstein, F.: Synthesis of kinematic structure of geared kinematic chains and other mechanisms. J. Mech. **5**(3), 357–392 (1970)

3. Davies, T.: Dual coupling networks. Proc. Inst. Mech. Eng. Part C J. Mech. Eng. Sci. **220**(8), 1237–1247 (2006)
4. Davies, T.: Freedom and constraint in coupling networks. Proc. Inst. Mech. Eng. Part C J. Mech. Eng. Sci. **220**(7), 989–1010 (2006)
5. Gogu, G.: Mobility of mechanisms: a critical review. Mech. Mach. Theory **40**(9), 1068–1097 (2005)
6. Martins, D., Carboni, A.P.: Variety and connectivity in kinematic chains. Mech. Mach. Theory **43**(10), 1236–1252 (2008)
7. McKay, B.D., Piperno, A.: Practical graph isomorphism, II. J. Symb. Comput. **60**, 94–112 (2014)
8. McKay, B.D., Piperno, A.: Nauty and Traces Users Guide (Version 2.6), Computer Science Department, Australian National University, Canberra, Australia (2016)
9. Simoni, R., Carboni, A., Martins, D.: Enumeration of kinematic chains and mechanisms. Proc. Inst. Mech. Eng. Part C J. Mech. Eng. Sci. **223**(4), 1017–1024 (2009)
10. Simoni, R., Carboni, A., Simas, H., Martins, D.: Enumeration of kinematic chains and mechanisms review. In: 13th World Congress in Mechanism and Machine Science, Guanajuato, México, pp. 19–25 (2011)
11. Tischler, C., Samuel, A., Hunt, K.: Kinematic chains for robot hands—II. Kinematic constraints, classification, connectivity, and actuation. Mech. Mach. Theory **30**(8), 1217–1239 (1995)
12. Tischler, C., Samuel, A., Hunt, K.: Selecting multi-freedom multi-loop kinematic chains to suit a given task. Mech. Mach. Theory **36**(8), 925–938 (2001)
13. Tsai, L.-W.: Mechanism Design: Enumeration of Kinematic Structures According to Function. CRC Press, Boca Raton (2000)
14. Yan, H.-S.: Creative Design of Mechanical Devices. Springer, Singapore (1998)

Mechanism Design and Kinematics Analysis of a Bat Robot

Deming Kong, Jing-Shan Zhao(✉), and Yaser Saffer Tollori

Department of Mechanical Engineering, Tsinghua University, Room A1033, Lee Shau Kee Science and Technology Building, Beijing 100084, People's Republic of China
jingshanzhao@mail.tsinghua.edu.cn

Abstract. This paper proposes a bat robot mechanism and investigates the kinematics of flying process. After observing the flight of bat for a long period of time and analyzing its flying kinematics, a bionic robot was synthesized based on the bat structure to realize the deploying and flapping movements of the double membranous wings. With screw theory, the primary motion of the membranous wings was checked, and five steering engines were selected for controlling the flapping flight of the bat robot collaboratively. The structure is optimized for a bench test. The following test is just for the measurement of the force output of the bat robot. Computer simulations of fluid field of flight in the ANSYS software proved the kinematics discipline of efficient flight of a bat. Prototype test indicates that the membranous wings could provide efficient flapping flight.

Keywords: Bat robot · Mechanism synthesis · Bionic design · Flapping wing · Folding and unfolding

1 Introduction

Bionic flying in the sky must overcome two challenges, one is to produce enough lift to conquer the self-weight of the robot and the other is to generate sufficient thrust to compensate for the drag in cruising. Many kinds of birds and insects can fly, but few of them can hover for a long period of time except fruit flies, hummingbirds and bats, while bat is the only kind of mammals that evolved the ability of flight. Currently, there are more than 900 kinds of bats in the world [1]. From the fossil of the bat of about 50 million years ago, we almost observe rare differences from the bat of nowadays [2]. That is, the bats had already obtained the flight ability for a rather long time ago. After such a long time of evolving, the body structure of a bat changes little. It must have superiority for the bat's flight. From the end of the 20th century [3–5] more and more scientists have been paying more attention to the kinematic analysis of the bat to uncover its fly secret and try to design efficient bionic flying robots.

Flying like a bird in the sky is the dream of people in the ancient times. And the mechanical pigeon made by Archytas of Tarentum in ancient Greek [6], boomerang in Australia [7], the Kongming lantern [2] and kite [8] in China were all the initial attempts of people to fly. However, the authentic try was starting from modern times.

J.C.M. Carvalho et al. (eds.), *Multibody Mechatronic Systems*,
Mechanisms and Machine Science 54, DOI 10.1007/978-3-319-67567-1_3

After long time exploring, the Wright brothers of America finally designed the plane to successfully fly in 1903 [9]. It marked that the dream of flying came true. From then on the manmade aircrafts had a spring up. Various kinds of airplanes [10], helicopters [11] and aircrafts [10] were emerged at the right moment. On the other hand, the bio-inspired micro flying robot also appeared in succession, especially flapping wing mechanisms [12]. The flights of the insect and hummingbird were studied [13, 14] and the scientist built the aerodynamic models to find out the principles of their flights [15]. The experimental characterization of fixed membranous wings was researched as well [16, 17]. And afterwards, the bio-inspired flapping robot was proposed and fabricated [18–21]. Most of the flapping robots which were used in the area of military reconnaissance played an important role. However, the lift of this kind of flying machines was mostly provided by flapping with high frequency [22–24]. How to reduce the self-weight of a robot and how to improve the propelling efficiency are two challenges of bionic design ahead.

Unlike hummingbirds' hovering with an extremely high flapping frequency typically around 50 times per second [25], the bat can hover with a much lower frequency from about 5 to 10 times per second. The scientists also found that the flight of bat is much more efficient than that of birds [26]. But the question is how the bat achieves that? 3D reconstruction of bat flight kinematics from sparse multiple views were made to study the bat's flight [27]. After researching the structure and the kinetics of the bat's wings, the researchers found that the bat could always get lift no matter whether the double wings lift up or stroke down [3, 28, 29]. Johansson, Wolf and Hedenstro compared quantitative measures of the circulation in the far wake of bird and bat species and found that bats have a significantly stronger normalized circulation of the start vortex than birds do [5, 26, 30, 31]. They found that when a bat flapping flies, the membrana dermalis and phalanx bone of the wings have certain deformations which could balance the air friction, so that the bat can fly with the half effort of bird.

Currently, the practical application about the bat in bionics mainly focuses on the ultrasonic wave [32, 33]. Bahlman [34] designed a mechanical bat to help scientists understand the mode of bat flight. Ghanbari et al. [35] proposed a model of flying bat robot with four degrees of freedom in each wing for providing the flight in straight path. Ramezani et al. [36] built a model called B2 which is a biomimetic micro aerial vehicle that possesses similar morphological properties to a bat in order to duplicate bats powered ballistic motion. He and Ma [37] built a bio-inspired bat robot model to analyze the aerodynamic lift of the flapping wing vehicle.

This paper focuses on the design of wing structure of a bat robot. We designed the structure as simple as possible and use the rigid structure to simulate the movement of the bat's double wings. We use the mathematical calculation method to design the wing structure moving in the form of nature. What's more, the robot has the capacity of supporting not only the self-weight of itself but also the loads it carries with a lower flapping frequency. A simple and light structure was made to realize the goals.

2 Structure Synthesis of a Bat Robot Mechanism

Wings of a bat can give the body additional lift required for supporting its weight in the sky (Fig. 1). And the force is generated by flapping the double wings, so flapping is the primary function that the robot must have. In fact, the wings show vaulted profile as the bat is flying. This kind of structure can improve the aerodynamic effect for flight according to the Bernoulli's principle of aerodynamics. It is conducive to the flight of bat. The double wings of bat could also keep straight to get fast speed in gliding. So the robot we built consists of the curved bars.

Fig. 1. The flight circle of the bat which is carrying a grape in the mouth.

The scientists found that there is a slight folding and unfolding movement of the wings to decrease the air drag when the bat flaps up and down [34]. And this requests the bat robot to have the capacity to fold and unfold in flight. Figure 2 illustrates the structure of the bat robot. It can flap, fold and unfold double wings. Each wing has one degree of freedom (DOF). θ is the angle of the arm and the body. It is a variable. When θ decreases, the arm is rotating around point A clockwise, and both the forearm and the fingers move towards its body. It is a process of folding wings. Vice versa, the arm will rotate around point A counterclockwise and the forearm and the fingers move away from the body when θ increases. θ could reach 70° for the completely unfolded wing and it is about 38° for folding process. All the movements remain in one plane.

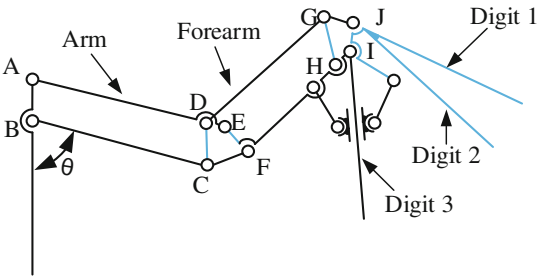

Fig. 2. Configurations of wings of a bat robot

We used the structure in Fig. 2 to realize the function of folding and unfolding. In this structure, there are several four-bar linkages connected with each other so that it forms a mechanical linkage of wing. Although the performance of the mechanical

elements cannot be comparable with the biological materials because of the larger stiffness and less plasticity, the mechanical structure can combine the mechanical elements to realize the complex function. It is controllable and it is visualized to reproduce the motions of a bat.

3 Kinematics Analysis of Wings

3.1 Folding and Unfolding Kinematics of Double Wings

We first discuss the relative motion of link CD with respect to the body AB. As link CD has two kinematic chains, AD and BC, we analyze the twists of them, individually. For link AD, there is

$$\$_{AD} = [\$_A \quad \$_D] \tag{1}$$

where $\$_A = [0 \quad 0 \quad 1 \quad 0 \quad 0 \quad 0]^T$, $\$_D = [0 \quad 0 \quad 1 \quad y_D \quad -x_D \quad 0]^T$.

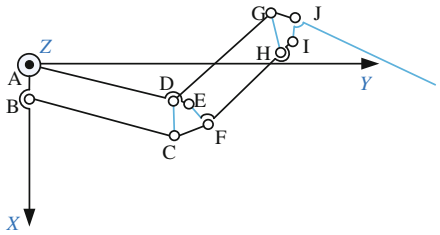

Fig. 3. Structure of the robotic wing composed of several four-bar linkages.

For link BC in the Fig. 3, there is

$$\$_{BC} = [\$_A \quad \$_D] \tag{2}$$

where $\$_B = [0 \quad 0 \quad 1 \quad 0 \quad -x_B \quad 0]^T$, $\$_C = [0 \quad 0 \quad 1 \quad y_C \quad -x_C \quad 0]^T$.

The free motion of link CD with respect to body AB satisfies that

$$\mathbf{A}x = 0 \tag{3}$$

where $\mathbf{A} = (\$)\mathbf{\Delta}$, $\Delta = \begin{bmatrix} 0 & \mathbf{I}_{3\times3} \\ \mathbf{I}_{3\times3} & 0 \end{bmatrix}$ and $\mathbf{I}_{3\times3} = \begin{bmatrix} 1 & 0 & 0 \\ 0 & 1 & 0 \\ 0 & 0 & 1 \end{bmatrix}$.

Associating Eqs. (1) and (3), and considering $\$ = \$_{AD}$, we obtain the reciprocal screws of link AD

$$\$_{AD}^{r} = [\$_1 \quad \$_2 \quad \$_3 \quad \$_4]$$

where $\$_1 = [0 \quad 0 \quad 1 \quad 0 \quad 0 \quad 0]^T$, $\$_2 = [0 \quad 0 \quad 0 \quad 1 \quad 0 \quad 0]^T$, $\$_3 = [0 \quad 0 \quad 0 \quad 0 \quad 1 \quad 0]^T$ and $\$_4 = \left[\frac{x_D}{a_1} \quad \frac{y_D}{a_1} \quad 0 \quad 0 \quad 0 \quad 0\right]^T$, and where $a_1 = \sqrt{x_D^2 + y_D^2}$.

Similarly, associating Eq. (2) with Eq. (3), and assuming $\$ = \$_{BC}$, we can solve the reciprocal screws of crank BC

$$\$_{BC}^{r} = [\$_5 \quad \$_6 \quad \$_7 \quad \$_8]$$

where $\$_5 = [0 \quad 0 \quad 1 \quad 0 \quad 0 \quad 0]^T$, $\$_6 = [0 \quad 0 \quad 0 \quad 1 \quad 0 \quad 0]^T$, $\$_7 = [0 \quad 0 \quad 0 \quad 0 \quad 1 \quad 0]^T$ and $\$_8 = \frac{1}{b_1}\left[\frac{x_C - x_B}{x_B y_C} \quad \frac{1}{x_B} \quad 0 \quad 0 \quad 0 \quad 1\right]^T$, and where $b_1 = \sqrt{\left(\frac{x_C - x_B}{x_B y_C}\right)^2 + \left(\frac{1}{x_B}\right)^2 + 1}$.

So the wrenches exerted by these two kinematic chains to link CD in matrix form can be expressed as

$$\$_{DC}^{r} = [\$_1 \quad \$_2 \quad \$_3 \quad \$_4 \quad \$_8] \tag{4}$$

Associating Eqs. (3) and (4), we get the wrench matrix

$$\mathbf{A} = \begin{bmatrix} 0 & 0 & 0 & 0 & 0 & 1 \\ 1 & 0 & 0 & 0 & 0 & 0 \\ 0 & 1 & 0 & 0 & 0 & 0 \\ 0 & 0 & 0 & \frac{x_D}{a_1} & \frac{y_D}{a_1} & 0 \\ 0 & 0 & \frac{1}{b_1} & \frac{x_C - x_B}{b_1 x_B y_C} & \frac{1}{b_1 x_B} & 0 \end{bmatrix}^T$$

, and the twist $\boldsymbol{x} = \left[0 \quad 0 \quad \frac{x_C y_D}{x_B y_C} - \frac{y_D}{y_C} - \frac{x_D}{x_B} y_D - x_D 0\right]^T$.

So the unit twist of link CD is

$$\$_{DC} = \left[0 \quad 0 \quad 1 \quad \frac{y_D}{\frac{x_C y_D}{x_B y_C} - \frac{y_D}{y_C} - \frac{x_D}{x_B}} \quad -\frac{x_D}{\frac{x_C y_D}{x_B y_C} - \frac{y_D}{y_C} - \frac{x_D}{x_B}} \quad 0\right]^T$$

Link DC just has one degree of freedom. The movement of DC is driven by the rotation of AD. And the relation between the movements of DC and AD will be analyzed later.

The structure in Fig. 3 is a special case. In Fig. 4, point P is the instantaneous center of the movement of link CD as it is the intersection of the extension cords of AD and BC. In the four-bar linkage ABCD, we get an equation set

$$\begin{cases} l_1 \sin\theta_1 - l_2 \sin\theta_2 = l_3 \sin\theta_3 \\ l_1 \cos\theta_1 + l_2 \cos\theta_2 = l_4 + l_3 \cos\theta_3 \end{cases} \tag{5}$$

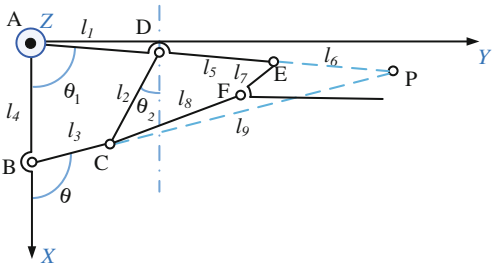

Fig. 4. Structure of the wing repaint as normal condition

Eliminating θ_3 yields

$$l_1 l_4 \cos\theta_1 + l_2 l_4 \cos\theta_2 - l_1 l_2 \cos(\theta_1 + \theta_1) = \frac{l_1^2 + l_2^2 + l_4^2 - l_3^2}{2} \tag{6}$$

The angular relationship between joint A and joint D can be obtained by calculating the derivatives of both sides of Eq. (6) with respect to time

$$\omega_2 = -\frac{l_1 l_2 \sin(\theta_1 + \theta_2) - l_1 l_4 \sin\theta_1}{l_1 l_2 \sin(\theta_1 + \theta_2) - l_2 l_4 \sin\theta_2}\omega_1 \tag{7}$$

We analyze CDP as fixed entirety here, it is rotating around point P at this moment, where it has an angular speed of ω_2. From the result we get in Eq. (7), ω_2 can be expressed as the function of ω_1 uniquely.

For CDEF in Fig. 5, we get the equation

$$\boldsymbol{v}_1 + \boldsymbol{v}_2 + \boldsymbol{v}_3 + \boldsymbol{v}_4 = \boldsymbol{v} \tag{8}$$

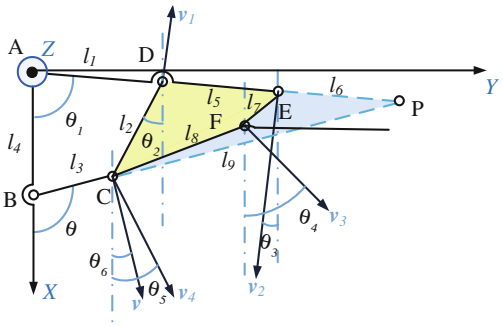

Fig. 5. Velocity analysis of the wing structure

According to the geometric calculation, we get the expression of the angular speed of all joints

$$\theta_3 = \frac{\pi}{2} - \theta_1,$$
$$\theta_4 = \theta_1 + \arccos\frac{l_2^2+l_5^2+l_7^2-l_8^2-2l_2l_5\cos(\theta_1+\theta_2)}{2l_7\sqrt{l_2^2+l_5^2-2l_2l_5\cos(\theta_1+\theta_2)}} + \arcsin\frac{l_2\sin(\theta_1+\theta_2)}{\sqrt{l_2^2+l_5^2-2l_2l_5\cos(\theta_1+\theta_2)}} - \frac{\pi}{2},$$
$$\theta_5 = \frac{\pi}{2} - \theta_2 - \arccos\frac{l_2^2+l_5^2+l_8^2-l_7^2-2l_2l_5\cos(\theta_1+\theta_2)}{2l_8\sqrt{l_2^2+l_5^2-2l_2l_5\cos(\theta_1+\theta_2)}} - \arcsin\frac{l_5\sin(\theta_1+\theta_2)}{\sqrt{l_2^2+l_5^2-2l_2l_5\cos(\theta_1+\theta_2)}},$$
$$\theta_6 = \frac{\pi}{2} - \arccos\frac{l_1^2+l_4^2+l_3^2-l_2^2-2l_1l_4\cos\theta_1}{2l_3\sqrt{l_1^2+l_4^2-2l_1l_4\cos\theta_1}} - \arcsin\frac{l_1\sin\theta_1}{\sqrt{l_1^2+l_4^2-2l_1l_4\cos\theta_1}}.$$

So we get the expressions of the linear speeds

$$\boldsymbol{v}_1 = (\cos\theta_1 \quad \sin\theta_1)\omega_2(l_5+l_6), \boldsymbol{v}_2 = (-\sin\theta_3 \quad -\cos\theta_3)\omega_1 l_5,$$
$$\boldsymbol{v}_3 = (\sin\theta_4 \quad -\cos\theta_4)\omega_3 l_7,\ \boldsymbol{v}_4 = (\sin\theta_5 \quad -\cos\theta_5)\omega_4 l_8,\ \boldsymbol{v} = (\sin\theta_6 \quad -\cos\theta_6)\omega_2 l_9.$$

Finally, we obtain an equation set of ω_3 and ω_4

$$\begin{cases} \sin\theta_4\omega_3 l_7 + \sin\theta_5\omega_4 l_8 = \sin\theta_6\omega_2 l_9 \\ \quad + \sin\theta_3\omega_1 l_5 - \cos\theta_1\omega_2(l_5+l_6) \\ \cos\theta_4\omega_3 l_7 + \cos\theta_5\omega_4 l_8 = \sin\theta_1\omega_2(l_5+l_6) \\ \quad + \cos\theta_6\omega_2 l_9 - \cos\theta_3\omega_1 l_5 \end{cases} \tag{9}$$

The result can be solved as

$$\begin{cases} \omega_3 = \frac{b_2 - a_2\cot\theta_5}{\cos\theta_4 l_7 - \cot\theta_5\sin\theta_4 l_7} \\ \omega_4 = \frac{b_2 - a_2\cot\theta_4}{\cos\theta_5 l_8 - \cot\theta_4\sin\theta_5 l_8} \end{cases} \tag{10}$$

where $a_2 = \sin\theta_6\omega_2 l_9 + \sin\theta_3\omega_1 l_5 - \cos\theta_1\omega_2(l_5+l_6)$, $b_2 = \sin\theta_1\omega_2(l_5+l_6) + \cos\theta_6\omega_2 l_9 - \cos\theta_3\omega_1 l_5$.

From Eqs. (7) and (10), we find that not only ω_2, but also ω_3 and ω_4 can be expressed as the functions of ω_1 uniquely. Similarly, as EF is fixed with FH, DEHG and GHIJ will be analyzed. As a result, the movements of executors DC, EF, GH and JI are all expressed by that of AD. So while AD is rotating around joint A, the executors have the exclusive output.

3.2 Size Synthesis of Double Wings

For the unknown factors upward, we have a detailed parsing process next. Figure 6 shows the condition of folding of the bat (left) and the condition of unfolding (right). Measuring the figures, we get the basic data to calculate the other factors we need in the left of Table 1.

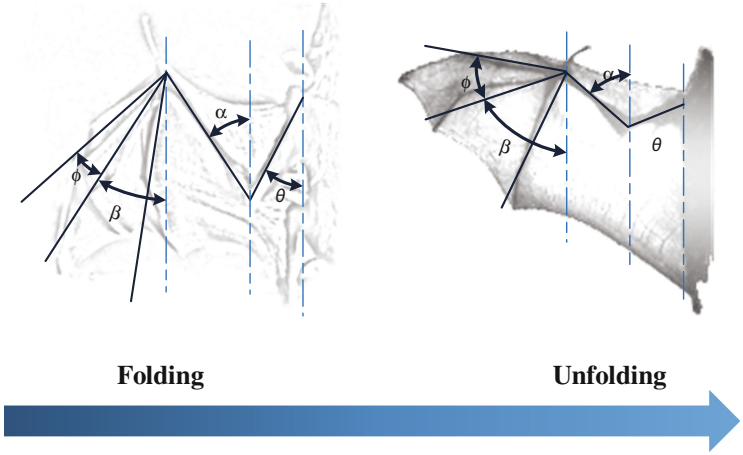

Fig. 6. The flying posture of the bat

Table 1. Design parameters

Objectives/degree			Results/degree		
θ	α	β	θ'	α'	β'
70	52	77	70	52.494	76.505
38	35	26	38	35.899	25.439

Measuring the angles between different digits in Fig. 6, we found that the angle ϕ changed little during folding and unfolding process. That is why we fixed digit 1 and 2 in the structure in Fig. 2. The angles of θ, α and β in the figures were also measured. The values are signed in the left of the table. Based on the values, the functions of the angles are deduced.

There are four four-bar linkages in the structure of the wing shown in Fig. 3. The expected values of α and β are listed in the left and the values we calculated are in the right. Both α and β can be expressed as the functions of θ. With the condition of the specified angle θ and the angles α, β which we want to get (left of Table 1), we get the relationship of the angles by using the geometrical relationship of the linkages.

$$\alpha = \arccos\left(\frac{1.3992 - 0.3004\cos\theta - 0.5\cos^2\theta - 0.5\sin\theta\sqrt{1.5410 - 0.0006\cos\theta - \cos^2\theta}}{2.09125 - 1.673\cos\theta}\right) + \arcsin\left(0.8056\sqrt{1.5410 - 0.0006\cos\theta - \cos^2\theta}\right) - \tfrac{5}{9}\pi \tag{11}$$

$$\beta = \frac{13}{9}\pi - \alpha - \arcsin\left(\frac{0.464\sin\mu}{\sqrt{0.4653 - 0.464\cos\mu}}\right) - \arccos\left(-\frac{0.3976 + 0.464\cos\mu}{1.484\sqrt{0.4653 - 0.464\cos\mu}}\right) \tag{12}$$

And

$$\mu = \pi - 0.1489 - \arcsin\left(\frac{0.5\sin(\alpha+\theta+\frac{5}{9}\pi - 1.5448)}{\sqrt{24.5125 - 4.9257\cos(\alpha+\theta+\frac{5}{9}\pi - 1.5448)}}\right) - \arccos\left(\frac{-0.2722 - 4.9257\cos(\alpha+\theta+\frac{5}{9}\pi - 1.5448)}{0.928\sqrt{24.5125 - 4.9257\cos(\alpha+\theta+\frac{5}{9}\pi - 1.5448)}}\right) \tag{13}$$

We take the derivative of the equation in the appendix and we get the angular speed of points D and J.

$$\frac{d\alpha}{d\theta} = f'(\theta) = \frac{\frac{0.3004\sin\theta + \cos\theta\sin\theta - \cos\theta f_4(\theta)/2 - \frac{0.25\sin\theta f_1(\theta)}{f_4(\theta)}}{f_1(\theta)} - \frac{1.673\sin\theta f_3(\theta)}{f_2^2(\theta)}}{\sqrt{1 - \frac{f_3^2(\theta)}{f_2^2(\theta)}}} + \frac{1007 f_1(\theta)}{\sqrt{(32.4496\cos^2\theta + 0.0195\cos\theta - 0.0048) f_4(\theta)}} \tag{14}$$

where:

$$\begin{aligned} f_1(\theta) &= 0.0006\cos\theta + 2\cos\theta\sin\theta, \\ f_2(\theta) &= 1.673\cos\theta - 2.09125, \\ f_3(\theta) &= 0.3004\cos\theta + 0.5\cos^2\theta + 0.5\sin\theta f_4(\theta) - 1.3992, \\ f_4(\theta) &= \sqrt{1.541 - 0.0006\cos\theta - \cos^2\theta}. \end{aligned}$$

And

$$\frac{d\beta}{d\theta} = f'(\theta) = \frac{\frac{0.464 f_1(\theta)\cos f_9(\theta)}{f_3(\theta)} - \frac{0.1076 f_1(\theta)\sin^2 f_9(\theta)}{f_2(\theta)}}{\sqrt{\frac{0.2153\sin^2 f_9(\theta)}{f_7(\theta) - 0.4653} + 1}} + \frac{\frac{0.3127 f_1(\theta)\sin f_9(\theta)}{f_3(\theta)} + \frac{0.1563 f_1(\theta)\sin f_9(\theta)[f_7(\theta) + 0.3976]}{f_2(\theta)}}{\sqrt{\frac{0.4541[f_7(\theta) + 0.3976]^2}{f_7(\theta) - 0.4653} + 1}} - f_4(\theta) - f_5(\theta) \tag{15}$$

where

$$f_1(\theta) = \frac{\frac{0.5[f_4(\theta)+f_5(\theta)+1]\cos f_{13}(\theta)}{f_{11}(\theta)} - \frac{1.2314[f_4(\theta)+f_5(\theta)+1]\sin^2 f_{13}(\theta)}{f_6(\theta)}}{\sqrt{\frac{\sin^2 f_{13}(\theta)}{4(f_{12}(\theta)-24.5125)}+1}},$$
$$-\frac{\frac{5.3079[f_4(\theta)+f_5(\theta)+1]\sin f_{13}(\theta)}{f_{10}(\theta)} + \frac{13.0725[f_4(\theta)+f_5(\theta)+1]\sin f_{13}(\theta)}{f_6(\theta)}}{\sqrt{1-[f_{10}(\theta)-0.2722]^2}},$$
$$f_2(\theta) = [0.4653 - f_7(\theta)]^{\frac{3}{2}},$$
$$f_3(\theta) = [0.4653 - f_7(\theta)]^{\frac{1}{2}},$$
$$f_4(\theta) = \frac{\frac{0.3004\sin\theta + \cos\theta\sin\theta - 0.5f_{16}(\theta)\cos\theta - \frac{0.25\sin\theta}{f_{16}(\theta)}}{f_{15}} - \frac{1.673f_{14}(\theta)\sin\theta}{f_{15}^2(\theta)}}{\sqrt{1-\frac{f_{14}^2(\theta)}{f_{15}^2(\theta)}}},$$
$$f_5(\theta) = \frac{1007f_8(\theta)}{f_{16}(\theta)\sqrt{32.4496\cos^2\theta + 0.0195\cos\theta - 0.0048}},$$
$$f_6(\theta) = [24.5125 - f_{12}(\theta)]^{\frac{3}{2}},$$
$$f_7(\theta) = 0.464\cos f_9(\theta),$$
$$f_8(\theta) = 0.0006\sin\theta + 2\cos\theta\sin\theta,$$
$$f_9(\theta) = \arcsin[\frac{\sin f_{13}(\theta)}{2f_{11}(\theta)}] + \arccos[-0.2722 - f_{10}(\theta)] - 2.9927,$$
$$f_{10}(\theta) = \frac{5.3079\cos f_{13}(\theta)}{f_{11}(\theta)},$$
$$f_{11}(\theta) = [24.5125 - f_{12}(\theta)]^{\frac{1}{2}},$$
$$f_{12}(\theta) = 4.9257\cos f_{13}(\theta),$$
$$f_{13}(\theta) = \theta + \arccos[\frac{f_{14}(\theta)}{f_{15}(\theta)}] + \arcsin[0.8056f_{15}(\theta)] - 1.5448,$$
$$f_{14}(\theta) = 0.3004\cos\theta + 0.5\cos^2\theta + 0.5f_{16}(\theta)\sin\theta - 1.5448,$$
$$f_{15}(\theta) = 1.673\cos\theta - 2.09125,$$
$$f_{16}(\theta) = \sqrt{-\cos^2\theta - 0.0006\cos\theta + 1.541}.$$

And the length of each link in the structure can be gained by associating Eqs. 11 and 12 above. The results simulated are listed in the right of Table 1.

3.3 Achievement of the Movement of Double Wings

We have presented that the movement of the bat is a combination of two parts. One is flapping, the other is folding and unfolding. The structure (Fig. 7) is symmetrical. There are two steering engines on the right part of the mechanism. And the function of engine 1 is providing the torque of folding and unfolding of the wing while engine 2 is providing a torque to flap up and down. Both of the movements have the same period. While the wing is flapping down to the bottom, the wing is driven by engine 1 to fold inside. While the wing is flapping up to the top, the wing is driven by engine 1 to unfold outside. In the structure, the purpose to use four steering engines to control the movement of the double wings is to make the movement of each wing be independent with each other. Because the postures of the bats are diverse, just like level flight, gliding, flashback and so on. And we want to make a model which is much more similar to the real bat.

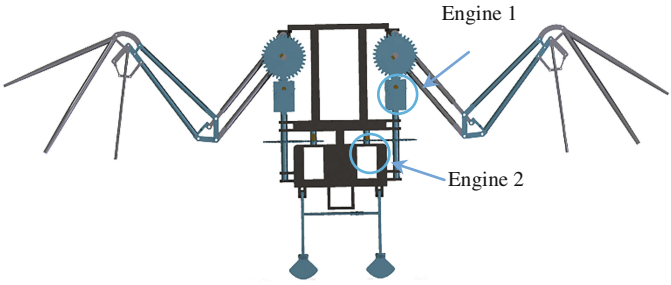

Fig. 7. Structure of the bat robot mechanism

Most parts of this mechanism are printed by a 3D printer with the material of Polylactic Acid (PLA). There are five steering engines in the mechanism (Fig. 8). The flapping motion is generated by the linkages and gears driven by steering engines 1–4. The movement of the legs are driven by steering engine 5. All the engines are controlled by the signal stored in the microcontroller. We divide the movement of the bat's wings into 3 simple movements. One is flapping, the second is folding and unfolding, and the third one is the movement of the legs. When the wings of the bat robot are flapping up, the legs will swing up and the wings will fold at the same time. While the wings of the bat robot are flapping down, the legs will also swing down and the wings will unfold. Kinematic experiments confirmed the function of wing mechanisms.

Fig. 8. Bat robot mechanism based on the kinematics analysis and computer simulation

4 Computer Simulation and Prototype Experiment

Two models of the bat were built in different flight attitudes used for the statics analysis (Fig. 9). The leg of the first model is not in the same plane as that of the body while the second one is in the same plane of the body. We used the sheet as the membrane of bat to simplify the models. The first model shows that the legs keep in one same plane as that of the body as the double wings beat upward. The second model denotes that the leg has an angle with the body when the wing is beating upward. With distributed surface force applying to the wings, the solid mechanics analysis was accomplished by the software ANSYS. The emulation images were obtained in Fig. 9 where (a), (b) and (c), illustrate the equivalent stress, equivalent elastic strain and total deformation of the first model, and (d), (e) and (f) are equivalent stress, equivalent elastic strain and total deformation of the second model.

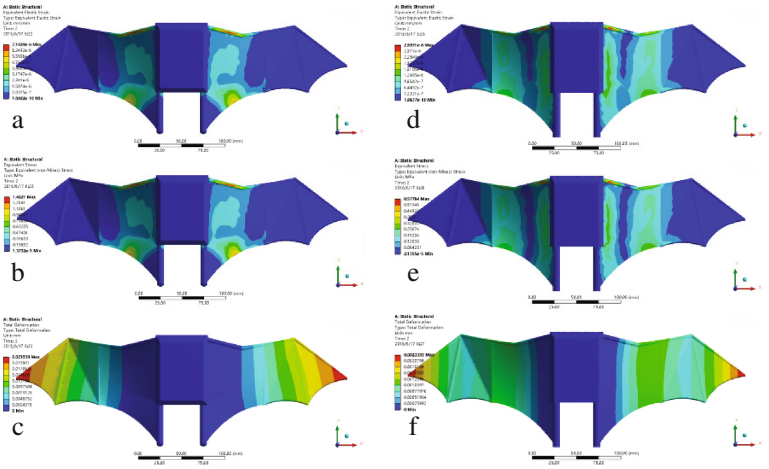

Fig. 9. Strain, stress and total deformation simulations on ANSYS

We found that these two models had quite obvious differences. The stress concentration can be found in the simulation of the first model. So the equivalent stress and elastic strain distributions of the second model are better than those of the first one. The first model has a linear deformation from the body to the wingtip while the second has an extremum in the middle of the wing. The forced movement of the second one is more coincident with the flapping of the wings. Because the deformation of the second one conform to the Bernoulli principle, the wings have a deformation that is needed to generate the lift even in the process of up-beating. It may also be the reason why the bat has a perfect flight in the low altitude with a low velocity and low flapping frequency.

5 Conclusions

We had given the method to design a bat robot. And the discussion of the degree of freedom was presented, too. Even though the basic data which was used for the calculation of the structure are measured in the pictures, the bat robot we made have realized the functions as what the real bats have. We expected to imitate the flight of bat by mixing several ordinary movements together. From the simulation of the models, we found that the stress and strain distributions of the membrane changed cyclically in flapping flight. However, the natural deformation of the membrane provides the excellent profile to generate the lift during up-beating.

References

1. Neuweiler, G.: The Biology of Bat. Oxford University Press, New York (2000)
2. Zhang, F.C.: Soaring in the Sky: Probe of the Animal Flight Origin. Shanghai Science and Technology Press, Shanghai (2003)

3. Aldridge, H.D.J.N.: Kinematics and aerodynamics of the Greater Horseshoe Bat, Rhinolophus Ferrumequinum, in horizontal flight at various flight speeds. J. Exp. Biol. **126**, 479–497 (1986). The Company of Biologists Limited
4. John, R.S.: The evolution of flight and echolocation in bats: another leap in the dark. Mammal Rev. **31**, 111–130 (2001)
5. Hedenström, A., Johansson, L.C., Wolf, M., Busse, R., Winter, Y., Spedding, G.R.: Bat flight generates complex aerodynamic tracks. Science **316**, 894–897 (2007)
6. Zhang, P.: The robot in history. New Speak Encyclopedic **10**, 45–49 (2015)
7. Boomerang history (2008). www.rangs.co.uk
8. Wang, J.C.: Kite: the ancestor of plane. Contemp. Miners **4**, 19 (1998)
9. FAI News: 100 Years Ago, the Dream of Icarus Became Reality (2003)
10. Li, C.Z.: The centennial development of airplane and aerodynamics. Mech. Pract. **25**, 1–13 (2003)
11. Yu, Z.: The overview of the development of helicopters. Technol. Helicopters **4**, 35–41 (2003)
12. Shen, H.P., Ma, X.M., Meng, Q.M., Li, Y.F., Ma, Z.H.: Rosearch progress on bionic robots and research issues of bionic mechanism. J. Changzhou Univ. **27**, 1–10 (2015)
13. Birch, J.M., Dickinson, M.H.: Spanwise flow and the attachment of the leading-edge vortex on insect wings. Nature **412**, 729–733 (2011)
14. Harbig, R.R.: Role of Wing Morphology in the Aerodynamics of Insect Flight. Monash University, Clayton (2014)
15. Roccia, B.A., Preidikman, S., Massa, J.C., Mook, D.T.: Development of a kinematical model to study the aerodynamics of flapping-wings. Int. J. Micro Air Veh. **3**, 61–88 (2011)
16. Richard, J.B., Frank, J.B., Ravi, V., Peter, G.I., Roger, D.Q.: A biologically inspired micro-vehicle capable of aerial and terrestrial locomotion. Mech. Mach. Theory **44**, 513–526 (2009)
17. Bret, S., Peter, I., Roberto, A., Wei, S.: Fixed membrane wing s for micro air vehicles: experimental characterization, numerical modeling, and tailoring. Mech. Mach. Theory **44**, 258–294 (2008)
18. Arabagi, V.G.: A miniature controllable flapping wing robot. Carnegie Mellon University (2011)
19. Khan, Z., Steelman, K., Agrawal, S.: Development of insect thorax based flapping mechanism. In: Kobe International Conference Center, pp. 3651–3656 (2009)
20. Asier, A.B.E.S.: Flapping wing devices for mars exploration: preliminary results from a novel flapping wing mechanism. Royal Military College of Canada (2008)
21. Michael, A.A.F., Tomonari, F.: Design of an active flapping wing mechanism and a micro aerial vehicle using a rotary actuator. Mech. Mach. Theory **45**, 137–146 (2010)
22. Ellington, C.P.: The Aerodynamics of Hovering Insect Flight IV Aerodynamic Mechanisms. University of Cambridge, Cambridge (1983)
23. Aono, H., Liang, F.Y., Liu, H.: Research article near- and far-field aerodynamics in insect hovering flight: an integrated computational study. J. Exp. Biol. **211**, 239–257 (2008)
24. Deng, X.Y.: Flapping flight for biomimetic robotic insects: system modeling and flight control in hover. University of California (2004)
25. Altshuler, D.L., Dudley, R., Ellington, C.P.: Aerodynamic forces of revolving hummingbird wings and wing models. J. Zool. **264**, 327–332 (2004)
26. Hedenström, A., Johansson, L.C.: Bat flight: aerodynamics, kinematics and flight morphology. J. Exp. Biol. **218**, 653–663 (2015)
27. Bergou, A.J., Swartz, S., Breuer, K., Taubin, G.: 3D Reconstruction of bat flight kinematics from sparse multiple views. In: IEEE, pp. 1618–1625 (2011)

28. Hubel, T.Y., Riskin, D.K., Swartz, S.M., Breuer, K.S.: Wake structure and wing kinematics: the flight of the lesser dog-faced fruit bat, Cynopterus brachyotis. J. Exp. Biol. **213**, 3427–3440 (2010)
29. Busse, R., Hedenström, A., Winter, Y., Johansson, L.C.: Kinematics and wing shape across flight speed in the bat, Leptonycteris yerbabuenae. Biol. Open **12**, 1226–1238 (2012)
30. Muijres, F.T., Johansson, L.C., Barfield, R., Wolf, M., Spedding, G.R., Hedenström, A.: Leading-edge vortex improves lift in slow-flying bats. Science **319**, 1250–1253 (2008)
31. Johansson, L.C., Wolf, M., Hedenström, A.: A quantitative comparison of bird and bat wakes. J. Roy. Soc. **7**, 61–66 (2010)
32. Fenton, M.B.: Echolocation: implications for ecology and evolution of bats. Q. Rev. Biol. **59**, 33–53 (1984)
33. Gerhard, N.: How bats detect flying insect. Phys. Today **33**(8), 34–40 (1980)
34. Bahlman, J.W., Swartz, S.M., Breuer, K.S.: Design and characterization of a multi-articulated robotic bat wing. Bioinspiration Biomimetics **8**, 1–17 (2013)
35. Ghanbari, A., Mottaghi, E., Qaredaghi, E.: A new model of bio-inspired bat robot. In: International Conference on Robotics and Mechatronics, pp. 403–406 (2013)
36. Ramezani, A., Shi, X.C., Chung, S.J., Hutchinson, S.: Lagrangian modeling and flight control of articulated-winged bat robot. In: International Conference on Intelligent Robots and Systems, pp. 2867–2874 (2015)
37. He, G.P., Ma, N.: Design and analysis of bat-like folding and flapping wings mechanism. J. North China Univ. Tech. **26**, 35–41 (2014)

Vector Analysis of the Cable Tension Conditions

T. Muraro(✉), D. Martins, and L.K. Sacht

Federal University of Santa Catarina, Florianópolis, Brazil
muraro.thais@gmail.com,
{daniel.martins,leonardo.sacht}@ufsc.br

Abstract. The use of cable-driven robots is growing because of several important features, such as their structural simplicity and reduced mass and production cost compared to rigid-structure robots. However, the cable-driven mechanisms present some drawbacks, such as the fact that the cables are always tensioned to avoid errors of trajectory of the end-effector. In addition, if this necessary traction exceeds a maximum limit, cable breakage may occur. In this sense, it is proposed in this paper a way to evaluate the cable tension conditions in order to maintain the traction in each cable within an acceptable range, that assure the good operation of the robot. For this, a planar truss of rigid links with revolute joints is considered and one of the links is replaced by a cable. Then, the schematic representation of the system is made and it is modeled statically by the Davies method. In this way a homogeneous linear system is obtained that is solved from the null space of the coefficient matrix and then finally the tension in the cable can be evaluated.

Keywords: Cable-driven mechanisms · Cable tension conditions · Davies method · Null space of matrix

1 Introduction

The study of cable-driven parallel mechanisms (CDPMs) began to be developed mainly from 1985, when Landsberg and Sheridan proposed replacing rigid links from a Stewart platform with cables [12]. Since then, many works have already been developed in this area, as well as important robots, which are used for different applications and at different scales.

The main challenge with respect to the mechanisms actuated by cables is precisely the fact that the cables can only "pull" the end-effector and not "push" it [3, 9]. In this sense, in order for the trajectory of the end-effector to be completely controlled, all cables must always be subjected to tension, a feature that avoids the sagged-cables. In spite of this, the tension to which the cables will be subjected can not exceed a certain maximum value [2, 3, 9, 14] so that they do not cause deformation or even the rupture of the cables.

The problem of sagged-cables has already been addressed in several works [1–4, 10, 11, 15–19], in which solutions are also proposed, mainly through the distribution of the cable tension to determine the movement control of the end-effector or the

J.C.M. Carvalho et al. (eds.), *Multibody Mechatronic Systems*,
Mechanisms and Machine Science 54, DOI 10.1007/978-3-319-67567-1_4

workspace. An important fact that is verified with this revision, is that none of them proposes the resolution through the Davies method.

In this paper we propose a way to approach the sagged-cables from the Davies method [7, 8], which is an important tool to solve static and kinematic analysis of mechanisms. The matrix equation obtained using the Davies method is solved using linear algebra knowledge within vector spaces. From this, it is possible to evaluate the magnitude of the tension force in the cables, have a vector view of these forces and determine traction restrictions.

2 Cable-Driven Parallel Mechanisms

Like the parallel mechanisms of rigid structure, the cable-driven mechanisms have also been the object of much interest and study in the last decades. They descend directly from the Stewart platform (1965), since, in 1985, Landsberger and Sheridan [12] proposed replacing the linear actuators of these rigid parallel structure with cables. In this sense, the robots actuated by cables are also parallel structures, nevertheless, cables take the place of the rigid legs. However, they have certain advantages compared to the classic parallel robots [5], since they are lighter, that is to say, of easy displacement and that a great number of cables can be had, which increases the supported load. Its constructive features are similar to those of a Stewart platform. In fact, a cable-driven mechanism is constituted by a mobile platform, where the end-effector is positioned, a fixed platform or base, whose purpose is to sustain the load moved and give the necessary rigidity to the robot, the cables, that allow the realization of the movement, and the engine or actuators that drive the cables movement.

This mechanism type has become more studied since the last two decades, mainly due to its large workspace and its structural simplicity [4], together with the reduced cost of production [1, 13]. Its application is more focused on situations where rigid and heavy manipulators are not the best choice. Although it has similar characteristics to the classic parallel robots, there are certain important differences [5]. Some of them can be characterized as advantages, such as the fact that the cables can be rolled up by the drums very quickly, while the moving mass of the robot is very small. This allows the robot to achieve acceleration and very high speeds in the end-effector [5, 14]. Also because the mass of the moving parts is very small, these robots become more energy efficient and thus suitable for the movement of heavier loads, acting as cranes. In addition, by increasing the number of cables, one can modify the workspace, increase the load capacity or even improve the safety of the one that is transported. Thus, a greater number of cables is allowed than the number of degrees of freedom of the end-effector and furthermore, if the position of these cables is favorable, the end-effector can also still overcome some obstacles.

Although a cable-driven robot has a number of advantages over the classic rigid and conventional robots, it also presents some problems in its use. The main of these problems was precisely inherited from the rigid parallel robots: restricted workspace [14]. It can be said that this disadvantage is aggravated, because the cables can only be pulled [9, 14]. However, it is possible to change the length of the kinematic chain through the cable winding drum, which overcomes the geometric limitation of the classic parallel robot

workspace [5], or even reposition the cable attachment points to the rigid structure, making it reconfigurable [13].

The motion control of this type of robot is also nontrivial, since there may be redundancy of traction, that is, there may be more cables than controllable degrees of freedom, and thus the distribution of cable tension must be evaluated and how its elasticity influences movement [5]. The kinematics of these manipulators is also complex and to control them it is very important to find a strategy where real-time computation is efficient [9].

3 The Davies Method

The Davies method is based on screw theory, graph theory, and Kirchhoff's laws. It generates results in the matrix form, requiring, in this way, a previous knowledge about the matrix algebra to apply it. This method can be used to carry out studies on kinematics as well as on static mechanisms. Regarding the use of Kirchhof's laws, the method is based on the Circuits Law for kinematics, while for performing static analysis, it is based on the Nodes Law [8].

In the static analysis of mechanisms the objective is to determine the existing requests in the joints and, when there is contact with the environment, the efforts existing in the end-effector. In the specific case of cable-driven mechanisms the main objective is to evaluate the distribution of tension in the cables according to the load carried, and with the pose of the mobile platform.

Although the main objective of the static analysis, for example, of cable actuated robots is the determination of the tensions in the cables, Davies method allows to determine at once all the requests existing in all the joints of the mechanism, thus configuring an advantage of this method. While tension in the cables can be used to analyze the work space, the efforts of the other joints are necessary for the complete design of the mechanism. In addition, the solution by the Davies method is obtained from the solution of systems of linear equations, which provides the visualization of the results through a vector approach.

The Davies method consists basically of four steps. Firstly, the schematic and the topological representations of the mechanism are made, with representation and identification of the joints and the links and also with the positioning of a coordinate system. Then the representation through an oriented graph is made. From the representations, all the characteristics of the system are determined, such as the number of actions C, and the parameters of the wrenches: orientation $\vec{S}$, position $\overrightarrow{S_0}$ and the pitch h. Also the features related to graphs are made, such as the number of chords I, and of cuts k. The third step consists in the matrix representation of the system. That is, the wrenches – in this case $\$_{a_{Fx}}, \$_{a_{Fy}}, \$_{b_{Fx}}, \$_{b_{Fy}}, \$_{c_{Fx}}, \$_{c_{Fy}}, \$_{c_{Mz}}, \$_{p_{Fx}}, \$_{p_{Fy}}$ and $\$_{p_{Mz}}$ – are described and the Cuts Matrix $[Q_A]_{k\times C}$, which relates the actions to the cuts, is constructed. From these mathematical entities the Actions Matrix $[A_D]_{\lambda\times C}$ and also the Network Unitary Actions Matrix $[\hat{A}_N]_{\lambda.k\times C}$ are determined. Note that λ is the order of the system i.e. in the planar case $\lambda = 3$ and in the spatial case $\lambda = 6$. And finally, in the last step, the laws of Kirchhoff are applied, generating the homogeneous system

$$\hat{A}_N \vec{\Psi} = \vec{0}, \tag{1}$$

where $\vec{\Psi}$ is the wrenches magnitudes vector.

The system must be solved by separating the variables between the primary ones (generally known and that determine the system completely) and the secondary ones (that one wishes to know). Thus, the system stop being homogeneous and the matrix of coefficients becomes square. In this way, only solution can be determined.

More information about the Davies method (details and examples) can be found in [6–8].

4 Methodology for the Evaluation of Cable Tension

Here we propose a methodology for evaluation the cable tension problem in planar cases. The tension problem, as explained previously, consists of the evaluation of the tensions of the cables in order to avoid sagged-cables, that is, the tension in each cable must be between a positive minimum value and a maximum value. Such limiting values are determined by several factors including, especially, cable and actuator characteristics. In this sense, the following steps are proposed to evaluate these tensions in the cables. The first one consists in the replacement of the cables by prismatic pairs connected to the rigid links through revolute joints. The second step is the resolution of the static problem following the steps of the Davies method until the application of the Kirchhoff's laws, that is, until to obtain the system of the Eq. 1. The next step is the resolution of the homogeneous system that involves the network unitary actions matrix through the determination of the matrix null space of it. In the fourth step it obtains convenient relations between the variables of the problem. These variables are the magnitudes of the screws that represent the system. Finally, the end step consists of generating a graphical representation of the relationships described in the previous step. In this paper, the components of the force in the cable, F_x and F_y, are plotted, which generates a vector representation of the feasible tensions in the cable, according to determined geometric features of the mechanism.

The first problem solved is that of a planar truss, in a horizontal plane, in which one of the rigid links is replaced by a cable. This problem has been identified as the simplest possible type because the weight force generated by the mass of the mobile link acts in a plane perpendicular to that of the motion. The second case proposed and studied is only a variation of the first case consisting of a planar truss, but in a vertical plane. The difference with respect to the previous case is that here we consider the gravity acting on the bar that is not fixed, that is, the weight force generated by the mass of that link acts in the same direction of the movement.

4.1 Case Study

The first case to be studied is, as explained earlier, the simplest case. It is considered a planar mechanism with three links, two rigid links being connected by a rotating joint and a cable, which is considered the third link, as shown in Fig. 1a. The placement of

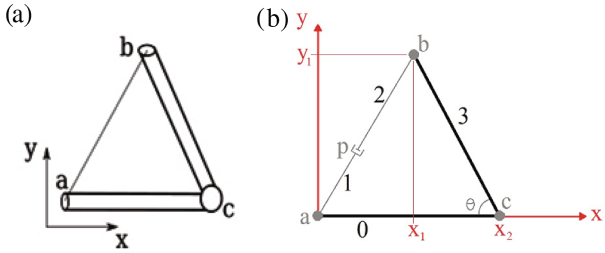

Fig. 1. Planar truss. (a) Physical model. (b) Representation in the coordinate system.

this cable is made so that the rigid links of the lattice can move around and thus assess conditions in which it breaks or becomes loose. The change in length of the cable, caused by the joint *c*, causes the opening angles formed by the cable and by each rigid link to also change. Thus, the joints *a* and *b*, rotating, were considered in the representation. To solve the problem, the link representing the cable has been replaced by a prismatic pair, connected to each rigid link through a rotating joint. This allows to evaluate the resultant force on the prismatic joint from the movement of the revolute joint *c*, and thus to determine whether the force evaluated is of traction or compression. The schematic representation with the cited substitution is shown in Fig. 1b. The joints are represented by the letters *a*, *b*, *c* and *p*, while the links are numbered from 0 to 3.

In order to use the Davies method for static analysis, we consider the couplings graph representation, showed in Fig. 2a. Using the Graph Theory, the number of chords *I* and cuts *k* is determined through the equations

$$I = e - v + 1 \tag{2}$$

and

$$k = v - 1 \tag{3}$$

respectively, where *e* is the number of the edges and *v* is the number of the vertices of the coupling graph (Fig. 2a).

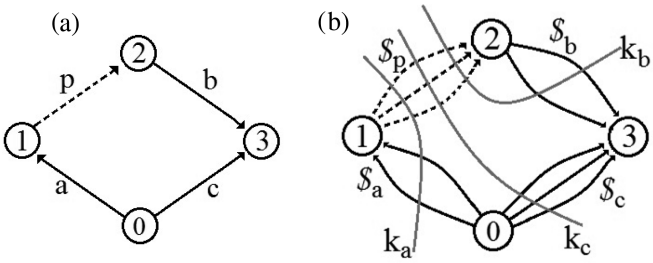

Fig. 2. Graph representation. (a) Coupling graph. (b) Actions unit graph.

The dotted edge of the coupling graph (Fig. 2a) represents a string and the lines that cut the edges are the cuts in the Fig. 2b. Since this problem is solved for the planar case, $\lambda = 3$, each joint can has a maximum of three actions – two of force and one of moment. In this sense, each non-actuated revolute joint has two force constraints, while the actuated one has the same two constraints besides of the momentum action, imposed by the engine actuation. Already for the prismatic joint, not being actuated, it is clear that its motion is conditioned to the actuation of the engine and then it is considered the existence of the momentum restriction and the two force restrictions imposed by the engine. In this sense, the action graph (Fig. 2b) contains the 10 edges representing actions.

Thus, one can determine the cuts matrix, which relates each action (in the columns) with each cut (in the rows). Then, using the cuts matrix and also the wrenches that represent the actions, the network unit actions matrix is determined

$$\hat{A}_N = \begin{bmatrix} y_1 & -x_1 & -1 & 0 & 0 & 0 & 0 & 0 & 0 & 0 \\ -1 & 0 & 0 & 1 & 0 & 0 & 0 & 0 & 0 & 0 \\ 0 & -1 & 0 & 0 & 1 & 0 & 0 & 0 & 0 & 0 \\ y_1 & -x_1 & -1 & 0 & 0 & -y_1 & x_1 & 0 & 0 & 0 \\ -1 & 0 & 0 & 0 & 0 & 1 & 0 & 0 & 0 & 0 \\ 0 & -1 & 0 & 0 & 0 & 0 & 1 & 0 & 0 & 0 \\ -y_1 & x_1 & 1 & 0 & 0 & 0 & 0 & 0 & x_2 & 1 \\ 1 & 0 & 0 & 0 & 0 & 0 & 0 & 1 & 0 & 0 \\ 0 & 1 & 0 & 0 & 0 & 0 & 0 & 0 & 1 & 0 \end{bmatrix} \tag{4}$$

By applying the cuts law, one gets the homogeneous system of the Eq. 1, where

$$\vec{\Psi}^T = [F_{p_x} F_{p_y} M_{pZ} F_{a_x} F_{a_y} F_{b_x} F_{b_y} F_{c_x} F_{c_y} M_{c_z}] \tag{5}$$

is the vector of linear system variables and the coefficient matrix is the one in Eq. 4.

So far, the steps of Davies method [6] have been followed literally. Now, the separation of variables in primary and secondary will not be done, as the method suggests. The idea is to use linear algebra knowledge to solve the problem, that is, to determine the null space of the coefficient matrix. For this, the "nullspace" function was used in the Maxima® program.

In order to obtain a more general equation, depending only on the θ angle, the following substitutions were made

$$x_1 = x_2 - |bc| \cos\theta \tag{6}$$

and

$$y_1 = |bc| \, sen\theta, \tag{7}$$

Thus, the system solution is given by

$$\begin{pmatrix} F_{p_x} \\ F_{p_y} \\ M_{p_z} \\ F_{a_x} \\ F_{a_y} \\ F_{b_x} \\ F_{b_y} \\ F_{c_x} \\ F_{c_y} \\ M_{c_z} \end{pmatrix} = \delta \begin{pmatrix} x_2 - |bc|\cos\theta \\ |bc|\, sen\theta \\ 0 \\ x_2 - |bc|\cos\theta \\ |bc|\, sen\theta \\ x_2 - |bc|\cos\theta \\ |bc|\, sen\theta \\ -(x_2 - |bc|\cos\theta) \\ -|bc| sen\theta \\ x_2 |bc|\, sen\theta \end{pmatrix}, \tag{8}$$

where δ is a real constant.

Note that the solution variables are only the constant δ and the θ angle, which is given by the problem geometry. Thus, by determining a value for any of the forces or moments, with the exception of M_{Cz}, because it is null, the system is completely determined. Note also that the set of forces and momentum relative to the prismatic joint is represented by the wrench

$$\$_p = F_{p_x} \begin{Bmatrix} -|bc|\, sen\theta \\ 1 \\ 0 \end{Bmatrix} + F_{p_y} \begin{Bmatrix} x_2 - |bc|\cos\theta \\ 0 \\ 1 \end{Bmatrix} + M_{p_z} \begin{Bmatrix} 1 \\ 0 \\ 0 \end{Bmatrix} = \delta \begin{Bmatrix} 0 \\ x_2 - |bc|\cos\theta \\ |bc|\, sen\theta \end{Bmatrix}. \tag{9}$$

It is known from the screw theory that the magnitude of the wrench is

$$|\overrightarrow{F_p}| = |\delta| \sqrt{x_2^2 - 2x_2|bc|\cos\theta + |bc|^2}. \tag{10}$$

The magnitude of the wrench represents the absolute value of the force, which in this case must be evaluated. This force represents the tension (or compression) in the cable which is subject an initial condition, to avoid sagged-cables,

$$F_p \geq 0. \tag{11}$$

In the second problem, the schematic representations are equal to the first problem. However, the addition of the gravity force adds one more edge to the action graph and them, one more column in the cuts matrix and also in the network unit action matrix. In this way, the system solution for Eq. 1 is as fallows, where δ and γ are real constants.

$$\begin{pmatrix} F_{p_x} \\ F_{p_y} \\ M_{p_z} \\ F_{a_x} \\ F_{a_y} \\ F_{b_x} \\ F_{b_y} \\ F_{c_x} \\ F_{c_y} \\ M_{c_z} \\ F_{\text{ext}} \end{pmatrix} = \delta \begin{pmatrix} 0 \\ 0 \\ 0 \\ 0 \\ 0 \\ 0 \\ 0 \\ 1 \\ \frac{|bc|\cos\theta}{2} - x_2 \\ -1 \end{pmatrix} + \gamma \begin{pmatrix} -(x_2 - |bc|\cos\theta) \\ -|bc|sen\theta \\ 0 \\ -(x_2 - |bc|\cos\theta) \\ -|bc|sen\theta \\ -(x_2 - |bc|\cos\theta) \\ -|bc|sen\theta \\ x_2 - |bc|\cos\theta \\ |bc|sen\theta \\ -x_2|bc|sen\theta \\ 0 \end{pmatrix}. \tag{12}$$

5 Results and Discussion

The results with respect to the truss system whit external force, in this case gravity, generated force maps equal to those of the truss case in the horizontal plane. In fact, the tension forces in the cables are not influenced by the weight of the rigid link, which will have an influence on the traction that must be exerted by the imposed actuator. In this sense, it can be verified that the procedure for solving this case is the same as in the previous case, unless the imposition of one more edge in the actions graph representing the force weight. It is also possible to verify that when considering, in Eq. 8, a null external force, the solution is the same as in the previous case, which validates the proposed methodology. In fact, the gravity will have no direct influence on the cable tension, but rather on the engine torque.

The methodology used produced interesting results regarding the tensile strength in the cable that was considered in the problem. A map of the tensions that can solve the system was generated, given a certain geometry of the truss. In the Fig. 3 is possible to see three graphs that present force maps for three different sizes of the truss. In the first one – Fig. 3a – the map was generated considering the fixed link with twice size of the other rigid link. In Fig. 3b, the map was generated for the two rigid links with identical sizes and for Fig. 3c the fixed link was considered half size of the other rigid link, with all measurements in meters.

These graphs present a greater region than the one that one intends to work, considering different geometries for the truss. However, it is an interesting result, since the sought-after set of the forces that are only tension is a sub-region of those shown in the graphics. In this sense, an important feature of the force maps is the possibility of making an initial estimate for the actuators. Given a region of the force map, that is, a desired set of forces, it is possible to properly restrict the range of or even to determine a single one and thus determine all other forces and moments acting on the system.

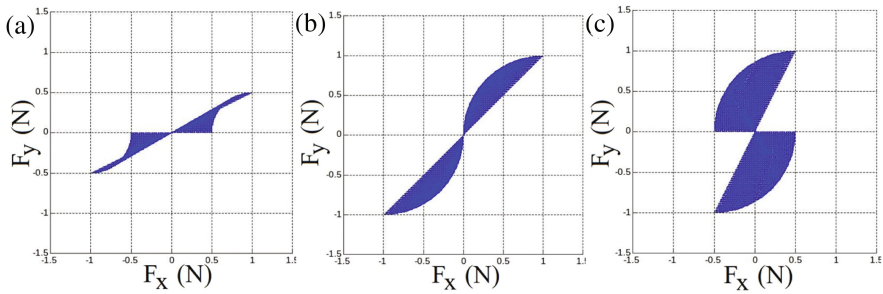

Fig. 3. Vector representation of the cable tension considering $-1 \leq \delta \leq 1$ and $0° \leq \theta \leq 90°$. (a) For $x_2 = 1$ and $|bc| = 0.5$. (b) For $x_2 = 1$ and $|bc| = 1$. (c) For $x_2 = 0.5$ and $|bc| = 1$.

6 Conclusions

Finally, the development of this methodology for the distribution of tension forces in the cables of CDPMs by adapting the Davies method contributes significantly to the studies of this type of mechanism. The determination of the workspace of CDPMs should become more evident, as well as the trajectory control of its end-effector, which has the contribution in this methodology. In addition, it is very useful to evaluate the force capability of a CDPM, besides expanding the use of the Davies method and assisting the design of the mechanism, facilitating, for example, the choice of actuators.

Acknowledgments. This work was supported by CNPq and CAPES.

References

1. Barrette, G., Gosselin, C.M.: Determination of the dynamic workspace of cable driven planar parallel mechanisms. J. Mech. Des. Trans. ASME **127**(2), 242–248 (2005)
2. Bosscher, P., Ebert-Uphoff, I.: Wrench-based analysis of cable-driven robots. In: Proceedings of the IEEE International Conference on Robotics and Automation, vol. 5, pp. 4950–4955. New Orleans (2004)
3. Bosscher, P., Riechel, A.T., Ebert-Uphoff, I.: Wrench-feasible workspace generation for cable-driven robots. IEEE Trans. Robot. **22**(5), 890–902 (2006)
4. Bosscher, P., Williams, R.L., Bryson, L.S., Castro-Lacouture, D.: Cable-suspended robotic contour crafting system. Autom. Constr. **17**(1), 45–55 (2007)
5. Bruckmann, T., Mikelsons, L., Brandt, T., Hiller, M., Schramm, D.: Wire robots Part i: kinematics, analysis & design. In: Parallel Manipulators, New Developments, InTech (2008)
6. Cazangi, H.R.: Aplicação do método de Davies para análise cinemática e estática de mecanismos com múltiplos graus de liberdade. Diss. Federal University of Santa Catarina (2008)
7. Davies, T. H.: The 1887 committee meets again: freedom and constraint. In: Ball 2000 Conference, University of Cambridge, Cambridge University Press, Trinity College, pp. 1–56 (2000)

8. Davies, T.: Freedom and constrain in coupling networks. In: Proceedings ImechE, vol. 220, pp. 989–1010 (2006)
9. Gosselin, C.: Cable-driven parallel mechanisms: state of the art and perspectives. Mech. Eng. Rev. **1**, 1–17 (2014)
10. Gouttefarde, M., Gosselin, C.M.: Analysis of the wrench-closure workspace of planar parallel cable-driven mechanisms. IEEE Trans. Robot. **22**(3), 434–445 (2006)
11. Gouttefarde, M., Merlet, J-P., Daney, D.: Wrench-feasible workspace of parallel cable-driven mechanisms. In: Robotics and Automation 2007 IEEE International Conference, pp. 1492–1497 (2007)
12. Lansdberger, S.E., Sheridan, T.B.: A new design for parallel link manipulators. In: Proceedings of the 1985 IEEE International Conference of Systems, Man and Cybernetics, Tucson, AZ, pp. 812–814 (1985)
13. Merlet, J-P.: Analysis of the influence of wires interference on the workspace of wire robots. In: Advances in Robot Kinematics. pp. 211–218. Kluwer Academic Publishers (2004)
14. Muraro, T.: Análise cinemática e estática de um mecanismo espacial atuado por cabos aplicado à movimentação de pacientes. Diss Federal University of Santa Catarina (2015)
15. Oh, S.R., Agrawal, S.K.: Cable suspended planar robots with redundant cables: controllers with positive tensions. IEEE Trans. Robot. **21**(3), 457–465 (2005)
16. Pham, C.B., Yeo, S.H., Yang, G., Kurbanhusen, M.S., Chen, I.M.: Force-closure workspace analysis of cable-driven parallel mechanisms. Mech. Mach. Theory **41**(1), 53–69 (2006)
17. Pusey, J., Fattah, A., Agrawal, S., Messina, E.: Design and workspace analysis of a 6–6 cable-suspended parallel robot. Mech. Mach. Theory **39**(7), 761–778 (2004)
18. Trevisani, A.: Underconstrained planar cable-direct-driven robots: a trajectory planning method ensuring positive and bounded cable tensions. Mechatronics **20**(1), 113–127 (2010)
19. Williams, R.L., Gallina, P.: Planar cable-direct-driven robots: design for wrench exertion. J. Intell. Robot. Syst. **35**(2), 203–219 (2002)

Actuated Degree-of-Control: A New Approach for Mechanisms Design

Estevan Hideki Murai[1(✉)], Roberto Simoni[2], and Daniel Martins[1]

[1] Federal University of Santa Catarina, Florianópolis, Santa Catarina, Brazil
eng.estevan.murai@gmail.com

[2] Federal University of Santa Catarina, Joinville, Santa Catarina, Brazil

Abstract. The identification of feasible kinematic structures is a challenge in early stages of mechanism design. Structural characteristics, such as connectivity, redundancy and variety can be used to identify promising chains. In this paper, a new structural characteristic is proposed; the actuated degree-of-control. Initially some structural characteristics are reviewed, then the actuated degree-of-control is proposed, focusing on its definition and purpose. Examples will show how the new structural characteristic can be used to aid the designer in the design process and how it differs from previous structural characteristics. Finally, a discussion is presented, showing the key points in the actuated degree-of-control.

Keywords: Actuated degree-of-control · Kinematic chain selection · Degree-of-control · Connectivity · Mechanism design

1 Introduction

In the early stages of mechanism design, the design decisions are often taken relying on the designer's experience, intuition and knowledge. A mechanism design challenge is the identification of promising kinematic structures according to functional and design requirements. Mechanism design methodologies together with structural characteristics can be used to aid the designer in selecting promising kinematic structures [1–3].

There are different approaches for mechanism design, such as graph-based mechanism synthesis [4–11], building blocks-based mechanism synthesis [12–15] and type synthesis of parallel mechanisms [16–20]. Here we focus on tools for mechanism design methodologies based on the graph approach, which use the mobility criterion. Despite the mobility criterion fails at some particular cases [21,22], for mechanisms with general dimensions and parameters this criterion is valid and quite useful at this early stage of mechanism design and it is a base for several enumeration techniques in the literature, see for instance Mruthyunjaya [22].

The enumeration-based approaches usually generate a great number of kinematic chains, making it harder for the designer to identify promising results to proceed with the synthesis or unfeasible results to reduce the number of options [1,2]. Structural characteristics such as connectivity, the degree-of-control and

J.C.M. Carvalho et al. (eds.), *Multibody Mechatronic Systems*,
Mechanisms and Machine Science 54, DOI 10.1007/978-3-319-67567-1_5

redundancy have been studied and used by several authors to aid in the kinematic chain selection [1–3,23–33]. Belfiore [3] proposed the degree-of-control and redundancy concepts to aid the designer in the selection of mechanisms with kinematic redundancy. Tischler [2] defined the variety to identify feasible chains, greatly reducing the number of outcomes.

It is desirable to have topological characteristics that are easily correlated to functional or design requirements, creating a bridge between feasible kinematic structures and functional and design requirements.

In this paper we propose a new structural characteristic: the actuated degree-of-control. Section 2 presents a review on some structural characteristics. Section 3 defines the actuated degree-of-control. Section 4 presents examples that compare the actuated degree-of-control with the degree-of-control, showing how the actuated degree-of-control can be used to aid the designer in the mechanism design process. Finally, Sect. 5 presents a discussion on both degree-of-control concepts. An algorithm for calculating the actuated degree-of-control will be proposed future works.

2 Review on Connectivity, Degree-of-Control and Redundancy

This section reviews the definition of connectivity, degree-of-control and redundancy, focusing on their use during mechanism design.

The connectivity was introduced by Hunt [23] as

> "...the concept of connectivity between two members is very simple, being nothing more than their number of relative [degrees of] freedoms" (pp. 30–31).

Phillips [24] introduced the concept of joint-in-the-bag for a better understanding of the connectivity. The connectivity is represented by a symmetric matrix $\mathbf{C}_{n\times n}$, being n the number of links in a kinematic chain. Although the concept of connectivity is clear, to devise an algorithm that yields the correct connectivity matrix for any kinematic chain is not straightforward. Several algorithms were proposed by Shoham and Roth [28], Belfiore and Benedetto [3], Liberati and Belfiore [29], Carboni and Martins [31,34] and, for the planar case, Huang et al. [1].

The degree-of-control concept was introduced by Belfiore and Benedetto [3] as

> "...the symmetric matrix whose element $K(i,j)$ is equal to the minimum number of independent actuating pairs needed to determine the relative position between the two links i and j" (p. 2).

The degree-of-control is represented by the symmetric matrix $\mathbf{K}_{n\times n}$, but differently from the connectivity, the degree-of-control is not upper bounded by the screw-system order λ. Belfiore and Benedetto [3] presented an algorithm to calculate the degree-of-control, Carboni and Martins [31,34] presented an algorithm which overcomes some deficiencies of previous algorithms.

The redundancy concept was introduced by Belfiore and Benedetto [3] as the number of degree-of-control that exceeds the connectivity between links i and j. The redundancy is represented by the symmetric matrix $\mathbf{R}_{n\times n}$ and can be obtained by a simple matrix subtraction of $\mathbf{C}$ from $\mathbf{K}$. As the degree-of-control is not upper bounded by the screw-system order, the redundancy matrix elements are non-negatives. Also, a kinematic chain presents redundancy if there is at least one pair of links i and j where $\mathbf{K}(i,j) > \mathbf{C}(i,j)$.

Belfiore and Di Benedetto [3] mention that "The redundancy matrix is defined to provide designers with a useful support in the first conceptual phase of the project of a new manipulator"(p. 1) and "The degrees-of-control and redundancy matrices have been also introduced, with the aim of extending the concept of connectivity to the class of redundant manipulators" (p. 2). Thus, it is implicit that the objective behind the degree-of-control and redundancy concepts is to aid in the designing of redundant manipulators or redundant mechanisms.

In field of parallel mechanisms synthesis, redundancy is classified in three types [35,36]: kinematic redundancy, actuation redundancy with in branch redundancy and actuation redundancy with branch redundancy. Regarding this types of redundancy, the redundancy defined by Belfiore and Benedetto is the kinematic redundancy.

The connectivity, degree-of-control and redundancy are structural characteristics related to the kinematic chain. Thus, when analyzing a mechanism, the matrices $\mathbf{C}$, $\mathbf{K}$ and $\mathbf{R}$ are established disregarding which is the reference link, which are the output links and in which pairs the actuators are placed. However, when designing a redundant mechanism, $\mathbf{C}$, $\mathbf{K}$ and $\mathbf{R}$ indicates which links presents redundancy and are feasible to be chosen as reference and output links.

To ilustrate $\mathbf{K}$, $\mathbf{C}$ and $\mathbf{R}$, a planar kinematic chain is presented in Fig. 1a and Eq. 1 shows the connectivity and redundancy for this chain while Eq. 2 shows the degree-of-control. The non-zero element $\mathbf{R}(1,9)$ in Eq. 1 indicates links 1 and 9 as promising choices for reference and output links when redundancy or dexterity are required.

$$\mathbf{C} = \begin{bmatrix} 0&1&2&3&2&1&3&3&3&3&3&3\\ 1&0&1&2&3&2&2&3&3&3&3&3\\ 2&1&0&1&2&3&1&2&3&3&3&3\\ 3&2&1&0&1&2&2&3&3&3&3&2\\ 2&3&2&1&0&1&3&3&3&3&2&1\\ 1&2&3&2&1&0&3&3&3&3&3&2\\ 3&2&1&2&3&3&0&1&2&3&3&3\\ 3&3&2&3&3&3&1&0&1&2&3&3\\ 3&3&3&3&3&3&2&1&0&1&2&3\\ 3&3&3&3&3&3&3&2&1&0&1&2\\ 3&3&3&3&2&3&3&3&2&1&0&1\\ 3&3&3&2&1&2&3&3&3&2&1&0 \end{bmatrix} \quad \mathbf{R} = \begin{bmatrix} 0&0&0&0&0&0&0&\mathbf{1}&\mathbf{2}&\mathbf{2}&\mathbf{1}&0\\ 0&0&0&0&0&0&0&0&\mathbf{1}&\mathbf{2}&\mathbf{2}&\mathbf{1}\\ 0&0&0&0&0&0&0&0&0&\mathbf{1}&\mathbf{1}&0\\ 0&0&0&0&0&0&0&0&\mathbf{1}&\mathbf{1}&0&0\\ 0&0&0&0&0&0&0&\mathbf{1}&\mathbf{1}&0&0&0\\ 0&0&0&0&0&0&\mathbf{1}&\mathbf{2}&\mathbf{2}&\mathbf{1}&0&0\\ 0&0&0&0&0&\mathbf{1}&0&0&0&0&\mathbf{1}&\mathbf{1}\\ \mathbf{1}&0&0&0&\mathbf{1}&\mathbf{2}&0&0&0&0&0&\mathbf{1}\\ \mathbf{2}&\mathbf{1}&0&\mathbf{1}&\mathbf{1}&\mathbf{2}&0&0&0&0&0&0\\ \mathbf{2}&\mathbf{2}&\mathbf{1}&\mathbf{1}&0&\mathbf{1}&0&0&0&0&0&0\\ \mathbf{1}&\mathbf{2}&\mathbf{1}&0&0&0&\mathbf{1}&0&0&0&0&0\\ 0&\mathbf{1}&0&0&0&0&\mathbf{1}&\mathbf{1}&0&0&0&0 \end{bmatrix} \tag{1}$$

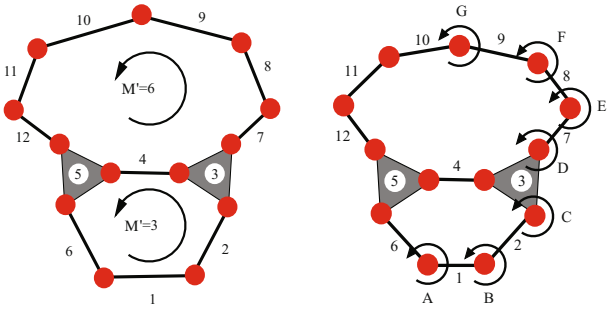

(a) Kinematic chain (b) Actuated chain

Fig. 1. Planar kinematic chain and actuators placement.

3 Actuated Degree-of-Control

The actuated degree-of-control is a structural characteristic proposed here which aims to aid the designer at the early stages of mechanism design. Differently from the previously presented structural characteristics, the actuated degree-of-control is applied to kinematic chains with all actuators located (or input pairs identified). Also, it can be applied for mechanisms with or without redundancy.

Definition: the actuated degree-of-control is the quantity of inputs that affect the relative positioning between two links in a kinematic chain with the actuated joints defined.

The actuated degree-of-control is represented by the symmetric matrix $\mathbf{K_A}_{n\times n}$. A possible way to determine the number of actuators that affect the relative positioning between two links using the gradual freezing approach. This approach was used by Mruthyunjaya and Raghavan [37] to analyze kinematic chains and by Liberati and Belfiore [29] to calculate a kinematic chain connectivity. However, when calculating the actuated degree-of-control only the kinematic pairs with actuators can be frozen. Then, different sets of actuators are frozen, looking for the minimum set that constrains the motion between those two links.

The kinematic chain from Fig. 1a is the same as the one in Fig. 1b but with the input pairs identified. The degree-of-control of the unactuated chain and the actuated degree-of-control for the actuated chain are respectively

$$\mathbf{K} = \begin{bmatrix} 0&1&2&3&2&1&3&4&5&5&4&3\\ 1&0&1&2&3&2&2&3&4&5&5&4\\ 2&1&0&1&2&3&1&2&3&4&4&3\\ 3&2&1&0&1&2&2&3&4&4&3&2\\ 2&3&2&1&0&1&3&4&4&3&2&1\\ 1&2&3&2&1&0&4&5&5&4&3&2\\ 3&2&1&2&3&4&0&1&2&3&4&4\\ 4&3&2&3&4&5&1&0&1&2&3&4\\ 5&4&3&4&4&5&2&1&0&1&2&3\\ 5&5&4&4&3&4&3&2&1&0&1&2\\ 4&5&4&3&2&3&4&3&2&1&0&1\\ 3&4&3&2&1&2&4&4&3&2&1&0 \end{bmatrix} \quad \mathbf{K_A} = \begin{bmatrix} 0&1&2&3&\mathbf{3}&1&3&4&5&\mathbf{6}&\mathbf{7}&\mathbf{7}\\ 1&0&1&\mathbf{3}&3&2&2&3&4&5&\mathbf{7}&\mathbf{7}\\ 2&1&0&\mathbf{3}&\mathbf{3}&3&1&2&3&4&\mathbf{7}&\mathbf{7}\\ 3&\mathbf{3}&\mathbf{3}&0&\mathbf{3}&\mathbf{3}&\mathbf{4}&\mathbf{5}&\mathbf{6}&\mathbf{7}&\mathbf{7}&\mathbf{7}\\ \mathbf{3}&3&\mathbf{3}&\mathbf{3}&0&\mathbf{3}&\mathbf{4}&\mathbf{5}&\mathbf{6}&\mathbf{7}&\mathbf{7}&\mathbf{7}\\ 1&2&3&\mathbf{3}&\mathbf{3}&0&4&5&\mathbf{6}&\mathbf{7}&\mathbf{7}&\mathbf{7}\\ 3&2&1&\mathbf{4}&\mathbf{4}&4&0&1&2&3&\mathbf{7}&\mathbf{7}\\ 4&3&2&\mathbf{5}&\mathbf{5}&5&1&0&1&2&\mathbf{7}&\mathbf{7}\\ 5&4&3&\mathbf{6}&\mathbf{6}&\mathbf{6}&2&1&0&1&\mathbf{7}&\mathbf{7}\\ \mathbf{6}&5&4&\mathbf{7}&\mathbf{7}&\mathbf{7}&3&2&1&0&\mathbf{7}&\mathbf{7}\\ \mathbf{7}&\mathbf{7}&\mathbf{7}&\mathbf{7}&\mathbf{7}&\mathbf{7}&\mathbf{7}&\mathbf{7}&\mathbf{7}&\mathbf{7}&0&\mathbf{7}\\ \mathbf{7}&\mathbf{7}&\mathbf{7}&\mathbf{7}&\mathbf{7}&\mathbf{7}&\mathbf{7}&\mathbf{7}&\mathbf{7}&\mathbf{7}&\mathbf{7}&0 \end{bmatrix} \tag{2}$$

This set of input pairs in the example of Fig. 1b is not unique and other sets could be devised. Different input pairs selections lead to a different actuated degree-of-control, although in simple cases the actuated degree-of-control can be the same, *e.g.*, kinematic chains with mobility one. The two matrices in Eq. 2 are different. This difference arises because the degree-of-control definition considers the minimum number of independent actuating pairs but it does not consider where the actuators pairs are while the actuated degree-of-control regards the input pairs selected as a requirement to be complied. In the mechanism design process, the actuated degree-of-control can be used to select the reference and the output links after all possible actuated chains are listed.

Finally, regarding the actuated degree-of-control:

- To calculate the actuated degree-of-control the input pairs must be identified.
- The inputs considered here are placed at pairs directly connecting two links.
- The actuator placement must be properly done. In this sense, a proper actuator placement results in all links having their position determined while no conflicts among actuators arise.
- When the kinematic chain has mobility one the degree-of-control, connectivity and actuated degree-of-control are identical matrices.

4 Comparison Between Degree-of-Control and Actuated Degree-of-Control

This section presents two examples to compare the degree-of-control and actuated degree-of-control and the purpose of their use in the design process.

4.1 Designing a Reciprocating Compressor with Variable Compression Ratio

Let us consider the design of a reciprocating compressor with variable compression ratio. Several design requirements and different concepts can be listed, but for the purpose of evaluating both concepts of degree-of-control let us consider a simple topology, with one independent loop and a fixed cylinder head.

The compressor requires two DOF, one for actuating the mechanism that compresses the air and another responsible for changing the compression ratio. For simplicity, we limit the scope to planar mechanisms ($\lambda = 3$), although other screw systems could be explored. Once the mobility, number of independent loops and the order of the screw system have been established, only one parallel kinematic chain can be generated ($M = 2$, $\nu = 1$, $\lambda = 3$). Different structural requirements could be used to generate more kinematic chains; however, the focus of this example is not to be a complete example of mechanism design but to show how these structural characteristics retrieve information on the kinematic chain. The enumeration method is out of scope of this paper, details on enumeration can be seen in [38–41].

Figures 2a and b shown respectively the kinematic chain (KC) generated and the kinematic chain with input pairs (IP) identified. The connectivity,

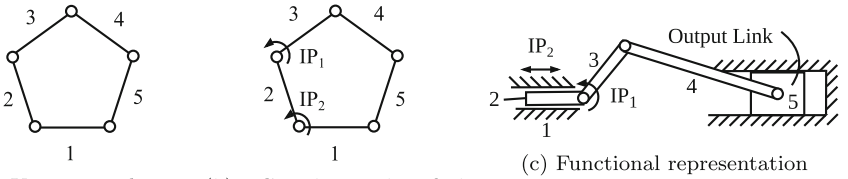

(a) Kinematic chain (b) KC with IPs identified (c) Functional representation

Fig. 2. Mechanism for a compressor with variable compression ratio.

degree-of-control and the actuated degree-of-control (for the chain in Fig. 2b) are respectively

$$\mathbf{C} = \mathbf{K} = \begin{bmatrix} 0\,1\,2\,2\,1 \\ 1\,0\,1\,2\,2 \\ 2\,1\,0\,1\,2 \\ 2\,2\,1\,0\,1 \\ 1\,2\,2\,1\,0 \end{bmatrix} \qquad \mathbf{K_A} = \begin{bmatrix} 0\,1\,2\,2\,\mathbf{2} \\ 1\,0\,1\,2\,2 \\ 2\,1\,0\,\mathbf{2}\,2 \\ 2\,2\,\mathbf{2}\,0\,\mathbf{2} \\ \mathbf{2}\,2\,2\,\mathbf{2}\,0 \end{bmatrix} \tag{3}$$

The mechanism does not present kinematic redundancy since the connectivity is equal to the degree-of-control. This can be verified because $M \leq \lambda$.

Different choices for input pairs are possible but do not affect the degree-of-control. Regarding the actuated degree-of-control, a different input pairs selection results in a different actuated degree-of-control matrix, but with similar outcome.

From the desired functionality two structural requirements can be listed:

- The actuated degree-of-control between piston and block is two. This requirement arises because both actuators should affect the piston positioning in relation to the block to achieve a variable compression ratio compressor.
- For the purpose of simplicity, the connectivity between block and piston is one. This requirement arises because in a reciprocating compressor it is usual to directly connect piston and block.

The pairs of links which present $\mathbf{C}_{i,j} = 1$ and $\mathbf{K_A}_{i,j} = 2$ are: (3, 4); (4, 5); (1, 5). Figure 2c shows the functional representation of one possible mechanism generated by choosing link 1 and 5 as block and piston, respectively. In this mechanism, an actuator moves link 2 along the prismatic pair between links 1 and 2, changing the crankshaft position (link 3) and hence, the compression ratio.

Figure 3a shows the functional representation of one possible mechanism generated by using link 2 as block and link 3 as piston. In t his case, only one actuator affects the piston position (IP_1) and the $\mathbf{K_A}_{i,j} = 2$ requirement is not satisfied. Figure 3b shows the functional representation of one possible mechanism generated by using link 2 as block and link 4 as piston. In this case, the piston is not directly connected to the block and the $\mathbf{C}_{i,j} = 1$ requirement is not satisfied.

The connectivity and the actuated degree-of-control are related to functional requirements. The connectivity requirement can be established by analyzing the

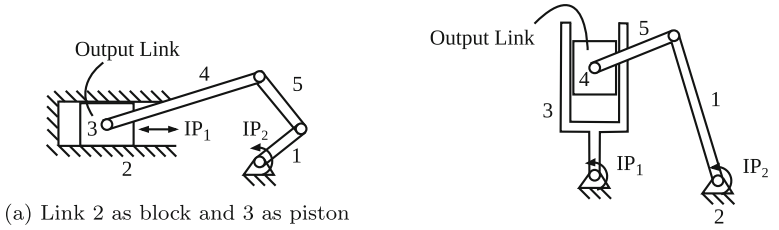

(a) Link 2 as block and 3 as piston

(b) Link 2 as block and 4 as piston

Fig. 3. Unfeasible mechanism for compressor with variable compression ratio.

desired degree-of-freedom for the output link and the actuated degree-of-control requirement can be established by analyzing how many actuators are desired to control the output link position.

The position of the piston in relation to the block is defined by both actuators, $\mathbf{K_A}(1,5) = 2$, although the degree-of-control indicates the minimum number of actuators is one, $\mathbf{K}(1,5) = 1$. The degree-of-control is useful when designing mechanisms with kinematic redundancy. It effectively indicates which pairs of link present kinematic redundancy, aiding the designer in the selection of reference and output links. However, the degree-of-control evaluates the minimum number of independent actuating pairs disregarding at which pairs the actuators are placed. Thus, the degree-of-control does not indicate how many actuators affect the relative positioning between two links (in mechanisms with or without kinematic redundancy) and cannot be used by the designer to chose links based on how many inputs control each link.

4.2 Designing a Mechanism with Two Inputs and Two Outputs

Let us consider the designing of a planar mechanism with mobility equals to two and two output links. For a given mechanism purpose, the first output link should be controlled by both input pairs while the second output link should be controlled only by one input pair. Examples of applications that can require two inputs and two outputs are stitching mechanisms and gripper mechanisms

To reduce the number of possibilities only kinematic chains with two independent loops and input pairs at the same polygonal links are analyzed. The four kinematic chains generated are shown in Fig. 4. The possible input pairs selections for the kinematic chains in Fig. 4 are exposed in Table 1, resulting in six different kinematic chains with actuators defined. Other input pairs placements are isomorphic or not at the same polygonal link. This procedure could be equally applied to other actuator choices or number of independent loops.

With the input pairs identified some symmetries of the kinematic chains are broken, yielding more possible combinations. The same asymmetry occurs after choosing one output link, resulting in less symmetries and more options for the second output link. The six actuated chains of Table 1 present 37 non-isomorphic inversions, and have around one thousand possible combinations for

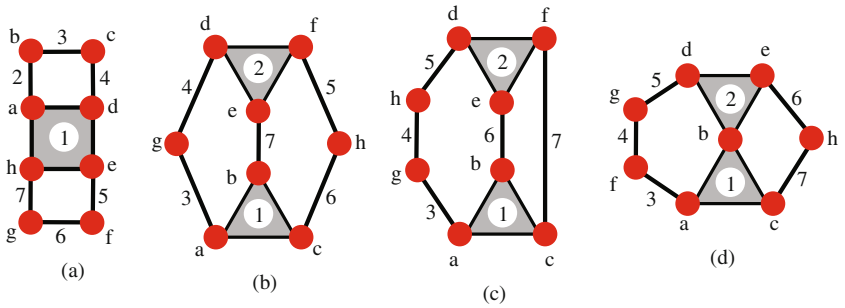

Fig. 4. Planar parallel kinematic chains for $M = 2$ and $\nu = 2$.

Table 1. Input pairs selections for kinematic chains in Fig. 4.

Kinematic chain	Fig. 4a	Fig. 4b I	Fig. 4b II	Fig. 4c	Fig. 4d I	Fig. 4d II
Input pairs	(a; h)	(a; b)	(a; c)	(a; b)	(a; b)	(a; c)
Actuated degree-of-control	$\mathbf{K_{A_I}}$	$\mathbf{K_{A_{II}}}$	$\mathbf{K_{A_{III}}}$	$\mathbf{K_{A_{IV}}}$	$\mathbf{K_{A_V}}$	$\mathbf{K_{A_{VI}}}$

non-isomorphic reference and output links selection. All combinations can be generated and then analyzed manually or automatically, however it is time-consuming. Among these combinations there are several unfeasible ones regarding the output links requirements and they must be eliminated. Other option is to use the actuated degree-of-control to identify beforehand the feasible options for reference and output links, as proposed in Sect. 4.1.

For each input pairs combination in the second line of Table 1 one actuated degree-of-control is evaluated. These matrices in the same order of Table 1 are

$$\mathbf{K_{A_I}} = \begin{bmatrix} 0&1&1&1&1&1&1 \\ 1&0&1&1&2&2&2 \\ 1&1&0&1&2&2&2 \\ 1&1&1&0&2&2&2 \\ 1&2&2&2&0&1&1 \\ 1&2&2&2&1&0&1 \\ 1&2&2&2&1&1&0 \end{bmatrix} \quad \mathbf{K_{A_{II}}} = \begin{bmatrix} 0&2&1&2&2&2&1 \\ 2&0&2&2&2&2&2 \\ 1&2&0&2&2&2&2 \\ 2&2&2&0&2&2&2 \\ 2&2&2&2&0&2&2 \\ 2&2&2&2&2&0&2 \\ 1&2&2&2&2&2&0 \end{bmatrix} \quad \mathbf{K_{A_{III}}} = \begin{bmatrix} 0&2&1&2&2&1&2 \\ 2&0&2&2&2&2&2 \\ 1&2&0&2&2&2&2 \\ 2&2&2&0&2&2&2 \\ 2&2&2&2&0&2&2 \\ 1&2&2&2&2&0&2 \\ 2&2&2&2&2&2&0 \end{bmatrix}$$

$$\mathbf{K_{A_{IV}}} = \begin{bmatrix} 0&1&1&2&2&1&1 \\ 1&0&2&2&2&1&1 \\ 1&2&0&2&2&2&2 \\ 2&2&2&0&2&2&2 \\ 2&2&2&2&0&2&2 \\ 1&1&2&2&2&0&1 \\ 1&1&2&2&2&1&0 \end{bmatrix} \quad \mathbf{K_{A_V}} = \begin{bmatrix} 0&1&1&2&2&1&1 \\ 1&0&2&2&2&1&1 \\ 1&2&0&2&2&2&2 \\ 2&2&2&0&2&2&2 \\ 2&2&2&2&0&2&2 \\ 1&1&2&2&2&0&1 \\ 1&1&2&2&2&1&0 \end{bmatrix} \quad \mathbf{K_{A_{VI}}} = \begin{bmatrix} 0&1&1&2&2&1&1 \\ 1&0&2&2&2&1&1 \\ 1&2&0&2&2&2&2 \\ 2&2&2&0&2&2&2 \\ 2&2&2&2&0&2&2 \\ 1&1&2&2&2&0&1 \\ 1&1&2&2&2&1&0 \end{bmatrix} \tag{4}$$

Although matrices $\mathbf{K_{A_{IV}}}$, $\mathbf{K_{A_V}}$ and $\mathbf{K_{A_{VI}}}$ are equal, their kinematic chain topologies are different in connection among links or actuators choice. Also, with the exception of $\mathbf{K_{A_I}}$, the other actuated degree-of-control differ from the degree-of-control of their respective chains.

The first line of matrix $\mathbf{K_{A_I}}$ in Eq. 4 shows that the quantity of inputs that determine the relative position between link 1 and any other link is always one. For instance, the relative position of links 1 and 3 is determined by one input at pair a, $\mathbf{K_{A_I}}(1,3) = 1$, as well as the relative position between links 1 and 5 by input at pair h, $\mathbf{K_{A_I}}(1,5) = 1$. Hence, link 1 is not a valid selection for the reference link because, given the design requirements, no other link is eligible for output link 1, which must be controlled by two inputs.

Similarly, the second line of matrix $\mathbf{K_{A_{II}}}$ in Eq. 4 shows that when link 2 is selected as reference link the remaining links have their position in relation to link 2 determined by both input pairs. Given the design requirements, it is not possible to select a link for output link 2. Thus, link 2 in this corresponding actuated kinematic chain is not a valid selection for reference link.

In this example, valid reference link selections have lines with both 1's and 2's in the actuated degree-of-control matrix. For instance, the sixth line of matrix $\mathbf{K_{A_{IV}}}$ has both 1's and 2's, being link 6 in this corresponding actuated chain a valid selection for reference link. Regarding this kinematic inversion, there are 6 different link options remaining for the first output and 5 different link options remaining for the second output, yielding up to 30 combinations. Notice that the actuators placement breaks the symmetry, increasing the number of possible combinations. Among those 30 combinations several are unfeasible according to the output requirements (quantity of inputs controlling each output). One possible solution is to generate and evaluate each combination regarding the requirements. However, the feasible candidates for output link 1 and 2 can be seen through an analysis of the sixth line elements. The third, fourth and fifth elements are valid options for the first output link ($\mathbf{K_{A_{IV}}}(6,3) = 2$, $\mathbf{K_{A_{IV}}}(6,4) = 2$ and $\mathbf{K_{A_{IV}}}(6,5) = 2$). The first, second and seventh elements are valid options for the second output link ($\mathbf{K_{A_{IV}}}(6,1) = 1$, $\mathbf{K_{A_{IV}}}(6,2) = 1$ and $\mathbf{K_{A_{IV}}}(6,7) = 1$). Thus, with 3 options for each output link, there are 9 feasible mechanisms.

Analyzing the six matrices, in total 24 feasible and non-isomorphic kinematic inversions are possible, *i.e.*, 24 lines with 1's and 2's. The first prediction was 37 inversions, but 13 inversions do not present valid choices for both output links. Repeating the procedure done to the sixth line of matrix $\mathbf{K_{A_{IV}}}$ to all the remaining 23 lines yields a total of 178 feasible non-isomorphic mechanisms with both output links selected.

This simple example shows how the actuated degree-of-control matrix can be used to identify feasible reference and output links, instead of generating all possible combinations of mechanisms with output links identified and then analyzing which are feasible and which are unfeasible.

5 Discussion on the Actuated Degree-of-Control

The degree-of-control is useful when designing mechanisms with kinematic redundancy [3]. In a mechanism design methodology, the degree-of-control can be used to identify which couples of links present kinematic redundancy in a kinematic chain; thus, aiding the designer while choosing reference and output links for a mechanism with kinematic redundancy.

The actuated degree-of-control is useful when designing mechanisms with or without kinematic redundancy. In a mechanism design methodology, the actuated degree-of-control can be used to identify which couples of links have their position controlled by a given number of inputs in a kinematic chain with actuators defined.

In general, the degree-of-control and actuated degree-of-control matrices are different. These differences arise because the degree-of-control considers the minimum number of independent actuating pairs disregarding where the input pairs are actually placed. Besides, the actuated degree-of-control matrix depends on the actuators placement, thus, while a kinematic chain has one degree-of-control matrix it can have several different actuated degree-of-control matrices. By definition, the actuated degree-of-control matrix yields the number of input pairs that control the position between each two links. As the actuated degree-of-control and the degree-of-control can be different, using the degree-of-control to select links according to how many inputs controls them can yield wrong results while discarding feasible options.

In the designing process, the desired motions between the reference and output links is usually known or determined in the early stages from the design requirements and the mechanism application. So, it is possible to establish or have an initial estimate on the number of actuators that should affect each output link, as Sect. 4.1 exemplifies it. On this point, the actuated degree-of-control is a tool that relates the desired functionality from the early stages of mechanism design to the kinematic structure selection stage, creating a bridge between them. As Sect. 4.2 exposes, the actuated degree-of-control can be effectively used to identify feasible sets of reference and output links in actuated chains, aiding the designer in this abstract step of mechanism design.

Some mechanism problems present design requirements regarding the reference link selection. When the reference link selection is constrained to a few links, then it is only necessary to evaluate the actuated degree-of-control in relation to those links, *i.e.*, evaluate the respective lines or columns of $\mathbf{K_A}$ instead of the whole matrix.

A complementary concept for actuated degree-of-control is to identify which are the inputs subset that affects the relative positioning between two links. This can be useful when designing mechanisms with multiple inputs and outputs, such that each output depends on an input subset. An actuated degree-of-control with distinguished inputs can be used to match the generated chain outputs and inputs with the desired characteristics for the outputs and inputs.

Finally, despite the main use of the actuated degree-of-control be related to the topological synthesis and analysis, the same concept has collateral effects on later phases of machine design such as dimensional synthesis and actuator selection.

6 Conclusions

In this paper the actuated degree-of-control was proposed. Differently from the existing structural characteristics, the actuated degree-of-control represents how many inputs affect the relative positioning between two links in a kinematic chain with actuators defined.

The examples showed how the difference between the degree-of-control and the actuated degree-of-control arises and how the actuated degree-of-control can be used to select feasible reference and output links in a kinematic chain with actuators placed. The actuated degree-of-control was used to identify which reference link choices do not yield output links controlled by the required amount of inputs. Also, for a feasible selection of reference link, the actuated degree-of-control showed which are the feasible options for output links given the number of inputs required to control the outputs.

The same method can be applied to more complex kinematic chains, regarding number of independent loops, inputs and outputs. It can also be used in chains with or without kinematic redundancy.

Acknowledgements. The authors would like to thank CNPq for the financial support.

References

1. Huang, P., Ding, H., Yang, W., Kecskeméthy, A.: Mech. Mach. Theory **109**, 195 (2017)
2. Tischler, C., Samuel, A., Hunt, K.H.: Mech. Mach. Theory **36**(8), 925 (2001)
3. Belfiore, N., Di Benedetto, A.: Int. J. Rob. Res. **19**(12), 1245 (2000)
4. Freudenstein, F., Maki, E.: Environ. Planning B **6**(4), 375 (1979)
5. Freudenstein, F., Maki, E.: J. Mech. Des. **105**(2), 259 (1983)
6. Olson, D.G., Erdman, A.G., Riley, D.R.: Mech. Mach. Theory **20**(4), 285 (1985)
7. Yan, H.S., Chen, J.J.: Mech. Mach. Theory **20**(6), 597 (1985)
8. Yan, H.S., Hwang, Y.W.: Mech. Mach. Theory **26**(6), 541 (1991)
9. Yan, H.S.: Mech. Mach. Theory **27**(3), 235 (1992)
10. Raghavan, M.: Mech. Mach. Theory **31**(8), 1141 (1996)
11. Yan, H.S.: Creative Design of Mechanical Devices. Springer, Singapura (1998)
12. Kota, S., Chiou, S.J.: Res. Eng. Des. **4**(2), 75 (1992)
13. Chiou, S.J., Kota, S.: Mech. Mach. Theory **34**(3), 467 (1999)
14. Yan, H.S., Ou, F.M.: Mech. Mach. Theory **40**(11), 1240 (2005)
15. Han, Y.H., Lee, K.: Comput. Ind. **57**(4), 305 (2006)
16. Huang, Z., Li, Q.: Int. J. Rob. Res. **21**(2), 131 (2002)
17. Lee, C.C., Hervé, J.M.: Mech. Mach. Theory **41**(4), 433 (2006)

18. Kong, X., Gosselin, C.: Type synthesis of parallel mechanisms. In: Springer Tracts in Advanced Robotics, Springer, Heidelberg (2007)
19. Gogu, G.: Structural Synthesis of Parallel Robots: Part 1: Methodology. Solid Mechanics and Its Applications Series. Springer, London (2009)
20. Meng, X., Gao, F., Wu, S., Ge, Q.J.: Mech. Mach. Theory **78**, 177 (2014)
21. Gogu, G.: Mech. Mach. Theory **40**(9), 1068 (2005)
22. Mruthyunjaya, T.S.: Mech. Mach. Theory **38**(4), 279 (2003)
23. Hunt, K.H.: Kinematic Geometry of Mechanisms. Oxford engineering science series. Clarendon Press, Oxford (1978)
24. Phillips, J.: Freedom in Machinery. Cambridge University Press, Cambridge (2007). No. vol. 1-2 in Freedom in Machinery
25. Hunt, K.H.: ASME J. Mech. Transm. Autom. Des. **105**(4), 705 (1983)
26. Tischler, C.R., Samuel, A.E., Hunt, K.H.: Mech. Mach. Theory **30**(8), 1193 (1995)
27. Tischler, C.R., Samuel, A.E., Hunt, K.H.: Mech. Mach. Theory **30**(8), 1217 (1995)
28. Shoham, M., Roth, B.: Mech. Mach. Theory **32**(3), 279 (1997)
29. Liberati, A., Belfiore, N.: Mech. Mach. Theory **41**(12), 1443 (2006)
30. PigaCarboni, A., Martins, D.: J. Mech. Des. (2007)
31. Martins, D., Carboni, A.P.: Mech. Mach. Theory **43**(10), 1236 (2008)
32. Simoni, R., Doria, C.M., Martins, D.: Robotica **31**(01), 61 (2013)
33. Simoni, R., Simas, H., Martins, D.: ASME 2015 International Design Engineering Technical Conferences and Computers and Information in Engineering Conference. American Society of Mechanical Engineers, p. V05CT08A031 (2015)
34. Carboni, A., Martins, D.: Proceedings of 19th International Congress of Mechanical Engineering. COBEM, Brasília (2007)
35. Ebrahimi, I., Carretero, J.A., Boudreau, R.: Mech. Mach. Theory **42**(8), 1007 (2007)
36. Firmani, F., Zibil, A., Nokleby, S.B., Podhorodeski, R.P.: Trans. Can. Soc. Mech. Eng. **31**(4), 469 (2007)
37. Mruthyunjaya, T., Raghavan, M.: Mech. Mach. Theory **19**(3), 357 (1984)
38. Simoni, R., Carboni, A., Simas, H., Martins, D.: Proceedings of 13th World Congress in Mechanism and Machine Science, pp. 19–25. IFToMM, Guanajuato (2011)
39. Ding, H., Hou, F., Kecskeméthy, A., Huang, Z.: Mech. Mach. Theory **47**, 1 (2012)
40. Ding, H.: Automatic structural synthesis of planar mechanisms and its application to creative design. Ph.D. thesis, Duisburg, Essen, Universität Duisburg-Essen, Diss. (2015)
41. Ding, H., Huang, P., Kecskeméthy, A.: The 14th IFToMM World Congress, pp. 25–30. Taiwan, Taipei, October 2015

Analysis of Self-aligning Mechanisms by Means of Matroid Theory

Andrea Piga Carboni(✉), Henrique Simas, and Daniel Martins

UFSC - Universidade Federal de Santa Catarina, Florianópolis, Brazil
andrea.piga@gmail.com, {henrique.simas,daniel.martins}@ufsc.br

Abstract. This papers deals with the investigation of the linear dependence and independence of freedoms and constraints in a given mechanism by the application of matroid theory. A new and original approach, based on matroid theory, is proposed and applied for solving two different problems of mechanism: enumeration and selection of self-aligning mechanism kinematically equivalent to a given mechanism. Two novel algorithms are presented and examples of application are provided.

Keywords: Overconstraint · Mechanism · Self-aligning · Matroid

1 Introduction

Self-aligning mechanisms are mechanisms which present no redundant constraints, where redundant constraints can be defined as those constraints whose elimination does not change the mobility of the mechanism.

The kinematic design, *i.e.* the use of exact constraints, is historically attributed to James Clerk Maxwell [25]. Later Pollard [30] and Hale and Slocum [18] applied the kinematic design principles to scientific instruments.

Reshetov [31] focuses on the concept of self-alignment for general mechanisms, appointing for the disadvantages of redundant constraints, such as call for higher accuracy in manufacture, increase in weight and size and general reduction of efficiency. Reshetov introduced a method for overconstraint evaluation, based on topology analysis of mechanisms. This method is based on visual inspection on the structure of a mechanism, and does not require any modelling of constraints in terms of screw theory.

A qualitative approach to self-aligning analysis is proposed by Kamm [20] and Blanding [2]. They claim the use of kinematic design principles as an essential requirement for the design of instruments and accurate mechanisms. An alternative approach for handling with redundant constraints is proposed by French and Council [17], based on kinematic and elastic design.

Whitney [36] and Shukla and Whitney [33] apply screw theory for determining overconstraint in assembly. Their method permits to evaluate the degree of overconstraint for a class of parallel mechanism. In [5], an extension of this method has been proposed by the author for mobility calculation of parallel mechanism.

J.C.M. Carvalho et al. (eds.), *Multibody Mechatronic Systems*,
Mechanisms and Machine Science 54, DOI 10.1007/978-3-319-67567-1_6

The correct evaluation of redundant constraints is of great importance in engineering simulation of multibody systems. Usually redundant constraints are detected and eliminated in order to perform kinematics and dynamics simulations. Wojtyra et al. [38] propose a method for redundant constraint detection based on the Jacobian formulation. An extension of this method for mechanisms with flexible bodies is presented in [39] and for mechanisms with Coulomb friction in [16]. In [26] an algorithm is proposed for the elimination of redundant loop constraints as pre-processing for multibody simulation.

In this paper a novel approach for identifying overconstraints in mechanisms is presented, and algorithms for enumerating self-aligning mechanism and selecting optimal self-aligning design are proposed.

2 Brief Review of Davies' Methodology and Matroid Theory

In this section an overview of Davies' methodology and matroid theory is briefly presented. The main contributions introduced by Davies and its applications can be found in [3,9–15,23]. Davies adapted Kirchhoff's circulation law and cutset law to multibody systems. The adaptation of Kirchhoff's laws is based on the representation of a coupling network [12] with n links and g joints by a graph, called a coupling graph G_C, in which every link (body) is represented by a node and every direct coupling between links by an edge. For a coupling network the cutset law can be written as:

$$\left[\hat{\boldsymbol{A}}_{\boldsymbol{N}}\right]_{\lambda k,C}[\boldsymbol{\Psi}]_C = [\boldsymbol{0}]_{\lambda k} \tag{1}$$

where k is the number of the cutsets in the coupling network, $C = \sum_{1}^{g} c_i$ is the gross degree of constraint, *i.e.* the sum of the degree of constraint c_i imposed by the couplings and $\boldsymbol{\Psi}$ is the vector of the action screws unknown magnitudes imposed by the couplings. Matrix $\hat{\boldsymbol{A}}_{\boldsymbol{N}}$ can be written as in Eq. (2).

$$\left[\hat{\boldsymbol{A}}_{\boldsymbol{N}}\right]_{\lambda k,C} = \begin{bmatrix} \left[\hat{\boldsymbol{A}}_{\boldsymbol{D}}\right]_{\lambda,C} & [\boldsymbol{Q_1}]_{C,C} \\ \left[\hat{\boldsymbol{A}}_{\boldsymbol{D}}\right]_{\lambda,C} & [\boldsymbol{Q_2}]_{C,C} \\ \vdots & \vdots \\ \left[\hat{\boldsymbol{A}}_{\boldsymbol{D}}\right]_{\lambda,C} & [\boldsymbol{Q_K}]_{C,C} \end{bmatrix} \tag{2}$$

$$\left[\hat{\boldsymbol{A}_{\boldsymbol{D}}}\right] = \left[\overbrace{\$^a_{a1}\ \$^a_{a2}\ \ldots}^{\text{Coupling a}} \middle| \overbrace{\$^a_{b1}\ \ldots\ldots}^{\text{Coupling b}} \middle| \overbrace{\ldots}^{\ldots} \middle| \overbrace{\ldots\ \$^a_C}^{\ldots}\right] \tag{3}$$

where $[\boldsymbol{Q_i}]_{C,C}$, $i = 1, 2, \ldots, k$ are diagonal matrices whose diagonal elements correspond to row i of cutset matrix $[\boldsymbol{Q_A}]_{k,C}$, derived from action graph G_A.

$\left[\hat{\boldsymbol{A}}_{\boldsymbol{D}}\right]$ is the unit action matrix containing one action screw for column as in Eq. (3), where k is the number of the cutsets in the coupling network and λ

is the order of the screw system to which all action screws belong (in the most general case $\lambda = 6$).

The concept of matroid is a combinatorial abstraction of matrices with respect to linear independence. It was first introduced by Hassler [37] as an abstraction of linear independence. Many alternative formulations of matroids can be found in literature [21,21,27–29,32,34] where multitude of non-obviously equivalent definitions goes by the name of cryptomorphism.

In this paper, the matroid theory developed from linear algebra is employed. Given matrix A in Eq. (5):

$$A = \begin{matrix} \begin{matrix} 1 & 2 & 3 & 4 & 5 \end{matrix} \\ \begin{bmatrix} 1 & 0 & 0 & 1 & 0 \\ 0 & 1 & 0 & 1 & 1 \\ 0 & 0 & 1 & 0 & 1 \end{bmatrix}_{3,5} \end{matrix} \tag{4}$$

$$\begin{aligned} \mathcal{I} = \{&\emptyset, \{1\}, \{2\}, \{3\}, \{4\}, \{5\}, \{1,2\}, \{1,3\}, \{1,4\}, \{1,5\}, \{2,3\}, \\ &\{2,4\}, \{2,5\}, \{3,4\}, \{3,5\}, \{4,5\}, \{1,2,3\}, \{1,2,5\}, \{1,3,4\}, \\ &\{1,3,5\}, \{1,4,5\}, \{2,3,4\}, \{2,4,5\}, \{3,4,5\}\}. \end{aligned} \tag{5}$$

whose columns are indexed by $E = \mathrm{Col}(A) = \{1, \ldots, 5\}$, the linear dependence and independence among column vectors $\{\boldsymbol{a_e}|e \in E\}$ is considered. A subset $I \subseteq E$ is said to be independent if the corresponding subfamily $\{\boldsymbol{a_e}|e \in I\}$ of column vectors is linearly independent. The family of independent subsets, denoted by $\mathcal{I} \subseteq 2^E$, *i.e.* all possible subsets of E, is defined as: $\mathcal{I} = \{I \subseteq E|\{\boldsymbol{a_e}|e \in I\}$ is linearly independent$\}$. For the matrix A of Eq. (4) $\mathcal{I}$ is presented in Eq. (5). Each one of the sets of Eq. (5) represents a linear independent set. Note that the set of columns $\{1, 2, 4\} \notin \mathcal{I}$, because column 4 can be obtained as a linear combination of columns 1 and 2. The following three properties [27] can be applied to $\mathcal{I}$:

1. $\emptyset \in \mathcal{I}$
2. $J \in \mathcal{I}$ and $I \subseteq J \Longrightarrow I \in \mathcal{I}$
3. $I, J \in \mathcal{I}, |I| < |J| \Longrightarrow (I \cup \{v\}) \in \mathcal{I}$ for some $\nu \in J \setminus I$

Property (2) states that all subsets of an independent set are independent sets. For example, set $\{1, 2, 3\} \in \mathcal{I}$ is an independent set thus subsets $\{1\}$, $\{2\}$, $\{3\}$, $\{1, 2\}$, $\{1, 3\}$ and $\{2, 3\}$ are all independent sets, as stated in Eq. (5). Because of property (2), it is redundant to enumerate all the members of $\mathcal{I}$. Instead the family $\mathcal{B}$ of the maximal members, *i.e.* the set with maximal cardinality, of $\mathcal{I}$ is sufficient: $\mathcal{B} = \{\{1, 2, 3\}, \{1, 2, 5\}, \{1, 3, 4\}, \{1, 3, 5\}, \{1, 4, 5\}, \{2, 3, 4\}, \{2, 4, 5\}, \{3, 4, 5\}\}$, which represent the family of bases of the column space of matrix $\boldsymbol{A}$. Thus a matrix gives rise to pairs $(E, \mathcal{I})$ and $(E, \mathcal{B})$, each representing the linear independence of linear structure of column vectors. $(E, \mathcal{I})$ and $(E, \mathcal{B})$ are equivalent and define the same combinatorial structure underlying linear independence. This structure is named matroid [27] and E is called the ground set of the matroid.

3 Analysis of Overconstrained Mechanisms by Means of Matroid Theory

The matroid formulation is applied to the unit action matrix $\left[\hat{\boldsymbol{A}}_{\boldsymbol{N}}\right]$, in a similar way it has been applied to the unit motion matrix $\left[\hat{\boldsymbol{M}}_{\boldsymbol{N}}\right]$ [4,6].

Matrix $\left[\hat{\boldsymbol{A}}_{\boldsymbol{N}}\right]$ presents the following structures:

$$\left[\hat{\boldsymbol{A}}_{\boldsymbol{N}}\right]_{\lambda k,C} = \begin{array}{c} \overbrace{\ldots}^{\text{Coupling a}}\ \overbrace{*\ \ldots}^{\text{Coupling b}}\ \overbrace{\ldots}^{\ldots}\ \overbrace{\ldots}^{\ldots} \\ \left[\begin{array}{cccccc} * * & \ldots & * & \ldots & \ldots & \ldots * \} \text{ dim. } 1 \\ * * & \ldots & * \ldots & \ldots & \ldots * \} \text{ dim. } 2 \\ & & & & & \vdots \\ * * & \ldots & * \ldots & \ldots & \ldots * \} \text{ dim. } \lambda \end{array}\right. \text{Cutset } 1 \\ \left[\begin{array}{cccccc} * * & \ldots & * \ldots & \ldots & \ldots * \} \text{ dim. } 1 \\ * * & \ldots & * \ldots & \ldots & \ldots * \} \text{ dim. } 2 \\ & & & & & \vdots \\ * * & \ldots & * \ldots & \ldots & \ldots * \} \text{ dim. } \lambda \end{array}\right. \text{Cutset } 2 \\ \vdots \\ \left[\begin{array}{cccccc} * * & \ldots & * \ldots & \ldots & \ldots * \} \text{ dim. } 1 \\ * * & \ldots & * \ldots & \ldots & \ldots * \} \text{ dim. } 2 \\ & & & & & \vdots \\ * * & \ldots & * \ldots & \ldots & \ldots * \} \text{ dim. } \lambda \end{array}\right. \text{Cutset } k \end{array} \tag{6}$$

where each column is uniquely determined by a single constraint imposed by a coupling. Dependence and independence of the mechanism's constraints can thus be analysed by studying the properties of $\left[\hat{\boldsymbol{A}}_{\boldsymbol{N}}\right]$. Independent columns of $\left[\hat{\boldsymbol{A}}_{\boldsymbol{N}}\right]$ identify a set of leading variables of the linear homogeneous system (1), *i.e.* a set of independent constraints of the mechanism. Each set of independent constraints form a basis for the constraint space of the mechanism, and can be regarded as a mechanism free of redundant constraints, *i.e.* a self-aligning mechanism, derived from the original one. Thus given a mechanism with C constraints and C_N redundant ones, a self-aligning mechanism kinematically equivalent to the original mechanism can be derived removing a set of C_N redundant constraints. The self-aligning mechanism derived thus has $C' = C - C_N$ constraints, all independent ones, and the linear homogeneous system (1) can be written as:

$$\left[\hat{\boldsymbol{A}}'_{\boldsymbol{N}}\right]_{\lambda k,C-C_N} [\boldsymbol{\Psi}]_{C-C_N,1} = [\boldsymbol{0}]_{\lambda k} \tag{7}$$

where $\left[\hat{\boldsymbol{A}}'_{\boldsymbol{N}}\right]_{\lambda k,C-C_N}$ has full rank: $rank(\left[\hat{\boldsymbol{A}}'_{\boldsymbol{N}}\right]_{\lambda k,C-C_N}) = C - C_N$. A new condition is herein stated for a self-aligning mechanism:

Condition 1. *For a mechanism with C constraints and C_N redundant ones in a given configuration, a set of $C' = C - C_N$ constraints represents a self-aligning mechanism kinematically equivalent to the original one, if and only if,*

in the given configuration, the corresponding matrix $\left[\hat{\boldsymbol{A}}'_{\boldsymbol{N}}\right]_{\lambda k, C-C_N}$, *obtained from* $\left[\hat{\boldsymbol{A}}_{\boldsymbol{N}}\right]_{\lambda k, C}$ *removing the* C_N *columns corresponding to the set of redundant constraint, has full rank:* $rank(\left[\hat{\boldsymbol{A}}'_{\boldsymbol{N}}\right]_{\lambda k, C-C_N}) = C - C_N$.

In general different basis can be chosen to span the constraint space, thus different self-aligning mechanism can be derived. All combination of $C - C_N$ columns of $\left[\hat{\boldsymbol{A}}_{\boldsymbol{N}}\right]_{\lambda k, C}$ can be tested for linear independence in order to find a basis for the constraint space [7]. This method is computationally heavily time-consuming because of the combinatorial explosion.

A new approach is proposed in this paper. Given a mechanism and its associated network unit action matrix $\left[\hat{\boldsymbol{A}}_{\boldsymbol{N}}\right]_{\lambda k, C}$, a linear matroid $\mathcal{M}_{A_N}$ is defined over the reals $\mathbb{R}$ from matrix $\left[\hat{\boldsymbol{A}}_{\boldsymbol{N}}\right]$, where the ground set $E(\mathcal{M}_{A_N})$ denotes the index set of the columns of $\left[\hat{\boldsymbol{A}}_{\boldsymbol{N}}\right]_{\lambda K, C}$ $E = \{1, 2, \ldots, C\}$.

For a subset X of E, let $\left[\hat{\boldsymbol{A}}_{\boldsymbol{N}}\right]_{\boldsymbol{X}}$ denote the submatrix of $\left[\hat{\boldsymbol{A}}_{\boldsymbol{N}}\right]$ consisting of those columns indexed by X. A family $\mathfrak{I}$ of subset can now be define for the matroid $\mathcal{M}$:

$$\mathfrak{I} = \{X \subseteq E \mid \text{rank } ([A_N]_X) = |X|\} \tag{8}$$

where a set X is independent if the corresponding columns are linearly independent. A basis B corresponds to a linearly independent set of columns of cardinality $\text{rank}(\left[\hat{\boldsymbol{A}}_{\boldsymbol{N}}\right]_B) = C - C_N$.

Thus the column space of $\left[\hat{\boldsymbol{A}}_{\boldsymbol{N}}\right]$ is spanned any basis B belonging to the collection of bases of the matroid $\mathcal{B}(\mathcal{M}_{A_N})$. Regarding that a basis B corresponds to a maximal set of independent columns of $\left[\hat{\boldsymbol{A}}_{\boldsymbol{N}}\right]$, any basis B of the matroid $\mathcal{M}_{A_N}$ represents a self-aligning mechanism kinematically equivalent to the original one.

The problem of enumerating all self-aligning mechanisms of a given mechanism has thus been turned into the problem of enumerating all the bases of matroid $\mathcal{M}_{A_N}$, which is a well-known problem in matroid theory. A new algorithm for enumeration of all self-aligning mechanism kinematically equivalent to a given mechanism is proposed in Algorithm (1).

The sets of variables corresponding to the bases of matroid represent the self-aligning mechanisms derived form the given mechanism.

In order to analyse the complexity of Algorithm (1), the worst case in terms of matrix $\left[\hat{\boldsymbol{A}}_{\boldsymbol{N}}\right]$ size is analysed. For a spatial ($\lambda = 6$) mechanism with n links and g joints, matrix $\left[\hat{\boldsymbol{A}}_{\boldsymbol{N}}\right]$ has size $6 \cdot (n-1) \times 5 \cdot g$ in the worst case. Each base of the matroid is enumerated in polynomial time $poly(5 \cdot g)$ [22,35].

Algorithm 1. Enumeration of all self-aligning mechanisms kinematically equivalent to a given mechanism

1: Create the network unit motion matrix $\left[\hat{\boldsymbol{A}}_{\boldsymbol{N}}\right]$;
2: Create the linear matroid $\mathcal{M}_{A_N}$ on the real field $\mathbb{R}$ defined over matrix $\left[\hat{\boldsymbol{A}}_{\boldsymbol{N}}\right]$;
3: Enumerate all bases B of matroid $\mathcal{M}_{A_N}$;

The cardinality of each base is the number of independent constraints, *i.e.* $C - C_N$ of the mechanism. Thus, in the worst case the number of $\mathcal{M}_{A_N}$ bases, *i.e.* the cardinality of $\mathcal{B}(\mathcal{M}_{A_N})$, is $(C - C_N)$-combination of the ground set E, *i.e.* $|\mathcal{B}^*(\mathcal{M}_{M_N})| = \begin{pmatrix} 5 \cdot g \\ C - C_N \end{pmatrix}$.

The correctness of Algorithm 1 can be shown in the following form: Steps 1 implement the Davies' method, well established in literature: given a mechanism, matrix $\left[\hat{\boldsymbol{A}}_{\boldsymbol{N}}\right]$ can always be obtained [8,15]. Given a matrix $\left[\hat{\boldsymbol{A}}_{\boldsymbol{N}}\right]$ a linear matroid $\mathcal{M}_{AN}$ can be defined [29] in Steps 2. In Step 3 all the bases of matroid $\mathcal{M}_{A_N}$ can be enumerated [22].

3.1 Example: Enumeration of Self-aligning Mechanisms for Planar Overconstrained Mechanism

Algorithm 1 is applied to the planar mechanism in Fig. 1a, with five links and six revolute couplings a, b, c, d, e and f. The mechanism has mobility $F_N = 1$ and $C_N = 1$ redundant restriction.

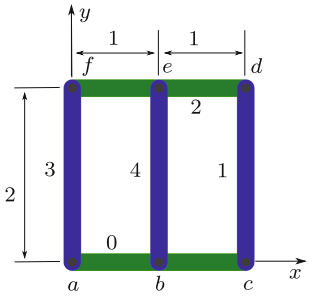

(a)

$$\left[\hat{\boldsymbol{A}}_{\boldsymbol{N}}\right]_{12,12} =$$

a_U	a_V	b_U	b_V	c_U	c_V	d_U	d_V	e_U	e_V	f_U	f_V
0	0	0	1	0	2	0	0	0	0	0	0
1	0	1	0	1	0	0	0	0	0	0	0
0	1	0	1	0	1	0	0	0	0	0	0
0	0	0	0	0	2	−2	2	0	0	0	0
0	0	0	0	1	0	1	0	0	0	0	0
0	0	0	0	0	1	0	1	0	0	0	0
0	0	0	0	0	2	0	0	−2	1	0	0
1	0	0	0	1	0	0	0	1	0	0	0
0	1	0	0	0	1	0	0	0	1	0	0
0	0	0	0	0	0	0	0	0	0	−2	0
1	0	0	0	0	0	0	0	0	0	1	0
0	1	0	0	0	0	0	0	0	0	0	1

(b)

Fig. 1. Planar mechanism with mobility $F_N = 1$ and redundant constraint $C_N = 1$ (a) and its corresponding network unit action matrix (b).

Recall that an action screw $\$^{\boldsymbol{a}}$ can be written in the in axis-coordinates [19] form $\$^{\boldsymbol{a}} = \left[R\ S\ T\ U\ V\ W\right]$, where $\boldsymbol{Q}$ is a force vector $\boldsymbol{Q} = \left[U\ V\ W\right]$ and $\boldsymbol{P}$ is a moment vector $\boldsymbol{P} = \left[R\ S\ T\right]$ around the origin. As the mechanism is planar, only the planar components of planar motion are considered, *i.e.* T, U and

V. The motion screws of the coupling network thus belong to the fifth special 3-system of screws [19]. The network unit action matrix is represented in Eq. (1b). A linear matroid $\mathcal{M}_{A_N}$ over the real number $\mathbb{R}$ is defined over matrix $\left[\hat{\boldsymbol{A}}_{\boldsymbol{N}}\right]$. The set of bases of the matroid are enumerated. Each basis correspond to a self-aligning mechanism kinematically equivalent to the one presented in Fig. 1a. The set of bases $\mathcal{B}$ of $\mathcal{M}_{A_N}$ is:

$$\mathcal{B}(\mathcal{M}_{A_N}) = \left\{ \begin{array}{ll} \{U_a, U_b, V_b, U_c, V_c, U_d, V_d, U_e, V_e, U_f, V_f\}, & (9) \\ \{U_a, V_a, U_b, U_c, V_c, U_d, V_d, U_e, V_e, U_f, V_f\}, & (10) \\ \{U_a, V_a, U_b, V_b, U_c, U_d, V_d, U_e, V_e, U_f, V_f\}, & (11) \\ \{U_a, V_a, U_b, V_b, U_c, V_c, U_d, U_e, V_e, U_f, V_f\}, & (12) \\ \{U_a, V_a, U_b, V_b, U_c, V_c, U_d, V_d, U_e, U_f, V_f\}, & (13) \\ \{U_a, V_a, U_b, V_b, U_c, V_c, U_d, V_d, U_e, V_e, U_f\} & (14) \end{array} \right\}$$

It can be observed that links 1, 3 and 4 must have the same length in order to assemble the mechanism with one degree of freedom, because of the presence of one redundant constraint. Moreover, in the given mechanism's configuration, the translation along y-axis is exactly the freedom which is overconstrained.

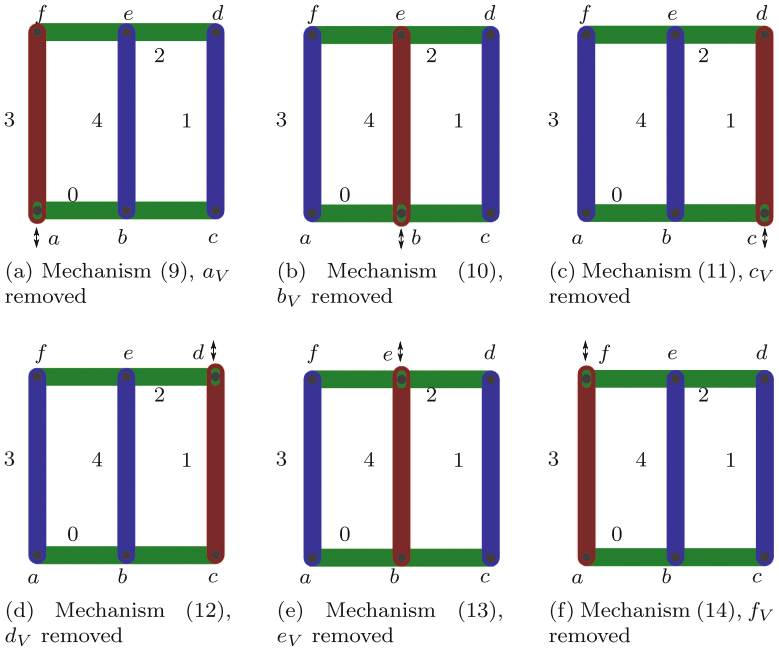

(a) Mechanism (9), a_V removed

(b) Mechanism (10), b_V removed

(c) Mechanism (11), c_V removed

(d) Mechanism (12), d_V removed

(e) Mechanism (13), e_V removed

(f) Mechanism (14), f_V removed

Fig. 2. The self-aligning mechanisms kinematically equivalent to the overconstrained mechanism shown in Fig. 1a.

Examining the result of the proposed algorithm, each one of the corresponding self-aligning mechanism obtained has exactly one constrained along y-axis removed from a coupling. Mechanism described by Set (9) has the constraint along y-axis removed from coupling a, *i.e.* the constraint a_V has been removed. The self-aligning mechanism enumerate by the algorithm are presented in Fig. 2, where the constraints removed are indicated.

Algorithm 1 can be applied to the *Tripteron* mechanism [24]. The mechanism considered presents a total of $C = 60$ constraints, of which $C_N = 3$ are redundant constraints. A linear matroid $\mathcal{M}_{A_N}$ over the real number $\mathbb{R}$ is defined over matrix $\left[\hat{\boldsymbol{A}}_{\boldsymbol{N}}\right]$. The set of bases of the matroid can thus be enumerated. Each basis correspond to a self-aligning mechanism kinematically equivalent to the original *Tripteron* mechanism. The Algorithm 1 enumerates a total of 512 distinct basis for the matroid $\mathcal{M}_{A_N}$, *i.e.* the mechanism *Tripteron* presents 512 self-aligning distinct mechanisms, all of them kinematically equivalent to the *Tripteron* mechanism.

It is important to regard that, as the complexity of the mechanism increases, the numbers of possible self-aligning mechanisms grows exponentially. It is thus important a way of selecting the best self-aligning mechanism with respect to some criteria. In the following, a new algorithm is proposed for selecting a self-aligning mechanism which best fits a criterion based on mechanism specifications.

3.2 Classification of Self-aligning Mechanism

Given a mechanism with g couplings imposing C constraints, a weight w_i is attributed to each allowed constraint c_i. The set of weights $\{w_i | w_i \in \mathcal{W}\}$ is chosen with respect to a set of criteria based on the mechanism specifications and each self-aligning mechanism can be classified in terms of the sum of weights attributed to the corresponding active couplings.

The matrix $\hat{\boldsymbol{A}}_{\boldsymbol{N}}$ of the mechanism is considered. Recalling that each column of $\hat{\boldsymbol{A}}_{\boldsymbol{N}}$ corresponds to a constraint imposed by the couplings of the mechanism, the set of weights $\{w_i | w_i \in \mathcal{W}\}$ can be considered assigned to the columns of $\hat{\boldsymbol{A}}_{\boldsymbol{N}}$. Thus the problem of selecting an optimal self-aligning mechanism is transformed in the problem of determining the maximum weight independent set in a matroid. This problem can be solved using a greedy algorithm in polynomial time [4]. The matroid $\mathcal{M}_{A_N}$ defined from matrix $\hat{\boldsymbol{A}}_{\boldsymbol{N}}$ of the given mechanism, as defined in the previous section, is considered. This matroid is thus a weighted matroid, with respect to which a greedy algorithm can be performed. The greedy algorithm for the matroid $\mathcal{M}_{A_N}$ returns the maximum weight basis for the matroid. This is exactly the maximum weight self-aligning mechanism, among all possible self-aligning mechanism kinematically equivalent, which best fits the criteria specified for the mechanism. A new algorithm for selecting an optimal self-aligning mechanism is herein proposed, based on the algebraic structure of matroid.

Thus the set of variables corresponding to this set is the self-aligning mechanism which best fits the mechanism specifications. The matroid structure guarantees that the solution encountered is the optimal one. The matroid formulation

Algorithm 2. Selection of self-aligning mechanism, kinematically equivalent to a given mechanism

1: Create the network unit action matrix $\left[\hat{\boldsymbol{A}}_{\boldsymbol{N}}\right]$ for the given mechanism;
2: Create the linear matroid $\mathcal{M}_{A_N}$ on the real field $\mathbb{R}$ defined from matrix $\left[\hat{\boldsymbol{A}}_{\boldsymbol{N}}\right]$;
3: Assign a weight to each constraint imposed by couplings in the mechanism, *i.e.* a weight is assigned to each column of $\left[\hat{\boldsymbol{A}}_{\boldsymbol{N}}\right]$, based on a set of criteria (mechanism specifications);
4: Apply greedy algorithm to matroid $\mathcal{M}_{A_N}$;
5: The greedy algorithm returns the maximum weight independent set for $\mathcal{M}_{A_N}$;

for a mechanism herein proposed allows thus to solve the problem of finding an optimal self-aligning mechanism with respect to a set of criteria established for the mechanism.

Algorithm complexity can now be calculated. For a spatial ($\lambda = 6$) mechanism with n links and g joints, matrix $\left[\hat{\boldsymbol{A}}_{\boldsymbol{N}}\right]$ has size $6 \cdot (n-1) \times 5 \cdot g$ in the worst case. The greedy algorithm has complexity $O(|E|f(rank(\mathcal{M})) + |E|log|E|)$ [1] where the cardinality of ground set E is $|E| = 5 \cdot g$ and the rank of the matroid is $rank(\mathcal{M}_{A_N}) = C - C_N$.

The correctness of Algorithm 2 can be shown in the following form: Steps 1 implement the Davies' method, well established in literature: given a mechanism matrix $\left[\hat{\boldsymbol{A}}_{\boldsymbol{N}}\right]$ can always be obtained [8,15]. Given a matrix $\left[\hat{\boldsymbol{A}}_{\boldsymbol{N}}\right]$ a linear matroid $\mathcal{M}_{A_N}$ can be defined [29] in Steps 2. Greedy algorithm can be applied to any matroid [29] in Step $3-5$.

3.3 Example: Selection of an Optimal Self-aligning Mechanism for Spatial Overconstrained Mechanism

The Algorithm 2 can be applied to the *Tripteron* mechanism. As presented in the previous section, the *Tripteron* mechanism presents 512 possible self-aligning mechanism, all kinematically equivalent to the *Tripteron*. In order to apply the algorithm, a set weights must be assigned to the columns $\left[\hat{\boldsymbol{A}}_{\boldsymbol{N}}\right]$. Considering the topology of the mechanism, the following criterion for selecting actuation scheme is adopted:

– *The self-aligning mechanism must contain the three prismatic couplings, which will be actuated. Furthermore revolute couplings in the set* $\{g, h, m, n, c, d\}$ *should be maintained. Furthermore any planar freedom in the set* $\{b, l, f\}$ *should be avoided,* i.e. *the planar constraints* U, V *and* W *should be maintained in joints* $\{b, l, f\}$.

This criterion is mostly for didactic purpose, and it aims to obtain a self-aligning mechanism easy to control and with standard joints (revolute, universal

and spherical), avoiding more complicated joints as the planar ones. Different criteria can be stated, corresponding to different weights sets. For the criterion considered, the set of weights $\{\mathcal{W}\}$ is assigned in Table 1.

Table 1. Constraints for *Tripteron* mechanism

Contr.	W	Contr.	W	Contr.	W	Contr.	W	Contr.	W	Contr.	W
$\boldsymbol{a_R}$	5	$\boldsymbol{c_S}$	5	$\boldsymbol{e_R}$	5	$\boldsymbol{g_R}$	5	$\boldsymbol{i_R}$	5	$\boldsymbol{m_R}$	5
$\boldsymbol{a_S}$	5	$\boldsymbol{c_T}$	5	$\boldsymbol{e_S}$	5	$\boldsymbol{g_T}$	5	$\boldsymbol{i_S}$	5	$\boldsymbol{m_S}$	5
$\boldsymbol{a_T}$	5	$\boldsymbol{c_U}$	5	$\boldsymbol{e_T}$	5	$\boldsymbol{g_U}$	5	$\boldsymbol{i_T}$	5	$\boldsymbol{m_U}$	5
$\boldsymbol{a_V}$	5	$\boldsymbol{c_V}$	5	$\boldsymbol{e_U}$	5	$\boldsymbol{g_V}$	5	$\boldsymbol{i_U}$	5	$\boldsymbol{m_V}$	5
$\boldsymbol{a_W}$	5	$\boldsymbol{c_W}$	5	$\boldsymbol{e_W}$	5	$\boldsymbol{g_W}$	5	$\boldsymbol{i_V}$	5	$\boldsymbol{m_W}$	5
$\boldsymbol{b_S}$	0	$\boldsymbol{d_S}$	5	$\boldsymbol{f_R}$	0	$\boldsymbol{h_R}$	5	$\boldsymbol{l_R}$	0	$\boldsymbol{n_R}$	5
$\boldsymbol{b_T}$	0	$\boldsymbol{d_T}$	5	$\boldsymbol{f_T}$	0	$\boldsymbol{h_T}$	5	$\boldsymbol{l_S}$	0	$\boldsymbol{n_S}$	5
$\boldsymbol{b_U}$	2	$\boldsymbol{d_U}$	5	$\boldsymbol{f_U}$	2	$\boldsymbol{h_T}$	5	$\boldsymbol{l_U}$	2	$\boldsymbol{n_U}$	5
$\boldsymbol{b_V}$	2	$\boldsymbol{d_V}$	5	$\boldsymbol{f_V}$	2	$\boldsymbol{h_V}$	5	$\boldsymbol{l_V}$	2	$\boldsymbol{n_V}$	5
$\boldsymbol{b_W}$	2	$\boldsymbol{d_W}$	5	$\boldsymbol{f_W}$	2	$\boldsymbol{h_W}$	5	$\boldsymbol{l_W}$	2	$\boldsymbol{n_W}$	5

With the criterion considered the algorithm proposed looks for a self-aligning mechanism by eliminating a set of planar constraints in couplings $\{b, f, l\}$. Applying Algorithm 2 to the mechanism, the maximum independent set of the matroid $\mathcal{M}_{A_N}$ obtained is presented in Fig. 3a.

$$\left\{ \begin{array}{c} a_R, a_S, a_T, a_V, a_W, b_T, b_U, b_V, b_W, \\ c_S, c_T, c_U, c_V, c_W, d_S, d_T, d_U, d_V, \\ d_W, e_R, e_S, e_T, e_U, e_W, f_U, f_V, f_W, \\ g_R, g_T, g_U, g_V, g_W, h_R, h_T, h_U, h_V, \\ h_W, i_R, i_S, i_T, i_U, i_V, l_R, l_S, l_U, \\ l_V, l_W, m_R, m_S, m_U, m_V, m_W, n_R, n_S, \\ n_U, n_V, n_W \end{array} \right\}$$

(a)

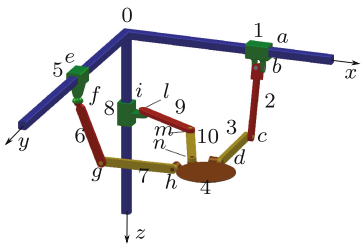

(b)

Fig. 3. Maximum independent set (a) and corresponding self-aligning mechanism (b)

The Set (Fig. 3a) describes a self-aligning mechanism kinematically equivalent to the *Tripteron*. This set describes the constraints which are maintained for each joint. For example for coupling a five constraints are maintained, more exactly R, S, T, V and W, thus a is a prismatic pair along x axis. On the other hand, for joint B four constraints are maintained, more exactly T, U, V and W, thus b is an universal pair with rotations along x and y axis. In the same

way all remaining joints can be obtained from Set (Fig. 3a). The corresponding self-aligning mechanism is presented in Fig. 3b.

It is important to notice that the greedy algorithm is guaranteed to find an optimal solution when performing on matroid structure. In general this solution is not unique. Thus Algorithm 2 proposed returns one possible self-aligning mechanism which satisfies the given criteria. All self-aligning mechanism satisfying the given criteria can be enumerated by calculating the weight of each basis enumerated by Algorithm 1 and selecting the maximal ones. Establishing the criteria in terms of the given specifications for a mechanism is thus of the greatest importance for the enumeration of interesting sets of self-aligning mechanisms.

4 Conclusions

This paper presents a new algorithm for enumerating self-aligning kinematically equivalent mechanisms based on Matroid theory. This algorithm enumerates all self-aligning mechanisms derived from an overconstrained one in polynomial time. With the increase of the complexity of mechanisms, the number of self-aligning solutions grows exponentially. Thus a further new algorithm is proposed for selecting an optimal self-aligning kinematically equivalent mechanism, based on a set of criteria describing mechanism specifications. The new algorithms apply matroid theory for investigating mechanisms, based on the freedom and constraint formulation introduced in this paper. The algorithms have all been implemented in SAGE software and examples of application for both algorithms are presented.

References

1. Bixby, R.E., Cunningham, W.H.: Matroid optimization and algorithms. In: Handbook of Combinatorics, vol. 1, pp. 551–609. MIT, Cambridge (1995). http://dl.acm.org/citation.cfm?id=233157.233193
2. Blanding, D.L.: Exact Constraint: Machine Design Using Kinematic Principles. ASME, New York (1999)
3. Campos, A., Gunther, R., Martins, D.: Differential kinematics of serial manipulators using virtual chains. J. Braz. Soc. Mech. Sci. Eng. XXVI **I**(4), 345–356 (2005)
4. Carboni, A.P.: Análise conceitual de estruturas cinemáticas planas e espaciais. Ph.D. thesis, Universidade Federal de Santa Catarina (2008)
5. Carboni, A.P., Simas, H., Martins, D.: Modelagem por helicoides de restrições redundantes. In: Cardona, A., Kohan, P.H., Quinteros, R.D., Storti, M.A. (eds.) MECOM - Mecánica Computacional, vol. XXXI, pp. 2803–2814. Asociación de Mecánica Computacional, Salta (2012)
6. Carboni, A.P., Simas, H., Martins, D.: Actuation scheme analysis based on matroid theory. Submitted to Mechansmism and Machine Theory (2018)
7. Carreto, V.: Estudo de mecanismos auto-alinháveis usando análise de dependências estáticas e cinemáticas. Master's thesis, Universidade Federal de Santa Catarina (2010). http://www.tede.ufsc.br/teses/PEMC1274-D.pdf

8. Davies, T.: Mechanical networks–II formulae for the degrees of mobility and redundancy. Mech. Mach. Theory **18**(2), 103–106 (1983). http://www.sciencedirect.com/science/article/B6V46-482GNP1-61/2/43272edab6520402afa74c3e38f2f2b0
9. Davies, T., Laus, L.P.: Coupling networks dual with planar revolute coupled linkages in critical configurations. In: 13th World Congress in Mechanism and Machine Science, Guanajuato, México, 19–25 June 2011. Paper number A11-305
10. Davies, T.H.: Kirchhoff's circulation law applied to multi-loop kinematic chains. Mech. Mach. Theory **16**(3), 171–183 (1981). http://www.sciencedirect.com/science/article/B6V46-482GN4J-PC/2/da424f56be0f7c29e7ddec5c95a7a7e7
11. Davies, T.H.: Circuit actions attributable to active couplings. Mech. Mach. Theory **30**(7), 1001–1012 (1995). http://www.sciencedirect.com/science/article/pii/0094114X9500022Q
12. Davies, T.H.: Couplings, coupling network and their graphs. Mech. Mach. Theory **30**(7), 991–1000 (1995). http://www.sciencedirect.com/science/article/B6V46-3YMFRH1-N/2/af193277f5af381883e4b8be6a26e94f
13. Davies, T.H.: The 1887 committee meets again. Subject: freedom and constraint. In: Ball 2000 Conference, University of Cambridge, Cambridge University Press, Trinity College Proceedings of a Symposium commemorating the Legacy, Works, and Life of Sir Robert Stawell Ball upon the 100th Anniversary of A Treatise on the Theory of Screws, pp. 1–56. University of Cambridge, Trinity College (2000). http://hdl.handle.net/2134/700
14. Davies, T.H.: Dual coupling networks. Proc. Inst. Mech. Eng. Part C J. Mech. Eng. Sci. **220**(8), 1237–1247 (2006). http://hdl.handle.net/2134/4667
15. Davies, T.H.: Freedom and constraint in coupling networks. Proc. Inst. Mech. Eng. Part C J. Mech. Eng. Sci. **220**(7), 989–1010 (2006)
16. Frączek, J., Wojtyra, M.: On the unique solvability of a direct dynamics problem for mechanisms with redundant constraints and coulomb friction in joints. Mech. Mach. Theory **46**(3), 312–334 (2011)
17. French, M.J., Council, D.: Conceptual Design for Engineers. Springer, New York (1999)
18. Hale, L.C., Slocum, A.H.: Optimal design techniques for kinematic couplings. J. Int. Soc. Precis. Eng. Nanotechnol. **25**(2), 114–127 (2001)
19. Hunt, K.H.: Kinematic Geometry of Mechanisms. The Oxford Engineering Science Series, vol. 7. Clarendon, Oxford (1978)
20. Kamm, L.: Designing Cost-efficient Mechanisms: Minimum Constraint Design, Designing with commercial Components, and Topics in Design Engineering. McGraw-Hill, New York (1990)
21. Katz, E.: Matroid theory for algebraic geometers (2014). http://arxiv.org/abs/1409.3503. Accepted, Simons Symposium volume
22. Khachiyan, L., Boros, E., Elbassioni, K., Gurvich, V., Makino, K.: On the complexity of some enumeration problems for matroids. SIAM J. Discrete Math. **19**(4), 966–984 (2005). http://rutcor.rutgers.edu/~boros/IDM/Papers/Cycles-in-matroids.pdf
23. Laus, L.P., Simas, H., Martins, D.: Efficiency of gear trains determined using graph and screw theories. Mech. Mach. Theory **52**, 296–325 (2012). http://www.sciencedirect.com/science/article/pii/S0094114X12000213
24. de Robotique de l'Université Laval, L.: Tripteron and quadrupteron. http://robot.gmc.ulaval.ca/en/research/theme104.html (2013). Accessed 19 July 2015
25. Maxwell, J.C.: The Scientific Papers of James Clerk Maxwell, vol. 2. Cambridge University Press, Cambridge (1890)

26. Müller, A.: A conservative elimination procedure for permanently redundant closure constraints in mbs-models with relative coordinates. Multibody Syst. Dyn. **16**(4), 309–330 (2006)
27. Murota, K.: Matrices and Matroids for Systems Analysis. Springer, Berlin (2000)
28. Neel, D.L., Neudauer, N.A.: Matroids you have known. Math. Mag. **82**(1), 26–41 (2009)
29. Oxley, J.G.: Matroid Theory, vol. 3. Oxford University Press, New York (2006)
30. Pollard, A.F.C.: The Kinematical Design of Couplings in Instrument Mechanisms. Adam Hilger Limited, London (1929)
31. Reshetov, L.: Self-Aligning Mechanism, vol. 2. MIR, Moscow (1979). Translated from Russian by Sachs, L.M
32. Rosen, K.H.: Handbook of Discrete and Combinatorial Mathematics. CRC Press, Washington, D.C. (2000)
33. Shukla, G., Whitney, D.E.: The path method for analyzing mobility and constraint of mechanism and assemblies. IEEE Trans. Autom. Sci. Eng. **2**(2), 184–192 (2005)
34. Truemper, K.: Matroid Decomposition. Academic Press, London (1992)
35. Uno, T.: A new approach for speeding up enumeration algorithms and its application for matroid bases. In: Computing and Combinatorics, pp. 349–359. Springer, Heidelberg (1999). http://research.nii.ac.jp/~uno/papers/cocoon99web.pdf
36. Whitney, D.E.: Mechanical Assemblies: Their Design, Manufacture, and Role in Product Development. Oxford University Press, New York (2004)
37. Whitney, H.: On the abstract properties of linear dependence. Am. J. Math. **57**(3), 509–533 (1935). http://graal.ens-lyon.fr/~abenoit/algo09/matroids.pdf
38. Wojtyra, M., Frä, J., et al.: Comparison of selected methods of handling redundant constraints in multibody systems simulations. J. Comput. Nonlinear Dyn. **8**(2), 021, 007 (2013)
39. Wojtyra, M., Frączek, J.: Joint reactions in rigid or flexible body mechanisms with redundant constraints. Bull. Pol. Acad. Sci. Tech. Sci. **60**(3), 617–626 (2012)

Review and Classification of Workpiece Toggle Clamping Devices

Mateus Viana de Oliveira e Costa(✉), Estevan Hideki Murai, Fabíola da Silva Rosa, and Daniel Martins

Federal University of Santa Catarina, Florianópolis, Santa Catarina, Brazil
mateusvoc@gmail.com

Abstract. Clamping devices are the elements that hold the workpiece during the machine operation. Since the workpiece can have any shape, there are many types of clampings. The toggle clamps present at least two equilibrium positions and they are the focus of this study. An extensive survey in academic, patent and commercial areas was made to analyze the clamping device state of technology. The objective of this article is to propose a new classification using the results of patent and commercial survey and to develop a innovation map of these mechanisms. This new classification, together with an innovation map, can be used to aid designers when creating a new clamping device.

Keywords: Toggle clamping device · Toggle clamp classification · Clamping mechanism · Mechanism design · Creative design

1 Introduction

During the manufacturing process, the workpiece is subject to many forces. A fixture is the tool that holds the workpiece during machining operation and it is often attached to the machine table [1]. Thus, a proper fixture design is related to the desired workpiece surface finish and dimensional accuracy, which determine the product quality. So, fixture devices are able to improve both the manufacture process quality and the final product quality [2].

Cecil [3] presents a clamping design methodology for automated fixture design. In Cecil's methodology, the designer can work on dimensional synthesis after selecting the type of clamping device. However, this approach does not consider number synthesis, being limited to a given kinematic chain. This limitation reduces the technological innovation potential for new clamping devices.

In this paper a survey on commercial devices and patents of toggle clamping devices is presented. Then we propose a new classification of clamping devices based on mechanism theory. The devices found in the survey are classified according to the proposed criterion and through the use of mechanisms atlas an innovation map is generated. This map can be used to aid the designer in the development of new mechanisms. Thus, innovation can be systematically searched through the use of an innovation map.

J.C.M. Carvalho et al. (eds.), *Multibody Mechatronic Systems*,
Mechanisms and Machine Science 54, DOI 10.1007/978-3-319-67567-1_7

2 Review on Clamping Devices

2.1 Academic Survey

There are many types of clamping devices, changing according to the application and workpiece shape. Boyes [4] classifies the clamps in six basic types: strap, screw, wedge, cam, toggle and rack-and-pinion. Figure 1 shows Boyes's classification.

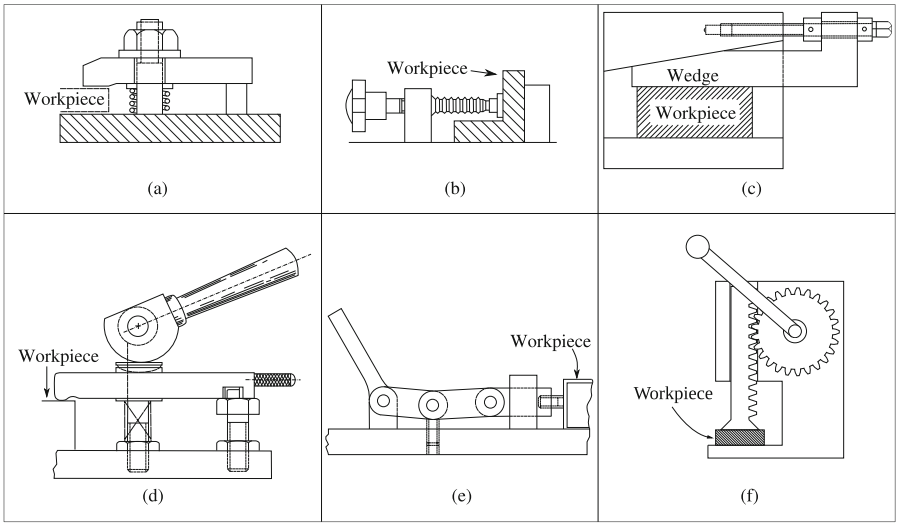

Fig. 1. Types of clamping devices: (a) strap, (b) screw, (c) wedge, (d) cam, (e) toggle, (f) rack-and-pinion. Adapted from [4].

The strap clamp is composed by a rectangular beam that contacts simultaneously the workpiece and a pivot point and is actuated by a component, such as a screw(Fig. 1a). The screw clamp acts based on the fastening of a screw attached to a fixed based (Fig. 1b). The wedge clamp is based on the motion of a inclined plane which gives the required clamping force (Fig. 1c). Cam clamps provides rapid and effective force using a cam shape piece to move the contact point and hold the workpiece (Fig. 1d). Toggle clamps are based on kinematic chains that have at least two equilibrium positions, providing heavy pressure and quick operation (Fig. 1e). The rack-and-pinion type uses the motion of a rack to transmit the clamping force (Fig. 1f) [4].

Boyes's classification aids designers in dimensional synthesis and provides a database to choose the best clamps to each application. Other authors propose similar classifications [1,2,5]. However, a classification based on working principle does not aid the designers in number synthesis stage, which is a stage with a high level of abstraction but holds a great innovation potential.

A mechanism design methodology is proposed by Yan [6] and applied to clamping devices. Yan's approach considers the clamping device in the closed position, *i.e.*, with the workpiece fixed. So, Yan searched for structures with negative mobility and three independent loops. Using enumerated techniques, 6 new design concepts were devised by Yan. Regarding Yan's methodology, it is constrained to explore kinematic chains with equal mobility and number of links and joints, reducing the search scope. However, promising and innovative solutions can exist outside those boundaries.

2.2 Commercial Clamping Devices

Seeking out to define the most significant features and characteristics of toggle clampings an extensive commercial research was made. In total 444 devices from five companies were analyzed. These devices are usually classified by the way the device secures the workpiece in four main types: hold-down, push-pull, latch and combination. In all the devices a rubber piece is used to create friction with the workpiece. The combination clamp touches the workpiece on two contact points and in more than one direction being able two hold the workpiece more precisely. These devices can be actuated by horizontal, vertical and angular handles.

The research has shown that most of the kinematic chains employed to build these devices are based in the four-bar mechanism. To build different types of clampings, companies employs several configurations for the handle, the clamping arm and the coupler. Just a few devices showed more complex kinematic chains. The major difference noticed among commercial clamps are accessories such as clamping arm spindles, quick release levers and additional locks.

2.3 Patent Survey

The patent survey was made using the search tools *Google patents* and *espacenet*. A total of 3198 patents related to clamping devices were analyzed, of which 228 were selected. A deep study extracted 41 representative patents of toggle clamps with different working principles.

This survey has shown that, similar to commercial clamping devices, most of the patents use the same working principle: four-bar linkage, Watt kinematic chain, Stephenson kinematic chain or a different inversion of the slider-crank mechanism. More details about the survey representative patents are exposed in Sect. 3.

3 Clamping Devices Classification Proposal

In this section a new classification for clamping devices is proposed, focusing on mechanism design. This classification, together with the innovation map exposed in Sect. 5, can be used to aid the designer when creating a new clamping device.

3.1 Considerations Regarding Accessories Features and Springs

Frequently, a clamping device is composed of a core mechanism responsible for the toggle locking action and accessories mechanisms which adds desirable features. Among the additional features found are adjustable fixing pressure, adjustable link size according to the workpiece size, different workpiece fixing posture, safe lock and quick release. These features are added to the core mechanism in peripheral mechanisms or by replacing a link with an adjustable link. See for instance Patent US4141543 [7], in which the possible embodiments include additional locking mechanisms using a ratchet or a pin in notch; a screw to adjust to different workpiece sizes; and push-pull or hold-down configuration. However, the core kinematic chain remains the same, a planar single-loop kinematic chain with mobility one.

Only the clamping device core is considered in this classification and accessory features are disregarded. This separates the device toggle locking action in the mechanism core from accessories features, making the design of new mechanisms easier. Also, accessories features can be added later to the new mechanism core as desired.

As the clamping device purpose is to fix a workpiece, the mechanism presents different degrees-of-freedom (DOF) from the opened to the closed position. In general, this is achieved by adding higher kinematic pairs to the kinematic chain, such as contact points, reducing the kinematic chain mobility. This is frequently associated with the singularity points at which the chain changes its configuration, such as elbow-up or elbow-down. The mechanisms are analyzed in the opened condition, so that their kinematic chains present a higher mobility.

Springs are often used in clamping devices to apply forces with a specific direction at a mechanism member. In some cases the spring function is to guarantee the kinematic pair closure, such as in patent US5527024A [8]. Springs with this function were disregarded to simplify both analysis and synthesis of new mechanism. When designing new clamping mechanisms with kinematic pairs that do not guarantee closure, the designer can add springs later to assure the pair closeness. In some cases the spring function is to reduce mobility by acting upon elements such that their positions are determined, as in patent GB2118896B [9]. In this patent, the spring length changes during the mechanism operation, allowing relative motion between the contacting elements. Thus, the spring was disregarded to obtain the mechanism mobility as it is during the device operation. Nevertheless, when designing new clamping devices with higher mobility, the designer can make use of springs to reduce the mechanism mobility on opened and closed position.

3.2 Clamping Device Classification Proposal

The clamp device classification is based on mechanism theory and the mechanisms are divided in three major classes according to their mobility:

Class M1: mechanisms in this class have mobility one. The core mechanisms in this class usually have less features. Accessories functions are done by adding

peripheral components. Examples of mechanisms in this class are patents EP128 5731B1 [10], US5921535A [11], US2744552A [12], US5647102A [13] and US6845 975B2 [14]. The product KIPP K0660, which is analyzed in Sect. 4.1, also belongs to this class.

Class M2: mechanisms in this class have mobility two. The added mobility is used to self-adjust the clamping device for different workpiece sizes or to adjust the fixing pressure. Examples of mechanisms in this class are patents GB2480434B [15], US3281140A [16] and GB2118896B [9].

Class M3: mechanisms in this class have mobility three. The core mechanisms in this class are able to self-adjust for different workpiece sizes and they present fixing pressure adjustment. The core mechanism of Bessey auto-adjust toggle clamp, as seen at patent US20100148414A1 [17], presents mobility three and the two adjustment capabilities mentioned.

It is desirable to have a device with few components to reduce manufacture and maintenance costs. Using the graph representation of a kinematic chain [18], the quantity of links (n) and the quantity of single DOF pairs (j) in a mechanism are related with the number of independent loops (ν) by the Euler's formula

$$\nu - 1 = j - n \tag{1}$$

The mechanisms can be further classified regarding their number of independent loops. Mechanisms with few links are desirable, however, in some cases loops are added to allow a different actuation. Patents US20060082040A1 [19], US5688014A [20] and US7178797B2 [21] show that an extra loop with a prismatic pair can be used to actuate the mechanism by pneumatic or hydraulic means.

Extra loops can also be used to devise a tandem holding arm, such as patent JP3671705B2 [22]; add a spring which can be used to adjust the fixing pressure, such as patent US2777347A [23]; and allow for a hold-down clamping device be used as a push-pull clamping device, such as Bessey STC-IHH15.

The core mechanism of clamping device AMF 6830 has one independent loop and mobility one, being classified as a M1L1. The mechanism from patent US68459 75B2 [14] presents two independent loops and mobility one, being classified as a M1L2. The mechanism from patent EP0163219B1 [24] has three independent loops and mobility one, belonging to class M1L3. Bessey presents two types of auto adjust toggle clamp. Patent US20100148414 A1 [17] shows the first type of Bessey auto adjust toggle clamp, here called Bessey 1. The mechanism from Bessey 1 has mobility three and one independent loop, belonging to class M3L1. Patent US20160184978A1 [25] shows the second type of Bessey auto adjust toggle clamp, here called Bessey 2. The mechanism from Bessey 2 has mobility three and four independent loops, thus, this mechanism is classified as M3L4. Analysis of Bessey 1 and 2 are exposed in Sects. 4.2 and 4.3, respectively.

Section 5 shows how this classification can be used to identify unexplored areas, which can be useful to systematically pursue innovation. Besides its application for designing new mechanisms, a classification based on mechanism theory can be easily extended, differently than a classification based on application

or working principle. As new mechanisms are developed, their core mechanisms can be analyzed and the corresponding class created.

4 Case Studies

After analyze almost 500 commercial clamping devices, the research has shown that, in a structural approach, the mechanisms available in the market are very similar and could be classified in a small number of classes. This paper summarizes theses devices into classes based on their mobility and number of independent loops. Three representative clamping device are analyzed as case studies, one for each of the following classes: M1L1, M3L1 and M3L4. As mentioned in Sect. 3, only the main kinematic chain of the device is analyzed. The motion of accessories attached to the equipment, such as clamping arm spindles, are not analyzed, since they can be added later and do not affect the core mechanism motion.

4.1 Class M1L1 - KIPP K0660

This class is composed by mechanisms with the following structural characteristics: $M = 1$ and $\nu = 1$. The most representative clamping device on this class is the KIPP K0660, a horizontal toggle clamp with flat foot and adjustable clamping spindle, which is shown in Fig. 2.

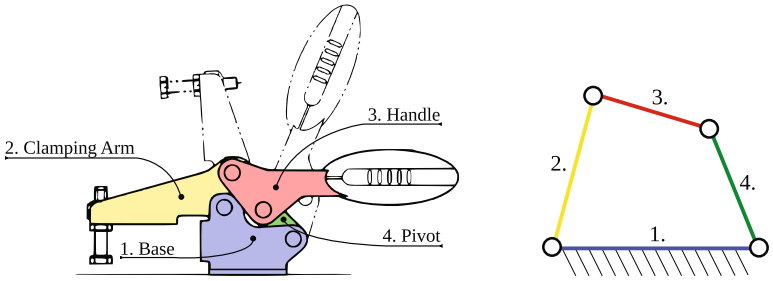

(a) Functional representation (b) Kinematic chain

Fig. 2. KIPP K0660 clamping device

This device won the 2011 iF product design award and has an special feature called KIPPlock. This feature changes the device's kinematic chain, merging links 1 and 2 into a single body by locking the rotative joint between them with a pin. The K0660 has a wide range of models, with clamping forces varying from 250 N to 2800N. The manual force needed to close the device goes from 80 N to 280N.

This toggle clamp is composed by four major elements (Fig. 2a), all connected to each other by rotative joints. The core mechanism, responsible for the toggle

action, is a four-bar linkage (Fig. 2b). The K0660's clamping principle is based on the singularity (Fig. 2a) created by the alignment of links 3 and 4, acting together with a stop surface on link 1.

4.2 Class M3L1 - Bessey 1

This class is composed by devices with a single loop and three degrees of freedom. Compared to the four-bar mechanism, the extra DOF can be used for additional features on the device. The representative device in this class is Bessey 1, the old generation of Bessey's auto-adjust toogle clamp. The three DOFs are used to execute the clamping action, the adjustment to various workpiece sizes and to change the holding force.

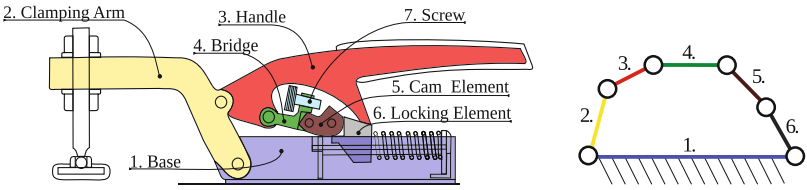

(a) Functional representation (b) Kinematic chain

Fig. 3. Bessey 1 - auto-adjust toggle clamp.

This device is divided into 6 main bodies (Fig. 3a). To achieve the holding position, with mobility 0, the device has to move through a certain number of singularity positions in the device's kinematic chain. The 3 DOFs need to be actuated only by the handle motion. The spring presented on the prismatic joint that connects the base and the pivot actuates one DOF and performs the equipment auto-adjustment capability. The second DOF is constrained from the device's kinematic chain when the cam shape of link 5 reaches the surface of link 4 (Fig. 3b), attaching those links together in one virtual link. The constant spring force and the physical connection between links 4 and 5 convert the device's kinematic chain into a single loop four bar mechanism. Thus, the last holding phase is achieved by the alignment of links 2 and the virtual link. The cam shape of link 5 also acts on the preload of the spring. The screw presented on link 5 defines which sector of the cam will affect the spring being able to change the spring preload, and thus, the clamping force.

4.3 Class M3L4 - Bessey 2

One of the most developed device found in the survey was the Bessey 2, the new generation of Bessey's auto-adjust toogle clamp. It has an auto-adjustment capability, being able to hold workpieces with various heights without any change on the adjustable clamping arm spindle. It also has a force adjustment feature,

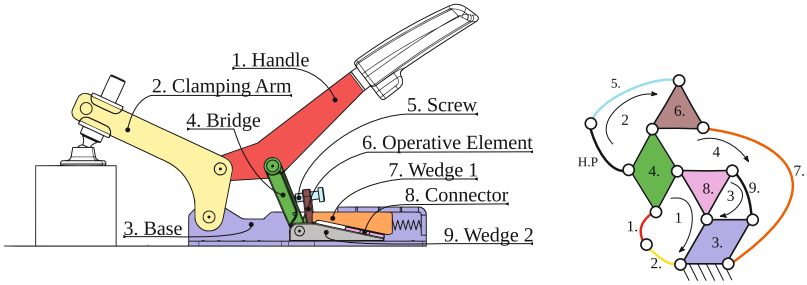

(a) Functional representation (b) Kinematic chain

Fig. 4. Bessey 2 - auto-adjust toggle clamp.

allowing the user to change the clamping force by a screw. This device is composed by 9 major components and it is the most representative member of the class with the structural characteristics: M = 3 and $\nu = 4$. The four loops that compose the device's kinematic chain can be seen in the Fig. 4. Notice that, the kinematic pairs that connects the links 3, 8 and 9 are all prismatic pairs which axes are parallel to the mechanism plane. Thus, the subchain composed of links 3, 8 and 9 are on the third special 2-system, according to Hunt [26], and this loop presents mobility 1.

The mobility 0 position is achieved by the settling of the wedges together with the singularity by alignment of the bridge element and the handle. After reaching the singularity point, if the handle is moved further, the mechanical interference with the base stops the clamping arm motion.

Loop 1. Clamping motion: it is built based on a five link kinematic chain and it has two DOF. The main components are the handle and the clamping arm. It has four revolute joints and one prismatic joint. It is actuated by the handle motion and affected by the sliding of wedge 1. After wedge 1 position is settled, the clampling will hold the workpiece when the handle and the bridge align, reaching the singularity position.

Loop 2. Force adjustment: the force adjustment capability is based on a screw that interacts with the device by a higher pair. The screw pushes the bridge element and making the operative element interact with the wedge 2 by another higher pair. The amount of screw that is screwed in affects the spring preload.

Loops 3 and 4. Reconfigurability: as said before, the screw motion (9) moves the wedge 2 through the operative element. The position of wedge 2 with respect to the base affects the wedge 1 position, changing the amount of force used to hold the workpiece. The motion of wedge 1 relative to the base also allows the device to hold different sizes of workpieces, changing loop 1 singularity point.

Although this mechanism presents more components, it also has interesting features, such as auto-adjust regarding the workpiece size and fixing pressure

adjustment. This features guarantee the same holding force while eliminating the need to manually adjust the clamping arm spindle for small variations on the workpiece size, reducing the setup time. In some cases the use of a more complex mechanism can be justified by achieving innovative designs with additional features.

5 Innovation Opportunities

Clamping devices are made to simplify the holding operation of workpieces. Devices which the core mechanism has only one DOF need manual adjustment to work with objects of various sizes. Usually this operation is done by adjusting a screw at the end of the clamping arm. The development of a clamping device with more than one DOF can allow several capabilities to the device, such as auto-adjustment.

As presented before, one of the main goals of the proposed classification is to guide the designer to new innovation opportunities in the designing of clamping devices. This strategy can lead to devices with more DOFs and more innovative devices. To build these new devices, various tools can be used as creativity sources, such as an atlas of generalized chains. For instance, the survey found only one of the 16 possible planar kinematic chains with $M = 1$ and $\nu = 3$. Figure 5 shows the remaining 15 unexplored options.

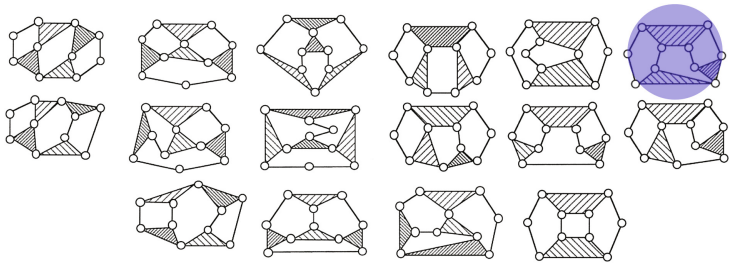

Fig. 5. Atlas of planar M1L3 chains. Adapted from [27].

Simoni et al. [28] present the quantity of possible kinematic chains for a given mobility and number of independent loops. Table 1 compares all possible kinematic chains with the configurations found in the commercial and patent surveys.

New clamping device patents can be issued with the already used kinematic chain, however, there is a great innovation potential unexplored within other structural characteristics. A more complex mechanism can be designed in exchange for additional features, which can improve the manufacturing process quality.

Table 1. Planar kinematic chains found on the survey.

M	1			2			3			
ν	1	2	3	1	2	3	1	2	3	4
Possible	1	2	16	1	3	35	1	5	74	1962
Found	1	2	1	1	1	0	1	0	0	1

6 Conclusions

This paper presented a survey on commercial devices and patents of toggle clamping mechanisms. A classification for these devices based on mechanism theory was proposed. Using the proposed criterion, it was noticed that the majority of commercial devices and patents, found in the survey, are variations of a few mechanisms. Most devices use four-bar mechanism, Watt kinematic chain, Stephenson kinematic chain or different inversions of the slider-crank mechanism.

However, a significant small amount of devices use mechanisms with a higher mobility or a higher number of independent loops. Two mechanisms with mobility three from Bessey were analyzed and it was noticed that they present auto-adjustment for different workpiece sizes and holding pressure adjustment. Thus, the use of kinematic chain with higher mobility can lead to innovative designs with additional desirable features.

The opportunities map show other kinematic chains that remain unexplored and can be used to pursue innovation. Therefore, by combining a state of the art survey, a mechanism based classification and a mechanism atlas it is possible to systematically search for innovation.

Acknowledgements. The authors would like to thank CNPq and CAPES for the financial support.

References

1. Joshi, P.H.: Jigs and Fixtures. Tata McGraw-Hill Education, New York (2010)
2. Pachbhai, S.S., Raut, L.P.: A review on design of fixtures. Int. J. Eng. Res. Gen. Sci. **2**(2), 2091–2730 (2014)
3. Cecil, J.: Computer-aided fixture design—a review and future trends. Int. J. Adv. Manuf. Technol. **18**(11), 784 (2001)
4. Boyes, W.E.: Handbook of Jig and Fixture Design. Society of Manufacturing Engineers, Dearborn (1989)
5. Hoffman, E.: Jig and Fixture Design. Cengage Learning, Cleveland (2012)
6. Yan, H.S.: Creative Design of Mechanical Devices. Springer, Singapore (1998)
7. Kato, K.: Toggle clamp device. US Patent 4,141,543 (1979)
8. Dysktra, H.: Toggle clamp with latch mechanism. US Patent 5,527,024 (1996)
9. Sweatman, O.M.: Toggle clamp locking device. GB 2,118,896 B (1982)
10. Dykstra, H.: Hold down toggle clamp. EP Patent 1,285,731 (2008)
11. Lutz, P.: Toggle clamp. US Patent 5,921,535 (1999)

12. Abraham, N.: Adjustable toggle actuated paper clamp. US Patent 2,744,552 (1956)
13. Sterling, J.: Quick release clamp. US Patent 5,647,102 (1997)
14. Tünkers, J.: Power-driven toggle-lever clamping device. US Patent 6,845,975 (2005)
15. Bishop, J.C.: Toggle clamp locking device. GB 2,480,434 B (2010)
16. Smierciak, W.: Sliding clamp. US Patent 3,281,140 (1966)
17. Poole, R., Poole, D.: Self adjusting toggle clamp. US Patent US20100148414 A1 (2010)
18. Mruthyunjaya, T.S.: Robust control of multilink flexible manipulators. Mech. Mach. Theory **38**(4), 367–377 (2003)
19. Shimizu, S., Kikuchi, N., Yurudume, T., Hoshino, H., Minagawa, T., Osaka, H., Noudou, M., Kishihara, S., Shikuwa, S.: Clamp device and clamp method for heat-treated article. US Patent App. 10/541, 331 (2006)
20. Kot, N.: Clamp having self-limiting internal overstress relief. US Patent 5,688,014 (1997)
21. Migliori, L.: Compact clamping device with side clamping member. US Patent 7,178,797 (2007)
22. Takashi, O.: Clamp device. JP 2000117574 A (2000)
23. Sendoykas, J.J.: Self-adjusting toggle clamp. US Patent 2,777,347 (1957)
24. Ehrenfied, M.: Tragplatte mit spannvorrichtung. EP Patent 0,163,219 (1988)
25. Roesch, H., Klein, T., Kloepfer, G.: Toggle clamp. US Patent 2016/0184978 A1
26. Hunt, K.H.: Kinematic Geometry of Mechanisms. Clarendon Press, Oxford (1978)
27. Tsai, L.W.: Mechanism Design: Enumeration of Kinematic Structures According to Function. CRC Press, Boca Raton (2001)
28. Simoni, R., Carboni, A., Simas, H., Martins, D.: 13th World Congress on Mechanism and Machine Science, Guanajuato, Mexico, pp. 19–25 (2011)

Supporting the Laminated Ferromagnetic Pole Pieces in a Magnetic Gear: A Structure Behaviour Analysis from a Multibody Model

M. Desvaux[1(✉)], B. Multon[1], H. Ben Ahmed[1], and S. Sire[2]

[1] SATIE Laboratory, ENS Rennes, Université Bretagne Loire, CNRS, Bruz, France
{melaine.desvaux, bernard.multon, hamid.benahmed}@ens-rennes.fr

[2] Université de Bretagne Occidentale, FRE CNRS 3744, IRDL, Brest, France
stephane.sire@univ-brest.fr

Abstract. This paper deals with the structure behaviour of a multi-bar system which maintains pole pieces in a magnetic gear. A simplified model of the system is proposed in order to be integrated in a multi-criteria global optimization for the sizing of a magnetic gear in wind power applications. For this purpose, the reduction of the computation time is taken into account. A geometry of the supporting bar is the defined and a Q bars structure is proposed. The study is based on a 1D model for each bar; variable radial and tangential magneto-mechanical pole pieces loads (generated by permanent magnets rings) are also considered. The resolution of the 6Q * 6Q system permits to determine quickly the evolution of displacements for each bar. An example of a magnetic gear with 151 pole pieces (i.e. 3,9 MW wind turbine) is proposed.

Keywords: Laminated pole pieces · Magnetic gear · Magneto-mechanical load · Multibody · Support bar

1 Introduction

Mechanical gearboxes, currently used in indirect drive electromechanical conversion chain (Fig. 1a), provide a lower capital expenditure and lower masses than the direct drive conversion chain [1] (Fig. 1b). In return, mechanical gearboxes induce production interruptions and repairs, which increase operating costs [2]. In this context, an interesting way is to develop a conversion chain with a medium-speed generator and a magnetic gear [3] (with non-contact power transmission) (Fig. 1c). The most studied topology of magnetic gears has been proposed by Martin [4] and was the subject of different behaviour studies proposed by Atallah [5].

This magnetic gear architecture shown in Fig. 2 potentially offers a higher performance with a high torque density and a high reliability than mechanical gearboxes [6] and even more for high torque applications like in high wind turbine (of the order of a few MN.m and a few MW) with only magnetic part consideration [7]. However, no magneto-mechanical sizing has been done on this magnetic gear (with an approach similar than [8] for a wind turbine generator) and it seems to have weaknesses in terms

J.C.M. Carvalho et al. (eds.), *Multibody Mechatronic Systems*,
Mechanisms and Machine Science 54, DOI 10.1007/978-3-319-67567-1_8

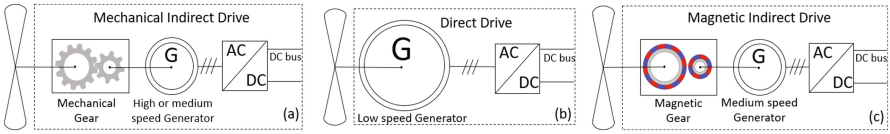

Fig. 1. Wind power conversion chains. (a) mechanical indirect drive, (b) direct drive, and (c) magnetic indirect drive

of mechanical strength which are subjected to radial and tangential loads from the magnetic field. Indeed, ferromagnetic pole pieces (see Fig. 3) are very elongated structures, laminated perpendicular to the axis of rotation (to minimize iron losses and conserve a high efficiency of the system) and subjected to magneto-mechanical loads.

The weaknesses of the poles pieces raises the question of the possibility to maintain mechanically this laminated pole pieces without lessening the magnetic properties (therefore without increasing air gaps and modifying magnetic field) in high power wind turbine applications (i.e. high dimensions and high pole numbers of the magnetic gear). It is then necessary to evaluate the stiffness of the pole pieces structure for different configurations. This evaluation must be done in a global multi-criteria mechatronic optimization.

The major contribution of this work is the definition of a multibody model of the pole pieces ring that permits to evaluate quickly the displacement generated by the magneto-mechanical variable loads. This multibody model could be integrated in a multi-criteria mechatronic optimization of a magnetic gear for wind turbine applications.

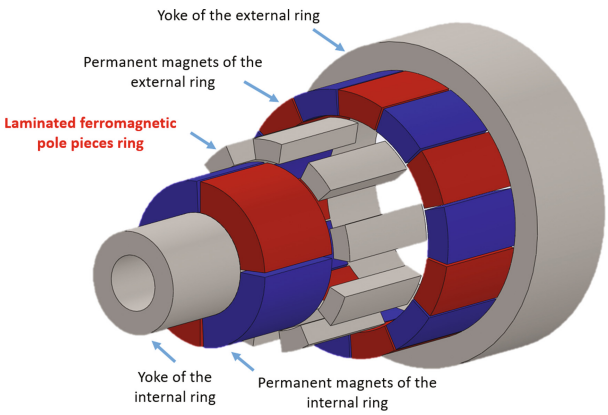

Fig. 2. Magnetic parts of the magnetic gear architecture in an exploded drawing with low pole numbers (in this example: $p_{LPN} = 2$, $p_{HPN} = 7$ and $Q = 9$).

2 Support Bars for Laminated Ferromagnetic Pole Pieces

2.1 General Principle of the Magnetic Gear

The magnetic gear is composed of three rings: a ring with p_{LPN} low pole number of pole pairs of permanent magnets and a ferromagnetic yoke, a ring with p_{HPN} high pole number of pole pairs of permanent magnets and a ferromagnetic yoke, a ring with Q ferromagnetic pole pieces (an example is given in Fig. 2 with low pole numbers, to improve readability: $p_{LPN} = 2$, $p_{HPN} = 7$ and $Q = 9$).

To achieve the power transmission, three rings pole numbers must respect Eq. (1). Depending on the fixed ring, the gear ratio G_{magn} is given by Eq. (2) where $\omega_{LPL/0}$, $\omega_{HPL/0}$ and $\omega_{Q/0}$ are the speed rotation of the internal ring (with low pole numbers), the external ring (with high pole numbers) and the pole pieces ring respectively, λ is defined in Eq. (3). For high power applications like offshore wind turbine, the number of pole increases with the diameter. A consequence can be a decrease of their rigidity.

$$p_{HPN} + p_{LPN} = Q \tag{1}$$

$$\begin{cases} \omega_{LPN/0} = 0 \rightarrow G_{magn} = \frac{\omega_{HPN/0}}{\omega_{Q/0}} = \frac{(\lambda - 1)}{\lambda} \\ \omega_{Q/0} = 0 \rightarrow G_{magn} = \frac{\omega_{LPN/0}}{\omega_{HPN/0}} = \lambda \\ \omega_{HPN/0} = 0 \rightarrow G_{magn} = \frac{\omega_{LPN/0}}{\omega_{Q/0}} = -(\lambda - 1) \end{cases} \tag{2}$$

$$\lambda = -\frac{p_{HPN}}{p_{LPN}} \tag{3}$$

2.2 Geometry of Support Bars

To support the laminated pole pieces of the magnetic gear, the support bar geometry shown in Fig. 3 is proposed. The support bar is composed of a massive magnetic insulator steel and a magnetic and electrical insulator skin. These support bars do not lessen the magnetic properties; they also do not modify the magnetic field and air gaps.

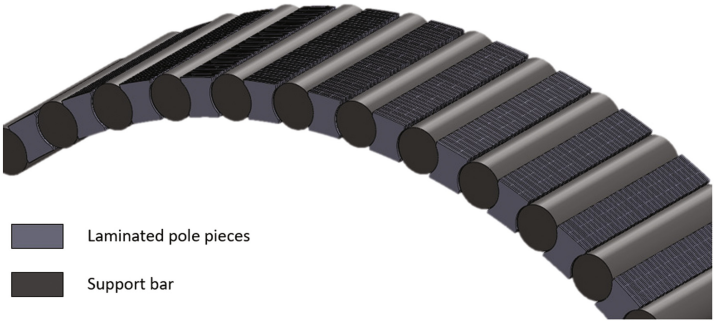

Fig. 3. Pole pieces ring with support bars (end bells are not represented)

Support bar will then transmit to the structural parts the magneto-mechanical load of the laminated pole pieces. Support bars are thus subjected to variable radial and tangential magneto-mechanical loads; their induced displacements and stresses must be then taken into account for their sizing (see [3]).

2.3 Magneto-Mechanical Loads Computation

To compute magneto-mechanical loads, it is possible to take into account exactly the exact geometry of pole pieces with a 2-D magnetic finite element model. This is shown in Fig. 4a for the magnetic field repartition of a part of the magnetic gear with $p_{LPN} = 2$, $p_{HPN} = 7$ and $Q = 9$. However, the fact of taking into account the adaptation of the geometry of the laminated pole pieces to be support by the support bars increases strongly the computation time of the magneto-mechanical loads determination. Figure 5 compares the magneto-mechanical loads obtained from a 2-D finite element magnetic model with the adapted geometry of pole pieces (presented in Fig. 4a) and with the theoretical geometry of pole pieces. This theoretical geometry of pole pieces presented in Fig. 4b induces a lower computation time of the magneto-mechanical loads since the mesh is simpler.

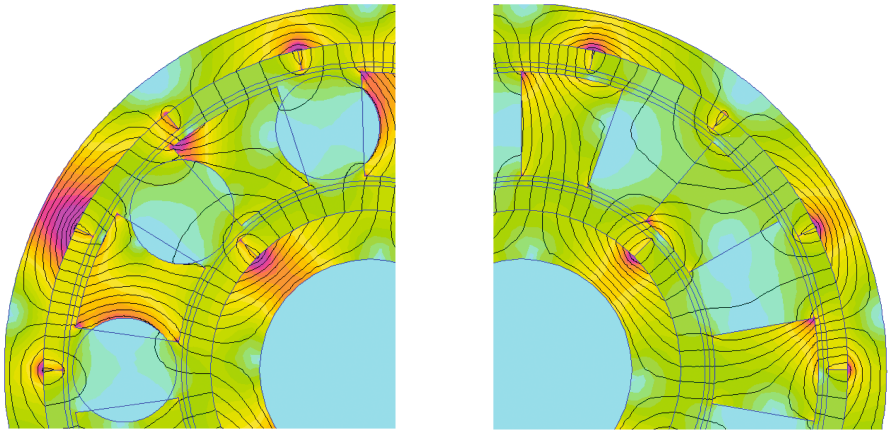

(a) (b)

Fig. 4. Magnetic field repartition obtain from 2-D finite element magnetic model with (a) the adapted geometry of pole pieces and (b) the theoretical geometry of pole pieces for the magnetic gear with $p_{LPN} = 2$, $p_{HPN} = 7$ and $Q = 9$.

The results of the comparison presented in Fig. 5 show that it is possible to compute the magneto-mechanical loads without taking into account to the adapted geometry of the pole pieces. The difference between these two models is indeed lower than 5%. The computation time is then reduced.

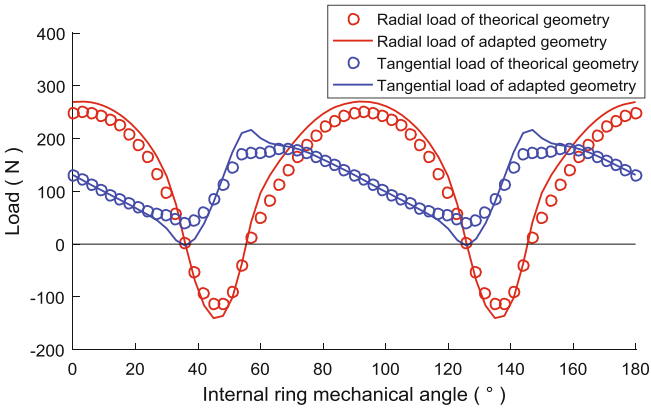

Fig. 5. Comparison between the magneto-mechanical loads obtained from a 2-D finite element magnetic model with the adapted geometry of pole pieces and with the theoretical geometry of pole pieces for a laminated pole piece of the magnetic gear (a gear with $p_{LPN} = 2$, $p_{HPN} = 7$ and $Q = 9$ is considered).

3 Multibody Model of the Pole Piece Ring

Loads that generate stresses and displacements are the magneto-mechanical radial and tangential loads ($\overrightarrow{F_r^{(q)}}$ and $\overrightarrow{F_\alpha^{(q)}}$) and the weight of the structure for the Q pole pieces and support bars (q corresponds to the number of the pole pieces, $1 \leq q \leq Q$). The geometry of the structural part of the pole pieces ring includes support bars and end bells. It is then possible to consider that a support bar is equivalent to a fixed end beam, considering that the end bells have a negligible deformation compared to support bars. Considering that the magneto-mechanical loads and the weights are applied in the middle of the pole pieces, the pole pieces ring can be modelled with the geometry described in Fig. 6a. Figure 6b defines the multibody model in the middle of the structure.

As shown in Fig. 6b, the multibody model is composed of $4Q$ bodies $S_i^{(q)}$ (with $i = 1..4$) and $4Q$ degrees of freedom ($2Q$ translation and $2Q$ rotation). The $2Q$ translations are linked to the stiffness of the support bars and the $2Q$ rotations correspond to the contacts between pole pieces and support bars. The stiffness of the support bars are determined from a fixed end beam 1-D model. The stiffness of pole pieces are considered negligible in this study because they are laminated.

This multibody model includes 8Q unknowns for each pole pieces ring. They correspond to the $2Q$ stiffnesses defined in Eq. (4), the $2Q$ fixed end reactions at the end of the support bars defined in Eq. (5) and the $4Q$ reactions from the contact between pole pieces and support bars defined in Eq. (6) as shown in Fig. 6b.

$$\begin{cases} \overrightarrow{T_x^{(q)}} = k_x^{(q)}.x^{(q)}.\overrightarrow{x_{S,q}} \\ \overrightarrow{T_y^{(q)}} = k_y^{(q)}.y^{(q)}.\overrightarrow{y_{S,q}} \end{cases} \tag{4}$$

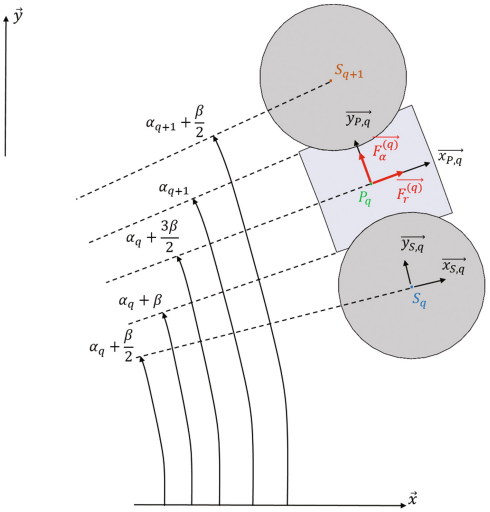

Fig. 6a. Multibody modelling of the pole pieces ring with the definition of the different bases

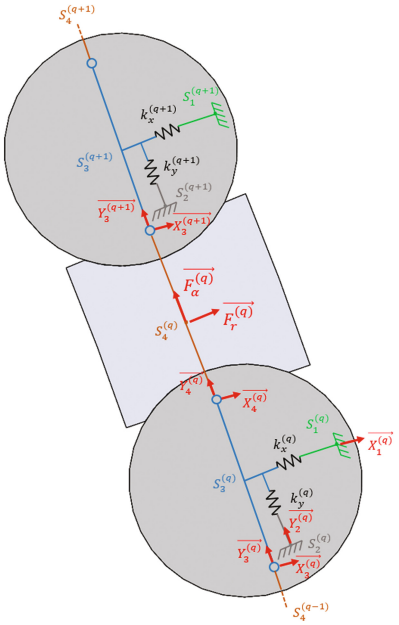

Fig. 6b. Multibody modelling of the pole pieces ring with the definition of the different loads and bodies.

$$\left\{\overrightarrow{X_1^{(q)}}, \overrightarrow{Y_2^{(q)}}\right\} \tag{5}$$

$$\left\{\overrightarrow{X_3^{(q)}}, \overrightarrow{Y_3^{(q)}}, \overrightarrow{X_4^{(q)}}, \overrightarrow{Y_4^{(q)}}\right\} \tag{6}$$

To determine the $2Q$ fixed end reaction unknowns, it is possible to consider only $S_1^{(q)}$ and determine $\overrightarrow{X_1^{(q)}}$ in function of $\overrightarrow{T_x^{(q)}}$ from the mechanical equilibrium, and consider only $S_2^{(q)}$ and determine $\overrightarrow{Y_2^{(q)}}$ in function of $\overrightarrow{T_y^{(q)}}$ from the equilibrium to obtain Eq. (7). It remains then $6Q$ unknowns to be determined. Contrary to the fixed end reaction unknowns, these $6Q$ unknowns are coupled and must be determined from $6Q$ coupled equations. Considering $S_3^{(q)}$ and then $S_4^{(q)}$, it is possible to obtain $6Q$ coupled relations from Eq. (8) where the two first equations are conditions for equilibrium (which give $4Q$ equations from projections) and the last equations are equilibrium of torque (which give $2Q$ equations). The $6Q$ coupled equations form the matrix system

defined in Eq. (9) where $[A]_{6Q,6Q}$ includes projections, $[B]_{6Q,1}$ the magneto-mechanical loads and weight and $[X]_{6Q,1}$ are the unknowns of the problem.

$$\begin{cases} Y_2^{(q)} = T_y^{(q)} \\ X_1^{(q)} = T_x^{(q)} \end{cases} \tag{7}$$

$$\begin{cases} \overrightarrow{X_4^{(q)}} + \overrightarrow{Y_4^{(q)}} + \overrightarrow{X_3^{(q+1)}} + \overrightarrow{Y_3^{(q+1)}} + \overrightarrow{F_r^{(q)}} + \overrightarrow{F_\alpha^{(q)}} + m_P^{(q)}.\vec{g} = \vec{0} \\ \overrightarrow{X_4^{(q)}} + \overrightarrow{Y_4^{(q)}} + \overrightarrow{X_3^{(q)}} + \overrightarrow{Y_3^{(q)}} + \overrightarrow{T_x^{(q)}} + \overrightarrow{T_y^{(q)}} + m_S^{(q)}.\vec{g} = \vec{0} \\ \overrightarrow{S_{q+1}S_q} \wedge \left(\overrightarrow{X_4^{(q)}} + \overrightarrow{Y_4^{(q)}} \right) + \overrightarrow{S_{q+1}P_q} \wedge \left(\overrightarrow{F_r^{(q)}} + \overrightarrow{F_\alpha^{(q)}} + m_P^{(q)}.\vec{g} \right) = \vec{0} \\ \overrightarrow{S_qS_{q+1}} \wedge \left(\overrightarrow{X_3^{(q+1)}} + \overrightarrow{Y_3^{(q+1)}} \right) + \overrightarrow{S_qP_q} \wedge \left(\overrightarrow{F_r^{(q)}} + \overrightarrow{F_\alpha^{(q)}} + m_P^{(q)}.\vec{g} \right) = \vec{0} \end{cases} \tag{8}$$

$$[A]_{6Q,6Q} * [X]_{6Q,1} = [B]_{6Q,1} \tag{9}$$

The last $6Q$ unknowns can be determined from a numerical resolution with an inversion of $[A]_{6Q,6Q}$ which permits to obtain the displacements in the middle of each support bar. Figure 7a shows the displacements of the support bars generated by the magneto-mechanical loads; Fig. 7b shows the displacements generated by the weight with a coefficient of amplification for the magnetic gear studied in [3]. For this magnetic gear, the maximum calculated radial displacement is 0.5 mm.

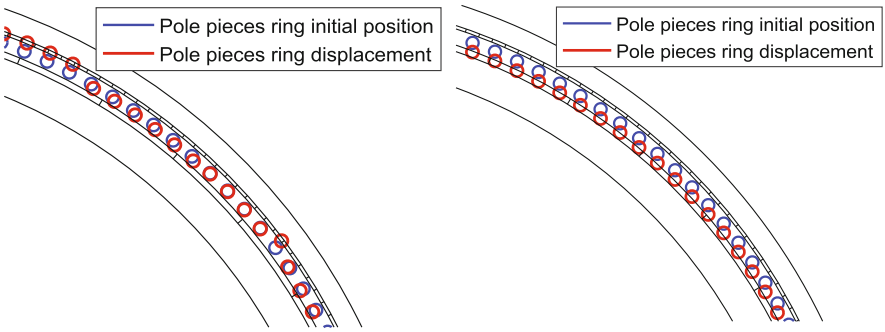

Fig. 7. Support bars displacements obtained from the multibody model (with a coefficient of amplification) generated by (a) the magneto-mechanical loads and (b) the weight, for the magnetic gear studied in [3].

4 Loose Coupling Mechatronic Resolution Procedure

The multibody model presented above aims to be integrated in a mechatronic multi-criteria optimization procedure. In this paper, we evaluate support bar displacements considering an acceptable computation time. In order to evaluate the computation time of the problem resolution and to verify if the model is adapted for the mechatronic resolution procedure, an example of the procedure progress is given for the magnetic gear [3] shown in Fig. 8. This magnetic gear includes 151 pole pieces.

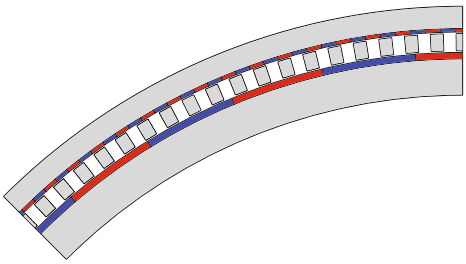

Fig. 8. Magnetic parts of the 3.9 MW and 15 rpm magnetic gear with $p_{LPN} = 20$, $p_{HPL} = 131$ and $Q = 151$, external diameter 3.8 m and active length 2 m.

Figure 9 describes the mechatronic optimization procedure that begins with an initial set of computation parameters. A 2-D magnetostatic computation can then be conducted from a finite element model or an analytical model [9]. This analysis provides the magneto-mechanical loads evolution which includes radial and tangential loads of pole pieces. From this computation, several criteria (objective functions and constraints) can be evaluated like magnetic losses or pole pieces ring displacement (this displacement can be considered as a constraint not to be exceed or an objective

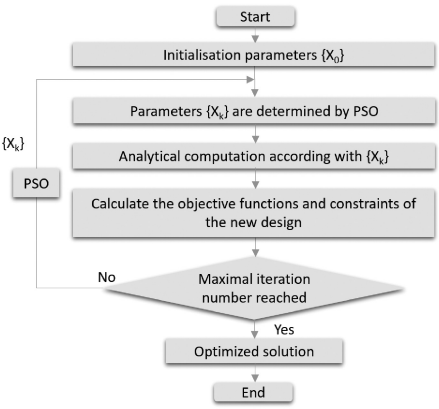

Fig. 9. Mechatronic optimization procedure description [3].

function to be minimized). This resolution procedure is then based on the hypothesis of a loose coupling between magneto-mechanical loads and displacement of pole pieces. To complete this optimization procedure, a Particle Swarm Optimization (PSO) algorithm [10] is computed.

The multibody model described above is then integrated in the mechatronic optimization procedure (block dedicated to the criteria evaluation). For the magnetic gear example [9], it is then possible to compute the evolution of the displacement of every support bars of the pole pieces ring. Figure 10 shows the evolution of the radial and tangential displacements of a support bar due to the magneto-mechanical loads and the weight of the structure with a constant rotational speed of 15 rpm for the external ring and 100 rpm for the internal ring.

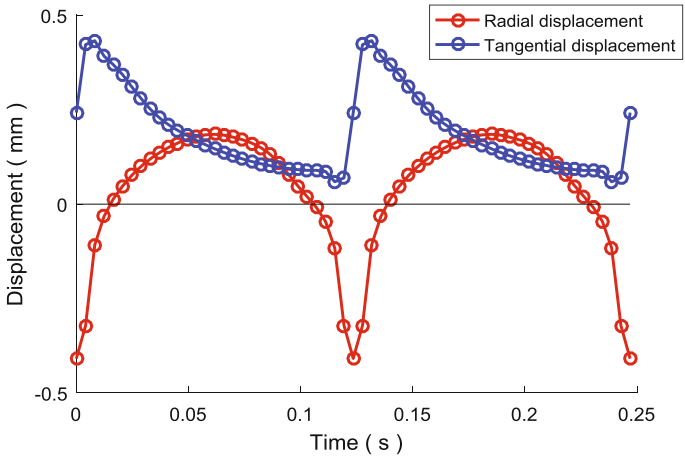

Fig. 10. Evolution of the radial and tangential displacements of a support bar due to the magneto-mechanical loads and the weight for the magnetic gear [3] with a constant rotational speed of 15 rpm for the external ring and 100 rpm for the internal ring.

Figure 10 shows a periodicity T of the radial a tangential displacements. This periodicity is generated by magneto-mechanical loads and corresponds to the periodicity of the permanent magnetic rings which depends on the rotational speed and the pole pair configuration of the rings as shown in Eq. (10).

$$T = \frac{2\pi}{p_{LPN}.\omega_{LPN/0}} = \frac{2\pi}{p_{HPN}.\omega_{HPN/0}} \tag{10}$$

For the magnetic gear described in [3], the computation time of the displacements for a single position of the different rings is equal to 0.03 s (with an Intel Xeon E5-1630 v3, 8 threads, 3.70 GHz) for all of the support bars. If the displacement evolution is computed for 30 positions of the permanent magnet rings, this multibody model then permits to perform the computation in approximately 1 s. This computation time value is then lower than every finite element mechanical model tested and is

acceptable for the 24 h multi-criteria mechatronic optimization procedure composed of approximately 200 particles and 100 iterations.

5 Conclusions

This paper presents a multibody model developed to evaluate displacements of a multi-bar structure that maintains laminated pole pieces of a magnetic gear. This model aims to be integrated in a multi-criteria mechatronic optimization for the sizing of a magnetic gear for wind power applications. This procedure needs to compute the support bar displacements quickly. The resolution of a 6Q * 6Q system permits to determine the evolution of displacements in 1 s for a magnetic gear with 151 pole pieces (i.e. 3,9 MW magnetic gear adapted for a wind turbine). The displacement evolution computed from the multibody model will permit to evaluate different sizing criteria like stress limit in pole pieces ring or maximal displacement tolerated in air-gaps. In prospect, the hypothesis of loose coupling between the magneto-mechanical loads and the displacement of pole pieces must be analyzed to validate the mechatronic resolution procedure.

References

1. Lacal Arántegui, R., Serrano Gonzáles, J.: 2014 JRC wind status report: Technology, market and economic aspects of wind energy in Europe (2015)
2. Keller, J., Guo, Y., Sethuraman, L.: Gearbox Reliability Collaborative Investigation of Gearbox Motion and High-Speed-Shaft Loads, NREL, Technical report TP-5000-65321 (2016)
3. Desvaux, M., et al.: Design and optimization of magnetic gears with arrangement and mechanical constraints for wind turbine applications. In: 2016 11th International Conference on Ecological Vehicles and Renewable Energies, EVER 2016 (2016)
4. Martin, T.B.: Magnetic transmission, Pat. US3378710 (1968)
5. Atallah, K., Howe, D.: A novel high-performance magnetic gear. IEEE Trans. Magn. **37**(4), 2844–2846 (2001)
6. Gouda, E., Mezani, S., Baghli, L., Rezzoug, A.: Comparative study between mechanical and magnetic planetary gears. IEEE Trans. Magn. **47**(2), 439–450 (2011)
7. Matt, D., et al.: Design of a mean power wind conversion chain with a magnetic speed multiplier. In: Advances in Wind Power, Chap. 10, pp. 247–266. InTech Book (2012)
8. Zavvos, A., Mcdonald, A.S., Mueller, M.: Structural optimisation tools for iron cored permanent magnet generators for large direct drive wind turbines. In: IET Conference on Renewable Power Generation (RPG 2011) (2011)
9. Desvaux, M., Traullé, B., Latimier, R.L.G., Sire, S., Multon, B., Ben Ahmed, H.: Computation time analysis of the magnetic gear analytical model. IEEE Trans. Magn. **53**(5), 1–10 (2017)
10. Niu, S., et al.: Design optimization of magnetic gears using mesh adjustable finite-element algorithm for improved torque. IEEE Trans. Magn. **48**(11), 4156–4159 (2012)

Kinematic Analysis

Kinematic Analysis for a Planar Redundant Serial Manipulator

Zijia Li(✉), Mathias Brandstötter, and Michael Hofbaur

Institute for Robotics and Mechatronics, Joanneum Research, Lakeside B08a, EG, 9020 Klagenfurt am Wörthersee, Austria
{zijia.li,mathias.brandstoetter,michael.hofbaur}@joanneum.at

Abstract. A planar serial manipulator with three rotational joints (planar 3R) can be seen to be a kinematically redundant system if only the position of the end-effector is taken into account. Configuration sets of serial manipulators of planar 3R will be considered in this work in detail. The configuration set is the solution set of all rotational joint angles (actually, we use the tangent of the half-angle) fulfilling the kinematic mapping. Then the configuration set will be an algebraic set if we fix the end-effector or the end-effector follows algebraic motions (for instance, algebraic curves in the special Euclidean group). We show the characteristic of configuration curves among the workspace in terms of the number of real connected components. The configuration curve has either one connected component or two connected components. Furthermore, we also studied the torque variation among the real connected components of the configuration set.

Keywords: Planar 3R · Torque · Gröbner Basis · Real connected components · Discriminant

1 Introduction

A kinematically redundant manipulator [1,24] has more joints (degrees of freedom) than required to execute its task. These extra degrees of freedom may be used to avoid collisions [16] and joint limits [4], but also to minimize joint torques [10]. This so-called redundancy resolution is mainly done through numerical computational methods. In this work we are more interested in the symbolic and geometrical redundancy solutions, e.g., [14,15,20,22,24]. The obtained results are extensive, hence, the interested reader is referred to [5,25,26]. Since we only consider rotational joints in this paper we follow the algebraic kinematics setting from [3,11,12].

A pose for the end-effector is the position and orientation of the end-effector, it is an element in special Euclidean group SE(3). For a fixed pose of the end-effector (when we fix the end-effector in space), a redundant serial manipulator

This research was funded by the Austrian Ministry for Transport, Innovation and Technology (BMVIT) within the framework of the sponsorship agreement formed for 2015–2018 under the project RedRobCo.

J.C.M. Carvalho et al. (eds.), *Multibody Mechatronic Systems*,
Mechanisms and Machine Science 54, DOI 10.1007/978-3-319-67567-1_9

will become a closed linkage which is a mechanical structure that consists of a finite number of rigid bodies and a finite number of joints that connect the links cyclically together. A sequence of joint angles is called a configuration for a closed linkage when one can connect the links following the rotation angles cyclically to form a loop. One configuration specifies a posture of the redundant manipulator. In other words, the posture depends on the sequence of joint angles (or the tangent of the half the joint angle) for a serial manipulator. By computational algebraic geometry, the set of all such configurations for a pose belong to an algebraic set (algebraic variety). For redundant serial manipulators, there are infinitely many configurations that can achieve the same end-effector pose. In other words, the variety is at least a one dimensional set.

It is known that redundant serial manipulators might not return to the same posture when its end-effector follows a closed trajectory [19]. So the question is, can we bring back the manipulator to the initial posture that it was in the beginning? The answer is "It depends!". Namely, it depends on the pose and the posture. Moreover, moving the manipulator to the same posture from another one without changing the end-effector pose might be not possible if two postures are in different real connected components of the variety of the configurations.

Hence, the question on when the manipulator is possible to return can be asked. Finding the answer on this question depends on further circumstances that arise in practice, e.g., joint limits of the rotational joints or self-collision (the manipulator collides with a part of itself). Both of these mechanical restrictions are complicate to study symbolically. In this paper we skip these real issues. Then only the number of real connected components of the varieties of configurations is crucial for this question. Namely, it might not be possible to return to the initial posture if the number of real connected components is bigger than 1. We study the configuration set of a redundant planar 3R serial manipulator to show this variation for its whole workspace (only in position, hence, orientation is ignored). The configuration set for a planar 3R serial manipulator with a fixed position of the end-effector is just a configuration curve for a single closed loop of planar 4R linkage. The maximal number of real connected components is 2 [23]. Furthermore, the Grashof condition can also give the answer: If the sum of the shortest and longest link of a planar quadrilateral linkage is less than or equal to the sum of the remaining two links, then the shortest link can rotate fully with respect to a neighboring link [7]. Namely, a closed planar 4R fulfilling Grashof condition has two connected components for its configuration curve. If a closed planar 4R does not fulfill the Grashof condition, its configuration curve has only one real branch. It should be mentioned, that we will consider only a 1-dof branch; the isolate configuration is not of interest for us.

Furthermore, the torque generated by a force at the end-effector depends on the configuration (posture) as well. We present torque variations for the redundant planar 3R among the connected components. It shows that minimum torques in two connected components can be different.

2 Preliminary Notations

In the beginning, we first recall several classical concepts and definitions followed from [8,9,17]: dual quaternions, the Study quadric, and the forward kinematics mapping.

We denote by SE(3) the group of Euclidean displacements, i.e., the group of maps from $\mathbb{R}^3$ to itself that preserve Euclidean distances and orientation.

We denote by $\mathbb{D} := \mathbb{R} + \epsilon\mathbb{R}$ the ring of dual numbers, with multiplication defined by $\epsilon^2 = 0$. The algebra $\mathbb{H}$ is the non-commutative algebra of quaternions, and $\mathbb{DH} := \mathbb{D} \otimes_{\mathbb{R}} \mathbb{H}$. The conjugate dual quaternion $\overline{h}$ of h is obtained by multiplying the vectorial part of h by -1.

By projectivizing $\mathbb{DH}$ as a real 8-dimensional vector space, we obtain $\mathbb{P}^7$. The condition that $h\overline{h}$ is strictly real, i.e., its dual part is zero, is a homogeneous quadratic equation. Its zero set, denoted by S, is called the Study quadric. The linear 3-space represented by all dual quaternions with zero primal part is denoted by E and is contained in the Study quadric. The complement $S - E$ is closed under multiplication and multiplicative inverse and therefore forms a group, which is isomorphic to SE(3) (see [13, Sect. 2.4]).

The structural design of manipulators is determined by its geometrical invariants of Denavit-Hartenberg parameters [6], i.e., twist angles, orthogonal distances and offsets. However, once the manipulator is assembled, we know all the rotation axes. A nonzero dual quaternion h represents a rotation (around an axis) if and only if $h\overline{h}$ and $h + \overline{h}$ are strictly real and its primal vectorial part is nonzero.

We give a formulation of the forward kinematics in the language of dual quaternions, based on the fact that SE(3) is isomorphic to the multiplicative group of dual quaternions with nonzero real norm modulo multiplication by nonzero real scalars. In the isomorphism described in [13, Sect. 2.4], the rotation with axis determined by $\mathbf{i}$ and angle q correspond to the dual quaternion $(\cos(\frac{q}{2}) - \sin(\frac{q}{2})\mathbf{i})$, which is projectively equivalent to $(1 - \tan(\frac{q}{2})\mathbf{i})$. So the forward kinematics mapping is

$$(1 - t_1 h_1)(1 - t_2 h_2) \cdots (1 - t_n h_n) \equiv h_e, \tag{1}$$

where $h_1, \ldots, h_n$ are dual quaternions specifying the rotation axes in the initial position of the robot, h_e is a dual quaternion specifying a pose of the end-effector, "$\equiv$" means projectively equivalent. For simplicity, we will use (1) from now on. The set G of all n-tuple $(t_1, \ldots, t_n) \in (\mathbb{P}^1)^n$ fulfilling (1) is called the *configuration set* (inverse kinematics) of the robot arm with respect to a fixed pose h_e. In order to solve (1), we multiply it with the conjugate of h_e from both side. We expand both sides into 8 dimensional vectors which gives us a system of equations.

3 Planar 3R Serial Manipulators

In the planar case, dual quaternions specifying the rotation axes with same directions can be written in a simpler form, e.g., as $h_1 = \mathbf{k} + \epsilon\mathbf{i}$, $h_2 = \mathbf{k} + \epsilon\mathbf{j}$.

The global geometric structure of a redundant planar 3R serial manipulator (see Fig. 1a), where only the position of the end-effector is analyzed, is considered in the following example.

Example 1

$$h_1 = \mathbf{k}, \quad h_2 = \mathbf{k} + d_1\epsilon\mathbf{j}, \quad h_3 = \mathbf{k} + (d_1 + d_2)\epsilon\mathbf{j}$$

Here, d_i denotes the length of the i-th link of the robot arm. Then the forward kinematics will be

$$(1 - t_1h_1)(1 - t_2h_2)(1 - t_3h_3) \equiv h_e.$$

The position of the end-effector will also depend on the distance d_3, which is the distance from the end-effector position P to the third joint axis. If we only consider the position of a planar manipulator, there are only two equations with respect to the two planar coordinates. By any given trajectory of the end-effector with $h_e = p_e + \epsilon q_e$ [18], the home position of the end-effector point P represented by $1 + (d_1 + d_2 + d_3)\mathbf{i}$ is mapped according to

$$x \mapsto p_e\overline{p_e} + p_e(d_1 + d_2 + d_3)\mathbf{i}\overline{p_e} + 2p_e\overline{q_e}.$$

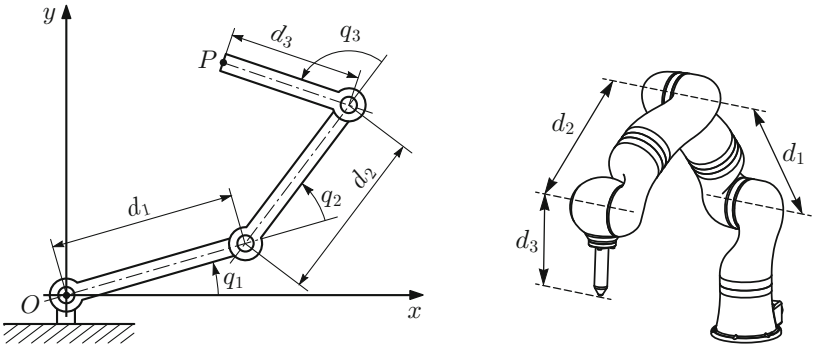

(a) Planar 3R manipulator. (b) KUKA LBR iiwa.

Fig. 1. Parameter definition of different manipulators.

For a reachable position, e.g., (x, y), of the end-effector (P is within the manipulators workspace) two equations define the inverse kinematics:

$$\begin{aligned}
&d_1t_1^2t_2^2t_3^2 - d_2t_1^2t_2^2t_3^2 + d_3t_1^2t_2^2t_3^2 + t_1^2t_2^2t_3^2x + d_1t_1^2t_2^2 + d_1t_1^2t_3^2 - d_1t_2^2t_3^2\\
&- d_2t_1^2t_2^2 + d_2t_1^2t_3^2 + 4d_2t_1t_2t_3^2 + d_2t_2^2t_3^2 - d_3t_1^2t_2^2 - 4d_3t_1^2t_2t_3 - d_3t_1^2t_3^2\\
&- 4d_3t_1t_2^2t_3 - 4d_3t_1t_2t_3^2 - d_3t_2^2t_3^2 + t_1^2t_2^2x + t_1^2t_3^2x + t_2^2t_3^2x + d_1t_1^2 - d_1t_2^2\\
&- d_1t_3^2 + d_2t_1^2 + 4d_2t_1t_2 + d_2t_2^2 - d_2t_3^2 + d_3t_1^2 + 4d_3t_1t_2 + 4d_3t_1t_3\\
&+ d_3t_2^2 + 4d_3t_2t_3 + d_3t_3^2 + t_1^2x + t_2^2x + t_3^2x - d_1 - d_2 - d_3 + x = 0,\\
&t_1^2t_2^2t_3^2y + 2d_1t_1t_2^2t_3^2 - 2d_2t_1^2t_2t_3^2 - 2d_2t_1t_2^2t_3^2 + 2d_3t_1^2t_2^2t_3 + 2d_3t_1^2t_2t_3^2\\
&+ 2d_3t_1t_2^2t_3^2 + t_1^2t_2^2y + t_1^2t_3^2y + t_2^2t_3^2y + 2d_1t_1t_2^2 + 2d_1t_1t_3^2 - 2d_2t_1^2t_2\\
&- 2d_2t_1t_2^2 + 2d_2t_1t_3^2 + 2d_2t_2t_3^2 - 2d_3t_1^2t_2 - 2d_3t_1^2t_3 - 2d_3t_1t_2^2 - 8d_3t_1t_2t_3\\
&- 2d_3t_1t_3^2 - 2d_3t_2^2t_3 - 2d_3t_2t_3^2 + t_1^2y + t_2^2y + t_3^2y + 2d_1t_1\\
&+ 2d_2t_1 + 2d_2t_2 + 2d_3t_1 + 2d_3t_2 + 2d_3t_3 + y = 0.
\end{aligned}$$

To avoid higher dimensional complex solutions, we use the inequality $(t_1^2+1)(t_2^2+1)(t_3^2+1) \neq 0$. With a Gröbner Basis approach, we can solve the system (two equations and the inequality) by adding a new variable (u) and a new equation: $(t_1^2+1)(t_2^2+1)(t_3^2+1)u - 1 = 0$ (Rabinowitsch trick). The projection to variable t_1, t_2, t_3 gives us the solution. Furthermore, we can do some projection with this solution for inspecting geometric properties. For instance, we project this curve to t_1, t_2 plane (with parameters d_1, d_2, d_3, x, y). Then we get

$$\begin{aligned}
&d_1^2t_1^2t_2^2 - 2d_1d_2t_1^2t_2^2 + 2d_1t_1^2t_2^2x + d_2^2t_1^2t_2^2 - 2d_2t_1^2t_2^2x - d_3^2t_1^2t_2^2 + t_1^2t_2^2x^2\\
&+ t_1^2t_2^2y^2 + 4d_1t_1t_2^2y - 4d_2t_1^2t_2y - 4d_2t_1t_2^2y + d_1^2t_1^2 + d_1^2t_2^2\\
&+ 2d_1d_2t_1^2 - 2d_1d_2t_2^2 + 2d_1t_1^2x - 2d_1t_2^2x + d_2^2t_1^2 + d_2^2t_2^2 + 2d_2t_1^2x \qquad (2)\\
&+ 8d_2t_1t_2x + 2d_2t_2^2x - d_3^2t_1^2 - d_3^2t_2^2 + t_1^2x^2 + t_1^2y^2 + t_2^2x^2 + t_2^2y^2 + 4d_1t_1y\\
&+ 4d_2t_1y + 4d_2t_2y + d_1^2 + 2d_1d_2 - 2d_1x + d_2^2 - 2d_2x - d_3^2 + x^2 + y^2 = 0.
\end{aligned}$$

Let us calculate the discriminants Δ_1 of the Eq. (2). First, the discriminant with respect to t_1 (the result is a polynomial of degree 4) can be computed to be

$$\begin{aligned}
\Delta_1 = &-4d_1^4t_2^4 + 16d_1^3d_2t_2^4 - 24d_1^2d_2^2t_2^4 + 8d_1^2d_3^2t_2^4 + 8d_1^2x^2t_2^4 + 8d_1^2y^2t_2^4\\
&+16d_1d_2^3t_2^4 - 16d_1d_2d_3^2t_2^4 - 16d_1d_2x^2t_2^4 - 16d_1d_2y^2t_2^4 - 4d_2^4t_2^4\\
&+ 8d_2^2d_3^2t_2^4 + 8d_2^2x^2t_2^4 + 8d_2^2y^2t_2^4 - 4d_3^4t_2^4 + 8d_3^2x^2t_2^4 + 8d_3^2y^2t_2^4\\
&- 4x^4t_2^4 - 8x^2y^2t_2^4 - 4y^4t_2^4 - 8d_1^4t_2^2 + 16d_1^2d_2^2t_2^2 + 16d_1^2d_3^2t_2^2\\
&+ 16d_1^2x^2t_2^2 + 16d_1^2y^2t_2^2 - 8d_2^4t_2^2 + 16d_2^2d_3^2t_2^2 + 16d_2^2x^2t_2^2 + 16d_2^2y^2t_2^2\\
&- 8d_3^4t_2^2 + 16d_3^2x^2t_2^2 + 16d_3^2y^2t_2^2 - 8x^4t_2^2 - 16x^2y^2t_2^2 - 8y^4t_2^2\\
&- 4d_1^4 - 16d_1^3d_2 - 24d_1^2d_2^2 + 8d_1^2d_3^2 + 8d_1^2x^2 + 8d_1^2y^2 - 16d_1d_2^3\\
&+ 16d_1d_2d_3^2 + 16d_1d_2x^2 + 16d_1d_2y^2 - 4d_2^4 + 8d_2^2d_3^2 + 8d_2^2x^2\\
&+ 8d_2^2y^2 - 4d_3^4 + 8d_3^2x^2 + 8d_3^2y^2 - 4x^4 - 8x^2y^2 - 4y^4.
\end{aligned}$$

Second, the discriminant Δ_2 with respect to t_2 of Δ_1 is

$$\begin{aligned}\Delta_2 = 294967296(x^2+y^2)^2 d_3^4 d_2^4 d_1^4((d_1+d_2-d_3)^2-(x^2+y^2))\\ ((d_1-d_2-d_3)^2-(x^2+y^2))((d_1-d_2+d_3)^2-(x^2+y^2))\\ ((d_1+d_2+d_3)^2-(x^2+y^2)).\end{aligned}$$

Remark 1. *One can see that x^2+y^2 is the link length of 4th link if we consider the planar serial 3R as a closed planar 4R linkage. Then the link length gives us the sign of the last discriminant. One can prove (by studying the sign change of the first discriminant) that the positive Δ_2 gives us 2 real connected components and a negative Δ_2 gives us 1 or 0 (depending on the workspace) real connected components.*

By Remark 1 we are able to draw the areas (rings) that corresponds to the number of connected components of the configuration curve. Here we use the link lengths of two different classes of industrial robots, the KUKA LBR iiwa and the Universal Robot variants, all of them used in a planar configuration. An example can be seen in Fig. 1b. By ignoring the other Denavit-Hartenberg parameters due to the planar operation of the robots, we list the reduced parameters d_1, d_2, d_3 (mm) in Table 1 to generate planar 3R.

Table 1. Reduced Denavit-Hartenberg parameters (mm).

Robot	d_1	d_2	d_3
KUKA LBR iiwa 7	400	400	126
KUKA LBR iiwa 14	420	400	126
UR3	243.65	213.25	85.35
UR10	612	572.3	115.7

Remark 2. *In Figs. 2 and 3, the green rings are the areas (the position of the end-effector) where only one real branch for the configuration curve (they are all in the workspace) exists; the red rings are the areas where two real connected components for the configuration curve are feasible.*

Remark 3. *It is known that the Denavit-Hartenberg parameters of KUKA LBR iiwa 7 and KUKAiiwa 14 are slightly different. One can realize that the number of rings changes with the variation of Denavit-Hartenberg parameters. Namely, in the left figure of Fig. 3 (corresponding to KUKA LBR iiwa 7), one ring is missing comparing to the right figure. The reason is that some of the radii (absolute values) $\gamma_1, \gamma_2, \gamma_3, \gamma_4$ can be equal, where $\gamma_1 = |d_1+d_2-d_3|$, $\gamma_2 = |d_1-d_2-d_3|$, $\gamma_3 = |d_1-d_2+d_3|$, $\gamma_4 = |d_1+d_2+d_3|$. In general, we should have four different circles with respect to four radii. However, for the Denavit-Hartenberg parameters of KUKA LBR iiwa 7, we only have three different circles because $\gamma_2 = \gamma_3$.*

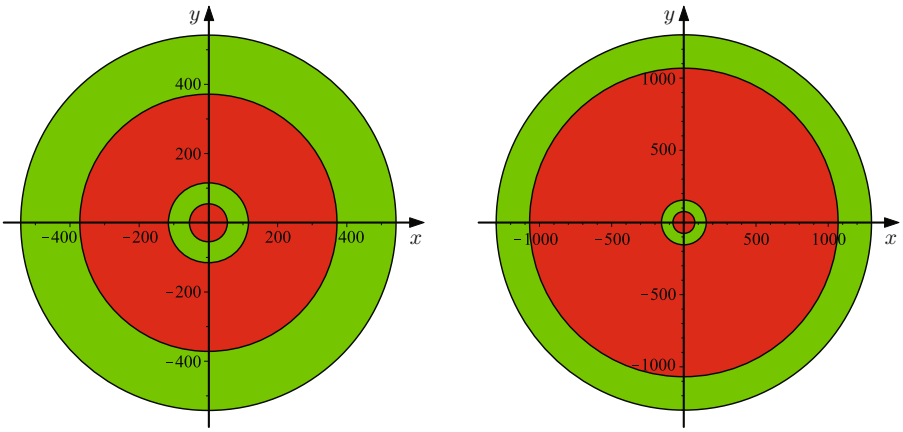

Fig. 2. Number of real connected components variation for (planar) Universal Robots UR3 (left) and Universal Robots UR10 (right). (Color figure online)

4 Torque Variation Among Different Configurations

The well known torque function $\tau = J^T F$ for planar serial manipulators [2,21] shows that the torque depends on the posture and the direction of the force, where J is the kinematics Jacobian matrix with only focusing on the position part, F is the force, τ is the torque vector that corresponds to the torques of each rotational joint.

The torque variation (vertical coordinate) in Fig. 4 shows that the minimum can be reached. In Fig. 5, we can see that the minimum of the torque variation

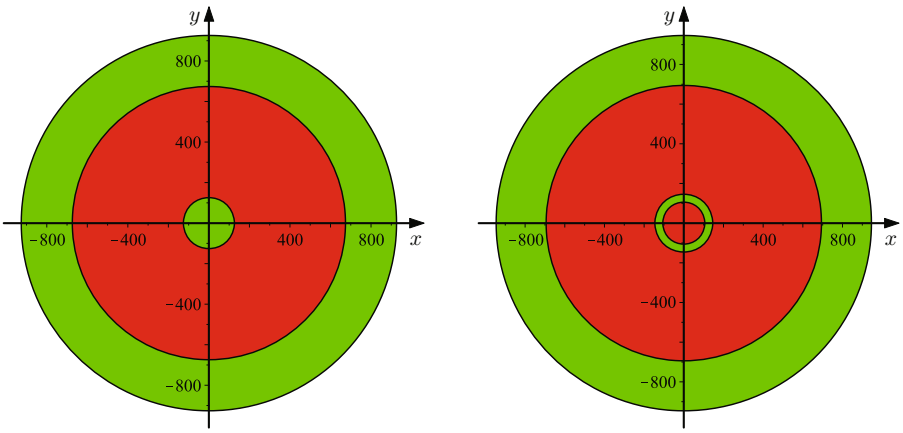

Fig. 3. Number of real connected components variation for (planar) KUKA LBR iiwa 7 (left) and KUKA LBR iiwa 14 (right). (Color figure online)

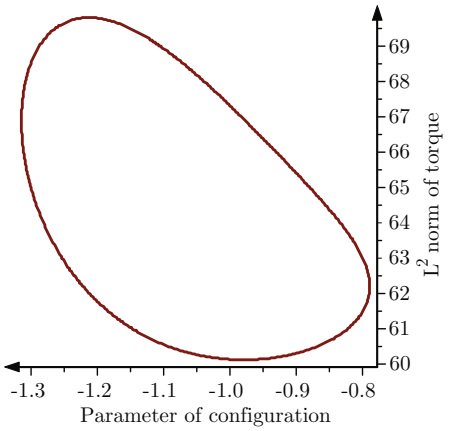

Fig. 4. Torque variations among the configuration curve with a pose such that there is only one real branch.

(vertical coordinate) among the two connected components is different. Here, the Euclidean norm of the torque is our objective function for showing the variation among all the configurations (parameter as horizontal coordinate) with a fixed position. We draw the Figs. 4 and 5 using a discretization of the configuration curves.

5 Discussion of Results and Future Research

The motivation for studying a computational, algebraic, geometrical framework for redundant serial manipulators was to look deep inside of the projective algebraic varieties (or manifold) respective algebraic tasks from a geometrical variation point (this is less studied) instead of a dynamics optimal point (this is more

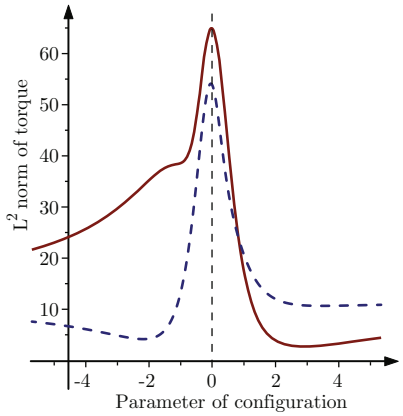

Fig. 5. Torque variations among the configuration curve with a pose such that there are two real connected components (the solid curve and the dashed curve).

and well studied). A deep investigation of a configuration set (variety) for the redundant manipulators can tell us some interesting facts from a geometric point of view by using knowledge from computational algebraic geometry. A variation of this information will provide a thorough understanding of manipulators. Here we mainly focused on planar 3R serial manipulators which are redundant when the orientation of the end-effector is neglected. However, the redundant planar 4R serial manipulator (when position and orientation is considered) is equivalent to the previous case in terms of configuration level. It is also simpler when we study the 1-D (redundant) configuration set (configuration curve). For instance, the decomposition of the real computation is easier when we study the curve instead of surface or even higher dimensional varieties. We show the determination of number of real connected components by using the discriminant of univariate polynomials. Through the study of the planar 3R, we can see that the global geometric analysis is important for understanding the redundancy. Even the local (with a fixed pose) minimization of torque might not be able to reach the global minimization because of the disconnected two real connected components of the configuration set.

Acknowledgements. We would like to thank Andrés Kecskeméthy (University of Duisburg-Essen), Josef Schicho (University of Linz) and Hans-Peter Schröcker (University Innsbruck) for the fruitful discussions.

References

1. Angeles, J., Fundamentals of Robotic Mechanical Systems, vol. 2. Springer, Berlin (2002)
2. Asada, H., Slotine, J.J.: Robot Analysis and Control. Wiley, New York (1986)
3. Brunnthaler, K., Schröcker, H.P., Husty, M.: A new method for the synthesis of Bennett mechanisms. In: Proceedings of CK 2005, International Workshop on Computational Kinematics, Cassino (2005)
4. Chan, T.F., Dubey, R.V.: A weighted least-norm solution based scheme for avoiding joint limits for redundant joint manipulators. IEEE Trans. Robotics Autom. **11**(2), 286–292 (1995)
5. Chiaverini, S., Oriolo, G., Walker, I.D.: Kinematically Redundant Manipulators, pp. 245–268. Springer, Heidelberg (2008)
6. Denavit, J., Hartenberg, R.S.: A kinematic notation for lower-pair mechanisms based on matrices. Trans. ASME J. Appl. Mech. **22**, 215–221 (1955)
7. Grashof, F.: Theoretische Maschinenlehre, vol. 3. L. Voss, Leipzig (1890)
8. Hegedüs, G., Schicho, J., Schröcker, H.P.: Factorization of rational curves in the study quadric. Mech. Mach. Theor. **69**, 142–152 (2013)
9. Hegedüs, G., Schicho, J., Schröcker, H.P.: The theory of bonds: a new method for the analysis of linkages. Mech. Mach. Theor. **70**, 407–424 (2013)
10. Hollerbach, J., Suh, K.: Redundancy resolution of manipulators through torque optimization. IEEE J. Robot. Autom. **3**(4), 308–316 (1987)
11. Husty, M.L., Pfurner, M., Schröcker, H.P.: A new and efficient algorithm for the inverse kinematics of a general serial 6R manipulator. Mech. Mach. Theor. **42**(1), 66–81 (2007)

12. Husty, M.L., Pfurner, M., Schröcker, H.P., Brunnthaler, K.: Algebraic methods in mechanism analysis and synthesis. Robotica **25**(06), 661–675 (2007)
13. Husty, M.L., Schröcker, H.P.: Algebraic geometry and kinematics. In: Emiris, I.Z., Sottile, F., Theobald, T. (eds.) Nonlinear Computational Geometry. The IMA Volumes in Mathematics and its Applications, vol. 151, pp. 85–107. Springer, New York (2010)
14. Kecskemethy, A., Krupp, T., Hiller, M.: Symbolic processing of multiloop mechanism dynamics using closed-form kinematics solutions. Multibody Syst. Dyn. **1**(1), 23–45 (1997)
15. Ketchel, J., Larochelle, P.: Collision detection of cylindrical rigid bodies for motion planning. In: Proceedings 2006 IEEE International Conference on Robotics and Automation, ICRA 2006, pp. 1530–1535. IEEE (2006)
16. Khatib, O.: Real-time obstacle avoidance for manipulators and mobile robots. In: Autonomous Robot Vehicles, pp. 396–404. Springer, New York (1986)
17. Li, Z.: Closed linkages with six revolute joints. Ph.D. thesis, Johannes Kepler University Linz (2015)
18. Li, Z., Schicho, J., Schröcker, H.P.: The rational motion of minimal dual quaternion degree with prescribed trajectory. Comput. Aided Geom. Des. **41**, 1–9 (2016)
19. Luo, S., Ahmad, S.: Predicting the drift motion for kinematically redundant robots. IEEE Trans. Syst. Man Cybern. **22**(4), 717–728 (1992)
20. Mohamed, H.A., Yahya, S., Moghavvemi, M., Yang, S.: A new inverse kinematics method for three dimensional redundant manipulators. In: ICCAS-SICE, pp. 1557–1562. IEEE (2009)
21. Paul, R.P.: Robot Manipulators: Mathematics, Programming, and Control: The Computer Control of Robot Manipulators. Richard Paul, MIT Press, Cambridge (1981)
22. Pfurner, M.: Closed form inverse kinematics solution for a redundant anthropomorphic robot arm. Comput. Aided Geom. Des. **47**, 163–171 (2016)
23. Schröcker, H.P., Husty, M.L., McCarthy, J.M.: Kinematic mapping based assembly mode evaluation of planar four-bar mechanisms. J. Mech. Des. **129**(9), 924–929 (2007)
24. Sciavicco, L., Siciliano, B.: Modelling and Control of Robot Manipulators. Springer, London (2012)
25. Selig, J.M.: Geometric Fundamentals of Robotics. Monographs in Computer Science, 2nd edn. Springer, New York (2005)
26. Siciliano, B.: Kinematic control of redundant robot manipulators: a tutorial. J. Intell. Robotic Syst. **3**(3), 201–212 (1990)

Workspace Analysis of a Parallel Manipulator Using Multi-objective Optimization and Bio-inspired Methods

R.S. Gonçalves[1(✉)], J.C.M. Carvalho[1], and F.S. Lobato[2]

[1] School of Mechanical Engineering, Federal University of Uberlândia, Uberlândia, Brazil
{rsgoncalves, jcmendes}@ufu.br
[2] School of Chemical Engineering, Federal University of Uberlândia, Uberlândia, Brazil
fslobato@ufu.br

Abstract. In robotic field, manipulators with parallel architecture have inherent advantages in relation to serial manipulators in various applications, such as high stiffness, accurate positioning and high movement velocities. In this context, the determination of volume position is one of the most important aspects considered during the manipulator project because it determines the geometrical limits of task that can be performed. In this contribution, Bio-inspired Optimization Methods (BiOM) are applied to solve a multi-objective problem that considers as objectives the maximization of volume position and the maximization of orientation workspace of CaPaMan (Cassino Parallel Manipulator). The strategy proposed consists in extension of the BiOM to problems with multiple objectives through the incorporation of two operators into the original algorithm: (i) the rank ordering, and (ii) the crowding distance. The results demonstrated that the proposed methodology represents an interesting approach to solve multi-objective problems in the robotic context.

Keywords: Parallel manipulators · Workspace optimization · CaPaMan · Bio-inspired optimization methods

1 Introduction

Naturally, realistic optimization problems can be easily found in different fields of science and engineering. This kind of problem, called Multi-Objective Optimization Problem (MOOP), consists of simultaneous optimization of two or more objectives (often conflicting). In the literature, there is no universal definition of optimal for MOOPs. However, there is a general concept that has to be taken into account for this kind of problem, namely, the Pareto's Curve (that is constituted for non-dominated solutions). A Pareto's Curve should present two characteristics [1]: (i) the non-dominated solutions should be well distributed, and (ii) convergence.

In the literature, two classes of methods for solving MOOPs can be found [1, 2]: Deterministic and Non-Deterministic approaches. First class consists in to transform the original multi-objective problem in to similar mono-objective problem considering

J.C.M. Carvalho et al. (eds.), *Multibody Mechatronic Systems*,
Mechanisms and Machine Science 54, DOI 10.1007/978-3-319-67567-1_10

a preference-based approach, in which a relative preference vector is used to scalarize multiple objectives. Non-deterministic methods not are based on the information about the gradient of objective function. In addition, these methodologies are based on natural selection processes, population genetics, and analogies with physical and chemical processes. In this context, Bio-inspired Optimization Methods (BiOM) belongs to class of Non-Deterministic methods and are based on capacity of communication among the individuals of population, capturing the interactions among the candidates to generate a population that is more adapted each generation.

Among the most recent BiOM, we can to cite the Bees Colony Algorithm - BCA [3], the Firefly Colony Algorithm - FCA [4], and the Fish Swarm Algorithm - FSA [5]. The BCA is based on the behavior of bees colonies in their search of raw materials for honey production. Basically, in this evolutionary strategy, groups of bees (called scouts) are recruited to explore new areas (design space) in search for pollen and nectar. After this first step, the bees return to hive and the acquired information is used to indicate the best regions visited (local search). This procedure continues until a stopping criterion is reached [6]. The FCA mimics the patterns of short and rhythmic flashes emitted by fireflies in order to attract other individuals to their vicinities [4]. In this case, the attractiveness is proportional to their brightness, and for any two fireflies, the less bright will attract (and thus move to) the brighter one. However, the brightness can decrease as their distance increases and if there are no fireflies brighter than a given firefly it will move randomly [4]. Finally, the FSA is a random search algorithm based on the behavior of fish swarm observed in nature [5]. This intelligent social behavior is related with interactions between all fish in a group during the search for food, when the fish discovers a region with more food, when the fish will swarm naturally in order to avoid danger and when fish stagnates in a region, a leap is required to look for food in other regions [5].

In robotic fields, one important application of MOOP is the optimization of the parallel manipulators workspace. Orientation workspace, reachable workspace and dexterous workspace are useful concepts in this context, and requires a tridimensional representation due to its complexity [7, 8]. The attention of parallel manipulator are focused to a number of possible industrial applications such as manipulation [9], packing [10], assembly and disassembly machines [11], motion simulation [12], milling machines [13] and in the field of medicine [14].

To parallel manipulators, a number of different objectives can be adopted depending on the resources and general nature of tasks to be performed, such as workspace, singularities, stiffness, and dexterity. Consequently, one of the problems facing the designer is how to choose performance criteria and justify the optimality of different designs [15]. A discussion on optimal design of CaPaMan architecture is presented in Ottaviano and Ceccarelli [16] and Castelli et al. [17], in order to obtain design parameters of the robot whose position workspace is suitably prescribed. Another work focuses the optimization of the orientation workspace of CaPaMan [18].

In this context, the main contribution, the BiOM is considered as optimization tool to solve a multi-objective optimization problem that considers the maximization of volume position and the maximization of orientation workspace of parallel manipulators. This work is organized as follows. Section 2 presents the description of the CaPaMan architecture (a 3-DOF spatial parallel manipulator, in order to obtain design

parameters of the robot whose position and orientation workspaces are prescribed in a suitable way). The mathematical formulation of multi-objective optimization is presented in Sect. 3. The BiOM and its extension for multi-objective context are presented in Sect. 4. Section 5 presents the methodology proposed in this work following by the results and discussion. Finally are presented the conclusions.

2 Description of CaPaMan Architecture

Ceccarelli in 1997 [12] presented a new 3 DOF parallel manipulator named as CaPaMan – Cassino Parallel Manipulator, which its structural parameters are shown in Fig. 1(a). As can see on Fig. 1(a), it is composed by a fixed plate *FP* and a movable platform *MP* connected by three mechanisms (legs) rotated of π/3 with respect to the neighbor one. Each leg is composed by an articulated parallelogram *AP*, a prismatic joint *SJ*, a connecting bar *CB* and a spherical joint *BJ*.

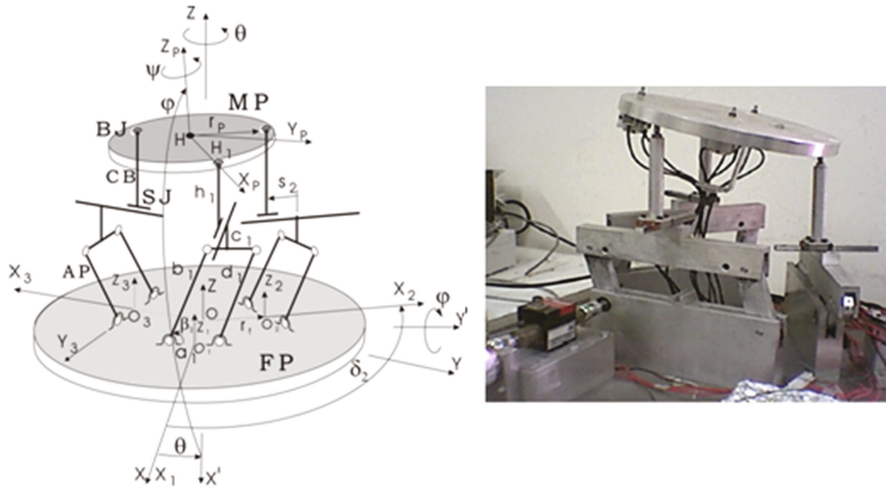

(a) (b)

Fig. 1. (a) Architecture and design parameters of CaPaMan; (b) Built prototype of CaPaMan [15].

Each leg mechanism is composed by the frame link a_k; the input crank b_k; the coupler link c_k; the follower crank d_k; and the connecting bar which its length is h_k, with $k = 1, 2, 3$. The input crank angle β_k and the stroke of the prismatic joint s_k are the kinematic variables. The size of the movable platform and the fixed plate are given by r_p and r_f, respectively. For the kinematic and dynamic analysis of CaPaMan [22, 23] a world frame *OXYZ* was fixed to the center point of *FP*, a moving frame $HX_PY_PZ_P$ was fixed to the center point of *MP*, and another frame $O_kX_kY_kZ_k$ (k = 1, 2, 3) was fixed to the middle point of the frame link a_k. Table 1 gives the dimensions of the built prototype of CaPaMan [22, 23]. The input crank angle β_k for the build prototype varies from $\pi/4$ to $3\pi/4$, but for the optimization process it varies from 0 to π.

Table 1. Design parameters of the built prototype of CaPaMan.

$a_k = c_k$ (mm)	$b_k = d_k$ (mm)	h_k (mm)	$r_p = r_f$ (mm)	β_k (rad)
200	80	96	109.50	$\pi/4$ to $3\pi/4$

More details for the kinematic and dynamic analysis of CaPaMan, as well the constructed prototype, can be found in [12, 22, 23].

The optimization problem enable to obtain the design parameters $a_k = c_k$, $b_k = d_k$, h_k and β_k, for three legs of CaPaMan when the size and shape of orientation and position workspace are suitably prescribed.

3 Mathematical Formulation of Optimization Problem

In the single-objective optimization context, the optimal design of CaPaMan architecture was addressed by Ottaviano and Ceccarelli [16]. These authors considered the maximization of workspace using a reference volume (parallelepiped), where a fixed volume is a goal to be achieved through a classical nonlinear programming methodology. In Ottaviano and Ceccarelli [18], a similar formulation for the optimal design of the same architecture was presented. By using a nonlinear programming methodology, the workspace orientation was considered. The corresponding results are summarized in Ceccarelli and Ottaviano [19], where the workspace positioning and orientation are considered simultaneously. All the approaches use the parallelepiped as reference geometry.

In this work is presented an analysis of the optimization problem of CaPaMan considering as objectives the maximization of workspace volume and the maximization of orientation by using three BiOM (multi-objective optimization bee colony algorithm, multi-objective optimization firefly colony algorithm and multi-objective optimization fish swarm algorithm). In order to compare the obtained results, it was also considered the non-dominated sorting genetic algorithms and the weighted sum method associated with the sequential quadratic programming. The first objective function is represented by Eq. (1):

$$\max f_1 = V \rightarrow \max f_1 = |\,(2x)\,(2y)\,(2z)\,| \tag{1}$$

where V is the optimal volume and the coordinate variables x, y and z are given in [12]. The second objective function is related to the orientation workspace, defined by Eq. (2):

$$\max f_2 = |(2\varphi)\,(2\psi)\,(2\theta)\,| \tag{2}$$

where ψ, θ, φ are angles that define the workspace orientation and are given in [12].

Based on the built prototype, Fig. 1(b), the associated constraints are given by:

$$\begin{gathered} |x| - 40 \leq 0\,;\ |y| - 40 \leq 0\,;\ |z| - 180 \leq 0\,;\ |\varphi| - 100^\circ \leq 0\,; \\ |\psi| - 100^\circ \leq 0\,;\ |\theta| - 230^\circ \leq 0\,;\ b_k \geq 0\,;\ h_k \geq 0\,;\ a_k \geq 0\,;\ 0^\circ \leq \beta_k \leq 180^\circ \end{gathered} \tag{3}$$

4 Multi-objective Optimization and Bio-inspired Optimization Methods

As mentioned earlier, the notion of optimality for MOOP was proposed by Edgeworth [20] and later generalized by Pareto [21]. This concept consists to finding non-dominated solutions (good tradeoffs among all the objectives). To solve this kind of problem considering the concept of non-dominated solutions, various Multiple-Objective Evolutionary Algorithms (MOEAs) can be found. In general, these methods can find multiple optimal solutions in one single simulation run due to their population-based search approach. Thus, MOEAs are ideally suited for multi-objective optimization problems.

In this context, due to success obtained by BiOM in different applications in science and engineering, several multi-objective algorithms based on these methods can be found. In this work, the MOBC (Multi-objective Optimization Bee Colony), MOFC (Multi-objective Optimization Firefly Colony) and MOFS (Multi-objective Optimization Fish Swarm) algorithms are used. Basically, in each approach, the BCA, FCA and FSA algorithms are considered as alternative to generate potential candidates to solve the MOOP proposed earlier. Each algorithm has the following structure: an initial population of size N is randomly generated considering the design space. Each candidate is evaluated considering all objectives. Following, all solutions are classified through the operator Fast Non-Dominated Sorting [1, 2] (this operator realizes the classification of non-dominated solutions). Thus, the population is sorted into non-dominated fronts F_j (classified solutions). This procedure is repeated until each vector is member of a front. A new candidate is generated considering a bio-inspired strategy (BCA, FCA or FSA). The Crowding Distance operator is applied to avoid a increase of population size during the evolutionary process [1]. Finally, this process continues until the number of generations is reached.

5 Workspace Analysis of a Parallel Manipulator

In order to evaluate the performance of the proposed methodology to solve the MOOP given by Eqs. (1) to (3), the following parameters were considered [3–5]: MOBC - number of scout bees (60), number of bees recruited for the best e sites (20), number of bees recruited for the other selected sites (20), number of sites selected for neighborhood search (5), number of top-rated (elite) sites among m selected sites (5), neighborhood search (10^{-3}) and generation number (250), MOFC - number of fireflies (100), maximum attractiveness value (0.9), absorption coefficient (0.7) and generation number (250), MOFS - number of fishes (100), weighted parameter value (1), control fish displacements (10^{-1}) and generation number (250). For the considered parameters, the number of objective function evaluations required for each bio-inspired algorithm is $100 \times 250 + 100$.

To compare the results obtained by using the BiOM, will be considered the Non-dominated Sorting Genetic Algorithms (NSGA II) (population size equal to 200, binary tournament, crossover probability equal to 0.9, mutation probability equal to

0.02 and 250 generations) and the Weighted Sum Method (WSM) associated with the Sequential Quadratic Programming (SQP).

The design variable vector considered in this application is [22]: $0.001 \leq b_1 = b_2 = b_3 \leq 0.3$, $0.001 \leq h_1 = h_2 = h_3 \leq 0.3$, $0 \leq \beta_1 = \beta_2 = \beta_3 \leq \pi$ and $0 < a_1 = a_2 = a_3 = a_k < 0.6$.

Table 2 presents the best point, in terms of to maximize volume (point A – MOBC, point C – MOFC and point E – MOFS, see Figs. 2 and 3, and maximize the positioning (point B – MOBC, point D – MOFC and point F – MOFS, see Figs. 2 and 3), respectively.

Table 2. Points belonging to Pareto's Curve.

		b_k (m)	h_k (m)	a_k (m)	$10^2 x f_1$ (m^3)	f_2 (rad^3)
MOBC	A	0.3	0.3	9.87E−5	3.59E−2	7.89
	B	0.3	0.3	5.51E−2	2.15E−1	0.00
MOFC	C	0.3	0.29	1.94E−2	3.05E−2	8.02
	D	0.3	0.3	3.62E−1	2.16E−1	0.00
MOFS	E	0.3	0.29	7.15E−2	2.34E−2	8.03
	F	0.3	0.3	1.19E−1	2.15E−1	0.00
NSGA II	G	0.3	0.29	7.04E−2	2.30E−2	8.02
	H	0.3	0.3	1.19E−1	2.10E−1	0.00
WSM	I	0.3	0.29	7.14E−2	2.33E−2	8.02
	J	0.3	0.29	1.20E−1	2.10E−1	0.00

In general way, the results obtained by using the BiOM are similar to found by using the NSGA II and the WSM, as observed in the Table 2. The results show upper values to b_k and h_k parameters, leading to maximization of volume and positioning of the movable platform in its workspace. In addition, lower values for the a_k parameter lead to maximization of workspace. The results presented on Figs. 2 and 3 are coherent with previous analysis of the CaPaMan workspace. Its structure, due to its particular geometry, presents a workspace similar to a bulk umbrella shaped volume with a hexagonal middle cross-section and six separate lower vertices. Another characteristic that can be noted is that its maximum workspace in volume is done when the movable platform is parallel to the base i.e., the orientation workspace is null. In opposite, when the maximum orientation workspace is obtained the volume workspace is minimum as can be seen on the analysis of its workspace characteristics shown in [12, 22]. In the optimization context, both algorithms were able to obtain satisfactory results in relation to objectives considered. Finally, in terms of the number of objective function evaluations, both algorithms presented the same computational cost.

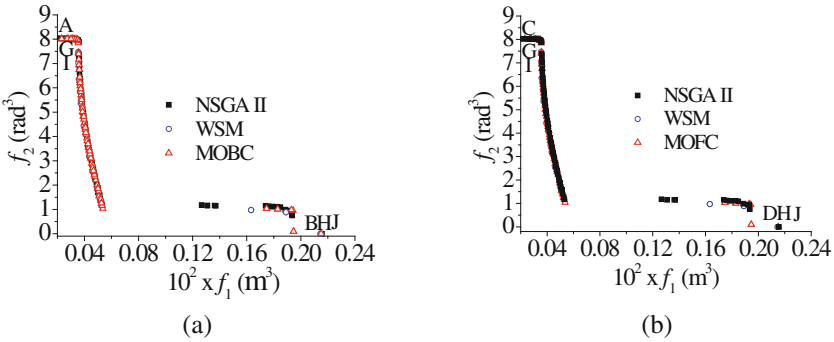

Fig. 2. (a) Pareto's Curve by using the NSGA II, WSM and MOBC. (b) Pareto's Curve by using the NSGA II, WSM and MOFC.

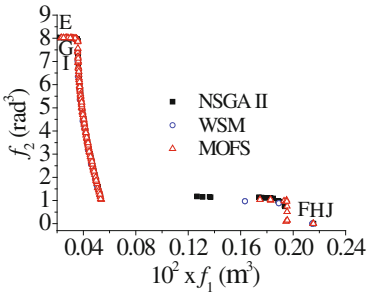

Fig. 3. Pareto's Curve by using the NSGA II, WSM and MOFS.

6 Conclusions

In this paper, the optimal design of a parallel robotic structure (CaPaMan) was studied. For this purpose, three Bio-inspired Optimization Methods (Bee Colony Algorithm, Firefly Colony Algorithm and Fish Swarm Algorithm) were extended to multi-objective context. This approach was applied to maximization of volume position and the orientation workspace.

The results obtained show that the methodology used represents an interesting approach to the treatment of the optimization problem formulated when compared with those obtained by the Non-dominated Sorting Genetic Algorithm (NSGA II) and the Weighted Sum Method (WSM).

It is important to observe that the methodology proposed in this work eliminate the necessity transformation of original multi-response problem in a similar with one objective, i.e., solve the original multi-objective problem.

Finally, due to the good performance found in numerical experiments, in the further work will be added other objectives, such as singularity and stiffness, when computing the optimal design, and can be efficiently used to analyze different parallel robotic structures.

Acknowledgments. The authors acknowledge the financial support provided by UFU, FEMEC, CAPES, FAPEMIG and CNPq agencies.

References

1. Deb, K.: Multi-Objective Optimization using Evolutionary Algorithms. Wiley, Chichester (2001). ISBN 0-471-87339-X
2. Lobato, F.S.: Multi-objective optimization to engineering system design. Thesis, School of Mechanical Engineering, Universidade Federal de Uberlândia, Brazil (2008). (in Portuguese)
3. Pham, D.T., Kog, E., Ghanbarzadeh, A., Otri, S., Rahim, S., Zaidi, M.: The Bees algorithm - a novel tool for complex optimization problems. In: Proceedings of 2nd International Virtual Conference on Intelligent Production Machines and Systems. Oxford, Elsevier (2006)
4. Yang, X.S.: Nature-Inspired Metaheuristic Algorithms. Luniver Press, Cambridge (2008)
5. Li, X.L., Shao, Z.J., Qian, J.X.: An optimizing method based on autonomous animate: fish swarm algorithm. Syst. Eng. Theor. Pract. **22**(11), 32–38 (2002)
6. Lucic, P., Teodorovic, D.: System: modeling combinatorial optimization transportation engineering problems by swarm intelligence. Preprints of the TRISTAN IV Triennial Symposium on Transportation Analysis, pp. 441–445 (2001)
7. Merlet, J.-P.: Determination de l'Espace de Travail d'un Robot Parallele pour une Orientation Constant. Mech. Mach. Theor. **29**(8), 1099–1113 (1994)
8. Huang, M.Z.: Design of a planar parallel robot for optimal workspace and dexterity. Inter. J. Adv. Rob. Syst. **8**(4), 176–183 (2011)
9. Stewart, D.: A platform with six degrees of freedom. Proc. Inst. Mech. Eng. **180**(15), 371–386 (1965). Part I
10. Clavel, R.: DELTA: a fast robot with parallel geometry. In: Proceedings of 18th International Symposium on Industrial Robots, Lausanne, pp. 91–100 (1988)
11. Pierrot, F., Dauchez, P., Fournier, A.: Hexa: a fast six-DOF fully parallel robot. In: Proceedings of International Conference on Advanced Robotics, Pisa, pp. 1159–1163 (1991)
12. Ceccarelli, M.: A new 3 DOF spatial parallel mechanism. Mech. Mach. Theor. **32**(8), 895–902 (1997)
13. Coelho, T.A.H., Batalha, G.F., Moraes, D.T.B., Boczko, M.: A prototype of a contour milling machine based on a parallel kinematic mechanism. In: Proceedings of the 32nd International Symposium on Robotics, Seoul, Korea (2001)
14. Gonçalves, R.S., Carvalho, J.C.M., Nunes, W.M., Rodrigues, L.A.O., Brabosa, A.M.: Cable-driven parallel manipulator for lower limb rehabilitation. Appl. Mech. Mater. **459**, 535–542 (2013)
15. Tsai, K.Y., Huang, K.D.: The design considerations of manipulators. In: Proceedings of the ASME Design Engineering Technical Conference and Computers and Information in Engineering Conference, Baltimore, Paper DETC2000/MECH-14089 (2000)
16. Ottaviano, E., Ceccarelli, M.: Optimal design of CaPaMan (Cassino Parallel Manipulator) with prescribed workspace. In: Proceedings of Computational Kinematics, Seoul (2001)
17. Castelli, G., Ottaviano, E., Ceccarelli, M.: A parametric study on position workspace capability of CAPAMAN. The Annals of "Dunarea de Jos" University of Galati Fascicle XIV Mechanical Engineering (2009)
18. Ottaviano, E., Ceccarelli, M.: Optimal design of CaPaMan (Cassino Parallel Manipulator) with a specified orientation workspace. Robotica **20**, 159–166 (2002)

19. Ceccarelli, M., Ottaviano, E.: An analytical design for CaPaMan with prescribed position and orientation. In: Proceedings of the ASME Design Engineering Technical Conference and Computers and Information in Engineering Conference, Baltimore (2000)
20. Edgeworth, F.Y.: Mathematical Psychics. P. Keagan, London (1881)
21. Pareto, V.: Manuale di Economia Politica, Societa Editrice Libraria, Milano, Italy (1906). Translated into English by A.S. Schwier as Manual of Political Economy. Macmillan, New York (1971)
22. Ceccarelli, M., Flgliolini, G.: Mechanical characteristics of CaPaMan (Cassino Parallel Manipulator). In: 3rd Asian Conference on Robotics and its Application, pp. 301–308 (1997)
23. Carvalho, J.C.M., Ceccarelli, M.: A dynamic analysis for Cassino parallel manipulator. In: Proceedings of 10th World Congress on Theory of Machines and Mechanisms/IFToMM 1999, Oulu, pp. 1202–1207 (1999)

Modeling of a Four-Legged Robot with Variable Center of Mass as a Cooperative Multirobot System

Cristiane P. Tonetto[1(✉)], Antônio Bento Filho[1], and Altamir Dias[2]

[1] Universidade Federal do Espírito Santo, Vitória, ES 29075-910, Brazil
{cristiane.tonetto,antonio.bento}@ufes.br
[2] Universidade Federal de Santa Catarina, Florianópolis, SC 88040-900, Brazil
altamir.dias@ufsc.br

Abstract. A multibody system, such as a multiple legged robot, can be modeled and controlled as a cooperative multirobot system (CMS), since it is expected that the several parts involved in the multibody to have a common purpose, in which they must cooperate in order to achieve success. This paper introduces the modeling of a four-legged robot as a set of five robot manipulators: four legs and one additional torso robot for center of mass change. The body's trajectory is defined and the legs must move cooperatively in order to keep the movement as defined, and the cooperation factor is used again with the torso compensation. The task of the torso robot is to keep the center of mass inside the supporting polygon composed by (at least) three legs, so that the system can remain stable at all times, and, because of that, must act cooperatively with the legs' movement. The kinematics are computed and simulated using the presented methodology, with screw theory, Assur virtual chains, graph theory and Davies method.

Keywords: Four-legged robot · Screw theory · Cooperative multirobot system

1 Introduction

Cooperative Multirobot System (CMS) are composed by robots that collaborate for the accomplishment of one or more tasks simultaneously, with some degree of interrelationship among them. In this definition, a four-legged robot can be modeled as a CMS, such that every leg is a single robot that composes this system and the main task imposed to the four-legged robot is a task of the CMS.

This approach allows the application of the methodologies developed generally for CMS in the four legged robot. On the condition where one leg is moving without ground contact, the other three establish a condition analogous to a parallel robot, or a multirobot sharing load. This condition allows them to displace the Base Plate in a specific desired way, referred as the main task of the robot.

J.C.M. Carvalho et al. (eds.), *Multibody Mechatronic Systems*,
Mechanisms and Machine Science 54, DOI 10.1007/978-3-319-67567-1_11

The global task of moving the robot includes some coordination effort, which is needed to plan the individual tasks of the legs lifting from the ground, and cooperative efforts, while the remaining legs must cooperatively share the load of the robot to be moved.

In addition to the study of this condition, this paper introduces the application of a fifth robot, which purpose is to assure the statically stable positions, by changing the center of mass of the system.

2 Kinematics for a Cooperative Multirobot System

2.1 Screw Theory

The methodology presented for kinematics computation of CMS is based on the screw theory. In this theory, a screw $\$$ is a geometric element defined by a directed line in space (not necessarily crossing the origin) and by a scalar parameter h, that defines the screw pitch [1]. One screw can be decomposed in a magnitude $\dot{q}$ and its normalized axis $\hat{\$}$. The axis $\hat{\$}$ is the geometric representation of the screw parameters:

$$\$ = \hat{\$}\dot{q}, \quad \text{where } \hat{\$} = \begin{bmatrix} s \\ s_o \times s + hs \end{bmatrix} \tag{1}$$

and also, s is an unitary vector with the direction of the axis related to the translation and rotation of the screw displacement. Since the axis not necessarily cross the origin, and s presents only the direction, the s_o vector defines the position of the axis related to the origin of the fixed coordinate system, h is the screw pitch and $s_o \times s$ is the cross product of s_o and s vectors.

Now, the screw can be adapted to each type of body motion. When the movement is a rotation, the screw pitch is null ($h = 0$), and Eq. (1) leads to $\hat{\$}_{revolute}$. Moreover, when the movement is a translation ($h = \infty$), Eq. (1) leads to $\hat{\$}_{translation}$.

$$\hat{\$}_{revolute} = \begin{bmatrix} s \\ s_o \times s \end{bmatrix}; \qquad \hat{\$}_{translation} = \begin{bmatrix} 0 \\ s \end{bmatrix} \tag{2}$$

So, the screw movement description may be used to define the differential displacement between two bodies related to a reference coordinate system (based on Chasles theorem and on Mozzi theorem). More details of the screw theory and its applications can be found in the following works: [1–3].

2.2 Successive Screw Method

This method can be extended to compute the screw due to the action of a body in another and as well as its coupling among them. The complete approach is presented in the research of Tsai [4], where he deduces the equations that model the rigid body displacements by using the Chasles theorem. Also, Tsai [4]

presents the Rodrigues matrix, written to evaluate the displacement of a rigid body in the space. So, the Rodrigues matrix is given by:

$$A_{\overrightarrow{s},\theta} = \begin{bmatrix} (s_x^2-1)(1-\cos\theta)+1 & s_x s_y(1-\cos\theta)-s_z\sin\theta & \dots \\ s_x s_y(1-\cos\theta)+s_z\sin\theta & (s_y^2-1)(1-\cos\theta)+1 & \dots \\ s_x s_z(1-\cos\theta)-s_y\sin\theta & s_y s_z(1-\cos\theta)+s_x\sin\theta & \dots \\ 0 & 0 & \dots \end{bmatrix} \quad (3)$$

$$\begin{bmatrix} \dots & s_x s_z(1-\cos\theta)+s_y\sin\theta & ts_x - s_{o_x}(a_{11}-1) - s_{o_y}a_{12} - s_{o_z}a_{13} \\ \dots & s_y s_z(1-\cos\theta)-s_x\sin\theta & ts_y - s_{o_x}a_{21} - s_{o_y}(a_{22}-1) - s_{o_z}a_{23} \\ \dots & (s_z^2-1)(1-\cos\theta)+1 & ts_z - s_{o_x}a_{31} - s_{o_y}a_{32} - s_{o_z}(a_{33}-1) \\ \dots & 0 & 1 \end{bmatrix}$$

In this Rodrigues matrix, θ is the angle of rotation around the s axis and t is the translational distance on the same axis.

By using the screw displacements concept for the kinematics analysis, the screw displacement of n successive screw displacements is just the premultiplication of the transformation matrix, given by:

$$A_r = A_1 A_2 A_3 \dots A_n \quad (4)$$

In this way, the position of the manipulator's end-effector can be computed, while the robot joints move, by using the screws evaluation procedures. In other words, the successive screw technique can be extended over the axis of the joints in order to calculate the robot effector pose. For the CMS, the screw technique is employed to establish the influence of each one of the joints over the others, and, thus, to get the s and s_o variables that includes such influence.

2.3 Assur Virtual Chains and Graph Theory

Another tool to study CMS is the Assur virtual chains. The Assur virtual chains, when added to a CMS, help to analyze the displacements of a kinematic chain or even to impose desired movement to a kinematic chain, as described before. By definition, a virtual chain is a kinematic chain composed by virtual links and joints, that can be added to a real kinematic chain without changing the main behavior of a real chain [5]. The virtual chain should be used to describe the relationship among robots links, tasks and parts in the scenario of CMS's planning.

Also, a CMS can be better represented by using graph theory, to visualize and compute interrelations between base, robots and tasks. Such relationships, represented by graphs, can be summarized in a circuit matrix B. This matrix B is a way to describe the presence of each edge in the graph meshes. The matrix is assembled so that each row is reserved to one mesh of the graph and each column to one edge. Each element of the matrix is defined as:

- 0, if the edge is not present on the mesh;
- 1, if the edge is on the mesh and on the same direction of the circuit (arbitrary chosen, but constant);
- −1, if the edge is on the mesh, but in the opposite direction of the circuit.

Together, Assur virtual chains and graph theory are very helpful to build the interrelationships in a CMS study.

2.4 Davies Method

The Davies method is a way to compute and relate the joints' velocities magnitudes of a close virtual chain. The method is an adaptation of the Kirchhoff circuit law and states that the sum of the relative speeds between kinematic pairs throughout any closed kinematic chain is null [2]:

$$\sum_{0}^{n} \$_i = \sum_{0}^{n} \hat{\$}_i \dot{q}_i = 0 \quad \Leftrightarrow \quad N\dot{q} = 0 \tag{5}$$

in which n is the number of joints of the system and N is the network matrix containing the normalized screws. To study the kinematic chain behavior it is better to classify the system' joints as primary N_p (joints used to define the movement) and secondary N_s (joints that will be computed in order to reach the desired movement). Thus, the Eq. (5) can be written as:

$$\begin{bmatrix} N_s \vdots N_p \end{bmatrix} \begin{bmatrix} \dot{q}_s \\ \cdots \\ \dot{q}_p \end{bmatrix} = 0 \quad \Leftrightarrow \quad N_s \dot{q}_s = -N_p \dot{q}_p \tag{6}$$

If N_s is invertible, the magnitude of the secondary joints can be computed by the following equation:

$$\dot{q}_s = -N_s^{-1} N_p \dot{q}_p \tag{7}$$

By substituting N_s, N_p and on Eq. (7), the secondary joints velocities magnitudes turn to be described as a function of the primary joints.

The gathering of these methods is applied in the kinematics computation for any multi-robot system, including cooperation [6]. The purpose of this paper is to apply such methodology in a four legged robot.

3 Guará Robot Overview

The configuration of a four legged robot consists in a rectangular plate equipped with a leg on each corner. Each leg is a robot manipulator, and can have from two up to six degrees of freedom.

An early implementation of a four legged robot made in *Universidade Federal do Espírito Santo* [7] was composed by four legs with four degrees of freedom each. This robot (as seen in Fig. 1) was named Guará.

This paper is part of the optimization effort for of Guará's design, including the investigation of the capabilities of simplified design (less joints) with more sophisticated simulation and trajectories programming techniques. The generalist approach of the proposed algorithms allows the evaluation of different degrees of freedom for the legs, as well as leg positioning, initial pose, joints ranges, links size, and additional manipulators.

In this way, the new proposed design is composed by four legs with three degrees of freedom each (all revolute joints). Additionally, a fifth simple robot (located in the middle of the plate, with one degree of freedom, revolute joint) is proposed, for controlling the center of mass of the system.

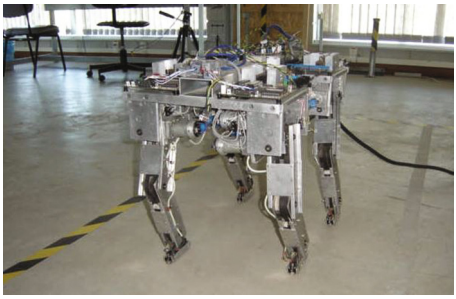

Fig. 1. Four legged robot Guará [8].

4 Guará's Kinematics Representation

4.1 Data Representation and Parameters

The data for one of the robots can be found on the Table 1 and the positioning of each leg and torso on the plate can be found on Table 2. A general view of this configuration can be seen on Fig. 2.

Table 1. Robots joints data.

Joint	s	s_o (mm)	Next link size (mm)
Leg's 1^{st} joint	(0, 0, 1)	(0, 0, 0)	0
Leg's 2^{nd} joint	(0, 1, 0)	(0, 0, 0)	120
Leg's 3^{rd} joint	(0, 1, 0)	(0, 0, 120)	100
Torso unique joint	(0, 0, 1)	(0, 0, 0)	100

Table 2. Robots positioning on the plate and initial joint configurations.

Robot	Position on plate (mm)	Joints initial configuration (rad)
Rear left leg (RLL)	(0, 0, 0)	(1.571, 3.500, −1.000)
Rear right leg (RRL)	(300, 0, 0)	(1.571, 3.500, −1.000)
Front left leg (FLL)	(0, 500, 0)	(1.571, 3.500, −1.000)
Front right leg (FRL)	(300, 500, 0)	(1.571, 3.500, −1.000)
Torso	(150, 200, 0)	(1.571)

For the graph representation, the four legged robot with torso is an specific case of the general modeling for cooperative multirobot system presented on [6,9]. The general model applied to multirobot systems allows each robot to

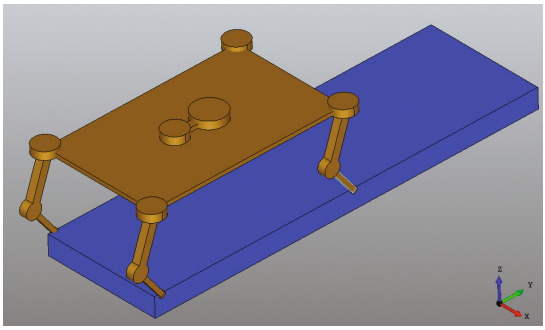

Fig. 2. Simulated configuration.

have a different moving base, with different tasks over a part, that is allowed to move related to the origin.

In the case of a four legged robot, the base is common for all the robots, and the part is the ground, which has no relative movement related to the origin. The graph representation for this case is presented on Fig. 3. This graph representation in condensed, so that the internal joints of robots and virtual chains are suppressed.

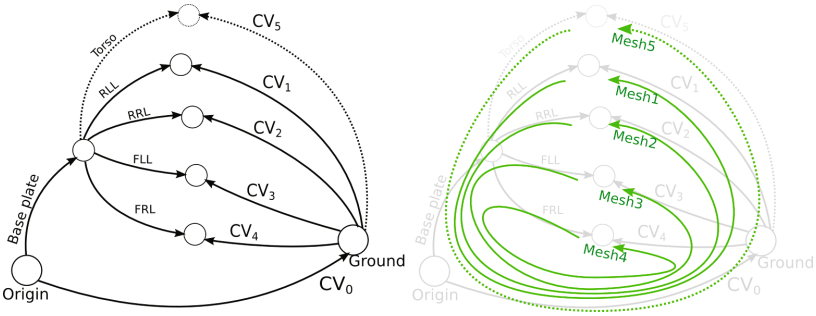

Fig. 3. Graph representation of the cooperative multirobot system (4 legs+torso).

The circuit matrix (B) associated with this graph is presented on Eq. 8. In this matrix representation the columns are presented in the compressed form. For example, CV_0 column refers to the six joints of the PPPS virtual chain.

$$
B = \begin{array}{c}
 \\
mesh_1 \\
mesh_2 \\
mesh_3 \\
mesh_4 \\
mesh_5
\end{array}
\begin{array}{c}
\begin{array}{cccccccccccc}
CV_0 & CV_1 & RLL & CV_2 & RRL & CV_3 & FLL & CV_4 & FRL & CV_5 & Torso & BasePlate
\end{array} \\
\left[\begin{array}{cccccccccccc}
1 & 1 & -1 & 0 & 0 & 0 & 0 & 0 & 0 & 0 & 0 & -1 \\
1 & 0 & 0 & 1 & -1 & 0 & 0 & 0 & 0 & 0 & 0 & -1 \\
1 & 0 & 0 & 0 & 0 & 1 & -1 & 0 & 0 & 0 & 0 & -1 \\
1 & 0 & 0 & 0 & 0 & 0 & 0 & 1 & -1 & 0 & 0 & -1 \\
1 & 0 & 0 & 0 & 0 & 0 & 0 & 0 & 0 & 1 & -1 & -1
\end{array}\right]
\end{array}
\tag{8}
$$

The normalized screw matrix D is defined as:

$$D = \left[\hat{\$}_{CV_0}\ \hat{\$}_{CV_1}\ \hat{\$}_{RLL}\ \hat{\$}_{CV_2}\ \hat{\$}_{RRL}\ \hat{\$}_{CV_3}\ \hat{\$}_{FLL}\ \hat{\$}_{CV_4}\ \hat{\$}_{FRL}\ \hat{\$}_{CV_5}\ \hat{\$}_{Torso}\ \hat{\$}_{BasePlate}\right] \quad (9)$$

In the screw matrix, each \$ is a matrix that includes all the screws of a given object. For example, the $\$_{CV_0}$ is a 6×6 sized matrix, including the normalized screws relative to the virtual chain. This leads to the Network Matrix N:

$$N = D \cdot diag\{B_i\} \quad (10)$$

where B_i is the vector extracted from the i^{th} row of the B matrix. The network matrix is split into primary matrix N_p and secondary matrix N_s. The primary matrix defines the tasks that need to be fulfilled, and the secondary matrix will be used to compute the joints values for the robots that are needed to fulfill the tasks.

$$N_p = \begin{bmatrix} \hat{\$}_{CV_0} & \hat{\$}_{CV_1} & 0 & 0 & 0 & 0 & -\hat{\$}_{BasePlate} \\ \hat{\$}_{CV_0} & 0 & \hat{\$}_{CV_2} & 0 & 0 & 0 & -\hat{\$}_{BasePlate} \\ \hat{\$}_{CV_0} & 0 & 0 & \hat{\$}_{CV_3} & 0 & 0 & -\hat{\$}_{BasePlate} \\ \hat{\$}_{CV_0} & 0 & 0 & 0 & \hat{\$}_{CV_4} & 0 & -\hat{\$}_{BasePlate} \\ \hat{\$}_{CV_0} & 0 & 0 & 0 & 0 & \hat{\$}_{CV_5} & -\hat{\$}_{BasePlate} \end{bmatrix} \quad (11)$$

$$N_s = \begin{bmatrix} -\hat{\$}_{RLL} & 0 & 0 & 0 & 0 \\ 0 & -\hat{\$}_{RRL} & 0 & 0 & 0 \\ 0 & 0 & -\hat{\$}_{FLL} & 0 & 0 \\ 0 & 0 & 0 & -\hat{\$}_{FRL} & 0 \\ 0 & 0 & 0 & 0 & -\hat{\$}_{Torso} \end{bmatrix} \quad (12)$$

The values of $\dot{q}_p$, N_s and N_p defined above are replaced on Eq. 7, thus making it possible to compute all the robots' joints speeds as a function of the speeds of the desired tasks.

4.2 Gait Planning

The first goal in a four legged robot is to complete the statically stable gait, which means that, during the walk, there must be at least three points of support at any given moment (three legs on the ground). This is the usual way that four legged animals move during walkings or slow runs. Whenever speed is necessary, there would be moments in which less than three legs, requiring even more coordination and balance. The purpose of this paper is to evaluate the applicability of a statically stable gait.

One example of such gait can be found on Fig. 4.

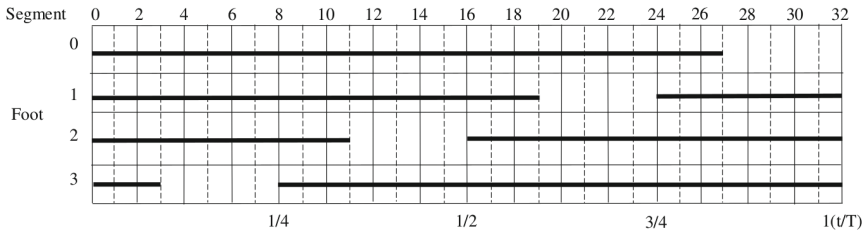

Fig. 4. Step pattern (black line meaning ground contact) [7].

This strategy has two advantages: first, it is easier to assure balance of the system, since only static evaluation must be made, and thus the balance is assured if the center of mass is located inside the ground contact polygon [7]; second, with three legs it is still possible to control the position and orientation of the plate, in an analogous situation of a parallel robot with three arms.

5 Results

5.1 Move Ahead Task

The move ahead task is the first task to be accomplished by the four-legged robotic system. The purpose is to go from an initial position to a position some place ahead, while maintaining the balance. The balance part will be considered on the next section, while this section explores the planning of the kinematics needed to accomplish the task.

One additional constraint imposed, in order to experiment the cooperative methodology is that it is desired to move the base plate with constant speed (linear advance on Y axis, since ahead direction is conventioned as $Y+$, as pictured on Fig. 5). This way, while one leg don't contact the ground, the other three legs must operate similar to a parallel robot, inducing the constant speed forward upon the plate, without rotating the plate in any direction.

In this formulation, there is the task of the base plate, and there is the planning of the gait, with the four legs moving without ground contact one at a time. Each leg has its own task planned, indicating if it contact the ground (constant position with $z = 0$) or is stepping forward. The tasks are planned so that the final pose equals the initial, making it possible to cycle through the movements in order to move ahead indefinitely.

The methodology defines the tasks as the primary joints on the kinematic chain, as the robots' joints are secondary. Applying Eq. 6 with the matrices defined on Eqs. 11 and 12, the robots joints could be found as presented on Fig. 6. It is possible to observe that the joints of the legs change even when the

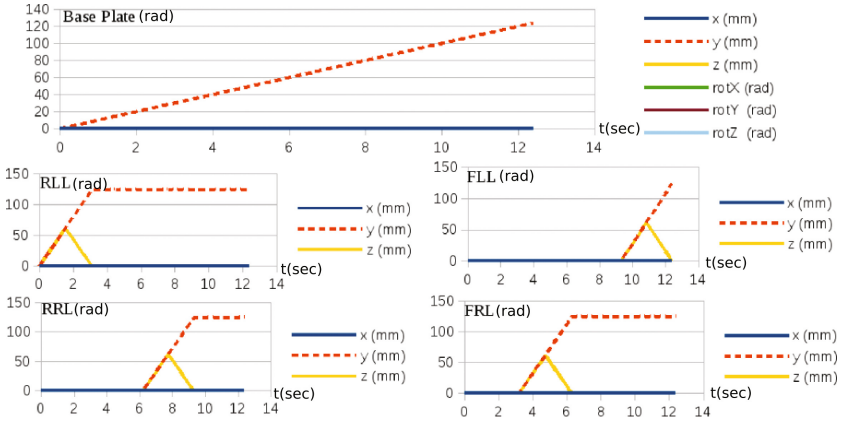

Fig. 5. Desired trajectories planned for the move ahead task (Primary joints).

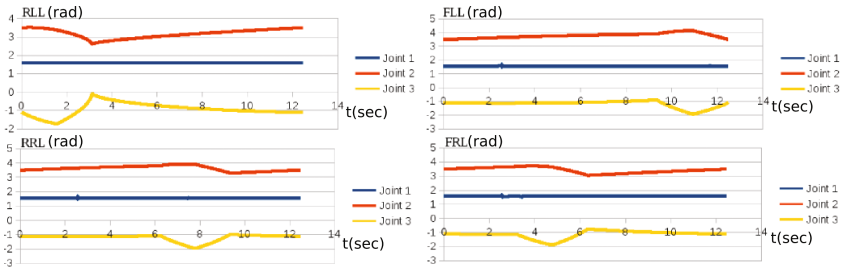

Fig. 6. Joints positions for the legs in order to accomplish the task.

end-effector (foot) is set on the ground. This is necessary in order to move the base plate forward with three legs while another doesn't have ground contact.

In this moment of the task experimentation, it is possible to verify more convenient dimensions of the links, as well as good initial position in order to complete the movement without singularity problems.

A view of the simulated environment can be seen on Fig. 7. It is noticeable that the Rear Right Leg is changing its pose during the task, even in the interval that it is contacting the ground (from "original" to "during 2^{nd} leg" frames).

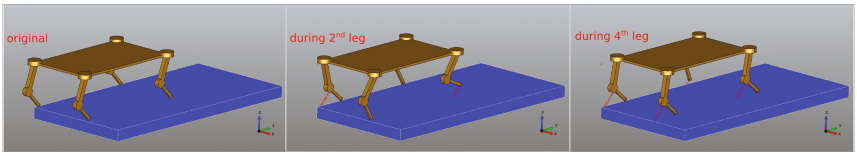

Fig. 7. Three different configurations for the move ahead task.

After accomplished this task, other tasks, such as the "move aside" task becomes trivial, by, for example, changing the Y axis movement to a X axis movement. Other possible change is to define a variable inclination of the base plate (in any given direction), since the virtual joints include revolute joints.

5.2 Center of Mass Control with the Fifth Robot

One important detail of the kinematics of the four-legged robot is the statically stable gait. This means that, in any given moment, the center of mass must remain inside the ground contact polygon.

Considering the base plate the most massive object and symmetrical legs implies that the center of mass is exactly on the middle of the base plate, making the gait as defined on the previous section a fragile stable system (the center of mass is located on the edge of the ground contact polygon).

For a statically stable gait, it is necessary to make sure that the center of mass is located inside the polygon, and the fragile stability isn't enough. The solution implemented on the Guará robot, for instance, was to tilt the base plate. This could be easily done by the correct definition of the base plate task, but it would violate the desired constraint.

The solution proposed is to implement a one joint robot over the base plate, with considerable mass that could actively change the center of mass to a desired position. This robot will be named Torso Robot. The task of such compensation robot is necessarily cooperative with the legs: each time a leg loses ground contact, the Torso must roll to a position where it ensures the position of the center of mass.

It is quite usual on the nature to see such behavior in animals, with the changing of the center of mass to a more stable position, even on walks or slow runs. On a horse, for example, it is usual to move the neck in order to guarantee the balance, as well as the torso [10].

The cooperative task computed for the torso robot, that makes the robot statically stable, is displayed on Fig. 8.

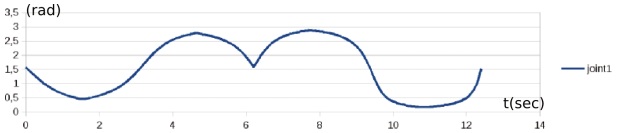

Fig. 8. Joint position for the 5^{th} robot.

In the Fig. 9 three different moments of the simulation is displayed, showing the mass on the end-effector of the torso robot inside the supporting polygon.

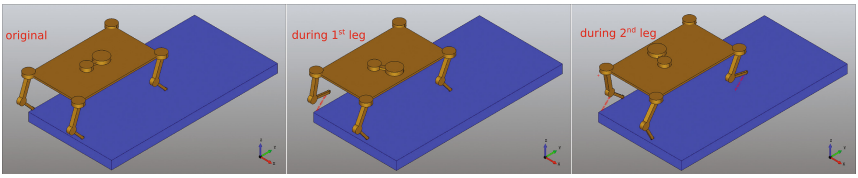

Fig. 9. Three different configurations for the center of mass control task.

6 Conclusions and Further Works

The application of the CMS methodology on multi-legged robot allows the testing of different configurations and parameters, as well as the capabilities of such robot, helping the design of the system. The addition of a fifth cooperating robot to compensate the center of mass so that the robot is always on a statically stable position seems to be a good design option that doesn't restrict the task definition of the Base Plate (as the Base Plate tilt would inevitably do).

As further works, in the simulation part, more complex trajectories can be implied, different solutions for the statical stability of the robot can be tested, as well as an adaptive method for unknown obstacles on the ground and the detection of positions near singularities. On the prototype part, the design options could be tested in a small-scale robot prototype.

References

1. Hunt, K.H.: Dont cross-thread the screw. In: A Symposium Commemorating the Legacy, Works, and Life of Sir Robert Stawell Ball Upon the 100th Anniversary of A Treatise on the Theory of Screws, pp. 1–36 (2000)
2. Davies, T.H.: Kirchhoffs circulation law applied to multi-loop kinematic chains. Mech. Mach. Theor. **16**, 171–183 (1981)
3. Rocha, C.R., Tonetto, C.P., Dias, A.: A comparison between the Denavit-Hartenberg and the screw-based methods used in kinematic modeling of robot manipulators. Robot. Comput. Integr. Manuf. **27**, 723–728 (2011). In: Conference papers of Flexible Automation and Intelligent Manufacturing
4. Tsai, L.-W.: Robot Analysis: The Mechanics of Serial and Parallel Manipulators. Wiley, New York (1999)
5. Campos, A., Guenther, R., Martin, D.: Differential kinematics of serial manipulators using virtual chains. In: Brazilian Society of Mechanical Sciences and Engineering. ABCM, vol. XXVII, pp. 345–356 (2005)
6. Tonetto, C.P., Rocha, C.R., Simas, H., Dias, A.: Kinematics programming for cooperating robotic systems. In: Camarinha-Matos, L.M., Shahamatnia, E., Nunes, G. (eds.) 3rd Doctoral Conference on Computing, Electrical and Industrial Systems (DoCEIS), Portugal. IFIP Advances in Information and Communication Technology, AICT, vol. 372, pp. 189–198. Springer (2012)
7. Filho, A.B., Amaral, P.F.S., Miglio Pinto B.G.: A divide and conquer approach for obstacles surpassing of a legged robot. In: Tan, H. (ed.) Informatics in Control, Automation and Robotics. Lecture Notes in Electrical Engineering, vol 132. Springer, Heidelberg (2011)

8. Filho, A.B., de Andrade, R.M.: A divide and conquer approach for obstacles overcoming of a legged robot. Int. J. Emerg. Technol. Adv. Eng. **5**(4), 56–68 (2015)
9. Tonetto, C.P., Rocha, C.R., Dias, A.: Kinematics programming for two cooperating robots performing tasks. In: ABCM Symposium Series in Mechatronics, vol. 6, pp. 578–587 (2014). PI.IV.10
10. Woodford, C.: Equine biomechanics and gait analysis. http://vipsvet.net/articles/biomechanics.pdf. Accessed 09 Mar 2017

Assembly Sequence Planning for Shape Heterogeneous Modular Robot Systems

Anelize Zomkowski Salvi(✉), Roberto Simoni, and Henrique Simas

UFSC - Universidade Federal de Santa Catarina, Florianópolis, Brazil
{anelize.salvi,roberto.simoni,henrique.simas}@ufsc.br

Abstract. Modular robots are robots capable of changing their morphology to perform various tasks and to adapt to different environments. In order to explore these versatile robots potentialities, they must be assembled and operated in as many different configurations as possible. This paper presents an original assembly sequence planning to target structures formed by shape heterogeneous modular robots systems. Each robot system is composed by any number of rectangular modules joined edge to edge, forming arbitrary shapes. The new planner is divided into three original algorithms and constitute a complete and novel method to build target structures without internal holes.

Keywords: Modular robot · Assembly · Heterogeneous systems

1 Introduction

Modular robots are robots capable of changing their morphology to perform various tasks and to adapt to different environments, for example, they can be employed to construct large marine structures, spatial applications, or even to construct furniture. In order to explore these versatile robots potentialities, they must be assembled and operated in as many configurations as possible.

An assembly is a collection of independent parts which forms a structure or product. The Assembly Sequence Planning (ASP) is the problem of finding a sequence of collision-free operations that brings the assembly parts together.

The traditional approach to assembly sequencing has been generalized in many directions. Concerning the assembly of mechanical products, according to [4], assembly generation methods lies in four general categories:

- Human interaction methods: this approach relies on user responses to a set of questions [3];
- Geometric feasible reasoning approaches: those methods plan feasible assembly paths [5,9,11,19].
- Knowledge-based reasoning approaches: that consider geometrical and non-geometrical informations, as human reasoning about the assembly process [2,6].
- Intelligent methods: uses multiple techniques as neural networks [1], heuristics [7,12,15] and optimization, among others.

J.C.M. Carvalho et al. (eds.), *Multibody Mechatronic Systems*,
Mechanisms and Machine Science 54, DOI 10.1007/978-3-319-67567-1_12

The ASP is an NP-hard problem [10], *i.e.* the problem complexity increases with the number of parts to be assembled. In fact, for n parts, the total number of possible sequences is n!. An inclusive survey on the ASP is presented in [8].

The assembly sequence problem for modular robots presents some peculiarities, specially about modules constraints. Paulus et al. [13,14], introduced the assembly sequence problem for rectangular modules. They addressed the problem of assembly large teams of autonomous robotic boats into floating platforms structures of arbitrary shapes, aggregating module by module to the target structure. A related problem is the assembling of two-dimensional structures by autonomous mobile robots transporting modular square building blocks. Werfel et al. [16], presented an algorithm for assembling arbitrary solid structures without internal holes out of square blocks. In [17], Werfel et al., introduced a rule based algorithm for target structures with holes. In [18], the authors presented another algorithm based on graph theory tools.

In this paper, a new assembly sequence planning for constructing planar target structures composed by any number of rectangular modules joined edge to edge is introduced. In order to assembly the target structure, the strategy of decomposing this structure into substructures is adopted. Each substructure is free-flying and composed by any number of rectangular modules joined edge to edge, forming arbitrary shapes. This kind of modular robot system is referred to as *shape heterogeneous modular robot systems*. Adopting this strategy, the main problem is how to join these robot systems, more precisely, how to determine the sequence of operations necessary to obtain the target structure from the robot systems. During assembly, easy accessibility of the individual modules must be guaranteed. This condition aggregates common modules mechanical restrictions, but other restrictions can be easily incorporated.

The new planner is divided into three novel algorithms presented in the next sections: Algorithm 1 (Assembly Order) summarizes the necessary steps to grown the target structures, Algorithm 2 (addEdge) aggregates the mechanical constraints and Algorithm 3 (deleteBranch) gives necessary conditions to delete a substructure to the growing target structure. To the best of the authors knowledge, this is the first work that shows how to build target structures composed by shape heterogeneous modular robots systems.

2 Preliminaries

This paper introduces a new assembly sequence planning for constructing planar target structures without internal holes. These structures are composed by shape heterogeneous robots systems. A configuration composed by 12 different robots system, labeled from A to L, is presented in Fig. 1. In this paper, each robot system is a collection of rectangular modules arranged in an arbitrary shape, where each robot module is represented by the coordinates of its centroid. For example, robot system F is composed by modules $\{(0,5);(0,6);(1,3);(1,4);(1,5)\}$.

During assembly, the following condition about accessibility must be verified: *Any rectangular module can not pass through a gap only as large as a side of*

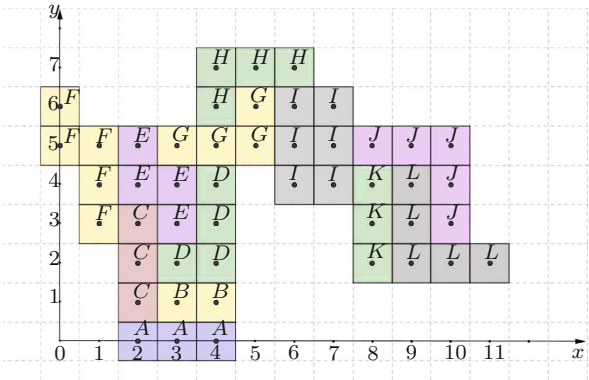

Fig. 1. A configuration composed by shape heterogeneous modular robots.

a module between two physical robots already assembled in the structure [13]. This condition aggregates common modules mechanical restrictions, but another restrictions can be easily incorporated.

Consider only the robots F, E and C in Fig. 1. These robots can not be assembled in the $F \rightarrow E \rightarrow$ C order, because when F and E are placed in the structure, C can not be added. More precisely, module $(2, 3) \in C$ can not be added to the structure without violating the accessibility condition.

Although, this paper uses the same accessibility condition for individual modules as [13], a different problem is herein addressed. In [13] target structures is assembled by adding module by module to the growing structure. In this paper, the target structure is assembled by joining modular robot systems composed by any number of modules and forming any arbitrary shape. To the best of the authors knowledge, this is the first work that shows how to build target structures composed by shape heterogeneous modular robots systems.

The problem of determining an assembly sequence can be regarded as the problem of choosing a path to transverse the whole structure adding as many robots as possible without violating the accessibility condition.

In this paper the target structure is modeled as an undirected graph: each module constituting the shape heterogeneous modular robots systems is represented by a vertex and robot systems neighborhood relations are represented by edges. Furthermore, powerful tools of graph theory are applied in order to find an assembly sequence that does not violate the accessibility condition, *i.e.* a feasible path to transverse the graph.

Next section introduces the new algorithms that constitute a complete and original method to assembly target structures without internal holes.

3 New Assembly Method for Heterogeneous Robots

In this paper, the target structure is represented by an undirected graph in the adjacency list form: each module is represented by a vertex and robot systems

neighborhood relations are represented by edges. Consider G the class that contains informations about the target structure and about the assembly sequence planning. In the class G:

- $G.adj[s]$ is the adjacency list of element s, in other words, it is the list of robots that are neighbors of s in the target structure;
- $G.Tree[s]$ is the list of elements added to an element s during the assembly process;
- $G.parent(s)$ is the parent of element s in the assembly process.

3.1 New Assembly Sequence Algorithms

The main Algorithm 1 (Assembly Order) is herein presented. This algorithm contains the necessary steps to plan the sequence in which the robots are added to the structure.

Algorithm 1 calls another two auxiliary procedures: Algorithm 2 (addEdge), that determines when a new robot can be added to the growing structure and Algorithm 3 (deleteBranch), that gives a strategy to delete a not allowed robot from the growing structure. These two algorithms are presented in the next subsections.

Algorithm 1. AssemblyOrder(G,s)

```
1: Label s as discovered
2: for each vertex w in G.adj[s] do
3:     if vertex w is labeled as undiscovered then
4:         if w can be added to the structure (AddEdge(G,w) is true) then
5:             G.Tree[s] ← w
6:             G.parent(w) = s
7:             label w as discovered
8:             AssemblyOrder(G,w)
9:         else
10:            deleteBranch(G,s)
11:            label s as undiscovered
12:            return
13: if Exists w in G.adj[s] marked as undiscovered then
14:     deleteBranch(G,s)
15:     label s as undiscovered
16:     return
```

In order to initialize the assembly process, select a robot s as starting point. Then, run Algorithm 1.

A brief explanation of Algorithm 1 (Assembly Order) is presented bellow.

Line 1: Add s to the structure (label s as discovered).
Lines 2–3: Select a neighbor robot w of s that is not in the structure (undiscovered).

Line 4: Check if it is possible to add w (accessibility condition - AddEdge), if it is possible, continue, otherwise, go to line 9.
Lines 5–7: Add w to the structure and mark s as parent of w.
Line 8: Call recursively the procedure AssemblyOrder(G,w), *i.e.* continue searching "deeper" for new robots (as in a depth-first search).
Lines 9–12: If w can not be added to the structure, then w's parent, s, can not be added to the structure. This implies that the entirely assembly tree branch starting in s must be deleted from the growing structure (what is done by the function deleteBranch(s)). For better understanding, consider only the robots F, E, C, G in Fig. 1. Suppose that the algorithm visits $F \rightarrow E \rightarrow G$, as shown in Figs. 2a and b (Steps 1–2). G has no neighbor to add, so the algorithm tries to add a new neighbor of G's parent, robot E. The only undiscovered neighbor of E is robot C, that can not be added to the structure (Step 3 in Figs. 2a and b). Thus, C's parent, robot E, can not be added to the structure at this point. As E has added robot G, this implies that G must be also deleted from the growing structure.
If G had added any neighbors to the growing structure, that neighbors would be also deleted. In other words, if E is deleted from the structure, all the assembly branch started in E must be deleted.
When the branch is deleted, the search returns to the previous added robot, in this case, F. New neighbors of F are explored (Step 4 in Fig. 2b). Finally, the correct sequence $F \rightarrow C \rightarrow E \rightarrow G$ is encountered (Steps 4–6 in Fig. 2b).
Lines 13–16: Given a robot s, when the recursion explores all neighbors of s, if any of these neighbors is still not added to the structure, then s can not also be added to the structure.

For better understanding, consider only the robots I, J, K, L in Fig. 1.

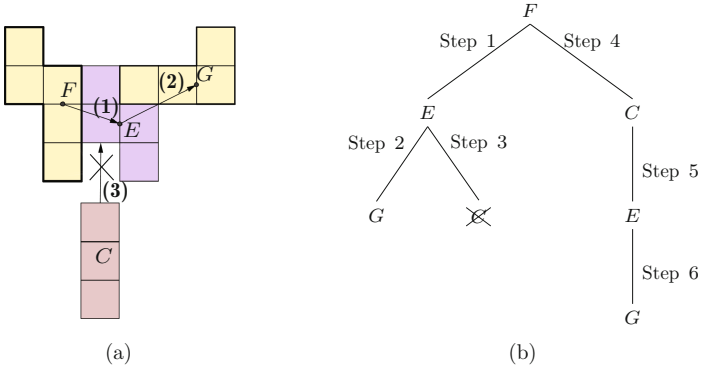

Fig. 2. (a) If the algorithms places $F \rightarrow E \rightarrow G$ and then E tries to place robot C, an incorrect assembly sequence is encountered. Thus, the parent of C, robot E, must be deleted from the structure along with G, the unique robot belonging to E's assembly tree branch (represented in (b)).

Consider the structure composed only by robot I, and that robots J, K, L must be added to this structure.

If robot J is added first, there are two possible orders $I \rightarrow J \rightarrow K \rightarrow L$ or $I \rightarrow J \rightarrow L \rightarrow K$. Let's analyze each case:

- Sequence $I \rightarrow J \rightarrow K \rightarrow L$: Due to the accessibility issue, L can't be added to the structure. K is marked as undiscovered by the rule in lines 9–12. Thus, by the end of this cycle, $I - J$ are marked as discovered, and $K - L$ as undiscovered;
- Sequence $I \rightarrow J \rightarrow L \rightarrow K$: Due to the accessibility issue, K can't be added to the structure. L is marked as undiscovered by the rule in lines 9–12. Thus, by the end of this cycle, $I - J$ are marked as discovered, and $K - L$ as undiscovered.

Thus, it can be concluded that after the neighboring checking cycle for J, not all of J's neighbors can be added to the growing structure. This implies that J can not be added to the structure. As in the first part of the Algorithm 1 J had already been marked as discovered, thus J needs to be remarked as undiscovered (in Line 15).

In the next two subsections Algorithm 2 (addEdge) and Algorithm 3 (deleteBranch) are presented.

3.2 Conditions to Add a New Robot to the Target Structure

The next algorithm gives a procedure to determine if a new robot can be added to the growing structure.

In order to determine if a new robot system can be added to the growing structure, this paper consider an oriented graph constructed as follows. Wherever a new robot s is added to the growing structure, construct oriented edges ending in s and starting in the s's already added neighbors.

For example, in Fig. 3a robot J is added to the configuration composed only by robot K, thus edge $K \rightarrow J$ is created. In Fig. 3b, robot L is added to the configuration composed by robots K, L, thus edges $K \rightarrow L$ and $J \rightarrow L$ are created.

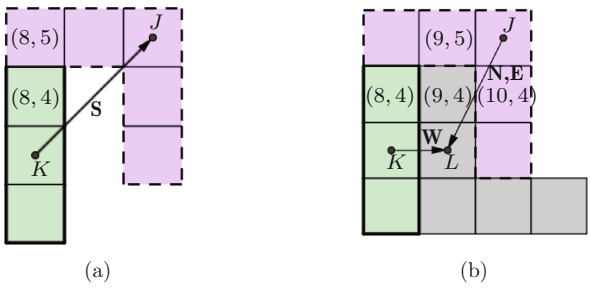

Fig. 3. (a) Robot J is added to the configuration composed only by robot K, thus edge $K \rightarrow J$ is created. (b) Robot L is added, thus edges $K \rightarrow L$ and $J \rightarrow L$ are created.

As seen in Fig. 3, each edge can receive one to four labels: north, south, east and west, according to the following rule.

An edge from robot A to robot B (edge $A \rightarrow B$) is labeled as:

- *North: if exists adjacent modules $a \in A$ and $b \in B$ such that module a is at north of module b ($a_x = b_x$ and $a_y = b_y + 1$);*
- *South: if exists adjacent modules $a \in A$ and $b \in B$ such that module a is at south of module b ($a_x = b_x$ and $a_y = b_y - 1$);*
- *East: if exists adjacent modules $a \in A$ and $b \in B$ such that module a is at east of module b ($a_y = b_y$ and $a_x = b_x + 1$);*
- *West: if exists adjacent modules $a \in A$ and $b \in B$ such that module a is at west of module b ($a_y = b_y$ and $a_x = b_x - 1$).*

where (a_x, a_y) and (b_x, b_y) are the coordinates of modules a and b, respectively.

Figure 3 represents the incorrect assembly order $K \rightarrow J \rightarrow L$ between robots K, L, J. In fact, L can not be added between K and J, if these pieces are already in the target configuration. Let's analyze this incorrect assembly order.

Step 1: When K is added, no edge is constructed;
Step 2: When J is added, an edge coming from his already added neighbor K is constructed. This edge is labeled as south, as shown in Fig. 3a. In fact, module $(8, 4) \in K$ is adjacent to the south of module $(8, 5) \in J$;
Step 3: When L is added, edges starting in his already placed neighbors K and J are constructed. These edges are shown in Fig. 3b and are labeled as:

- West: module $(8, 4) \in K$ is adjacent to the west of module $(9, 4) \in L$;
- North: $(9, 5) \in J$ is adjacent to the north of module $(9, 4) \in L$;
- East: module $(10, 4) \in J$ is adjacent to the east of module $(9, 4) \in L$.

In Fig. 3b the presence of west and east edges formalize the fact that L is going to be added in a constricted space between K and J, representing an incorrect assembly order.

The same analysis holds for north-south edges. In fact, the presence of north-south or east-west edges pairs ending at a robot shows that this robot can not be added to the structure.

Thus, in order to determine if a new robot s can be added to the growing structure, Algorithm 2 (AddEdge) considers all edges arriving in s. These edges start at s's neighbors already added to the growing structure. AddEdge checks if these edges are in conflict, *i.e.* if exists north-south or east-west edges pairs. If no conflict occurs, the algorithm returns true, signalizing that the new robot can be added to the growing structure. Otherwise, it returns false.

It is important to notice that in this construction, the case where a module is blocked by diagonal neighbors is not considered. However, as the configuration does not contain holes, if a module is blocked for diagonal neighbors, successive modules added to the structure will be blocked by north, south, west or east neighbors, thus the algorithm will detect an incorrect assembly sequence.

Algorithm 2. AddEdge(G,s)

```
for each vertex w in G.adj[s] do
    if vertex w is labeled as discovered then
        Create edge (w, s)
Check if any created edges are in conflict
if A conflict occurs then
    Return false
else
    Return true
```

3.3 Deleting a Branch from the Structure

For better understanding, of Algorithm 3, consider that an element s must be deleted from the assembly planning. When s was added by Algorithm 1 (Assembly Order) to the growing structure, it was marked as discovered and added to his parent adjacent list. Thus, in order to delete s it is necessary to:

- Mark s as undiscovered;
- Delete s from G.Tree[parent(s)].

An example of this procedure was shown in Fig. 2b, more precisely in Step 3. In that step, robot E tried to add robot C. Due to the accessibility issue, C could not be added to the growing structure. Thus, Algorithm 1 (Assembly Order) called the deleteBranch procedure for robot E (C's parent). As E had added robot G, E and G was both deleted from the growing structure. The function deleteBranch(E):

- Marked E as undiscovered and deleted it from G.Tree[F];
- Marked G as undiscovered and deleted it from G.Tree[E].

If G had added any neighbors to the growing structure, that neighbors would had been deleted in an analogues process, and so on.

This suggest a recursively implementation of the deletion process.

Algorithm 3 summarize this idea.

Algorithm 3. deleteBranch(G,s)

```
Remove s from G.Tree[parent(s)];
while G.Tree[s] isn't empty do
    Pop the fist element w from G.Tree[s];
    Mark w as undiscovered;
    deleteBranch(G,w);
```

4 Results

Considering the configuration in Fig. 1, given an arbitrary choice of the starting robot for the assembling process, the algorithm took 8 ms on average for the Assembly Planner running on a 4 GB, 1.6 GHz machine to compute the assembly sequence.

However, for n heterogeneous robots systems, the worst case for the number of possible sequences evaluated in Algorithm 1 (Assembly Order) is $(n-1)!$. Thus, the average time depends mostly of the number of robots composing the target structure, which highlights the algorithm complexity.

However, if the number of robots is large, an hierarchical strategy can be adopted: robots can first be aggregated in bigger components and then the algorithm is applied. To the best of the authors knowledge, this is the first work that shows how to build target structures composed by shape heterogeneous modular robots systems, thus the results can not be compared with literature.

5 Conclusions

This paper introduced an original assembly sequence planning to build target structures composed by shape heterogeneous modular robots systems. Three algorithms, original contributions of this paper, were presented: Algorithm 1 (Assembly Order), Algorithm 2 (addEdge), Algorithm 3 (deleteBranch). They constitute a complete and original method to assembly target structures without internal holes. Results were presented and discussed. To the best of the authors knowledge, this is the first work that shows how to build target structures composed by shape heterogeneous modular robots systems.

References

1. Chen, W.C., Tai, P.H., Deng, W.J., Hsieh, L.F.: A three-stage integrated approach for assembly sequence planning using neural networks. Expert Syst. Appl. **34**(3), 1777–1786 (2008). doi:10.1016/j.eswa.2007.01.034. http://www.sciencedirect.com/science/article/pii/S0957417407000541
2. Dong, T., Tong, R., Zhang, L., Dong, J.: A knowledge-based approach to assembly sequence planning. Int. J. Adv. Manuf. Technol. **32**(11), 1232–1244 (2007). doi:10.1007/s00170-006-0438-1.
3. Fazio, T.D., Whitney, D.: Simplified generation of all mechanical assembly sequences. IEEE J. Robot. Autom. **3**(6), 640–658 (1987). doi:10.1109/JRA.1987.1087132
4. Ghandi, S., Masehian, E.: A breakout local search (BLS) method for solving the assembly sequence planning problem. Eng. Appl. Artif. Intell. **39**, 245–266 (2015). doi:10.1016/j.engappai.2014.12.009. http://www.sciencedirect.com/science/article/pii/S0952197614003017
5. Halperin, D., Latombe, J.C., Wilson, R.H.: A general framework for assembly planning: the motion space approach. Algorithmica **26**(3), 577–601 (2000). doi:10.1007/s004539910025.

6. Hsu, Y.Y., Chen, W.C., Tai, P.H., Tsai, Y.T.: A Knowledge-Based Engineering System for Assembly Sequence Planning, pp. 123–126. Springer, London (2010). doi:10.1007/978-1-84996-432-6_28.
7. Ibrahim, I., Ibrahim, Z., Ahmad, H., Jusof, M.F.M., Yusof, Z.M., Nawawi, S.W., Mubin, M.: An assembly sequence planning approach with a rule-based multi-state gravitational search algorithm. Int. J. Adv. Manuf. Technol. **79**(5), 1363–1376 (2015). doi:10.1007/s00170-015-6857-0.
8. Jiménez, P.: Survey on assembly sequencing: a combinatorial and geometrical perspective. J. Intell. Manuf. **24**(2), 235–250 (2013). doi:10.1007/s10845-011-0578-5.
9. Lee, S., Shin, Y.G.: Assembly Coplanner : Cooperative Assembly Planner based on Subassembly Extraction, pp. 315–339. Springer, Boston (1991). doi:10.1007/978-1-4615-4038-0_13.
10. Lv, H., Lu, C.: An assembly sequence planning approach with a discrete particle swarm optimization algorithm. Int. J. Adv. Manuf. Technol. **50**(5), 761–770 (2010). doi:10.1007/s00170-010-2519-4.
11. de Mello, L.S.H., Sanderson, A.C.: And/or graph representation of assembly plans. In: Proceedings of the Fifth AAAI National Conference on Artificial Intelligence, AAAI 1986, pp. 1113–1119. AAAI Press (1986). http://dl.acm.org/citation.cfm?id=2887770.2887953
12. Pan, H., Hou, W.J., Li, T.M.: Genetic algorithm for assembly sequences planning based on heuristic assembly knowledge. In: Frontiers of Manufacturing and Design Science, Applied Mechanics and Materials, vol. 44, pp. 3657–3661. Trans Tech Publications (2011). doi:10.4028/www.scientific.net/AMM.44-47.3657
13. Paulos, J., Eckenstein, N., Tosun, T., Seo, J., Davey, J., Greco, J., Kumar, V., Yim, M.: Automated self-assembly of large maritime structures by a team of robotic boats. IEEE Trans. Autom. Sci. Eng. **12**(3), 958–968 (2015). doi:10.1109/TASE.2015.2416678
14. Seo, J., Yim, M., Kumar, V.: Assembly sequence planning for constructing planar structures with rectangular modules. In: 2016 IEEE International Conference on Robotics and Automation (ICRA), pp. 5477–5482 (2016). doi:10.1109/ICRA.2016.7487761
15. Wang, J., Liu, J., Zhong, Y.: A novel ant colony algorithm for assembly sequence planning. Int. J. Adv. Manuf. Technol. **25**(11), 1137–1143 (2005). doi:10.1007/s00170-003-1952-z
16. Werfel, J., Bar-Yam, Y., Rus, D., Nagpal, R.: Distributed construction by mobile robots with enhanced building blocks. In: Proceedings 2006 IEEE International Conference on Robotics and Automation, ICRA 2006, pp. 2787–2794 (2006). doi:10.1109/ROBOT.2006.1642123
17. Werfel, J., Ingber, D., Nagpal, R.: Collective construction of environmentally-adaptive structures. In: 2007 IEEE/RSJ International Conference on Intelligent Robots and Systems, pp. 2345–2352 (2007). doi:10.1109/IROS.2007.4399462
18. Werfel, J., Nagpal, R.: Extended stigmergy in collective construction. IEEE Intell. Syst. **21**(2), 20–28 (2006). doi:10.1109/MIS.2006.25
19. Wilson, R.H., Latombe, J.C.: Geometric reasoning about mechanical assembly. Artif. Intell. **71**(2), 371–396 (1994). doi:10.1016/0004-3702(94)90048-5. http://www.sciencedirect.com/science/article/pii/0004370294900485

Static Analysis

Kinetostatics and Optimal Design of a 2PRPU Shoenflies-Motion Generator

H. Simas[1(✉)] and R. Di Gregorio[2]

[1] Federal University of Santa Catarina, Florianópolis, Brazil
henrique.simas@ufsc.br
[2] University of Ferrara, Ferrara, Italy
raffaele.digregorio@unife.it

Abstract. Schoenflies-motion generators (SMGs) are 4-degrees-of-freedom (dof) manipulators whose end effector can perform translations along three independent directions and rotations around one fixed direction (Schoenflies motions). The authors, in a previous paper, showed that a 2PRPU SMG has a simple position analysis and singularities that leave a wide free-from-singularity workspace. The present paper addresses the kinetostatics and the optimal design of this SMG.

Keywords: Parallel manipulators · Schoenflies motions · Kinetostatics · Useful workspace

1 Introduction

Pick-and-place tasks are typical industrial applications that Shoenflies Motion Generators (SMGs) can accomplish. In the literature (see, for instance, [1–4]), SMGs with parallel architecture have been proposed.

Figure 1(a) shows a single-loop SMG of type 2PRPU[1] the authors proposed in a previous paper [5]. This SMG is obtained by adding a rotation amplifier that drives a gripper hinged on the mobile platform of the single-loop of 2PRPU type shown in Fig. 1(b). With reference to Fig. 1(b), the frame (base) and the mobile platform (platform) are fixed to the Cartesian references $O_b x_b y_b z_b$ and $O_e x_e y_e z_e$, respectively, and are connected to each other by two PRPU limbs with the PR chain, adjacent to the base, that constitutes a C pair, whose axis is parallel to the axis of the first R pair of the U joint. The platform is connected to the two limbs by two R pairs (i.e., the 2nd ones of the two U joints) with parallel axes and keeps these axes always parallel during motion.

In Fig. 1, the axes of the two C pairs are one parallel to the x_b axis and the other to the y_b axis; whereas, the axes of the 2nd R pairs of the two U joints are both parallel to the z_b axis. A_1 and A_2 are the centers of the two U joints. B_1 (B_2) is the foot of the perpendicular from A_1 (A_2) to the x_b axis (y_b axis). The rotation amplifier is constituted

[1] Hereafter, R, P, U, and C stand for revolute pair, prismatic pair, universal joint, and cylindrical pair, respectively. The underlining indicates the actuated joints and the sequence of joint types, which are encountered by moving from the base to the platform on a limb, is given with a string of capital letters.

J.C.M. Carvalho et al. (eds.), *Multibody Mechatronic Systems*,
Mechanisms and Machine Science 54, DOI 10.1007/978-3-319-67567-1_13

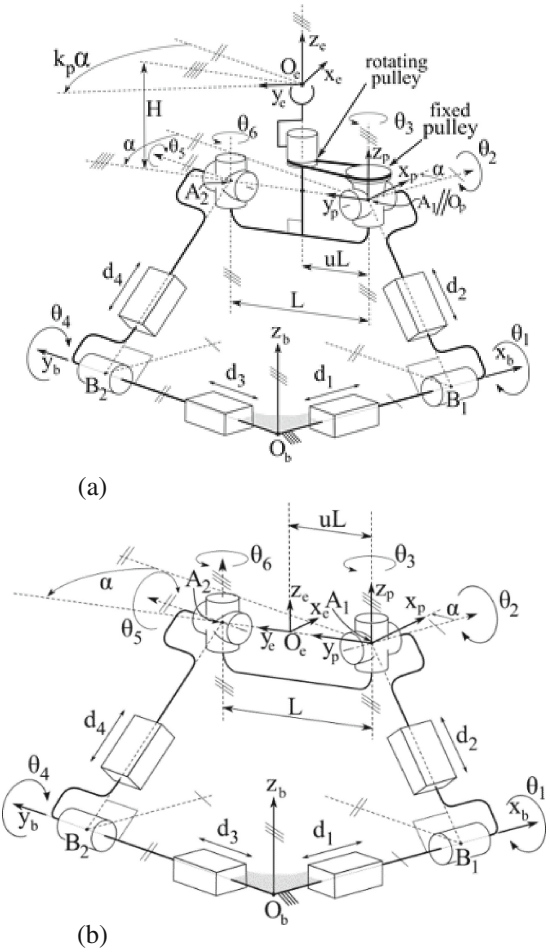

Fig. 1. Kinematic scheme of the SMG presented in [4] (parallelepipeds and cylinders denote P and R pairs, respectively): (a) complete scheme, (b) single-loop of 2PRPU type

by a toothed belt that transmits the motion from a "fixed" pulley embedded in the hub of the 2nd R pair of the U joint with center at A_1 to another "rotating" pulley embedded in the gripper. k_p is the ratio between the angular velocities of the gripper and of the platform (i.e., the angular-velocity ratio of this rotation amplifier).

With reference to Fig. 1, d_1 and d_3 are the signed distances of the points B_1 and B_2, respectively, from O_b and are the joint variables of the two P pairs adjacent to the base. d_2 and d_4 are the variable lengths (limbs' lengths) of the segments B_1A_1 and B_2A_2, respectively, and are the joint variables of the remaining two P pairs. L is the constant length of the segment A_1A_2 and u is a constant coefficient ranging from 0 to 1. α is the angle, counterclockwise with respect to the direction of the z_b axis, that the segment A_1A_2 form with the direction of the y_b axis, and identifies the platform orientation. Eventually, the angles θ_i for i = 1,…,6 are the joint variables of the six R pairs. θ_1 and

θ_2 (θ_4 and θ_5) are defined counterclockwise with respect to the direction of the x_b axis (the y_b axis); whereas, θ_3 and θ_6 are defined counterclockwise with respect to the direction of the z_b axis. θ_1 (θ_4) is equal to 0 when the vector ($\mathbf{A}_1$–$\mathbf{B}_1$) [the vector ($\mathbf{A}_2$–$\mathbf{B}_2$)] has the same direction of the y_b axis (the x_b axis). The four P pairs are the actuated joints.

The directions of the axes of the 2nd R pairs of the two U joints must be parallel to each other and, simultaneously, perpendicular to the axes of the 1st R pairs of the two U joints, whose directions are fixed by the limb geometry. Thus, the orientations of the planes that contain the two R-pair axes of each U joint do not change during motion and the platform can only perform Schoenflies motions with rotation axis parallel to the z_b axis.

Position analysis, singularity analysis and dexterous workspace of this SMG have been studied in [5]. They showed that it has a simple kinematics with a wide free-from-singularity dexterous workspace. Here, its kinetostatics performances are studied and the optimal location of the useful workspace inside the regions of the free-from-singularity dexterous workspace with high kinetostatics performances is presented.

2 Kinetostatic Performances

Hereafter, the four-tuple $\mathbf{q} = (d_1, d_2, d_3, d_4)^T$ collects all the actuated-joint variables and locates the points of the joint space. The position vector $\mathbf{A}_1 = (A_{1x}, A_{1y}, A_{1z})^T$, which collects the coordinates of the platform point A_1 in $O_b x_b y_b z_b$, and the angle α uniquely identify the platform pose, and the four-tuple $\boldsymbol{\kappa} = (A_{1x}, A_{1y}, A_{1z}, \alpha)^T$ is adopted to locate the points of the operational space. Also, the position vector $\mathbf{A}_2 = (A_{2x}, A_{2y}, A_{2z})^T$ collects the coordinates of the platform point A_2 in $O_b x_b y_b z_b$.

By using these notations, the following instantaneous input-output relationship (InI/O) has been deduced in [5] for the studied SMG

$$\mathbf{M}\dot{\boldsymbol{\kappa}} = \mathbf{N}\dot{\mathbf{q}} \tag{1}$$

where the Jacobian matrices M and N are defined as follows

$$\mathbf{M} = \begin{bmatrix} 1 & 0 & 0 & 0 \\ 0 & A_{1y} & A_{1z} & 0 \\ 0 & 1 & 0 & -L\sin\alpha \\ A_{1x} - L\sin\alpha & 0 & A_{1z} & L\cos\alpha(L\sin\alpha - A_{1x})] \end{bmatrix}; \mathbf{N} = \begin{bmatrix} 1 & 0 & 0 & 0 \\ 0 & d_2 & 0 & 0 \\ 0 & 0 & 1 & 0 \\ 0 & 0 & 0 & d_4 \end{bmatrix} \tag{2}$$

Equation 1 brought to conclude (see [5] for details) that parallel singularities occur when either of the following relationships are satisfied

$$A_{1z} = 0 \tag{3a}$$

$$A_{1y}\sin\alpha + A_{2x}\cos\alpha = 0 \tag{3b}$$

From statics point of view, Eq. (1) can be exploited to deduce the relationship between the four-tuple $\boldsymbol{\tau} = (\tau_1, \tau_2, \tau_3, \tau_4)^T$ that collects the generalized forces applied by the actuators and the wrench $(\mathbf{f}^T, \mathbf{m}^T)^T$ the platform applies to the external world as follows[2]. The power balance on the SMG is $\mathbf{f}^T \dot{\mathbf{A}}_1 + m_z \dot{\alpha} = \boldsymbol{\tau}^T \dot{\mathbf{q}}$ which, if Eq. (1) is used to eliminate $\dot{\mathbf{A}}_1$ and $\dot{\alpha}$, becomes $[(\mathbf{f}^T, m_z)\,\mathbf{M}^{-1}\mathbf{N} - \boldsymbol{\tau}^T]\,\dot{\mathbf{q}} = 0$. The last equation is satisfied for any $\dot{\mathbf{q}}$ if and only if the following input-output static (StI/O) relationship holds:

$$\mathbf{J}^{-T}\left(\mathbf{f}^T,\ m_z\right)^T = \boldsymbol{\tau} \tag{4}$$

where $\mathbf{J}^{-T} = \mathbf{N}^T\mathbf{M}^{-T}$.

2.1 Deduction of a Meaningful Performance Index

The StI/O can be rewritten as follows

$$\mathbf{U}_f\mathbf{f} + \mathbf{u}_\alpha m_z = (\tau_1, \tau_2, \tau_3)^T \tag{5a}$$

$$\mathbf{v}_f^T\mathbf{f} + v_\alpha m_z = \tau_4 \tag{5b}$$

Where

$$\mathbf{J}^{-T} = \begin{bmatrix} \mathbf{U}_f & \mathbf{u}_\alpha \\ \mathbf{v}_f^T & v_\alpha \end{bmatrix},\quad \mathbf{U}_f = \begin{bmatrix} 1 & \dfrac{A_{2x}\sin\alpha}{A_{1y}\sin\alpha + A_{2x}\cos\alpha} & \dfrac{-A_{1y}A_{2x}\sin\alpha}{A_{1z}\left(A_{1y}\sin\alpha + A_{2x}\cos\alpha\right)} \\ 0 & \dfrac{d_2\sin\alpha}{A_{1y}\sin\alpha + A_{2x}\cos\alpha} & \dfrac{d_2A_{2x}\cos\alpha}{A_{1z}\left(A_{1y}\sin\alpha + A_{2x}\cos\alpha\right)} \\ 0 & \dfrac{A_{2x}\cos\alpha}{A_{1y}\sin\alpha + A_{2x}\cos\alpha} & \dfrac{-A_{1y}A_{2x}\cos\alpha}{A_{1z}\left(A_{1y}\sin\alpha + A_{2x}\cos\alpha\right)} \end{bmatrix}$$

$$\mathbf{u}_\alpha = \left(\frac{A_{2x}}{L\left(A_{1y}\sin\alpha + A_{2x}\cos\alpha\right)},\ \frac{d_2}{L\left(A_{1y}\sin\alpha + A_{2x}\cos\alpha\right)},\ \frac{-A_{1y}}{L\left(A_{1y}\sin\alpha + A_{2x}\cos\alpha\right)}\right)^T$$

$$\mathbf{v}_f^T = \left(0,\ \frac{-d_4\sin\alpha}{A_{1y}\sin\alpha + A_{2x}\cos\alpha},\ \frac{d_4A_{1y}\sin\alpha}{A_{1z}\left(A_{1y}\sin\alpha + A_{2x}\cos\alpha\right)}\right)$$

$$v_\alpha = \frac{-d_4}{L\left(A_{1y}\sin\alpha + A_{2x}\cos\alpha\right)}$$

Exploiting Eq. (5b) to linearly eliminate m_z transforms Eq. (5a) as follows

$$\mathbf{f} = \mathbf{J}_f\boldsymbol{\tau} \tag{6}$$

where $\mathbf{J}_f = \mathbf{E}^{-1}\mathbf{F}$ with $\mathbf{E} = [\mathbf{U}_f - (\mathbf{u}_\alpha\,\mathbf{v}_f^T/v_\alpha)]$, $\mathbf{F} = [\mathbf{1}_{3x3}, -\mathbf{u}_\alpha/v_\alpha]$ and $\mathbf{1}_{3x3}$ is the 3×3 identity matrix.

[2] Hereafter, $\mathbf{f} = (f_x, f_y, f_z)^T$ is the resultant force and $\mathbf{m} = (m_x, m_y, m_z)^T$ is the resultant moment about A_1 of the force system the platform applies to the external world.

Equation (6) implicitly takes into account m_z and, with respect to Eq. (4), has the advantage that both the input $\boldsymbol{\tau}$ and the output $\mathbf{f}$ are homogenous vectors whose entries are all forces. Thus, the condition $\mathbf{f}\cdot\mathbf{f} = 1$ is dimensionally consistent and, when Eq. (6) is introduced, yields the following four-dimensional ellipsoid

$$\boldsymbol{\tau}^T \mathbf{J}_f^T \mathbf{J}_f \boldsymbol{\tau} = 1 \tag{7}$$

which is dimensionally consistent, too.

The shape of ellipsoid (7) depends on the SMG configuration through $\mathbf{J}_f$. The semi-axes lengths of this ellipsoid are the inverse of the singular values[3] of $\mathbf{J}_f$. Also, the minimum, λ_{min}, and maximum, λ_{max}, lengths of the semi-axes of ellipsoid (7) at a given configuration correspond to the minimum and maximum values, respectively, of $|\boldsymbol{\tau}|$ necessary to equilibrate a unit resultant force applied to the platform at that configuration. Therefore, the following local index, CI, can be adopted as a measure of the kinetostatic performance of the SMG at a given configuration:

$$CI = \frac{\lambda_{min}}{\lambda_{max}} \tag{8}$$

The above-defined CI ranges from 0 to 1: the higher the CI, the better the performance is. It corresponds to the conditioning index [6] of the Jacobian matrix $\mathbf{J}_f$ and can be used for any SMG. Accordingly, the global performance of the SMG can be measured by the global conditioning index [6], GCI, defined as the average value of CI on the useful workspace. Moreover, the concept of isotropic configuration [7] of a SMG can be referred to the SMG configurations with CI = 1.

2.2 Evaluation of the Kinetostatics Performances

In [5], the analysis of the singularity conditions (3a) and (3b) brought to conclude that, for $\alpha \in [0°, 90°]$ and $A_{1z} \geq 0$, if the projections of A_1 and A_2 (see Fig. 1) lie on the first quadrant of the $x_b y_b$ plane (i.e., when A_1 and A_2 are inside the first octant of $O_b x_b y_b z_b$) parallel singularities occur only when the manipulator is flattened on the coordinate planes. Thus, if the coordinate planes are excluded, the first octant is a free-from-singularity region. In this octant, even though the platform rotation is limited, the gripper rotation (Fig. 1) can be a complete rotation by choosing a suitable value of the angular-velocity ratio k_p of the rotation amplifier.

If the dexterous workspace [4, 8] is represented by giving the positions that the platform point O_e (see Fig. 1(b)) can reach with any platform orientation $\alpha \in [0°, 90°]$, its shape for[4] $(d_{2max}/d_{2min}) = 3$, $u = 0.5$, $L = 100$ l.u., $d_{2min} = d_{4min} = 3L$, and $d_{2max} = d_{4max}$ (l.u. stands for length unit) is depicted in Fig. 2. This workspace is the

[3] The "singular values" of a real matrix $\mathbf{A}$ are the square roots of the eigenvalues of the positive-semidefinite matrix $\mathbf{A}^T\mathbf{A}$. Also, the spectral norm of $\mathbf{A}$ is the square root of the largest eigenvalue of $\mathbf{A}^T\mathbf{A}$; thus, the spectral norm of $\mathbf{A}$ is equal to its largest singular value.

[4] These geometric values have been found in [5] acceptable to have a dexterous workspace wide enough for practical applications.

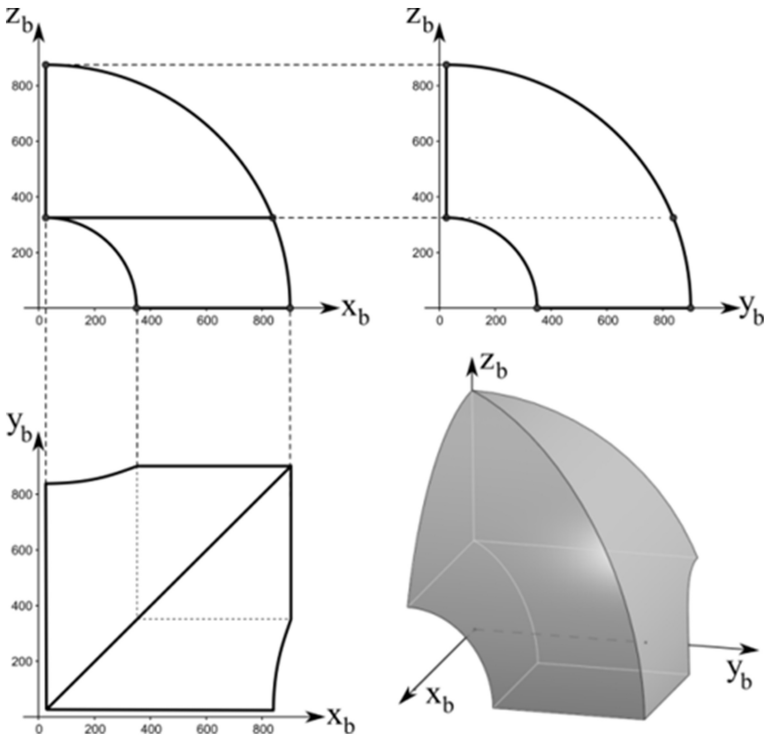

Fig. 2. Free-from-singularity dexterous workspace of the 1st octant [(d_{2max}/d_{2min}) = 3, u = 0.5, L = 100 l.u., $d_{2min} = d_{4min} = 3L$, and $d_{2max} = d_{4max}$ (l.u. stands for length unit)].

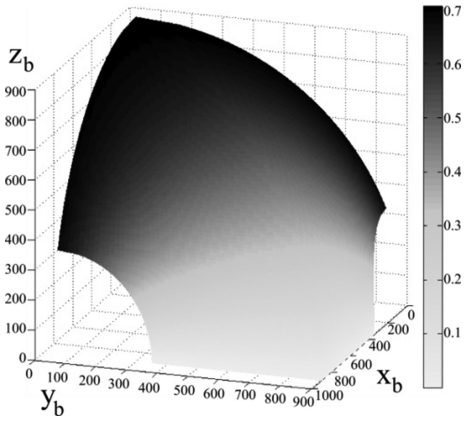

Fig. 3. CI values corresponding to the SMG configurations located on the boundaries of the dexterous workspace of Fig. 2 (the gray scale gives the value of CI).

common intersection of two right circular cylindrical shells with axes parallel to x_b and y_b due to the two PRPU limbs (see [5] for details). Also, the CI values corresponding to the SMG configurations located on the boundary surface of this workspace are shown in Fig. 3. This figure shows that the CI value increases with the z coordinate of O_e and reaches the maximum value $CI_{max} = 0.707$. Thus, the SMG must work in the upper part of its dexterous workspace to have good kinetostatic performances.

3 Optimal Location of the Useful Workspace

The useful workspace is a regular geometric object (e.g., a cube, a ball, etc.) [9] located in the region of the operational workspace that satisfies all the kinetostatics requirements. Here, by keeping the geometric data adopted to draw Fig. 2, the useful workspace is chosen equal to a rectangular parallelepiped with two sides lying on the boundary surfaces of the dexterous workspace, which is located in the upper region of this workspace (Fig. 4). Figure 5 shows simultaneously its projection on the x_bz_b and y_bz_b planes with d_p that corresponds to d_4 or d_2 for the x_bz_b or y_bz_b plane, respectively.

By using the notations of Fig. 5, the volume, V_u, of the useful workspace is

$$V_u = b^2h \tag{9}$$

and the following geometric relationships hold

$$c_z = h + z_{min} \tag{10a}$$

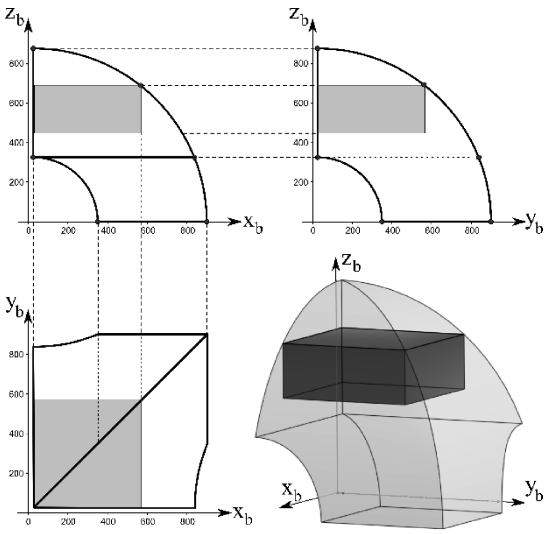

Fig. 4. Useful workspace with CI $\geq$ 0.45 inside the dexterous workspace.

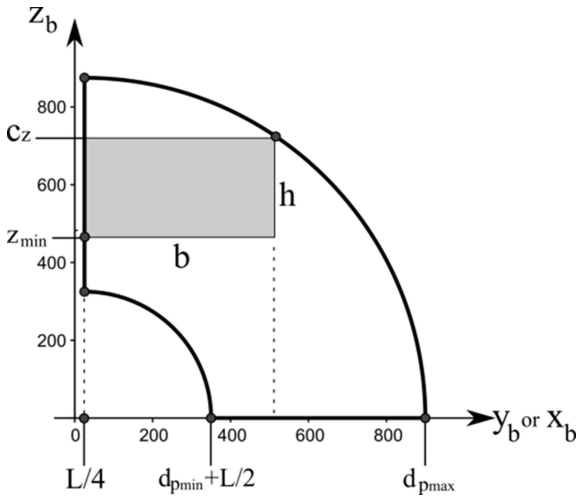

Fig. 5. Useful workspace (gray rectangle) projected onto the x_bz_b-and y_bz_b-planes (d_p corresponds to d_4 or d_2 for the x_bz_b or y_bz_b plane, respectively).

$$b^2 = \left(d_{pmax} - \frac{L}{4}\right)^2 - c_z^2 \tag{10b}$$

The introduction of Eq. (10a) into Eq. (10b) and of the resulting expression into Eq. (9) yields the following explicit expression of V_u as a function of h

$$V_u = \left[\left(d_{pmax} - \frac{L}{4}\right)^2 - (h + z_{min})^2\right] h \tag{11}$$

By equating to zero the derivative of function (11) with respect to h, the following expression of h that maximizes V_u is obtained

$$h = -\frac{2}{3} z_{min} + \frac{1}{3}\sqrt{3\left(d_{pmax} - \frac{L}{4}\right)^2 + z_{min}^2} \tag{12}$$

whose introduction into Eq. (11) yields the optimal value of V_u as a function of z_{min}. Also, the value of volume, V_o, of the dexterous workspace has been computed by using a CAD tool.

Figure 6 shows a dimensionless diagram that, for each value of z_{min}/L, yields V_u/V_o, the maximum, CI_{max}, and the minimum, CI_{min}, values of CI in the useful workspace and the GCI. This diagram shows that the GCI has always values greater than 0.602 (i.e., near to CI_{max} = 0.707); whereas, CI_{min} and V_u/V_o strongly depend on z_{min}/L with CI_{min} that is always greater than 0.332 and V_u/V_o that is always lower than 34.4%. Such high GCI brings to conclude that only small parts of the useful workspace have CI values near

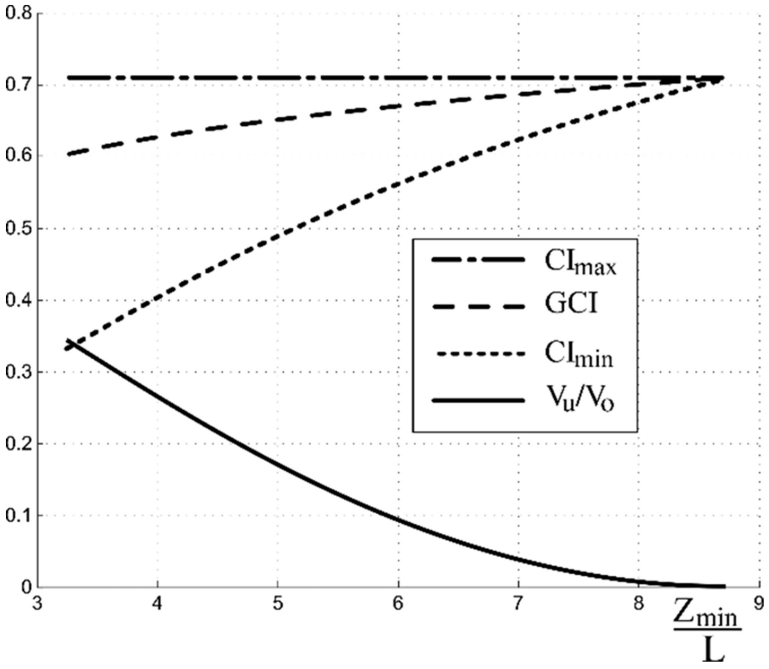

Fig. 6. Diagrams of V_u/V_o, CI_{min}, CI_{max}, and GCI as a function of z_{min}/L

to CI_{min}. Anyway, choosing $CI_{min} = 0.45$ could be a good compromise (see Fig. 6) since it yields $z_{min} = 4.54$ L, $h = 2.24$ L, $b = 5.52$ L, $(V_u/V_o) = 20.9\%$, and GCI = 0.639. The useful workspace of Fig. 4 refers to this case and shows that it is interesting for practical applications.

4 Conclusions

The kinetostatic performances and the optimal location of the useful workspace of an SMG previously proposed by the authors have been studied.

The kinetostatic performances have been evaluated by introducing a novel technique that could be applied to any SMG. Such technique brings to determine a reduced form of the static input-output relationship, which has homogeneous inputs and outputs, and uses the Jacobian of this relationship to calculate the conditioning index and the global conditioning index.

The results of this study show that a useful workspace with sizes that are interesting for practical applications, and with satisfactory kinetostatic performance can be found for this SMG.

Acknowledgments. This work has been developed at the Laboratory of Advanced Mechanics (MECH-LAV) of Ferrara Technopole, supported by FIR2016 funds, by Regione Emilia Romagna (District Councillorship for Productive Assets, Economic Development, Telematic

Plan) POR-FESR 2007–2013, Attività I.1.1, and by the Raul Guenther Laboratory of Applied Robotics (LAR-UFSC) of Federal University of Santa Catarina, supported by Brazil's federal agencies for research: CNPq, CAPES and FINEP.

References

1. Lee, C.-C., Hervé, J.M.: Type Synthesis of primitive Schoenflies-motion generators. Mech. Mach. Theory **44**, 1980–1997 (2009)
2. Lee, C.-C., Hervé, J.M.: Isoconstrained parallel generators of schoenflies motion. ASME J. Mech. Rob. 3(2), 021006-1–021006-10 (2011)
3. Kong, X., Gosselin, C.M.: Type synthesis of 3T1R 4-DOF parallel manipulators based on screw theory. IEEE Trans. Rob. Autom. **20**, 181–190 (2004)
4. Zhao, J., Feng, Z., Chu, F., Ma, N.: Advanced Theory of Constraint and Motion Analysis for Robot Mechanisms. Elsevier Academic Press (2014). ISBN 978-0-12-420162-0
5. Simas, H., Di Gregorio, R.: Position analysis, singularity loci and workspace of a novel 2PRPU Schoenflies-motion generator. ASME J. Mech. Rob., Paper no. JMR-17-1036 (2017, submitted)
6. Gosselin, C., Angeles, J.: A global performance index for the kinematic optimization of robotic manipulators. J. Mech. Des. **113**(3), 220–226 (1991)
7. Angeles, J.: Fundamentals of Robotic Mechanical Systems. Springer, Swizterland (2014). ISBN 978-3-319-30762-6
8. Siciliano, B., Sciavicco, L., Villani, L., Oriolo, G.: Robotics: Modelling, Planning and Control, p. 85. Springer, London (2009). ISBN 978-1-84628-641-4
9. Lou, Y., Liu, G., Chen, N., Li, Z.: Optimal design of parallel manipulators for maximum effective regular workspace. In: Proceedings of the 2005 IEEE/RSJ International Conference on Intelligent Robots and Systems, Edmonton, Canada, pp. 795–800 (2005)

Influence of the Working Mode on the Maximum Isotropic Force Capability Maps for a 3RRR Planar Parallel Manipulator

L. Mejia[1(✉)], D. Ponce[2], J.C. Herrera[3], H. Simas[3], and D. Martins[3]

[1] Department of Automation and Control, Federal University of Santa Catarina, Blumenau, Santa Catarina 89036-256, Brazil
leonardo.mejia.rincon@ufsc.br

[2] Department of Engineering, Federal University of Santa Catarina, Blumenau, Santa Catarina 89036-256, Brazil
daniel.alejandro@ufsc.br

[3] Department of Mechanical Engineering, Federal University of Santa Catarina, Florianópolis, Santa Catarina 88040-900, Brazil
camilo.herrera@posgrad.ufsc.br, {henrique.simas,daniel.martins}@ufsc.br

Abstract. This paper shows how different working modes in a symmetrical 3RRR planar parallel manipulator can influence its maximum isotropic force capability maps. Herein, a new method to obtain analytically the maximum isotropic force with a prescribed moment is proposed. The proposed method is obtained from a general static model of the studied manipulator obtained by employing the screw theory and the Davies method as primary mathematical tools. Finally, some maximum isotropic force capability maps are obtained for different working modes in the studied manipulator in order to analyse their influence.

Keywords: Wrench capability · Davies method · Isotropic force · Maximum isotropic wrench capability maps

1 Introduction

In recent years, industrial robots have become more and more complex and their use has been widely disseminated. Nowadays, robots are not simply machines that can be reprogrammed in order to execute different repetitive tasks, but very sophisticated devices that can actively interact with the environment [1].

In this sense, the interaction of robots with the environment needs to get an especial attention because once a robot comes into contact with a surface, internal forces that can be lead the robot to its force capability limit can appear [1].

The force capability of a robot or a manipulator is defined as the maximum force that can be applied (or sustained) by such a device. This property changes its magnitude as a function of the applied force's direction and in order to deal with these variations, an important property known as the maximum isotropic force capability can be considered. The maximum isotropic force capability in a

J.C.M. Carvalho et al. (eds.), *Multibody Mechatronic Systems*,
Mechanisms and Machine Science 54, DOI 10.1007/978-3-319-67567-1_14

robot or a manipulator is defined as the maximum force that such a device can apply (or sustain) in all directions [2].

The main objective of this study is to develop a method to obtain the maximum isotropic force capability for a 3RRR symmetrical planar parallel manipulator (SPPM) in static or quasi-static conditions. Additionally, the maximum isotropic force capability is evaluated within the entire workspace of the studied manipulator in order to obtain a complete map of the behavior of this property as a function of a chosen working mode.

2 Related Work

The interest in measuring the force and velocity capabilities of robots and mechanisms began in the mid-1980s when Yoshikawa [3] introduced the concepts of force and velocity manipulability ellipsoid. Along the last years, several researchers have proposed new methodologies and indices that best describe such a capabilities.

Several studies related to the force capability in robots and manipulators have been presented recently. Zhao et al. [4] analyzed the force capabilities of two mechanisms based on the force manipulability ellipsoid. Mejia et al. [5,6] and Weihmann et al. [2] presented new methodological solutions to obtain the force capability in planar manipulators by using differential evolution algorithms.

Mejia et al. [7,8] proposed several closed-form solutions to obtain the maximum force with a prescribed moment in parallel mechanisms with a net degree of constraint equal to three, four, five or six.

Firmani et al. [9] presented some new wrench capability indices to evaluate the force capabilities in planar manipulators. Three of the most important indices presented by Firmani et al. were the maximum absolute force (F_{av}), the maximum force with a prescribed moment (F_{app}) and the maximum isotropic force (F_{iso}) [2]. F_{iso} is the main indice studied in this paper. Figure 1 shows a *"3RRR symmetrical planar parallel manipulator"* with a graphical representation of three of its main force capability indices: the F_{app}, the F_{av} and the F_{iso}.

3 Geometry of the Studied Manipulator

In this paper, a *"3RRR symmetrical planar parallel manipulator"* is studied. Such a parallel manipulator has its fixed and mobile platforms joined by using three limbs and each limb has three rotational joints which axes are perpendicular to the $(x-y)$ plane. The first of the three joints in each limb is actuated.

The studied manipulator has the mobile and fixed platforms formed by equilateral triangles with sides l_m and l_f respectively. The limbs are formed by two links with longitudes l_1 and l_2 respectively. A *"3RRR symmetrical planar parallel manipulator (SPPM)"* was represented schematically in Fig. 1.

The studied *"3RRR symmetrical planar parallel manipulator"* is a mechanism with nine joints and eight links, and its mobility can be calculated using

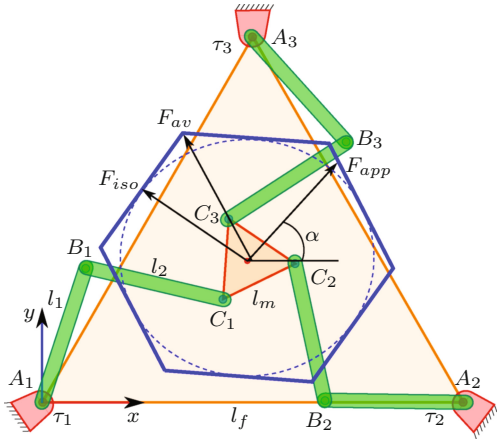

Fig. 1. A 3RRR symmetrical planar parallel manipulator with a graphical representation of three of its main force capability indices

the Chebychev-Grubler-Kutzbach criterion, as shown in Eq. (1).

$$M = \lambda(n - j - 1) + \sum_{i=1}^{j} f_i = 3(8 - 9 - 1) + 9 = 3 \tag{1}$$

In the studied *"3RRR symmetrical planar parallel manipulator"*, the fixed base is considered as the frame of the system, the l_1 links belonging to the three limbs are considered as the inputs links and the mobile platform is considered as the end effector link. The primary actuation is applied to the active joints A_1, A_2 and A_3 of the fixed platform.

4 Statics of the Studied Manipulator

Static analysis of mechanisms and robots makes use of the static force equilibrium equations in order to obtain the wrenches requirements at the end effector in relation to the forces and moments applied at the joints. Some well known methodologies to solve the statics of mechanisms and robots have been proposed in the literature, nevertheless, in this paper the method presented by Davies [10] is used in order to solve the statics of the studied SPPM. The Davies method is a systematic procedure that relate the joint moments and forces in closed kinematic chains [11]. This method is based on the ***Kirchhoff cut-set laws***, ***screw theory***, and ***graph theory*** in order to obtain matricial expressions that model the statics of a robotic mechanism [7].

The Davies method for static analysis can be described in a simplified way through the following steps: (1) draw the kinematic chain identifying all of its *"n"* links and *"e"* direct couplings, (2) Draw the coupling graph **"**G_C**"** using the links of the mechanism as the vertices of the graph, and the joints of the mechanism as the edges of the graph, (3) Generate the action graph **"**G_A**"** from **"**G_C**"** through

unfolding single actions from direct couplings. In this step, each edge of "G_C" representing a coupling is replaced in "G_A" by "c" constraint edges in parallel, (4) Write the cut-set matrix $[Q_N]_{k,e}$ with suitable signs, (5) Write a wrench $\$_J$ for each edge from "G_A", (6) Replace each wrench $\$_J$ in the cut-set matrix $[Q_N]_{k,e}$ in order to obtain the generalized action matrix $[A_N]_{3k,e}$, (7) Operate algebraically the generalized action matrix $[A_N]_{3k,e}$ in order to statically solve the system.

More explanations about the use of the Davies' Method can be found in [2,7,10–13].

Once the Davies method has been applied in order to obtain the backward statics of the SPPM, it is possible to represent the wrenches at the actuated joints of the manipulator $[\tau_{A_1}, \tau_{A_2}, \tau_{A_3}]^T$ as a generalized function of a coefficient matrix [A] and a vector containing the 3 primary actions $[F_x, F_y, M_z]^T$ as shown in Eq. (2). In this equation the $a_{1,1}, \ldots, a_{3,3}$ elements represent kinematic expressions as a function of the manipulator joint positions, the $[F_x, F_y, M_z]^T$ elements represent the wrenches at the manipulator's end effector and the $\tau_{A_1}, \tau_{A_2}, \tau_{A_3}$ elements represent the wrenches at the actuated joints.

$$\begin{bmatrix} \tau_{A_1} \\ \tau_{A_2} \\ \tau_{A_3} \end{bmatrix} = \begin{bmatrix} a_{1,1} & a_{1,2} & a_{1,3} \\ a_{2,1} & a_{2,2} & a_{2,3} \\ a_{3,1} & a_{3,2} & a_{3,3} \end{bmatrix} \cdot \begin{bmatrix} F_x \\ F_y \\ M_z \end{bmatrix} \tag{2}$$

5 Scaling Factor Method to Obtain the Maximum Isotropic Force with a Prescribed Moment (F_{iso})

In this section, a modified scaling factor method to obtain the maximum isotropic force with a prescribed moment is proposed. Formally, the maximum isotropic force can be defined as the maximum force that a manipulator can apply (or sustain) in all directions [2]. The method proposed in this section solves the main problem identified in the literature for another maximum force capabilities methods. Such a problem is directly related with the variations in the forces' magnitudes as a function of the direction of the applied wrenches.

Initially, the proposed method requires a unit wrench $\$_F$ to be imposed at the end effector of the manipulator, such unit wrench must include an associated value μ as the component of the moment in z. The unit wrench is represented as $\$_F = [\cos(\theta), \sin(\theta), \mu]^T$, and the backward statics equation shown in Eq. (2) can be rewritten as:

$$\begin{bmatrix} \tau_{A_1} \\ \tau_{A_2} \\ \tau_{A_3} \end{bmatrix} = \begin{bmatrix} a_{1,1} & a_{1,2} & a_{1,3} \\ a_{2,1} & a_{2,2} & a_{2,3} \\ a_{3,1} & a_{3,2} & a_{3,3} \end{bmatrix} \cdot \begin{bmatrix} \cos(\theta) \\ \sin(\theta) \\ \mu \end{bmatrix} \tag{3}$$

In order to solve the maximum isotropic force capability problem (F_{iso}), first, an expansion for Eq. (3) can be obtained as:

$$\tau_i(\theta, \mu) = a_{i,1} \cdot \cos(\theta) + a_{i,2} \cdot \sin(\theta) + a_{i,3} \cdot \mu \qquad i = 1, 2, 3 \tag{4}$$

then, assuming the existence of an scaling factor (Ψ) saturating the actuated joints and the knowledge of the maximum value of wrench accepted at each actuated joint ($\tau_{i_{max}}$), two conditions need to be respected simultaneously, these conditions are shown in Eqs. (5) and (6).

$$\tau_i \cdot \Psi = \tau_{i_{max}} \qquad i = 1, 2, 3 \tag{5}$$

$$\mu \cdot \Psi = M_d \qquad i = 1, 2, 3 \tag{6}$$

multiplying Eq. (4) by Ψ and substituting Eqs. (5) and (6) in this equation, we can obtain a generalized equation that describes the scaling factor Ψ as a function of the direction for the application of the force (θ) as shown in Eq. (7).

$$\Psi(\theta) = \frac{\tau_{i_{max}} - a_{3i} \cdot M_d}{a_{3i-2} \cdot \cos(\theta) + a_{3i-1} \cdot \sin(\theta)} \tag{7}$$

Due that the numerator in Eq. (7) is assumed as a constant, the maximum value that the scaling factor $\Psi(\theta)$ can assume is obtained when the denominator in Eq. (7) is minimum. In this way, by deriving the denominator in Eq. (7), equating to zero and solving, it is possible to obtain the critical values for the direction θ which minimize the values of the scaling factor Ψ as shown in Eq. (8).

$$\theta_{crit} = \tan^{-1}\left(\frac{a_{3i-2}}{a_{3i-1}}\right) \tag{8}$$

The values obtained for $\theta_{i_{crit}}$ are the possible directions in which the maximum isotropic force can be found. By evaluating those values obtained from Eq. (8) into the Eq. (7) and manipulating algebraically, we obtain a generalized expression that defines the maximum isotropic force as shown in Eq. (9).

$$\psi_i = \frac{(\tau_{i_{max}} - a_{i,3} \cdot M_d)}{\sqrt{(a_{i,1})^2 + (a_{i,2})^2}} \qquad i = 1, 2, 3 \tag{9}$$

The scaling factors of Eq. (9) can be placed in a set. The scaling factor (Ψ) in this set with the minimum value is the maximum factor which all joint torques/forces can be scaled by and still remain at or below their corresponding maximum values, and represents the maximum isotropic force of the robotic manipulator i.e.:

$$\Psi = \min(\psi_i) \qquad i = 1, 2, 3 \tag{10}$$

6 Influence of the Working Mode on the Maximum Isotropic Force Capability Maps for the Studied SPPM's

The serial planar parallel manipulator under study presents eight inverse kinematic solutions associated with the possible postures that such a manipulator can adopt. The set of these possible manipulator's postures without any serial singularity represents its possible working modes.

Assembly modes represent the different solutions to the direct kinematic problem whereas ***Working modes*** represent the solutions to the inverse kinematic problem [14]. In this paper we only studied the influence of the *working modes* on the maximum isotropic force capability maps for a 3RRR SPPM. The eight possible working modes (WM_1 to WM_8) for the studied manipulator are shown in Fig. 2.

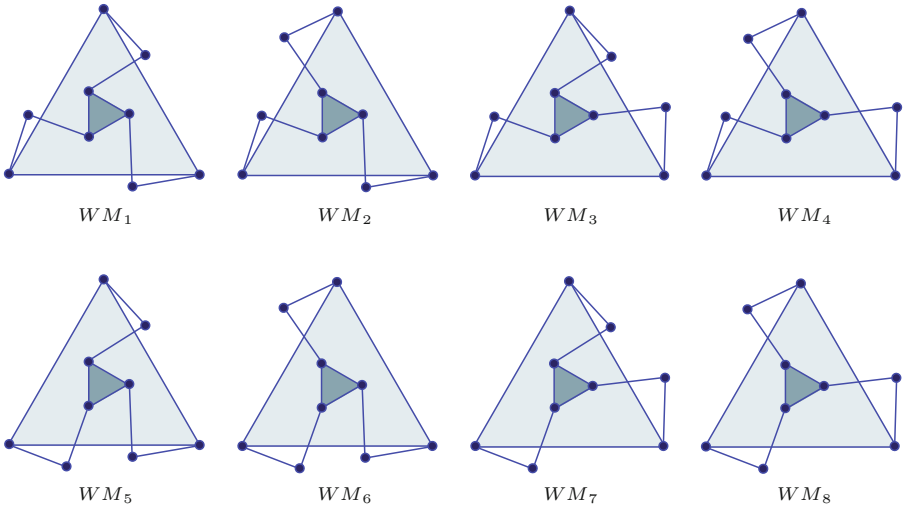

Fig. 2. The eight possible working modes for a 3RRR PPM

7 Results

By applying the proposed Scaling Factor Method to obtain the maximum isotropic force with a prescribed moment (F_{iso}) (shown in Sect. 5), for all reachable positions in the manipulator's workspace, it is possible to obtain a complete map representing the behavior of the F_{iso} along the different regions of the workspace. It allow us to evaluate the places where the manipulator could execute a determined task in a more efficient way. Figure 3 shows the different maximum isotropic force capability maps for the studied SPPM in each of its different working modes and in agreement with the ones shown in Fig. 2.

From Fig. 3, it is possible to observe that the studied SSPM have several symmetries that influence in a direct way the geometrical representation of the maximum isotropic force capability maps. In order to explain this phenomenon, suppose the working modes WM_1 and WM_8 shown in Fig. 2. Observe that these manipulators have all their legs located in an opposite direction, and as result of this kind of variation, their corresponding maximum isotropic force capability maps have a reflection symmetry (as shown in WM_1 and WM_8 in

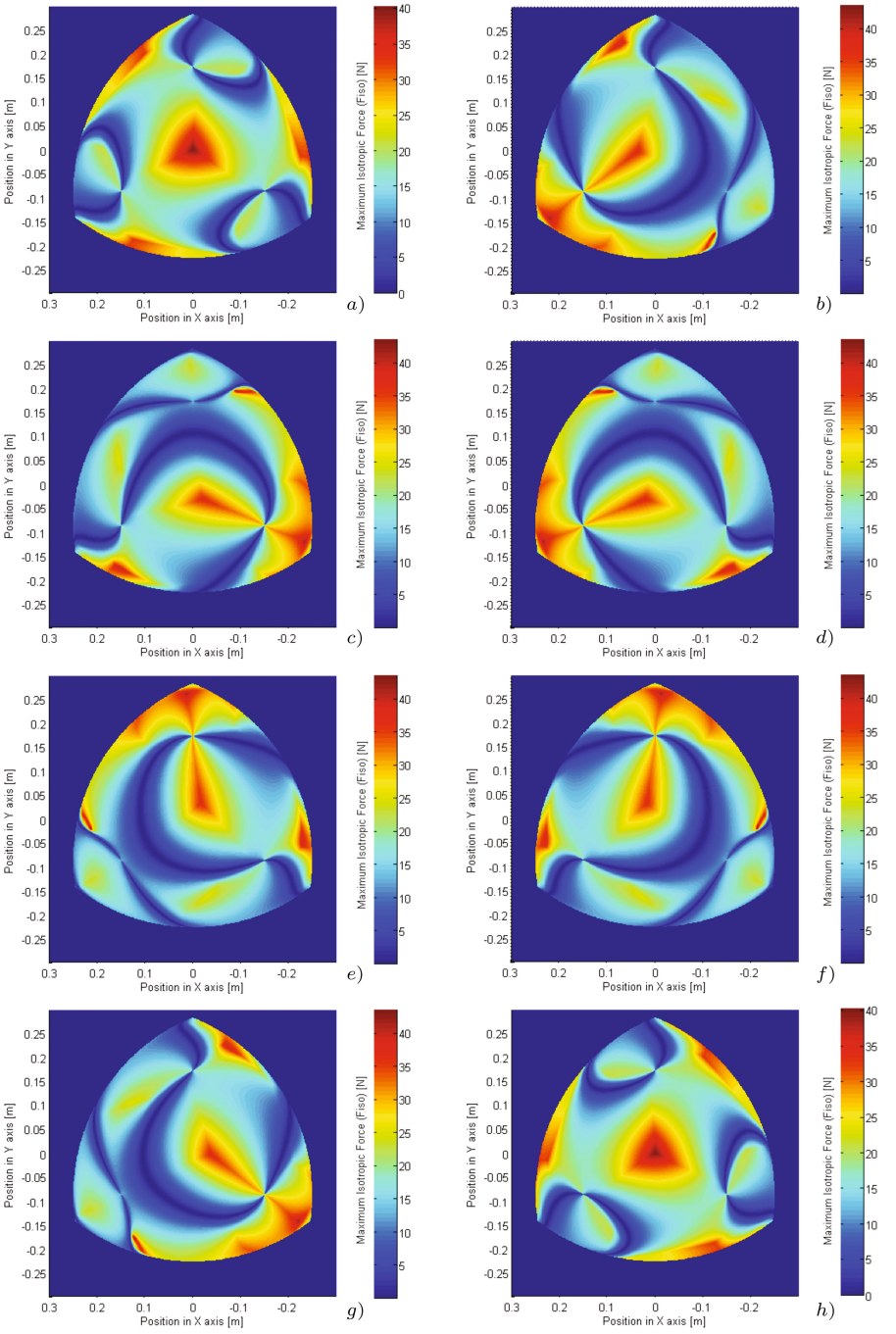

Fig. 3. Maximum isotropic force capability maps for a 3$\underline{\text{R}}$RR SSPM in: (a) WM1; (b) WM2; (c) WM3; (d) WM4; (e) WM5; (f) WM6; (g) WM7 and (h) WM8

Fig. 3). The symmetries presented in the maximum force capability maps can not be disconsidered because for different predefined tasks different working modes could be required.

Another phenomenon found when the working mode in parallel manipulators is changed is the superposition, that represents an extended map of the manipulator's maximum isotropic force capabilities. Figure 4 shows an extended maximum isotropic force capability map, by using overlapping of the previously obtained force capability maps in Fig. 3.

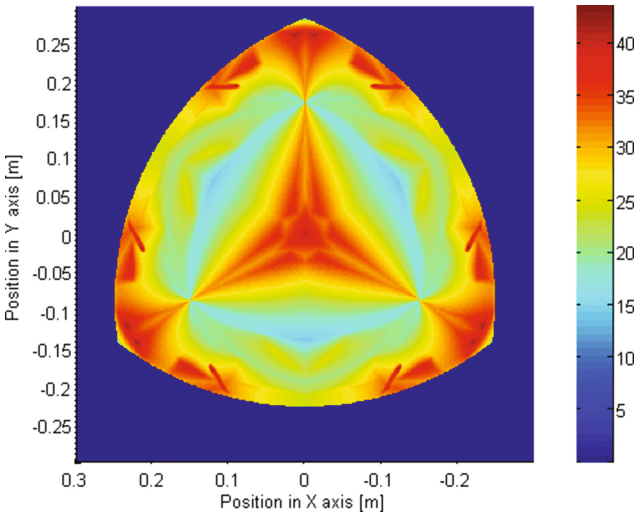

Fig. 4. General maximum isotropic force capability map for all working modes in a 3RRR planar parallel manipulator

8 Conclusions

This paper studied the influence that several variations in the working modes of a 3RRR symmetrical parallel manipulator can have on their maximum isotropic force capability, opening the possibility to visualize the best regions where the manipulator can act in order to improve its efficiency.

A new method to obtain analytically the maximum isotropic force with a prescribed moment was proposed. The proposed method in this paper uses a general static model as an starting point to solve the problem of the maximum isotropic force. Authors used the formalism presented by Davies as the primary mathematical tool to analyze the mechanisms statically.

The present study may be extended in various ways. Manipulators with different DOFs, kinematic chains and including dynamic behavior may be studied, and variations on the imposed moment may be considered in future researches.

Acknowledgements. Authors would like to thank to the Federal University of Santa Catarina which has made the present work possible.

References

1. Weihmann, L.: FModelagem e otimização de forças e torques aplicados por robôs com redundância cinemática e de atuação em contato com o meio, Universidade Federal de Santa Catarina (2011)
2. Weihmann, L., Martins, L., Coelho, L.S.: Force capabilities of kinematically redundant planar parallel manipulators. In: 13th World Congress in Mechanism and Machine Science, vol. I, p. 483 (2011)
3. Yoshikawa, T.: Manipulability and redundancy control of robotic mechanisms. In: The Second International Symposium on Robotics Research, vol. I, pp. 1004–1009 (1985)
4. Zhao, Y., Lin, Z.Q., Wang, H.: Manipulation performance analysis of heavy manipulators. J. Chin. Mech. Eng. **46**(11), 69–75 (2010)
5. Mejia, L., Simas, H., Martins, D.: Force capability polytope of a 3RRR planar parallel manipulator. In: Proceedings of Romansy 2014 XX CISM-IFToMM Symposium on Theory and Practice of Robots and Manipulators, 1st edn., pp. 537–545 (2014)
6. Mejia, L., Simas, H., Martins, D.: Force capability polytope of a 4RRR redundant planar parallel manipulator. In: Advances in Robot Kinematics, 1st edn., pp. 87–94 (2014)
7. Mejia, L., Simas, H., Martins, D.: Force capability in general 3DoF planar mechanisms. Mech. Mach. Theory **91**, 120–134 (2015)
8. Mejia, L., Simas, H., Martins, D.: Wrench capability in redundant planar parallel manipulators with net degree of constraint equal to four, five or six. Mech. Mach. Theory **106**, 58–79 (2016)
9. Firmani, F., Zibil, A., Nokleby, S.B., Podhorodeski, R.P.: Wrench capabilities of planar parallel manipulators. Part II: wrench polytopes and performance indices. Robotica **26**, 803–815 (2008)
10. Davies, T.H.: Mechanical networks III: wrenches on circuit screws. Mech. Mach. Theory **18**, 107–112 (1983)
11. Cazangi, H.R.: Aplicação do método de Davies para Análise Cinemática e Estática de Mecanismos de Múltiplos Graus de Liberdade, Universidade Federal de Santa Catarina, I (2008)
12. Davies, T.H.: Mechanical networks I: passivity and redundancy. Mech. Mach. Theory **18**, 95–101 (1983)
13. Davies, T.H.: Mechanical networks II: formulae for the degrees of mobility and redundancy. Mech. Mach. Theory **18**, 103–106 (1983)
14. Chablat, D., Wenger, P.: Working modes and aspects in fully-parallel manipulator. In: Proceedings of the IEEE International Conference on Robotics and Automation (1998)

Maximum Isotropic Force Capability Maps in Planar Cooperative Systems: A Practical Case Study

Juan Camilo Herrera Pineda[1(✉)], Leonardo Mejia Rincon[1], Roberto Simoni[2], and Henrique Simas[1]

[1] Federal University of Santa Catarina, Florinpolis, Santa Catarina 88040-900, Brazil
camherrera837@hotmail.com
[2] Federal University of Santa Catarina, Joinville, Santa Catarina 89218-000, Brazil

Abstract. In robotics, the force capability is defined as the maximum wrench that can be applied (or sustained) by a manipulator. This property is dependent on the robot's posture, actuation limits and redundancies and, by considering all possible directions of the applied wrench, a polar force capability plot can be generated for a given pose. The concept of isotropic force capability appeared as a subset of the classic force capability and it was formally defined as the maximum magnitude force that a robot can apply or support in all directions according to a posture. A relevant condition which must be studied is when there is load distribution processes between cooperative robots, e.g. when two or more arms are carrying the same load, if the load distribution fails, one of the arms may overload causing structural or material damage during the process. The main objective of this paper is to develop a method to determine the area in the workspace of a cooperative robot composed by two planar serial $3R$ manipulators which presents the maximum isotropic force capability. The isotropic force capability maps are generated for three different load's orientations and four working modes and they are compared among themselves.

Keywords: Isotropic force capability · Cooperative robots · Davies' method · Screw theory

1 Introduction

Power tools are being increasingly demanded in the industrial scope due to the need for adaptability, productivity and quality that are extremely important. This scenario includes industrial robots, which have a larger workspace and a lower investment compared to a 5-axis tool machine [2].

The task space capability of a manipulator to perform motion and/or to exert forces and moments are of fundamental importance in robotics. Its evaluation can be useful to determine the structure and size of the manipulator that best fit the designer's requirements or it can be used to find a better configuration or a better operation point for a manipulator to perform a given task [4,5].

J.C.M. Carvalho et al. (eds.), *Multibody Mechatronic Systems*,
Mechanisms and Machine Science 54, DOI 10.1007/978-3-319-67567-1_15

In robotics, the force capability is defined as the maximum wrench that can be applied (or sustained) by a manipulator in a certain pose, based on the limits of the actuators [13]. The force capability of a cooperative robot system depends on its posture, actuation limits and redundancies [15] and, by considering all possible directions of the applied wrench, a polar force capability plot can be generated for a given pose. The concept of isotropic force capability appeared as a subset of the classic force capability and it was formally defined as the maximum magnitude force that a robot can apply or support in all directions according to a posture [11].

The cooperative work between two manipulators has had in recent years a significant growth given the advantages it offers. The first of these advantages is that it allows to perform tasks which are impossible to achieve by a single manipulator, e.g. a manipulator can not move a beam that exceeds its load capacity, but two working coordinately can do so. Thus a relevant condition which must be studied is when there are load distribution processes between cooperative robots, e.g. when two or more arms are carrying the same load, if the load distribution fails, one of the arms may overload causing structural or material damage during the process. The main objective of this paper is to develop a method to determine the area in the workspace of a cooperative robot composed by two planar serial $3R$ manipulators which presents the maximum isotropic force capability. In Sect. 2, it is introduced the Davies method to determine the static model of the cooperative robotic system, from which is developed the method to determine the isotropic force capability, shown in Sect. 3. A dynamic model is not developed as only the task of the transport of loads, which does not demand high velocities, is considered. The isotropic force capability maps are generated for three different load's orientations and four working modes and they are compared among themselves in Sect. 4. Finally, Sect. 5 presents the final considerations about the results achieved in this paper.

2 Statics of Cooperative Robots

The static analysis of cooperative robots allows to know the forces and the moments acting at the manipulator's joints and at the manipulator's end effector when it comes in contact with the environment. In the direct static analysis, the wrenches at the end effector are determined through the forces and moments applied at the manipulator's joints while in the backward static analysis, the wrenches at the end effector are known and allow to estimate the efforts in the joints.

The static analysis can be developed through different methods, such as the vector method, dual vectors and dual quaternions, virtual work and the Davies method using screw theory. In this paper it is employed the Davies method [8] because it permits to obtain the static model of the mechanism in a simple way and it is easily adaptable. This method is a powerful tool based on graph theory,

screw theory and Kirchhoff-Davies theory. The main steps of the method are briefly explained below [14].

1. Given a mechanism, draw its kinematic chain identifying all of its n links and e direct couplings.
2. Draw the coupling graph G_C using the links of the mechanism as the vertices of the graph, and the joints of the mechanism as the edges of the graph.
3. Generate the action graph G_A from G_C through unfolding single actions from direct couplings. In this step, each edge G_C of representing a coupling is replaced in G_A by c constraint edges in parallel.
   - Assign positive directions to each edge with an arrow pointing from the minor to major vertex.
   - Locate the number of cuts ($k = n - 1$) and chords ($l = e - n + 1$) in the action graph and depict them.
4. Write the cut-set matrix $[Q_N]_{k,e}$ with suitable signs.
5. Write a wrench $\$_J$ for each edge from G_A as follows:

$$\$_J = \begin{bmatrix} -y \\ 1 \\ 0 \end{bmatrix} J_{F_x} + \begin{bmatrix} x \\ 0 \\ 1 \end{bmatrix} J_{F_y} + \begin{bmatrix} 1 \\ 0 \\ 0 \end{bmatrix} J_{M_z} \tag{1}$$

6. Replace each wrench $\$_J$ in the cut-set matrix $[Q_N]_{k,e}$ in order to obtain the generalized action matrix $[A_N]_{3k,e}$.
7. Operate algebraically the generalized action matrix $[A_N]_{3k,e}$ in order to statically solve the system.

For further information about the Davies method, see [3,6–8,10,14,15]. An intrinsic property obtained from the Davies method is the net degree of constraint (C_N), which represents the number of variables that must be known to determinate completely the mechanism's static state. It is calculated by the expression:

$$C_N = C - \lambda k \tag{2}$$

where C is the sum of the number of internal constraints of all the mechanism's joints, λ is the order of screw system e.g. for a planar mechanism, $\lambda = 3$ and k is the number of cuts.

2.1 Davies Method in Cooperative Robots

The cooperative robot shown in Fig. 1(a) is composed by two 3R planar serial robots and is depicted by the action graph in Fig. 1(b), where the vertices correspond to the links and the edges represent the actions in the joints. The cooperative robot system is transporting a load whose weight is the sum of a component in x (f_x) and another in y (f_y). All the joints have two constraints

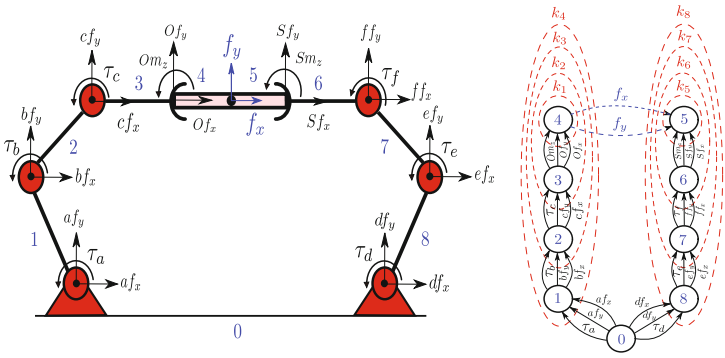

Fig. 1. (a) Planar serial cooperative robotic system. (b) Action graph.

of force, one in x and other in y, indicated by the letter representing the joint plus the force direction (e.g. af_x, af_y), and a torque as active coupling (e.g. τ_a). The two end effectors have three active couplings each: a force in x, a force in y and a moment in z, where Of_x, Of_y and Om_z belong to the master serial robot and Sf_x, Sf_y and Sm_z belong to the slave serial robot.

By employing the Eq. (2), the net degree of constraint of the cooperative robot is defined as:

$$C_N = 26 - 3 \cdot 8 = 26 - 24 = 2 \tag{3}$$

This result means that among the variables of the cooperative robot's backward static model, two must be known (*primary variables*) to describe the behavior of the remaining ones (*secondary variables*). In the static model of the cooperative robotic system in Fig. 1(a) the primary variables are f_x and f_y and secondary variables are the torques in the joints and moments in the end effector:

$$\begin{bmatrix} \tau_a \\ \tau_b \\ \tau_c \\ Om_z \\ \tau_d \\ \tau_e \\ \tau_f \\ Sm_z \end{bmatrix} = \begin{bmatrix} a_{1,1} & a_{1,2} \\ a_{2,1} & a_{2,2} \\ a_{3,1} & a_{3,2} \\ a_{4,1} & a_{4,2} \\ a_{5,1} & a_{5,2} \\ a_{6,1} & a_{6,2} \\ a_{7,1} & a_{7,2} \\ a_{8,1} & a_{8,2} \end{bmatrix} \begin{bmatrix} f_x \\ f_y \end{bmatrix} \tag{4}$$

The 8×2 matrix in Eq. (4) is the transposed Jacobian of the cooperative robot, where the elements $a_{1,1}, \cdots, a_{4,1}$ and $a_{1,2}, \cdots, a_{4,2}$ represent the position of the joints and of the end effector of the master serial robot and the elements $a_{5,1}, \cdots, a_{8,1}$ and $a_{5,2}, \cdots, a_{8,2}$ represent the position of the joints and of the end

effector of the slave serial robot shown in Fig. 1(a). From Eq. (4) we can determine which is the maximum force that the final actuators can realize without exceeding the limits of the actuators.

The knowledge of this problem allowed to develop important tools to know the potential of the generation of torques or forces in the actuators and the direction of the forces applied in the final effector [9]. In this sense comes the concept of ***isotropic force capability***, which consists of the maximum magnitude of force that a robot can apply or support in all directions according to a posture [1]. In order to obtain the isotropic force in a cooperative robotic system, in this paper is presented a method based on the scaling factor method presented by [13] and the modified scaling factor method presented by [12].

3 Isotropic Force Capability for a Cooperative Robotic System

In order to calculate the isotropic force capability for the cooperative robotic system shown in Fig. 1(a), a unitary action with a desired direction is applied to determine the joint of the manipulator that is the relatively most charged. The limits of the actuators are taken in consideration through a unit wrench $\$_F$, representing the desired wrench direction as shown in Eq. (5), where f_{app} is the wrench intensity of $\$F_{app}$.

$$\$F_{app} = f_{app}\$_F \tag{5}$$

Using the unit wrench $\$_F = [\cos(\theta), \sin(\theta), 0]^T$ in order to represent the desired direction of the force, and eliminating the third element of $\$_F$ as there is no moment in the particular case depicted in Fig. 1(a), the backward statics equation shown in Eq. (4) can be rewritten as:

$$\begin{bmatrix} \tau_a \\ \tau_b \\ \tau_c \\ Om_z \\ \tau_d \\ \tau_e \\ \tau_f \\ Sm_z \end{bmatrix} = \begin{bmatrix} a_{1,1} & a_{1,2} \\ a_{2,1} & a_{2,2} \\ a_{3,1} & a_{3,2} \\ a_{4,1} & a_{4,2} \\ a_{5,1} & a_{5,2} \\ a_{6,1} & a_{6,2} \\ a_{7,1} & a_{7,2} \\ a_{8,1} & a_{8,2} \end{bmatrix} \begin{bmatrix} \cos(\theta) \\ \sin(\theta) \end{bmatrix} \tag{6}$$

The primary actions $(\tau_1(\theta), \tau_2(\theta), ..., \tau_8(\theta)) = (\tau_a, \tau_b, ..., Sm_z)$ can be calculated as a function of θ as shown below:

$$\tau_i(\theta) = a_{i,1}\cos(\theta) + a_{i,2}\sin(\theta) \qquad i = 1, ..., 8 \tag{7}$$

Since the maximum torque limits (τ_{imax}) are known for all actuated joints i, scaling factors for each one can be found using Eq. (8) [13].

$$\psi_i = \left|\frac{\tau_{imax}}{\tau_i(\theta)}\right| = \left|\frac{\tau_{imax}}{a_{i,1}\cos(\theta) + a_{i,2}\sin(\theta)}\right| \qquad i = 1, ..., 8 \tag{8}$$

where ψ_i is the scaling factor for each actuated joint i, and $\tau_i(\theta)$ is the torque of the i^{th} actuated joint for a unit wrench in the desired force direction, obtained from Eq. (7). The results of Eq. (8) can be placed in a set of scaling factors, which in the studied case is composed by eight elements.

To maximize the set of scaling factors ψ_i, the denominator of the Eq. (8) must be minimize by finding the critical angles. In such a way the denominator is derived and equated it to zero:

$$D' \rightarrow -a_{i,1}\sin(\theta) + a_{i,2}\cos(\theta) = 0 \qquad i = 1, ..., 8 \tag{9}$$

Dividing both sides of the Eq. (9) by $\cos(\theta)$, the equation can be rewritten as follows:

$$D' \rightarrow -a_{i,1}\tan(\theta) + a_{i,2} = 0 \qquad i = 1, ..., 8 \tag{10}$$

Isolating θ, the critical angles θ_c are determined:

$$\theta_c = \tan^{-1}\left(\frac{a_{i,2}}{a_{i,1}}\right) \qquad i = 1, ..., 8 \tag{11}$$

Replacing Eq. (11) in (8) and applying the following trigonometric proprieties:

$$\cos\left(\tan^{-1}(x)\right) = \frac{1}{\sqrt{1+x^2}} \qquad \sin\left(\tan^{-1}(x)\right) = \frac{x}{\sqrt{1+x^2}} \tag{12}$$

The Eq. (8) can be rewritten as:

$$\psi_i = \frac{\tau_{i_{max}}}{\sqrt{{a_{i,1}}^2 + {a_{i,2}}^2}} \qquad i = 1, ..., 8 \tag{13}$$

The isotropic force capability is the minimal value of the scaling factor set ψ_i:

$$F_{iso} = \min(\psi_i) \qquad i = 1, ..., 8 \tag{14}$$

4 Maximum Isotropic Force Capability Maps

The isotropic force capability maps are obtained for the complete workspace of the cooperative robotic system shown in Fig. 1(a), for a specific orientation of the load in the xy-plane for all possible working modes, shown in Fig. 2. The load's orientations considered in this paper are represented in Fig. 3. The isotropic force capability is calculated for each point inside the work space, considering a mesh of 0,01 m, totaling $1,8 \times 10^6$ points. The adopted parameters for the calculation of the isotropic force capability are shown in Table 1.

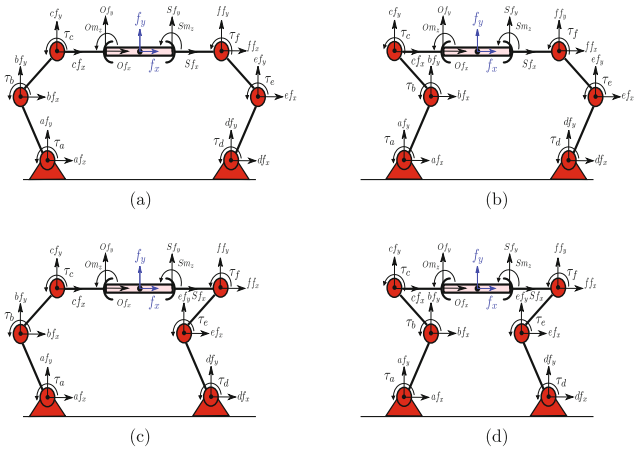

Fig. 2. The four work modes of the cooperative robot of Fig. 1(a) used to obtain isotropic force capability maps.

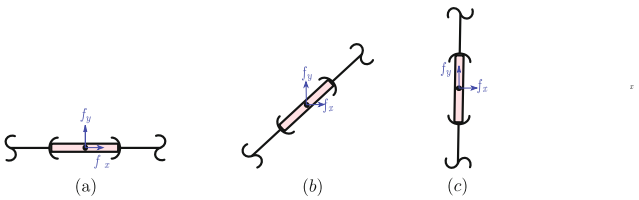

Fig. 3. Load's orientations considered to build the isotropic force capability maps: (a) 0°, (b) 45°, (c) 90°.

Table 1. Parameters of the cooperative robotic system.

Master serial robot	Value	Slave serial robot	Value
Length of link 1	3 m	length of link 8	3 m
Length of link 2	2 m	length of link 7	2 m
Length of link 3	1 m	length of link 6	1 m
$\tau_{a_{max}}$	40 N	$\tau_{d_{max}}$	40 N
$\tau_{b_{max}}$	30 N	$\tau_{e_{max}}$	30 N
$\tau_{c_{max}}$	20 N	$\tau_{f_{max}}$	20 N
$Om_{z_{max}}$	10 N	$Sm_{z_{max}}$	10 N

The isotropic force capability maps are presented in Figs. 4, 5 and 6. In those figures, the color tones indicate the isotropic forces capability intensity that the end effector can apply or support within his workspace. The deep blue area indicates the region which cannot be reached by the end effector.

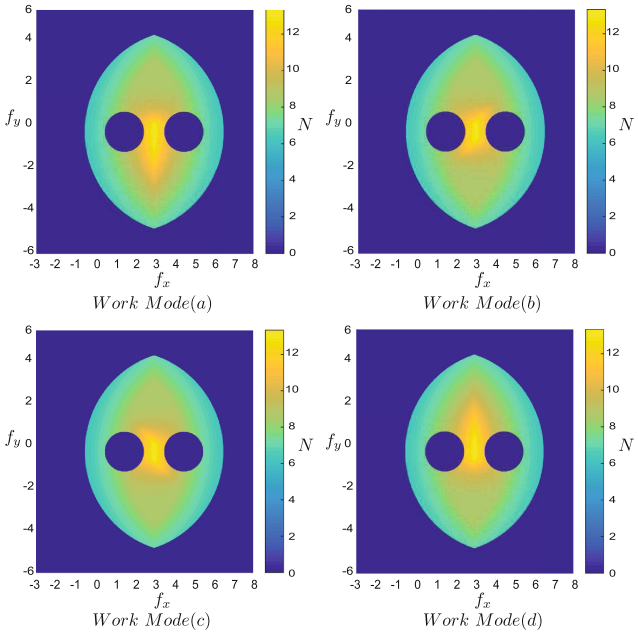

Fig. 4. Isotropic force capability maps for the load orientation represented in Fig. 3(a) (Color figure online)

By comparing the three load's orientations, it can be noted that in Fig. 4, in spite of the cooperative robot workspace being larger than the ones in Figs. 5 and 6, the area corresponding to the greatest values of isotropic force capability is smaller. Also it can be inferred that changes in the working mode have not a high impact on the case where the load orientation is 0°.

In Fig. 5, it is possible to see that the working mode has an effect on the cooperative robot's performance, e.g. for the working modes (a), (b) and (d), the area with higher isotropic force capability intensity occupy almost all the workspace, what does not occur in work mode (c).

In Fig. 6, the working modes influence the isotropic force capability intensity too, being the working mode (b) the most effective as the region with the greater values of force fill up the work space.

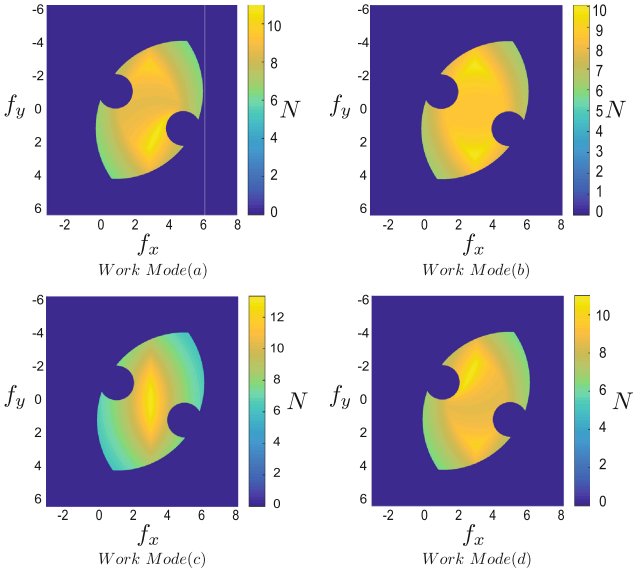

Fig. 5. Isotropic force capability maps for the load orientation represented in Fig. 3(b) (Color figure online)

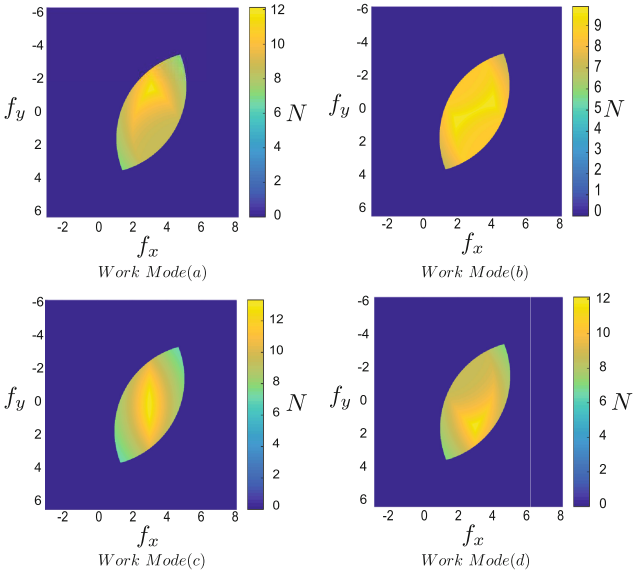

Fig. 6. Isotropic force capability maps for the load orientation represented in Fig. 3(c) (Color figure online)

5 Conclusion

The Davies method associated with the screw theory is an important tool to determine the static models in cooperative robotic systems necessary to analyze the force capability.

The isotropic force capability method is a breakthrough in the study of the force capability of cooperative manipulators. This method allowed for the first time to determine the isotropic force capability for the whole workspace of the cooperative robot, in a faster and direct way, without the use of optimization algorithms, generating maps that indicate the areas where the force is more intense, being useful in processes that require a certain force for the execution of a task. The completeness of these maps has the advantage of showing which working modes have the best performance to develop a task, being an important tool in applications that require to know the areas with greater capability of forces, before executing the task. The method proposed in this paper is based on the work of Mejia et al. [12] and represents a generalization of their proposal. At this moment, the method can only be used in cooperative planar manipulators that individually satisfy the condition $C_N = 3$, whether serial, parallel or hybrid. Future studies aim to extend the isotropic force capability method to spatial mechanisms, including the dynamic analysis and the consideration of gravitational forces.

Acknowledgements. The authors would like to thank to the Federal University of Santa Catarina, and the National Council for Scientific and Technological Development (CNPq).

References

1. Angeles, J., López-Cajún, C.S.: Kinematic isotropy and the conditioning index of serial robotic manipulators. Int. J. Robot. Res. **11**(6), 560–571 (1992)
2. Bi, S., Liang, J.: Robotic drilling system for titanium structures. Int. J. Adv. Manuf. Technol. **54**(5–8), 767–774 (2011)
3. Cazangi, H.R., et al.: Aplicação do método de davies para análise cinemática e estática de mecanismos com múltiplos graus de liberdade (2008)
4. Chiacchio, P., Bouffard-Vercelli, Y., Pierrot, F.: Evaluation of force capabilities for redundant manipulators. In: 1996 Proceedings of IEEE International Conference on Robotics and Automation, vol. 4, pp. 3520–3525. IEEE (1996)
5. Chiu, S.L.: Task compatibility of manipulator postures. Int. J. Robot. Res. **7**(5), 13–21 (1988)
6. Davies, T.: Mechanical networks - I passivity and redundancy. Mech. Mach. Theory **18**(2), 95–101 (1983)
7. Davies, T.: Mechanical networks - II formulae for the degrees of mobility and redundancy. Mech. Mach. Theory **18**(2), 103–106 (1983)
8. Davies, T.: Mechanical networks - III wrenches on circuit screws. Mech. Mach. Theory **18**(2), 107–112 (1983)
9. Firmani, F., Zibil, A., Nokleby, S.B., Podhorodeski, R.P.: Wrench capabilities of planar parallel manipulators. Part I: wrench polytopes and performance indices. Robotica **26**(06), 791–802 (2008)

10. Frantz, J.C., et al.: Análise estática de sistemas robóticos cooperativos (2015)
11. Legnani, G., Tosi, D., Fassi, I., Giberti, H., Cinquemani, S.: The point of isotropy and other properties of serial and parallel manipulators. Mech. Mach. Theory **45**(10), 1407–1423 (2010)
12. Mejia, L., Frantz, J., Simas, J., Martins, D.: Modified scaling factor method for the obtention of the wrench capabilities in cooperative planar manipulators. In: Proceedings of the 14th IFToMM World Congress, pp. 572–581 (2015)
13. Nokleby, S.B., Fisher, R., Podhorodeski, R.P., Firmani, F.: Force capabilities of redundantly-actuated parallel manipulators. Mech. Mach. Theory **40**(5), 578–599 (2005)
14. Weihmann, L., et al.: Modelagem e otimização de forças e torques aplicados por robôs com redundância cinemática e de atuação em contato com o meio (2011)
15. Weihmann, L., Martins, D., Coelho, L., Bernert, D.: Force capabilities of kinematically redundant planar parallel manipulators. In: 13th World Congress in Mechanism and Machine Science, p. 483 (2011)

Balancing Conditions of the RSS'R, Spatial Mechanism

An Alternative Method Using Natural Coordinates

Mario Acevedo(✉)

Facultad de Ingeniera, Universidad Panamericana,
Augusto Rodin 498, 03920 Ciudad de México, México
mario.acevedo@up.edu.mx

Abstract. Dynamic balancing of rigid body linkages with constant mass links is a traditional but still very active research area in mechanical engineering. It has some difficulties but the initial one is to derive the so-called balancing conditions, that are helpful to obtain different configurations for the balanced mechanism. The objective of this work is to illustrate the application of a general method to find the force and moment balancing conditions of planar and spatial linkages. It is applied for the dynamic balancing of the RSS'R spatial mechanism. The method is based on the use of Natural Coordinates so the whole system is represented only by a set of *basic points*, avoiding the use of angular coordinates. This facilitates obtaining the expressions for the linear momentum and for the angular momentum required to extract the shaking force and the shaking moment balancing conditions for the linkage. These conditions are interpreted and used to propose different design alternatives which can lead to a convenient design.

Keywords: Dynamic balancing · Shaking force · Shaking moment · Counterweights · Natural coordinates

1 Introduction

Dynamic balancing (force and moment balancing) of rigid body linkages with constant mass links, is a traditional but still very active research area in mechanical engineering, see [1]. Its benefits are well known [2–5], and the different methods used to achieve this goal have been recently documented with illustrative examples at [6]. A very interesting multi-body systems approach can also be found in [7].

But dynamic balancing of linkages has some difficulties named, to derive the so-called balancing conditions and to obtain the different balanced configurations of the mechanism. Thus a general method to find the force balancing conditions of spatial linkages, based on the use of Natural Coordinates [8], is demonstrated in this work. Although it has been introduced and applied to planar systems in [9,10].

J.C.M. Carvalho et al. (eds.), *Multibody Mechatronic Systems*,
Mechanisms and Machine Science 54, DOI 10.1007/978-3-319-67567-1_16

The method is direct due to the fact that with the Natural Coordinates the whole system can be represented by a set of *basic points* [8], avoiding the use of angular coordinates. It can be easily automated within a computer algebra system. This facilitates obtaining the expressions for the linear momentum and for the angular momentum required to extract dynamic balancing conditions. This means the shaking force and the shaking moment balancing conditions for the linkage. These conditions are interpreted and used to propose and evaluate different design alternatives which can lead to an efficient design.

In this case the method has been used to find the dynamic balancing conditions of the spatial RSS'R four bar mechanism (see Fig. 1). The obtained conditions are interpreted and used to show and alternative design which has been validated through dynamic simulation using ADAMS.

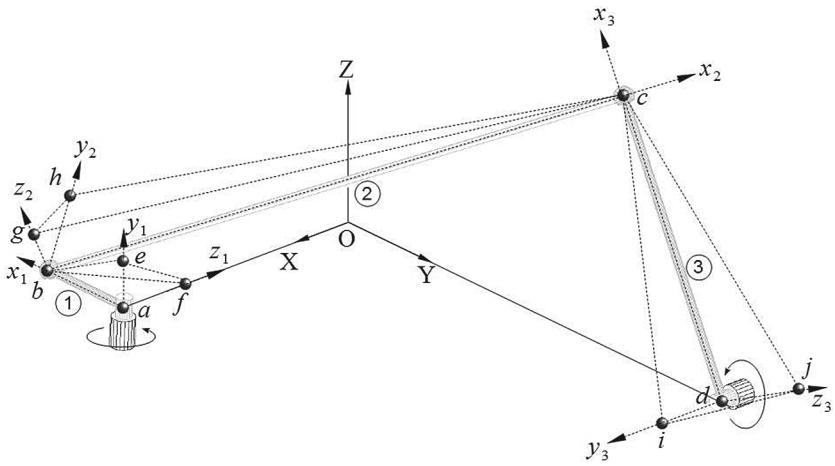

Fig. 1. A generic RSS'R mechanism defined using natural coordinates.

2 The Method

The starting part of the method is to define each body by a set of four basic points, see Fig. 2. In this way the mass matrix of the generic body, $\mathbf{M}$, is constant and calculated by using a base defined by three vectors: $(\mathbf{r}_j - \mathbf{r}_i)$, $(\mathbf{r}_k - \mathbf{r}_i)$, $(\mathbf{r}_l - \mathbf{r}_i)$. Where $\mathbf{r}_n$ is the position vector of the point n in the body. In this way the mass matrix of a body with mass m and an inertia tensor defined by:

$$\mathbf{J} = \begin{bmatrix} J_{xx} & J_{xy} & J_{xz} \\ J_{yx} & J_{yy} & J_{yz} \\ J_{zx} & J_{zy} & J_{zz} \end{bmatrix}$$

can be expressed as:

$$\mathbf{M} = \begin{bmatrix} (m_a)\mathbf{I} & (m_b)\mathbf{I} & (m_c)\mathbf{I} & (m_d)\mathbf{I} \\ (m_b)\mathbf{I} & \left(\frac{J_{xx}}{l_{ij}^2}\right)\mathbf{I} & \left(\frac{J_{xy}}{l_{ij}\cdot l_{ik}}\right)\mathbf{I} & \left(\frac{J_{xz}}{l_{ij}\cdot l_{il}}\right)\mathbf{I} \\ (m_c)\mathbf{I} & \left(\frac{J_{xy}}{l_{ij}\cdot l_{ik}}\right)\mathbf{I} & \left(\frac{J_{yy}}{l_{ik}^2}\right)\mathbf{I} & \left(\frac{J_{yz}}{l_{ik}\cdot l_{il}}\right)\mathbf{I} \\ (m_d)\mathbf{I} & \left(\frac{J_{xz}}{l_{ij}\cdot l_{il}}\right)\mathbf{I} & \left(\frac{J_{yz}}{l_{ik}\cdot l_{il}}\right)\mathbf{I} & \left(\frac{J_{zz}}{l_{il}^2}\right)\mathbf{I} \end{bmatrix} \tag{1}$$

where:

$$m_a = m - x\frac{2m}{l_{ij}} - y\frac{2m}{l_{ik}} - z\frac{2m}{l_{il}} + \frac{J_{xx}}{l_{ij}^2} + \frac{J_{yy}}{l_{ik}^2} + \frac{J_{zz}}{l_{il}^2} + \frac{2J_{xy}}{l_{ij}l_{ik}} + \frac{2J_{yz}}{l_{ik}l_{il}} + \frac{2J_{xz}}{l_{ij}l_{il}}$$

$$m_b = x\frac{m}{l_{ij}} - \frac{J_{xx}}{l_{ij}^2} - \frac{J_{xy}}{l_{ij}l_{ik}} - \frac{J_{xz}}{l_{ij}l_{il}}$$

$$m_c = y\frac{m}{l_{ik}} - \frac{J_{yy}}{l_{ik}^2} - \frac{J_{xy}}{l_{ij}l_{ik}} - \frac{J_{yz}}{l_{ik}l_{il}}$$

$$m_d = z\frac{m}{l_{il}} - \frac{J_{zz}}{l_{il}^2} - \frac{J_{xz}}{l_{ij}l_{il}} - \frac{J_{yz}}{l_{ik}l_{il}}$$

and $\mathbf{I}$ is the (3×3) identity matrix.

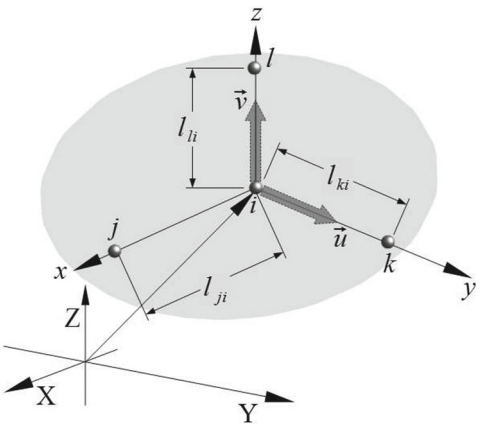

Fig. 2. A general body defined by four basic points.

It should be noted that all terms in $\mathbf{J}$ must be calculated with respect to the point i. On the other hand x, y and z are the components of the position vector that locates the center of mass of the body with respect to point i, expressed

in the body's local reference frame. A detailed explanation about the use of the Natural Coordinates and the way to calculate the mass matrix of a given body can be found at [8].

In this way it is possible to calculate the linear momentum and the angular momentum of the body in an easy and direct way, using a set of point masses located at points: i, j, k and l.

The same simple procedure used to calculate the linear and angular momentum of a body is used to calculate the linear and angular momentum of an entire mechanism, once its whole mass matrix is calculated. Thus the only difficulty in the application of the method in case of a mechanical system is the mass matrix assemblage (identify the correct location of each term in the matrix).

2.1 Linear Momentum of a Body Defined with a Set of Points

Without loss of generality, a way to illustrate the calculation of the linear momentum of a system defined using a set of points is to present the calculation of the linear momentum of a body.

Taking into account the body of Fig. 1, first a set of linear momentum vectors is calculated as:

$$\begin{bmatrix} (m_a)\mathbf{I} & (m_b)\mathbf{I} & (m_c)\mathbf{I} & (m_d)\mathbf{I} \\ (m_b)\mathbf{I} & \left(\frac{J_{xx}}{l_{ij}^2}\right)\mathbf{I} & \left(\frac{J_{xy}}{l_{ij}\cdot l_{ik}}\right)\mathbf{I} & \left(\frac{J_{xz}}{l_{ij}\cdot l_{il}}\right)\mathbf{I} \\ (m_c)\mathbf{I} & \left(\frac{J_{xy}}{l_{ij}\cdot l_{ik}}\right)\mathbf{I} & \left(\frac{J_{yy}}{l_{ik}^2}\right)\mathbf{I} & \left(\frac{J_{yz}}{l_{ik}\cdot l_{il}}\right)\mathbf{I} \\ (m_d)\mathbf{I} & \left(\frac{J_{xz}}{l_{ij}\cdot l_{il}}\right)\mathbf{I} & \left(\frac{J_{yz}}{l_{ik}\cdot l_{il}}\right)\mathbf{I} & \left(\frac{J_{zz}}{l_{il}^2}\right)\mathbf{I} \end{bmatrix} \begin{bmatrix} \mathbf{v}_i \\ \mathbf{v}_j \\ \mathbf{v}_k \\ \mathbf{v}_l \end{bmatrix} \tag{2}$$

Then for example the linear momentum associated to the point i is:

$$\mathbf{l}_i = (m_a)\mathbf{I}\mathbf{v}_i + (m_b)\mathbf{I}\mathbf{v}_j + (m_c)\mathbf{I}\mathbf{v}_k + (m_d)\mathbf{I}\mathbf{v}_l$$

So the total linear momentum of the body is calculated by the sum of the linear momentum of each point as:

$$\mathbf{l} = \mathbf{l}_i + \mathbf{l}_j + \mathbf{l}_k + \mathbf{l}_l \tag{3}$$

in this case expressed by:

$$\mathbf{l} = (m - \frac{mx}{l_{ij}} - \frac{my}{l_{ik}} - \frac{mz}{l_{il}})\mathbf{v}_i + (\frac{mx}{l_{ij}})\mathbf{v}_j + (\frac{my}{l_{ik}})\mathbf{v}_k + (\frac{mz}{l_{il}})\mathbf{v}_l \tag{4}$$

The force balancing conditions for the body can be obtained taking into account the kinematic pair that joints it to the base and through the analysis of the expression (4). A constant (usually zero) linear momentum warranties null shaking force.

If, for example, the body is attached to the ground by a revolute joint positioned at point i, then $\mathbf{v}_i = 0$. On the other hand in general the velocities of points j, k and l are different from zero. Thus in order to obtain constant (in this case zero) linear momentum the center of mass must be positioned at point i. This means that $x = 0$, $y = 0$ and $z = 0$, which are precisely the force balancing conditions.

In practice this can be achieved adding a counterweight located in the opposite direction of the center of mass.

2.2 Angular Momentum of a Body Defined with a Set of Points

The angular momentum of the body can be calculated simply as:

$$\mathbf{h} = \begin{bmatrix} \tilde{\mathbf{r}}_i & \tilde{\mathbf{r}}_j & \tilde{\mathbf{r}}_k & \tilde{\mathbf{r}}_l \end{bmatrix} \begin{bmatrix} (m_a)\mathbf{I} & (m_b)\mathbf{I} & (m_c)\mathbf{I} & (m_d)\mathbf{I} \\ (m_b)\mathbf{I} & \left(\frac{J_{xx}}{l_{ij}^2}\right)\mathbf{I} & \left(\frac{J_{xy}}{l_{ij}\cdot l_{ik}}\right)\mathbf{I} & \left(\frac{J_{xz}}{l_{ij}\cdot l_{il}}\right)\mathbf{I} \\ (m_c)\mathbf{I} & \left(\frac{J_{xy}}{l_{ij}\cdot l_{ik}}\right)\mathbf{I} & \left(\frac{J_{yy}}{l_{ik}^2}\right)\mathbf{I} & \left(\frac{J_{yz}}{l_{ik}\cdot l_{il}}\right)\mathbf{I} \\ (m_d)\mathbf{I} & \left(\frac{J_{xz}}{l_{ij}\cdot l_{il}}\right)\mathbf{I} & \left(\frac{J_{yz}}{l_{ik}\cdot l_{il}}\right)\mathbf{I} & \left(\frac{J_{zz}}{l_{il}^2}\right)\mathbf{I} \end{bmatrix} \begin{bmatrix} \mathbf{v}_i \\ \mathbf{v}_j \\ \mathbf{v}_k \\ \mathbf{v}_l \end{bmatrix} \tag{5}$$

This expression can be reduced substituting the shaking force balancing conditions in the mass matrix, which depends precisely on the center of mass coordinates.

3 Shaking Force and Shaking Moment Balancing Conditions of the RSS'R Spatial Mechanisms

As could be seen from the previous section, the key step in the use of a set of points to define the mechanism is the mass matrix assemblage.

A generic spatial RSS'R mechanism is presented in Fig. 1. A set of 10 points are used to complete the model. Point b is shared between body 1 (the crank) and body 2 (the coupler), while point c is shared between body 2 and body 3 (the rocker).

The mass matrix can be assembled in different ways. In this case the mass matrix is ordered by body, starting with body 1, then body 2, and finally body 3. The local reference frames are located at points a, b, and d respectively. Thus the mass matrix of the system is assembled considering the following order of points: a, b, e, f, c, g, h, d, i, j. The resulting mass matrix is presented in Eq. (6).

$$\mathbf{M} = \begin{bmatrix}
(m_a)_1\mathbf{I} & (m_b)_1\mathbf{I} & (m_c)_1\mathbf{I} & (m_d)_1\mathbf{I} & \mathbf{0} & \mathbf{0} & \mathbf{0} & \mathbf{0} & \mathbf{0} & \mathbf{0} \\
(m_b)_1\mathbf{I} & \left[\frac{J_{xx}}{l_{ab}^2} + (m_a)_2\right]\mathbf{I} & \frac{J_{xy}}{l_{ab}\cdot l_{ae}}\mathbf{I} & \frac{J_{xz}}{l_{ab}\cdot l_{af}}\mathbf{I} & (m_b)_2\mathbf{I} & (m_c)_2\mathbf{I} & (m_d)_2\mathbf{I} & \mathbf{0} & \mathbf{0} & \mathbf{0} \\
(m_c)_1\mathbf{I} & \frac{J_{xy}}{l_{ab}\cdot l_{ae}})\mathbf{I} & \frac{J_{yy}}{l_{ae}^2}\mathbf{I} & \frac{J_{yz}}{l_{ae}\cdot l_{af}}\mathbf{I} & \mathbf{0} & \mathbf{0} & \mathbf{0} & \mathbf{0} & \mathbf{0} & \mathbf{0} \\
(m_d)_1\mathbf{I} & \frac{J_{xz}}{l_{ab}\cdot l_{af}}\mathbf{I} & \frac{J_{yz}}{l_{ae}\cdot l_{af}}\mathbf{I} & \frac{J_{zz}}{l_{af}^2}\mathbf{I} & \mathbf{0} & \mathbf{0} & \mathbf{0} & \mathbf{0} & \mathbf{0} & \mathbf{0} \\
\mathbf{0} & (m_b)_2\mathbf{I} & \mathbf{0} & \mathbf{0} & \left[\frac{J_{xx}}{l_{bc}^2} + (m_b)_3\right]\mathbf{I} & \frac{J_{xy}}{l_{bc}\cdot l_{bg}}\mathbf{I} & \frac{J_{xz}}{l_{bc}\cdot l_{bh}}\mathbf{I} & \frac{J_{xx}}{l_{bc}^2}\mathbf{I} & \frac{J_{xy}}{l_{bc}\cdot l_{bg}}\mathbf{I} & \frac{J_{xz}}{l_{bc}\cdot l_{bh}}\mathbf{I} \\
\mathbf{0} & (m_c)_2\mathbf{I} & \mathbf{0} & \mathbf{0} & \frac{J_{xy}}{l_{bc}\cdot l_{bg}}\mathbf{I} & \frac{J_{yy}}{l_{bg}^2}\mathbf{I} & \frac{J_{yz}}{l_{bg}\cdot l_{bh}}\mathbf{I} & \mathbf{0} & \mathbf{0} & \mathbf{0} \\
\mathbf{0} & (m_d)_2\mathbf{I} & \mathbf{0} & \mathbf{0} & \frac{J_{xz}}{l_{bc}\cdot l_{bh}}\mathbf{I} & \frac{J_{yz}}{l_{bg}\cdot l_{bh}}\mathbf{I} & \frac{J_{zz}}{l_{bh}^2}\mathbf{I} & \mathbf{0} & \mathbf{0} & \mathbf{0} \\
\mathbf{0} & \mathbf{0} & \mathbf{0} & \mathbf{0} & \frac{J_{xx}}{l_{dc}^2}\mathbf{I} & \mathbf{0} & \mathbf{0} & (m_a)_3\mathbf{I} & (m_c)_3\mathbf{I} & (m_d)_3\mathbf{I} \\
\mathbf{0} & \mathbf{0} & \mathbf{0} & \mathbf{0} & \frac{J_{xy}}{l_{dc}\cdot l_{di}}\mathbf{I} & \mathbf{0} & \mathbf{0} & (m_c)_3\mathbf{I} & \frac{J_{yy}}{l_{di}^2}\mathbf{I} & \frac{J_{yz}}{l_{di}\cdot l_{dj}}\mathbf{I} \\
\mathbf{0} & \mathbf{0} & \mathbf{0} & \mathbf{0} & \frac{J_{xz}}{l_{dc}\cdot l_{dj}}\mathbf{I} & \mathbf{0} & \mathbf{0} & (m_d)_3\mathbf{I} & \frac{J_{yz}}{l_{di}\cdot l_{dj}}\mathbf{I} & \frac{J_{zz}}{l_{dj}^2}\mathbf{I}
\end{bmatrix} \tag{6}$$

3.1 Shaking Force Balancing Conditions

To obtain the shaking force balancing conditions of the mechanism it is necessary first to multiply the mass matrix, Eq. (6), times the vector of velocities:

$$\dot{\mathbf{q}}^T = \begin{bmatrix} \mathbf{v}_a & \mathbf{v}_b & \mathbf{v}_e & \mathbf{v}_f & \mathbf{v}_c & \mathbf{v}_g & \mathbf{v}_h & \mathbf{v}_d & \mathbf{v}_i & \mathbf{v}_j \end{bmatrix} \tag{7}$$

to obtain the set of linear momentum vectors for the whole system.

These linear momentum vectors are summed to obtain the total linear momentum of the system. In this case $\mathbf{v}_a = 0$, $\mathbf{v}_d = 0$, $\mathbf{v}_e = 0$, and $\mathbf{v}_i = 0$. Once this values are substituted and reducing all terms the total linear momentum of the system is:

$$\begin{aligned} \mathbf{l} = & \left[m_2 + \frac{m_1 x_1}{l_{ab}} - \frac{m_2 x_2}{l_{bc}} - \frac{m_2 y_2}{l_{bg}} - \frac{m_2 z_2}{l_{bh}} \right] \mathbf{v}_b \\ & + \left[\frac{m_3 x_3}{l_{dc}} + \frac{m_2 x_2}{l_{bc}} \right] \mathbf{v}_c + \left[\frac{m_1 z_1}{l_{af}} \right] \mathbf{v}_f \\ & + \left[\frac{m_2 y_2}{l_{bg}} \right] \mathbf{v}_g + \left[\frac{m_2 z_2}{l_{bh}} \right] \mathbf{v}_h + \left[\frac{m_3 z_3}{l_{dj}} \right] \mathbf{v}_j. \end{aligned} \tag{8}$$

3.2 Shaking Moment Balancing Conditions

To calculate the total angular momentum of the system it is necessary to multiply the mass matrix, Eq. (6), times the vector of velocities, Eq. (7). Then to get the total angular momentum of the system this product is pre-multiplied by a (3×10) matrix composed by the skew-symmetric matrices calculated with the components of the position vectors of the points. Taking into account that $\mathbf{v}_a = 0$, $\mathbf{v}_e = 0$, $\mathbf{v}_d = 0$ and $\mathbf{v}_i = 0$ the total angular momentum of the systems can be calculated as:

$$\tilde{\mathbf{R}} \begin{bmatrix} (m_b)_1\mathbf{I} & (m_d)_1\mathbf{I} & \mathbf{0} & \mathbf{0} & \mathbf{0} & \mathbf{0} \\ \left[\frac{J_{xx}}{l_{ab}^2} + (m_a)_2\right]\mathbf{I} & \frac{J_{xz}}{l_{ab}\cdot l_{af}}\mathbf{I} & (m_b)_2\mathbf{I} & (m_c)_2\mathbf{I} & (m_d)_2\mathbf{I} & \mathbf{0} \\ \frac{J_{xy}}{l_{ab}\cdot l_{ae}}\mathbf{I} & \frac{J_{yz}}{l_{ae}\cdot l_{af}}\mathbf{I} & \mathbf{0} & \mathbf{0} & \mathbf{0} & \mathbf{0} \\ \frac{J_{xz}}{l_{ab}\cdot l_{af}}\mathbf{I} & \frac{J_{zz}}{l_{af}^2}\mathbf{I} & \mathbf{0} & \mathbf{0} & \mathbf{0} & \mathbf{0} \\ (m_b)_2\mathbf{I} & \mathbf{0} & \left[\frac{J_{xx}}{l_{bc}^2} + (m_b)_3\right]\mathbf{I} & \frac{J_{xy}}{l_{bc}\cdot l_{bg}}\mathbf{I} & \frac{J_{xz}}{l_{bc}\cdot l_{bh}}\mathbf{I} & \frac{J_{xz}}{l_{bc}\cdot l_{bh}}\mathbf{I} \\ (m_c)_2\mathbf{I} & \mathbf{0} & \frac{J_{xy}}{l_{bc}\cdot l_{bg}}\mathbf{I} & \frac{J_{yy}}{l_{bg}^2}\mathbf{I} & \frac{J_{yz}}{l_{bg}\cdot l_{bh}}\mathbf{I} & \mathbf{0} \\ (m_d)_2\mathbf{I} & \mathbf{0} & \frac{J_{xz}}{l_{bc}\cdot l_{bh}}\mathbf{I} & \frac{J_{yz}}{l_{bg}\cdot l_{bh}}\mathbf{I} & \frac{J_{zz}}{l_{bh}^2}\mathbf{I} & \mathbf{0} \\ \mathbf{0} & \mathbf{0} & \frac{J_{xx}}{l_{dc}^2}\mathbf{I} & \mathbf{0} & \mathbf{0} & (m_d)_3\mathbf{I} \\ \mathbf{0} & \mathbf{0} & \frac{J_{xy}}{l_{dc}\cdot l_{di}}\mathbf{I} & \mathbf{0} & \mathbf{0} & \frac{J_{yz}}{l_{di}\cdot l_{dj}}\mathbf{I} \\ \mathbf{0} & \mathbf{0} & \frac{J_{xz}}{l_{dc}\cdot l_{dj}}\mathbf{I} & \mathbf{0} & \mathbf{0} & \frac{J_{zz}}{l_{dj}^2}\mathbf{I} \end{bmatrix} \begin{bmatrix} \mathbf{v}_b \\ \mathbf{v}_f \\ \mathbf{v}_c \\ \mathbf{v}_g \\ \mathbf{v}_h \\ \mathbf{v}_j \end{bmatrix} \tag{9}$$

where

$$\tilde{\mathbf{R}} = \left[\tilde{\mathbf{r}}_a\ \tilde{\mathbf{r}}_b\ \tilde{\mathbf{r}}_e\ \tilde{\mathbf{r}}_f\ \tilde{\mathbf{r}}_c\ \tilde{\mathbf{r}}_g\ \tilde{\mathbf{r}}_h\ \tilde{\mathbf{r}}_d\ \tilde{\mathbf{r}}_i\ \tilde{\mathbf{r}}_j\right] \tag{10}$$

Multiplying all terms in Eq. (9), simplifying considering an inline mechanism and substituting the coupler by a dynamic equivalent of two concentrated masses located at the points b and c, as proposed in [11], the total angular momentum of the system is:

$$\mathbf{h} = \begin{bmatrix} \left\{\frac{m_2}{2} + (Jxx)_3 + (Jzz)_3\right\}\omega_3 \\ 0 \\ \left\{\frac{m_2}{2} + (Jxx)_1 + (Jzz)_1\right\}\omega_1 \end{bmatrix} \tag{11}$$

Thus to make the angular momentum constant, a necessary condition to get zero shaking moment, a set of counter-rotary counterweights should be added to the crank and to the rocker.

4 Numerical Example

In order to show the practical application of the equations developed through the paper, force balancing of an specific RSS'R spatial mechanism is presented in this section.

The same mechanism formerly proposed in [11] is used to develop the example. It is represented in Fig. 1 and has the following parameters: $l_{Oa} = 0.1\,\text{m}$, $l_{ab} = 0.05\,\text{m}$, $l_{bc} = 0.3\,\text{m}$, $l_{cd} = 0.15\,\text{m}$, and $l_{Od} = 0.25\,\text{m}$. All bodies are made of steel ($\rho = 7,801\frac{\text{kg}}{\text{m}^3}$) with $m_1 = 0.0109\,\text{kg}$, $m_2 = 0.036\,\text{kg}$, and $m_3 = 0.0207\,\text{kg}$. The constant angular velocity of the crank, body 1, is $\omega_1 = 2\pi\frac{\text{rad}}{\text{s}}$.

To balance the mechanism by force it is necessary to achieve a constant (zero) linear momentum. Using Eq. (8) it can be noted that This can be done by fulfilling the following shaking force balancing conditions:

$$\begin{aligned} \left[m_2 + \frac{m_1 x_1}{l_{ab}} - \frac{m_2 x_2}{l_{bc}} - \frac{m_2 y_2}{l_{bg}} - \frac{m_2 z_2}{l_{bh}}\right] &= 0 \\ \left[\frac{m_3 x_3}{l_{dc}} + \frac{m_2 x_2}{l_{bc}}\right] &= 0 \\ \left[\frac{m_1 z_1}{l_{af}}\right] = 0 \quad \left[\frac{m_2 y_2}{l_{bg}}\right] = 0 \quad \left[\frac{m_2 z_2}{l_{bh}}\right] = 0 \quad \left[\frac{m_3 z_3}{l_{dj}}\right] &= 0 \end{aligned} \tag{12}$$

An alternative solution to fulfill these conditions is to make the crank be an inline body, making $z_1 = 0$. In addition leave body 2 unaltered and also inline, making:

$$x_2 = \frac{l_{bc}}{2};\ y_2 = 0;\ z_2 = 0$$

Finally $z_3 = 0$ in body 3. This determines the necessary location of the center of mass of body 1 as:

$$x_1 = -\left(\frac{m_2}{m_1}\right) l_{ab};\ y_1 = 0;\ z_1 = 0$$

as well as the center of mass of body 3 as:

$$x_3 = -\left(\frac{1}{2}\right)\left(\frac{m_2}{m_3}\right) l_{dc};\ y_3 = 0;\ z_3 = 0$$

In practice this has been achieved by adding two counterweights, one at the crank (body 1) and one at the rocker (body 3), as shown in Fig. 3. Both counterweights made of brass ($\rho = 8,545 \frac{\text{kg}}{\text{m}^3}$).

The counterweight attached to the crank has thickness equal to 0.01 m and a diameter of 0.0093317 m. The counterweight attached to the rocker has thickness equal to 0.01 m and a diameter of 0.014371 m.

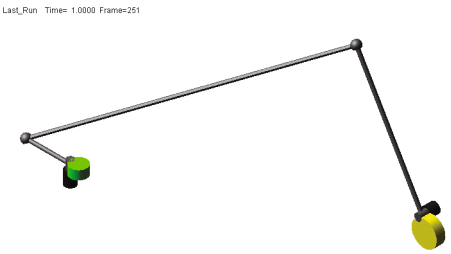

Fig. 3. Solution to the proposed mechanism, balanced by two counterweights made of brass.

The Fig. 4 shows a comparison of the shaking force between the original mechanism and the balanced mechanisms. These results have been generated by simulation using ADAMS.

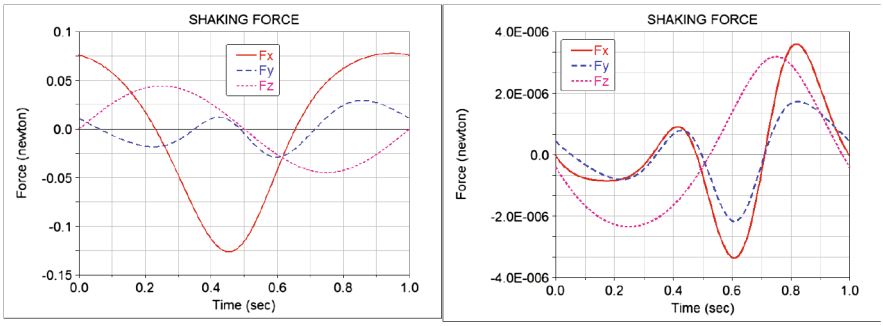

Fig. 4. Comparison of the shaking force, non-balanced mechanism on the left and mechanism balanced on the right.

5 Conclusions

An alternative method to obtain the shaking force and shaking moment balancing conditions necessary for the dynamic balancing of the RSS'R spatial mechanism has been showed. The method, based on the use of Natural Coordinates, is efficient when using a computer algebra software. It can be applied to complex mechanisms, such as spatial robots, to find force balancing conditions. Its application to find moment balancing conditions of complex systems should be evaluated in more detail.

References

1. Zhang, D., Wei, B.: Dynamic Balancing of Mechanisms and Synthesizing of Parallel Robots. Springer, Cham (2015)
2. Lowen, G.G., Berkoft, R.S.: J. Mech. **3**, 221 (1968)
3. Arakelian, V., Dahan, M., Smith, M.: A historical review of the evolution of the theory on balancing of mechanisms. In: Ceccarelli, M. (ed.) Proceedings of International Symposium on History of Machines and Mechanisms, HMM 2000, pp. 291–300. Springer, Kluwer Academic Publishers, Dordrecht, Boston, London (2000)
4. Arakelian, V.H., Smith, M.R.: ASME J. Mech. Des. **127**(2), 334 (2005)
5. Arakelian, V.H., Smith, M.R.: ASME J. Mech. Des. **127**(2), 1034 (2005)
6. Arakelian, V., Briot, S.: Balancing of Linkages and Robot Manipulators. Advanced Methods with Illustrative Examples. Springer, Cham (2015)
7. Chaudhary, H., Saha, S.K.: Dynamics and Balancing of Multibody Systems, 3rd edn. Springer, Cham (2009)
8. García de Jalón, J., Bayo, E.: Kinematic and Dynamic Simulation of Multibody Systems: The Real-Time Challenge. Springer, Cham (1994)
9. Acevedo, M.: Proceedings of ASME IDETC/CIE, Boston, Massachusetts, USA, 2–5 August 2015
10. Acevedo, M.: Proceedings of the 14th IFToMM World Congress, Taipei, Taiwan, 25–30 October 2015
11. Arakelian, V.H.: Proc. IMechE Part K J. Multi-body. Dynamics **221**, 303 (2007)

Dynamic Analysis

Elastodynamic Performance of a Planar Parallel Mechanism Under Uncertainties

Fabian Andres Lara-Molina[1(✉)], Edson Hideki Koroishi[1], and Thamiris Lima Costa[2]

[1] Department of Mechanical Engineering, Federal University of Technology - Paraná, Cornélio Procópio, PR, Brazil
fabianmolina@utfpr.edu.br

[2] Department of Automation and Systems (DAS), Federal University of Santa Catarina, Florianópolis, SC, Brazil

Abstract. The analysis of the elastodynamic performance of the parallel mechanisms is necessary for their optimal design. This paper aims at evaluating the elastodynamics of a planar parallel mechanism with flexible joints subjected to uncertainties. Therefore, the elastodynamic performance is analyzed over the design space that considers all the possible combinations of the lengths of the links of the mechanism. The uncertainties in the stiffness of the active joints are modeled as random variables. The elastodynamic performance subjected to uncertainties is evaluated numerically by using the Monte Carlo Simulation.

Keywords: Parallel manipulator · Elastodynamics · Uncertainties

1 Introduction

The elastodynamic performance of the parallel mechanisms with flexible elements is an important issue mainly for their mechanical design and also for the development of new control algorithms [11].

In this direction, the parallel mechanisms with flexible links or flexible joints have been extensively studied. Thus, several works have been focused on the optimal design procedure [1], analysis of the elastodynamic performance [7] and development of motion control laws [11] among other important aspects of parallel mechanism with flexible elements. In the other hand, several contributions have studied the effect of uncertainties in parallel mechanisms [5,6].

Specifically, this contribution presents a novel study in order to analyze the elastodynamic performance of a planar parallel mechanism with flexible active joints by considering uncertainties in the stiffness parameters. Initially, the analysis of the elastodynamics is based on the complete kinematic and dynamic model of parallel mechanism that is formulated taking into account the flexible joints. Then, the uncertainties are modeled as random variables and they are included in the stiffness of the active joints. The elastodynamic criterion is formulated based on the dynamic model. Finally, the elastodynamic performance subjected

J.C.M. Carvalho et al. (eds.), *Multibody Mechatronic Systems*,
Mechanisms and Machine Science 54, DOI 10.1007/978-3-319-67567-1_17

to uncertainties is evaluated within the design space by means of the Monte Carlo Simulation.

2 Mechanism Modeling

The planar parallel mechanism is show in Fig. 1. The mechanism has two identical kinematic chains. Each kinematic chain have an active joint (A_i), a passive joint (B_i) for $i = 1, 2$, and two rigid links. Moreover, a flexible active joint is considered. The end-effector of the mechanism is located at $\mathbf{p}$ which position is defined by the Cartesian coordinates $(\overline{x}_p, \overline{y}_p)$. Finally, an inertial frame O is defined in the middle of A_1A_2. The acceleration of the gravity acts in the $-z$ direction that is perpendicular to the plane that contains the mechanism.

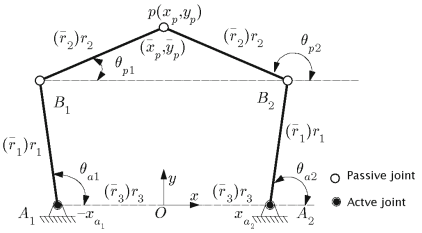

Fig. 1. The planar parallel mechanism.

The link lengths are denoted by $\overline{r}_1$, $\overline{r}_2$ and $\overline{r}_3$ as shown in the Fig. 1. The link lengths are defined between zero and infinite. Nevertheless, these dimensional link lengths should be non-dimensionalized with the purpose of analyzing the effects of link lengths in the model of the mechanism. Thus, the auxiliary an variable $D = (\overline{r}_1 + \overline{r}_2 + \overline{r}_3)/3$ is defined. The three non-dimensional parameters (r_i, for $i = 1, 2, 3$) are defined by:

$$r_1 = \overline{r}_1/D \qquad r_2 = \overline{r}_2/D \qquad r_3 = \overline{r}_3/D \tag{1}$$

Where $r_1 + r_2 + r_3 = 3$. Furthermore, the end-effector coordinates are also non-dimensionalized as follows: $x_p = \overline{x}_p/D \quad y_p = \overline{y}_p/D$.

2.1 Kinematic Model

The Cartesian vector $\mathbf{p} = \begin{bmatrix} x_p \; y_p \end{bmatrix}^T$ defines the position of the end-effector with reference to the inertial frame O. Moreover, the position of the points B_i (for $i = 1, 2$) with reference to the inertial frame O are $\mathbf{b}_1 = \begin{bmatrix} r_1 \cos(\theta_{a1}) - r_3 \; r_1 \sin(\theta_{a1}) \end{bmatrix}^T$ and $\mathbf{b}_2 = \begin{bmatrix} r_1 \cos(\theta_{a2}) + r_3 \; r_1 \sin(\theta_{a2}) \end{bmatrix}^T$, respectively. θ_{a1} and θ_{a2} are the angular positions of the active joint. The inverse

kinematics is formulated by considering the kinematic constraint $|\mathbf{b}_i\mathbf{p}| = r_2$, therefore:

$$(x_p - r_1\cos(\theta_{a1}) + r_3)^2 + (y_p - r_1\sin(\theta_{a1}))^2 = r_2^2 \tag{2}$$

$$(x_p - r_1\cos(\theta_{a2}) - r_3)^2 + (y_p - r_1\sin(\theta_{a2}))^2 = r_2^2 \tag{3}$$

2.1.1 Jacobian Matrix

The Jacobian matrix of the mechanism is derived by differentiating with respect to time Eqs. (2) and (3), then this expression is written in the matrix form:

$$\mathbf{A}\dot{\boldsymbol{\theta}}a = \mathbf{B}\dot{\mathbf{p}} \tag{4}$$

where $\dot{\mathbf{p}} = \begin{bmatrix}\dot{x}_p & \dot{y}_p\end{bmatrix}^T$, $\dot{\boldsymbol{\theta}}a = \begin{bmatrix}\dot{\theta}_{a1} & \dot{\theta}_{a2}\end{bmatrix}^T$ and the 2×2 matrices $\mathbf{A}$ and $\mathbf{B}$.

$$\mathbf{J} = \mathbf{A}^{-1}\mathbf{B} \tag{5}$$

2.1.2 Workspace

Initially, the usable workspace is defined as the area wherein the end-effector can reach free of singular loci. Additionally, the Maximum Inscribed Circle (MIC) is an useful measure to assess the size of the usable workspace. The MIC is a circle that is inscribed within the usable workspace and it is tangent with singular loci [9]. The Maximum Inscribed Workspace (MIW) is defined as the workspace bounded by the MIC. The MIC as a function of the link lengths is defined by the follow expression:

$$x^2 + (y - y_{MIC})^2 = r_{MIC}^2 \tag{6}$$

where r_{MIC} is the radius and $(0, y_{MIC})$ is the center of the MIC. For the cases that $r_1 + r_3 < r_2$, the MIC is defined by:

$$r_{MIC} = (r_1 + r_2 - |r_1 - r_2|)/2 \quad \text{and} \quad y_{MIC} = \sqrt{(r_1 + r_2 + |r_1 - r_2|)^2/4 - r_3^2} \tag{7}$$

For the cases that $r_1 + r_3 > r_2$, the radius and center of the MIC are defined by:

$$r_{MIC} = |y_{MIC}| - y_{col} \quad \text{and} \quad y_{MIC} = \frac{(r_1 + r_2 + y_{col})^2 - r_3^2}{2(r_1 + r_2 + y_{col})} \tag{8}$$

with $y_{col} = \sqrt{r_1^2 - (r_2 - r_3)^2}$.

2.2 Dynamic Model

Initially, the dynamics of each kinematic chain together with the flexible active joint is considered separately in order to derive the complete dynamic model of the mechanism. Then, the total dynamics of the parallel mechanism is obtained by applying the kinematic constraints of the both kinematic chains.

The dynamic parameters should also be non-dimensionalized. By considering the masses of the first and second links of the $i-th$ kinematic chain, respectively: $\overline{m}_{1i}$, $\overline{m}_{2i}$ and the stiffness of the active joints: $\overline{k}_1$ and $\overline{k}_2$, thus, m_t and k_t are defined as follow: $m_t = (\overline{m}_{1i} + \overline{m}_{2i})/2$ and $k_t = (\overline{k}_1 + \overline{k}_2)/2$. Consequently, the non-dimensional masses of the links and the stiffness of the joints are defined as follow:

$$m_{1i} = \overline{m}_{1i}/m_t \qquad m_{2i} = \overline{m}_{2i}/m_t \qquad m_{1i} + m_{2i} = 2$$
$$k_1 = \overline{k}_1/k_t \qquad k_2 = \overline{k}_2/k_t \qquad k_1 + k_2 = 2$$

The links are considered as slender rods. Thus, the inertial moment and center of mass of the links can be defined as a function of the non-dimensional masses and lengths of the links as follows: $d_{1i} = r_1/2$, $d_{2i} = r_2/2$, $I_{z1i} = \frac{1}{12} m_1 r_1^2$, $I_{z2i} = \frac{1}{12} m_2 r_2^2$.

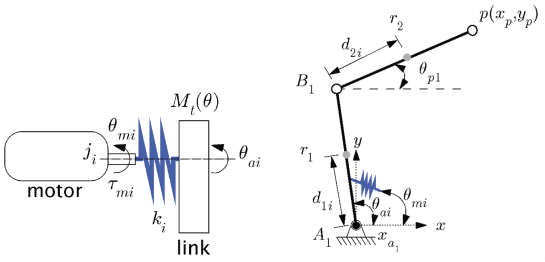

(a) Flexible joint. (b) Kinematic chain of the mechanism.

Fig. 2. Flexible active joint and kinematic chain.

2.2.1 Dynamic of the Kinematic Chains

The model of the flexible joint is shown in the Fig. 2(a). $\boldsymbol{\tau}_m = \begin{bmatrix}\tau_{m1} & \tau_{m2}\end{bmatrix}^T$ is the torque applied by the motors after the reduction, $\boldsymbol{\theta}_m = \begin{bmatrix}\theta_{m1} & \theta_{m2}\end{bmatrix}^T$ is the angular position of the motor.

A single kinematic chain is shown in the Fig. 2(b). Each kinematic chain is modeled separately in order to simplify the total dynamics modeling of the mechanism. The dynamic equation is obtained by using the Lagrange formulation as presented by [4]. Then, the dynamic model of the two kinematic chains is formulated by combining the model of both kinematic chains, thus:

$$\mathbf{M}(\boldsymbol{\theta})\ddot{\boldsymbol{\theta}} + \mathbf{C}\left(\boldsymbol{\theta}, \dot{\boldsymbol{\theta}}\right)\dot{\boldsymbol{\theta}} + \mathbf{f} + \mathbf{f}_k = \boldsymbol{\tau} \tag{9}$$

with:

- $\boldsymbol{\theta} = (\boldsymbol{\theta}_a^T, \boldsymbol{\theta}_p^T)^T$, $\dot{\boldsymbol{\theta}} = (\dot{\boldsymbol{\theta}}_a^T, \dot{\boldsymbol{\theta}}_p^T)^T$, $\mathbf{f} = (\mathbf{f}_a^T, \mathbf{f}_p^T)^T$ and $\boldsymbol{\tau} = (\boldsymbol{\tau}_a^T, \boldsymbol{\tau}_p^T)^T$.
- $\mathbf{f}_k = (\mathbf{f}_{ka}^T, \mathbf{f}_{kp}^T)^T$ is the elastic torque in active and passive joints respectively.

- $\mathbf{f}_{kp} = (0,0)^T$ is stiffness of passive joints and no torque is applied in passive joints, thus $\boldsymbol{\tau}_p = (0,0)^T$.
- $\mathbf{f}_p = (0,0)^T$ is the friction in passive joints.
- $\mathbf{M}(\boldsymbol{\theta})$ and $\mathbf{C}\left(\boldsymbol{\theta}, \dot{\boldsymbol{\theta}}\right)$ are the mass and Coriolis matrices of both kinematic chains.

2.2.2 Complete Dynamic Model

The complete dynamic model of the parallel mechanism is derived by considering the coupling of both kinematic chains at the passive joint of point p located at end-effector. By using the D'Alembert's principle and the principle of virtual work, the torques of the active joint $\boldsymbol{\tau}_a$ and torque of the joints $\boldsymbol{\tau}$ satisfy the relation:

$$\boldsymbol{\tau}_a = \Psi^T \boldsymbol{\tau} \tag{10}$$

with $\Psi = \partial\boldsymbol{\theta}/\partial\boldsymbol{\theta}_a$. Therefore, the total dynamic equation is expressed as follows:

$$\mathbf{M}_t \ddot{\boldsymbol{\theta}}_a + \mathbf{C}_t \dot{\boldsymbol{\theta}}_a + \mathbf{f}_a + \mathbf{f}_{ka} = \boldsymbol{\tau}_a \tag{11}$$

where $\mathbf{M}_t = \Psi^T \mathbf{M}(\boldsymbol{\theta})\Psi$ and $\mathbf{C}_t = \Psi^T \mathbf{M}(\boldsymbol{\theta})\dot{\Psi} + \Psi^T \mathbf{C}\left(\boldsymbol{\theta}, \dot{\boldsymbol{\theta}}\right)\Psi$. Additionally, no torque is applied directly to the active joints by the motors, thus $\boldsymbol{\tau}_a = (0,0)^T$. Thus, the complete dynamic of Eq. (11) can be written as follows:

$$\mathbf{M}_t \ddot{\boldsymbol{\theta}}_a + \mathbf{C}_t \dot{\boldsymbol{\theta}}_a + \mathbf{f}_a + \mathbf{K}(\boldsymbol{\theta}_a - \boldsymbol{\theta}_m) = 0 \tag{12}$$

Finally, based on Eq. (12) and using the Jacobian matrix, the dynamics in the Cartesian coordinates can be express at a fixed posture and without frictions in the joints, i.e. $\dot{\boldsymbol{\theta}} = \begin{bmatrix} 0 & 0 & 0 & 0 \end{bmatrix}^T$ and $\mathbf{f}_a = \begin{bmatrix} 0 & 0 & 0 & 0 \end{bmatrix}^T$ [2]; thus:

$$\mathbf{J}^{-T}\mathbf{M}_t\mathbf{J}^{-1}\ddot{\boldsymbol{\theta}}_a + \mathbf{J}^{-T}\mathbf{K}\mathbf{J}^{-1}(\boldsymbol{\theta}_a - \boldsymbol{\theta}_m) = 0 \tag{13}$$

3 Uncertainties Modeling and Analysis

Typically, the parameters of the mechanism suffer from small variations during their operation. The uncertainties allow including these aforementioned variations of the parameters in the numerical model of the mechanism. Consequently, the stiffness of the active joints include the uncertainties.

The uncertainties are modeled as small variations about the nominal value of each parameter. These uncertainties are modeled by means of random variables, thus:

$$a_0(\theta) = a_0 + a_0 \delta_a \xi(\theta) \tag{14}$$

where a_0 is the mean or nominal value of the parameter, δ_a is the maximum percentage dispersion and $\xi(\theta)$ is the unit normal random variable with θ being a random process. The unit normal random variable is governed by a normal distribution, this distribution was selected in order to evaluate the uncertain parameters in this contribution.

The so-called Monte Carlo method combined with the Latin Hypercube sampling [3] is used to map these uncertain random parameters on the elastodynamic model of the mechanism. In this way, the elastodynamic performance of the mechanism subjected to uncertainties is evaluated.

4 Performance Indices

Several performance criteria have been used with the propose of analyze the performance of parallel mechanism. In this direction, the concept of the atlases of the performance criteria. i.e., a desired performance criteria is evaluated for all the combinations of the design variables. For the parallel mechanism analyzed in this contribution, the elastodynamic performance is examined for every single length of the non-dimensional links on the design space.

4.1 The Design Space

The design space allows assessing as a function of the non-dimensional link lengths of the mechanism. Thus, the design space permits to evaluate the elastodynamic performance criteria within a sets that contains all the possible combinations the non-dimensional length. For this contribution, the elastodynamic performance subjected to uncertainties is evaluated over the design space.

The design space of this parallel mechanism was previously defined by [8]. The non-dimensional length of links were previously defined in Eq. (1). The non-dimensional link lengths are constrained in order to ensure the geometric definition of the mechanism, thus:

$$0 < r_1, r_2 < 3 \qquad \text{and} \qquad 0 \leq r_3 \leq 1.5 \tag{15}$$

By applying these constraints to the definition of the non-dimensional link lengths definition ($r_1 + r_2 + r_3 = 3$), the design space is shown in Fig. 5(a). Moreover, two orthogonal coordinates s and t are defined to establish a planar configuration of the design space that is presented in the Fig. 3(b), thus:

$$s = 2r_1/\sqrt{3} + r_3/\sqrt{3} \qquad \text{and} \qquad t = r_3 \tag{16}$$

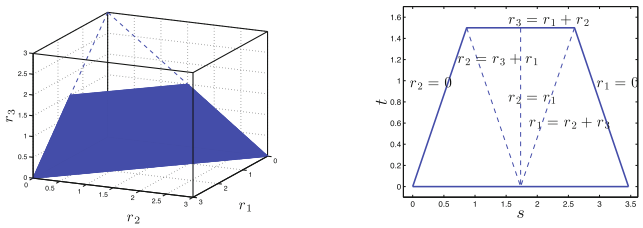

(a) (b)

Fig. 3. Design space of the planar parallel mechanism.

The design space can be split in several sub-regions; these subregions are bounded by the dotted lines where r_1, r_2 and r_3 assume certain lengths as presented in Fig. 3(b).

4.2 Elastodynamic Performance

The elastodynamic performance consists in evaluating the vibratory characteristics of the mechanism that are produced by flexible elements of the structure [10]. The elastodynamics is evaluated by computing the natural modes and frequencies at a specific posture of the mechanism. The analysis of the elastodynamic performance derived based on Eq. (13), thus:

$$\mathbf{M}_C\ddot{\boldsymbol{\theta}}_a + \mathbf{K}_C(\boldsymbol{\theta}_a - \boldsymbol{\theta}_m) = 0 \tag{17}$$

Where $\mathbf{M}_C = \mathbf{J}^{-T}\mathbf{M}_t\mathbf{J}^{-1}$ and $\mathbf{K}_C = \mathbf{J}^{-T}\mathbf{K}\mathbf{J}^{-1}$.

The elastodynamic performance depends on the posture of the mechanism because total inertia and Jacobian matrices are dependent on the position of active joints. The natural modes and frequencies are obtained by solving the associated eigenvalue problem of Eq. (17); thus, $(\mathbf{K}_C - \boldsymbol{\lambda}_T^2\mathbf{M}_C)\boldsymbol{\theta}_a = 0$, leads to the set of eigenvalues ($\boldsymbol{\lambda}_T = \begin{bmatrix}\lambda_1 \dots \lambda_n\end{bmatrix}$) and eigenvector ($\boldsymbol{\phi}_T = \begin{bmatrix}\phi_1 \dots \phi_n\end{bmatrix}$), respectively.

An optimal elastodynamic performance is obtained while the mechanism operates below the smallest natural frequency during the motion in order to avoid undesirable vibrations produced by the resonance effect. Therefore, the elastodynamic performance could be assessed as a function of the link lengths by determining the smallest eigenvalue over the MIW, thus:

$$\lambda_e = \min_{MIW}(\boldsymbol{\lambda}_T(r_1, r_2, r_3)) \tag{18}$$

One can observe that the elastodynamic performance enhances by maximizing the smallest natural frequency, this behavior could be obtained by selecting the proper link lengths r_1, r_2 and r_3.

5 Results

The nondimensional dynamic parameters adopted in this contribution are: $m_{1i} = 1.2$, $m_{2i} = 0.8$, i.e., the mass of the second link is 20% smaller than the mass of the second link. The stiffness of the elastic joints is equal, thus $k_1 = 1$ and $k_2 = 1$. Additionally, the uncertainties are introduced in these parameters by considering the 5% of dispersion in the masses and stiffness according to Eq. (14).

Initially, the atlas of the elastodynamic performance subjected to uncertainties was calculated by the aids of the expression given in the Eq. (18) together with the Monte Carlo Simulation (see Fig. 4). The elastodynamics atlas is completely defined by two parts, first by the mean atlas ($mean(\lambda_e)$) and second, by the maximum variation of the smallest natural frequency that is defined by

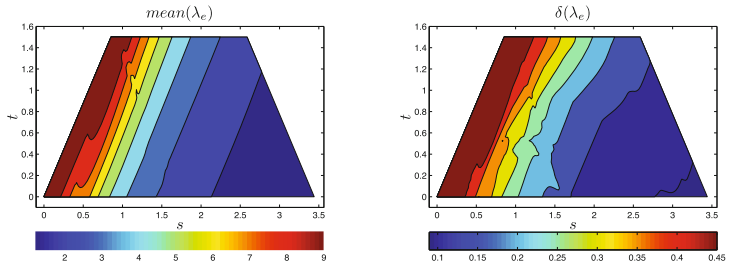

Fig. 4. Elastodynamic atlas subjected to uncertainties.

$\delta(\lambda_e) = \max(\lambda_e) - \min(\lambda_e)$. As seen in Fig. 4(a), the atlas shows that the elastodynamics mainly varies along s coordinate, consequently, the elastodynamics is mainly function of r_1 and r_2 because the link lengths of the kinematic chains modifies the Jacobian and the total inertia matrix $\mathbf{M}_C$ defined in Eq. (17). Furthermore, one can perceive in the atlas of Fig. 4(a) that elastodynamic exhibits a slight variation on the $t = r_3$ coordinate. Consequently, the smallest natural frequency is maximized for links lengths that follow the relation $r_1 \leq r_2$ characterized in a specific region of the atlas. This region is located in the left border of the design space as showed in Fig. 4(a). Nevertheless, when the smallest natural frequency increases, the effects of uncertainties gets more preponderant as Fig. 4(b). Therefore, the elastodynamic performance subject to uncertainties exhibits a compromise between the elastodynamic behavior of mechanism and the effect of uncertainties.

Finally, the elastodynamic performance is evaluated by considering two specific sets of link lengths, s and t coordinates, by considering the elastodynamic atlas subjected to uncertainties. Consequently, the local elastodynamics is evaluated for each single posture within the usable workspace. First, it is selected the case (a): $s = 1.85$ and $t = 0.8$ that corresponds to $r_1 = 1.20$, $r_2 = 1.0$ and $r_3 = 0.8$ (see Fig. 5); then, it is selected the case (b): $s = 0.75$ and $t = 1.00$ that corresponds to $r_1 = 0.15$, $r_2 = 1.85$ and $r_3 = 1.00$ (see Fig. 6).

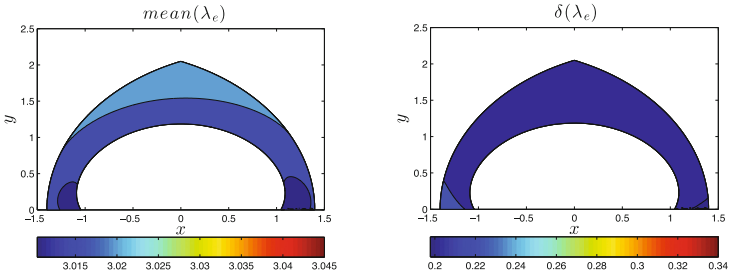

Fig. 5. Case (a): Local Elastodynamic performance over the usable workspace.

In the case (a) is observed that the smallest eigenvalue has a homogeneous value over the usable workspace (see Fig. 5(a)) and additionally, the effects of uncertainties are small compared with the dispersion of uncertainties. The case (b) exhibits the smallest natural frequency has a small variation over the usable workspace (see Fig. 6(a)) and, it is observed an important influence of the uncertainties over the usable workspace(see Fig. 6(b)). Another notable difference between the two cases is the size of the usable workspace, it is observed that the workspace in case (a) is bigger than case (b).

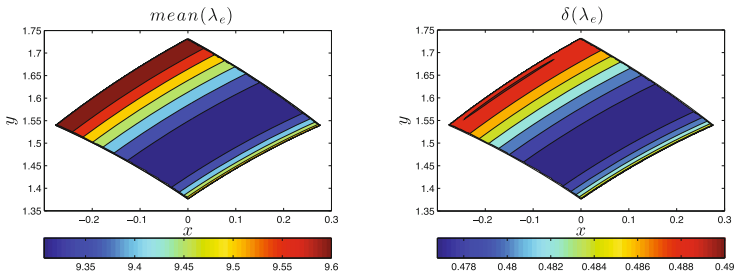

(a) (b)

Fig. 6. Case (b): Local Elastodynamic performance over the usable workspace.

6 Conclusion

This paper presented a study that analyzes the elastodynamics of a planar parallel mechanism under uncertainties. The elastodynamic performance of the mechanism was analyzed as a function of the link lengths, i.e., within the design space. This analysis allows illustrating the elastodynamics subjected to uncertainties in the stiffness of the active joints. The results exhibit a compromise between the elastodynamic performance and uncertainties effects. Therefore, additional proprieties, such as workspace size, should be taken into account in order select the most favorable link lengths. Future works will deal with the optimal design of parallel flexible mechanism subjected to uncertainties.

Acknowledgements. The authors express their acknowledgements to the Graduate Program in Mechanical Engineering of the Federal University of Technology - Paraná funded by CAPES.

References

1. Alessandro, C., Rosario, S.: Elastodynamic optimization of a 3T1R parallel manipulator. Mech. Mach. Theory **73**, 184–196 (2014)
2. Angeles, J., Park, F.C.: Performance evaluation and design criteria. In: Springer Handbook of Robotics, pp. 229–244. Springer (2008)

3. Florian, A.: An efficient sampling scheme: updated Latin hypercube sampling. Probab. Eng. Mech. **7**(2), 123–130 (1992)
4. Khalil, W., Dombre, E.: Modeling. Identification and Control of Robots. Butterworth-Heinemann, Sterling (2004)
5. Lara-Molina, F., Koroishi, E., Dumur, D., Steffen, V.: Stochastic analysis of a 6-DOF fully parallel robot under uncertain parameters. IFAC-PapersOnLine **48**(19), 214–219 (2015)
6. Lara-Molina, F.A., Dumur, D., Koroishi, E.H.: Uncertainty analysis of a 2-DOF planar parallel robot by means of fuzzy dynamic approach. In: 2016 XIII Latin American Robotics Symposium and IV Brazilian Robotics Symposium (LARS/SBR), pp. 275–280 (2016)
7. Lara-Molina, F.A., Koroishi, E.H., Dumur, D.: Design criteria of 2-DOF planar parallel manipulator with flexible joints. In: 2016 12th IEEE International Conference on Industry Applications (INDUSCON), pp. 1–6 (2016). doi:10.1109/INDUSCON.2016.7874544
8. Liu, X.J., Wang, J., Pritschow, G.: Kinematics, singularity and workspace of planar 5R symmetrical parallel mechanisms. Mech. Mach. Theory **41**(2), 145–169 (2006)
9. Liu, X.J., Wang, J., Pritschow, G.: Performance atlases and optimum design of planar 5R symmetrical parallel mechanisms. Mech. Mach. Theory **41**(2), 119–144 (2006)
10. Siciliano, B., Khatib, O.: Springer Handbook of Robotics. Springer Science & Business Media, New York (2008)
11. Zhang, X., Mills, J.K., Cleghorn, W.L.: Vibration control of elastodynamic response of a 3-PRR flexible parallel manipulator using PZT transducers. Robotica **26**(05), 655–665 (2008)

Complex Modelling and Dynamical Analysis of Parallel Cable Mechanisms

Radek Bulín(✉), Michal Hajžman, and Pavel Polach

University of West Bohemia, Univerzitní 22, Pilsen, Czech Republic
{rbulin,ppolach}@ntis.zcu.cz, mhajzman@kme.zcu.cz

Abstract. This paper deals with the modelling of flexible cables, which are parts of multibody systems. The common approaches suitable for the cable modelling are summarized. Force representation of a cable, a point-mass model and an absolute nodal coordinate formulation are discussed. The experimental results from the weight-fibre-pulley-drive mechanical system are used to compare possibilities of common modelling approaches. Then the widely used MSC.Adams software is employed for modelling the Quadrosphere mechanism, which contains flexible fibers. The results of dynamical analysis are presented.

Keywords: Cable · Mechanism · Dynamics · Experiment · Simulation

1 Introduction

Parallel kinematic mechanisms (PKMs) are characterized by one or more closed-loop kinematical chains and exhibit higher stiffness, payload capacity and agility comparing to standard serial kinematic mechanism. A comprehensive review of PKMs was introduced in [6].

Special variants of PKMs are cable driven parallel mechanisms or robots, where rigid links of PKMs are replaced by cables [1]. Advantages of cable driven parallel mechanisms are easy reconfigurability, smaller mass, larger workspace and high acceleration capability. Optimal force distribution in cables for over-constrained cable driven PKMs was solved in [4]. Static and dynamic stiffness analyses were discussed in [11]. Dynamical properties of cable driven PKMs can be improved employing [12] hybrid-driven based PKMs.

Various modelling techniques for the dynamical modelling of cables in the framework of multibody dynamics are summarized in this paper. The application of a simple mechanical system composed of a drive, a pulley and a weight joined by a cable is introduced and the results of simulations are compared with experimental results. Further, the complex example of so called Quadrosphere parallel mechanism driven by four cables is shown and the results of the chosen simulations are discussed.

J.C.M. Carvalho et al. (eds.), *Multibody Mechatronic Systems*,
Mechanisms and Machine Science 54, DOI 10.1007/978-3-319-67567-1_18

2 Cable Modelling Techniques

In most cases, the cables, fibers or ropes are very flexible, thus they should be described by proper mathematical models in order to reflect their behaviour. There are several methods of cables modelling, the most common are described in this section.

2.1 Force Representation of the Cable

One of the basic and most effective ways of including cables into multibody system equations of motion is the force representation of cable using nonlinear forces. For the description of this approach, the simple mechanical system of mass M attached to the base frame by one cable, see Fig. 1(a), was used. The equation of motion for such a system can be written as

$$m\ddot{\mathbf{r}} + b\dot{\mathbf{d}} + k\mathbf{d} = \mathbf{F}_e, \tag{1}$$

where m is the weight of the attached mass, $\mathbf{r}$ is the position vector of the mass, b is the damping coefficient of the cable, k is the stiffness of the cable, $\mathbf{F}_e$ is the vector of external forces acting on the mass and finally $\mathbf{d}$ is the vector of deformation of the cable and $\dot{\mathbf{d}}$ is its time derivative. Since the cables are active only in tension, the longitudinal deformation of the cable can be expressed as

$$\mathbf{d} = \begin{cases} -\left(|\mathbf{r}_f| - l_0\right)\frac{\mathbf{r}_f}{|\mathbf{r}_f|} & \text{for} \quad |\mathbf{r}_f| \geq l_0, \\ 0 & \text{for} \quad |\mathbf{r}_f| < l_0, \end{cases} \tag{2}$$

where vector $\mathbf{r}_f = \mathbf{r} - \mathbf{r}_0$, $\mathbf{r}_0$ is the position vector of the cable attachment and l_0 is the cable free length. The minus sign represents the fact that the cable forces act in the opposite direction to the vector $\mathbf{r}_f$.

Because this force representation of cable does not describe the bending and inertia properties of the cable, it is suitable only for thin and light cables. The main advantages of this model are easy implementation and the ability of obtaining results in real time, which is useful in control problems.

2.2 Point-Mass Representation of the Cable

In this approach, the cable is divided into point-masses which are interconnected by springs, see Fig. 1(b). Each point-mass is represented by the following equation of motion

$$m_i\ddot{\mathbf{r}}_i + b_i\dot{\mathbf{d}}_i + b_{i+1}\dot{\mathbf{d}}_{i+1} + k_i\mathbf{d}_i + k_{i+1}\mathbf{d}_{i+1} = \mathbf{F}_{e,i}, \tag{3}$$

where m_i is the weight of the cable point-mass i, b_i is the damping coefficient of the cable part between nodes $i-1$ and i, k_i is the stiffness of the cable part

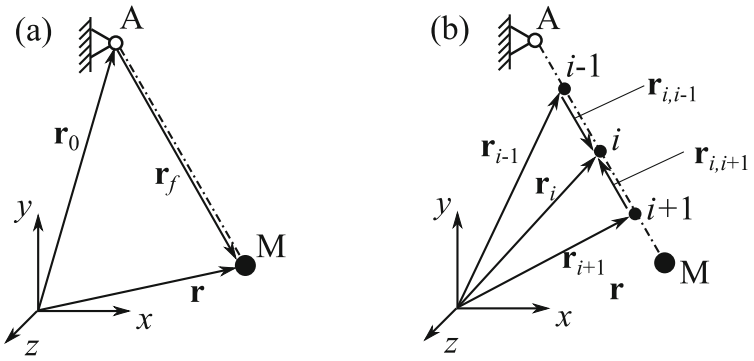

Fig. 1. Scheme of force representation of the cable (a) and point-mass representation of the cable (b)

between nodes $i-1$ and i, $\mathbf{r}_i$ is the position vector of point-mass i, $\mathbf{F}_{e,i}$ is the vector of external forces applied to point-mass i. The deformation of the cable between nodes $i-1$ and i is denoted as $\mathbf{d}_i$ and deformation between nodes i and $i+1$ is denoted as $\mathbf{d}_{i+1}$. These deformation can be expressed as

$$\begin{aligned}
\mathbf{d}_i &= \begin{cases} -\left(|\mathbf{r}_{i,i-1}| - l_{0,i}\right) \frac{\mathbf{r}_{i,i-1}}{|\mathbf{r}_{i,i-1}|} & \text{for} \quad |\mathbf{r}_{i,i-1}| \geq l_{0,i}, \\ 0 & \text{for} \quad |\mathbf{r}_{i,i-1}| < l_{0,i}, \end{cases} \\
\mathbf{d}_{i+1} &= \begin{cases} -\left(|\mathbf{r}_{i,i+1}| - l_{0,i+1}\right) \frac{\mathbf{r}_{i,i+1}}{|\mathbf{r}_{i,i+1}|} & \text{for} \quad |\mathbf{r}_{i,i+1}| \geq l_{0,i+1}, \\ 0 & \text{for} \quad |\mathbf{r}_{i,i+1}| < l_{0,i+1}, \end{cases}
\end{aligned} \tag{4}$$

where $l_{0,i}$ and $l_{0,i+1}$ is the free length of cable part between the nodes $i-1$ and i and between nodes i and $i+1$, respectively.

This cable modelling approach describes the inertia properties of the cable and the resultant equations of motion of all point-masses (3) together with the equation of motion of mass M, which has analogical structure as Eq. (1), can be written in a matrix form. This approach can be also enhanced by adding bending stiffnesses of the cable segments in order to describe also bending behaviour.

2.3 ANCF Cable Model

One of the complex way of cable representation is the Absolute nodal coordinate formulation (ANCF) method, which is based on the finite element method, but instead of deformations and small rotations as the nodal coordinates it uses positions of nodes in global coordinate system and slopes (gradients) in the nodes. A planar ANCF beam element of length l with two nodes (see Fig. 1) is described in this section. The derivation of spatial ANCF beam element is analogical (Fig. 2).

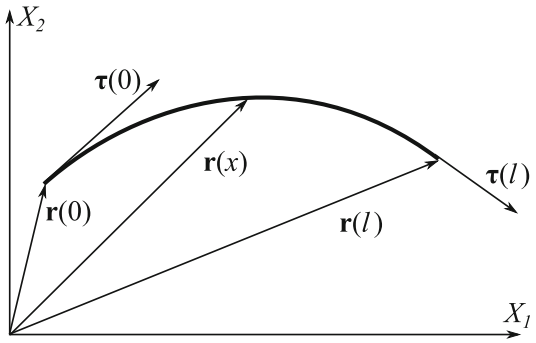

Fig. 2. ANCF planar beam.

Global position $\mathbf{r} = [\, r_x,\, r_y \,]^T$ of an arbitrary beam point determined by parameter x can be written as

$$\mathbf{r}(x) = \mathbf{S}(x)\mathbf{e}, \quad \mathbf{e} = [\, e_1 \;\, e_2 \;\, \ldots \;\, e_8 \,]^T, \tag{5}$$

where $\mathbf{S} \in R^{2,8}$ is the global shape function matrix, $\mathbf{e}$ is the vector of element nodal coordinates and $x \in (0,\, l)$ is the curve parameter. The global shape function matrix $\mathbf{S}$ is derived in the form

$$\mathbf{S} = [s_1\mathbf{I},\; s_2\mathbf{I},\; s_3\mathbf{I},\; s_4\mathbf{I}], \quad \mathbf{I} = \begin{bmatrix} 1 & 0 \\ 0 & 1 \end{bmatrix}, \tag{6}$$

where the shape functions $s_f = s_f(x)$ $(f = 1,\; 2,\; 3,\; 4)$ can be expressed as

$$\begin{aligned} s_1 &= 1 - 3\xi^2 + 2\xi^3, & s_2 &= l(\xi - 2\xi^2 + \xi^3), \\ s_3 &= 3\xi^2 - 2\xi^3, & s_4 &= l(\xi^3 - \xi^2), \end{aligned} \tag{7}$$

with the dimensionless parameter $\xi = x/l$.

Kinetic energy of the element with material density ρ is

$$E_k = \frac{1}{2}\int_0^l \rho A \dot{\mathbf{r}}^T \dot{\mathbf{r}}\, \mathrm{d}x = \frac{1}{2}\dot{\mathbf{e}}^T \int_0^l \rho A \mathbf{S}^T \mathbf{S}\, \mathrm{d}x\, \dot{\mathbf{e}} = \frac{1}{2}\dot{\mathbf{e}}^T \mathbf{M}_e \dot{\mathbf{e}}, \tag{8}$$

where $\mathbf{M}_e$ is the element mass matrix. Strain energy E_p of the element is used for the derivation of elastic forces in the ANCF beam element and the form of an adopted elasticity model determines the complexity of the whole model. In [2], there are several approaches, which employ the separation of the strain energy of longitudinal deformation E_{pl} and the strain energy of transverse (bending) deformation E_{pt} as

$$E_p = E_{pl} + E_{pt} = \frac{1}{2}\int_0^l EA\varepsilon^2\, \mathrm{d}x + \int_0^l EI\kappa^2\, \mathrm{d}x, \tag{9}$$

where E is the Young modulus, A is the area of the cross-section and I is the second moment of the area about a transverse axis. The possible models are then

classified according to the expressions for longitudinal strain ε and curvature κ. General expressions for these quantities are

$$\varepsilon = \frac{1}{2}(\mathbf{r}'^T\mathbf{r}' - 1), \quad \kappa = \left|\frac{\mathrm{d}^2\mathbf{r}}{\mathrm{d}\bar{s}^2}\right|, \tag{10}$$

where $\bar{s}$ is the arc length of the curve and $\mathbf{r}' = \frac{\partial \mathbf{r}}{\partial x}$. Berzeri and Shabana [2] introduced several suitable models for both longitudinal and transverse elastic forces, whereas the formulation denoted L2T2 is employed in this paper in order to investigate the cable-pulley interaction in the weight-fibre-pulley-drive mechanical system.

Standard procedures (e.g. the Lagrange equations or the principle of virtual work) can be used in order to derive a mathematical model of the planar ANCF beam element. It must be noted, that this approach leads to constant mass matrix and nonlinear stiffness matrix of the element.

3 Application on the Test Configuration

Investigation of the fibre behaviour was performed on an experimental configuration of weight-fibre-pulley-drive mechanical system (see Fig. 3), which is described in [8,9]. A carbon cable with a silicone coating is driven with one motor and is led over a pulley of diameter 80 mm. The cable length is 1.82 m (the cable weight is 4.95 g). At one end, the cable is fixed to the drive, at the another end, the cable is fixed to the steel weight of 8.131 kg which moves in a prismatic linkage on an inclined plane of an angle $\alpha = 30°$. The weight, pulley and drive are considered rigid bodies. The cable is investigated using the force representation of cable [8–10] and the ANCF cable model [3,5].

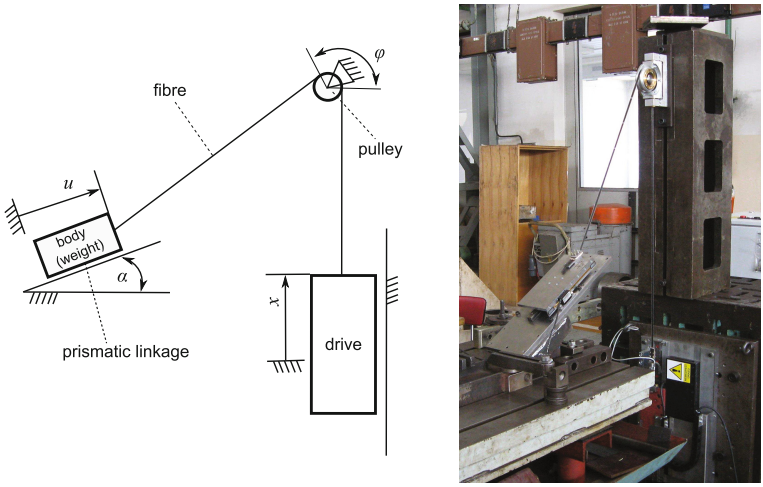

Fig. 3. Scheme and a real experimental mechanical system.

The model that uses the force representation of the cable was implemented in the *alaska* simulation tool. In the case of the ANCF cable model, the contact between the cable and the pulley was modelled using normal contact forces and tangential friction forces in accordance to [3,7], which allows the disengagement of the contact. An in-house modelling tool in the MATLAB system based on the proposed modelling methodology was created. For both models, the prismatic linkage between the weight and the base and between the drive and the base is considered. The revolute joint is considered between the pulley and the base, so the pulley has one rotational degree of freedom.

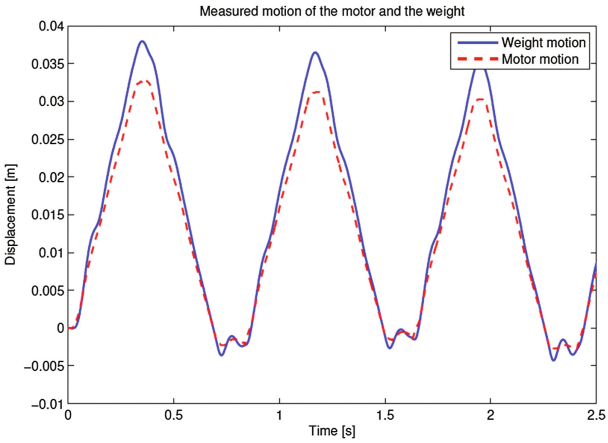

Fig. 4. Measured motion of the drive and the weight.

Time history of a particular signal defining the motion of the drive is in Fig. 4 with the resultant measured position of the weight. The measured motion of the drive was used as an input signal for the numerical simulations in the form of kinematic excitation. The calculated dynamic responses of the weight using the force representation of the cable and the complex model employing the ANCF beam element with cable-pulley interaction modelling are shown in Fig. 5. It is apparent, that the complex ANCF model is in better compliance with the measured data. From the mathematical formulation it is evident that the ANCF method must be more precise than the force representation of fibre, but it is also more computationally demanding. Thus, it would be beneficial to use the simpler force representation of the cable in the case of quick simulations and control problems.

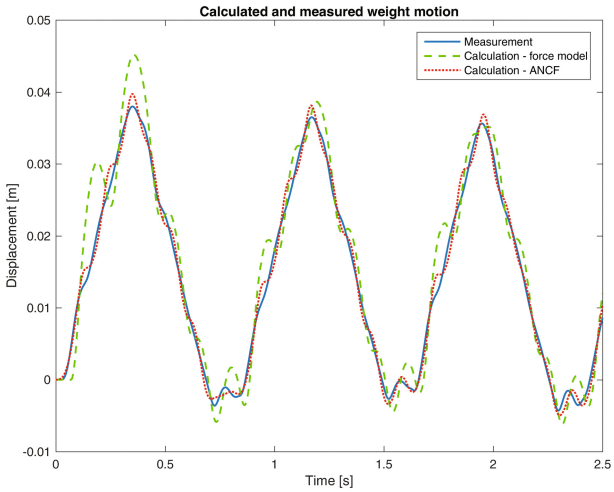

Fig. 5. Measured and calculated displacement of the weight.

4 Modelling of Parallel Mechanism

After the numerical investigation of various cable modelling techniques, the parallel mechanism called Quadrosphere was modelled in the MSC.Adams commercial software. The Quadrosphere, see Fig. 6, is a mechanism consisting of a platform connected with a spherical joint, whose three rotation cardan angles are accurately measured. The actual position of the platform is determined by four fibers. Each fiber leads from each corner of the platform to the vertically placed linear drive through a guiding pulley.

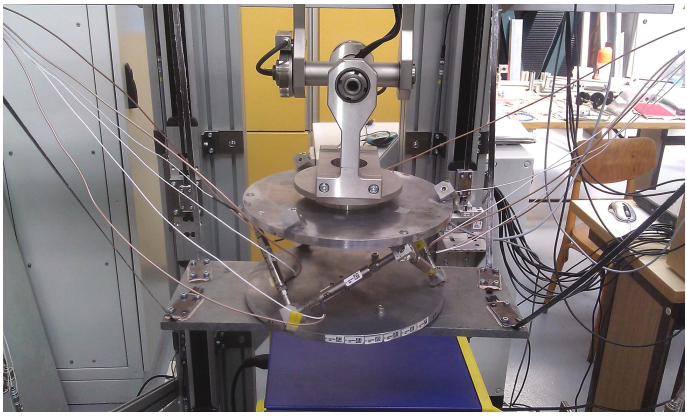

Fig. 6. The Quadrosphere mechanism with the platform and the installed active piezo structure.

The active piezo structure can be attached to the platform to obtain the multi-level controlled mechanism, which serves as a demonstrator of controlling possibilities. In our case, we investigate the arrangement without the active structure.

The Quadrosphere model contains several rigid bodies, see the kinematic scheme in Fig. 7. In this scheme, R means rotational constraint, T means translational constraint and the dot-dash line represents the cable. The spherical joint is composed of an upper fork, which can rotate along vertical axis x, a cardan cross and a bottom fork that holds the platform. Each pulley is installed in a pulley holder which can rotate along vertical direction. Four drives are represented by rigid bodies which can translate only in vertical direction. The platform has three degrees of freedom and its position is determined by the positions of drives.

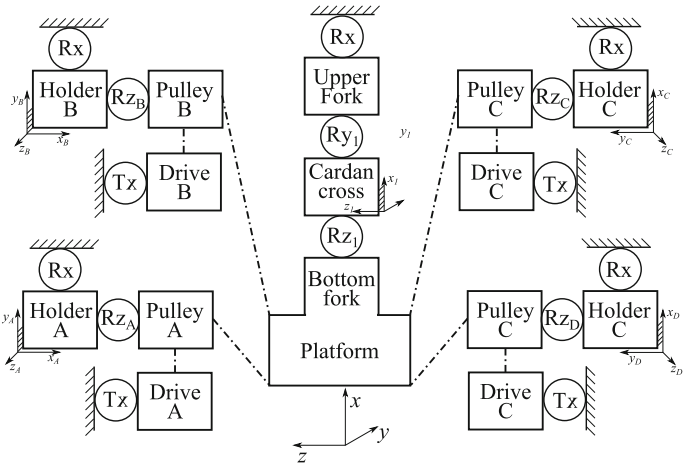

Fig. 7. Kinematic scheme of the Quadrosphere mechanism.

For the modelling of cables, the Cable module of MSC.Adams Machinery toolbox was used. Three computational models were created, each uses another settings of this module. Model 1 has the cables modelled using the simplified method. Model 2 and model 3 use the discretized method for cables with a different size of cable elements. The cable element of model 2 is 16 mm long, whereas model 3 uses cable elements of the size of 40 mm. It must be noted that the simplified model corresponds with the force representation of the cable and the discretized model corresponds with the point-mass representation, which includes the bending behaviour of the cable (Fig. 8).

At first, computational models of the Quadrosphere were verified according to the experimental modal analysis. Eigenfrequencies obtained from the experiment and by numerical analysis using the MSC.Adams Vibration plugin are summarized in Table 1. During modal analysis, the movement of drives was locked and the fibers were pretensioned by 50 N. Since the platform has three degrees of

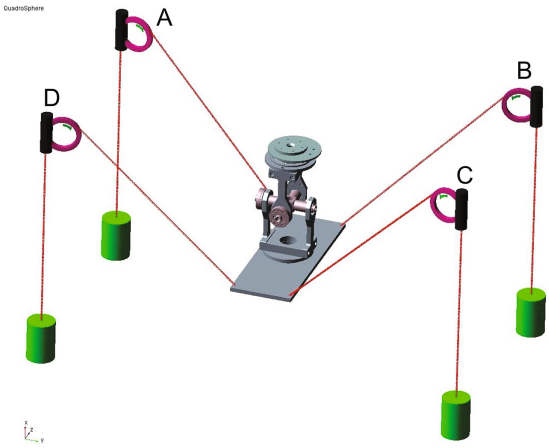

Fig. 8. Visualisation of the Quadrosphere mechanism in MSC.Adams.

Table 1. Results of modal analysis

Mode shape	Experiment	Eigenfrequencies [Hz]		
		Model 1	Model 2	Model 3
Platform rotation φ_y	36.05	39.98 (111%)	40.50 (112%)	38.7 (107%)
Platform rotation φ_z	42.72	42.83 (100%)	43.19 (101%)	43.03 (101%)
Platform rotation φ_x	48.05	46.16 (96%)	48.21 (100%)	57.46 (120%)

freedom $\varphi_x, \varphi_y, \varphi_z$, only the eigenfrequencies of dominant mode shapes that correspond to the excitation of each degree of freedom are compared. The results show that modal characteristics of model 1 and model 2 are in a good compliance with the experimental results. Model 3 differs significantly in the third eigenfrequency. This is caused by poor fiber discretization.

5 Conclusions

In this paper, the cable modelling techniques are summarized and used in two specific applications. The experimental results from the weight-fibre-pulley-drive mechanical system were used to compare possibilities of common modelling approaches. Further the widely used MSC.Adams software was employed for the modelling of the Quadrosphere mechanism, which contains flexible fibers and the results of dynamical analysis were shown. It can be concluded that the cable modelling technique based on the force representation could be used in future developments in the case of the Quadrosphere parallel kinematic mechanism.

The proposed Quadrosphere model will be used in the development of a hierarchical motion control of lightweight multi-level mechanisms consisting of the

large motion level realized by the cable driven PKM (Quadrosphere) and the small motion levels realized using active structures. The aim of such multi-level structures is the widening of frequency bandwidth of their feedback motion control. The superimposed active structures can improve the positioning accuracy and operational speed of the end-effectors of recently developed cable driven parallel mechanisms of different types.

Acknowledgements. The paper has originated in the framework of solving the project of the Czech Science Foundation No. 15-20134S entitled Multi-level Light Mechanisms with Active Structures.

References

1. Behzadipour, S., Khajepour, A.: A new cable-based parallel robot with three degrees of freedom. Multibody Syst. Dyn. **13**, 371–383 (2005)
2. Berzeri, M., Shabana, A.A.: Development of simple models for elastic forces in the absolute nodal coordinate formulation. J. Sound Vib. **235**, 539–565 (2000)
3. Bulín, R., Hajžman, M., Polach, P.: Nonlinear dynamics of a cable-pulley system using the absolute nodal coordinate formulation. Mech. Res. Commun. (2016, in press). http://dx.doi.org/10.1016/j.mechrescom.2017.01.001
4. Gosselin, C., Grenier, M.: On the determination of the force distribution in over-constrained cable-driven parallel mechanisms. Meccanica **46**, 3–15 (2011)
5. Hajžman, M., Bulín, R., Polach, P.: Nonlinear analysis of the cable-pulley interaction. In: Proceedings of ECCOMAS Thematic Conference on Multibody Dynamics 2015, pp. 554–564. Universitat Politcnica de Catalunya, Barcelona (2015)
6. Luces, M., Mills, J.K., Benhabib, B.: A review of redundant parallel kinematic mechanisms. J. Intell. Rob. Syst. (2016). doi:10.1007/s10846-016-0430-4
7. Lugrís, U., Escalona, J., Dopico, D., Cuadrado, J.: Efficient and accurate simulation of the Rope-Sheave interaction in weight-lifting machines. Proc. Inst. Mech. Eng. Part K J. Multi-body Dyn. **225**(4), 331–343 (2011)
8. Polach, P., Hajžman, M., Václavík, J., Šika, Z., Svatoš, P.: Model parameters influence of a simple mechanical system with fibre and pulley with respect to experimental measurements. In: Proceedings of ECCOMAS Thematic Conference Multibody Dynamics 2013, pp. 473–482. University of Zagreb, Zagreb (2013)
9. Polach, P., Hajžman, M., Václavík, J., Šika, Z., Valášek, M.: Investigation of a laboratory mechanical system with fibre and pulley. Int. J. Dyn. Control **3**(1), 78–86 (2015)
10. Polach, P., Hajžman, M.: Influence of the fibre spring-damper model in a simple laboratory mechanical system on the coincidence with the experimental results. In: Proceedings of ECCOMAS Thematic Conference on Multibody Dynamics 2015, pp. 419–430. Universitat Politcnica de Catalunya, Barcelona (2015)
11. Yuan, H., Courteille, E., Deblaise, D.: Static and dynamic stiffness analyses of cable-driven parallel robots with non-negligible cable mass and elasticity. Mech. Mach. Theory **85**, 64–81 (2015)
12. Zi, B., Ding, H., Cao, J., Zhu, Z., Kecskemthy, A.: Integrated mechanism design and control for completely restrained hybrid-driven based cable parallel manipulators. J. Intell. Rob. Syst. **74**, 643–661 (2014)

A New Methodology for the Balancing of Mechanisms Using the Davies' Method

Julio Cesar Frantz[1(✉)], Leonardo Mejia Rincon[2], Henrique Simas[1], and Daniel Martins[1]

[1] Department of Mechanical Engineering, Federal University of Santa Catarina, Florianópolis, Santa Catarina, Brazil
julio.frantz@posgrad.ufsc.br, {henrique.simas,daniel.martins}@ufsc.br
[2] Department of Automation and Control, Federal University of Santa Catarina, Blumenau, Santa Catarina, Brazil
leonardo.mejia.rincon@ufsc.br

Abstract. A general method for balance of planar mechanisms is presented in this paper. In order to determine the force that causes unbalanced, called shaking forces, the dynamics equations of motion for mechanisms are formulated systematically using the Davies' method. The formulation leads to an optimization scheme for the mass distribution to improve the dynamic performances of mechanisms. The method is illustrated with a slider-crank mechanism. Balancing of shaking forces shows a significant improvement in the dynamic performances compared to that of the original mechanisms.

Keywords: Dynamics · Shaking force · Balancing · Davies' method

1 Introduction

Despite large research effort in the field of balance of mechanisms, modelling the behaviour of unbalanced forces are still considered important and a major challenge in recent investigations [13]. The development of models using Fourier series in analytical way can be difficult to interpretate, due to the complexity of the equations. Also, an approach that considered the behaviour of others forces in the model, as example, gravitational force, can be difficult to integrate with analytical models.

In order to address the issues previously discussed we proposed a method based in a synthetical view which can not only be used to solve the internal unbalanced forces, but integrated also external forces which are applied to the structure. The method is validated using a planar slider-crank mechanism (Fig. 1), but it has the potential to be expanded in order to use it in spatial mechanisms.

An overview on balancing techniques is presented in Sect. 2. Section 3 describe the proposed methodology and summarises scientific contributions of this paper. The mechanical design of the slider-crank mechanism is presented in Sect. 4 along

J.C.M. Carvalho et al. (eds.), *Multibody Mechatronic Systems*,
Mechanisms and Machine Science 54, DOI 10.1007/978-3-319-67567-1_19

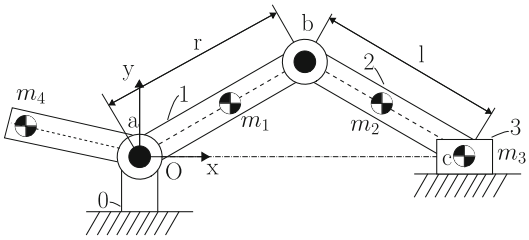

Fig. 1. Slider-crank mechanism

the equivalent masses model. Section 5 present the solution of the accelerations center of mass and Sect. 6 the solution of the inertial equations. The optimization algorithm used is briefly introduced in Sect. 7. Section 8 present the results for the shaking forces and Sect. 9 the conclusions of the paper.

2 Background

Different approaches has been developed for the balance of mechanisms. In [2,11] a method based on the conditions of the angular and linear moment being equal to zero was used. In [3,13] a closed analytical condition has been found to determine the position of the center of mass of a mechanism and the conditions for being stationary. Both methods are convenient for the analytical solution of the problem but sometimes leads to complex solutions, requiring significant algebraic effort to the derivation of the balance conditions.

In [4,6] a fast Fourier transform analysis is derived and investigated to the partial balancing of high-speed machinery by the use of counterweights mounted on shafts. This solution has found wide application as it may be accomplished by attaching balancing elements to the crank. However, for mechanisms with more degrees of freedom (DOFs), the dynamic balance conditions become increasingly to find as the number of bodies increase. In [8] a screw-based dynamic balancing approach has been developed to obtain the balancing conditions directly from the momentum equations. Using Screw theory it has been found that a simplification of the balancing process is obtained. On overview of the theory of balancing mechanism is given in [1].

In this paper, the Davies' method is used to solve the dynamic balance for a planar slider-crank mechanism. The method is based on Graph theory, Screw theory and an adaptation of the Kirchhoff's laws and is applied to solve both differential kinematics and statics of mechanism [5,7,9]. Recently, the method was used to solve the rollover of long combination vehicles, treating the acceleration of the last unit (trailer) and the stiffness of the suspension system [10]. Because of this combination of powerful mathematical tools, as Graph theory and Screw theory, and also for the adaptation from electric circuits, the Davies' method have been proved to be more general and straight forward than other tools.

3 Methodology

In this section, a new methodology is derived and presented to solve the shaking forces in a slider-crank mechanism. The methodology is based on the Davies' method to solve the inertial equations and after an optimization method to describe the position of the counterweights to reduce the shaking forces in the mechanism.

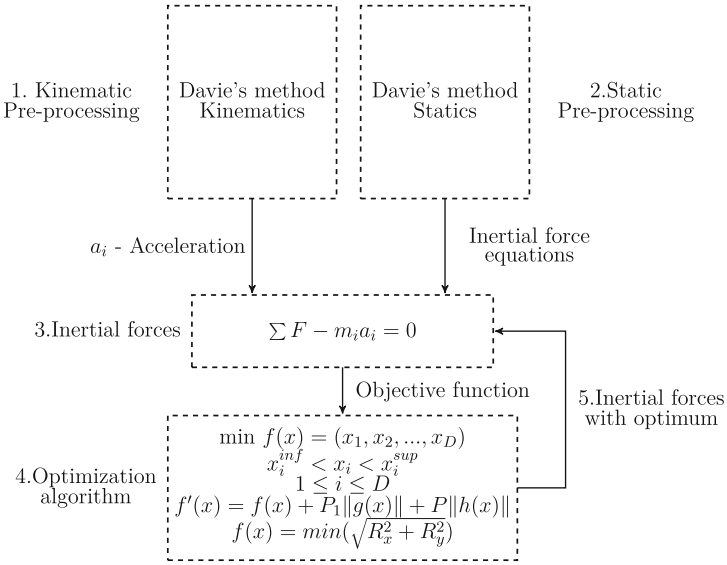

Fig. 2. Flowchart of the methodology

Figure 2 shows the flow chart of the methodology: the first step is solving the accelerations of the center of mass of each link of the mechanism and the inertial forces acting in each link, as we call the kinematic pre-processing and static pre-processing. Once the accelerations and the inertial forces are known, to solve the shaking forces, an objective function is built, using a convenient number of optimization variables. In this paper, the differential evolution optimization method was used to solve the minimization of the shaking forces.

4 System Modeling

The slider-crank mechanism is divided by a crankshaft (1), connecting rod (2) and slider block (3). The respectively total mass of the crankshaft, connecting rod and slider block is m_1, m_2 and m_3. The length of the crankshaft and connecting rod is, respectively, r and l. To balance the shaking forces in the mechanism, a counterweight with total mass m_4 is add in the crankshaft (Fig. 1). The weight and the position of the counterweight it will be determined by the optimization method.

To solve the inertial forces in the slider-crank it is necessary to know the position of each center of mass of each link and the counterweight. For this solution, it is better to represent the masses of the links as equivalent masses. For the dynamic equivalence, it is necessary to assume three conditions [2].

- The mass of the model must be equal that of the original body.
- The center of gravity must be in the same location as that of the original body.
- The mass moment of inertia must equal that of the original body.

Figure 3 shows the equivalent mass of the crankshaft. The total mass of the crankshaft m_1 can be represented as an equivalent mass in the point b.

$$m_{1_b}\, r = m_1\, r_{G_2}$$
$$m_{1_b} = m_1 \frac{r_{G_2}}{r} \tag{1}$$

For the connecting rod, the total mass can be derived in three masses: m_{2_b}, m_{2_g} and m_{2_c} (Fig. 3).

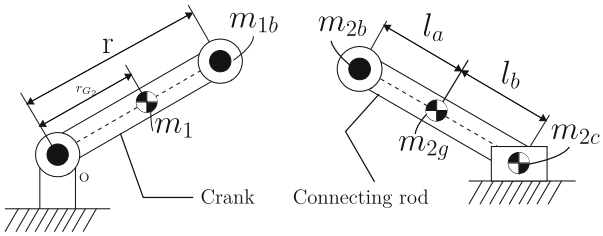

Fig. 3. Equivalent mass model

The equivalent mass system is obtained by the Eqs. 2, 3 and 4.

$$m_{2_b} + m_{2_g} + m_{2_c} = m_2 \tag{2}$$
$$m_{2_b}\, l_a + m_{2_g}\, 0 + m_{2_c}\, l_b = 0 \tag{3}$$
$$m_{2_b}\, l_a^2 + m_{2_g}\, 0 + m_{2_c}\, l_b^2 = J_S \tag{4}$$

Solving m_{2_b} in Eq. 3, we obtain,

$$m_{2_b} = \frac{m_{2_c}\, l_b}{l_a} \tag{5}$$

Now, applying Eq. 5 in Eq. 4,

$$m_{2_c} = \frac{J_S}{l_b\, l_a + l_b^2} \tag{6}$$

Knowing the moment of inertia J_S, it is possible to describe the equivalent masses of the link. These simplifications lead to the equivalent masses model of the slider-crank.

5 Solving the Acceleration

As stated previously, the Davies' method is used in this paper to solve the kinematics of the slider-crank. The first step in the solution of the shaking forces, it is necessary to know the accelerations of the center of mass of each link of the mechanism. For the slider-crank, it is necessary to know the acceleration of the counterweight (S_3), joints b and c of the connecting rod, and the center of mass S_2 of the connecting rod, as shown in Fig. 4(a).

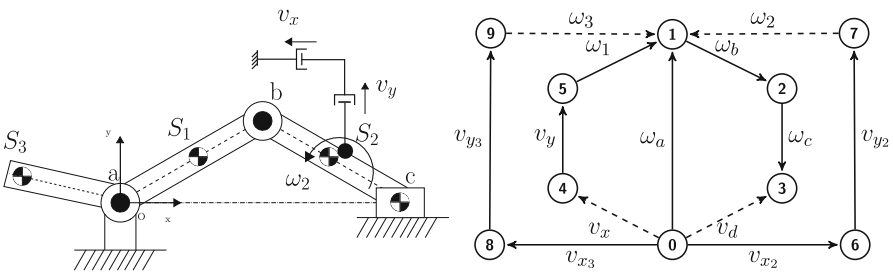

(a) Kinematic parameters (b) Motion graph

Fig. 4. Kinematic parameters and motion graph of the slider-crank

To describe the acceleration of the connecting rod center of mass it is applied an assur virtual chain, composed by prismatic kinematic pairs at x and y axis, and one revolute joint about the z axis, as we called a PPR assur virtual chain. The prismatic joint is used in these case to solve the linear velocities of the center of mass v_x and v_y.

Using graph theory we can represent the whole velocities in the slider-crank as a graph called the motion graph G_M. The slider-crank is composed by three revolute joints a, b and c and one prismatic joint d. The DOF of the revolute joint are the angular velocities about the z axis ω_a, ω_b and ω_c. And the DOF of the prismatic joint is the velocity in the x axis called v_d. In the motion graph, each edge represents the degrees of freedom f of the coupling (joint). The motion graph G_M of the slider-crank mechanism is shown in Fig. 4(b).

In the motion graph, we represent also the degrees of freedom of the assur virtual chain, in this case 3 virtual chains to describe the velocities of the center of mass b, S_2 and S_3. A set of f independent motions represented by twists is written in the circuit matrix $\{B_M\}_{l,F}$. The number of circuits l is 4 and the gross network degree of freedom F is 13, so the circuit matrix G_M is

$$[B_M]_{4\times 13} = \begin{bmatrix} -1 & -1 & -1 & 1 & 0 & 0 & 0 & 0 & 0 & 0 & 0 & 0 & 0 \\ -1 & 0 & 0 & 0 & 1 & 1 & 1 & 0 & 0 & 0 & 0 & 0 & 0 \\ -1 & 0 & 0 & 0 & 0 & 0 & 0 & 1 & 1 & 1 & 0 & 0 & 0 \\ -1 & 0 & 0 & 0 & 0 & 0 & 0 & 0 & 0 & 0 & 1 & 1 & 1 \end{bmatrix} \tag{7}$$

The solution of the kinematic magnitudes of the slider-crank is obtained applying the circuit-law in the unit motion matrix [5]. The solution of the secondary variables $[\Psi_p]$ is obtained in Eq. 8.

$$\begin{Bmatrix} v_{b_x} \\ v_{b_y} \\ v_{S_{2_x}} \\ v_{S_{2_y}} \\ v_{c_x} \\ v_{S_{3_x}} \\ v_{S_{3_y}} \end{Bmatrix} = \begin{Bmatrix} -y_b \\ x_b \\ \frac{-(y_{S_2}\, x_b - y_b\, x_c)}{x_b - x_c} \\ \frac{x_b\,(x_{S_2} - x_c)}{x_b - x_c} \\ \frac{-(x_b\, y_c - y_b\, x_c)}{x_b - x_c} \\ -y_{S_3} \\ x_{S_3} \end{Bmatrix} \omega_a \tag{8}$$

where $[x_i, y_i]$ are the coordinates of each joint and center of mass illustrated in Fig. 4. Once the velocities are known, the accelerations are easily obtained applying the derivative.

6 Solving the Inertial Forces

We can apply the Davies' method to solve the reactions forces at the frame of the slider-crank. The reactions forces R_x and R_y can be represented by the inertial forces acting in each link. The inertial forces due to the acceleration of the link act in a straight line passing through the center of mass of the link. The inertial forces F_i acting in each link are shown in Fig. 5.

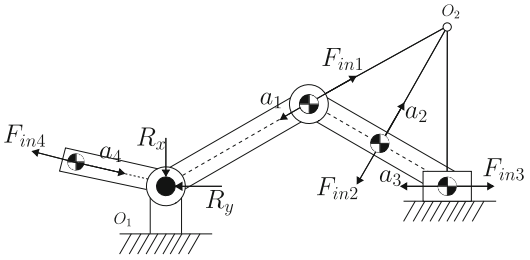

Fig. 5. Inertial forces acting in the slider-crank.

As in the kinematic solution, the actions in the mechanism can be represented by a graph called action graph G_A. In the action graph, each constraint in a joint is represented as a set of edges in parallel. The inertial forces acting in each link of the slider-crank mechanism can be represented as a screw with six coordinates. Here we call the screw as and inertial screw. The inertial screw is composed by one unitary vector with six coordinates and an scalar representing its magnitude. The magnitude is the properly inertial force, as estimated by the second Newton law: $\Psi = -m\, a$.

The negative in the inertial force is written in the vector of six coordinates. Written the inertial force in each axis of the coordinate system O_{xyz}, the inertial screw is

$$\$^{in} = \begin{Bmatrix} \boldsymbol{M}^{in} \\ -- \\ \boldsymbol{R}^{in} \end{Bmatrix} = \begin{Bmatrix} \boldsymbol{S}_0 \times \boldsymbol{R}^{in} \\ - - - \\ f_x^{in} \\ f_y^{in} \\ f_z^{in} \end{Bmatrix} = \begin{Bmatrix} m\,(z_i\,a_y\,-\,y_i\,a_z) \\ m\,(x_i\,a_z\,-\,z_i\,a_x) \\ m\,(y_i\,a_x\,-\,x_i\,a_y) \\ - - - - - - - - \\ -m\,a_x \\ -m\,a_y \\ -m\,a_z \end{Bmatrix}$$

$$\$^{in} = \begin{Bmatrix} 0 \\ -z_i \\ y_i \\ -- \\ -1 \\ 0 \\ 0 \end{Bmatrix} m\,a_x + \begin{Bmatrix} z_i \\ 0 \\ -x_i \\ -- \\ 0 \\ -1 \\ 0 \end{Bmatrix} m\,a_y + \begin{Bmatrix} -y_i \\ x_i \\ 0 \\ -- \\ 0 \\ 0 \\ -1 \end{Bmatrix} m\,a_z \tag{9}$$

As the slider-crank mechanism is in the planar case ($\lambda = 3$), it is possible to eliminate the rows 1, 2 and 6 of the vector. The set of inertial screws and wrenches it is written in the cutset matrix $\{Q_A\}_{k,C}$. The number of cut-sets k is 3 and the gross network degree of freedom C is 17, so the cutset matrix will be in the form $\{Q_A\}_{3,17}$. For brevity, the cut-set matrix it is not showed here.

Using the cut-set law the algebraic sum of the normalized wrenches that belong to the same cut must be equal to zero [5]. So it is possible to obtain the action unit matrix $[\hat{A}_N]_{\lambda k,C} = [\hat{A}_N]_{9,17}$. Using as primary variables the magnitudes of the inertial screws, and solving the action unit matrix using the Gauss-Jordan elimination method, the solution of the system provides the following equations,

$$R_x = -F_{in_{1_x}} - F_{in_{2_x}} - F_{in_{3_x}} - F_{in_{4_x}} \tag{10}$$

$$R_y = -F_{in_{1_y}} - F_{in_{2_y}} - F_{in_{4_y}} \tag{11}$$

Equations 10 and 11 describe the shaking forces at the frame of the slider-crank in function of the inertial forces acting in each link. In the next section, the construction of the objective function to minimize these shaking forces will be explained.

7 Objective Function

The strategy used in this paper to solve the optimization problem was the Differential Evolution (DE) proposed in [12]. The objective function to the problem of minimization of shaking forces in the slider-crank was built using three variables. The first variable is the mass of the counterweight m_4. The two others variables describe the position of the counterweight relative to the coordinate system O_{xyz}. r_2 is the length of the link counterweight and γ is the angle between

the crankshaft. Here the objective function is written in the way to minimize the force (R) of the shaking force,

$$\begin{aligned} minimize: R(m_4, r_2, \gamma) = R = min(\sqrt{R_x^2 + R_y^2}) = \ldots \\ \ldots = \sqrt{-F_{in_{1_x}} - (m_A - \overline{m}_b)\, a_{2_x} - F_{in_{3_x}} - F_{in_{4_x}}} \\ + \sqrt{-F_{in_{1_y}} - (m_A - \overline{m}_b)\, a_{2_y} - F_{in_{4_y}}} \end{aligned} \tag{12}$$

Equation 12 shows that the two components of the shaking force are written in function of the optimization variables (m_4, r_2, γ). To solve the problem it is necessary to write a set of inequality constraints for each optimization variables, indicating the limits of each variable. For this problem the inequality constraints is,

$$subject\,to: \quad g_1(m_4): \quad 0 \leqslant m_4 \leqslant m_{4_{max}} \tag{13}$$

$$g_2(r_2): \quad 0 \leqslant r_2 \leqslant r_{2_{max}} \tag{14}$$

$$g_3(\gamma): \quad 0 \leqslant \gamma \leqslant 2\pi \tag{15}$$

8 Results

The methodology is validated by calculating the shaking forces at the frame of the slider-crank using Matlab®. The data used for the slider-crank is: $r = 0.4$ [m], $l = 0.15$ [m], the masses and moment of inertia of the crank, connecting rod and slider, respectively $m_1 = 0.5$ [kgf] and $J_{S_1} = 1.8e^{-5}$ [kg m^2], $m_2 = 0.1$ [kgf] and $J_{S_2} = 9.50e^{-7}$[kg m^2], $m_3 = 0.5$ [kgf] and $J_{S_3} = 5.05e^{-7}$[kg m^2]. The angular velocity is $\omega_a = 300$ [rpm]. Figures 6 and 7 shows the shaking force R_x and R_y at the frame of the slider-crank without counterweight. Figures 8 and 9 shows the maximum force and the forces R_x and R_y for the case when the counterweight is add to the crankshaft.

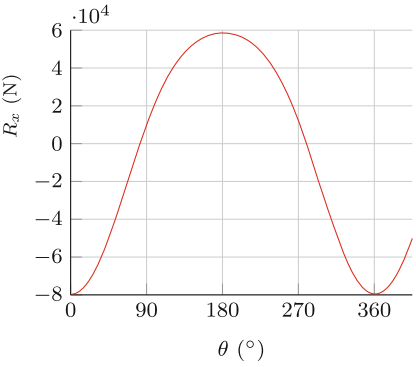

Fig. 6. Unbalanced shaking force R_x

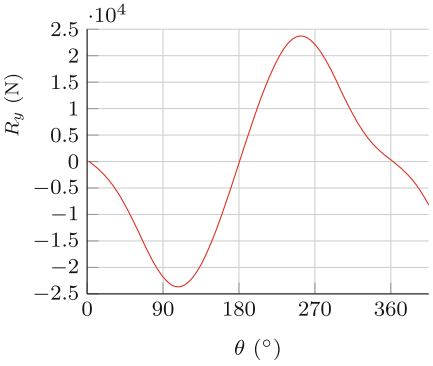

Fig. 7. Unbalanced shaking force R_y

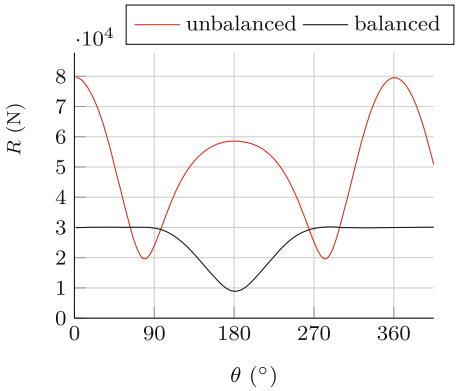

Fig. 8. Maximum shaking force

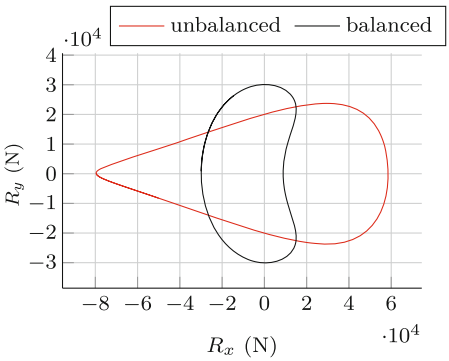

Fig. 9. Shaking forces Rx and Ry

9 Conclusion

In this paper a new methodology to derive the equations of the shaking forces in a slider-crank mechanism by using the Davies' method was presented. The results using the method show that the equations are obtained with a minimum effort. The method shows a great potential to be applied in spatial mechanisms and also to include external forces within the model. Compared to another methods that use Fourier analysis this method treats the shaking forces as a unique approximation. Another advantage is that the approach is formulated as a general mathematical optimization problem. Future works involve including other variables in the optimization algorithm, such as dimensions and weight of the connecting rod.

Acknowledgements. This work was conducted during a scholarship supported by the Program PGPTA 59/2014 financed by CAPES.

References

1. Arakelian, V., Smith, M.R.: Shaking force and shaking moment balancing of mechanisms: a historical review with new examples. J. Mech. Des. **127**(2), 334–339 (2005)
2. Baranov, G.G.: Curso de la teoría de mecanismos y máquinas. Mir, Moscow (1979)
3. Berkof, R.S., Lowen, G.G.: A new method for completely force balancing simple linkages. J. Eng. Ind. **91**, 21–26 (1969)
4. Chiou, S.T., Davies, T.H.: The ideal locations for the contra-rotating shafts of generalized Lanchester balancers. Proc. Inst. Mech. Eng. Part C J. Mech. Eng. Sci. **208**(1), 29–37 (1994)
5. Davies, T.H.: Freedom and constraint in coupling networks. Proc. Inst. Mech. Eng. Part C J. Mech. Eng. Sci. **220**(7), 989–1010 (2006)
6. Davies, T.H., Niu, G.H.: On the retrospective balancing of installed planar mechanisms. Proc. Inst. Mech. Eng. Part C J. Mech. Eng. Sci. **208**, 39–45 (1994)

7. Frantz, J.C., Mejia, L., Simas, H., Martins, D.: Analysis of wrench capability for cooperative robotic systems. In: Proceedings of 23rd ABCM International Congress of Mechanical Engineering - COBEM (2015)
8. Jong, J.J., Dijk, J., Herder, J.L.: A screw-based dynamic balancing approach, applied to a 5-bar mechanism. In: 15th Advances in Robot Kinematics, France (2016)
9. Mejia, L., Frantz, J.C., Simas, H., Martins, D.: Wrench capability polytopes in redundant parallel manipulators. In: Proceedings of 23rd ABCM International Congress of Mechanical Engineering - COBEM (2015)
10. Moreno, G.G., Nicolazzi, L., Vieira, R.S., Martins, D.: Three-dimensional analysis of the rollover risk of heavy vehicles using Davies method. In: Proceedings of the 14th IFToMM World Congress, pp. 195–204 (2015)
11. Paul, B.: Kinematics and Dynamics of Planar Machinery. Prentice Hall, Englewood Cliffs (1979)
12. Storn, R., Price, K.: Differential evolution-a simple and efficient heuristic for global optimization over continuous spaces. J. Global Optim. **11**, 341–359 (1997)
13. van der Wijk, V.: Methodology for analysis and synthesis of inherently force and moment-balanced mechanisms. Universiteit Twente (2014)

The Dynamic Synthesis of an Energy-Efficient Watt-II-Mechanism

F. Schwarzfischer(✉), M. Hüsing, and B. Corves

Department of Mechanism Science and Dynamics of Machines,
RWTH Aachen University, Aachen, Germany
schwarzfischer@igm.rwth-aachen.de

Abstract. Mechanisms form part of many different production machines, e.g. weaving machines, printing machines or packaging machines. The energy-efficiency of their built-in mechanisms is crucial for the profitability of these machines. In many cases a considerable part of the energy to drive the mechanisms has to be applied to accelerate and decelerate links of these mechanisms. When a mechanism is driven in its so-called Eigenmotion, no energy-input for accelerating and decelerating its links has to be applied as the kinetic energy stays constant over the whole motion. In this contribution, the basic principles of energy-efficient mechanisms with a constant level of kinetic energy during its operation are discussed. A new method of designing such mechanisms is shown on the example of a six bar Watt-II-Mechanism.

Keywords: Eigenmotion · Dynamic balancing · Mechanism synthesis · Dynamic synthesis

1 Introduction

Processes in production machines often require the non-uniform movement of parts. This non-uniform movement can be either created by the use of servomotors or by the application of mechanisms or a combination of both [4, 10].

In the following only mechanisms with a rotating input link (crank) are considered. In order to drive a mechanism, an input torque T_D has to be provided. This input torque can be written as a sum:

$$T_D = T_{kin} + T_{pot} + T_{diss} + T_{proc} \tag{1}$$

T_{kin} is the necessary torque to accelerate and decelerate the links of the mechanism. T_{pot} has to be provided to overcome the resistances resulting from gravity and springs. T_{diss} and T_{proc} comprise the resistances following from dissipation effects and process forces. In case of high-speed applications with low process forces the torque T_{kin} is dominant. It can be derived using the Lagrange Equations of 2nd kind [2]:

$$T_{kin} = \frac{d}{dt}\left(\frac{\partial E_{kin}}{\partial \dot{\varphi}}\right) - \frac{\partial E_{kin}}{\partial \varphi} \tag{2}$$

J.C.M. Carvalho et al. (eds.), *Multibody Mechatronic Systems*,
Mechanisms and Machine Science 54, DOI 10.1007/978-3-319-67567-1_20

The crank angle of the mechanism is denoted by φ. E_{kin} is the kinetic energy of its links. Obviously a constant level of kinetic energy leads to very efficient mechanisms as T_{kin} vanishes. A specific velocity profile can be found for every mechanism with one degree of freedom (1-DOF) in order to achieve a constant level of kinetic energy. This periodic motion is called the Eigenmotion [2, 3].

The task of mechanism synthesis is to find the optimal kinematic parameters of a mechanism in order to fulfil a desired motion [4, 10]. Dynamic balancing comprises the methods to change the dynamic properties of a mechanism by changing the mass parameters, which comprise the masses, the position of the centers of gravity and the mass moments of inertia of the different links. The goals of dynamic balancing can be the reduction of shaking forces and torques or joint forces or the lowering of the input torque. The dynamic synthesis of a mechanism comprises the methods of the dynamic balancing. Apart of the mass parameters also kinematic parameters are taken into account. The aim of this synthesis is to find a mechanism which fulfills a desired motion but also meets certain requirements regarding the dynamic properties [2, 3, 11].

Examples for the dynamic synthesis of mechanisms can be found in [3, 8, 11]. Due to the oftentimes high number of parameters, the application of optimization algorithms is common is this field. An example is given in [8].

The aim of this paper is to develop a method for the synthesis of mechanisms with a constant level of kinetic energy. The method will be introduced on the example of the synthesis of a Watt-II-Mechanism. The synthesis will be formulated as an optimization problem which will be solved using a genetic algorithm.

2 State of the Art

In the first part of this section, the basic equations of the dynamics of 1-DoF-mechanisms (in the following referred to as mechanisms) are presented. The second part covers the basics of mathematical optimization.

2.1 Dynamics of Mechanisms

The kinetic energy of a mechanism is the sum of the kinetic energy of its links. For a planar mechanism with n links it can be written as follows:

$$E_{\text{kin}} = \frac{1}{2}\sum_{k=1}^{n} m_k v_{\text{CG},k}^2 + \frac{1}{2}\sum_{k=1}^{n} J_k \omega_k^2 \tag{3}$$

The mass is referred to as m, the mass moment of inertia is denoted by J. The angular velocity is denoted as ω, the translational velocity of the center of gravity ('CG') as v. The kinetic energy can be rewritten as follows:

$$E_{\text{kin}} = \dot{\varphi}^2 \left(\frac{1}{2}\sum_{k=1}^{n} m_k \left[\left(\frac{\mathrm{d}x_{\text{CG},k}}{\mathrm{d}\varphi} \right)^2 + \left(\frac{\mathrm{d}y_{\text{CG},k}}{\mathrm{d}\varphi} \right)^2 \right] + \frac{1}{2}\sum_{k=1}^{n} J_k \left(\frac{\mathrm{d}\varphi_k}{\mathrm{d}\varphi} \right)^2 \right) \tag{4}$$

The angle φ denotes the input angle (crank angle). Its derivative with respect to time is the input velocity of the mechanism. Setting the kinetic energy equal to a constant value at an initial state '0', Eq. (4) can be solved for the input velocity:

$$\dot{\varphi}_{\mathrm{e}} = \frac{\sqrt{E_{\mathrm{kin}}(\varphi_0, \dot{\varphi}_0)}}{\sqrt{\frac{1}{2}\sum_{k=1}^{n} m_k \left[\left(\frac{\mathrm{d}x_{\mathrm{CG},k}}{\mathrm{d}\varphi} \right)^2 + \left(\frac{\mathrm{d}y_{\mathrm{CG},k}}{\mathrm{d}\varphi} \right)^2 \right] + \frac{1}{2}\sum_{k=1}^{n} J_k \left(\frac{\mathrm{d}\varphi_k}{\mathrm{d}\varphi} \right)^2}} \tag{5}$$

This particular velocity is called the Eigenmotion of the mechanism (index 'e'). It depends on the kinematic parameters of the mechanism, its mass parameters and the initial kinetic energy of the mechanism. The characteristics of the Eigenmotion depend on the kinematic and on the mass parameters. The cycle time T of the Eigenmotion can be adjusted by in- or decreasing the initial kinetic energy of the mechanism, that is adjusting the initial angular velocity of the crank [2, 3, 11].

Experiments have shown that driving a mechanism in its Eigenmotion is a suitable course of action in order to save energy [9].

2.2 Mathematical Optimization

The objective of optimization techniques is to find the best design of a variety of alternatives. Therefore a function is analyzed. This so-called objective function f is expressed in terms of a set of design parameters $\boldsymbol{x}$. The goal of the optimization process is to find a certain set of parameters, which minimizes or maximizes the objective function. Furthermore, constraints can be taken into account. Constraints can be formulated as equality constraint equations h or as inequality constraint equations g and are also dependent on the design parameters. Acceptable combinations of the design parameters have to satisfy these constraint equations. The formal statement of the minimization formulation of an optimization problem is:

$$\begin{aligned} &\textit{minimize } f(\boldsymbol{x}) \\ &\textit{subject to} \quad \boldsymbol{h}(\boldsymbol{x}) = 0, \\ &\qquad\qquad\quad \boldsymbol{g}(\boldsymbol{x}) \leq 0, \\ &\qquad\qquad\quad \boldsymbol{x} \in X \subseteq \mathbb{R}^n \end{aligned} \tag{6}$$

Hereby, $\boldsymbol{h(x)}$ is a vector containing all equality constraints $h(\boldsymbol{x})$ meanwhile $\boldsymbol{g(x)}$ is a vector containing the inequality constraints $g(\boldsymbol{x})$. Maximization formulations can be transformed into minimization formulations by multiplying the objective function by minus one. Therefore in the following only minimization formulations are contemplated. In the case of some of the design parameters being restricted to be integers the optimization problem is denominated a mixed-integer optimization problem. Algorithms to find solutions of optimization problems are called optimization algorithms [6, 7].

3 Dynamic Synthesis of a Watt-II-Mechanism

In this section the formulation of the synthesis of a Watt-II-Mechanism with a constant level of kinetic energy as a minimization problem is presented. First the optimization problem is defined. Afterwards the design parameters are elaborated. The objective function is defined. Finally the optimization constraints are set up. The presented procedure can also be applied to other 1-DOF-mechanisms.

3.1 Problem Description

The goal of the synthesis is to find a mechanism, which fulfills a desired motion when driven in its Eigenmotion. In many applications, only a part of the output motion is relevant. Figure 1 shows this task.

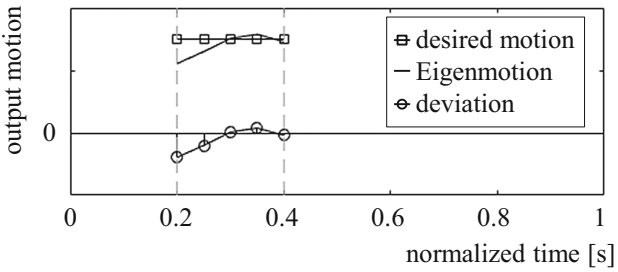

Fig. 1. Comparing the Eigenmotion and the desired motion of a mechanism

The Eigenmotion in the form of the output motion has to be compared to the desired output motion. The difference of both motions, that is the deviation of the Eigenmotion from the desired motion, has to be minimized. This minimization problem has to be described within the objective function.

Both motions are plotted over the normalized time, which means that their cycle time T is equal to one second. The cycle time can later be adjusted by increasing or decreasing the initial velocity $\dot{\varphi}_0$, see Eq. (5).

3.2 Design Parameters

The structure of the mechanism as well as the nomenclature is shown in Fig. 2.

The contemplated Watt-II-Mechanism is a plane, sequential arrangement of two fourbar mechanisms. The mechanism is composed of a crank-rocker-mechanism A_0-A-B-B_0 and a rocker-slider-mechanism B_0-C-D as shown in Fig. 2.

The dyad between the joints A and B_0 can be either closed in B or in B'. In order to distinguish between these two mounting positions a variable K is introduced. K is equal to +1 in case of the mounting position A-B-B_0 and equal to −1 in case of the mounting position A-B′-B_0 of the first fourbar mechanism.

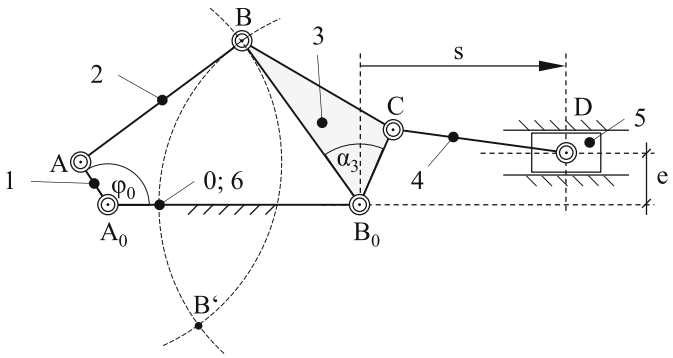

Fig. 2. The parameters of the Watt-II-Mechanism

The Eigenmotion of the mechanism depends on the kinematic parameters $\boldsymbol{p}_{\text{e,kin}}$ and on the mass parameters $\boldsymbol{p}_{\text{e,mass}}$.

$$\begin{aligned}\boldsymbol{p}_{\text{e,kin}} &= (l_0, l_1, l_2, l_{3B}, l_{3C}, l_4, e, \alpha_3, K, \varphi_0)\\ \boldsymbol{p}_{\text{e,mass}} &= (m_1, J_1, x_{\text{CG},1}, y_{\text{CG},1}, m_2, J_2, x_{\text{CG},2}, y_{\text{CG},2}, m_3, J_3, \ldots\\ &\quad x_{\text{CG},3}, y_{\text{CG},3}, m_4, J_4, x_{\text{CG},4}, y_{\text{CG},4}, m_5, J_5, x_{\text{CG},5}, y_{\text{CG},5})\end{aligned} \tag{7}$$

The index numbers of the parameters indicate the corresponding links according to Fig. 2. The length l_{3B} is the length between the joints B_0 and B, l_{3C} denotes the length between the joints B_0 and C. The coordinates of the centers of gravity of the links are indicated in local, body-fixed coordinate systems. Due to the fact, that the mechanism is a plane mechanism, only the J_{zz} components of the mass moment of inertia tensors of the moved links have to be considered. The component J_{zz} of the link k will be denoted by J_k. Furthermore, no z-components have to be taken into account in order to describe the position of the centers of gravity. The parameters J_5, $x_{\text{CG},5}$ and $y_{\text{CG},5}$ do not have to be considered in order to calculate the Eigenmotion, as the slider only performs a translational motion. Therefore 27 parameters have to be considered. In the following, assumptions are made in order to decrease the number of design parameters. Therefore the parameters m_1, J_1, $x_{\text{CG},1}$ and $y_{\text{CG},1}$ of the crank are substituted by J_{1v}, which is defined as follows:

$$J_{1v} = J_1 + m_1(x_{\text{CG},1}^2 + y_{\text{CG},1}^2) \tag{8}$$

In case of the rocker, the parameter J_{3v} is introduced.

$$J_{3v} = J_3 + m_3\left(x_{\text{CG},3}^2 + y_{\text{CG},3}^2\right) \tag{9}$$

The coupler (C) links are said to have a geometry according to Fig. 3. The thickness of the coupler link is denoted by t_C. The density is named ρ_C.

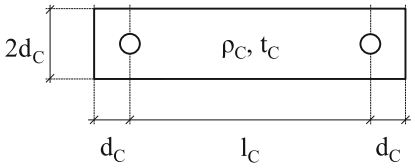

Fig. 3. Geometry of the coupler links

For this geometry the properties of the coupler links can be calculated as follows.

$$\begin{aligned} m_C &= \rho_C \cdot (l_C + 2d_C) \cdot 2d_C \cdot t_C \\ J_C &= \frac{m_C}{12}\left((l_C + 2d_C)^2 + (2d_C)^2\right) \\ x_{\mathrm{CG},C} &= \frac{l_C}{2}, y_{\mathrm{CG},C} = 0 \end{aligned} \tag{10}$$

Hereby the local coordinate system is placed in one joint and its x-axis points to the other joint. Introducing

$$P_C = \rho_C \cdot t_C \tag{11}$$

and setting the mass of the slider m_5 to a fixed value the number of design parameters can be decreased to 16:

$$\boldsymbol{p} = (l_0, l_1, l_2, l_{3B}, l_{3C}, l_4, e, \alpha_3, K, \varphi_0, J_{1v}, d_2, P_2, J_{3v}, d_4, P_4). \tag{12}$$

3.3 Objective Function

Within the objective function the Eigenmotion has to be compared to the desired motion. Therefore the Eigenmotion has to be calculated for a set of parameters according to Eq. (12). Equation (5) is therefore reformulated using the assumptions made in Sect. 3.2. Subsequently, the Eigenmotion $\dot{\varphi}_\mathrm{e}$ has to be integrated in order to achieve the trend of the input angle φ_e over the time. Inserting φ_e into the kinematic transfer function of the mechanism, the output stroke s_e can be calculated. The output stroke can then be compared to the desired output motion. Equation (13) shows the objective function as a sum of least squares for all relevant points i of the output function. The goal of the optimization is to minimize the value of F.

$$F = \sum_{i=1}^{N} (s_\mathrm{e} - s_\mathrm{desired})^2. \tag{13}$$

3.4 Constraints

The optimization problem is formulated as a constrained optimization problem. In order to achieve a workable mechanism, the chain A_0-A-B-B_0 according to Fig. 2 has

to fulfill the Grashof condition. The chain B_0-C-D has to be closable. Upper and lower limits (boundaries) of the design parameters, so-called box constraints, have to be set. Apart of these constraints, further constraints can be implemented.

4 Results of the Dynamic Synthesis

In this section the result of the dynamic synthesis of the Watt-II-Mechanism is presented. First, the aim of the synthesis is formulated. Afterwards the results of the synthesis are discussed.

4.1 Optimization Problem

The motion task is defined according to Fig. 1. The output motion should have a dwell between 0.2 s and 0.4 s of normalized time. During this dwell the output stroke should be approximately 0.80 m. The minimum stroke should be 0.45 m within a tolerance of 0.0005 m.

Table 1. Upper (ub) and lower boundaries (lb) of the design parameters

Parameter	lb	ub	Parameter	lb	ub
l_0	0.1 m	1.0 m	K	−1	1
l_1	0.1 m	1.0 m	φ_0	0	2π
l_2	0.1 m	1.0 m	J_{1v}	0	15 kg m^2
l_{3B}	0.1 m	1.0 m	d_2	0.03 m	0.04 m
l_{3C}	0.1 m	1.0 m	P_2	40.5 kg/m^2	236.1 kg/m^2
l_4	0.1 m	0.5 m	J_{3v}	0	15 kg m^2
e	−0.5 m	0.5 m	d_4	0.03 m	0.04 m
α_3	0	2π	P_4	40.5 kg/m^2	236.1 kg/m^2

In order to obtain a feasible mechanism, the range of the design parameters has to be limited. Table 1 gives an overview over the upper and lower boundary of the design parameters. K deserves special attention as it is defined as an integer parameter, which can only reach the values −1 or +1. The lower and upper boundaries for P_2 and P_4 are calculated as follows:

$$\begin{aligned} P_{2,\min} = P_{4,\min} &= \rho_{\min} \cdot t_{\min} = 2700 \frac{\text{kg}}{\text{m}^3} \cdot 0.015 \text{ m} \\ P_{2,\max} = P_{4,\max} &= \rho_{\max} \cdot t_{\max} = 7870 \frac{\text{kg}}{\text{m}^3} \cdot 0.030 \text{ m} \end{aligned} \tag{14}$$

The mass of the output link is preset. It is equal to 2 kg.

Additionally to the constraints listed in Sect. 3.4 further constraints are implemented. Minimum mass moments $J_{1v,\min}$ and $J_{3v,\min}$ and maximum mass moments

$J_{1v,\max}$ and $J_{3v,\max}$ are introduced. They are calculated according to Fig. 3 and the minimum and maximum values listed in the following table. In case of $J_{1v,\min}$ and $J_{1v,\max}$ the reduced mass moment of a servomotor is added (Table 2).

Table 2. Minimum and maximum dimensions of crank and rocker

Mass moment	d [m]	t [m]	ρ [kg/m^3]
$J_{1v,min}$	0.035	0.015	2700
$J_{1v,max}$	0.050	0.035	7870
$J_{3v,min}$	0.035	0.015	2700
$J_{3v,max}$	0.050	0.035	7870

The minimum value of the output stroke is set also defined as a constraint. As mentioned above it should be equal to 0.45 m within a tolerance of 0.0005 m.

4.2 Results

The result of the dynamic synthesis is shown in Fig. 4. A genetic algorithm (GA) was used to solve the optimization problem. Information on the GA can be found in [5]. The output values of the GA were used as initial values for local optimization using a barrier-method. Information on this method can be found in [6, 7]. Figure 4 shows that the mechanism performs an approximated dwell at the desired time. According to [1] the quality of the dwell can be assessed as follows:

$$p = \frac{s_D}{s_M} = \frac{8.044 \cdot 10^{-4}}{0.35} = 2.298 \cdot 10^{-3} \tag{15}$$

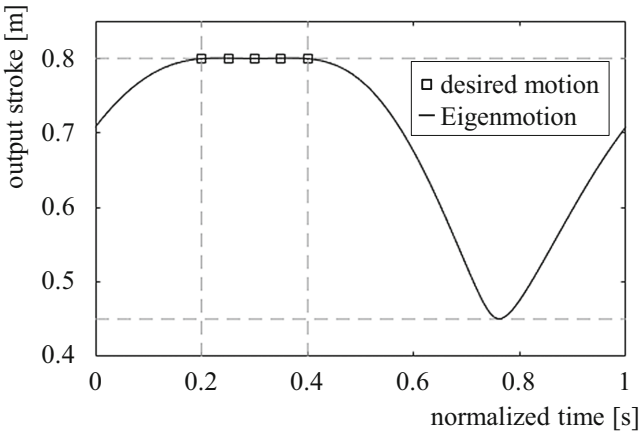

Fig. 4. The result of the dynamic synthesis

Table 3 lists the values of the optimal design parameters.

Table 3. Values of the design parameters for the result of the optimization

Parameters	Result	Parameters	Result
l_0	0.9439 m	K	1
l_1	0.4650 m	φ_0	2.1293
l_2	0.8973 m	J_{1v}	0.8905 kg m^2
l_{3B}	0.8448 m	d_2	0.0400 m
l_{3C}	0.3121 m	P_2	139.5169 kg/m^2
l_4	0.5000 m	J_{3v}	4.8572 kg m^2
e	0.1379 m	d_4	0.0300 m
α_3	2.4481	P_4	146.6220 kg/m^2

Taking into account Eq. (14) the properties of the coupler links can be derived from P_2 and P_4. Steel is chosen to be the material of the coupler links:

$$\begin{aligned} t_2 &= \frac{P_2}{7870\ \text{kg/m}^3} = 17.73 \cdot 10^{-3}\ \text{m} \\ t_4 &= \frac{P_4}{7870\ \text{kg/m}^3} = 18.63 \cdot 10^{-3}\ \text{m} \end{aligned} \tag{16}$$

The design parameters J_{1v} and J_{3v} can be used to derive feasible crank and rocker geometries. The constraints discussed in Sect. 4.1 assure that feasible links can be found that satisfy these design parameters.

5 Conclusion

A method to synthesize a mechanism in order to fulfill a desired motion with a constant level of kinetic energy was presented. This is desirable as a constant level of kinetic energy leads to a low input torque.

The synthesis of a Watt-II-Dwell-Mechanism was presented as an example for the application of the new method. The novelty of this method is, that the mechanism synthesis is conducted in such manner, that the resulting mechanism fulfills a desired motion when driven in its Eigenmotion. Therefore, kinematic parameters as well as mass properties of the mechanism have to be considered. To meet the goal of the synthesis, the mechanism synthesis approach was formulated as a minimization problem. The example was solved using a genetic algorithm.

It was shown that with this method the design of feasible, highly energy-efficient mechanisms is possible. The design of feasible, more complex link geometries in accordance with the outcome of the synthesis process can be the subject of further investigation.

References

1. Dittrich, G., Unger, W.: Rechnerunterstützte Synthese ebener Kurbelgetriebe zur Erzeugung vorgegebener Bewegungsabläufe in Verarbeitungsmaschinen. VS Verlag für Sozialwissenschaften, Wiesbaden (1978). ISBN 3531027506
2. Dresig, H., Holzweißig, F.: Dynamics of Machinery, Theory and Applications, Springer, Heidelberg (2010). ISBN 3540899391
3. Dresig, H., Vul'fson, I.I.: Dynamik der Mechanismen. Springer, New York, Wien (1989). ISBN 9783326003610
4. Kerle, H.; Corves, B.; Hüsing, M.: Getriebetechnik, Grundlagen, Entwicklung und Anwendung ungleichmäßig übersetzter Getriebe, 4th edn. Vieweg+Teubner, Wiesbaden (2011). ISBN 978-3-8348-0961-2
5. Mitchell, M.: An Introduction to Genetic Algorithms. MIT Press, Cambridge (2001). ISBN 0262631857
6. Nocedal, J., Wright, S.J.: Numerical Optimization, 2nd edn. Springer, New York (2006). ISBN 9780387987934
7. Papalambros, P.Y., Wilde, D.J.: Principles of Optimal Design, Modeling and Computation, 2nd edn. Cambridge University Press, Cambridge (2000). ISBN 051162641X
8. Soong, R.-C., Yan, H.-S.: Simultaneous minimization of shaking moment, driving torque, and bearing reactions of complete force balanced linkages. J. Chin. Soc. Mech. Eng. **28**(3), 243–254 (2007)
9. Thümmel, T.: Experimentelle Mechanismendynamik, Messung, Modellierung, Simulation, Verifikation, Interpretation und Beeinflussung typischer Schwingungsphänomene an einem Mechanismenprüfstand. VDI-Verl., Als Ms. gedr, Düsseldorf (2012). ISBN 3183345110
10. Uicker, J.J., Pennock, G.R., Shigley, J.E.: Theory of Machines and Mechanisms, 4th edn. Oxford University Press, New York (2011). ISBN 0195371232
11. VDI-Richtlinie 2149, Blatt 1: Getriebedynamik: Starrkörper Mechanismen, Standard, VDI, Beuth (2008)

Multibody Dynamic Analysis of a High-Altitude Long-Endurance Aircraft Concept

L.M. Nitardi[1(✉)], B.A. Roccia[1,2], S. Preidikman[2], and F.G. Flores[2]

[1] Grupo de Matemática Aplicada, Facultad de Ingeniería, Universidad Nacional de Río Cuarto, Río Cuarto, Argentina
[2] Instituto de Estudios Avanzados en Ingeniería y Tecnología (IDIT) UNC-CONICET, y Departamento de Estructuras, FCEFYN, Universidad Nacional de Córdoba, Córdoba, Argentina

Abstract. A new generation of unmanned-air-vehicles (UAVs) called extremely flexible (X) high-altitude long-endurance (HALE) aircrafts are being actively studied today. These special kind of UAVs are characterized by highly flexible structural members undergoing complex motions in space. In this paper, the authors present a numerical framework to study the dynamical behavior of a X-HALE-UAV concept. The aircraft is modeled as a set of rigid bodies linked each other through elastic joints. The motion equations for the entire UAV are derived by using an energetic approach based on Lagrange's equations for constrained systems, which are differential-algebraic of index-3 in nature. All governing equations are numerically integrated by means of different time-marching schemes such as: (*i*) direct-based methods (Newmark, Hughes-Hilber-Taylor and α-generalized); and (*ii*) index reduction-based techniques along with standard packages for ordinary differential equations (ODEs). The simulation tool developed is validated comparing results against well-documented problems. Finally, numerical simulations of a simplified concept of X-HALE-UAV is presented.

Keywords: X-HALE-UAV · Multibody dynamics · Numerical simulations

1 Introduction

During the 80's, it was understood that an airplane powered by the sun can, in principle, stay aloft for weeks or months at a time. Under these assumptions, AeroVironment developed and designed the first solar rechargeable aircraft HALSOL (high-altitude solar vehicle) [1]. Ten years later, under the sponsorship of the Ballistic Missile Defense Organization, this aircraft was redesigned giving rise to a metamorphosed vehicle renamed Pathfinder. In order to guarantee the continuous development of these aeronautical systems, NASA founded the ERAST (*Environment Research Aircraft and Sensor*) program, frame in which the vehicles Pathfinder and Centurion evolved in the Helios prototype HP03 (long-endurance configuration) [2]. In the course of ERAST project, significant advances were made related to HALE-UAVs. At the beginning, the aeroelastic behavior of these aeronautical platforms were studied

J.C.M. Carvalho et al. (eds.), *Multibody Mechatronic Systems*,
Mechanisms and Machine Science 54, DOI 10.1007/978-3-319-67567-1_21

by using linear assumptions, commonly used for the design of conventional aircrafts. Unfortunately, the overconfidence in results predicted by these analyses tools led to the catastrophic accident involving the NASA's Helios aircraft. In the light of this event, the recommendation from NASA was: "*[that] more advanced, multidisciplinary (structures, aeroelastic, aerodynamics, atmospheric, materials, propulsion, controls, etc.) time-domain analysis methods appropriate to highly flexible, morphing vehicles [be developed]*" [3].

Despite a long history of studies related to dynamics of flexible aircrafts, most of them consider linear models, or at most, nonlinear rigid models for the vehicle coupled with linear structural models [4, 5]. In order to tackle this problem, at the University of Michigan, a research team develop the code UM/NAST (*the University of Michigan's nonlinear aeroelastic simulation toolbox*). This analysis tool allowed to obtain some important insights into the aeroelastic behavior of HALE-based aircrafts, such as: aeroelastic modeling [6], flutter boundaries [7], wind gust responses [8], and global optimization studies [9], among others. Since 2000 up today, a number of numerical simulation codes intended for analyzing/designing very flexible aircrafts have been developed: the code ASWING developed by Drela at the Massachusetts Institute of Technology [10], the simulation framework called NATASHA (*Nonlinear Aeroelastic Trim and Stability of HALE Aircraft*) [11], and the code NANSI (*Nonlinear-Aerodynamic/Nonlinear-Structure Interaction*) developed at the Virginia Polytechnic Institute [12].

Regarding the different approaches followed to model the dynamics of HALE-UAVs, a review of the state of the art can be found in references [13, 14]. Recently, Argüello et al. [15] developed a dynamic model for a HALE aircraft concept by using a hybrid formulation founded on Newton/Euler's equations combined with Lagrange's equations.

Despite the contributions made by all these works, there are still major questions related to the aeroelastic behavior of HALE aircrafts, mostly due to the strong coupling and feedback effects between these highly flexible structures and the surrounding fluid.

Under the fore-mentioned initiatives, in this paper the authors present an enlarged numerical tool based on the multibody dynamic description for HALE-UAVs [16], previously developed by the authors of this work. Here, the computational simulation environment is enhanced by adding a new set of numerical integrators, commonly used in multibody dynamics, such as the Hughes-Hilber-Taylor (HHT) algorithm and the α-generalized. The aircraft is modeled as a collection of rigid bodies elastically connected to one another and supported by a flexible platform that simulates the wind tunnel base. In this first stage, the non-conservative loads coming from the aerodynamic are not taking into account. The motion equations for the multibody system were obtained through an energetic approach based on Lagrange's equations for constrained systems and then implemented in an interactive numerical simulation framework built in MATLAB®.

Finally, the simulation tool is validated by comparing numerical results with well-documented problems and against solutions obtained by software broadly used in the field of computational mechanics, such as SIMPACT.

2 Model for Vehicle Dynamics

The aircraft is modeled as a collection of rigid bodies (fuselage, wings, engines and landing gear) linked each other rigidly or by elastic joints. The fuselage (generally represented by a cube) is connected to the wind tunnel by means of 12 linear springs and 12 dampers (see Fig. 1a). The configuration space of the entire multibody system is described by a set of redundant coordinates, which are not independent, these are linked through constraint equations. The constraints are directly introduced in the equations of motion by means of Lagrange's multipliers [16].

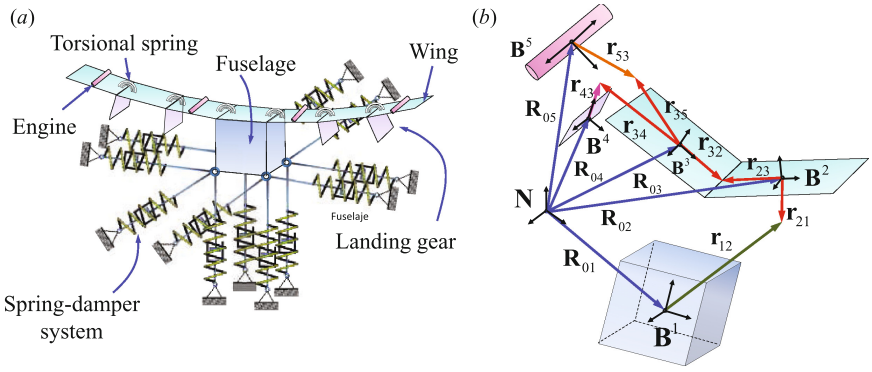

Fig. 1. Model representation, (*a*) Conceptual design of a X-HALE-UAV, (*b*) definition of reference frames

In this work, the authors use $N_E + N_W + N_L + N_F + 1$ reference systems, where: N_E, N_W, N_L and N_F are the number of engines, wings, landing gears and fuselages, respectively. The remaining one is to account for the inertial frame of reference (see Fig. 1b).

The nomenclature adopted for the reference frames are: (*i*) $\mathbf{N} = \left\{\hat{\mathbf{n}}_1, \hat{\mathbf{n}}_2, \hat{\mathbf{n}}_3\right\}$ for the Newton's inertial reference frame; and (*ii*) $\mathbf{B}^i = \left\{\hat{\mathbf{b}}_1^i, \hat{\mathbf{b}}_2^i, \hat{\mathbf{b}}_3^i\right\}$, $i = 1, \ldots, n_b$ (where $n_b = N_E + N_W + N_L + N_F + 1$) for the body-fixed frame attached at the mass center of the ith body.

The location of each body in space is identified by using a set of seven absolute coordinates. Three of them are used to define the position of the mass center of the body, and the remaining four are used to specify its orientation (unitary quaternions). It makes a total of $n_{coord} = 7n_b$ coordinates for the entire multibody system. These coordinates are not independent, but are related through n_c constraint equations, resulting at last in a dynamical system with $n_{\mathrm{DOF}} = 7n_b - n_{coord}$ degrees of freedom.

It is noteworthy that a rotation parameterization by means of unitary quaternions introduces an additional constraint equation per each body [17]. The set of absolute coordinates for each body is given by,

$$\mathbf{q}_i = \{q_{i1}, q_{i2}, q_{i3}, q_{i4}, q_{i5}, q_{i6}, q_{i7}\}^T \; i = 1, \ldots, n_b \tag{1}$$

and the set of coordinates for the entire multibody system is expressed as,

$$\mathbf{q} = \left\{\mathbf{q}_1^T, \mathbf{q}_2^T, \mathbf{q}_3^T, \ldots, \mathbf{q}_{n_b}^T\right\}^T. \tag{2}$$

2.1 Constraint Equations

For each body, there are three different constraint equations: (*i*) position constraints, for specifying the connection point between the components of the multibody system; (*ii*) orientation constraints, for specifying the relative orientation between two or more components of the multibody system, and (*iii*) unitary quaternion constraints, due to the additional requirement arising from a parameterization based on unitary quaternions. All constraint equations are written with respect to the inertial frame of reference, **N**. Equation (3) presents the constraint equations for the *i*th body. Such equations for the rest of the bodies are obtained with the same procedure. These are:

$$\begin{aligned}
{}^{Pos}\varphi_{ij}^{r} &= \left(\left[\mathbf{R}_{0i} + \mathbf{A}_i\mathbf{r}_{ij}\right] - \left[\mathbf{R}_{0j} + \mathbf{A}_j\mathbf{r}_{ji}\right]\right) \cdot \hat{\mathbf{n}}_r = 0, \;\; \text{for} \;\; r = 1, 2, 3, \\
{}^{Ort}\varphi_{ij}^{1} &= \left(\hat{\mathbf{b}}_1^j\right)^T \left[\mathbf{A}_j^T\mathbf{A}_i\right] \hat{\mathbf{b}}_2^i = 0, \\
{}^{Ort}\varphi_{ij}^{2} &= \left(\hat{\mathbf{b}}_2^j\right)^T \left[\mathbf{A}_j^T\mathbf{A}_i\right] \hat{\mathbf{b}}_3^i = 0, \\
{}^{Ort}\varphi_{ij}^{3} &= \left(\hat{\mathbf{b}}_3^j\right)^T \left[\mathbf{A}_j^T\mathbf{A}_i\right] \hat{\mathbf{b}}_1^i = 0, \;\; \text{and} \\
{}^{U-Q}\varphi_i &= \sum_{k=4}^{7} q_{ik}^2 - 1 = 0,
\end{aligned} \tag{3}$$

where the superscripts *Pos*, *Ort* and *U-Q* indicate the character of the constraint, *i.e.*, position, orientation and unitary quaternion, respectively. $\mathbf{R}_{0i}$ ($\mathbf{R}_{0j}$) is position vector of the mass center of the *i*th (*j*th) body relative to the origin of the inertial frame, $\mathbf{r}_{ij}$ ($\mathbf{r}_{ji}$) is the position vector of connection point between the body *i*(*j*) and the body *j*(*i*) relative to the origin of the frame $\mathbf{B}^i$ ($\mathbf{B}^j$), $\mathbf{A}_i$ ($\mathbf{A}_j$) is the matrix rotation (in terms of Euler parameters) which orientates frame $\mathbf{B}^i$ ($\mathbf{B}^j$) with respect to **N**.

The set of Eq. (3) stablish that the frames $\mathbf{B}^i$ and $\mathbf{B}^j$ are coincident for all time. However, the dynamic system studied in this work contains *hinge joints*. Equation (3) can be slightly modified in order to represent these type of joints, which permit a relative rotation around one defined axis [18]. Finally, the global constraint vector for the multibody system can be expressed as follows,

$$\mathbf{\Phi}(\mathbf{q}) = \left\{ \ldots, {}^{Con}\varphi_{ij}^{r}, \ldots, {}^{Ort}\varphi_{ij}^{1}, {}^{Ort}\varphi_{ij}^{2}, {}^{Ort}\varphi_{ij}^{3}, \ldots, {}^{U-Q}\varphi_{1}, \ldots, {}^{U-Q}\varphi_{n_b} \right\}. \tag{4}$$

2.2 Generalized Loads

The generalized loads associated with the set of absolute coordinates are determined by using the principle of virtual work. The virtual work of an external force, $\mathbf{F}_{pj}$, applied to a point P belonging to the jth body can be expressed as,

$$\overline{\delta W_{pj}} = \mathbf{F}_{pj} \cdot \delta \mathbf{R}_{pj} = \mathbf{F}_{pj} \cdot \left[\delta \mathbf{R}_{0j} + \frac{\partial}{\partial \bar{\mathbf{q}}_j} \left(\mathbf{A}_j \mathbf{r}_{pj} \right) \, \delta \bar{\mathbf{q}}_j \right]. \tag{5}$$

Here $\delta \mathbf{R}_{pj}$ is a virtual displacement of the point P belonging to the jth body, $\mathbf{r}_{pj}$ is the position vector of the point P relative to the origin of the frame $\mathbf{B}^j$, and $\bar{\mathbf{q}}_j$ is the set of Euler parameters associated to the jth body. Following the procedure exposed by Nikravesh [16], and after some algebraic manipulations, the generalized loads of the kth spring-damper system connected to the vertex u of the fuselage and associated to the set of coordinates $\mathbf{q}_1$ are,

$$\mathbf{Q}_{1k}^{S} + \mathbf{Q}_{1k}^{D} = \left[\left(\mathbf{F}_{uk}^{S} + \mathbf{F}_{uk}^{D} \right)^T \quad 2\mathbf{m}_{uk}^T \mathbf{G}_1 \right], \tag{6}$$

where $\mathbf{F}_{uk}^{S}$ ($\mathbf{F}_{uk}^{D}$) is the force exerted by the kth spring (damper) on the vertex u, $\mathbf{m}_{uk}^T = \left[\tilde{\mathbf{r}}_{u1} \left(\mathbf{F}_{uk}^{R} + \mathbf{F}_{uk}^{A} \right) \right]^T$, $\tilde{\mathbf{r}}_{u1}$ is a skew-symmetric matrix whose axial vector is $\mathbf{r}_{uj}$ ($u = p$) defined above, and $\mathbf{G}_1$ is a matrix containing the Euler parameters that orientate the fuselage with respect $\mathbf{N}$, given by,

$$\mathbf{G}_j = \begin{bmatrix} -q_{j5} & q_{j4} & -q_{j7} & q_{j6} \\ -q_{j6} & q_{j7} & q_{j4} & -q_{j5} \\ -q_{j7} & -q_{j5} & q_{j5} & q_{j4} \end{bmatrix}, j = 1 \text{ for the fuselage.} \tag{7}$$

On the other hand, the torsional springs are exclusively located on the hinge joints (wing-wing connection), where a pure moment $\mathbf{T}_j$ is generated. The generalized loads due to $\mathbf{T}_j$ and associated to the set of coordinates $\mathbf{q}_j$ (which describe the space configuration of the jth wing) are written as follow,

$$\mathbf{Q}_j^{Tor} = \left[\mathbf{0}_{1\times 3} \quad 2\mathbf{T}_j^T \mathbf{G}_j \right]. \tag{8}$$

Finally, the generalized loads due to the action of the gravitational field associated to the set of coordinates of each body j of the multibody system is computed as,

$$\mathbf{Q}_j^{g} = \left[\left(\mathbf{F}_j^{g} \right)^T \quad \mathbf{0}_{1\times 3} \right], \tag{9}$$

where $\mathbf{F}_j^g = -m_j g\,\hat{\mathbf{n}}_3$, m_j is the mass of the jth body, and g is the gravity acceleration constant.

2.3 Equations of Motion

Following the procedure described by Shabana [19], the general form of the dynamic equations for the jth body are given by,

$$\mathbf{M}_j\ddot{\mathbf{q}}_j + \mathbf{B}_{\mathbf{q}_j}^T\boldsymbol{\lambda}_j = \mathbf{Q}_j^v + \left(\mathbf{Q}_j^{nc}\right)^T + \left(\mathbf{Q}_j^c\right)^T. \tag{10}$$

Here, $\mathbf{M}_j$ is the mass matrix, which is differentiable, symmetric and at least positive-semi-definite; $\mathbf{B}_{\mathbf{q}_j}$ is the Jacobian matrix of constraints associated with the coordinates $\mathbf{q}_j$; $\mathbf{Q}_j^v$ is a quadratic velocity vector that arises from differentiating the kinetic energy with respect to time and with respect to the generalized coordinates of the jth body; $\boldsymbol{\lambda}_j$ s the vector of Lagrange multipliers for the jth body; $\mathbf{Q}_j^{nc}$ represent the set of non-conservative loads (here coming from dampers); and $\mathbf{Q}_j^c$ represent the set of conservative loads (due to springs and gravitation).

Finally, the equations of motion for the complete multibody system are obtained by assembling the equations of motion for each body complemented with constraint equations, as

$$\begin{aligned} &\mathbf{M}\ddot{\mathbf{q}} + \mathbf{B}_{\mathbf{q}}^T\boldsymbol{\lambda} = \mathbf{Q}^v + (\mathbf{Q}^{nc})^T + (\mathbf{Q}^c)^T, \\ &\boldsymbol{\Phi}(\mathbf{q}) = \mathbf{0}. \end{aligned} \tag{11}$$

The term $\mathbf{B}_{\mathbf{q}}^T\boldsymbol{\lambda}$ represents the generalized constraint forces. The meaning of each multiplier depends on the specific manner in which the constraint was written [20].

3 Numerical Results

The equations of motions expressed in (11) are numerically integrated in time-domain by using two strategies: *(i)* an index reduction of the index 3 DAEs; and (*ii*) the direct integration of the index 3 DAEs. The former consists in differentiate the constraint equations twice with respect to time, often called constraint acceleration level. This new system of index 1 DAEs can be integrated by standard packages for ordinary differential equations (ODEs). However, as consequence of the reduction index, the constraint position level $\boldsymbol{\Phi}(\mathbf{q}) = \mathbf{0}$ and constraint velocity level $\dot{\Phi}(\mathbf{q}, \dot{\mathbf{q}}) = \mathbf{0}$, are no longer satisfied, i.e., there is a drift of the constraints. In order to control/eliminate this numerical drift, the simulation framework implements two stabilization schemes: (*i*) Baumgarte's technique [20]; and (*ii*) the coordinate projection method [21, 22].

The last strategy utilize implicit formulas to directly integrate the system (11) such as: Newmark, Hughes-Hilber-Taylor (HHT), and α-generalized. This election allows one to use the iterative character of the implicit schemes to solve the constraint

equations with a user-defined precision. A detailed explanation to numerically implementing these schemes can be found in [18].

In Subsect. 3.1 the current numerical tool is validated by comparing results against the responses published in reference [15] and those obtained by the finite element code SIMPACT [23]. Finally, in Subsect. 3.2 the authors present numerical simulations of a conceptual design of an X-HALE-UAV aircraft.

3.1 Validations

The setup of the numerical experiment consist only of the fuselage (cube) mounted on the 12 springs without consider the dampers. The lack of dampers results in a dynamic system very sensitive to the system parameters, external disturbances and the numerical integrators used to obtain the system response. On this basis, it was decided to include the validation considering only the springs. The data problem are: spring stiffness $k = 1.0$ N/m, spring natural length $l_0 = 10.0$ m, fuselage mass $m = 1.0$ kg, and gravity acceleration $g = 9.81$ m/s^2. The initial conditions are all zero, except for an initial rotation of 10º about the axis $\hat{\mathbf{n}}_2$ (see Fig. 2a). The integrators used are central difference, the four-order method of Hamming, and α-generalized ($\alpha_f = 0.5$ and $\alpha_m = 0.4988$). The time step used for all integrators is $\Delta t = 0.001$ s.

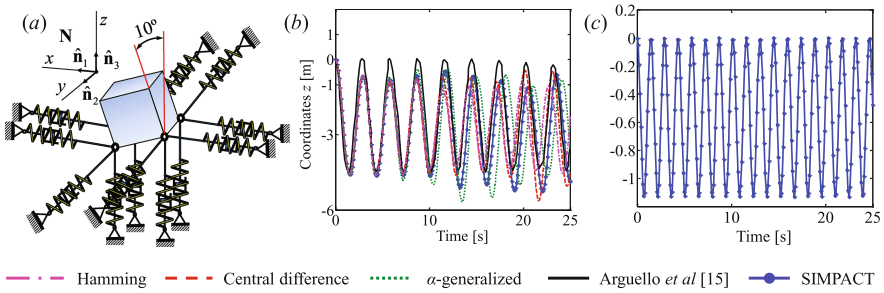

Fig. 2. (*a*) Initial configuration, (*b*) coordinate z of the mass center of the cube ($l_0 = 10.0$ m, $k = 1.0$ N/m), (c) coordinate z of the mass center of the cube ($l_0 = 2.5$ m, $k = 4.0$ N/m)

Figure 2b shows the coordinate z of the mass center of the fuselage versus time. As it can be appreciated, the response obtained with the current numerical tool differs from $t = 4$ s of those obtained by Argüello et al. [15] and SIMPACT. This fact is initially attributed to the features of a highly flexible dynamic system resulting from to choose a large natural length and low stiffness for the springs. As consequence, any perturbation on the system (coming from numerical issues for instance) affects the precision of the integrators, which in turn are very different in nature (explicit, implicit, second-order, four-order, etc.).

On the contrary, if the natural length is shortened, $l_0/4 = 2.5$ m, and the spring stiffness is increased, $k = 4.0$ N/m, the resulting dynamic system is less flexible. Figure 2c shows the time evolution of the coordinate z of the fuselage. Now, the response obtained by the three integrators matches the one simulated by SIMPACT.

3.2 Dynamics of a X-HALE-UAV Concept

In this subsection, the dynamic behavior of an X-HALE-UAV concept is presented. It consists of five wings, two landing gear, two engines, and one fuselage. The parameters of the system are: wing mass $m_W = 1.0$ kg, landing gear mass $m_L = 1.0$ kg, mass of engines $m_E = 0.1$ kg, fuselage mass $m_F = 0.1$ kg, length side of the cube that simulates the Fuselage $L_F = 1.0$ m, square wings of side $L_W = 1.0$ m, rectangular plates simulating the landing gears of side $L_L = 1.0$ m and $h_L = 0.5$ m, length of the engines $L_E = 1.0$ m and diameter $d_M = 0.1$ m, spring stiffness $k = 50$ N/m, spring natural length $l_0 = 2.5$ m, torsional stiffness $k_T = 50$ N/rad, and damper constants $c = 0.1$ Ns/m. The UAV has a symmetrical configuration and, in the initial configuration, the outer wings have a relative angle to each other of 10° (see Fig. 3a). The gravity acceleration constant is $g = 9.81$ m/s^2.

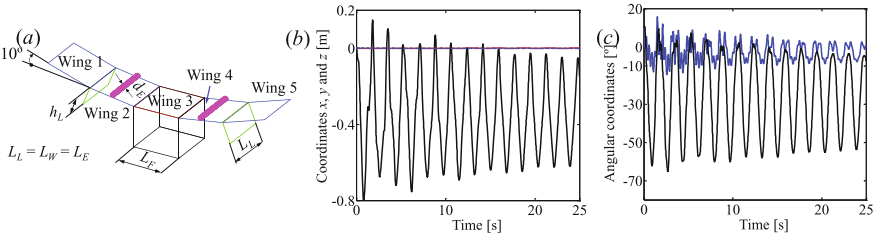

Fig. 3. (*a*) X-HALE-UAV configuration, (*b*) coordinate of the fuselage mass center (black for $z(t)$, red for $x(t)$, blue for $y(t)$), (*c*) relative angular coordinates (blue for wing 1–2 joint, black for wing 2–3 joint) (Color figure online)

The aeronautical system is released from rest (where the springs are undeformed). Finally, the integration schemes used are: (*i*) the four-order method of Hamming along with a stabilization procedure based on coordinate projection (*S-Both*^{2}) [21]; (*ii*) Central difference, stabilized with *S-Both*^{2} (DC + *S-Both*^{2}); and (*iii*) generalized Alpha ($\alpha_f = 0.473$ and $\alpha_m = 0.421$). The adopted time step is $\Delta t = 0.001$ s.

Figure 3b shows the time evolution of the coordinates of the mass center of the aircraft's fuselage while Fig. 3c shows the angular coordinates describing the orientation of a wing relative to the contiguous one versus time (only for the set of wings located at the right).

It should be noted that all the integration produced exactly the same response for the dynamical system studied. As can be seen in Fig. 3b, the x and y coordinates of the mass center of the fuselage are practically zero (red curve), while the z coordinate exhibit an oscillatory behavior. One component of this oscillation arises from release the system from a position that does not match the static equilibrium position. The other component is associated with the oscillatory movement of the wing sections. As time passes, it can be seen that the first component disappears as a result of the dissipation introduced by the dampers. With respect to the angular coordinates, the wing connection near the fuselage (wing 2–3 joint) shows a greater oscillation amplitude when compared with those connections located at the ends (wing 1–2 joint).

4 Conclusions

In this work, a general rigid multibody model for studying the dynamics of a X-HALE aircraft has been presented. Such model was successfully implemented in a simulation tool entirely elaborated in MATLAB®, which allows to integrate all the governing equations in the time domain through different integration schemes.

The numerical tool was validated by comparing current results with data published in the literature and against solutions obtained by programs broadly used in computational mechanics.

From the results presented in the preceding sections it can be concluded that the simulation framework is well-suited to carry out numerical studies of HALE-based aircrafts characterized by large wing deflections. Although good results have been obtained, the implemented time-marching algorithms shows some numerical stability problems when the linear springs become less rigid or for configurations involving initial rotations of the fuselage. As future work, the model here presented will be enhanced by means of: (*i*) the incorporation of a flexible model for the wing sections; and (*ii*) the combination of the structural model with the non-linear and non-stationary vortex network method (UVLM) in order to study the aeroelastic behavior of these highly flexible structures.

References

1. Colella, N.J., Wenneker, G.S.: Pathfinder and the Development of Solar Rechargeable Aircraft. E&TR, pp. 1–9 (1994)
2. Gibbs, Y.: NASA Armstrong Fact Sheet: Solar-Power Research, (2015). http://www.nasa.gov
3. Noll, T.E., Brown, J.M., Perez-Davis, M.E., Ishmael, S.D., Tiffany, G.C., Gaier, M.: Investigation of the Helios Prototype Aircraft Mishap. Mishap Report, vol. I. NASA (2004). http://www.nasa.gov/pdf/64317main/helios.pdf
4. Schimdt, D.K., Raney, D.L.: Modeling and simulation of flexible flight vehicles. J. Guid. Control Dyn. **24**(3), 539–546 (2001)
5. Reschke, C.: Flight loads analysis with inertially coupled equations of motion. In: AIAA Atmospheric Flight Mechanics Conference and Exhibit, AIAA Paper 2005–6026, pp. 1–21. San Francisco, 15–18 August 2005

6. Shearer, C.M., Cesnik, C.E.S.: Nonlinear flight dynamics of very flexible aircraft. J. Aircraft **44**(5), 1528–1545 (2007)
7. Cesnik, C.E.S., Ortega-Morales, M.: Active aeroelastic tailoring of slender flexible wings. In: Proceedings of the International Forum on Aeroelasticity and Structural Dynamics, Madrid, Spain (2001)
8. Su, W., Cesnik, C.E.S.: Dynamic response of highly flexible flying wings. AIAA J. **49**(2), 324–339 (2011)
9. Cesnik, C.E.S., Brown, E.L.: Active warping control of a joined wing airplane configuration. In: Proceedings of the 44th AIAA/ASME/ASCE/AHS/ASC Structures, Structural Dynamics, and Material Conference, AIAA Paper 2003–1715, Hampton, Virginia, 7–10 April 2003
10. Drela, M.: Integrated simulation model for preliminary aerodynamic, structural, and control-law design of aircraft. In: Proceedings of the 40th AIAA/ASME/ASCE/AHS/ASC Structures, Structural Dynamics, and Materials Conference and Exhibit, AIAA Paper 1999–1394, pp. 1644–1656. St. Louis, Missouri, 12–15 April 1999
11. Patil, M.J., Hodges, D.H.: Flight dynamics of highly flexible flying wings. J. Aircr. **43**(6), 1790–1798 (2006)
12. Wang, Z., Chen, P.C., Liu, D.D., Mook, D.T.: Nonlinear-aerodynamics/nonlinear-structure interaction methodology for a high-altitude long-endurance wing. J. Aircr. **47**(2), 556–566 (2010)
13. Cesnik, C.E.S., Su, W.: Nonlinear aeroelastic modeling and analysis of fully flexible aircraft. In: Proceedings of the 46th AIAA/ASME/ASCE/AHS/ASC Structures, Structural Dynamics and Materials Conference, AIAA Paper 2005–2169, Austin, TX, 18–21 April 2005
14. Wang, R., Zhou, X., Zhou, Z.: Longitudinal flight dynamics and control of highly flexible solar UAV, pp. 1–4. IEEE (ICIECS) (2010)
15. Arguello, M., Preidikman, S., Roccia, B.A.: Desarrollo de simulaciones numéricas para estudiar la dinámica de un concepto de aeronave X-HALE-UAV. Revista Facultad de Ciencias Exactas y Naturales **2**(2), 16–24 (2014)
16. Nitardi, L.M., Roccia, B.A., Preidikman, S., Flores F.G.: Estudio de la dinámica de un concepto de aeronave X-HALE-UAV: un enfoque multicuerpo. Mecánica Computacional ENIEF 2016, vol. XXXIV, pp. 2781–2807 (2016)
17. Nikravesh, P.E.: Computer-Aided Analysis of Mechanical Systems. Prentice Hall, Upper Saddle River (1988)
18. Shuster, M.D.: A survey of attitude representations. J. Astronaut. Sci. **41**(4), 439–517 (1993)
19. Géradin, M., Cardona, A.: Flexible mulibody dynamics: a finite element approach. Wiley, New York (2001)
20. Shabana, A.A.: Dynamics of multibody systems, 3rd edn. Cambridge University Press, Cambridge (2010)
21. Bauchau, O.A.: Flexible multibody dynamics. Springer, New York (2011)
22. Ascher, U.M., Chin, H., Petzold, L.R., Reich, S.: Stabilization of constrained mechanical systems with DAEs and invariant manifolds. J. Mech, Struct. Mach. **23**, 135–158 (1995)
23. Roccia, B.A., Preidikman, S., Gebhardt, C.G., Massa, J.C.: Dynamics of micro-air-vehicles with flapping wings: a multibody system approach. IEEE Lat. Am. Trans. **11**(1), 189–195 (2013)

Control of Mechatronic Systems

High-Order Sliding Mode Control for Solar Tracker Manipulator

I. Gutierrez[1(✉)], E. Hernandez-Martinez[2], A. Oropeza[2], and Sajjad Keshtkar[1]

[1] Automatic Control Department, Cinvestav, Mexico
igutierrez@ctrl.cinvestav.mx, diesel253m@gmail.com
[2] Instituto Politécnico Nacional, ESIME Ticoman, Mexico City, Mexico
{euhernandezm,aoropeza}@ipn.mx

Abstract. In this paper, a continuous sliding mode algorithm for a system with relative degree three is presented. The studied mechanism is a class of nonlinear system with electro-mechanical actuators which includes both matched and unmatched bounded perturbations /uncertainties. The proposed homogeneous continuous control algorithm produces a continuous control signal ensuring finite time convergence of the states to the desired trajectory. Moreover, the control signal compensates the bounded perturbation in finite time, i.e. its value converges to the opposite value of the perturbation. The quality of the presented controller is proved via numerical simulations.

Keywords: Continuous sliding mode control · Non-linear system · 2 DoF platform · Robust control

1 Introduction

In physical systems there exists always a discrepancy between the actual plant and its mathematical model used for the controller design [1]. These discrepancies can be raised considerably with the unknown external disturbances, plant parameters and unmodeled dynamics. Sliding mode control (SMC) is considered as one of the most efficient methods for the control and observation under these uncertainty conditions [2–4]. The algorithms based on sliding mode can keep the desired (sliding) variable at zero after a finite time, while compensating theoretically exactly matched bounded uncertainties/perturbations. The main disadvantage of these types of controllers is the presence of the discontinuous term in the control law which causes the high-activity (chattering) in the actuator and consequently its damage.

The amplitude of the chattering can be reduced by the adjustment of the sliding mode controller gain. On the other hand, an overestimation of the controller gains is usually taken since the bounds of the perturbation is unknown and, consequently, leads to a high amplitude of the chattering effect. Some authors present an adaptive version of sliding mode gains which guarantees the minimum values of the chattering effect. For example, in [5, 6] the authors adapt the gains, according to the value of the estimated perturbation. The adaptive gain follows the *equivalent control*, which is obtained by filtering out the control signal with a low-pass filter. In these works,

J.C.M. Carvalho et al. (eds.), *Multibody Mechatronic Systems*,
Mechanisms and Machine Science 54, DOI 10.1007/978-3-319-67567-1_22

the controller gain obtained online provides a less-risky condition for the actuators but the discontinuity still remains. The main disadvantage of this method is that the boundaries of the derivative of the perturbation must be exactly known.

Another approach is to increase the sliding mode controller gain until the sliding mode is detected and reduce the gain until the sliding mode is lost and then increase the gain again until the sliding mode is attained. These controllers called twisting or super-twisting controllers are proposed, for example, in [7] and in [8]. In these approaches, the adaptive gain can increase or decrease, but only convergence to a neighborhood of the origin can be guaranteed.

Recently, a new class of homogeneous continuous SMC of the systems with relative degree two based on a generalization of the high-order algorithms were announced [9]. In this paper, we propose a continuous algorithm, for a system with relative degree three. The goal of this paper is to present a homogeneous control for uncertain second-order plants, having the following advantages:

- Compensate bounded uncertainties/perturbations
- Guarantee a continuous control signal
- Finite-time convergence

As a physical plant, we use a two degree of freedom platform with two electric actuators. The electromagnetic torque generated at the direct-current electrical motor is transmitted to the ball-screw mechanism causing the change of the lengths of the actuator. The changes in the actuator lead to the movement of the moving platform. This platform can be used as a solar tracker or as an antenna positioner. The paper is organized as follows: In Sect. 2, the mathematical model of the system and the problem is stated. In Sect. 3 the controller design is presented. In Sect. 4, the designed controller is proposed for a mechanical system and the simulation is given. The conclusions are denoted in Sect. 5.

2 Model Description and Mathematical Model

The 2 degree of freedom platform represented in the Fig. 1 consists of two actuated rods (linear actuators) and one passive rod attached to a triangular base with spherical joints. Each linear actuator is made of upper and lower rods, connected to each other by a translational kinematic pair (screw mechanism). The movable platform is attached to the other side's upper legs via Hook's joint. An anti-plunging strut, connected rigidly to the base and from the other end of Hooke's joint to the moving platform, inhibits the translational movements and one rotation, giving the system the desired DOF. Additionally, this strut can serve as weight compensator. The orientation of the moving platform is regulated by changing the lengths of two active rods. This causes a corresponding change in the angle of the inclination of the panel with respect to the ground.

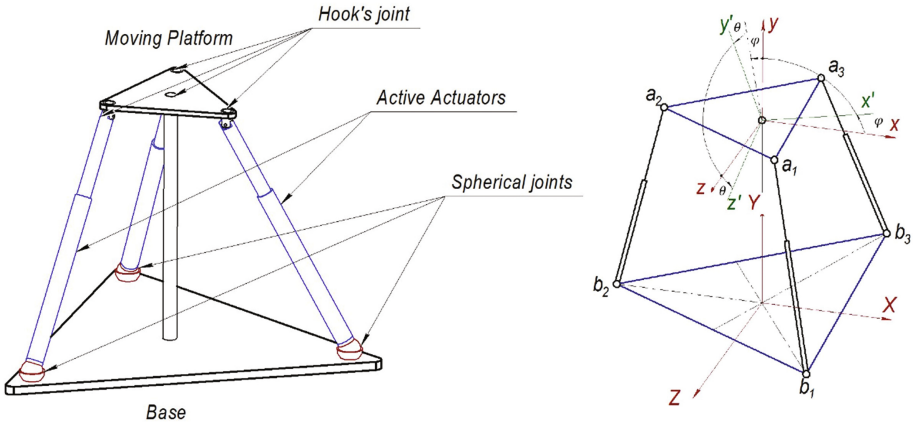

Fig. 1. Platform with two degrees of freedom.

The mathematical model of the system [10] can be described by the generalized coordinate vector $q = [\varphi \quad \theta]^T$, where φ and θ represent two angular rotations of the platform. Considering the world coordinate system W, and a frame coordinate system P, the vector line $L_i = a_i - b_i$, where $a_i = {}^{W}R_P \, {}^{P}a_i$ is the coordinate of the joints of the moving platform and b_i The coordinates of the link in the Ground. The rotation matrix ${}^{W}R_P$ Is given by

$$ {}^{W}R_P = \begin{bmatrix} \cos\varphi & -\cos\theta\sin\varphi & \sin\theta\sin\varphi \\ \sin\varphi & \cos\theta\cos\varphi & -\cos\theta\cos\varphi \\ 0 & \sin\theta & \cos\theta \end{bmatrix} $$

The length l_i of link i will be simply computed from $l_i = \sqrt{L_i \cdot L_i}$ and the unit vector along the axis of the prismatic joint of link i : $n_i = \frac{L_i}{l_i}$. The angular velocity of the system in the inertial frame is given by

$$ \omega = \begin{bmatrix} \dot{\theta} \\ \dot{\varphi}\sin\theta \\ \dot{\varphi}\cos\theta \end{bmatrix} $$

and the Jacobian expression is written as

$$ \mathbf{J}^{-1} = \begin{bmatrix} ({}^{W}R_P \, {}^{P}\mathbf{a}_1 \times \mathbf{n}_1)^T \\ ({}^{W}R_P \, {}^{P}\mathbf{a}_2 \times \mathbf{n}_2)^T \end{bmatrix} \begin{bmatrix} 0 & \cos\varphi \\ 0 & \sin\varphi \\ 1 & 0 \end{bmatrix} \tag{1} $$

*Note that, $\mathbf{J}^{-1}$ is non-singular if the link rods are not parallel to each other, nor align with the platform.

2.1 Kinetic Energy and Dynamic Equations

If we denote the angular velocity by ${}^{P}\omega$, and the inertia matrix of the platform with respect to the moving frame P by ${}^{P}I \in \mathbb{R}^{3\times3}$, we can write the kinetic energy of the system by

$$T = \frac{1}{2}\,{}^{P}\omega^{\intercal}\,{}^{P}I\,{}^{P}\omega$$

It is assumed that the center of mass of the platform is loaded by a static rod, since the position of the center of mass does not change, then the potential energy neither change, this latest is set arbitrarily to zero; we can write then the Euler-Lagrange equations,

$$M(\mathbf{q})\ddot{\mathbf{q}} + C(\mathbf{q},\dot{\mathbf{q}})\dot{\mathbf{q}} = \boldsymbol{\tau} \tag{2}$$

where $\mathrm{M}(\mathbf{q})$ is positive definite inertia matrix and a skew-symmetric matrix $\mathrm{C}(\mathbf{q},\dot{\mathbf{q}})$ represents the corriolis and centrifugal forces.

Considering $\dot{\mathrm{G}} = \mathbf{J}^{-1}\dot{\mathbf{q}}$ the actuator dynamics can be represented as

$$M_a\ddot{G} + V_a\dot{G} + K_a\mathbf{F} = \boldsymbol{\tau}_m \tag{2a}$$

where

$\mathrm{M_a}$: actuator inertia matrix,
$\mathrm{V_a}$: viscous damping coefficient,
$\mathrm{K_a}$: actuator gain matrix,
$\mathbf{F}$: forces induced by the platform in the actuators,
τ_{m}: vector of motor torques.
So the expression (2) and (2a) can be rewritten as

$$M_A(\mathbf{q})\ddot{\mathbf{q}} + C_A(\mathbf{q},\dot{\mathbf{q}}) = \boldsymbol{\tau}_m \tag{3}$$

where

$$M_A(\mathbf{q}) := M_a\mathbf{J}^{-1} + K_a\mathbf{J}^{\intercal}M(\mathbf{q})$$

$$C_A(\mathbf{q},\dot{\mathbf{q}}) := \left(K_a\mathbf{J}^{\intercal}C(\mathbf{q},\dot{\mathbf{q}}) + M_a\frac{d}{dt}\left(\mathbf{J}^{-1}\right) + V_a\mathbf{J}^{-1}\right)\dot{\mathbf{q}}$$

Finally, including the dynamic of the motor as

$$L\frac{d\boldsymbol{i}}{dt} + R\boldsymbol{i} + K_b\dot{\Theta}_{\boldsymbol{m}} = \mathbf{v} \tag{4}$$

where

L : motor armature inductance matrix,
R: motor armature resistance matrix,

K_b : motor back emf matrix,
v: input voltages.
and with the next equalities

$$\boldsymbol{\tau}_m = K_m \mathbf{i}$$

$$\dot{\Theta}_{\boldsymbol{m}} = K_n \dot{G}$$

where
K_m : motor torque matrix,
$\boldsymbol{\Theta}_{\boldsymbol{m}}$: motor angular position,
K_n : actuator constant that depends on gear ratio and pitch.
we obtain the third order differential equation

$$\frac{d}{dt}\begin{bmatrix}\mathbf{q}\\ \dot{\mathbf{q}}\\ \mathbf{i}\end{bmatrix} = \begin{bmatrix}\dot{\mathbf{q}}\\ M_A^{-1}(\mathbf{q})K_m\boldsymbol{i} - M_A^{-1}(\mathbf{q})C_A(\mathbf{q},\dot{\mathbf{q}})\\ -\mathrm{L}^{-1}(\boldsymbol{Ri} + \boldsymbol{K_b}K_n\dot{\mathbf{q}})\end{bmatrix} + \begin{bmatrix}0\\ 0\\ \mathrm{L}^{-1}\end{bmatrix}\mathbf{v} + \begin{bmatrix}0\\ \xi(\mathbf{q},t)\\ \mu(\mathbf{i},t)\end{bmatrix} \tag{5}$$

where $\xi(\mathbf{q},t)$ and $\mu(\mathbf{i},t)$ are perturbations due to unmodeled dynamics or parametric uncertainty.

3 Control Design and Main Result

The perturbed system (5) can be represented in the space-state form

$$\dot{\mathbf{x}} = \mathrm{f}(\mathbf{x}) + \mathrm{B}\mathbf{u} + \phi(\mathbf{x},\mathrm{t})$$

where $\mathbf{x} = [\mathbf{x}_1, \mathbf{x}_2, \mathbf{x}_3] = [\mathbf{q}, \dot{\mathbf{q}}, \mathbf{i}] \in \mathbb{R}^6$ are the states, $\mathrm{u} \in \mathbb{R}^2$ is the control signal and $\phi(\mathbf{x},\mathrm{t})$ is the perturbation, which is bounded constant, i.e. $\left\|\dot{\phi}(\mathbf{x},\mathrm{t})\right\| \leq \Delta$ almost everywhere. The problem is to design a time continuous control law, such that $\mathbf{x}_1$ tends to the desired value while $\mathbf{x}_2$ and $\mathbf{x}_3$ also converge in finite time despite of the perturbation $\phi(\mathbf{x},\mathrm{t})$. Moreover, after a finite time the control should compensate the perturbation i.e. $\mathrm{u}(\mathrm{t}) \equiv -\phi(\mathbf{x},\mathrm{t})$. The problem can be resolved as follows:

First, we choose a new variable

$$\boldsymbol{\delta}_1 = \dot{\boldsymbol{e}} + C_1\boldsymbol{e}$$

with

$$\dot{\boldsymbol{e}} = \boldsymbol{x}_2^* - \boldsymbol{x}_2$$

$$\boldsymbol{e} = \boldsymbol{x}_1^* - \boldsymbol{x}_1$$

Here $\mathbf{x}_1^*$ and $\mathbf{x}_2^*$ are desired values and C_1 is any positive definite matrix. With this we can define the new representation of the system, where the system parameters enter

as an additional term considered as a perturbation. The mathematical model now has the relative degree two (another method can be found in [10]) as follows:

$$\dot{\boldsymbol{\delta}}_1 = \boldsymbol{\delta}_2$$

$$\dot{\boldsymbol{\delta}}_2 = \boldsymbol{u} + \zeta(\boldsymbol{x}, t)$$

Where $\zeta(\mathbf{x}, \mathrm{t})$ includes the external perturbations as well the unmodelled dynamics. Now, following [9] the control problem can be solved by the dynamic feedback control law

$$\begin{aligned} \boldsymbol{u} &= -k_1 \lfloor \boldsymbol{\delta}_1 \rceil^{\frac{1}{3}} - k_2 \lfloor \boldsymbol{\delta}_2 \rceil^{\frac{1}{2}} + z \\ \dot{z} &= -k_3 \lfloor \boldsymbol{\delta}_1 \rceil^{0} - k_4 \lfloor \boldsymbol{\delta}_2 \rceil^{0} \end{aligned} \tag{6}$$

where $k_1, k_2, k_3, k_4 > 0$ are constant parameters. $z^p := |z|^p \mathrm{sign}(z)$ where $z, p \in \mathbb{R}$. The second equation in (6) has the high-order continuous structure. Its purpose is to reject derivative of the bounded perturbation. This integral form appears in the controller producing a continuous control signal. The proof of the stability and the finite time convergence of the proposed feedback controller can be fined in [9].

4 Numerical Simulations

We illustrate the behavior of the proposed controller for the system by some simulations. We will compare the result with back-stepping control and twisting controller [11], [12] to demonstrate the quality of the continuous SMC.

Consider the following bounded perturbations

$$\phi(\boldsymbol{x}, t) = \begin{bmatrix} 0 \\ 0,1 \sin(10t) \\ 0,2 \cos(10t) \end{bmatrix}$$

and the reference signals

$$\mathbf{x}_1 = \begin{bmatrix} \varphi \\ \theta \end{bmatrix} = \begin{bmatrix} \frac{\pi}{4} \cos(0,5t) \\ \frac{\pi}{4} \sin(0,5t) \end{bmatrix}$$

As one can see from the Figs. 2 and 3 all proposed controllers can regulate the system in less than 10 s. However, it can be seen the clear difference between the precision that provide each algorithm. As one knows the sliding mode controllers follow the reference perfectly, while the backstepping controller is not robust to the perturbations.

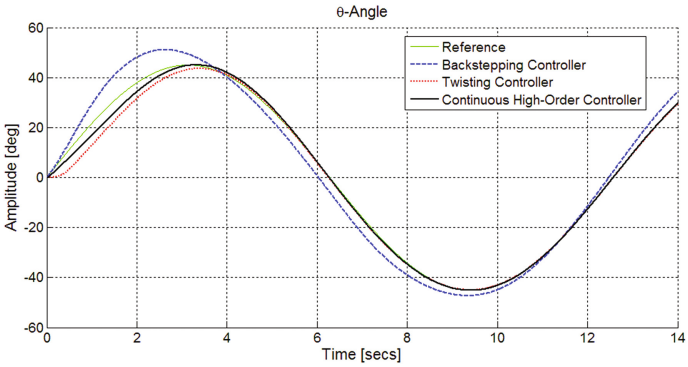

Fig. 2. The tracking of an angle θ.

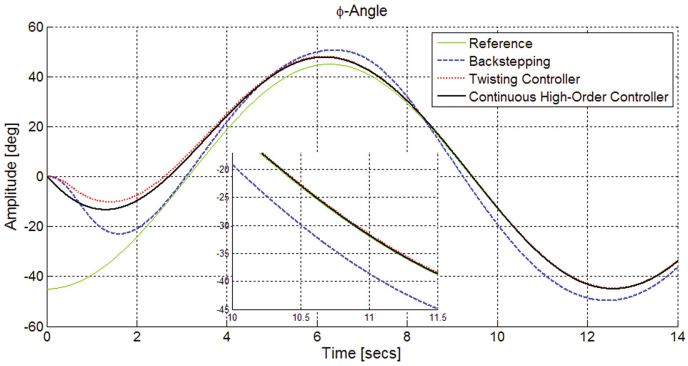

Fig. 3. The tracking of an angle φ.

More clear illustration of the behavior and advantage of the continuous SMC can be seen in the Fig. 4. Here one can see the error of tracking and the fact that the proposed control can compensate successfully the perturbation and parasitic effects.

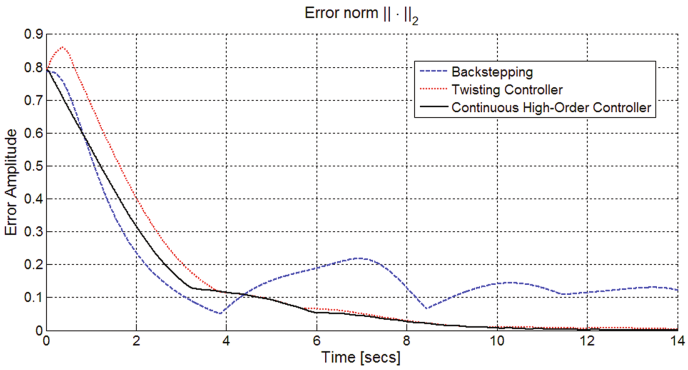

Fig. 4. Error of tracking of an angle φ.

Figure 5 shows the control signals (voltage) of the electric motors. Compared with the classical sliding mode control, the presented algorithms provide a continuous signal and less chattering effect which guarantees a suitable condition for the actuators.

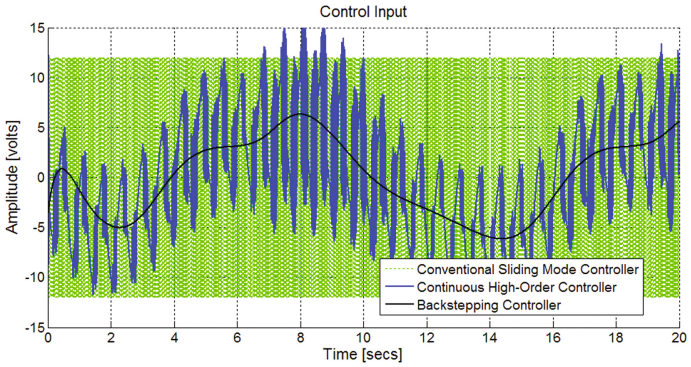

Fig. 5. Control input signals.

5 Conclusions

The description and mathematical model of a two degree of freedom platform is presented. A nonlinear feedback control based on continuous sliding mode control is proposed to regulate the system in the presence of perturbations/uncertainties. The behavior of the controller and its comparison with existing ones are proven via simulation. The control provides a major compensation of the perturbations in finite time.

Acknowledgments. Authors are grateful to CONACYT-Mexico and SIP-IPN for supporting part of this work through grants AEM-Conacyt 262887 and SIP20171092, respectively.

References

1. Shevchenko, G.V.: A new 3 D.O.F. Numerical method for solving a nonlinear time-optimal control problem with additive control. Comput. Math. Math. Phys. **47**(1), 1768–1778 (2007)
2. Utkin, V.: Sliding Modes in the Control and Optimization. Springer, Heidelberg (1992)
3. Ablameyko, S.V., Biryukov, A.S., Dokukin, A.A., D'yakonov, A.G., Zhuravlev, Y.I., Krasnoproshin, V.V., Obraztsov, V.A., Romanov, M.Y., Ryazanov, V.V.: Practical algorithms for algebraic and logical correction in precedent-based recognition problems. Comput. Math. Math. Phys. **54**(12), 1915–1928 (2014)
4. Shtessel, Y., Edwards, C., Fridman, L., Levant, A.: Sliding Mode Control and Observation. Birkhäuser Mathematics, Basel (2014)
5. Keshtkar, S., Poznyak, A.: Tethered space orientation via adaptive sliding mode. Robust Nonlinear Control **26**(8), 1632–1646 (2016)
6. Utkin, V., Poznyak, A.: Adaptive sliding mode control with application to super-twist algorithm: equivalent control method. Automatica **49**(1), 39–47 (2013)

7. Fridman, L., Moreno, J., Bandyopadhyay, B., Chalanga, A.: Continuous nested algorithms: the fifth generation of sliding mode controllers. In: Yu, X., Efe, O. (eds.) Recent Advances in Sliding Modes—Control to Intelligent Mechatronics. Studies in Systems, Decision and Control, vol. 24, pp. 5–35. Springer, Cham (2015)
8. Sanchez, T., Moreno, J.: A constructive Lyapunov function design method for a class of homogeneous systems. In: IEEE 53rd Annual Conference on Decision and Control, pp. 5500–5505. Los Angeles (2014)
9. Moreno, J., Negrete, D.Y., Torres-Gonzalez, V., Leonid, F.: Adaptive continuous twisting algorithm. Int. J. Control **89**(9), 1798–1806 (2015)
10. Harib, K., Srinivasan, K.: Kinematic and dynamic analysis of Stewart platform-based on machine tool structures. Robotica **21**, 541–554 (2003)
11. Kulikov, G.Y.: Solving the order reduction phenomenon in variable step size quasi-consistent nordsieck methods. Comput. Math. Math. Phys. **52**(11), 1547–1564 (2012)
12. Kulikov, G.Y.: Method of fast expansions for solving nolinear differential equations. Comput. Math. Math. Phys. **54**(1), 11–21 (2014)

Towards a Servovision Based Control for a Planar Parallel Manipulator

Fernanda Thaís Colombo(✉) and Maíra Martins da Silva

São Carlos Engineering School, University of São Paulo, Av. Trab. São-Carlense, 400 - Pq Arnold Schimidt, São Carlos, SP 13566-590, Brazil
fernanda.colombo@usp.br, mairams@sc.usp.br

Abstract. The control of parallel kinematic machines requires the use of complex strategies due to the coupling of the kinematic chains. The usual strategies for controlling serial manipulators should be reassessed for successfully controlling parallel manipulators. For instance, the usual joint space computed torque control strategy requires the calculation of the manipulator's inverse kinematics. The inverse kinematics of a parallel manipulator can be cumbersome. This issue may yield unsatisfactory performance and/or stability. The usual Cartesian space computed torque control strategy demands the measurement of the end-effector's pose. This measurement can be a challenging task. In this work, the pose of the end-effector of a 3$\underline{\text{R}}$RR parallel manipulator is estimated using a fixed camera and image processing algorithms during the execution of a predefined task. This is the first step for implementing the Cartesian space computed torque control for the manipulator under study.

Keywords: Parallel kinematic manipulator · Servovision · Camera calibration · Image processing

1 Introduction

The control of parallel kinematic machines requires the use of complex strategies due to the coupling of the kinematic chains. The usual strategies for controlling serial manipulators should be reassessed for successfully controlling parallel manipulators. Among them, two computed torque control strategies are widely used for controlling serial manipulators: the joint space and the Cartesian space [1].

The joint space computed torque control demands the measurement of the actual joints' positions and velocities. On the one hand, this approach is widely employed for serial manipulators since the end-effector's pose can be completely defined by their joints' positions and velocities using the forward kinematic model. The joints' positions and velocities are readily available since the joints are active and are measured by encoders. On the other hand, this approach may not be fully suitable for PKMs since the end-effector's pose is not readily available. In fact, it can only be calculated by evaluating the kinematic constraint equations due to the presence of close-loop kinematic chains and passive joints.

J.C.M. Carvalho et al. (eds.), *Multibody Mechatronic Systems*,
Mechanisms and Machine Science 54, DOI 10.1007/978-3-319-67567-1_23

This complexity imposes serious difficulties for the controller design, such as lack of speed and performance, stability issues, among others.

The Cartesian space computed torque control demands the measurement of the end-effector's pose. This data can be directly exploited by the control scheme. Although mathematically simpler, this choice imposes a significant technical challenge: the measurement of the end-effector's pose. This measurement should not only be fast and accurate, but also should not rely on modeling errors and/or system's nonlinearities [2]. By aiming to ensure fast and reliable measurements of the end-effector's pose, computer vision techniques could be exploited [2]. For instance, Andreff et al. [3] proposed an image-based visual servoing for controlling a Gough-Stewart parallel manipulator. The use of visual feedback to control the manipulator's motion plays an important role in the visual servoing. In fact, the end-effector's pose can be directly measured by detecting the positions of certain features in the image captured by a digital camera. Corke [4] presented a tutorial on many relevant topics on visual servoing, such as coordinate transformations and digital image processing techniques.

In this manuscript, the authors present the implementation of a position based visual servoing technique to be explored in a Cartesian space computed torque control of the 3RRR manipulator. This planar PKM is illustrated in Fig. 1. The rest of the manuscript is organized as follows. Section 2 presents the inverse kinematics model of the 3RRR manipulator. Section 3 presents a brief description of the 3RRR prototype, the exploited image processing method and

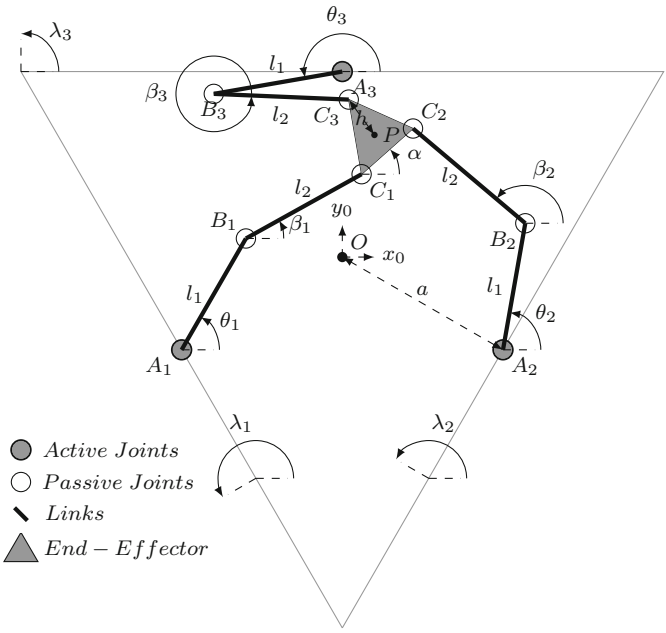

Fig. 1. Illustration of the 3RRR manipulator

the details on the camera's calibration. The experimental measurement of the end-effector's pose using the servovision system is presented and discussed in Sect. 4. Finally, conclusions are drawn in Sect. 5.

2 Kinematic Modelling of the 3RRR manipulator

The parallel kinematic manipulator under study is the 3RRR. As illustrated in Fig. 1, the end-effector is connected to the ground by 3 kinematic chains. Each kinematic chain is composed of two links, one active revolute joint (R) and two passive revolute joints (RR). A global coordinate system $O(x_0, y_0)$ is fixed to the equilateral triangle's barycenter illustrated in Fig. 1. The angles θ_i and β_i describe the kinematic configuration of the manipulator. The subscript i is related to each kinematic chain and can vary from 1 to 3. The lengths of the links are l_1 and l_2. The distance between the origin O and the active joints A_i is a, the distance between the point P and the passive joints C_i is h, and the angles of each side of the triangle are given by λ_i.

The inverse kinematic model evaluates the position $\{\theta_1, \theta_2, \theta_3\}$ of the active joints for a certain end-effector pose $\{x, y, \alpha\}$ and is described hereafter. The position of the joints A_i, B_i and C_i in the global coordinate system can be denoted by position vectors $\mathbf{r}_{A_i}$, $\mathbf{r}_{B_i}$ and $\mathbf{r}_{C_i}$, respectively. By evaluating the kinematic constraints, the vectors $\mathbf{r}_{B_i}$ and $\mathbf{r}_{C_i}$ can be expressed as:

$$\mathbf{r}_{B_i} = \mathbf{r}_{A_i} + l_1 \begin{bmatrix} cos\theta_i \\ sin\theta_i \end{bmatrix} \quad \text{and} \tag{1}$$

$$\mathbf{r}_{C_i} = \mathbf{r}_{B_i} + l_2 \begin{bmatrix} cos\beta_i \\ sin\beta_i \end{bmatrix}, \tag{2}$$

respectively. The auxiliary variables μ_i and ρ_i can defined by:

$$\mu_i = x + h\ cos(\lambda_i + \alpha) - a\ cos(\lambda_i) \quad \text{and} \tag{3}$$

$$\rho_i = y + h\ sin(\lambda_i + \alpha) - a\ sin(\lambda_i), \tag{4}$$

respectively. Using these variables, the following geometrical constraint $\left\|\overrightarrow{B_iC_i}\right\| = \|\mathbf{r}_{C_i} - \mathbf{r}_{B_i}\| = l_2$ can be rewritten as:

$$\left\| \begin{bmatrix} \mu_i - l_1 cos(\theta_i) \\ \rho_i - l_1 sin(\theta_i) \end{bmatrix} \right\| = \left\| l_2 \begin{bmatrix} cos(\beta_i) \\ sin(\beta_i) \end{bmatrix} \right\| = l_2. \tag{5}$$

Considering that $e_{i1} = -2l_1\rho_i$, $e_{i2} = -2l_1\mu_i$ and $e_{i3} = \mu_i^2 + \rho_i^2 + l_1^2 - l_2^2$, the Eq. 5 can be rewritten as:

$$e_{i1} sin\theta_i + e_{i2} cos\theta_i + e_{i3} = 0. \tag{6}$$

Therefore, the inverse kinematics of the 3RRR manipulator is as follows:

$$\theta_i = 2\tan^{-1}\left(\frac{-e_{i1} \pm \sqrt{e_{i1}^2 + e_{i2}^2 - e_{i3}^2}}{e_{i3} - e_{i2}}\right) \quad \text{and} \tag{7}$$

$$\beta_i = \tan^{-1}\left(\frac{\rho_i - l_1 \sin(\theta_i)}{\mu_i - l_i \cos(\theta_i)}\right). \tag{8}$$

The inverse dynamic model of the 3RRR manipulator can be found by exploring the Virtual Work Principle and/or the Newton-Euler formulation. Using this model, one can derive the required torque to perform a predefined trajectory. Details can be found in [5]. As it can be observed, these inverse models are composed of trigonometric relations. These relations might become rather complex for spatial manipulators. This complexity imposes challenges to the implementation of the joint space computed torque control.

3 Materials and Methods

3.1 Prototype

The 3PRRR manipulator built at EESC-USP is a kinematically redundant manipulator. This planar manipulator presents 3 degrees of freedom and can be actuated by up to six brushless servomotors *Maxon E60*. These servomotors work together with six control boards *EPOS 2* 50/5. By actuating the prismatic joint (P), the user can add kinematic redundancies to the manipulator. Since the main objective of this work is the implementation a servovision technique to allow the design of a Cartesian space computed torque control of the non-redundant 3RRR manipulator, the prismatic joints are locked. The communication scheme is illustrated in Fig. 2. The control boards are connected through CAN protocol. The communication between the first EPOS with the computer is via USB.

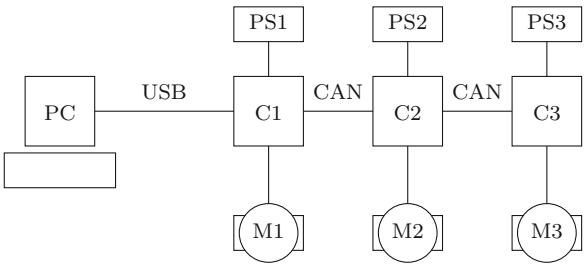

Fig. 2. Communication Scheme between the boards and the computer

The control board EPOS presents several control modes. In this work, the *Interpolated Position Mode* is selected since it guarantees performance and robustness. In this mode, the discrete positions and velocities given by the user are interpolated through splines and these signals are used as reference signals to the linear position feedforward and position feedback control strategies The feedforward and feedback gains have been adjusted manually in a human machine interface that has been built in Matlab.

3.2 Image Processing

In order to implement the Cartesian space computed torque control for the 3RRR manipulator, the pose of its end-effector should be directly measured. In this manuscript, a position based visual servoing is exploited to accomplish this task. The end-effector's pose $\{x, y, \alpha\}$ can be determined by measuring the position of two points in the end-effector. In this way, in order to use visual computing techniques, some key points are selected at this part. These points are illustrated in Fig. 3. At this figure, the point P is at the center of the equilateral triangle, the points G and R are at the same distance from the point P and the segment line between the points G and R is parallel to the side $\overline{C_1C_2}$.

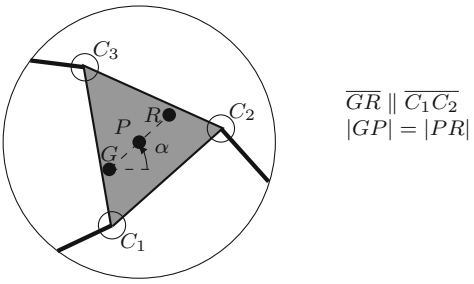

Fig. 3. The key points at the end-effector's manipulator

In the image plane, the coordinates of a point are defined by $\{u, v\}$ in pixels, ordered from left to right and top to bottom, respectively. So, the position $\{u_P, v_P\}$ in the image plane of the end-effector can be found by using the coordinates in pixels of the points G and R,

$$u_p = \frac{u_G + u_R}{2} \quad \text{and} \quad v_p = \frac{v_G + v_R}{2}, \tag{9}$$

and the angular position α of the end-effector can be found by using the coordinates in pixels of the points G and R,

$$\alpha = \arctan\left(\frac{v_R - v_G}{u_R - u_G}\right). \tag{10}$$

The positions of the points G and R are represented by small green and red circles, as illustrated in the Fig. 4, respectively. These features can be identified using a color camera. In fact, a digital image in the RGB color model is formed by 3 matrices corresponding to its red, green and blue components. For instance, a red pixel must not only have a high value in the red component, but also low values of the green and blue components, as in the rule $Red\ Pixels : r - g/2 - b/2 > Threshold$. This rule can be used for identifying the red pixels. The same strategy can be exploited for identifying the green pixels. Finally, the position of the point R can be found by calculating the average position of all red pixels, whilst the position of the point G by calculating the average position of all green pixels.

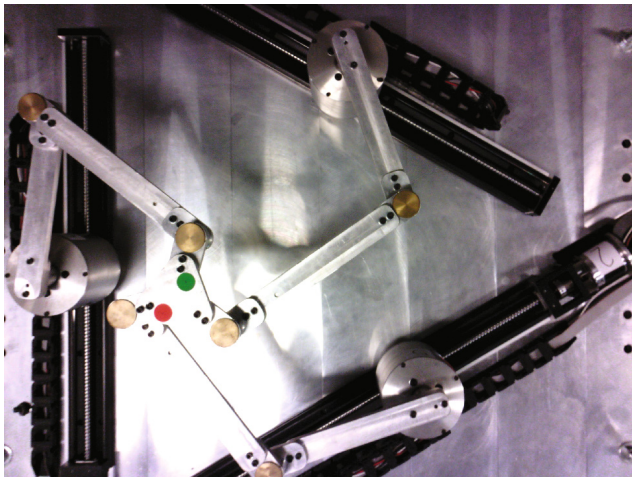

Fig. 4. 3RRR manipulator with green and red circular markers in the end-effector (Color figure online)

3.3 Camera

The images of the 3RRR are obtained with an *oCam-5CRO-U* digital camera. Due to its USB 3.0 interface, the data can be transferred to a computer at a high rate yielding higher frame rates and/or resolution. For position based visual servoing, the positions in the image plane of certain features should be detected and then transformed to the global coordinate system, using geometrical properties and intrinsic parameters of the camera. These intrinsic parameters, such as focal length, optical center and skew, can be obtained by performing the camera's calibration.

In this work, this calibration was performed by using the *Zhang's method* [6]. One advantage of this method is that it takes into account the distortion of the lens. This method requires a planar pattern with known metric to be photographed in at least 3 different orientations by the camera. A checkerboard was used as a planar pattern and several pictures with different poses were taken, as can be seen in Fig. 5 while the camera focus was kept constant.

This method, which is available in *Computer Vision System Toolbox* in Matlab, was able to detect the checkerboard pattern successfully. As illustrated in Fig. 6, all corners of the internal squares of the pattern were detected. Since the theoretical distance between those points is known, they can be used for calculating the parameters of the camera's model. Figure 6 shows the detected points and the reprojected ones based on the camera's model. As it can be verified, the scheme has been capable of not only identifying the corners but also calculating their positions correctly and depicting them in the figure (reprojected points).

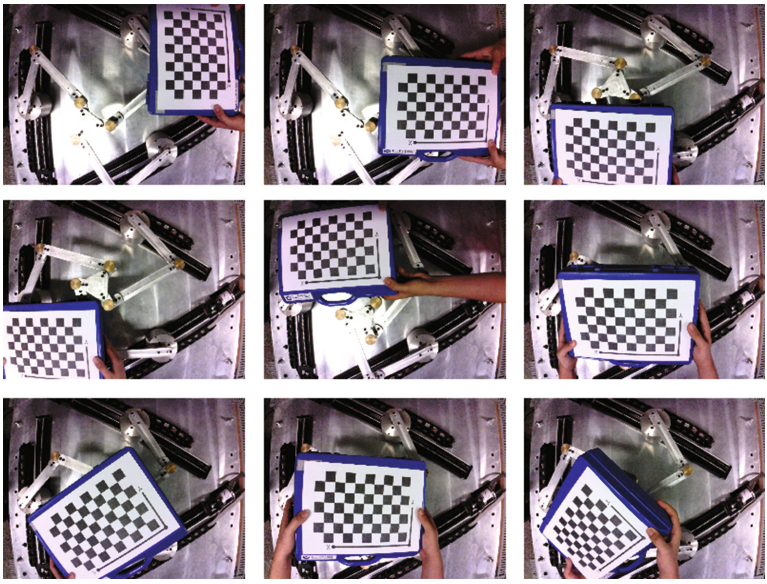

Fig. 5. Pictures for the Calibration: the checkerboard pattern in different orientations and positions

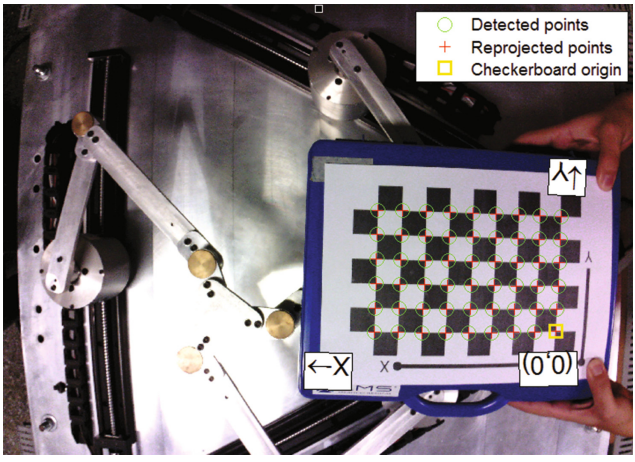

Fig. 6. Detected and reprojected points of the checkerboard pattern

Moreover, the distortion coefficients obtained in the calibration could be used for removing the images' distortion caused by the lenses. In Fig. 7(a), the radial distortion is highlighted by the bending of some edges. In Fig. 7(b), this effect has been eliminated.

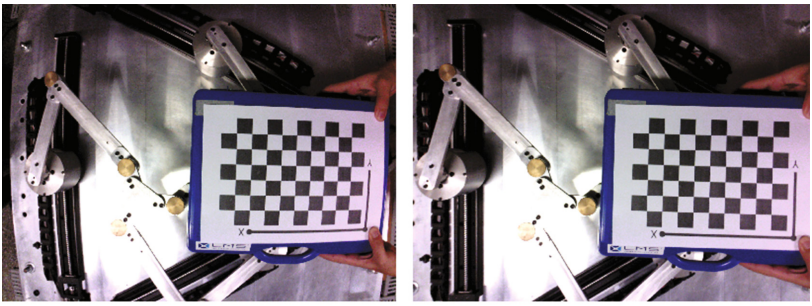

Fig. 7. (a) Original image with radial distortion and (b) Corrected image

4 Results and Discussion

After the calibration of the camera, the pose of the manipulator's end-effector $\{x, y, \alpha\}$ could be identified using the aforementioned visual servoing scheme. Both green and red markers located at the end-effector, as depicted in Fig. 8(a), are detected successfully, as illustrated by the two highlighted circles in Fig. 8(b). The points G and R are detected as the center of the green and red markers, respectively, and are illustrated as white dots in Fig. 9.

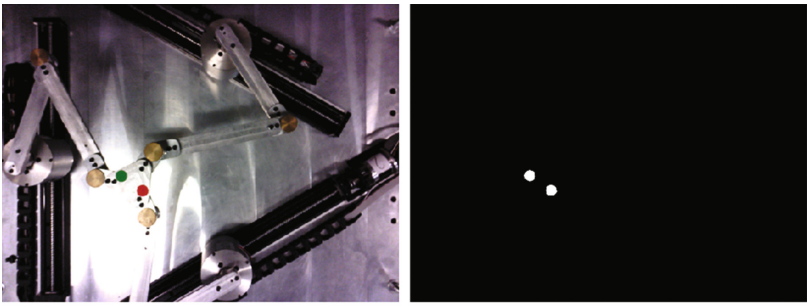

Fig. 8. (a) Undistorted image of the 3RRR manipulator and (b) The detection of the green and red markers (Color figure online)

This visual servoing scheme has been exploited for measuring the end-effector's pose of the manipulator during the execution of two tasks, A and B. The end-effector's pose can be also calculated using the direct kinematic model and the encoders' measurements of the active joints. Both tasks are point-to-point trajectories. For the execution of the task A, shown in Fig. 10(a), the end-effector moved from $\mathbf{X}_0 = [13.9, 7.88, 0]^T$ to $\mathbf{X}_1 = [-6.9, -39.4, 0]^T$ in 1.6 s. For the execution of

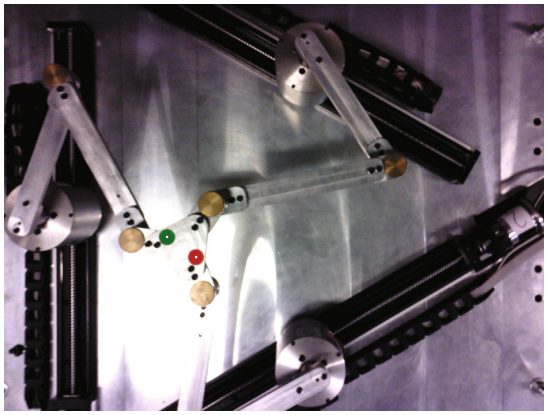

Fig. 9. Points G and R found as the centers of the green and red markers, respectively (Color figure online)

the task B, shown in Fig. 10(b), the end-effector moved from $\mathbf{X}_0 = [0, 119, 0]^T$ to $\mathbf{X}_1 = [0, -70, 0]^T$ and return to $\mathbf{X}_0$ in 2.2 s. The velocity and acceleration of the end-effector were null at the points $\mathbf{X}_0$ and $\mathbf{X}_1$ for both tasks. The translational dimensions are in mm and the rotational dimension in *rad*. The camera was set to its default resolution and frame rate of 640 × 480 at 20 fps.

As seen in Figs. 10, the encoder based motion and the camera based motion measurements differ considerably. In fact, the camera based motion measurements are showing that the actual control strategies, described in Sect. 3.1, are promoting a poor reference tracking performance. The control strategy, with linear position feedforward and position feedback, is purely based on the measurements done using the encoders. This might not deliver the desired reference tracking performance.

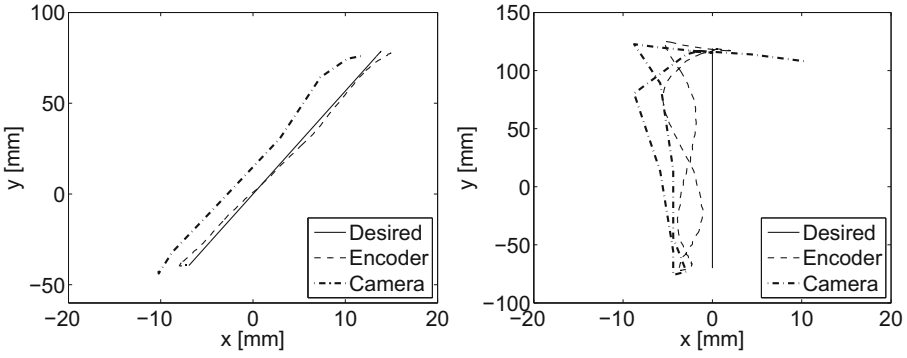

Fig. 10. Comparison between the desired motion, the encoder based motion measurement and the camera based motion measurement: (a) Task A and (b) Task B

5 Conclusions

Several control strategies, such as the Cartesian space computed torque control, require the measurement of the position of the manipulator's end-effector. In this manuscript, this is accomplished by using a visual servoing technique. This data can be further explored in a control strategy analysis.

Acknowledgements. This research is supported by FAPESP 2014/01809-0 and by CNPq 405569/2016-5. Fernanda T. Colombo is thankful for her scholarship FAPESP 2015/25936-4.

References

1. Paccot, F., Andreff, N., Martinet, P.: Revisiting the major dynamic control strategies of parallel robots. In: Control Conference, 2007 European, pp. 4377–4384 (2007)
2. Paccot, F., Lemoine, P., Andreff, N., Chablat, D., Martinet, P.: A vision-based computed torque control for parallel kinematic machines. IEEE International Conference on Robotics and Automation: ICRA **2008**, 1556–1561 (2008)
3. Andreff, N., Dallej, T., Martinet, P.: Image-based Visual Servoing of a GoughStewart parallel manipulator using Leg observations. Int. J. Robot. Res. Spec. Issue Vis. Robot. Jt. Int. J. Comput. Vis. **26**(7), 677–687 (2007)
4. Hutchinson, S., Hager, G.D., Corke, P.I.: A tutorial on visual servo control. IEEE Trans. Robot. Autom. **12**(5), 651–670 (1996)
5. Fontes, J.V., da Silva, M.M.: On the dynamic performance of parallel kinematic manipulators with actuation and kinematic redundancies. Mech. Mach. Theory **103**, 148–166 (2016)
6. Zhang, Z.: A flexible new technique for camera calibration. IEEE Trans. Pattern Anal. Mach. Intell. **22**(11), 1330–1334 (2000)

Multibody Model of the VVER 1000 Nuclear Reactor Control Assembly and Simulation of Its Moving Parts Drop

P. Polach(✉) and M. Hajžman

Research and Testing Institute Pilsen, Pilsen, Czech Republic
{polach,hajzman}@vzuplzen.cz

Abstract. The paper deals with the control assembly of the VVER 1000 nuclear reactor. The rod control cluster assembly is the moving part of the control assembly. After the rod control cluster assembly drop to the lower part of the core, a nuclear reaction stops. Multibody model of the control assembly intended for the simulations of the rod control cluster assembly moving parts drop during the seismic event was created and enables investigating the influence of deformations of fuel assembly guide tubes. The aim of this model creation is the proof that under the given conditions the rod control cluster assembly fulfils the demands that are made on the time of its drop from the point of view of the operating safety of the VVER 1000 nuclear reactor. Results of simulations are presented.

Keywords: Nuclear reactor · Control assembly · Drop · Tube deformation · Seismic excitation

1 Introduction

Approaches of multibody systems modelling and analysis are useful due to their ability to handle complex systems of bodies with nonlinear behaviour, which is also the case of dynamical analyses in nuclear engineering. The motion of important parts of nuclear reactors called control assemblies could be efficiently analysed [3] using these approaches. The purpose of the control assemblies is to control the power of a nuclear reactor (i.e. to control nuclear reaction). The second important function is to stop the nuclear reaction in the case of a defined emergency state.

Different control systems composed of various mechanical parts and transmissions can be found in various nuclear reactors based on their type [8]. From the viewpoint of multibody modelling, they can be simplified to the typical problem of a long thin rod moving through guide tubes and driven by a motor. The effects of contacts and influences of cooling water surrounding the control assembly in the nuclear reactor would be considered in the mathematical models.

The problem of mechanical behaviour of a control assembly during the emergency drop is not commonly studied in the available literature and therefore the investigation

J.C.M. Carvalho et al. (eds.), *Multibody Mechatronic Systems*,
Mechanisms and Machine Science 54, DOI 10.1007/978-3-319-67567-1_24

of this problem is a challenge. Some basic studies can be found in [3] or [5], but they are not focused on mechanical behaviour in a sufficient detail. Authors of this paper presented several approaches to modelling the flexible falling rod in [8–10] and more detailed (similar) models of control assemblies in [14, 15].

Spatial multibody model of the LKP-M/3 control assembly of the VVER 1000 nuclear reactor was created in the Alaska simulation tool [1]. Model is intended for the simulations of the rod control cluster assembly drop during the seismic event and enables investigating the influence of deformations of fuel assembly guide tubes [13]. The significant computed quantity is the total time of the drop. After the drop of the rod control cluster assembly to the lower part of the core a nuclear reaction stops. Novelty of this work consists in the creation of a unique computational methodology for the nonlinear dynamic analysis of nuclear reactors with and without seismic excitation considering the deformations of fuel assembly guide tubes. The methodology is further applied to the analysis of a particular control assembly of the VVER 1000 nuclear reactor. Reason for solving the presented problem was the proof that under the given conditions the rod control cluster assembly fulfils the demands that are made on the time of its drop from the point of view of the operating safety of the VVER 1000 nuclear reactor.

2 Structure of the Reactor and the Control Assembly

The VVER 1000 nuclear reactor is a pressurized water-cooled and water-moderated reactor developed in the Soviet Union. It consists of a reactor pressure vessel with an interior structure and a reactor upper block with control assembly drives (see scheme in Fig. 1). The core of the nuclear reactor containing fuel assemblies is its active zone with running nuclear reaction. Fuel assemblies are placed on the core support plate. The block of protective tubes, which is above the core with fuel assemblies, helps to guide and to protect control assemblies during their motion.

The VVER 1000 reactor contains 163 fuel assemblies and 61 control assemblies (e.g. [19]). A moveable part of the control assembly, i.e. the rod control cluster assembly (this part is the necessary condition for the stopping of nuclear reaction), is composed of a suspension bar, a spider and 18 long thin absorber rods.

A detailed scheme of the control assembly is shown in Fig. 2 (rectangles represent parts of the mechanism that are coupled by elastic elements with possible clearances; the objects in Fig. 2 are not displayed in a real scale factor. The suspension bar is divided into an upper and a lower part with a bayonet joint for connecting with a spider of the control element. The suspension bar of the rod control cluster assembly is driven by a linear stepper motor, the mechanism of which is based on the usage of electro-magnets. In case of an emergency state the lifting system mechanism is set off and the rod control cluster assemblies can drop down through the protective tubes to the reactor core with fuel assemblies and stop the nuclear reaction. Other functional subsystems plotted in Fig. 2 do not influence the dynamic behaviour in the course of

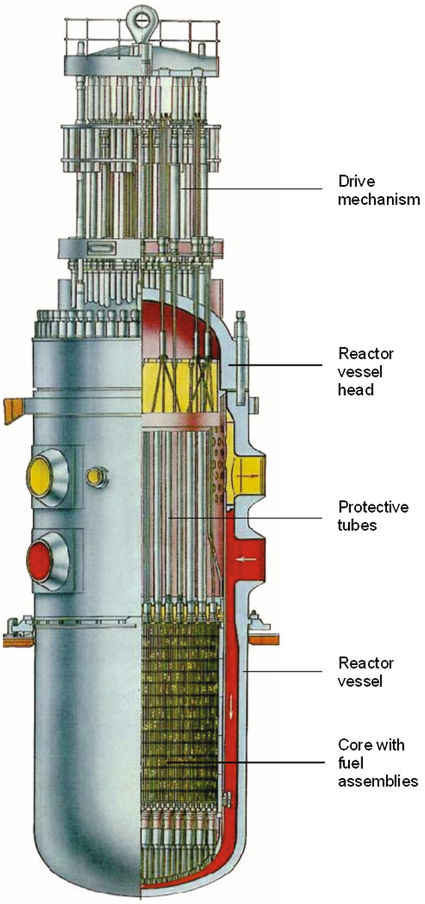

Fig. 1. Scheme of the VVER 1000 reactor

the studied rod control cluster assembly drop. The spider and the absorber rods of the rod control cluster assembly are schematically drawn in Fig. 2.

When the absorber rods reach the lower part of the core, they pass through the guide channel narrowing, which has the function of hydraulic shock absorbers for the stop of the rod control cluster assemblies drop.

3 Multibody Model of the Control Assembly

As it has been already stated, spatial multibody model of the LKP-M/3 control assembly of the VVER 1000 nuclear reactor was created in the Alaska simulation tool [1] on the basis of the technical documentation provided by the control assembly producer ŠKODA JS a.s. (the Czech Republic). The (similar) control assembly multibody models are described in more detail in [13] or [14] (these models do not

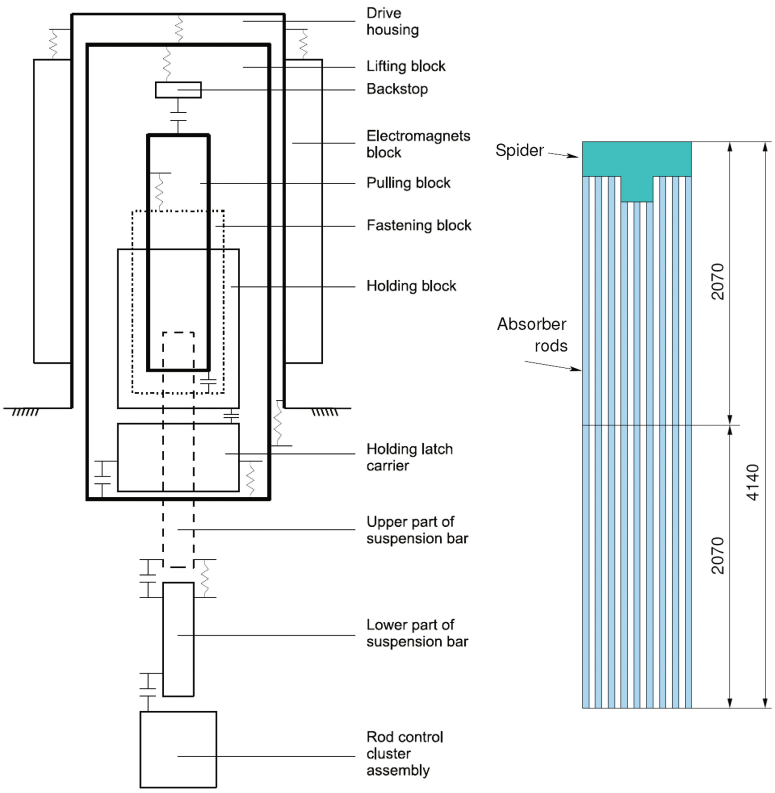

Fig. 2. Functional scheme of the control assembly without casing (not in a real scale factor) and scheme of the rod control cluster assembly (dimensions are in millimeters)

Table 1. Basic summary data about multibody model of the control assembly

Number of (rigid) bodies	23
Number of kinematic joints	23
Number of degrees of freedom	49
Number of contact points in vertical direction	11
Number of contact positions in horizontal plane	58

enables to consider both the seismic excitation and the deformations of fuel assembly guide tubes). Basic summary information about the multibody model is given in Table 1.

In the multibody model it is necessary to consider many contact positions in a horizontal plane for investigating limit curves of deformations of fuel assembly guide tubes [13–15] (see Table 2). Due to the simulation of the worst case for the time of the rod control cluster assembly drop, the initial position of the rod control cluster assembly in the multibody model is chosen in the maximum operation stroke, i.e. a lower end of the absorber rods is at distance of 3.586 m from the mechanical stop [13].

Table 2. Contact positions of bodies in horizontal plane in the multibody model

Contact between bodies (see Fig. 3)		Number of contact positions
First body	Second body	
Upper part of suspension bar	Lifting block	1
Upper part of suspension bar	Pulling block	2
Upper part of suspension bar	Frame	1
Cluster spider	Frame	6
Upper parts of 1st to 6th threes of absorber rods	Frame	18
Lower parts of 1st to 6th threes of absorber rods	Frame	30

Dynamic aspects of the control assembly that do not influence the rod control cluster assembly drop are neglected in the computational model.

The multibody model includes the influences of the fluid, the contacts and impacts of the rod control cluster assembly with the adjacent structural parts inside the reactor, deformations of fuel assembly guide tubes and seismic excitation. Not all influences and specific behaviour could be considered in detail in the model, but some aspects of the control assembly are and will be studied in more detail in future works.

Kinematic scheme of the control assembly multibody model is shown in Fig. 3, where circles represent kinematic joints (BUNC – unconstrained, PRI – prismatic in vertical axis, UNI – universal around horizontal axes) and quadrangles represent rigid bodies.

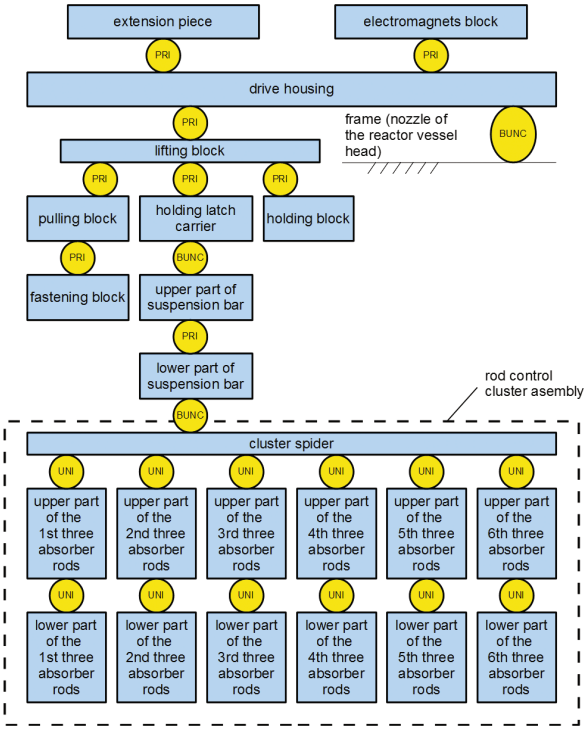

Fig. 3. Kinematic scheme of the control assembly multibody model

Due to virtual division of the rod control cluster assembly into thirteen rigid bodies (the purpose of this virtual division is partial considering the elastic properties of the rod control cluster assembly) certain distinguishing names of its parts were introduced (cluster spider, upper parts of the 1st to 6th threes absorber rods and lower parts of upper parts of the 1st to 6th threes absorber rods). The terminology is evident from Fig. 3 (or partly from Fig. 2 left). This modelling enables, using appropriately chosen torsional stiffness in the kinematic joints, to "tune" the values of the lowest natural frequencies corresponding to bending vibration modes to the natural frequencies obtained from the FEM model of the rod control cluster assembly.

The best way of introducing the seismic excitation in the computational model and the fuel assembly guide tubes deformations are presented e.g. in [13, 14].

Motion of body "drive housing" are defined by seismic excitations, which are specified by time histories of the absolute displacements in three directions (see example of time history of seismic excitation in Fig. 4). Considered deformation of fuel assembly guide tubes, that corresponds with the first bending mode shape of the fuel assembly guide tubes, is given in Fig. 5 (for VVANTAGE-6 fuel assembly in the Temelín Nuclear Power Plant, the Czech Republic).

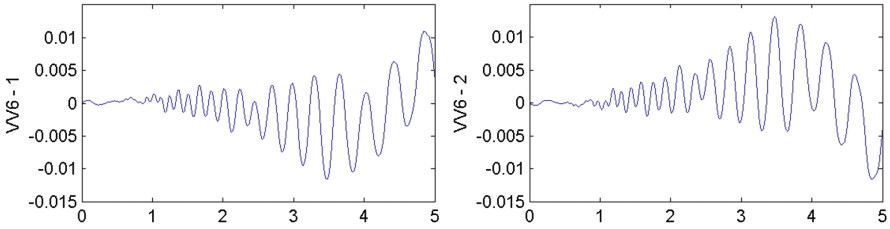

Fig. 4. Time histories [s] of the absolute displacements [m] of the body "drive housing" in horizontal directions during the seismic event in the Temelín Nuclear Power Plant

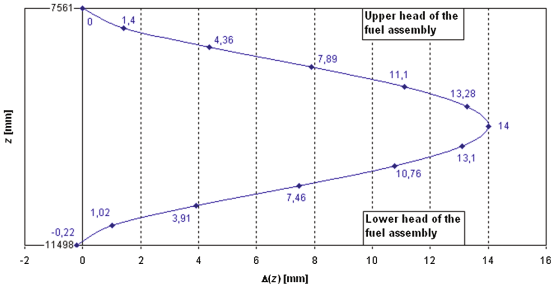

Fig. 5. Deformations of fuel assembly guide tubes (for VVANTAGE-6 fuel assembly)

Possible contacts and impacts of the moving parts with adjacent structural parts inside the reactor are very important and significant aspects of the rod control cluster assembly drop modelling. Many publications studying contact problems were released, e.g. [2, 7, 11, 12, 16, 18].

The problem can be divided into two steps – the first one is the determination of the contact occurrence and contact position and the second one is the calculation of the impact force acting on the bodies. Approach to the solution of this problem for the LKP-M/3 control assembly of the VVER 1000 nuclear reactor is given e.g. in [13–15].

The impact (normal) forces are introduced as the applied forces in the multibody model of the LKP-M/3 control assembly. Their instantaneous value is given by the *bistop* function [1]. After introducing axis *u,* direction of which is given by connecting point and instantaneous position of contact point, and independent variable u in its direction, impact (normal) force is calculated using the *bistop* function

$$F = bistop\,(u,\dot{u},u_1,u_2,c,d,e,b) = \begin{cases} -c\cdot(u_1-u)^e + step(u,u_1-d,b,u_1,0)\cdot\dot{u}, & u\le u_1 \\ 0, & u_1<u<u_2 \\ c\cdot(u-u_2)^e + step(u,u_2,0,u_2+d,b)\cdot\dot{u}, & u_2\le u, \end{cases} \tag{1}$$

where u is the independent variable, $\dot{u}$ is the first-order derivative of u and c, d, e, b are the coefficients determining the course of the function when one of the boundary values u_1 or u_2 is exceeded.

Function *step* approximates a step function by evaluating a cubic polynomial, which starts at initial ordinate value h_0 at $u = u_0$ and ends at final ordinate value h_1 at $u = u_E$

$$step(u,u_0,h_0,u_E,h_1) = \begin{cases} h_0, & u\le u_0 \\ h_0+(h_1-h_0)\cdot\left(\frac{u-u_0}{u_E-u_0}\right)^2\cdot\left(3-2\cdot\frac{u-u_0}{u_E-u_0}\right), & u_0<u<u_E \\ h_1, & u_E\le u. \end{cases} \tag{2}$$

The second most problematic factor in the control assembly multibody model is the influence of the pressurized water (coolant) that flows through the reactor interior structure and acts against the rod control cluster assembly motion. Like in the case of the contacts and impacts, this issue is frequently studied in the theoretical way (e.g. [6, 17]). It is evident that the main influence of coolant is the hydraulic resistance and friction slowing down the rigid body motion (e.g. [4]). Approach to solution of this problem for the LKP-M/3 control assembly of the VVER 1000 nuclear reactor is given e.g. in [13, 14].

4 Simulation Results

As it was already stated, due to the simulation of the least favourable situation for the rod control cluster assembly drop time in the multibody model initial position of the rod control cluster assembly is selected in the position of the maximum operation stroke.

Time histories of the distance of the lower end of absorber rods from the mechanical stop are in Fig. 6 and time histories of the velocity of the rod control cluster assembly drop are in Fig. 7.

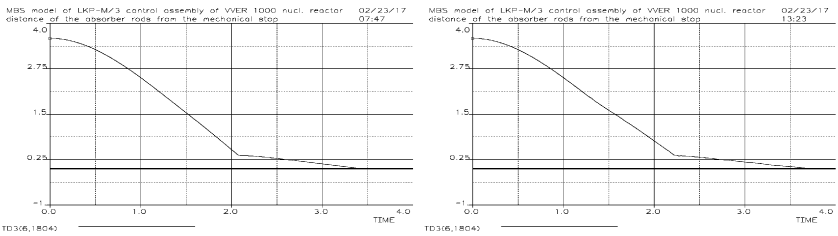

Fig. 6. Time histories [s] of distance [m] of the lower end of absorber rods from the mechanical stop at deformations of fuel assembly guide tubes: without any excitation (left); during the seismic event (right)

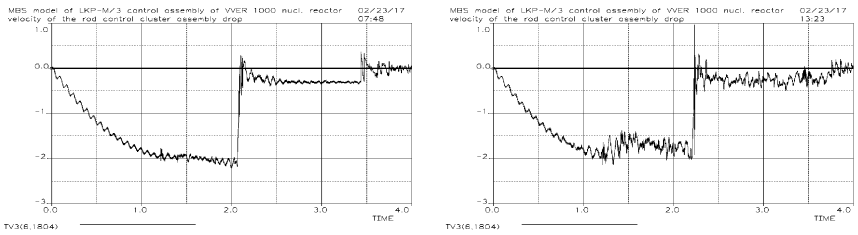

Fig. 7. Time histories [s] of the velocity [m/s] of the rod control cluster assembly drop at deformations of fuel assembly guide tubes: without any excitation (left); during the seismic event (right)

The design of the LKP-M/3 control assembly of the VVER 1000 nuclear reactor should meet the condition that the drop time should not exceed 4 s. This value is required for the time of the rod control cluster assembly drop from its initial position to the mechanical stop considering safety stop of the nuclear reaction.

On the basis of simulation results (see Fig. 6) it could be stated that the design of the LKP-M/3 control assembly fulfils the requirements for the time of the rod control cluster assembly drop at deformations of fuel assembly guide tubes and in addition in the case of a seismic event, too (in the Temelín Nuclear Power Plant).

5 Conclusions

The paper presents spatial multibody model of the LKP-M/3 control assembly of the VVER 1000 nuclear reactor created in the Alaska simulation tool [1]. The model is intended for the simulations of the rod control cluster assembly drop during the seismic event and enables investigating the influence of deformations of fuel assembly guide tubes [13]. The multibody model includes the influences of the coolant and the contacts and impacts of the rod control cluster assembly with the adjacent structural parts inside the reactor.

The simulations of the control assembly moving parts drop to investigate the total drop time at deformation of fuel assembly guide tubes without any excitation and during

a seismic event were performed. On the basis of the simulations' results it is possible to state that the drop time fulfils the prescribed maximum time of the drop given for the nuclear power plants safety estimation (in the Temelín Nuclear Power Plant).

Acknowledgments. The paper has originated in the framework of institutional support for the long-time conception development of the research institution provided by the Ministry of Industry and Trade of the Czech Republic to Research and Testing Institute Plzeň.

References

1. Alaska 9, Modeling and Simulation of mechatronical Systems. Institut für Mechatronik e. V., Chemnitz (2017)
2. Ben-Dor, G., Dubinsky, A., Elperin, T.: Some inverse problems in penetration mechanics. Mech. Based Des. Struct. Mach. **38**, 468–480 (2010)
3. Bosselut, D., Andriambololona, H., Longatte, E., Pauthenet, J.: Insertion and drop of control rod in assembly simulations and parametric analysis. In: Technical Meeting on Structural Behaviour of Fuel Assemblies for Water Cooled Reactors, IAEA-TECDOC-1454, pp. 189–194 (2004)
4. Chang, K.-H.: Computer-aided modeling and simulation for recreational waterslides. Mech. Based Des. Struct. Mach. **35**, 229–243 (2007)
5. Collard, B.: RCCA drop kinetics test, calculation and analysis, abnormal friction force evaluation. In: Proceedings of the 7th International Conference on Nuclear Engineering, Tokyo, CD-ROM (1999)
6. Feireisl, E.: On the motion of rigid bodies in a viscous fluid. Appl. Math. **47**, 463–484 (2002)
7. Flores, P., Lankarani, H.M.: Contact Force Models for Multibody Dynamics. Springer, New York (2016)
8. Hajžman, M., Polach, P.: Nonlinear dynamic analysis of flexible control rods in nuclear reactors. In: Proceedings of The Third Asian Conference on Multibody Dynamics, CD-ROM, Tokyo (2006)
9. Hajžman, M., Polach, P.: Modelling of flexible rods falling in fluid with possible contacts. In: Proceedings of the III European Conference on Computational Mechanics: Solids, Structures and Coupled Problems in Engineering, CD-ROM, Lisbon (2006)
10. Hajžman, M., Polach, P.: Two approaches to the modelling of the control rods in nuclear reactors. In: Proceedings of The Fourth Asian Conference on Multibody Dynamics ACMD2008, CD-ROM, Jeju (2008)
11. Klisch, T.: Contact mechanics in multibody systems. Multibody Sys. Dyn. **2**, 335–354 (1998)
12. Machado, M., Moreira, P., Flores, P., Lankarani, H.M.: Compliant contact force models in multibody dynamics: evolution of the Hertz contact theory. Mech. Mach. Theory **53**, 99–121 (2012)
13. Polach, P., Hajžman, M.: Verification of the multibody model of the LKP-M/3 control assembly intended for the control assembly moving parts drop calculation at the seismic event on the basis of experimental measurement results, research report VYZ 1236/09. ŠKODA VÝZKUM s.r.o, Plzeň (2009). (in Czech)
14. Polach, P., Hajžman, M.: Approaches to the creation of multibody models of the VVER 1000 nuclear reactor control assembly. In: Proceedings of the ECCOMAS Congress, Hersonissos, (2016). https://eccomas2016.org/proceedings

15. Polach, P., Hajžman, M., Bulín, R.: Determination of deformation limit of fuel assembly guide tubes of the VVER 1000 nuclear reactor. In: Proceedings of The 8th Asian Conference on Multibody System Dynamics ACMD, USB flash drive, Kanazawa (2016)
16. Popov, V.L.: Contact Mechanics and Friction, Physical Principles and Applications. Springer, New York (2010)
17. Sarrate, J., Huerta, A., Donea, J.: Arbitrary Lagrangian-Eulerian formulation for fluid-rigid body interaction. Comput. Methods Appl. Mech. Eng. **190**, 3171–3188 (2001)
18. Schiehlen, W., Seifried, R.: Three approaches for Elastodynamic contact in multibody systems. Multibody Sys. Dyn. **12**, 1–16 (2004)
19. Zeman, V., Hlaváč, Z.: Dynamic response of VVER 1000 type reactor excited by pressure pulsation. Eng. Mech. **15**, 435–446 (2008)

Single-State Friction Model for Control Purposes

Fernando J. Villegas(✉), Rogelio L. Hecker, and Gustavo M. Flores

Facultad de Ingeniería, Universidad Nacional de La Pampa,
CONICET, Santa Rosa, Argentina
fvillegas@ing.unlpam.edu.ar

Abstract. Friction is a complex phenomenon which has negative effects on the precision of positioning systems. Therefore, friction models for use in friction compensation have to show a good performance while remaining simple enough for its use in control algorithms. In this work, a single-state friction model for control purposes is proposed, aiming to simplify the implementation of such control algorithms, while keeping a good performance in friction compensation. This model has been tested on an experimental setup based on a linear motor, and its performance is compared to that of the Generalized Maxwell-slip (GMS) model, showing better performance on the tracking error for low accelerations.

Keywords: Friction model · Precise positioning · Linear motor

1 Introduction

Friction is a complex phenomenon which has important effects in servo mechanisms [1,2], such as tracking errors in precision positioning [3]. This is particularly important in positioning systems which are too sensitive to external forces, like those with linear motors. One way to mitigate its effect is by feedforward control using a convenient friction model.

In this way, the modeling of friction force for control purposes must be able to represent relevant friction properties while at the same time remain simple enough for its online calculation [4]. These properties include those displayed during the sliding regime, dominated by the Stribeck effect, and during the presliding regime represented by a hysteresis behavior.

The Stribeck effect corresponds to the negative slope exhibited by friction force as a function of steady-state velocity for low velocities, and it is considered an important factor in stick-slip phenomena [4]. The curve which depicts friction force as a function of steady state velocity is called Stribeck curve. However, when velocity is varying, friction force does not follow the Stribeck curve, it rather follows an hysteresis path around it. Such hysteretic behavior is called friction lag.

The previous properties are exhibited for non-zero velocities. However, when the bodies in contact begin to move from zero velocity, initially friction force

J.C.M. Carvalho et al. (eds.), *Multibody Mechatronic Systems*,
Mechanisms and Machine Science 54, DOI 10.1007/978-3-319-67567-1_25

depends only on displacement, characterized by a hysteresis behavior. The particular type of hysteresis exhibited by this presliding friction has several properties. One is rate-independence [3], which is clearly seen when tracking a sinusoidal reference, as the frequency of the reference has no influence on the shape and area of the hysteresis loop [5]. Another property is what is called non-local memory, for which the output at any time instant depends not only on any past value and the input history since then, but also on the past extremum values [4]. The described phenomena of this regime particularly affect the errors of trajectory tracking when zero velocity is crossed.

Several friction models have been proposed in the last decades for control purposes. A popular one is the LuGre model [6], which however is unable to represent hysteresis with nonlocal memory [4], and even might exhibit spurious drifting behavior [7]. Other models have been proposed in order to overcome these limitations. In particular the Leuven [8] and GMS [4,9] models are capable of representing hysteresis with nonlocal memory, and particularly the GMS model included improvements in friction lag representation.

The GMS model represents friction as a combination of N single-state dynamic elements. As a result, the hysteresis branches resembles a polygonal curve, whose number of segments increase with N. Modifications of this model has been proposed in [10,11], in order to avoid switching dynamics. However, the same multi-state structure is maintained.

Aiming to reduce the number of states while obtaining smooth slope changes inside the hysteresis loop, a two-state model [12] has been derived from the GMS model, through mathematical manipulations and simplifications. Lower errors were obtained with this model compared to those with the GMS model, when applied to feedforward friction compensation in a linear motor system. The lower performance of the GMS was attributed to the reaction of the integral control, from the position closed loop, with the discontinuities of the slope change in the hysteresis branches.

Although the model in [12] has only two states, it is relatively complex and presents impulsive behavior. The aim of this work is to obtain a simplified single-state version of this model which might keep the advantages in feedforward friction compensation of the two-state model. In order to do this, an outline of the two-state model is given in Sect. 2, continuing in Sect. 3 with a discussion on the manner in which such simplification can be achieved. Then, the proposed single-state model is presented in Sect. 4, showing also part of its behavior in simulation. After that, the performance of the proposed model in feedforward friction compensation for an experimental setup is shown in Sect. 5, where it is compared with a 5-element GMS model. Finally, this work ends in Sect. 6 with the conclusions.

2 Two-State Friction Model

The two-state friction model in [12], which has been derived from the GMS model, is a dynamic model in which friction force is given by $F = F_h + F_l + \sigma_2 v$,

that is the sum of a viscous friction component, being σ_2 the viscous friction coefficient, and two states whose dynamics during motion is given by

$$\begin{aligned} \frac{dF_h}{dt} &= \kappa\left(\xi(t)\right) v(t) + \gamma\left(\xi(t)\right) \frac{d}{dt} s(v(t)) \\ \frac{dF_l}{dt} &= -\frac{C}{|s(v(t))|} F_l - \gamma\left(\xi(t)\right) \frac{d}{dt} s(v(t)) \end{aligned} \tag{1}$$

Here $\xi(t) = \frac{x(t)-x_k}{s(v(t))-s_k}$, $x(t)$ stands for position, $v(t)$ for velocity, $s(v)$ is a curve which describes the Stribeck effect, and such that friction force for a steady state velocity v is given by $s(v) + \sigma_2 v$. A common parameterization for $s(v)$ [4] which is the one used in this work is

$$s(v) = \operatorname{sgn}(v) \left(F_c + (F_s - F_c) e^{-\left|\frac{v}{V_s}\right|^{\delta_{V_s}}} \right) \tag{2}$$

being F_c the Coulomb force, F_s the static force, V_s the Stribeck velocity and δ_{V_s} the Stribeck shape factor.

The values with k as subindex can be considered as constants which are updated under certain events on the hysteresis curve, such as motion reversal. In fact, Eq. (1) determines the evolution of the two friction states during motion between two equation updates driven by the mentioned events. More precisely, x_k represents the position during the last reference event, while s_k is the value of $s(v)$ immediately before that event, and thus its sign will be the opposite of that of $s(v(t))$, being t the current time.

The state F_h represents the contribution of presliding hysteresis and Stribeck curve to the friction force, respectively through first and second term in the F_h state equation. The relative contribution of these two effects on F_h are weighted by the functions κ and γ, whose shapes take the general form shown in Fig. 1. That is, κ is a nonincreasing continuous function while γ is nondecreasing. Precisely, in Eq. (1) it can be seen that κ will determine the shape of the hysteresis curve, and once outside the presliding region, corresponding to the value l_1 in Fig. 1, the contribution of the κ term vanishes, at least until an equation update event occurs. Meanwhile, the value of γ outside the presliding region is 1, thus it can be seen that if the presliding region is left at time t_l, from there on the contribution of the γ term is of the form $s(v(t)) - s(v(t_l))$, accounting for the speed dependence of the Stribeck curve.

As for the state F_l, it is clear that is driven out of zero by variations in $s(v(t))$, specially outside the presliding region where γ attains its maximum value, and without this variation it will tend to return to zero. This suitably represents the effect known as friction lag where, for a velocity change, the friction force does not follow the Stribeck curve, but rather shows some hysteresis around it until a new steady state value is reached. The shape associated to friction lag is clearly seen on the friction force modeled when a varying positive velocity is applied to the two-state model, as shown in Fig. 2, where the hysteresis shape can be seen around the Stribeck curve.

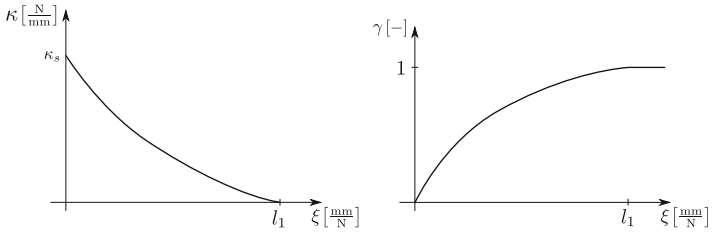

Fig. 1. Functions κ and γ of the two-state model

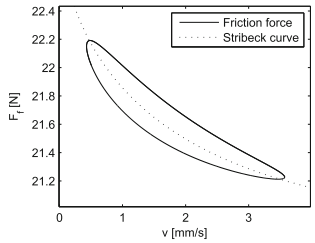

Fig. 2. Friction lag as represented by the two-state model

The other model parameters are given by C, a parameter related to friction lag, l_1, which determines the extent of presliding region, and those needed to parameterize functions κ and γ which determine hysteresis curve.

3 Simplification of the Two-State Friction Model

Although the two-state model has allowed to reduce tracking error and at the same time reduce the number of states and parameters needed for friction modeling, it has several aspects of increased complexity, such as its impulsive behavior. This impulsive behavior is expressed in its set of rules [12] which determine the procedure on equation update events, and can be associated mainly with two aspects. One is the modeling of friction lag, and the other is the velocity dependence of presliding hysteresis exhibited by this model.

Regarding the modeling of friction lag it should be noted that in a typical application, such as our experimental setup, this effect can be masked by local variations in friction force. This problem with the friction force variation was noted by [4] in a machine tool table setup. Therefore, it should be considered whether the increase in complexity associated to friction lag modeling is worthwhile. Thus, in the model proposed this effect is neglected, which can be done disregarding the state F_l altogether.

As for presliding hysteresis, this phenomenon is considered to be frequency-independent [5]. However, the presliding hysteresis for the two-state model has some degree of dependence on speed. This behavior is a result of the dependence

on velocity exhibited by the GMS model during presliding regime, associated to the transition mechanism between presliding and gross-sliding regime.

Notice that speed dependence could be eliminated in the two-state model, disregarding the variation of $s(v(t))$ during the presliding regime. Thus, if $s(v)$ is constant during this regime, the second term on the F_h equation is zero, and F_h will depend only on position, as $s(v(t))$ is constant. One way in which this can be done is considering a constant low velocity during presliding regime, such that when leaving the presliding region, the friction force will be equal to F_s in Eq. (2).

However, the described approach has the consequence that once outside presliding region, there will be no more variation of F_h, so such model would be unable to depict Stribeck curve. In order to compensate for this, somehow the effect of the γ term outside the presliding region, that is, the contribution of the form $s(v(t)) - s(v(t_l))$ to the friction force must be added.

One manner in which this can be done, is to use an approach similar to that used in [13] to simplify the LuGre model. There, simplified expressions for the model depending on the particular friction regime involved were considered, and the full friction force was obtained from these expressions, weighed by suitable transition functions. This is the approach used in the simplified model proposed in the next section, adding a term accounting for the Stribeck curve variation with velocity, combining it with a friction state representing solely presliding hysteresis through a suitable transition curve.

4 Proposed Friction Model

Considering the guidelines in the prior section, a simplified friction model for control purposes is proposed. This is a single-state model, in which the dynamics of its only state during motion is given by

$$\frac{dF_H}{dt} = \kappa\left(|\xi(t)|\right) v(t) \tag{3}$$

All quantities in Eq. (3) are defined just as in the two-state model except for $\xi(t)$, which is given by $\xi(t) = \frac{x(t)-x_k}{z_k}$.

Like in the two-state model, k is the index of the last point of motion reversal used as reference for the current motion, except in the case of two bodies which had never undergo relative motion, in which case $k = 0$ corresponds to the initial state, referred from here on as zero state. Thus, $\xi(t)$ represents the distance from the last reference position, modified by a scale factor given by z_k. If the bodies have never had relative movement and $k = 0$, $z_k = F_s$, the static friction force, otherwise $z_k = 2F_s$.

With this state, and following the prior section, the friction force is given by

$$F_f(t) = F_H(t) + \sigma_x\left(\xi(t)\right)\left(s(v(t)) - \alpha_k F_s + \sigma_2 v(t)\right) \tag{4}$$

Here α_k is 1 or -1 according to the direction of motion, and can be considered as $\alpha_k = \text{sgn}(x(t) - x_k)$ which during motion would be equal to $\text{sgn}(v(t))$ or $\text{sgn}(s(v(t)))$.

The function σ_x is such that $\sigma_x(\xi) = 0$ for $|\xi| \leq l_1$ and $\sigma_x(\xi) = 1$ for $|\xi| \geq l_u$ with a continuous monotonic transition between both values. Here, l_1 is the value where $\kappa(\xi)$ becomes zero, and defines the extent of the presliding region, while $l_u > l_1$ defines the displacement from which friction force will start to follow the Stribeck curve.

Notice that, as discussed in the previous section, the state F_H now represents solely the effect of presliding hysteresis, which is combined with the friction behavior for gross-sliding through the transition function σ_x. Also, two main contributions can be appreciated in the expression for sliding friction which is enclosed in parentheses. One is the term of viscous friction, $\sigma_2 v(t)$, while the other two terms account for the variation in $s(v(t))$ expected from the Stribeck curve.

As for the changes in k and the reference position x_k, these are determined by the following rules

Rule 1 If motion reverses at a point x_d, k is incremented by 1 and the value $x(t_k) = x_d$ is saved to the stack.

Rule 2 When a loop is closed, that is when

$$^{k}\Delta x(t) = -\left(^{k-1}\Delta x(t_k)\right) \tag{5}$$

and friction is still in presliding regime, i.e.

$$|^{k-1}\Delta x(t_k)| \leq 2 l_1 F_s \tag{6}$$

Then k is decremented in 2, and the last 2 elements of the stack are removed.

Rule 3 (Only when the system begins from zero state) When $k = 1$, $|^{1}\Delta x(t)| = 2|\Delta x(t_1)|$, and $|\Delta x(t_1)| \leq l_1 F_s$, k returns to 0 and the remaining value on the stack is removed.

To have a more graphical description of the above rules, consider the depiction of a trajectory exhibiting hysteresis with nonlocal memory in Fig. 3.

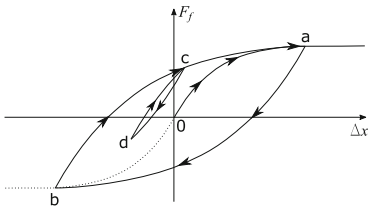

Fig. 3. Friction force as a function of displacement in presliding regime

The first rule applies at points in which the trajectory undergoes motion reversal, such as a, b, d and c when coming from b. The second rule applies when an inner loop is closed, such as happens when point c is reached when coming from d. In such a case points c and d are forgotten and point b is the new reference in the F_H equation. Notice that the plot represents the case of a system beginning from zero state, shown as point 0. Thus, if at point b the trajectory would follow the dotted line, rule 3 would apply.

As with the two-state model, these rules are needed for representing presliding hysteresis with nonlocal memory. However, in contrast to that model there are no impulsive changes in the F_H state. This is a result of avoiding friction lag and making presliding hysteresis frequency-independent.

It should be noticed that the determination of the model parameters will be done in the same manner as with the two-state model, that is, following the procedure detailed in [12].

Simulations with the proposed model have been performed to show that the model properly account for two important properties of friction. The depiction of presliding hysteresis with nonlocal memory by this model can be seen in Fig. 4a. Also, the representation of Stribeck curve by the model can be seen in Fig. 4b, where a varying positive velocity has been input to the model, resulting on a plot of the Stribeck curve for $v > 0$.

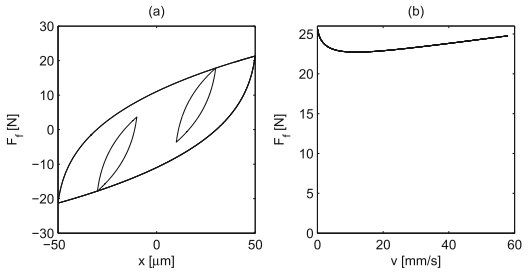

Fig. 4. Presliding hysteresis with nonlocal memory (a) and Stribeck curve (b) as represented by the proposed model

5 Experimental Results

The performance of the proposed model in friction compensation has been tested against a 5-element GMS model in the experimental setup shown in Fig. 5a. This is a linear drive based on a permanent magnet linear synchronous motor. Here the friction force comes from the four ball runner blocks sliding over linear guides. More details about the particular system can be found in [14].

The controller is a state-space controller with full-state observer and integral action where the friction model has been used for feedforward friction compensation. A schematic representation of the whole control structure is shown in Fig. 5b. Either the parameterization of function κ as well as the parameters of

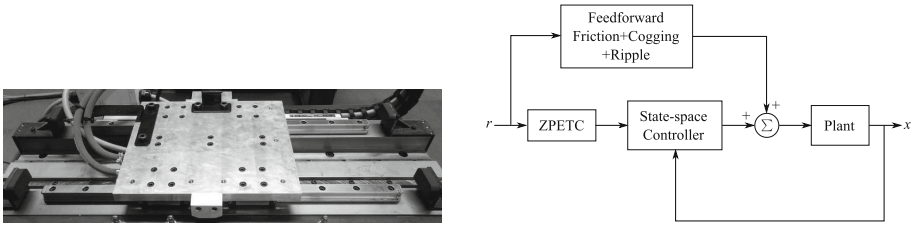

Fig. 5. Linear motor stage (a) and control structure (b) for the experiment

the proposed model are the same shown for the two-state model in [12], where details about the parameters of the 5-element GMS model and the controller itself can also be found.

In order to test the performance of feedforward friction compensation, rather than the dynamic performance of the state-space controller, slow sinusoidal references (6 s period) has been input to the control system. The first reference had an amplitude of 5 mm, driving the system outside the presliding regime. The maximum error for this trajectory reaches 12.5 μm for the GMS model and 9.8 μm for the single-state model. A period of the reference trajectory is shown in Fig. 6a, and the error plots for this fragment are shown in Figs. 6b and c.

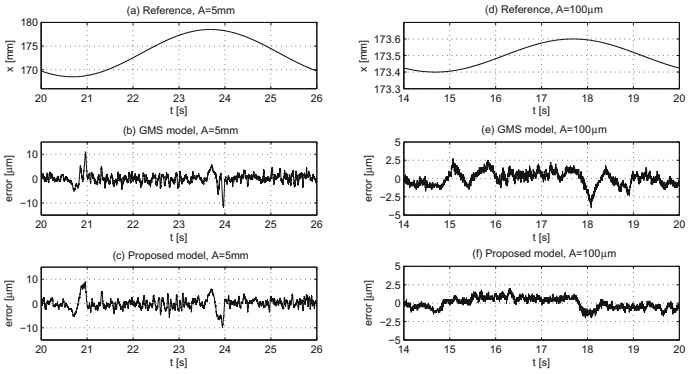

Fig. 6. Tracking error in feedforward compensation for reference amplitudes of 5 mm and 100 μm and maximum accelerations of 5.48 mm/s^2 and 0.11 mm/s^2 respectively

The peak errors are coincident with the points of zero velocity of the sinusoidal reference. Thus, in order to have a better view of this behavior, a lower amplitude input of 100 μm has been tested. The maximum tracking error in this case reaches 4 μm for the GMS model and 2.2 μm for the single-state model. A period of the reference trajectory is shown in Fig. 6d and the error plots for this fragment are shown in Figs. 6e and f.

As pointed out in [12] the peaks exhibited by the error for the GMS model seem to be associated to the abrupt changes of slope described by GMS model in presliding hysteresis. As the proposed model exhibits a smooth change in slope along hysteresis branches, this seems to be the cause for an improved performance of the proposed model. However, when reference acceleration is increased, which would increase the importance of the neglected term in Eq. (1), the performance of the proposed model deteriorates as shown in Table 1. Here are given values of maximum position error for friction feedforward using the GMS (e_{GMS}) and the proposed (e_{prop}) model, as well as the relative difference between both errors $\epsilon_e = \frac{e_{prop} - e_{GMS}}{e_{GMS}}$. It can be seen that for accelerations up to $7.68\,\mathrm{mm/s^2}$ the use of the proposed model in friction compensation results in maximum errors from 3.17% to 45% lower than those obtained with the GMS model. However, for higher accelerations the maximum error is lower for the GMS model.

Table 1. Maximum error for each model and relative difference between errors for several references

A[mm]	v_{max}[mm/s]	a_{max}[mm/s^2]	e_{GMS}[µm]	e_{prop}[µm]	ϵ_e[%]
0.05	0.052	0.055	2.7	2.2	−18.52
0.1	0.105	0.11	4	2.2	−45
0.25	0.262	0.27	4	3.2	−20
5	5.236	5.48	12.5	9.8	−21.6
7	7.33	7.68	15.75	15.25	−3.17
8	8.38	8.77	16.25	17	4.62
10	10.47	10.97	17	17.5	2.94
0.1	1.047	10.97	9.75	13	33,3
20	20.94	21.93	20	23.5	17.5
5	10.47	21.93	20.5	23.25	13.41

6 Conclusions

A single-state friction model has been proposed for feedforward friction compensation, based on the two-state friction model in [12]. This single-state model is capable of accurately represent the frequency-independent presliding hysteresis with nonlocal memory, as well as the Stribeck curve

As done in [12] for the two-state model, the proposed single-state model has been tested against the GMS model in feedforward friction compensation. In fact, its performance has been tested for tracking of sinusoidal references on an experimental setup consisting of a linear motor and compared to that of a 5-element GMS model in the same conditions. The results display improvements in maximum tracking error for accelerations of up to $7.68\,\mathrm{mm/s^2}$. For higher accelerations the performance of the proposed model is below that of the GMS model.

References

1. Armstrong-Hélouvry, B., Dupont, P., de Wit, C.C.: A survey of models, analysis tools and compensation methods for the control of machines with friction. Automatica **30**, 1083–1138 (1994)
2. Feng, B., Zhang, D., Yang, J., Guo, S.: A novel time-varying friction compensation method for servomechanism. Math. Probl. Eng. (2015). doi:10.1155/2015/269391
3. Al-Bender, F., De Moerlooze, K.: Characterization and modeling of friction and wear: an overview. Int. J. Sustain. Constr. Des. **2**, 19–28 (2011)
4. Lampaert, V. Modelling and control of dry sliding friction in mechanical systems. Ph.D. thesis, Katholieke Universiteit Leuven (2003)
5. Prajogo, T.: Experimental study of pre-rolling friction for motion-reversal error compensation on machine tool drive systems. Ph.D. thesis, Katholieke Universiteit Leuven (1999)
6. de Wit, C.C.: Olsson, H., Åström, K.J., Lischinsky, P.: A new model for control of systems with friction. IEEE Trans. Autom. Control **40**, 419–425 (1995)
7. Dupont, P., Hayward, V., Armstrong, B., Altpeter, F.: Single state elastoplastic friction models. IEEE Trans. Autom. Control **47**, 787–792 (2002)
8. Swevers, J., Al-Bender, F., Ganseman, C.G., Prajogo, T.: An integrated friction model structure with improved presliding behavior for accurate friction compensation. IEEE Trans. Autom. Control **4**, 676–686 (2000)
9. Al-Bender, F., Lampaert, V., Swevers, J.: The generalized Maxwell-Slip model: a novel model for friction simulation and compensation. IEEE Trans. Autom. Control **50**, 1883–1887 (2005)
10. Boegli, M., De Laet, T., De Schutter, J., Swevers, J.: Moving horizon for friction state and parameter estimation. In: Proceedings of the 2013 European Control Conference, pp. 4142–4147. Zurich (2013)
11. Boegli, M., De Laet, T., De Schutter, J., Swevers, J.: A smoothed GMS friction model suited for gradient-based friction state and parameter estimation. IEEE/ASME Trans. Mechatron. **19**, 1593–1602 (2014)
12. Villegas, F., Hecker, R., Peña, M.: Two-state GMS-based friction model for precise control applications. Int. J. Precis. Eng. Manuf. **17**, 553–564 (2016)
13. Lu, L., Yao, B., Wang, Q., Chen, Z.: Adaptive robust control of linear motors with dynamic friction compensation using modified LuGre model. Automatica **45**, 2890–2896 (2009)
14. Villegas, F., Hecker, R., Peña, M., Vicente, D., Flores, M.: Modeling of a linear motor feed drive including pre-rolling friction and aperiodic cogging and ripple. Int. J. Adv. Manuf. Technol. **73**, 267–277 (2014)

Design of a Robotic Speech-to-Sign Language Transliterating System

E. López-Zapata(✉), M. Campos-Trinidad, R. Salazar-Arévalo, and J. Acostupa-Del Carpio

National University of Engineering, Lima, Peru
edlopez96s6@gmail.com, mjcampost4l96@gmail.com, ressar0702@gmail.com, jjacostupa@gmail.com

Abstract. The present paper shows the work done on the design of a robotic humanoid arm, whose objective is to perform the transliteration of sound language, commonly used, to sign language, used by people with hearing disabilities. It is proposed the use of a screw, coupled to hydraulic transmission, to act on a pullets system on each finger and not keep the motor energized. Through a dynamic analysis it has been obtained the necessary torque for each joint in the arm to perform the correct movement of the servo motors. In addition to this, a script has been made in order to do some tests for speech-recognition and an Android application as a tool for an easier way to process it.

Keywords: Robotics · Speech recognition · Transliteration

1 Introduction

From the WHO (World Health Organization) terminology on disability, the group of people with decreased hearing capacity can be restricted in two groups. The first consists of people with hearing impairment, with a reduced hearing capacity that does not affect their life significantly. Then, the second group consists of people who need constant help on their daily living activities. This group is conformed of people with hearing disability.

Hearing impairment exists because both congenital and acquisition causes (WHO). In a related research, [1] it is mentioned that the percentage of hearing disability is 5% of the world population (World Disability Report). The percentage of hearing impairment is 0.8% of the Peruvian population. This is approximately 255,000 Peruvians according to INEI (National Institute of Statistics and Informatics, by its acronym in Spanish).

Given this, a need to reduce the communication gap between people with hearing disabilities and the majority of the population that uses voice-based language is raised. For this purpose, CONADIS (National Council for the Integration of Peoples with Disabilities, by its acronym in Spanish) suggests the implementation of a humanoid robotic system that allows the interpretation of the voice language of a sign language and vice versa. The present paper shows the progress obtained in the design of the proposed arm.

J.C.M. Carvalho et al. (eds.), *Multibody Mechatronic Systems*,
Mechanisms and Machine Science 54, DOI 10.1007/978-3-319-67567-1_26

2 Kinematic Analysis

In this section, the forward and inverse kinematics of the designed arm will be performed.

2.1 Forward Kinematics

The forward kinematics problem is concerned with the relationship between the joints of the robot manipulator and the position and orientation of the tool or end-actuator. A common proceeding for selecting frames of reference in robotic applications is the Denavit-Hartenberg convention, where each homogeneous transformation A_i is represented as a product of four basic transformations as Eq. (1) shows [2].

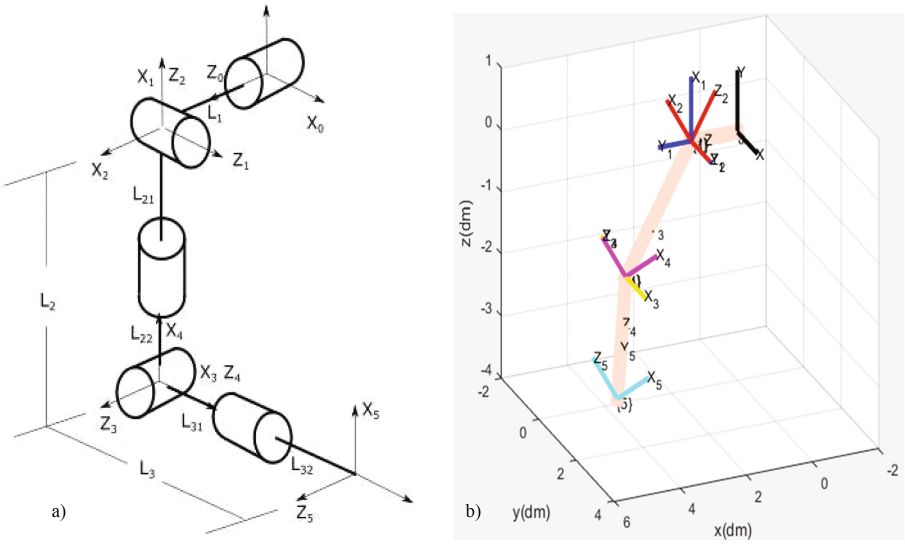

Fig. 1. Simulated model of the robotic arm.

The robotic system is represented in Fig. 1a, where the second and fourth coordinate frames has been attached to the previous one in order to do a good configuration of the parameters for the Denavit-Hartenberg convention. The simulated model can be observed in Fig. 1b, where it can be appreciated how the whole system is composed.

$$A_i = Rot_{z,\theta_i} Trans_{x,d_i} Trans_{x,a_i} Rot_{x,\alpha_i} \tag{1}$$

2.2 Inverse Kinematics

When performing inverse kinematics, different angular configurations that satisfy the condition of getting to the desired coordinate points become available. To solve this problem, it is necessary to make some restrictions. First, Eq. 2 calculates $\boldsymbol{\theta}_1$.

$$\theta_1 = tan^{-1}(-\frac{Y_0}{Z_0}) \tag{2}$$

The next task is to find the angles θ_2 and θ_4. Figure 2a helps to have an idea of the configuration of the arm in the new plane. The front view of the plane X_1Z_1 is shown in Fig. 2b.

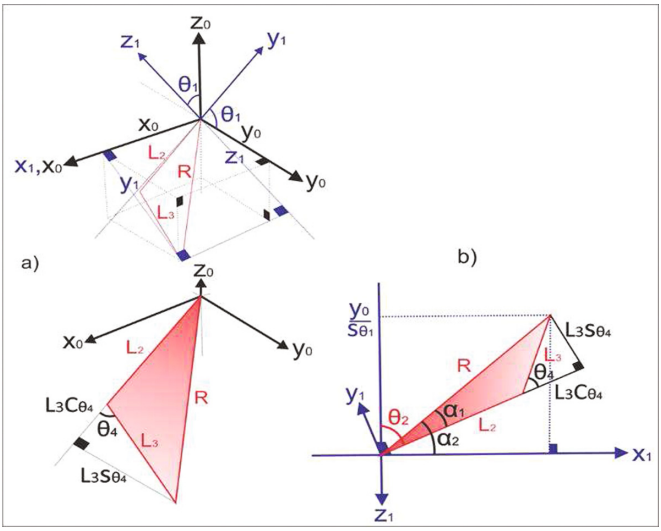

Fig. 2. (a) Inverse kinematic. (b) Front view of the plane X_1Z_1

With this view, the existing geometric relations can be applied (Eq. 3).

$$\begin{gathered} R^2 = L_2^2 + L_3^2 + 2L_2L_3cos\theta_4 \quad cos\theta_4 = \frac{R^2 - L_2^2 - L_3^2}{2L_2L_3} = D \\ \theta_4 = tan^{-1}(\pm\frac{\sqrt{1-D^2}}{D}) \end{gathered} \tag{3}$$

The sign will allow to choose between elbow up (+) or down (−) (Eq. 4).

$$\begin{gathered} \alpha_1 = tan^{-1}(\frac{L_3 \sin\theta_4}{L_3\cos\theta_4 + L_2}) \quad \alpha_2 = tan^{-1}(\frac{X_1}{Z_1}) \\ \theta_2 = \pi - (\alpha_1 - \alpha_2) \end{gathered} \tag{4}$$

The angles θ_3 and θ_5 are not relevant to define the final position.

3 Dynamic Analysis

Two subsystems were considered: one for the hand, which shows the movement of the fingers, and the other for the arm, which involves since the shoulder to the wrist.

3.1 Hand

The proposed model of a hand has 3 degrees of freedom for the index, middle, ring and pinky fingers, as shown in Fig. 3a. For the thumb, 2 links and an additional degree of freedom are proposed.

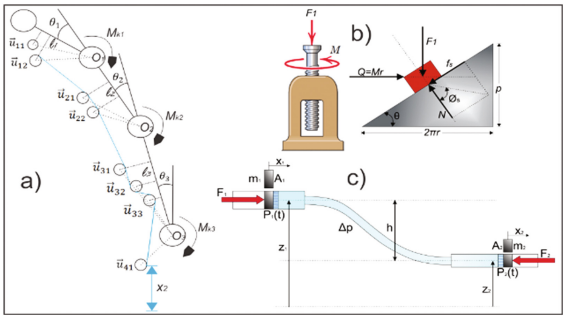

Fig. 3. Schemes design (a) System of pulleys (b) Worm screw (c) Hydraulic transmission system

The actuation of each finger is carried out by a worm screw (Fig. 3b), which rotates piston 1 and piston 2 by means of fluid (Fig. 3c) to finally get movement in the system of pulleys installed on each finger (Fig. 3a).

From Fig. 3b, the amount of the torque M necessary to move a load of weight F_1, can be obtained, depending on the average radius of the thread (using + sing in Eq. 5). But whenever the angle $\emptyset_s$ is greater than θ, the screw will remain in its position without needing a torque. In order to return the load, a torque of less intensity in the opposite direction is necessary (using – sign in Eq. 5) [3].

$$M = F_1 r \tan\left(\emptyset_s \pm \theta\right) \tag{5}$$

By using Newton's law in the plunger and conservation of energy in the fluid, some differential equations can be obtained (considering $A_1 = 2A_2$) [4].

The results of solving these equations will be the velocity at which the finger must be actuated and is shown in Eq. 6.

$$\dot{x}_2(t) = \sqrt{\frac{k_3}{k_2}}\left(\frac{10^{\sqrt{k_2 k_3}t} - 1}{10^{\sqrt{k_2 k_3}t} + 1}\right) \tag{6}$$

$$k_1 = \frac{2m_2}{m_1}\; k_2 = \frac{3k_1A_2\gamma}{4m_2g(2k_1+1)} \quad k_3 = \frac{k_1A_2F_1 - k_1A_1F_2 + k_1A_1A_2h_p\gamma}{m_2(k_1A_1 + A_2)}$$

The speed was obtained by numerical derivation of 4 Taylor terms of a real data obtained by image processing and was compared with the speed of Eq. 6 (Fig. 4).

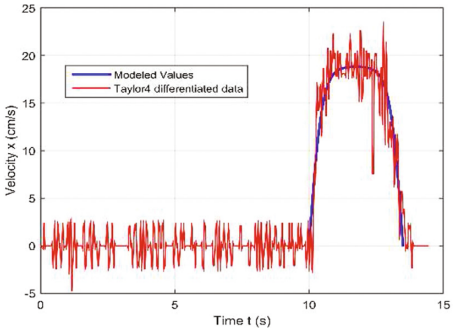

Fig. 4. Comparison of the model and the Tylor terms

Finally, the force F_2 will be transmitted in the system of pulleys, generating a tension of the same magnitude in all the points. In each case, crossed and normal pulleys, the direction of the force will be obtained by working on its respective coordinate system by a rotation matrix. Then, the restituting moment is calculated for each link, according to our geometric arrangement (Fig. 5).

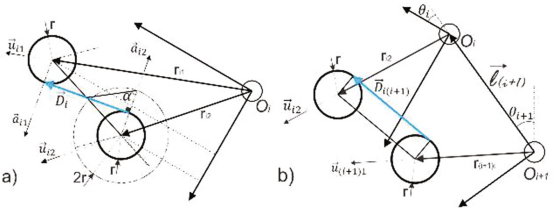

Fig. 5. Scheme of the fingers dynamics. (a) Crossed pulleys (b) Normal pulleys

3.2 Arm

Euler-Lagrange equations, because of its mechanical and computational scalability for complex systems, have been used for this study to get the dynamic model. Equation 7 shows how to form the Lagrangian of a system, which is necessary to determinate the Euler-Lagrange equations [2].

$$\mathcal{L} = K - P = \mathcal{L}\left(q_{(t)}, \dot{q}_{(t)}\right), K = \sum_{i=1}^{k} \frac{1}{2}\left(v_i^T m_i v_i\right) + \frac{1}{2}\left(\omega_i^T I_i \omega_i\right), P = -\sum_{i=1}^{k} g^T r_{ci} m_i \quad (7)$$

Then the Lagrange equation is (Eq. 8):

$$\frac{d}{dt}\left(\frac{\partial L}{\partial \dot{q}_i}\right) - \frac{\partial L}{\partial q_i} = \tau_i(t); 1 \leq i \leq 5 \tag{8}$$

Being the Lagrange equation in matrix form (Eq. 9):

$$\tau(t) = D(q)\ddot{q} + C(q, \dot{q})\dot{q}(t) + g(q) \tag{9}$$

4 3D Design

In the design of humanoid hands and hand prostheses there is usually a mechanism that requires a motor to be permanently fed in order to maintain a fixed position of the fingers [4]. Because of this, a power screw feed mechanism is proposed, which uses the qualities of friction to transmit a torque and keep it without the need to maintain it.

In this type of systems, standard ACME threads are used due to their easy machining. However, with the use of CAD software and a 3D printer, ABS high resistance parts for small non-industrial systems can be designed and obtained.

The load will be transmitted by means of a fluid, in this case, water. This will take advantage of Pascal's principle to take better advantage of the high load that can be handled and convert part of it into speed. In addition, this will allow to locate the actuator at convenience. The only drawback would be the manufacture of the pistons. However, it is preferred to use #3 and #5 syringes and a 4 mm pneumatic tubing.

The power screw assembly takes into consideration the resistance of the ABS in the screw overhang, the ratio of angles for anti-return and the necessary advance in the piston system (Fig. 6a).

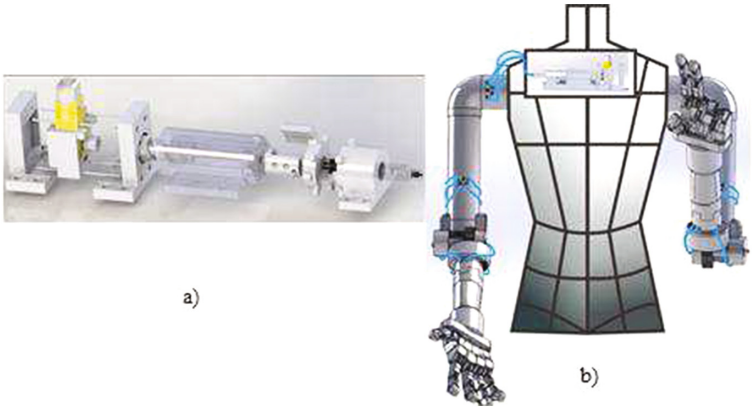

Fig. 6. (a) 3D Design (b) Exploded view of the power screw assembly

Finally, Fig. 6b shows the 3D design worked so far, it is appreciated that it is possible to use the space corresponding to the trunk to locate the actuator screws and their respective controllers.

5 Speech Recognition

In this section, we will describe the technique applied for speech recognition.

5.1 Speech Recognition Software

A first script for speech-recognition was developed in MatLab. This script consists of a records an audio sample and chooses from a small database the best fitting word by means of a simplified algorithm inspired in the Linear Predictive Coding (LPC) [5].

The script was trained with a small database of ten different words, which are the numbers from 0 to 9 in Spanish. In the following table, the results of a brief testing is shown (Table 1).

Table 1. Accuracy of the LPC speech recognition system developed in Matlab

Word	Accuracy (%)	Number of samples	Accuracy (%)
0 'Cero'	85.19	5 'Cinco'	96.00
1 'Uno'	100.00	6 'Seis'	64.00
2 'Dos'	96.15	7 'Siete'	100.00
3 'Tres'	72.00	8 'Ocho'	96.00
4 'Cuatro'	84.00	9 'Nueve'	96.00

The testing shows an overall accuracy of 88.93%. Most of the errors came from words that share a similar intonation. It was also observed that this system is heavily affected by external noise. This result is a milestone that must be surpassed by other software alternatives considered for this project.

A demo of an Android app that listens in real time and gives text output using the Google Speech Recognition API® was mad. On the final version, this app will recognize each word and communicate with the processing unit, which will store the sign language database.

5.2 Acquisition of Data for Sign Language Movement

The database which will contain information about the position and orientation of the arms and the fingers.

For the arms, a motion capture platform was created. For the calculation of the trajectory, the linear acceleration on each axis of the accelerometer must be obtained. However, the readings have also a gravity component, which has to be filtered. For this we will use Euler angles, obtained from the gyroscope (Eq. 10).

$$R = \begin{bmatrix} c\theta c\psi & s\phi s\theta c\psi - c\phi s\psi & c\phi s\theta c\psi + s\phi s\psi \\ c\theta s\psi & s\phi s\theta s\psi + c\phi c\psi & c\phi s\theta s\psi - s\phi c\psi \\ -s\theta & s\phi c\theta & c\phi c\theta \end{bmatrix} \tag{10}$$

Where ψ, θ *and* ϕ are the yaw, pitch and roll angles respectively (Fig. 7).

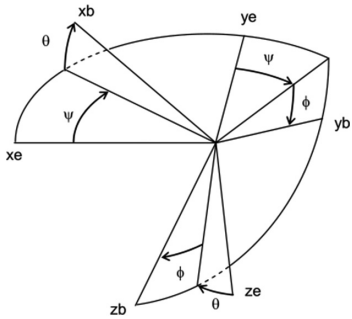

Fig. 7. Illustration of the orientation angles [6]

Once the rotational matrix is calculated, it is possible to estimate and remove the gravity component from the accelerometer readings (Eq. 11).

$$\bar{a}_l = R^T \bar{a}_{acc} + \bar{g} \tag{11}$$

Where $\bar{a}_l$ is the linear acceleration, R^T is the transpose of the rotational matrix, $\bar{a}_{acc}$ is the vector measured with the three-axis accelerometer and $\bar{g}$ is the gravity vector measured in the reference frame of the ground ($-9.81\ \hat{k}$ was used).

With the linear acceleration, the velocity and position of the sensor is calculated through numerical integration. Using a sample rate of 40 Hz, an example of a calculated trajectory is shown in Fig. 8.

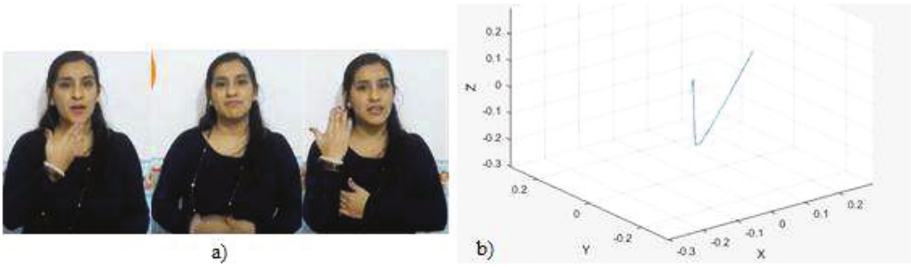

Fig. 8. Expression 'Good Morning' (a) Real gesture in the Peruvian sign language. (b) Trajectory obtained with the inertial sensors of a smartphone

It is expected to complete a database of 200–300 words for the Peruvian sign language. Is also possible to build similar databases for other sign languages. In the future is also planned to redo the process with an Inertial Measurement Unit (IMU) in order to improve accuracy.

6 Conclusions

Our design uses 3D printing to manufacture hard machined parts, which allow a mechanical locking system to be used to reduce energy consumption. For the movement of the fingers the number of variables to be controlled from 3 angles of each phalanx to an angle of rotation in the motor was reduced by means of the use of conductive pulleys and hydraulic transmission.

A mobile app will be used for real-time speech recognition. A database for hand-sign language will be built using motion capture for the arms movement, and manual input in a transcripting software for the hand shapes.

References

1. Ahmed, M., Idrees, M., Abideen, Z., Mumtaz, R., Khalique, S.: Deaf talk using 3D animated sign language, a sign language interpreter using Microsoft's Kinect. IEEE SAI Comput. Conf. **2016**, 330–335 (2016)
2. Spong, M., Hutchinson, S., Vidyasagar, M.: Robot Modeling and Control, pp. 65–100, 187–215. Wiley, New York (2006)
3. Meriam, J.: Engineering Mechanics Statics, pp. 58–360. Wadsworth, Belmont (2006)
4. Diaz, J., Dorador, J.: Mecanismos de transmisión y actuadores utilizados en prótesis de mano. In: Memorias del XV Congreso internacional anual de la SOMIM, pp. 335–345 (2009)
5. O'Shaughnessy, D.: Linear predictive coding. In: IEEE ponentials, pp. 29–32 (2002)
6. Premerlani, W., Bizard, P.: Direction Cosine Matrix IMU: Theory, p. 8 (2009)

Modelling and Simulation

Robust Critical Inverse Condition Number for a 3RRR Robot Using Failure Maps

Hiparco Lins Vieira(✉), João Vitor de Carvalho Fontes, Andre Teófilo Beck, and Maíra Martins da Silva

São Carlos Engineering School, University of São Paulo, Av. Trab. São-Carlense, 400 - Pq Arnold Schimidt, São Carlos, SP 13566-590, Brazil
{hiparcolins,fontesjvc}@usp.br, {atbeck,mairams}@sc.usp.br

Abstract. Industrial manipulators must be robust with regard to manufacturing tolerances and uncertainties. This paper presents a study of the effects of geometrical uncertainties of a planar parallel manipulator on its kinematic performance and robustness, regarding possible failures. The parallel manipulator under study is a 3RRR, which is composed of a single end-effector connected to the ground by three identical kinematic chains. Each kinematic chain is composed of two passive and one active revolute joints. Among others, parallel manipulators may suffer from two important failures: when the end-effector reaches (i) the workspace's limitation and (ii) a singular region. Both failures can be assessed by calculating the inverse of the condition number of the Jacobian matrix. In order to evaluate geometrical uncertainties, a Monte Carlo simulation is performed to estimate the probability of both types of failures. Failure Maps are depicted by plotting the probability of failure on the workspace, exhibiting the most affected regions. Based on this information, a robust inverse critical condition number is proposed. This information can be exploited for robustifying the control design and the motion planning of parallel manipulators.

Keywords: Parallel manipulators · Condition Number · Failure Maps · Monte Carlo simulation

1 Introduction

Whilst parallel manipulators (PKMs) can present higher dynamic performance [1], reach improved motion/force transmission rates [2] and be more energy efficient [3,4] than serial manipulators, the presence of singularities in their workspace can jeopardize its practical applicability. Strategies for dealing with this limitation have been addressed by the scientific community. Among them, one can highlight the exploitation of singularity-free paths [5,6] and the use of kinematic redundancies [7,8].

Considering the presence of singularities in the workspace of PKMs as an important drawback, the assessment of their existence is essential during their

J.C.M. Carvalho et al. (eds.), *Multibody Mechatronic Systems*,
Mechanisms and Machine Science 54, DOI 10.1007/978-3-319-67567-1_27

design. Singular regions should be avoided and considered during control design and motion planing of PKMs. Cha et al. [9] have concluded that the Condition Number (CN) of the Jacobian matrix can be used to evaluate the closeness of the end-effector and a singularity. In fact, while the $CN \rightarrow 1$ indicates that the end-effector is not near a singular configuration, $CN \rightarrow \infty$ indicates that the end-effector is close to singular regions.

Parametric uncertainties can be found in these manipulators due to their manufacturing process. These geometrical uncertainties may impact their performance. In this way, strategies for robustifying their performance require the assessment of the impact of relevant geometrical uncertainties. Few approaches for addressing this issue have been proposed in the literature. For instance, Merlet [10] developed and exploited Interval Analysis for studying uncertainties in robotics. Real applications were addressed by them. The main disadvantage of using Interval Analysis for evaluating the impact of uncertainties in the manipulator's performance is caused by the accumulation of the errors. Due to this issue, unrealistic intervals can be found [11]. This can be overcome by mathematically treating the equations [10], which might impose difficulties for this kind of study.

In this way, works on failures caused by uncertainties in robotics could bring relevant results to the field of mechanism and machine design. In this work, the main objective is to evaluate the impact of geometrical uncertainties on the failures due to singularities of a planar parallel manipulator, the 3$\underline{\text{R}}$RR. This manipulator, illustrated in Fig. 1, is composed of three identical kinematic chains with one active ($\underline{\text{R}}$) and two passive (RR) revolute joints. The proposed study is carried out by evaluating the CN under some possible geometrical uncertainties. The variability of the CN under these uncertainties can be approximated by a normal distribution according to Monte Carlo simulations. Using this fact, the probability of failure of a kinematic configuration can be calculated and depicted on the workspace.

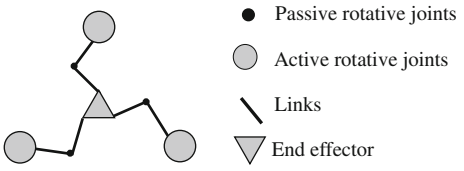

Fig. 1. Illustrations of the non-redundant manipulator 3$\underline{\text{R}}$RR.

The rest of the manuscript is organized as it follows. Sections 2 and 3 describe the kinematic model of the 3$\underline{\text{R}}$RR manipulator and the failure modes, respectively. Section 4 describes the methodology for evaluating the uncertainties and the probability of failure. Numerical results are discussed in Sect. 4. Conclusions are drawn in Sect. 5.

2 Kinematic Model

In this section, the kinematic model of a 3PRRR manipulator, illustrated in Fig. 2, is presented. This manipulator presents an extra active prismatic joint in each kinematic chain. By actuating these joints, the system became kinematically redundant [8]. In this work, the kinematic redundancies are not addressed. So, the kinematic model of the non-redundant manipulator 3RRR considers $\gamma_1 = 0$, $\gamma_2 = 120°$, $\gamma_3 = -120°$ and $\zeta_1 = \zeta_2 = \zeta_3 = 0$.

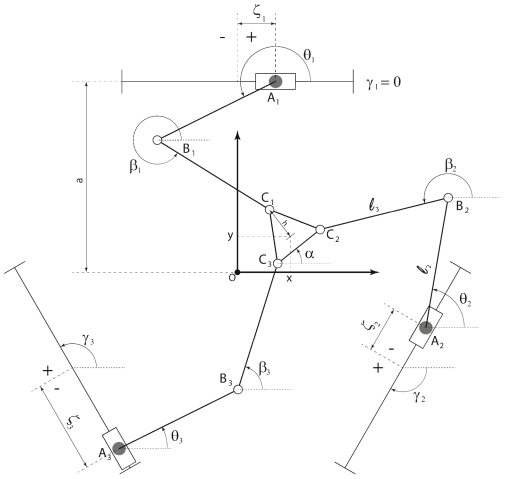

Fig. 2. Geometrical scheme of the 3PRRR manipulator

Using the inverse kinematic model one can calculate the active joints' inputs, $\mathbf{\Theta} = (\theta_1, \theta_2, \theta_3)$, for a given end-effector's pose (configuration), $\mathbf{X} = (x, y, \alpha)$. The parameter a represents the distance between the workspace center and the center of the linear guides. The distance of the center of the end-effector to C_i is h. The lengths of the links are given by l_{2i} (A_iB_i) and l_{3i} (B_iC_i), according to Fig. 2. The angles θ_i and β_i represent, respectively, the orientation of the links A_iB_i and B_iC_i. Since $\|r_{Ci} - r_{Bi}\| = l_{3i}$, θ_i can be related with x, y and α by the following geometrical constraint:

$$\left\| \begin{matrix} \rho_{xi} - l_{2i}\cos(\theta_i) \\ \rho_{yi} - l_{2i}\sin(\theta_i) \end{matrix} \right\| = l_{3i}^2, \tag{1}$$

where ρ_{xi} and ρ_{yi} can be found by:

$$\begin{bmatrix} \rho_{xi} \\ \rho_{yi} \end{bmatrix} = \begin{bmatrix} x \\ y \end{bmatrix} + h \begin{bmatrix} \cos(\alpha + \gamma_i \pm \frac{\pi}{2}) \\ \sin(\alpha + \gamma_i \pm \frac{\pi}{2}) \end{bmatrix} - a \begin{bmatrix} \cos(\gamma_i \pm \frac{\pi}{2}) \\ \sin(\gamma_i \pm \frac{\pi}{2}) \end{bmatrix}. \tag{2}$$

Using the definition of the Euclidean norm, Eq. 1 can be rearranged:

$$\rho_{xi}^2 + \rho_{yi}^2 + l_{2i}^2 - l_{3i}^2 - 2l_{2i}(\rho_{xi}\cos(\theta_i) + \rho_{yi}\sin(\theta_i)) = 0. \tag{3}$$

The active joints' inputs can be calculated by applying the Weierstrass Substitution to Eq. 3, yielding:

$$\theta_i = 2\arctan\left(\frac{-k_{i3} \pm \sqrt{k_{i2}^2 + k_{i3}^2 - k_{i1}^2}}{k_{i1} - k_{i2}}\right), \tag{4}$$

where

$$k_{i1} = \rho_{xi}^2 + \rho_{yi}^2 + l_{2i}^2 - l_{3i}^2, \tag{5}$$

$$k_{i2} = -2l_{2i}\rho_{xi}, \tag{6}$$

$$k_{i3} = -2l_{2i}\rho_{yi}. \tag{7}$$

And, β_i can be calculated by:

$$\beta_i = \arctan\left(\frac{\rho_{yi} - l_{2i}\sin(\theta_i)}{\rho_{xi} - l_{2i}\cos(\theta_i)}\right). \tag{8}$$

As aforementioned, the CN of the Jacobian matrix is a valuable information for identifying the singular regions. The Jacobian matrix $\mathbf{J}$ is obtained by the relation $\mathbf{J} = \mathbf{A}^{-1}\mathbf{B}$, where the matrices $\mathbf{A}$ and $\mathbf{B}$ are found by:

$$\mathbf{A}\dot{\mathbf{X}} = \mathbf{B}\dot{\mathbf{\Theta}}. \tag{9}$$

The singularities occur when matrices $\mathbf{A}$ and/or $\mathbf{B}$ are singular. These matrices can be calculated by taking the time derivation of the geometrical constraint given by Eq. 3, yielding:

$$\dot{x}l_{3i}\cos(\beta_i) + \dot{y}l_{3i}\sin(\beta_i) + \dot{\alpha}l_{3i}h\sin(\beta_i - \gamma_i - \alpha \pm \frac{\pi}{2}) = \dot{\theta}_i l_{2i} l_{3i}\sin(\beta_i - \theta_i). \tag{10}$$

This expression can be rewritten in the matrix format $\mathbf{A}\dot{\mathbf{X}} = \mathbf{B}\dot{\mathbf{\Theta}}$, yielding the following matrices:

$$\mathbf{A} = \begin{bmatrix} l_{31}\cos(\beta_1) & l_{31}\sin(\beta_1) & l_{31}h\sin(\beta_1 - \gamma_1 - \alpha \pm \frac{\pi}{2}) \\ l_{32}\cos(\beta_2) & l_{32}\sin(\beta_2) & l_{32}h\sin(\beta_2 - \gamma_2 - \alpha \pm \frac{\pi}{2}) \\ l_{33}\cos(\beta_3) & l_{33}\sin(\beta_3) & l_{33}h\sin(\beta_3 - \gamma_3 - \alpha \pm \frac{\pi}{2}) \end{bmatrix}, \tag{11}$$

$$\mathbf{B} = \begin{bmatrix} l_{21}l_{31}\sin(\beta_1 - \theta_1) & 0 & 0 \\ 0 & l_{22}l_{32}\sin(\beta_2 - \theta_2) & 0 \\ 0 & 0 & l_{23}l_{33}\sin(\beta_3 - \theta_3) \end{bmatrix}. \tag{12}$$

3 Failure Modes

In this section, details on the failure modes are given. Parallel manipulators may suffer from two important failures, when the end-effector reaches: (i) the workspace's limitation and (ii) a singular region. In this way, the definitions of workspace and singular regions are firstly given. Then, the failure modes are introduced.

3.1 3$\underline{\text{R}}$RR's Workspace

The 3$\underline{\text{R}}$RR workspace is determined by the union of all reachable configurations of the manipulator's end-effector [12,13]. For each chain, both outer and inner radii are defined by the maximum ($max|A_iD|$) and minimum ($min|A_iD|$) reachable distances, respectively. In this way, the workspace is delimited by ring-shape regions. The value of A_iD is determined by:

$$\overrightarrow{\mathbf{A_iD}} = l_{i2}\begin{bmatrix}\cos(\theta_i)\\ \sin(\theta_i)\end{bmatrix} + l_{i3}\begin{bmatrix}\cos(\beta_i)\\ \sin(\beta_i)\end{bmatrix} + h\begin{bmatrix}\cos(\alpha+30°)\\ \sin(\alpha+30°)\end{bmatrix}. \tag{13}$$

Subsequently, the ring-shape region of the ith chain is represented by RS_i. The 3$\underline{\text{R}}$RR workspace (WS) is obtained by the intersection between the three ring-shape regions of each kinematic chain. The nominal workspace is the set of all end-effector's reachable configurations built with the nominal parameter values.

3.2 Singularity Regions

The CN of the Jacobian matrix approaches infinity as the manipulator approximates a singularity [9]. Conversely, it approaches an unity value as the manipulator moves away from the singularities. The CN of a matrix $\mathbf{F}$ is the ratio between the maximum σ_{max} and minimum σ_{min} singular values of $\mathbf{F}$:

$$CN(\mathbf{F}) = \frac{\sigma_{max}}{\sigma_{min}}. \tag{14}$$

Alternatively, the inverse condition number (iCN) can also be used to the identification of singular regions. In singular configurations, $iCN = 0$. In fully isotropic positions, $iCN = 1$ [9]. This number can be calculated as the inverse of the CN:

$$iCN(\mathbf{F}) = \frac{1}{CN} = \frac{\sigma_{min}}{\sigma_{max}}. \tag{15}$$

Singularity regions in the workspace are related to the matrix $\mathbf{A}$ as discussed in [9]. As the $\mathbf{A}$ is not dimensionally homogeneous due to the presence of translational and rotational degrees of freedom, an evaluation of its iCN may provide imprecise results. To overcome this situation, $\mathbf{A}$ must be normalized, using the characteristic length L [14]. In [15], a convenient characteristic length is proposed for a 3$\underline{\text{R}}$RR manipulator, $L = \sqrt{2}h$. The normalized matrix $\overline{\mathbf{A}}$ is found by dividing the third column of $\mathbf{A}$ by L. In this work, the iCN of matrix $\overline{\mathbf{A}}$ is exploited for assessing the singularities inside of the manipulator's workspace.

3.3 Failure Modes

In order to define the failure modes, one should define a bound for the iCN. This bound is the limit where the end-effector's configuration can approach without

having any substantial decrease in its accuracy/performance. In this manuscript, this bound is defined as the critical inverse condition number ($CiCN$). Its value is task dependent. Moreover, due to uncertainties, the manipulator may present failure modes. Regarding geometrical uncertainties, two failure modes are investigated:

Failure (i) or WS Failure: happens when the real iCN is null ($iCN = 0$), i.e., when the end-effector reaches the workspace's limits or a singularity due to uncertainties.

Failure (ii) or iCN Failure: happens when the real iCN is greater than zero and lower or equal to the $CiCN$ ($0 < iCN \leq CiCN$), i.e., when the manipulator is not in a singularity, however, it violates the $CiCN$ due to uncertainties.

4 Methodology

This section presents the methodology for deriving the Failure Maps and the Robust Critical Inverse Condition Numbers ($RCiCN$), which identifies the value of iCN where the probability of failure is null.

As aforementioned, in this manuscript, the geometrical uncertainties of the length of the links are evaluated. The length of each link is assumed to present a Gaussian distribution. For evaluating the impact of these uncertainties at different end-effector's pose, the workspace was divided in a grid with p possible end-effector's positions (x, y). At every possible position, g possible end-effector's orientations (α) have been evaluated. In this way, a Failure Map is depicted for each end-effector's orientation. The values of p and g should be selected according to the task and accuracy's requirements. For each end-effector's position at the workspace's grid, a Monte Carlo simulation is performed with n_s simulations. This is done by randomly selecting the lengths of the six links, according to a probability distribution function.

Once the Monte Carlo algorithm is finished, a great amount of data is obtained. Since the failure probability depends on the $CiCN$ value, its impractical to access all data and compute the failure probabilities when the task and the $CiCN$ change, especially in real-time applications. Thus, an alternative is to fit the data by a probability distribution function.

Figure 3 shows the histogram of the iCN for a given end-effector's pose ($x = 0.15$ m, $y = 0.15$ m e $\alpha = \pi/3$). The occurrences of $iCN = 0$ illustrate the incident of WS Failure. The occurrences of $0 < iCN \leq CiCN$, the iCN Failure, follow a probability distribution function, similar to a Gaussian distribution. The iCN and WS Failures are depicted in Fig. 3.

The probability of the occurrence of the WS failure, P_{WS}, can be calculated for each position at the grid by the ratio between c_{wsf} and n_s, where c_{wsf} is the number of simulations in which $iCN = 0$. The probability of the occurrence of a iCN Failure, P_{iCN}, can be calculated by:

$$P_{iCN} = (1 - P_{WS}) \int_0^{CiCN} f(x)dx, \tag{16}$$

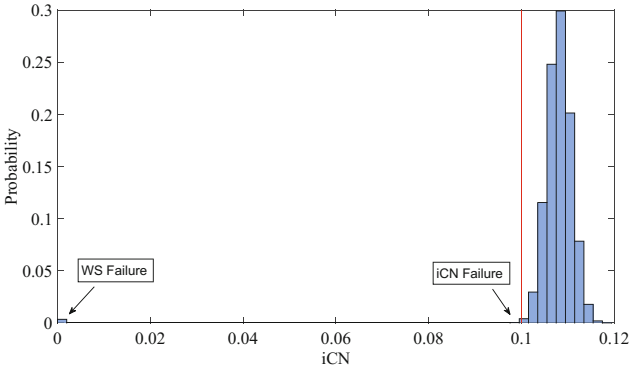

Fig. 3. The occurrences of WS Failure and iCN Failure. The red line represents the CiCN. (Color figure online)

where $f(x) = \frac{1}{\sigma\sqrt{(2\pi)}} e^{-\frac{1}{2}(\frac{x-\mu}{\sigma})^2}$ is a probability distribution function that describes the distribution of the iCN Failure. In our simulations, the Gaussian distribution provided good results for the failure probability. For each position of the grid at the workspace, it presents a mean μ and a standard deviation σ. The probability of failure P_f for both failure modes for each position at the grid is obtaining by:

$$P_f = P_{WS} + P_{iCN}. \tag{17}$$

While the Gaussian distribution is comprehended in the interval $]-\infty, +\infty[$, the iCN varies from 0 to 1. Thus, an approximation error is resulted from Eq. 16, since the distribution's tails were neglected. However, in approximately 98.3% of all configurations, this error was insignificant. In the remaining samples, where the error was not superior to 0.10, the term $(1 - P_{WS})$ was so small that the probability of failure P_f had no significant changes. Failure Maps are depicted by plotting P_f at each position at the grid on the workspace. The precision of the failure probability is directly related with n_s. As n_s approaches infinity, the WS failure probability approaches to its exact value.

5 Numerical Results

The manipulator's nominal parameters are $l_{i2} = 0.191$ m, $l_{i3} = 0.232$ m, $h = 0.0597$ m and $a = 0.2598$ m. The random variables l_{i2} and l_{i3}, $i = 1, 2, 3$, are sampled according to two Gaussian distributions: $\mathcal{N}(0.191, 0.0006)$ and $\mathcal{N}(0.232, 0.0006)$, respectively. The grid was built using $g = 5$ and $p = 0.005$ m. In this way, the grid had 108×108 positions. Five orientation values, α, were investigated $-30°$, $-15°$, $0°$, $15°$ and $30°$. During the Monte Carlo simulations, $40,000$ different combinations of the links' length for each position at the grid were evaluated. The $CiCN$ was defined as 0.1.

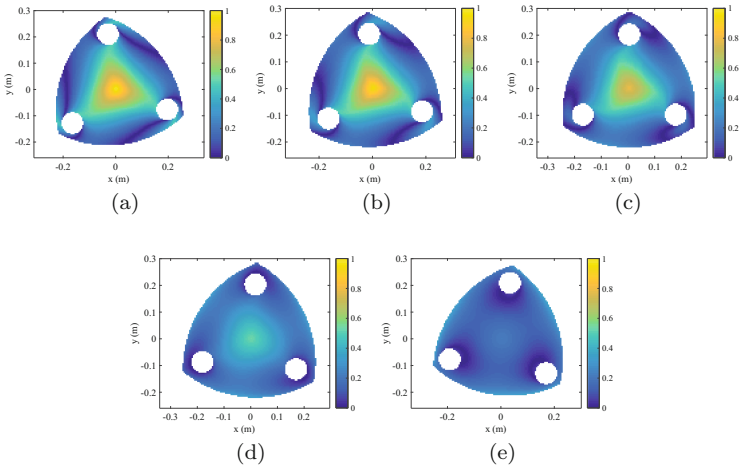

Fig. 4. The iCN maps for different values of α: (a) $\alpha = -30^o$, (b) $\alpha = -15^o$, (c) $\alpha = 0^o$, (d) $\alpha = 15^o$ and (e) $\alpha = 30^o$

Figure 4 shows the values of iCN for each position at the grid on the workspace, the iCN Map. For each value of α, a map is depicted. The iCN values were calculated using the nominal parameters. The three circles in the workspace represent unreachable regions. One can observe that higher values of iCN are located in the center of workspace. The regions with lower values of iCN are represented in dark blue. Another interesting aspect is the contribution of α to the iCN map. For instance, the regions with low values of iCN of the maps for $\alpha = -30^o$ (Fig. 4(a)) and for $\alpha = 30^o$ (Fig. 4(e)) are located in different regions of the workspace.

Figure 5 depicts the Failure Maps, considering both WS and iCN Failures, for several values of α. It is possible to note that some configurations are very sensitive to the geometrical uncertainties. In fact, some of them present $P_f > 0.5$. The comparison between the iCN Maps and the Failure Maps, Figs. (4 and 5), shows that the probability of failure is higher near singular regions.

The definition of a Robust Critical Inverse Condition Number, denoted as $RCiCN$, can be useful during the design of control systems and planning the execution of trajectories. This number reveals the regions that are free of any kind of failure. The $RCiCN$ can be found by identifying the maximum iCN value for all configurations that present any kind of failure during the Monte Carlo simulations. Considering that, configurations with $iCN > 0.5311$ are free of the WS Failure and $iCN > 0.5310$ are free of the iCN Failure. In this case, one can define that the $RCiCN = 0.5311$. One should notice that the $RCiCN$ depends on the number of investigated configurations. As the number of possible configurations and the Monte Carlo samples approach infinity, the $RCiCN$ approaches its exact value.

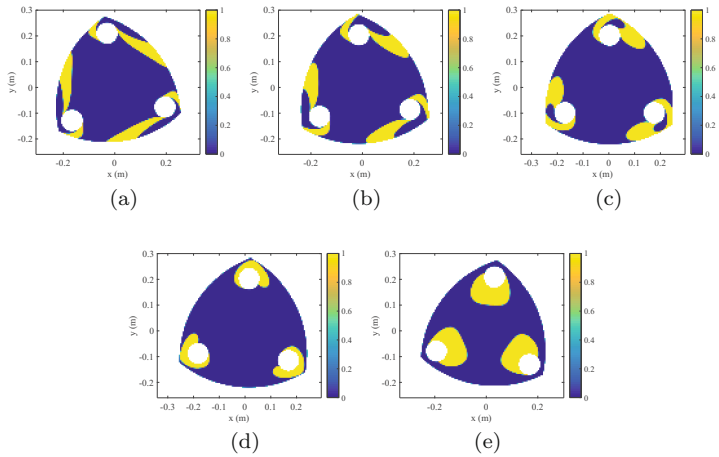

Fig. 5. Failure maps for different values of α. (a) $\alpha = -30^o$, (b) $\alpha = -15^o$, (c) $\alpha = 0^o$, (d) $\alpha = 15^o$ and (e) $\alpha = 30^o$.

6 Conclusions

This paper presented a method for determining a robust critical condition number for a planar parallel manipulator under geometrical uncertainties based on Failure Maps. A Monte Carlo simulation is performed to evaluate the impact of the geometrical uncertainties in the 3$\underline{\text{R}}$RR manipulator's conditioning. Two failure modes were considered: when the end-effector reaches (i) the workspace's limits or singularities and (ii) singular regions. The mathematical approach for assessing both failures was described. By plotting the probability of a failure on the workspace, Failure Maps can be depicted, showing that the regions with higher failure probability are located between well and ill-conditioned regions. Moreover, a robust critical condition number was computed for each failure mode. This information can be exploited for robustifying the control design and the motion planning of parallel manipulators.

Acknowledgements. This research is supported by FAPESP 2014/01809-0. Moreover, Joao V.C. Fontes and H.L. Vieira are grateful for their CNPq grants.

References

1. Fontes, J.V., da Silva, M.M.: On the dynamic performance of parallel kinematic manipulators with actuation and kinematic redundancies. Mech. Mach. Theor. **103**, 148–166 (2016). http://dx.doi.org/10.1016/j.mechmachtheory.2016.05.004
2. Xie, F., Liu, X.J., Wang, J.: Performance evaluation of redundant parallel manipulators assimilating motion/force transmissibility. Int. J. Adv. Robot. Syst. **8**(5) (2016). http://dx.doi.org/10.5772/50904

3. Li, Y., Bone, G.M.: Are parallel manipulators more energy efficient? In: Proceedings 2001 IEEE International Symposium on Computational Intelligence in Robotics and Automation (Cat. No.01EX515), pp. 41–46 (2001). http://dx.doi.org/10.1109/CIRA.2001.1013170
4. Ruiz, A.G., Fontes, J.V.C., da Silva, M.M.: The influence of kinematic redundancies in the energy efficiency of planar parallel manipulators. In: ASME International Mechanical Engineering Congress and Exposition, No. IMECE2015-50278. http://dx.doi.org/10.1115/IMECE2015-50278
5. Dash, A.K., Chen, I-M., Yeo, S.H., Yang, G.: Singularity-free path planning of parallel manipulators using clustering algorithm and line geometry. In: Proceedings in ICRA 2003 IEEE International Conference on Robotics and Automation, vol. 1, pp. 761–766. http://dx.doi.org/10.1109/ROBOT.2003.1241685
6. Bohigas, O., Henderson, M.E., Ros, L., Manubens, M., Porta, J.M.: Planning singularity-free paths on closed-chain manipulators. IEEE Trans. Robot. **29**(4), 888–898 (2013). http://dx.doi.org/10.1109/10.1109/TRO.2013.2260679
7. Kotlarski, J., Heimann, B., Ortmaier, T.: Influence of kinematic redundancy on the singularity-free workspace of parallel kinematic machines. Front. Mech. Eng. **7**(2), 120–134 (2012). http://dx.doi.org/10.1016/10.1007/s11465-012-0321-8
8. Santos, J.C., Frederice, D., Fontes, J.V.C., da Silva, M.M.: Numerical analysis and prototyping details of a planar parallel redundant manipulator. In: 12th Latin American Robotics Symposium and 3rd Brazilian Symposium on Robotics (LARS-SBR), pp. 55–60 (2015). http://dx.doi.org/10.1109/LARS-SBR.2015.30
9. Cha, S.H., Lasky, T.A., Velinsky, S.A.: Determination of the kinematically redundant active prismatic joint variable ranges of a planar parallel mechanism for singularity-free trajectories. Mech. Mach. Theor. **44**(5), 1032–1044 (2009). http://dx.doi.org/10.1016/j.mechmachtheory.2008.05.010
10. Merlet, J.P.: Interval analysis and robotics. In: Robotics Research. Springer Tracts in Advanced Robotics, vol. 66, 147–156
11. Bastos, R.F., Fontes, J.V.C., da Silva, M.M.: Interval kinematic and dynamic analysis of a planar parallel kinematic manipulator. In: Proceedings of Third International Symposium on Uncertainty Quantification and Stochastic Modeling, UNCERTAINTIES 2016, So Sebastião (2016)
12. Wu, J., Zhang, B., Wang, L.: A measure for evaluation of maximum acceleration of redundant and nonredundant parallel manipulators. J. Mech. Robot. **8**(2), 021001-021001-8 (2015). http://dx.doi.org/10.1115/1.4031500
13. Gosselin, C., Angeles, J.: Singularity analysis of closed-loop kinematic chains. IEEE Trans. Robot. Autom. **6**(3), 281–290 (1990). http://dx.doi.org/10.1109/70.56660
14. Mohammadi, H.R., Zsombor-murray, P.J.D., Angeles, J.: The isotropic design of two general classes of planar parallel manipulators. J. Robot. Syst. **12**(12), 795–805 (1995). http://dx.doi.org/10.1002/rob.4620121204
15. Alba-Gomez, O., Wenger, P., Pamanes, A.: Consistent kinetostatic indices for planar 3-DOF parallel manipulators, application to the optimal kinematic inversion. In: ASME International Design Engineering Technical Conferences and Computers and Information in Engineering Conference: 29th Mechanisms and Robotics Conference, Parts A and B, vol. 7, pp. 765–774. doi:10.1115/DETC2005-84326

Simulation of a Serial Robot Calibration Through Screw Theory

L.K. Kato(✉), T.L.F.C. Pinto, H. Simas, and D. Martins

Federal University of Santa Catarina, Florianópolis, Brazil
lucaskkato@gmail.com, tiago.tlp@gmail.com,
{henrique.simas,daniel.martins}@ufsc.br

Abstract. Robot manipulators are essential in tasks in which speed, accuracy and repeatability are required. As the increasing of data needed (end effector posture, speed and acceleration) to complete a specific task, the robot offline programming is necessary. But, the biggest issue around these procedures is the difference between the nominal robot model and the real one. So, the calibration of these kinds of mechanisms is important. This paper presents an alternative way to represent the kinematic model through screw theory and its calibration, considering joint offsets and link deviation. The simulation result shows, for each kinematic parameter, values which reduce the end effector posture error of a serial manipulator.

Keywords: Robot calibration · Screw theory · Robot clearances · Link deviation · Robot screw kinematic model

1 Introduction

Robot manipulators can be programmed in two ways: online and offline programming. The first procedure is used by 90% of industrial robots, which position and orientation accuracy is not relevant comparing to its repeatability, according to [16]. The second procedure is based on simulating robot postures in terms of its kinematic model. Unfortunately, the nominal model is different from the real, because of geometric and non-geometric errors in the mechanism [12].

Geometric errors are caused by joint and link offsets. The first is related to the difference between joint transducer information and actual joint angle displacement. The second is related to manufacturing errors. Non-geometric errors are caused by joint and link compliance, clearance, backlash and friction. Among all of these error causes, the geometric errors are responsible for 95% of the robot posture errors [6, 12]. To reduce the end effector (EE) slop, a calibration procedure can be made.

Robot calibration consists in estimate kinematic model parameter to reduce posture deviances caused by joint and link errors [27]. This process is fragmented in four steps: Modeling, measurement, estimation and implementation [6, 12–14].

- **Modeling**
  The kinematic model is commonly formulated by Denavit-Hartenberg (DH) convention [1, 13, 14, 19, 21, 27], but the screw based model has some advantages over

J.C.M. Carvalho et al. (eds.), *Multibody Mechatronic Systems*,
Mechanisms and Machine Science 54, DOI 10.1007/978-3-319-67567-1_28

DH convention as described in [17]. The base frame can be located arbitrarily, and the Jacobian is formed by normalized screws directly after the Rodrigues parameters identification [4, 23].
While clearances, joint offsets and link tolerances are represented as variations in DH parameters, in a screw model, they can be considered as virtual joints of revolute or prismatic kinematic pairs [11].

- **Measurement**
  In this step, a contact or noncontact measurement machine is used to get the EE posture with high accuracy. The most common contact equipment is the coordinate measuring machine with cartesian or anthropomorphic (measuring arm) configuration. The noncontact ones have many varieties, like laser tracker, laser scanner, cameras and indoor positioning systems [15].
  At the stage of this work a measure machine was not used, instead, a simulation of robot postures was implemented with joint and link offset. Also, as there are infinities robot configuration for measurements possibilities and the identification parameters depend on them, optimal measurement configurations are interesting to consider. Some researchers have already done this analysis [10, 14] for a 6° of freedom anthropomorphic robot based on optimality conditions [22]. The result of Klimchik [10] was implemented in this work.
  The set of data obtained by forward kinematic is applied to the next step to estimate kinematic parameters.
- **Estimation**
  In the first simulation step, the postures are generated considering predefined systematic and random errors for revolute virtual joints and only systematic errors for prismatic virtual joints. The systematic errors represent a fixed deviation in joint variables, caused by the robot home position readings by encoders and link manufacturing errors. The random ones, for joints, represent those errors sources which change along the robot movement and for different configurations, like joint compliance, clearance, backlash and friction. For links, these random errors represent link compliance caused by thermal and gravitational effects, which was not considered in this work.
  After the error posture acquisition the kinematic parameters can be estimated through linear or non-linear least square minimization [4].
- **Implementation or correction**
  After the parameter identification the robot posture is corrected changing its kinematic parameter in controller, compensating joint variables or the desired path [24, 26]. This step is implemented on forward kinematic simulation.

2 Kinematic Robot Modeling

The first step for the calibration simulation is defining the robot kinematic model. A serial robot with 6 revolute joints is modeled with joint and link offset as illustrated in Fig. 1.

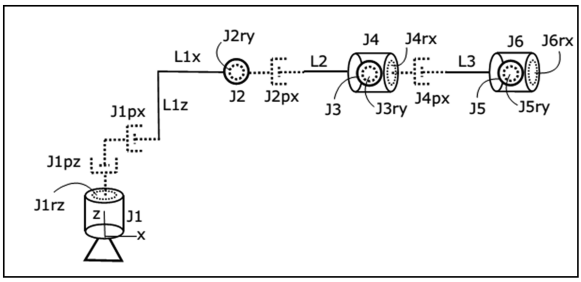

Fig. 1. 6R spatial robot with joint and link offsets

Each joint has its angular offset and its consecutive link offset. For joint 1 the notation J1rz represents a revolute virtual joint in z axis and J1pz, a prismatic virtual joint in z axis, while J1 is the nominal joint representation.

For the EE posture simulations, a set of robot configuration is defined first and for each configuration another set of random values are applied for each virtual joint, considering a predefined systematic errors for each one. For the random values, a uniform distribution is considered and its boundaries are set to be at least a hundredth of degrees in comparison to systematic errors of virtual revolute joint.

With those predefinitions the EE postures are obtained by Successive Screw Displacement (SSD) [23, 25]. It differs from DH in its input parameters to form the homogeneous transformation matrices and the screw frames. While DH needs four parameters constant, the SSD needs two vectors and two constants for each joint. The vectors are the screw axis and its inertial moment from the reference frame when kinematics analysis is considered [2]. The other constants are the rotation and translation screw movements. Also, in DH, joint frames are settled accordingly to the robot configuration and each frame is defined from the previous frame, except for the base frame.

In the transformation matrices in SSD, each screw frame is relative to the base frame and not from the previous as DH convention [23].

The joint and link offsets are estimated through to posture errors which were measured through this simulation. The next section details the identification parameter procedure with nonlinear least square optimization.

3 Screws Parameters Identification

The main difference between conventional inverse kinematics and the procedure used to calibrate the robot is the Jacobian matrix and error posture vector. While the goal of conventional approach is to move the actual EE posture “p” to a desired one, estimating joint variables “q”, the calibration consists in estimate joint variables or screw parameters that minimize posture error for all robot configurations in the workspace. This process is called Absolute Accuracy Calibration [7].

To find a good approximation, three steps have to be made: Objective function, parameter estimation and EE posture update.

3.1 Objective Function

The problem begins with the nominal robot model and its posture, defined by forward kinematic, as in Eq. (1).

$$P = T_n \cdot R_0 = \begin{bmatrix} R & p \\ 0 & 1 \end{bmatrix} \tag{1}$$

where T_n stands for the matrix from successes screw displacement of all joint screws, as in Eq. (2).

$$T_n = \prod_{i=1}^{n} A_i \tag{2}$$

Each transformation matrix A_i is formed by screw parameters (s, s_0, θ, t) [23]. The vector s is the screw normalized axis; s_0 is a coordinate in s relative to a reference frame; θ is the angular rotation of s and t, a translation movement in the same direction of s. The matrix R_0 is a homogeneous matrix composed by an identity matrix and EE position of robot zero position, e.g. all joint variables are in its zero reference (q = 0).

The row, pitch and yaw angles Eq. (3) are calculated from orientation matrix R from Eq. (1) [23].

$$\theta = \begin{bmatrix} R & P & Y \end{bmatrix}^T \tag{3}$$

Now the EE posture error is determined with the nominal and nominal plus virtual joints robot model. So, a matrix error Eq. (4) is formed for all robot configurations.

$$\varepsilon_i = \begin{bmatrix} \theta_{si} \\ p_{si} \end{bmatrix} - \begin{bmatrix} \theta_i \\ p_i \end{bmatrix} = \begin{bmatrix} \varepsilon_{\theta i} \\ \varepsilon_{pi} \end{bmatrix} \tag{4}$$

The variable θ_{si} stands for i-th simulated EE orientation and θ_i is the i-th EE orientation provided by analytical forward kinematic as in Eq. (1) and similarly for EE position.

The objective function (O.F.) to be minimized is defined in Eq. (5):

$$\text{O.F.} = \sum_{i=1}^{m} \left\| \varepsilon_{pi} \right\|^2 \frac{1}{W^2} + \sum_{i=1}^{m} \left\| \varepsilon_{\theta i} \right\|^2 \tag{5}$$

where O.F. is the function to be minimized subject to virtual joints variable limits specified in Sect. 4. As the O.F. sums errors with different units (mm and radians), which is inconsistent in engineering point of view, a constant "W" is applied to the position errors [18] with the same unit and its value is defined on simulation varying from 0.01 to 100. This constant value is chosen according to the parameter estimation, also described in Sect. 4.

3.2 Parameter Estimation and Posture Update

At this stage an advantage of screw modeling over DH is observed. Each Jacobian column is a joint screw, while in DH notation, is a parameter (d, a, α, θ) [20] related to link frames translation and rotation. So the Jacobian based on screw can be separated in nominal and virtual joints as in Eq. (6).

$$\dot{p} = J_v \dot{q}_v + J_n \dot{q}_n \tag{6}$$

The subscripts "v" and "n" stand for virtual and nominal, respectively. So, the virtual joints are considered as the unique error source, and it is equivalent to consider all remain nominal joints as a rigid structure. So, the minimization finds just the virtual joints parameters with a non-linear least square function from MatLab program (lsqnonlin).

The function output provide these virtual joint values which is compared with those predefined in the first simulation step, when a forward kinematic was made with systematic and random errors. This comparison measures the estimation quality. In real experiments, the systematic error is unknown, but this previous analysis guarantees the calibration procedure effectiveness.

The next section presents simulation results for an anthropomorphic robot considering real dimensions of an ABB IRB 1600 robot.

4 Calibration Simulation of an Industrial Robot

This section presents the steps for calibration simulation for an industrial robot considering a set of optimal robot measured configurations suggested by [10], described in Table 1.

Table 1. Optimal measurement for calibration [10]

Joint coordinate	Configuration 1	Configuration 2	Configuration 3	Configuration 4
q1	−90°	0°	90°	180°
q2	−30°	−60°	−90°	−120°
q3	90°	−90°	−90°	90°
q4	0°	180°	90°	−90°
q5	120°	−120°	−60°	60°
q6	−120°	120°	60°	−60°

Some researchers suggest 40 to 60 robot configuration to do the calibration [9, 14] achieving position EE errors (Euclidean distance) mean from 0.9 to 1 mm with standard deviation of 0.3 to 0.5 mm when kinematic calibration is implemented, and when link compliance is considered, the final robot error postures achieve 0.364 mm. These values are adopted as the reference to achieve this work.

For the first simulation step it is necessary to determine posture errors varying joint and link offsets and its uncertainty range or standard deviation, which is defined in the next subsection.

4.1 Sensitivity Analysis

In order to predict the virtual joint uncertainty in terms of those related to EE positions, a sensitivity analysis is made. The forward kinematic is implemented choosing these 4 optimal configurations. For each of them it is added four configurations chosen randomly in uniform distribution with a limit of ±30°. Also, each configuration is repeated 10.000 times. All this process is done for different uniformly distributed values of revolute virtual joint uncertainty.

These uncertainties are added in the screw parameter (θ) without joint and link offset (systematic error). The results are shown in Fig. 2 for standard deviation position error caused by only virtual revolute joints.

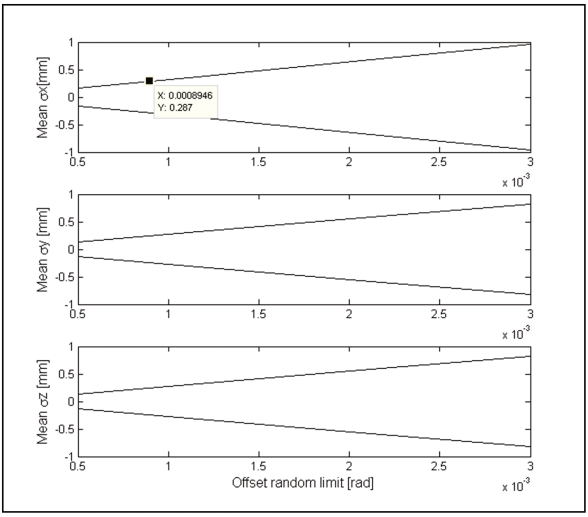

Fig. 2. Sensitivity analysis

Considering a standard deviation of 0.5 mm, the equivalent in each Cartesian coordinates is 0.287 mm. From Fig. 2, the limits for random values for virtual revolute joint are $\pm 8.946 \cdot 10^{-4}$ rad or ±0.051° and it is used in the next step.

4.2 Posture Error Simulation and Offset Estimation

The screw parameters (θ, t) are defined at this step. The systematic error in revolute joints (joint offset) appears despite the method implemented in industrial robots to calibrate the encoder's zero position, also called revolution counters update [7], depends on operators visual capability. These two parameters are defined in Table 2.

Table 2. Screw parameters (θ, t) for virtual joints

Virtual joint	Systematic	Random
Revolute	1.210°	±0.051°
Prismatic	0.300 mm	0

The systematic error for prismatic virtual joints (link offset) is chosen according to ISO 2768 [8], which specify general tolerances for linear dimensions. The reference adopted for linear dimension is the largest robot link (600 mm). So, the linear fine tolerance that covers this dimension is ±0.3 mm. For revolute virtual joint, the systematic error is based on the largest joint offset estimation from [5]. Also, the objective function in Eq. 5 has its constraints equations based on the range of [−1.21°, 1.21°] for joint offset and [−0.3 mm, 0.3 mm] for link offset. With these assumptions, the forward kinematic can be evaluated as in sensitivity analysis, but with 3 replication for each configuration, totalizing 60 robot configurations. The measurement noise is defined as ±0.013 mm for a measure arm system [3].

After the posture simulation, these data are used to estimate the systematic errors from virtual joints (offsets). In practice, these offsets are unknown. The estimation results are shown in Tables 3 and 4 considering different weights for the objective function.

Table 3. Selection weight (W) for the object function

W	Position error [mm]			Euclidian	Orientation error [°]			[Dimensionless]
	εx	εy	εz	Distance error [mm]	εRow	εPitch	εYaw	Obj. Func.
0.01	0.171	0.198	0.250	0.421	0.550	0.028	0.022	$3.122 \cdot 10^{8}$
0.1	0.171	0.198	0.250	0.421	0.042	0.028	0.022	31219.6
1	0.171	0.198	0.250	0.421	0.026	0.029	0.022	3.122
10	0.172	0.197	0.253	0.423	0.030	0.040	0.040	$3.141 \cdot 10^{-4}$
100	0.200	0.199	0.251	0.440	0.036	0.039	0.047	$4.269 \cdot 10^{-8}$

From Table 3 the result is similar to other works [9, 14], emphasizing object function advantage on considering position and orientation error and pondering it. The possible weights to use in real calibration are (0.1; 1; 10; 100) resulting in minors Euclidean distance error.

Finally, Table 4 shows the effectiveness of virtual joints estimation. For all revolute joints the approximation error was less than 1 μrad, except for joint 6, and for prismatic, around 30 μm, less than tolerance considered.

Table 4. Parameter estimation result

Virtual joints	From forward kinematic simulation	From estimation	Error
J1rz	0.021 rad	0. 021 rad	0
J1pz	0.300 mm	0.321 mm	0.021
J1px	0. 300 mm	0.327 mm	0.027
J2rz	0. 021 rad	0.021 rad	0
J2pz	0. 300 mm	0.324 mm	0.024
J3rz	0. 021 rad	0.021 rad	0
J4rx	0. 021 rad	0.022 rad	0.001
J4px	0. 300 mm	0.318 mm	0.018
J5rz	0. 021 rad	0.021 rad	0
J6rx	0. 021 rad	0.012 rad	−0.09

5 Conclusions

This work deals with a calibration procedure considering screw theory in the kinematic model. In the beginning a simulation process is made to get end effector postures for a set of robot configurations with virtual joints representing joint and link offset, consequently a posture error is evaluated with nominal postures. These errors are used to estimate the virtual joints parameters. In the estimation process, joint parameters are found with a non-linear least square minimization.

The results show that the quantity of robot configuration was enough to estimate the joint and link offset error providing reasonable posture errors comparing to similar works with the same robot model.

With screw kinematic modeling it is possible to separate those virtual joints, which simulate posture source errors from nominal joints reducing the number of parameters to be estimated, comparing to conventional methods, as DH.

Acknowledgments. The researcher is supported by CAPES foundation.

References

1. Abderrahim, M., Whittaker, A.: kinematic model identification of industrial manipulators. Robot. Comput. Integr. Manuf. **16**, 1–8 (2000)
2. Cazangi, H.R.: Aplicação do Método de Davies para Análise Cinemática e Estática de Mecanismos com Múltiplos Graus de Liberdade. Master thesis. Universidade Federal de Santa Catarina, Florianópolis (2008)
3. Certi Foundation: Calibration Certification of a Measure Arm (Faro). Dimensioal Metrology Laboratory (2016)
4. Erthal, J.L.: Estudo de Métodos para a Solução da Cinemátic Inversa de Robôs Industriais para Implementação Computacional. Master thesis. Universidade Federal de Santa Catarina, Florianópolis (1992)

5. Gao, B., Liu, Y., Xi, N., Shen, Y.: Developing an efficient calibration system for joint offset of industrial robots. J. Appl. Math. **2014**, 9 (2014)
6. Ginani, L.S., Motta, J.M.S.T.: Theoretical and practical aspects of robot calibration with experimental verification. Braz. Soc. Mech. Sci. **33**, 15–21 (2011)
7. IRB1600: Product Manual. ABB Automation Technologies, Sweden (2005)
8. ISO 2768-1: General Tolerances – Part 1: Linear and Angular Dimensions Tolerances without Individual Tolerance Indication. International Organization for Standardization, Switzerland (1989)
9. Kamali, K., Joubair, A., Bonev, I.A., Bigras, P.: Elasto-geometrical calibration of an industrial robot under multidirectional external loads using a laser tracker. In: IEEE International Conference on Robotics and Automation (ICRA) (2016)
10. Klimchik, A., Caro, S., Pashkevich, A.: Optimal pose selection for calibration of planar anthropomorphic manipulators. Precis. Eng. **40**, 214–229 (2015)
11. Kumaraswamy, U., Shunmugam, M.S., Sujatha, S.: A unified framework for tolerance analysis of planar and spatial mechanisms using screw theory. Mech. Mach. Theor. **69**, 168–184 (2013)
12. Mooring, B., Roth, Z., Driels, M.: Fundamentals of Manipulator Calibration. Wiley, New York (1991)
13. Nguyen, H., Zhou, J., Kang, H.: A new full pose measurement method for robot calibration. Sensors **13**, 9132–9147 (2013)
14. Nubiola, A., Bonev, I.: Absolute calibration of an ABB IRB 1600 robot using a laser tracker. Robot. Comput. Integr. Manuf. **29**, 236–245 (2013)
15. Nubiola, A., Bonev, I.: Absolute robot calibration with a single telescoping ballbar. Precis. Eng. **38**, 472–480 (2014)
16. Robot Programming Methods (n.d.). http://www.bara.org.uk/robots/robot-programming-methods.html. Accessed 12 Mar 2017
17. Rocha, C., Tonetto, C., Dias, A.: A comparison between the Denavit – Hartenberg and the screw-based methods used in kinematic modeling of robot manipulators. Robot. Comput. Integr. Manuf. **27**, 723–728 (2011)
18. Saldias, D.P., Radavelli, L.A., Roesler, R.M., Martins, D.: Kinematic synthesis of the passive human knee joint by differential evolution and quaternions algebra: a preliminary study. In: IEEE RAS & EMBS International Conference on Biomedical Robotics and Biomechatronics (2014)
19. Santolaria, J., Guillomí, D., Cajal, C., Albajez, J., Aguilar, J.: Modelling and calibration technique of laser triangulation sensors for integration in robot arms and articulated arm coordinate measuring machines. Sensors **9**, 7374–7396 (2009)
20. Siciliano, B., Sciavicco, L., Villani, L., Oriolo, G.: Robotics: Modelling, Planning and Control. Springer, London (2010)
21. Souza, C.: Metodologia de Calibração de TCP para Robôs Industriais Utilizando Visao Computacional. Master thesis. Centro Universitário FEI. São Bernardo do Campo (2014)
22. Sun, Y., Hollerbach, J.M.: Observability index selection for robot calibration. In: IEEE Robotics and Automation (2008)
23. Tsai, L.-W.: Robot Analysis: The Mechanics of Serial and Parallel Manipulators. Wiley, New York (1999)
24. Veischegger, W., Wu, C.: Robot calibration and compensation. IEEE Robot. Autom. **4**, 643–656 (1988)
25. Wu, A., Shi, Z., Li, Y., Wu, M., et al.: Formal kinematic analysis of a general 6R manipulator using the screw theory. In: Mathematical Problems in Engineering. Hindawi Publishing Corp. (2015)

26. Wu, Y., Klimchik, A., Caro, S., Furet, B., Pashkevich, A.: Geometric calibration of industrial robots using enhanced partial pose measurements and design of experiments. Robot. Comput. Integr. Manuf. **35**, 151–168 (2015)
27. Zhuang, H., Roth, L.W.Z.: Error-model-based robot calibration using a modified CPC model. Robot. Comput. Integr. Manuf. **10**, 287–299 (1993)

Comparative Study of Autonomous Aerial Navigation Methods Oriented to Environmental Monitoring

J. López, A. Mauricio, A. Rojas, E. Dianderas, J. Vargas-Machuca, and R. Rodríguez(✉)

National Research Institute, National University of Engineering, 210 Tupac Amaru Ave. Bldg. A - Off. A1-221, 4453 Lima, Peru
robust@uni.edu.pe

Abstract. Autonomous robots have allowed automation of a wide range of environmental monitoring processes, these include spatial extension mapping, remote sensing and acquisition of environmental data. Among these applications, the acquisition of environmental data has received a growing interest because of its scientific and social importance. The collected information could be air pollution data to evaluate air quality or impacts of environmental disasters, or humidity and speed of winds data to evaluate quickly and directly climate anomalies. Motivated by fast paced advances in this priority area, this work develops and compares the most used techniques of path planning in autonomous robots under physical constraints of environmental monitoring.

Keywords: Autonomous robots · Environmental monitoring · Pollution detection · Path planning

1 Introduction

Air quality is determined based on the concentrations of some pollutants, such as ozone, carbon monoxide, sulfur oxides, nitrogen oxides and lead. At present the levels of concentration of these pollutants are very high mainly in big cities, which implies a risk in human health and a latent risk of environmental disaster. Therefore, the monitoring of pollutants is the basis for effective prevention and treatment of accidents and environmental disasters.

The environmental monitoring systems have been developed in two distinct manners. The first approach consists of a fixed network of sensors which collect measurements in order to plot environmental profiles, this scheme requires fixed data collection nodes which imply expensive assembly, complex protocols of communication and coverage area limitations. The second approach involves the use of mobile monitoring systems equipped with appropriate sensors, which allows

The present work would not be possible without the funds of the National Research Institute of the National University of Engineering (IGI-UNI).

J.C.M. Carvalho et al. (eds.), *Multibody Mechatronic Systems*,
Mechanisms and Machine Science 54, DOI 10.1007/978-3-319-67567-1_29

a more dynamic, flexible and adequate solution to plot environmental profiles. With this scheme, the coverage area ceases to be a limitation because it can be modified without higher costs, although a multi-robot cooperative solution could be better depending on coverage area size.

According to [1–3], unmanned aerial vehicles (UAVs) are commonly used as mobile monitoring systems due to good results obtained in multiple tests. This promotes the development of new methods oriented to improve the autonomy of UAVs considering the restrictions that each application implies.

The organization of the paper is as follows. Section 2 shows the develop of various methods of path planning based on the traveling salesman problem (TSP). Results are presented in Sect. 3, which includes comparison tables of compile-time and travel distances and Sect. 4 presents the final conclusions and future works.

2 Path Planning Based on TSP

Complex maps reduction problem for autonomous robots applications has been mentioned in several works [6–13] for building up simple discrete maps that allow to use techniques based on graphs so as to improve response time and reduce stored data. In environmental monitoring applications, maps can be defined as polygons in open spaces without walls or obstacles.

A discrete map is defined as a graph $G = (V(G), E(G))$ where $V(G)$ are the vertices of the graph and $E(G)$ are the edges of the graph. These maps have allowed the advance of many areas of robotics, such as navigation based on Graph-SLAM [4,5] or the establishment of communication policies between cooperative systems [3,5]. For this work, we will use the Hamiltonian cycles for navigation, this problem is also known as the traveling salesman problem (TSP). A graph G is Hamiltonian if there exists at least one cycle containing all vertices of $V(G)$.

The TSP can be defined as the shortest Hamiltonian graph of G with a matrix cost $D = [d_{ij}]$, d_{ij} is the distance between the vertices i and j, $d_{ij} = \infty$ in case they have no connection or $i = j$. Let $L = [1, 2, .., n]$ be a Hamiltonian cycle of the graph G, $l \in L$ a stretch of the path and X_{xyl} is defined in Eq. 1.

$$X_{xyl} = \begin{cases} 1 & \textit{If } l \textit{ goes from } i \textit{ to } j \\ 0 & \textit{else} \end{cases} \tag{1}$$

Since Eq. 2 is the cost function to be optimized in the TSP.

$$min\ Z = \sum_{i \in V} \sum_{j \in V} d_{ij} X_{ijl} \tag{2}$$

Subject by the following restrictions:

$$\sum_{i \in V} X_{ijl} = 1, i = 1, 2, .., n \wedge \sum_{j \in V} X_{ijl} = 1, j = 1, 2, .., n \tag{3}$$

Equation 3 indicates that each vertex is allowed to reach a single previous vertex and a single next vertex. Also, remember the solution must be a Hamiltonian cycle. There are several algorithms that solve the TSP in reasonable time but without guaranteeing the optimal route and vice versa [6].

According to [6], heuristics methods use favorable rules to locate the best solution in a limited exploration because local minima, among them highlight the Lin-Kernigham and 2-opt algorithms. While meta-heuristics depend on initialization values, but thanks to their inner movements they can escape from local minima, among them highlight the genetic and ant colony algorithms.

In the following subsections, we present a concise review of most used methods to solve the TSP.

2.1 Ant Colony Algorithm

Based on the natural behavior of ants, it is a probabilistic technique to find optimal solutions by making a positive or negative feedback on any solution found before, so the route with more pheromones (positive reinforcement) will be the most traveled, the algorithm contemplates a pheromones dissipation model in order to avoid local minima [7,8].

The algorithm starts in an initial population of artificial ants that randomly draw a solution (a Hamiltonian path) and leave their trace inversely proportional to the cycle cost. Then the old trail is evaporated and the current one provided by the last ants is added. A new group of ants is released in search of random solutions, but more likely to choose routes with more pheromones, and the process is repeated until the solution can not be further improved or until a number of iterations are completed. Considering the initial node i and the set of alternative edges $X = a_{i1}, a_{i2}, ..., a_{ij}$ that ant k must choose. The selection rule is the probability distribution presented in Eq. 4.

$$P(a_{xy}|X) = \frac{\tau_{xy}^{\alpha} * \eta_{xy}^{\beta}}{\sum_X \tau_{xy}^{\alpha} * \eta_{xy}^{\beta}} \tag{4}$$

Where:

τ_{xy}: Is the amount of pheromones that are deposited in the edge a_{xy}.

η_{xy}: Is the convenience of deciding a random route.

α, β: Positive parameters that determine the relation between τ_{xy} and η_{xy}.

The value τ_{xy} is assigned a minimum value to guarantee the same possibility for the other routes to be choosen. The function η_{xy} usually assigns each path a value $\frac{1}{c_{ij}}$, where c_{ij} is the size of edge a_{ij}, thus favoring edges of small cost. Values α and β define the convergence time and the search dynamics of the algorithm. Pheromones evaporate over time (iterations), decreasing their concentration and impact on new ants. The Eq. 5 shows pheromone evaporation equation.

$$\tau_{xy}^{k+1} = (1 - \rho)\tau_{xy}^{k} \tag{5}$$

For the route evaluation by iteration a residual value of pheromones is used being L the cost of the Hamiltonian cycle traced by the ant k. The pheromone deposit function in each edge is:

$$\Delta\tau_{xy}^{k} = \begin{cases} \frac{1}{L_k} & \textit{If the edge was used} \\ 0 & \textit{If the edge was not used} \end{cases} \tag{6}$$

Adding 6 to 5, the final pheromone equation for a group of ants H is:

$$\tau_{xy} = (1-\rho)\tau_{xy} + \rho \sum_{H} \Delta\tau_{xy}^{k} \tag{7}$$

Although evaporation serves to avoid premature convergence, however, supersaturation may occur on edges. To solve it, the Max-Min criterion is added, which are both lower and higher limits of pheromone values. The Algorithm 1 summarizes step by step the solution of the TSP by colony of ants.

Data: Graph $G = (V(G), E(G))$
Result: Cycle T
Initialization;
Pheromones equal to the minimum value;
while *better routes appear* **do**
  Hamiltonian cycle random construction from $N \rightarrow T$;
  Pheromones evaporation;
  Pheromones actualization;
  Choose maximum pheromone value;
end

Algorithm 1. Ant colony algorithm

2.2 2-Opt Algorithm

The 2-opt exchange is a basic algorithm that consists choosing two pairs of edges from different vertices in a Hamiltonian cycle [9,10], them break and build a new cycle by intersecting the free vertices to form new edges as shown in Fig. 1. New cycle is compared to the previous cycles and only the one with the lowest cost

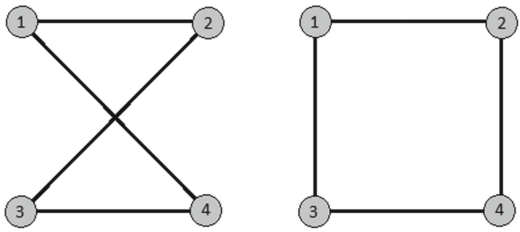

Fig. 1. 2-opt exchange of edges.

is stored. This process is repeated in all vertices looking for the optimal cycle locally. The Algorithm 2 explains step by step the process described above.

Data: Graph $G = (V(G), E(G))$
Result: Cycle T
Initialization;
Choose and initial Hamiltonian cycle T;
Flag up;
while *flag up* **do**
  Flag down;
  Label all vertices V as not scanned;
  while *flag up* **do**
    Choose a not explored vertex i;
    Examine all 2-opt moves that include $i - edge$;
    if *any examined move reduce the cycle length* **then**
      Flag up
    else
      Label vertex i as scanned;
    end
  end
end

Algorithm 2. 2-opt algorithm

2.3 Lin-Kernighan Algorithm

This algorithm is considered among the most used heuristics in local search [6,11]. It consists of comparing two routes and eliminating the one with greater cost. The algorithm starts with an initial Hamiltonian path or cycle obtained by some previous method (can even be random) and then search for local improvements by generating a new route which, if better, will replace the current one.

To improve the 2-opt algorithm, k edges are chosen instead of two. The edges combine to get several cycles and look for the best possible. This is called $k-opt$ motions used for $k - opt$ algorithms. By increasing k, the possibilities increase to examinate the Hamiltonian cycle. The combinations to eliminate the k edge in the cycle is the combinatorial $\binom{n}{k}$. The time to analyze all these cases is order $O(n^k)$ so it is only used for small ks.

This method looks for several simple and compound procedures [12]. Not necessarily every movement improves the cycle, but the compound and total movement improves it. In this way it seeks to escape the local minimums. Its heuristic starts in $k-opt$ search that generates optimal solutions where k is variable. This algorithm is very varied, but we consider the simplest version based on 2-opt. It is possible that the 2-opt algorithm stops at a local minimum T because the 2-opt exchanges have already been done without an improvement in cost. However, it is possible that at least one bad 2-exchange were performed to move from cycle T to cycle T' and then look for 2-exchange from cycle T' to T''

until find the shortest. Algorithm 3 shows how to implement the Lin-Kernighan method.

Data: Graph $G = (V(G), E(G))$
Result: Cycle T
Initialization;
Choose and initial Hamiltonian cycle T;
while *stop criterion is not met* **do**
  Label all vertices V as not scanned;
  while *all V are not scanned* **do**
    Choose a not explored vertex t_i;
    $G* = 0$ (Improvements made) and $i = 1$;
    Examine all 2-opt moves that include $i - edge$ in T;
    Find x_i in $S = T - [x_i, ..., x_i - 1]$ to break T;
    Find y_i in $S - [y_i, ..., y_i - 1]$ to replace broken parts of T;
    New T' is formed with gain $G* = 0$;
    if *any examined move reduce the cycle length* **then**
      $T_{best} \rightarrow T$
    end
    Label vertex t_i as scanned;
  end
end

Algorithm 3. Lin-Kernighan algorithm

2.4 Genetic Algorithm

Based on [10,13], to apply the genetic algorithms to the TSP, the chromosomes are first represented as permuted vectors which contain the vertices connection order of a Hamiltonian cycle T. For a graph G with n vertices, the initial cycle is expressed as $T = (g_0, g_1, ..., g_n)$ where g_k gene is a vertex of $V(G)$. After generating the first population X_0, a selection is made per tournament, chromosomes or individuals are selected in pairs and the one with lowest cost is chosen. Then a random crossing is done in pairs through a partially mapped inheritance, being $T_1 = (g_0, g_1, ..., g_n)$ and $T_2 = (g_m, g_{m+1}, ..., g_{m+n})$ a pair of parents, their first son S_1 will inherit genes from T_1 up to the gene g_k which is chosen randomly, and its genes are completed with the second parent. The second child receives the remaining genes from each parent, such that the children are $S_1 = (g_0, ..., g_k, g_{k+m+1}, ..., g_{m+n})$ and $S_2 = (g_m, ..., g_{k+m}, g_{k+1}, ..., g_n)$.

The crossing generates Hamiltonian cycles by not repeating the genes which represent the vertices. In order to avoid rapid convergence and local minima, it is necessary to make random mutations in the population, for our case we used the reciprocal exchange method that consists of exchanging the position of two

or more genes to obtain another Hamiltonian cycle. Algorithm 4 shows the steps to implement a genetic algorithm oriented to solve of the TSP.

Data: Graph $G = (V(G), E(G))$
Result: Cycle T
Initialization;
Generate a random population X of N chromosomes;
Encode the population X by some representation;
while *better routes appear* **do**
  Assess the fitness value of each chromosome in X;
  Select the chromosomes that will be parents;
  Choose the best chromosome $\rightarrow T$;
  Cross parents in pairs to obtain a new generation;
  Make mutations on some chromosomes;
  Replaces the weaker X with the new generation;
end

Algorithm 4. Genetic algorithm

3 Simulation and Results

In this section, we present the results of path planning algorithms. The comparison is made based on the run-time in seconds and the total distance traveled, this distance is taken as reference and without units in the comparison. The results were obtained from an Intel (R) Core i7-4790 CPU @ 3.60 GHz 3.60 GHz computer with 4.00 GB RAM and 1600 Hz speed using MatLab.

First the local search algorithms are compared. Table 1 shows the comparison between of 2-opt and Lin-Kernighan algorithms. In this case it is observed that the Lin-kernighan algorithm is slightly superior to the 2-opt algorithm in the cycle cost, but quite inferior in the convergence time. The time trends follow the order of computational costs $O(n^2)$ in 2-opt case and $O(n^3)$ in Lin-kernighan case.

Table 1. Results of 2-opt and Lin-Kernighan algorithms.

Number of	2-opt		Lin-Kernighan	
vertices	Time (s)	Cost (distance)	Time (s)	Cost (distance)
10	0.0039	96.88	0.0095	96.88
49	0.0802	497.11	0.4355	476.76
84	0.3495	818.00	2.0796	804.68
172	1.4015	1711.10	15.1032	1702.50
273	5.9199	2819.10	75.7097	2764.10

Efficiency of the ant colony algorithm depends on α and β. To compare, two good sets of parameters are used [8], which are shown in Table 2. Table 3 shows the superiority of the first set, both in convergence time and cycle cost, this proves that increasing β improves the results.

For the genetic algorithms analysis, a local optimization 2-opt is added in order to evaluate the improvement in the cycle cost in relation to convergence time variation. Table 4 shows the parameters for each algorithm, while Table 5 shows the results of the simulation. The 2-opt genetic algorithm significantly improves its result but adds a considerable computational cost despite reducing the number of generations and the chromosomes population.

Finally, we compare the best cases regarding the cycle cost. We chose the algorithms that showed lower cycle cost because that is the main objective of the TSP. Table 6 shows the results of Lin-Kernighan, ant colony and 2-opt genetic algorithms.

As a result, the Lin-Kernighan algorithm is the best, both in cycle cost and in convergence time, followed by the genetic algorithm with local optimization. Figure 2 shows the comparison of the results for the 52 vertices case from Table 6. Figure 2b shows that the ant colony algorithm generates route crossings because it has not been modified with a local optimization method.

Table 2. Sets of parameters for the ant colony algorithm.

Parameters	α	β	ρ	τ_{ij}min	τ_{ij}max
Case 1	1	10	0.1	0.01	0.5
Case 2	1	6	0.2	0.01	0.5

Table 3. Comparison of 2 set of parameters for the ant colony algorithm.

Number of vertices	Ant colony case 1		Ant colony case 2	
	Time (s)	Cost (distance)	Time (s)	Cost (distance)
10	0.1610	102.88	0.1636	102.88
43	5.3609	421.94	5.1238	425.08
63	14.4409	623.90	13.9181	653.23
93	43.6180	918.42	42.7420	982.04
150	148.6530	1599.40	168.8473	1724.00

Table 4. Parameters for genetic algorithms.

Type of algorithm	Parameters		
	Chromosome population	Generations	Probability of mutation
Simple genetic	100	10000	0.2
2-opt genetic	10	100	0.1

Table 5. Results of simple genetic and 2-opt genetic algorithms.

Number of vertices	Genetic algorithm		2-opt Genetic algorithm	
	Time (s)	Cost (distance)	Time (s)	Cost (distance)
13	7.2886	119.54	0.8088	119.54
42	10.9917	478.71	7.1665	399.28
67	15.7654	776.90	17.7476	648.75
128	34.4900	1785.00	67.0130	1268.10
185	60.7306	2947.90	143.4611	1848.70

Table 6. Comparison of the three algorithms with best results.

Number vertices	Lin-Kernighan		Ant colony		2-opt GA	
	Time (s)	Cost[a]	Time (s)	Cost[a]	Time (s)	Cost[a]
7	0.0057	74.2	0.074	77.1	0.46	74.2
20	0.0242	186.2	0.866	186.2	1.48	186.2
43	0.2729	413.8	5.617	414.3	8.14	417.6
53	0.5498	517.7	8.191	517.7	11.79	521.6
75	1.7515	734.6	22.379	742.2	23.33	741.6
108	4.0502	1074.8	59.171	1111.7	45.97	1081.8
168	19.8271	1644.6	183.656	1783.3	118.38	1675.4
213	28.8552	2130.4	390.282	2348.2	185.15	2153.3
301	92.0820	2994.4	1010.493	3367.5	359.74	3022.3
Mean	**16.4798**	**1085.63**	**186.7476**	**1172.02**	**83.8267**	**1097.11**

[a] The cycle cost is measured in distance

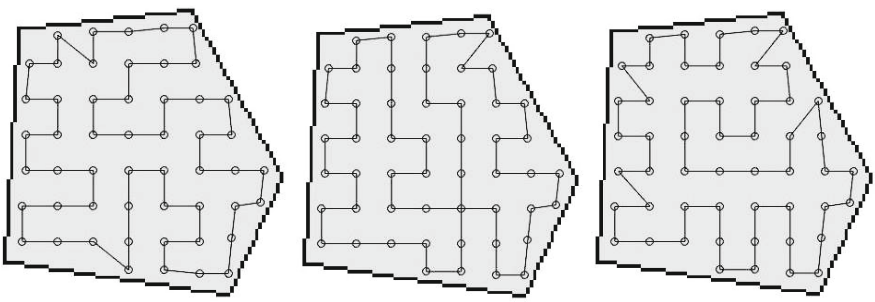

(a) Lin-Kernighan algorithm (b) Ant Colony algorithm (c) 2-opt Genetic algorithm

Fig. 2. Resultant paths for each algorithm with 52 vertices.

4 Conclusions and Future Work

Convergence times of each algorithm would vary depending on the relation between its computational cost and number of vertices. About the compared algorithms, each method can be optimized either by choosing a set of parameters like the ant colony algorithm or by an external optimization method like the Lin-Kernigham. Based on the results, we conclude that the Lin-Kernigham algorithm is the most efficient for the TSP problem applied to environmental monitoring, although its computational cost is high its metrics on average place it well above. Finally, the next step is to implement the selected algorithm in a UAV, although it is likely that the requirements for the coverage of large areas require a multi-robot solution.

References

1. Koh, L.P., Wich, S.A.: Dawn of drone ecology: low-cost autonomous aerial vehicles for conservation. Tropical conservation. Science **5**(2), 121–132 (2012)
2. Stanisław, A., Piwowarski, D.: Multicopter platform prototype for environmental monitoring. J. Cleaner Prod. **155**, 204–211 (2016)
3. Sahingoz, O.K.: Flyable path planning for a multi-UAV system with Genetic Algorithms and Bezier curves. In: 2013 International Conference on Unmanned Aircraft Systems. IEEE (2013)
4. Fermin-Leon, L., Neira, J., Castellanos, J.A.: Path planning in graph SLAM using Expected uncertainty. In: 2016 IEEE/RSJ International Conference on Intelligent Robots and Systems. IEEE (2016)
5. Isaac, D., Liu, M., Siegwart, R.: A framework for multi-robot pose graph SLAM. In: IEEE International Conference on Real-time Computing and Robotics. IEEE (2016)
6. Zongxu, M., Hoos, H.H., Stützle, T.: The impact of automated algorithm configuration on the scaling behaviour of state-of-the-art inexact TSP solvers. In: International Conference on Learning and Intelligent Optimization. Springer International Publishing (2016)
7. Razif, R., et al.: Mobile robot path planning using Ant Colony Optimization. In: 2016 2nd IEEE International Symposium on Robotics and Manufacturing Automation. IEEE (2016)
8. Olivas, F., et al.: Ant colony optimization with dynamic parameter adaptation based on interval Type-2 fuzzy logic systems. Appl. Soft Comput. **53**, 74–87 (2017)
9. Khoufi, I., et al.: Optimized trajectory of a robot deploying wireless sensor nodes. In: 2014 IFIP, Wireless Days. IEEE (2014)
10. Sahingoz, O.K.: Generation of Bezier curve-based flyable trajectories for multi-UAV systems with parallel genetic algorithm. J. Intell. Robot. Syst. **74**(1–2), 499 (2014)
11. Kulich, M., Juan José, M.-B., Libor, P.: A meta-heuristic based goal-selection strategy for mobile robot search in an unknown environment. Comput. Oper. Res. **84**, 178–187 (2016)
12. Hernandez, K., Bacca, B., Posso, B.: Multi-goal path planning autonomous system for picking up and delivery tasks in mobile robotics. IEEE Lat. Am. Trans. **15**(2), 232–238 (2017)
13. Wang, X., et al.: Double global optimum genetic algorithm-particle swarm optimization-based welding robot path planning. In: Eng. Optim. **48**(2), 299–316 (2016)

Simulation and Experimental Verification of a Global Redundancy Resolution for a 3PRRR Prototype

João Vitor de Carvalho Fontes(✉) and Maíra Martins da Silva

São Carlos School of Engineering, University of São Paulo, São Paulo, Brazil
joao.fontes@usp.br

Abstract. Parallel manipulators have kinematic chains connected to each other in a common point, the end effector. This design grants desirable characteristics to parallel manipulators, for instance high rigidity and load distribution. However they suffer from singularities inside their workspace which may cause low precision and high efforts. Aiming to overcome this problem, kinematic redundancy can be used to design new redundant manipulators which can avoid singularities and improve some manipulator's characteristics with a proper redundancy resolution. Two approaches of a global redundancy resolution to avoid singularities and improve the manipulator's dynamic performance in a 3PRRR manipulator prototype are presented. The experimental results show that the implemented redundancy resolution is suitable for the application.

Keywords: Parallel manipulator · Kinematic redundancy · Redundancy resolution · Experimental verification

1 Introduction

Kinematically redundant manipulators have more actuators than degrees of freedom (DOFs) which lead to infinite number of solutions for the inverse kinematic. The problem of select one solution among them is addressed as redundancy resolution, when solved, defines the behavior of the manipulator's extra DOFs while the end effector is performing a task. Moreover these extra DOFs can be used to improve different manipulator's characteristics [1].

Redundancy resolution methods can be classified in local or global. Local methods consist of moving the redundant joints following a function gradient that improves some manipulator's characteristics for each time step. On the other hand, global redundancy resolution is able to optimize a manipulator's characteristic considering the total time interval of a task [2].

Regarding parallel manipulators, kinematic redundancy has emerged as a solution for parallel manipulator's drawbacks. Some authors, e.g. [3–5], have suggested that the inclusion of kinematic redundancy on parallel manipulators may eliminate or reduce the presence of singularities enlarging the usable workspace. In addition, it has been demonstrated that kinematic redundancy can improve

J.C.M. Carvalho et al. (eds.), *Multibody Mechatronic Systems*,
Mechanisms and Machine Science 54, DOI 10.1007/978-3-319-67567-1_30

accuracy [6,7], motion/force transmissibility [8], dynamic performance [9–11], energy efficiency [12] of parallel manipulators.

Despite many evidences, no work has experimentally demonstrated the impact of several degrees of kinematic redundancies and global redundancy resolution to improve dynamic performance on parallel manipulators. Extra degrees of kinematic redundancies demand the employment of redundancy resolution approaches to solve the inverse kinematics problem satisfactorily.

In this manuscript, the kinematically redundant 3PRRR manipulator is experimentally exploited. The redundancy resolution is solved via an global optimization problem that describes a tracking problem aiming to improve the dynamic performance. Two approaches are proposed: the prepositioning and the ongoing positioning strategies [11,13].

Figure 1 illustrates the planar non redundant parallel manipulator 3RRR and a redundant manipulator 3PRRR. These manipulators presents three kinematic chains composed of one active revolute joint (R) and two passive revolute joints (RR). The inclusion of extra active prismatic joints (P) is responsible for the kinematic redundancies.

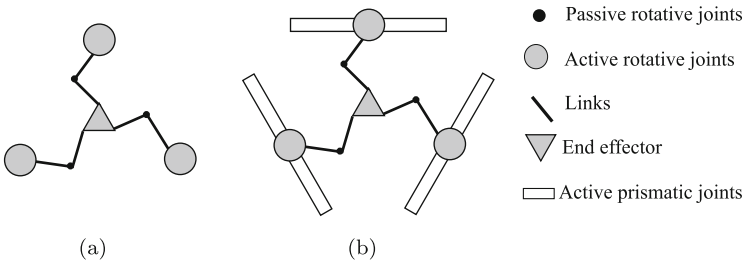

Fig. 1. Illustrations of (a) the non-redundant manipulator 3RRR and (b) the kinematically redundant manipulator 3PRRR.

The experimental prototype is described in Sect. 2. Section 3 summarizes the kinematic and dynamic models of the manipulators. Both global approaches are described in Sect. 4. Numerical and experimental results are discussed in Sect. 5. Finally, conclusions are drawn in Sect. 6.

2 Prototype Description

In this section, the prototype 3PRRR is described. The end effector of this planar manipulator presents three DOFs. The actuation of the prismatic joints allow the manipulator's reconfiguration. Each kinematic chain presents an active prismatic joint and an active revolute joint. The actuation of these joints is performed by brushless Maxon EC60 flat motors. They might deliver 100 W of power. The nominal torque of these motors is 0.257 N.m @ 3580 rpm. Maxon planetary gearheads GP52C with a reduction rate of 3.5:1 resulting in a nominal

torque of 0.82 N.m @ 1200 rpm. The linear motion is performed by three table systems with ball screw HIWIN KK60-10-C-E-600-A-1-F0-S3. Its stroke range is 600 mm (Fig. 2).

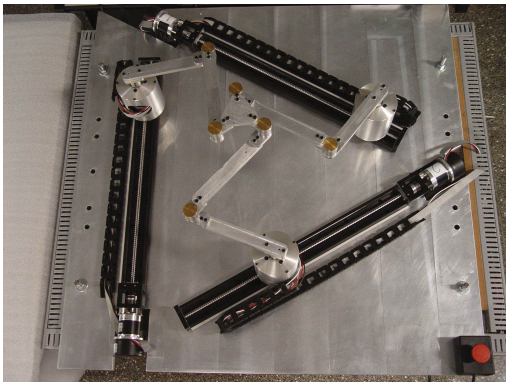

Fig. 2. The prototype 3PRRR

3 Kinematic and Dynamic Modeling

In this section, the model of the 3PRRR manipulator is presented. Figure 3 illustrates a scheme of the geometry of the 3PRRR. The subscript $i = 1, \ldots, 3$ describes the kinematic chain. There are revolute joints in A_i, B_i and C_i, where A_i is active and B_i and C_i are passive. The angles θ_i and β_i represent the orientation of the links A_iB_i and B_iC_i, respectively. The lengths of links A_iB_i and B_iC_i are, respectively, l_1 and l_2. Active prismatic joints can modify the

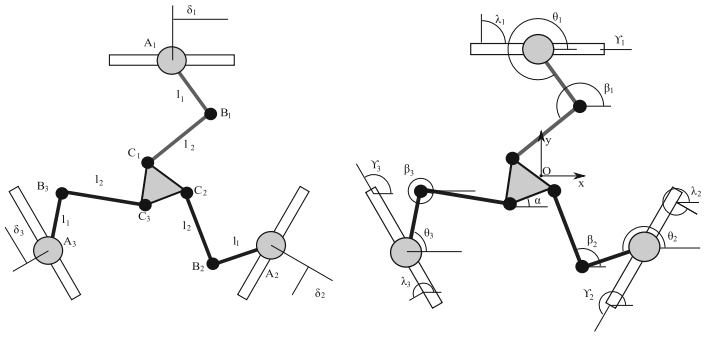

Fig. 3. Model parameters of the redundant manipulator 3PRRR: (a) Points and link lengths; (b) Angles and coordinate system.

position of the point A_i. Using this linear actuators the position of A_i can be modified according to the position δ_i and the orientation γ_i (see Fig. 3). The distance between the manipulator's center and the central position of the linear actuators is represented by a. The Cartesian position of the end effector is (x, y) with orientation α. The distance of C_i to the center of the end effector is h. Details on this description can be found in [11].

3.1 Kinematic Analysis

The inverse kinematic model is used to determine the active joints' inputs $\boldsymbol{\Theta} = [\theta_1, \theta_2, \theta_3, \delta_1, \delta_2, \delta_3]^T$ that yield a desired end effector's pose $\mathbf{X} = [x, y, \alpha]^T$. So, considering that the values of the redundant actuators' inputs δ_1, δ_2 and δ_3 will be defined by redundancy resolution, the inverse kinematics of the manipulator is described as follows.

First, the variables ρ_{xi} and ρ_{yi} are introduced as:

$$\begin{bmatrix}\rho_{xi}\\ \rho_{yi}\end{bmatrix} = \begin{bmatrix}x\\ y\end{bmatrix} + h\begin{bmatrix}\cos(\alpha+\lambda_i)\\ \sin(\alpha+\lambda_i)\end{bmatrix} - \delta_i\begin{bmatrix}\cos(\gamma_i)\\ \sin(\gamma_i)\end{bmatrix} - a\begin{bmatrix}\cos(\lambda_i)\\ \sin(\lambda_i)\end{bmatrix}. \tag{1}$$

The following geometrical constraint can be imposed according to the length of the links:

$$e_{i1} + e_{i2}\cos(\theta_i) + e_{i3}\sin(\theta_i) = 0, \tag{2}$$

where

$$e_{i1} = -2l_1\rho_{yi}, \quad e_{i2} = -2l_1\rho_{xi} \quad e_{i3} = \rho_{xi}^2 + \rho_{yi}^2 + l_1^2 - l_2^2. \tag{3}$$

The tangent half-angle substitution is employed to solve Eq. 2 for θ_i yielding:

$$\theta_i = 2\tan^{-1}\left(\frac{-e_{i1} \pm \sqrt{e_{i1}^2 + e_{i2}^2 - e_{i3}^2}}{e_{i3} - e_{i2}}\right). \tag{4}$$

Using the result of θ_i, the angle β_i can also be determined by

$$\beta_i = \tan^{-1}\left(\frac{\rho_{yi} - l_1\sin(\theta_i)}{\rho_{xi} - l_i\cos(\theta_i)}\right). \tag{5}$$

One way to determine the Jacobian matrix $\mathbf{J}$ is by taking the time derivative of the constraint relation described by Eq. 2. This approach yields:

$$\begin{aligned}\dot{x}[l_2\cos(\beta_i)] + \dot{y}[l_2\sin(\beta_i)] + \dot{\alpha}[l_2 h\sin(\beta_i - \lambda_i - \alpha)] \\ = \dot{\theta}_i[l_1 l_2\sin(\beta_i - \theta_i)] + \dot{\delta}_i[l_2\cos(\beta_i - \gamma_i)].\end{aligned} \tag{6}$$

Equation 6 can be rewritten in a matrix form yielding

$$\mathbf{A}\dot{\mathbf{X}} = \mathbf{B}\dot{\boldsymbol{\Theta}}. \tag{7}$$

The matrices $\mathbf{A}$ and $\mathbf{B}$ can be defined as:

$$\mathbf{A} = \begin{bmatrix} a_{11} & a_{12} & a_{13} \\ a_{21} & a_{22} & a_{23} \\ a_{31} & a_{32} & a_{33} \end{bmatrix} \text{ and } \mathbf{B} = \begin{bmatrix} b_{11} & 0 & 0 & b_{14} & 0 & 0 \\ 0 & b_{22} & 0 & 0 & b_{25} & 0 \\ 0 & 0 & b_{33} & 0 & 0 & b_{36} \end{bmatrix}. \tag{8}$$

where $a_{i1} = l_2 \cos(\beta_i)$, $a_{i2} = l_2 \sin(\beta_i)$, $a_{i3} = l_2 h \sin(\beta_i - \lambda_i - \alpha)$, $b_{ii} = l_1 l_2 \sin(\beta_i - \theta_i)$ and $b_{ii+3} = l_2 \cos(\beta_i - \gamma_i)$.

The Jacobian matrix can be defined as:

$$\mathbf{J} = \mathbf{A}^{-1}\mathbf{B} \tag{9}$$

The velocities and accelerations of the end effector can be calculated by taking the time derivatives of the position vector, $\dot{\mathbf{X}} = \mathbf{J}\dot{\boldsymbol{\Theta}}$ and $\ddot{\mathbf{X}} = \mathbf{J}\ddot{\boldsymbol{\Theta}} + \dot{\mathbf{J}}\dot{\boldsymbol{\Theta}}$, respectively. The dynamic model is defined using virtual work. Thus, it is necessary to obtain Jacobian matrices $\mathbf{K}_{ij}$ for each moving body of the manipulator. This can be found in [11].

3.2 Dynamic Analysis

The equations of motion of the non-redundant manipulators are derived in this section using the Newton-Euler formulation and the previously described kinematics.

Using the components of the vector $\mathbf{p}_{ij} = [\mathbf{F}_{ij}; M_{ij}]$ composed by the combination of forces and moment applied on the body j of the chain i, the vector $\mathbf{d}_{ij} = [r_{x_{ij}} \quad r_{y_{ij}} \quad \phi_{ij}]^T$ and the components of the vector $\mathbf{p}_e = [\mathbf{F}_e; M_e]$ composed by the forces and moment applied on the end effector, the relation between the generalized efforts $\boldsymbol{\tau}$ applied by the actuators and the forces and moments on the system can be expressed using the Principle of Virtual Work [14]. This strategy yields the following relation:

$$\boldsymbol{\tau}^T \delta\boldsymbol{\Theta} = \mathbf{p}_e^T \delta\mathbf{X} + \sum_{i=1}^{3}\sum_{j=0}^{2} \mathbf{p}_{ij}^T \delta\mathbf{d}_{ij}, \tag{10}$$

Using the definitions of the Jacobian matrices, Eq. 10 can be rewritten in terms of the virtual displacement, $\delta\boldsymbol{\Theta}$. Since these displacements are non-zero, the equations of motion can be completely defined by:

$$\boldsymbol{\tau} = \mathbf{J}^T \mathbf{p}_e + \sum_{i=1}^{3}\sum_{j=0}^{2} \mathbf{K}_{ij}^T \mathbf{p}_{ij} = \mathbf{M}\ddot{\boldsymbol{\Theta}} + \mathbf{V}\dot{\boldsymbol{\Theta}}. \tag{11}$$

4 Redundancy Resolution

In this work, the absolute value of the maximum required torque during the execution of a preselected trajectory of the end effector should be minimized, $\|\boldsymbol{\tau}\|$. The variables of this optimization problem are the positions $\delta_i(t)$ of the redundant actuators which are limited by the length of the linear guides.

Although high torques can be required in tasks nearby singularities, only $\|\boldsymbol{\tau}\|$ not suffices the requirements to avoid parallel singularities. Therefore, an index related to the singularity definitions must be added to the cost function in order to ensure the singularity avoidance.

Since the Jacobian $\mathbf{A}$ is dimensionally heterogeneous, performance indices derived from this matrix can be misleading. To solve that, the matrix $\mathbf{A}$ must be homogenized using the manipulator's characteristic length $Lc = \sqrt{2}h$ [15,16], as follows:

$$\mathbf{A}' = \begin{bmatrix} a_{11} & a_{12} & a_{13}/Lc \\ a_{21} & a_{22} & a_{23}/Lc \\ a_{31} & a_{32} & a_{33}/Lc \end{bmatrix} \tag{12}$$

As a result, the condition number $\kappa(\mathbf{A}')$ of the homogenized Jacobian matrix $\mathbf{A}'$ behaves as a measurement of the closeness between the end effector and parallel singularities.

$$\kappa(\mathbf{A}') = \frac{max\ \nu(\mathbf{A}')}{min\ \nu(\mathbf{A}')} \tag{13}$$

where $\nu(\mathbf{A}')$ are the singular values of the matrix $\mathbf{A}'$ and the condition number is bounded, $1 \leq \kappa(\mathbf{A}') \leq \infty$.

In order to compose the multiobjective function using maximum performed torque and maximum reached conditioning index, both indices are normalized using predefined values of each index, $\kappa(\mathbf{A}')_{max}$ and $\boldsymbol{\tau}_{max}$

$$f = \frac{\|\boldsymbol{\tau}\|_\infty}{\boldsymbol{\tau}_{max}} + \frac{\|\kappa(\mathbf{A}')\|_\infty}{\kappa(\mathbf{A}')_{max}} \tag{14}$$

$$\begin{aligned} \delta_{i,opt}(t) &= arg \quad min\ _{\delta_i(t)}\ f \\ subject\ to: &\ \ \delta_{min} \leq \delta_i(t) \leq \delta_{max} \end{aligned} \tag{15}$$

Using the presented cost function (15), two approaches for the redundancy resolution are applied. The prepositioning approach consists in determining which are the best positions of kinematically redundant actuators, the positions of the linear guides δ_i, before moving the end effector. Note that the values δ_i are the same throughout the entire execution of the end effector's trajectory. So, in this case, the optimization problem has just one optimization variable for each kinematic chain with a redundant actuator, a fixed δ_{fixed_i}. The optimal values of this variable, $\delta_{fixed_i,opt}$, can be found by the following optimization problem:

$$\begin{aligned} \delta_{fixed_i,opt} &= arg \quad min\ _{\delta_{fixed_i}}\ f \\ subject\ to:\ \delta_{min} &\leq \delta_{fixed_i} \leq \delta_{max}. \end{aligned} \tag{16}$$

In the ongoing positioning approach, the redundant actuators are allowed to move the linear guides while the end effector performs the desired task. In order to calculate appropriate movements for the redundant actuators, a parametric trajectory is predefined which is selected in such a way that only the initial and final positions are considered as optimization variables. Thus, this parametric trajectory is defined as a polynomial of degree five that describes the movement of δ_i from δ_{0_i} to δ_{f_i} between the times t_0 and t_f seconds with initial and final velocities/accelerations equal to zero.

In this case, the optimization problem has, for each degree of kinematic redundancy, two variables, δ_{0_i} and δ_{f_i}. The optimal values of these variables, $\delta_{0_i,opt}$ and $\delta_{f_i,opt}$, can be found by:

$$\begin{aligned} [\delta_{0_i,opt}, \delta_{f_i,opt}] &= arg \quad min\ _{[\delta_{0_i},\delta_{f_i}]}\ f \\ subject\ to: \quad \delta_{min} \leq \delta_{0_i} \leq \delta_{max} \quad \delta_{min} &\leq \delta_{f_i} \leq \delta_{max} \quad \delta_{min} \leq \delta_i \leq \delta_{max}. \end{aligned} \tag{17}$$

5 Results

The results refer to a comparison of a same task performed in simulated and experimental environment. The task is a simple trajectory represented by a straight line as shown in Fig. 5. The end effector starts from the position (−0.0208 m, 0.1182 m) with posture angle (α) equal to zero and reaches, in a second, the end point, (0.0104 m, −0.0591 m), without changing the posture angle.

The objective function (Eq. 15) has two values for normalization, the expected maximum torque value (τ_{max}) and the expected maximum condition number (κ_{max}). For the presented task, these values for normalization were defined as $\tau_{max} = 0.2$ N.m and $\kappa_{max} = 1.5$.

In order to compare the redundancy resolution methods, the final values of the objective function, maximum conditioning number, maximum calculated torque and maximum experimental torque, were organized in Table 1. It is possible to evaluate that the ongoing positioning method present a lower objective function than prepositioning.

Simulated and experimental results are presented in Figs. 5 and 6. In these graphs, the performed torques are labeled as motor 1, motor 2 and motor 3 for the non redundant actuators and as motor 4, motor 5 and motor 6 for the redundant actuators (Fig. 4).

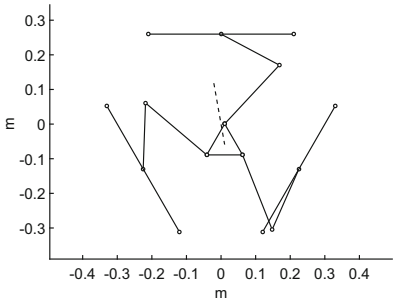

Fig. 4. Performed trajectory by all manipulators.

Table 1. Final value of the cost function and maximal values of the condition number, calculated torque, experimental torque for each manipulator and redundancy resolution executing the predefined task.

Manipulator and redundancy resolution	Cost function	Condition number	Calculated torque (N.m)	Exp. torque (N.m)
3PRRR prepositioning	2.0915	1.6638	0.1965	0.2503
3PRRR on going positioning	1.9910	1.5463	0.1920	0.2265

The simulated and experimental torques for the 3PRRR manipulator when executing the prepositioning approach are presented in Fig. 5. Since this approach actuates only the non redundant joints, only the efforts for motors 1, 2 and 3 are shown. One can notice that the experimental and calculated efforts are alike, however there are some unmodeled dynamics.

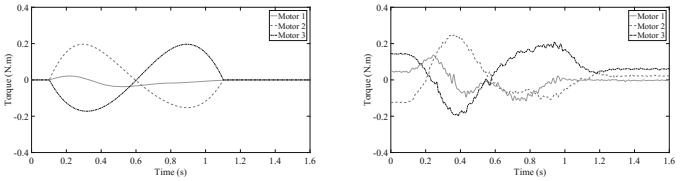

Fig. 5. (a) Calculated and (b) experimental torques performed by the motors of the redundant manipulator 3PRRR when performed the prepositioning optimization.

The efforts of all six motors for the case of ongoing positioning for the 3PRRR manipulator are shown in the Fig. 6. In this case, the behavior of the simulated and experimental efforts are similar and all efforts reach in some time a value near the maximum torque for this case, 0.2265 N.m (Table 1).

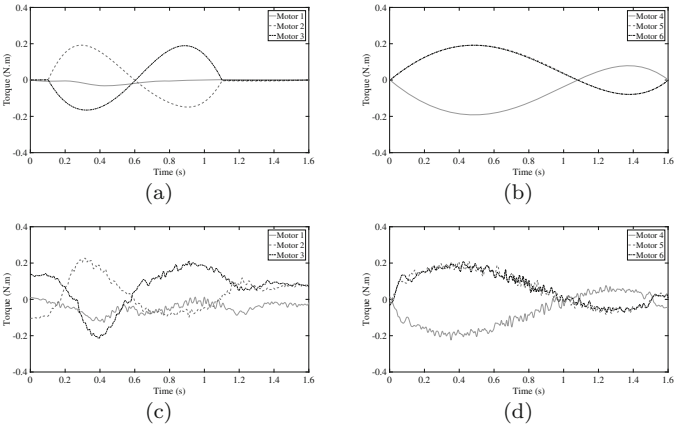

Fig. 6. (a, b) Calculated and (c, d) experimental torques performed by the motors of the redundant manipulator 3PRRR when performed the on going positioning optimization.

6 Conclusion

Parallel manipulators present singularities in their workspace. In order to avoid these drawbacks, kinematic redundancy can be applied as stated in the literature. Few works exploited experimentally redundancy resolution in parallel manipulators with several degrees of kinematic redundancy.

In this manuscript, a prototype with three degrees of kinematic redundancy was presented and a proper redundancy resolution with two approaches to avoid parallel singularities and improve dynamic performance is implemented.

The experimental results show that the prototype works as expected, following the simulated results. In addition, the ongoing positioning approach presented a better performance than the prepositioning approach.

Acknowledgements. This research is supported by FAPESP 2014/01809-0 and FP7-EMVeM (Energy Efficiency Management for Vehicles and Machines). Moreover, Joao V.C. Fontes and H.L. Vieira are thankful for their CNPq grants.

References

1. Müller, A.: On the terminology for redundant parallel manipulators. In: 32nd Mechanisms and Robotics Conference, Brooklyn, New York, USA, vol. 2, pp. 1121–1130. ASME (2008)
2. Ahuactzin, J.M., Gupta, K.K.: The kinematic roadmap: a motion planning based global approach for inverse kinematics of redundant robots. IEEE Trans. Robot. Autom. **15**, 653–669 (1999)
3. Kotlarski, J., Abdellatif, H., Ortmaier, T., Heimann, B.: Enlarging the useable workspace of planar parallel robots using mechanisms of variable geometry. In: ASME/IFToMM International Conference on Reconfigurable Mechanisms and Robots, ReMAR 2009, London, UK, pp. 63–72, June 2009

4. Mohamed, M.G., Gosselin, C.M.: Design and analysis of kinematically redundant parallel manipulators with configurable platforms. IEEE Trans. Robot. **21**, 277–287 (2005)
5. Cha, S.-H., Lasky, T.A., Velinsky, S.A.: Singularity avoidance for the 3-RRR mechanism using kinematic redundancy. In: Proceedings 2007 IEEE International Conference on Robotics and Automation, Rome, Italy, pp. 1195–1200. IEEE, April 2007
6. Kotlarski, J., Abdellatif, H., Heimann, B.: Improving the pose accuracy of a planar 3RRR parallel manipulator using kinematic redundancy and optimized switching patterns. In: IEEE International Conference on Robotics and Automation, ICRA 2008, Pasadena, CA, USA, pp. 3863–3868, May 2008
7. Kotlarski, J., Heimann, B., Ortmaier, T.: Experimental validation of the influence of kinematic redundancy on the pose accuracy of parallel kinematic machines. In: 2011 IEEE International Conference on Robotics and Automation (ICRA), Shanghai, China, pp. 1923–1929 (2011)
8. Xie, F., Liu, X.-J., Wang, J.: Performance evaluation of redundant parallel manipulators assimilating motion/force transmissibility. Int. J. Adv. Robot. Syst. **8**(5), 113–124 (2011)
9. Fontes, J.V.C., Santos, J.C., Da Silva, M.M.: Optimization strategies for actuators of kinematically redundant manipulators to achieve high dynamic performance. In: 2014 Joint Conference on Robotics: SBR-LARS Robotics Symposium and Robocontrol, São Carlos, Brazil, pp. 31–36, October 2014
10. Wu, J., Wang, J., You, Z.: A comparison study on the dynamics of planar 3-DOF 4-RRR, 3-RRR and 2-RRR parallel manipulators. Robot. Comput. Integr. Manuf. **27**, 150–156 (2011)
11. Fontes, J.V., da Silva, M.M.: On the dynamic performance of parallel kinematic manipulators with actuation and kinematic redundancies. Mech. Mach. Theor. **103**, 148–166 (2016)
12. Ruiz, A.G., Fontes, J.V.C., da Silva, M.M.: The Impact of kinematic and actuation redundancy on the energy efficiency of planar parallel kinematic machines. In: Proceedings of 17th International Symposium on Dynamic Problems of Mechanics, Natal, Brazil (2015)
13. Kotlarski, J., Thanh, T.D., Heimann, B., Ortmaier, T.: Optimization strategies for additional actuators of kinematically redundant parallel kinematic machines. In: 2010 IEEE International Conference on Robotics and Automation (ICRA), Anchorage, AK, USA, pp. 656–661 (2010)
14. Wu, J., Wang, J., Wang, L., You, Z.: Performance comparison of three planar 3-DOF parallel manipulators with 4-RRR, 3-RRR and 2-RRR structures. Mechatronics **20**, 510–517 (2010)
15. Alba-Gomez, O., Wenger, P., Pamanes, A.: Consistent kinetostatic indices for planar 3-DOF parallel manipulators, application to the optimal kinematic inversion. In: 29th Mechanisms and Robotics Conference, Parts A and B, vol. 7, pp. 765–774. ASME (2005)
16. Reveles, D.R., Pamanes, J.A.G., Wenger, P.: Trajectory planning of kinematically redundant parallel manipulators by using multiple working modes. Mech. Mach. Theor. **98**, 216–230 (2016)

A Computational Aeroelastic Framework for Studying Non-conventional Aeronautical Systems

S. Preidikman[1,2(✉)], B.A. Roccia[1,2,3], M.L. Verstraete[2,3], L.R. Ceballos[1,3], and B. Balachandran[4]

[1] Facultad de Ciencias Exactas, Físicas y Naturales, Universidad Nacional de Córdoba, Córdoba, Argentina
[2] Consejo Nacional de Investigaciones Científicas y Técnicas, CONICET, Buenos Aires, Argentina
[3] Grupo de Matemática Aplicada, Facultad de Ingeniería, Universidad Nacional de Río Cuarto, Río Cuarto, Argentina
[4] University of Maryland at College Park, College Park, MD, USA

Abstract. A computational co-simulation framework to study the aeroelastic behavior of a variety of aeronautical systems characterized by highly flexible structures undergoing complex motions in space and immersed in a low-subsonic flow is presented. The authors combine a non-linear aerodynamic model based on an extended version of the unsteady vortex-lattice method with a non-linear structural model based on a segregated formulation of Lagrange's equations obtained with the Floating Frame of Reference formalism. The structural model construction allows for hybrid combinations of different models typically used with multi-body systems, such as models based on rigid-body dynamics, assumed-modes techniques, and finite-element methods. The governing equations are numerically integrated in the time domain to obtain the structural response and the consistent flowfield around it. The integration is based on the fourth-order predictor-corrector method of Hamming. The findings are found to capture known non-linear behavior of these non-conventional flight systems. The developed framework should be relevant for conducting aeroelastic studies on a wide variety of aeronautical systems such as: micro-air-vehicles (MAVs) inspired by biology, morphing wings, and joined-wing aircrafts, among others.

Keywords: Aeroelasticity · Multibody dynamics · Aeronautical systems · Unsteady aerodynamics · Co-simulation

1 Introduction

Over the past decade, the aeronautical industry has been enriched by a great diversity of innovative and non-conventional designs such as the so-called High-Altitude Long-Endurance (HALE) vehicles based on both joined and strut-braced wings [1, 2], morphing wings aircrafts [3, 4], and Micro-Air-Vehicles (MAVs) inspired by biology [5, 6], among others. All these physical systems are characterized by highly flexible

J.C.M. Carvalho et al. (eds.), *Multibody Mechatronic Systems*,
Mechanisms and Machine Science 54, DOI 10.1007/978-3-319-67567-1_31

structures undergoing complex motions in space and, therefore, untreatable by means of closed-analytic approaches.

A number of different approaches were proposed to study the aeroelastic behavior of HALE aircrafts, which can be summarized as follows: strategies based on Rational Function Approximations (RFA) [7]; approaches founded in vortex methods coupled with several linear and non-linear structural models [8, 9]; and codes that use Euler/Navier-Stokes solvers coupled with various structural models [10]. It is worthwhile to mention the work of Zhao and Ren [11], who presented a multi-body dynamic approach for a flexible aircraft, where the aerodynamic loads are computed by using the strip theory combined with the ONERA aerodynamic model.

Like in the case of aircrafts, several numerical models have been proposed to investigate the dynamic response and aeroelastic limit states of morphing wings. Most of them intended for studying the static [12] and dynamic instabilities [13] of the wing in a fixed stage, i.e. once the wing ended its morphing process. On the other hand, very few works were found to deal with the aeroelastic characterization during the morphing process [14], perhaps because of the additional complication associated to a time-dependent wing geometry.

Finally, early aeroelastic studies for micro-air-vehicles were based on either two-dimensional models or other simplified aerodynamic approaches relying on thin-airfoil theory, unsteady panel methods or Euler methods and on linear beam finite elements [15]. Later on, several works on this subject were published by using approaches founded on Computational Fluid Dynamics (CFD) solvers coupled with a variety of structural models [16–18].

Computational difficulties and costs associated with the use of CFD models have led to alternative approaches. For example, the utilization of the unsteady vortex-lattice method (UVLM) has been gaining ground in the study of unsteady problems, in which free-wake methods become a necessity due to the geometric complexity of the aeronautical systems under analysis. Such a method was intensively used to investigate flapping-wing kinematics [19, 20], rotorcraft [21], and morphing wings [22].

In this paper, the authors present an extended unified aeroelastic framework based on the approach originally proposed by Preidikman and Mook [23] and Preidikman [24]. In these prior studies, the structures were much simpler than those considered here, and they were represented by means of traditional beam formulations based on assumed-modes/finite-element methods. In the authors' novel methodology, the dynamical system is partitioned into two subsystems (the structural and aerodynamic models) that communicate with each other across the boundary of the flow field (the surface of the structure) in a strong way. The computational environment can be considered a *strong co-simulation framework* [25]. Initial steps taken in this direction are presented in reference [26].

2 Aerodynamic Model

The aerodynamic loads are computed with the Unsteady Vortex-Lattice Method (UVLM) [20, 22, 24]. This method can be used to model flows over 3D lifting and non-lifting surfaces undergoing arbitrary time-dependent deformations and any motion

in space. UVLM can accurately describe aerodynamic interference among bodies. The bound-vortex sheets, which model the boundary layers, are replaced by a lattice of short, straight vortex segments with circulation $\Gamma(t)$. These segments are used to divide the wing surface into a number of elements of area (the so-called panels that generally are nonplanar). The model is completed by joining free vortex lines, representing the wakes, to the bound-vortex lattice along the separation edges, such as the trailing edges, wing-tips, and leading edges of the lifting surfaces. The locations at which separations occur are input data. However, in the wakes the positions of the vortex segments and their circulations are determined as part of the solution. The aerodynamic loads acting on the wings are computed based on the pressure differential between the top and bottom surfaces, which are computed for each panel by using the unsteady Bernoulli equation.

3 Flexible Multi-Body Model

The equations governing the structure were developed for large rotations and displacements, called *primary motions*, and small/moderate rotations and displacements with respect to a moving reference frame, called *secondary motions*. The primary motions describe the position and orientation of each body as a whole, and the secondary motions describe deformations. The Floating Frame of Reference (FFR) formalism and Lagrange's method for constrained systems [27] were used to derive the equations of motion. The aeronautical system is modeled as a collection of n_b rigid and deformable bodies subjected to n_c constraints, which are used to impose the connections and pre-defined motions. This approach requires the specification of $n_b + 1$ reference frames in order to describe the kinematics of the multi-body system: (*i*) an inertial system $\mathbf{N}$; and (*ii*) a reference system fixed to each body k, $\mathbf{B}^k$.

3.1 Equations of Motion

In order to simplify the manipulation, Lagrange's equations are separated into two groups: one corresponding to the set of coordinates used to describe translation and rotation of the FFR, $\mathbf{q}^k$, and the second to $\mathbf{p}^k$. Following the procedure presented by Shabana [27] and after some algebraic manipulations, the equations for *primary* and *secondary motions* for the k-th body are as follows:

$$\begin{aligned}
&\mathbf{M}^k\ddot{\mathbf{q}}^k + \left(\mathfrak{M}^k\right)^T\ddot{\mathbf{p}}^k + \mathbf{B}_{\mathbf{q}^k}^T\boldsymbol{\lambda}_k = \left(\boldsymbol{Q}_q^k\right)^T,\\
&\mathbf{m}^k\ddot{\mathbf{p}}^k + \mathfrak{M}^k\ddot{\mathbf{q}}^k + \mathbf{K}^k\mathbf{p}^k + \mathbf{B}_{\mathbf{p}^k}^T\boldsymbol{\lambda}_k = \left(\boldsymbol{Q}_p^k\right)^T,\\
&\boldsymbol{\Phi}^k\left(\mathbf{q}^{k-1}, \mathbf{q}^k, \mathbf{q}^{k+1}, \mathbf{p}^{k-1}, \mathbf{p}^k, \mathbf{p}^{k+1}; t\right) = \mathbf{0}, \quad \text{for } k = 1, \ldots, n_b.
\end{aligned} \tag{2}$$

Here, $\mathbf{M}^k$ is the mass matrix for primary motions, which is differentiable, symmetric and at least positive-semi-definite; $\mathfrak{M}^k$ is the mass matrix that couples primary and secondary motions; $\mathbf{m}^k$ is the metric tensor for secondary motions, which is constant, symmetric, positive-definite, and its matrix representation is the "elastic mass matrix";

$\mathbf{K}^k$ is the stiffness matrix for the secondary motions; $\boldsymbol{\lambda}^k$ is the vector of Lagrange multipliers; $\mathbf{B}_{\mathbf{q}^k}\left(\mathbf{B}_{\mathbf{p}^k}\right)$ is the Jacobian tensor of constraints associated with the coordinates $\mathbf{q}^k(\mathbf{p}^k)$; and $\boldsymbol{Q}_q^k\left(\boldsymbol{Q}_p^k\right)$ is the generalized load vector corresponding to the vector $\mathbf{q}^k(\mathbf{p}^k)$; and $\boldsymbol{\Phi}^k$ is the set of holonomic-reonomic constraint equations associated with the k-th body. It should be noted that $\mathbf{q} \in \mathbb{R}^{m\times 1}$ for $m \leq n_b$ and $\mathbf{p} \in \mathbb{R}^{n\times 1}$ for $n \leq n_b$. The total number of coordinates is calculated through $6n_b + \sum_{k=1}^{n_b} N_k = n_{coord}$ (N_k is the number of elastic generalized coordinates of the k-th body). Thus, the number of degrees of freedom is $n_{dof} = n_{coord} - n_c$. A beam element based on Euler-Bernoulli/Rayleigh theory is used. Hermite polynomials are used to interpolate displacement/rotation fields in each finite element from nodal values. First-order polynomials are used to interpolate elongation and torsion, and third-order polynomials are used to interpolate bending [28]. Finally, the equations of motion for the complete multi-body system are obtained by assembling the equations of motion for each body.

4 Inter-model Connection

At each time step, as shown in Fig. 1, there is a bi-directional exchange of information between the simulators for aerodynamics and structural dynamics. Since the structural mesh's topology is generally very complex, the classical methods for transferring information between the models, such as those used by Preidikman [24], are inadequate. To circumvent this problem, the authors propose the use of an interpolation procedure based on Radial Basis Functions (RBFs) [29].

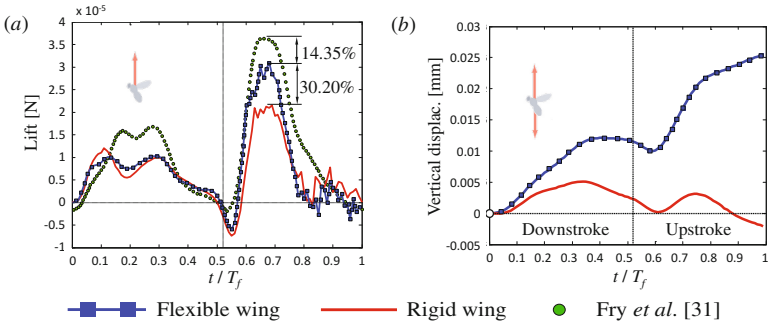

Fig. 1. Aerodynamic force and structure response, adapted from [26], (*a*) Lift force (green circular marks), (*b*) vertical displacement (Color figure online)

First, a linear relationship between the generalized displacements associated with both the aerodynamic mesh and structural mesh is established through a coupling matrix. In particular, such a linear transformation has been developed for combining UVLM grids with structural meshes based on beam finite elements. As the coupling

matrix only depends on the kind of RBFs used and the clouds of points to be interpolated, the same formulation is valid for other types of finite element meshes.

5 Numerical Results

In this section, results obtained with the implementation of the proposed methodology written in Fortran 90 are presented. The implementation is structured in a modular organization; that is, so that each part can be individually removed and replaced, as well as, the capability of adding new models without modifying the general structure of the program.

5.1 Aerial Vehicles with Flapping Wings

In this section, the numerical results obtained for the dynamic behavior of a fruit fly (*Drosophila Melanogaster*) in hovering flight are presented. The general equations of motion were adapted to consider only imposed deformations. These include torsion and bending in the directions normal and parallel to the wing's chord. Details of the kinematics and the dynamic models that allow one to prescribe such patterns of deformation are given in reference [30]. Data reported by Fry et al. [31] on the actual kinematics of a fruit fly in hover were used to describe the wing motion over a flapping cycle. For this numerical experiment the following parameters were chosen: flapping frequency n_f = 210 Hz; wing span R = 2.5 mm; wing area S = 2.21 mm^2; air density ρ_{air} = 1.2 kg/m^3; and insect's mass of 0.84 mg. Only the first stroke cycle was simulated, which was discretized into 100 time-steps. Two cases are presented next. In the first, the authors consider a rigid wing, and in the second, the authors consider a flexible wing with prescribed deformation. In order to show the role of the wing's flexibility in the production of lift, the parameters that regulate the deformation were tuned in order to increase the lift force throughout the stroke cycle with respect to the rigid-wing model. The set of initial conditions for the two cases of study consist of a body angle of 75º and a stroke plane angle of 15º. These values produce a horizontal stroke plane. Both the linear and angular velocity of the MAV's fuselage are zero at $t = t_0$.

The most important requirement of hovering flight is undoubtedly that the value of the vertical force must compensate for the insect's weight. In Fig. 1*a*, a peak force can be observed at the center of each halfstroke, mainly during the upstroke. The peak force produced by the flexible wing is approximately 30% higher than what the rigid-wing model predicts. This fact is also reflected in Fig. 1*b*, in which the degree of freedom associated with the vertical displacement of the center of mass of the central body has been plotted. In order to assess the quality of numerical simulations, the aerodynamic forces obtained numerically are compared with experimental measurements reported by Fry et al. [31] showing a good agreement. Nevertheless, lift levels predicted by the numerical model are lower than those measured experimentally (approximately 14% lower for flexible wing case). Possibly, this fact is due to two factors: (*i*) LEV phenomenon is not taken into account, and (*ii*) the wing deformation is not exactly that showed by insects, but it is prescribed my means of harmonic functions.

5.2 Morphing Wings

In this subsection, the authors present numerical results related to the aeroelastic behavior of an aerial-robot wing model whose planform geometry is based on the seagull wing. The wing's structural skeleton consists of a set of structural elements modeled as beams with rectangular cross-sections (width = 2 cm and height = 0.6 cm) and material properties: density ρ_b = 1187 kg/m3, Young's modulus E = 3.18 GPa and shear modulus G = 1.35 GPa. The inner and outer wing sections are oriented in space through the dihedral angles θ_B and θ_C (see Fig. 2*b*). However, the wings do not have a prescribed motion (pitching, flapping, lagging) and the wing's roots are considered to be clamped to the fuselage. This dynamic configuration deactivates the large rotations and displacements associated with primary motions; therefore, the set of governing Eq. (2) is reduced to the well-known set of classical ODEs for structural dynamics.

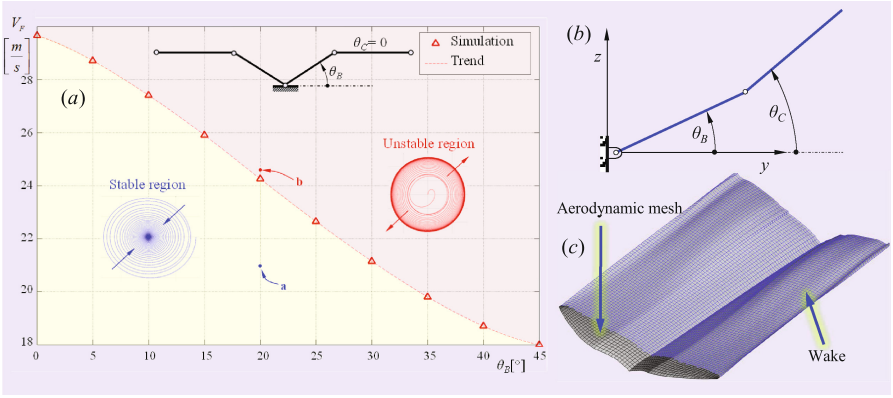

Fig. 2. (*a*) Flutter speed versus dihedral angle of the inner wing, (*b*) definition of the inner and outer dihedral angles, (*c*) wing and wake dynamics during flutter (29.66 m/s)

The numerical experiment consist of compute the flutter velocity for different dihedral angles, ranging from θ_B = 0º to θ_B = 45º, with steps of $\Delta\theta$ = 5º. θ_C = 0º was used for all values of θ_B. Due to the lack of primary motions, the dihedral angles remain constant during the whole simulation. Additionally, the angle of attack is α = 0º for all simulations. In Fig. 2*a*, the authors show the flutter speed versus the dihedral angle of the inner wing θ_B. It can be observed that V_F decreases linearly from 29.66 m/s (for θ_B = 0º) to a minimum of 18 m/s for θ_B = 45º.

In Fig. 2*a*, the curve represents a boundary for the stable and unstable regions. All flight conditions located below the curve (point a) lead to a response that tends to a static equilibrium position for any perturbation. On the contrary, the response for flight

conditions located above the curve (point b) achieves a periodic motion with an amplitude that depends on the flight speed, which could lead to a collapse of the structure. In the phase portrait, this behavior is characterized by the presence of a limit cycle oscillation (LCO). In Fig. 3*c*, the authors show the wing (bound-vortex lattice) and the wakes (free-vortex lattice) at the flutter speed.

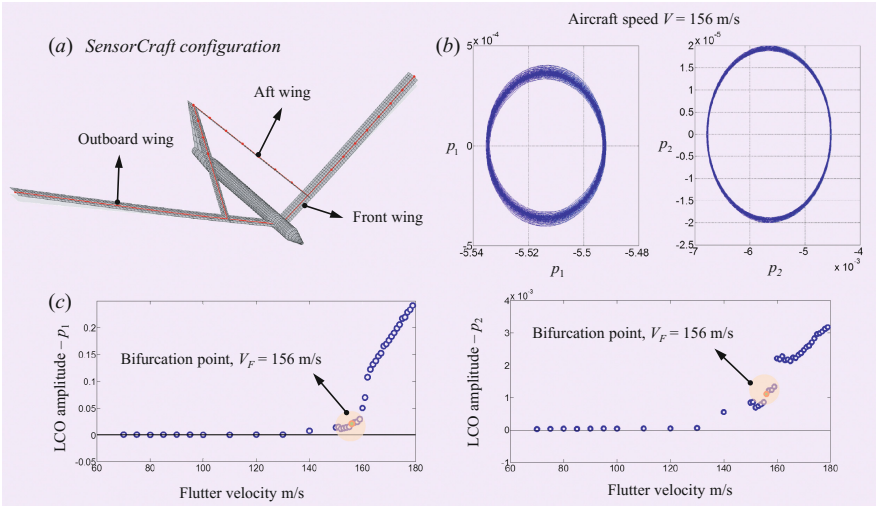

Fig. 3. (*a*) SensorCraft configuration, (*b*) LCO for p_1 and p_2, (*c*) bifurcation diagram for p_1 and p_2

5.3 Joined-Wings Aircraft – SensorCraft Configuration

In this subsection, the authors present numerical results of the aeroelastic behavior of a joined-wings aircraft based on the SensorCraft concept [2]. The computational model consist of: (*i*) a finite-element mesh for the structural discretization of 19 beam elements; and (*ii*) an aerodynamic grid for the entire aircraft of 1410 panels. Because of a SensorCraft-based configuration, the lifting surfaces are composed by three well-differentiated parts: the front wing, the aft wing and the outboard wing (see Fig. 3*a*). The material properties for all of them is aeronautic aluminum 2024-T3. Regarding the geometric cross-section properties, these are: area $A = 0.01744$ m^2, second moment of the cross-section $I_y = 0.330274 \times 10^{-3}$ m^4 and $I_z = 0.757632 \times 10^{-2}$ m^4, polar moment of inertia $J_p = 0.790659$ m^4, and torsional moment of the cross-section $J_{Torsion} = 0.105536 \times 10^{-2}$ m^4.

Because of the lack of primary motions, the governing equations are similar to those obtained in Subsect. 5.2 for morphing wings. Furthermore, a reduced order model is built from the full finite-element formulation by expressing secondary motions as linear combination of the first 10 free vibration modes of the structure, whose natural frequencies are listed in Table 1.

Table 1. Natural frequencies

Mode i →	1	2	3	4	5	6	7	8	9	10
ω_i [Hz] →	0.37	0.87	1.55	2.22	2.53	2.67	3.76	4.59	5.06	6.06

The procedure followed to determine the critical velocity (flutter speed) is time-consuming. During each run of the aeroelastic code, 240 s of physical time are simulated. The set of initial conditions is equal to zero and the air density is $\rho_{air} = 0.1152$ kg/m^3. After an exploration process ranging from 110 m/s to 160 m/s, a critical velocity (for the aircraft configuration analyzed) was found to be 156 m/s. At this velocity, the time evolution of the generalized coordinates shows a brief transient followed by an oscillatory behavior with constant amplitude. Specifically, the phase portrait of the first two generalized coordinates, p_1 and p_2, exhibit a limit cycle oscillation (see Fig. 3*b*).

In Fig. 3*c* the authors built a bifurcation diagram for coordinates p_1 and p_2, where the LCO amplitude is plotted versus the aircraft speed. In such diagram, a dispersion on the LCO's amplitudes can be observed at low velocities, *i.e*. subcritical. To circumvent this problem, the simulation time should be longer in order to achieve a full steady-state regime.

6 Conclusions

A combined structural and aerodynamic model for studying the aeroelastic behavior of aeronautical systems with flexible wings has been presented and aeroelasticity studies have been carried out for systems with flexible wings. The modular approach is based on the following: (*i*) a general, non-linear-unsteady vortex-lattice method, (*ii*) a segregated version of Lagrange's equations and the Floating Frame of Reference formalism for constrained systems, (*iii*) tight coupling of the aerodynamic model (UVLM) with the structural model, *iv*) Radial Basis Functions to transfer information between the aerodynamic and structural grids, and (*v*) an efficient and novel algorithm, based on a computational platform with modular structure, to integrate the equations interactively and simultaneously in the time domain.

As illustrated by the examples, the authors' methodology is well-suited to carry out fully coupled aeroelastic simulations for MAVs with flapping wings, morphing wings and joined-wings aircrafts. The very promising features warrant further investigations in this address, and although the proposed model constitutes a good starting point to improve the understanding of the aeroelastic behavior of a number of aeronautical applications, more research will be necessary. Their development paves the way to advance the current methodology by implementing a vortex-particle method to improve the description of the wakes and a fast multi-pole method for computing the velocity field, and by including various other beam and shell elements.

Acknowledgments. The authors gratefully acknowledge the partial support received from the Consejo Nacional de Investigaciones Científicas y Técnicas, Argentina, the U.S. National Science Foundation through Grant No. CMMI-1250187, the U.S. Air Force Office of Scientific Research through Grant No. FA95501510134, and the Minta Martin Foundation. In addition, the authors would like to thank the Grupo de Matemática Aplicada (GMA), Engineering School, Universidad Nacional de Río Cuarto, Argentina.

References

1. Lucia, D.J.: The sensorcraft configurations: a non-linear aeroservoelastic challenge for aviation. In: Proceedings of 46th AIAA/ASME/ASCE/AHS/ASC Structures, Structural Dynamics and Materials Conference, AIAA Paper 2005-1943, Austin, TX, USA, 18–21 April 2005
2. Cavallaro, R., Demasi, L.: Challenges, ideas, and innovations of joined-wings configurations: a concept from the past, and opportunity for the future. Prog. Aerosp. Sci. **87**, 1–93 (2016)
3. Barbarino, S., Bilgen, O., Ajaj, R.M., Friswell, M.I., Inman, D.J.: A review of morphing aircraft. J. Intell. Mater. Syst. Struct. **22**, 823–877 (2011)
4. Valasek, J.: Morphing Aerospace Vehicles and Structures. Wiley, UK (2012)
5. Lentink, D., Biewener, A.A.: Nature-inspired flight – beyond the leap. Bioinspir. Biomim. **5**, 040201 (2010). 9 pp.
6. Taha, H.E., Hajj, M.R., Nayfeh, A.H.: Flight dynamics and control of flapping-wing MAVs: a review. J. Nonlinear Dyn. **70**(2), 907–939 (2012)
7. Baldelli, D.H., Chen, P.C., Panza, J.: Unified aeroelastic and flight dynamic formulation via rational function approximations. J. Aircr. **43**(3), 763–772 (2006)
8. Varello, A., Carrera, E., Demasi, L.: Vortex lattice method coupled with advanced one-dimensional structural models. ASD J. **2**(2), 53–78 (2011)
9. De Souza, C.E., da Silva, R.G.A., Cesnik, C.E.S.: Nonlinear aeroelastic framework based on vortex lattice method and co-rotational shell finite element. In: 53rd AIAA/ASME/ASCE/AHS/ASC Structures, Structural Dynamics and Materials Conference, AIAA Paper 2012-1976, Honolulu, Hawaii, USA, 23–26 April 2012
10. Hallissy, B.P., Cesnik, C.E.S.: High-fidelity aeroelastic analysis of very flexible aircraft. In: 52nd AIAA/ASME/ASCE/AHS/ASC Structures, Structural Dynamics and Materials Conference, AIAA Paper 2011-1914, Denver, Colorado, USA, 4–7 April 2011
11. Zhao, Z., Ren, G.: Multibody dynamic approach of flight dynamics and nonlinear aeroelasticity of flexible aircraft. AIAA J. **49**(1), 41–54 (2011)
12. Thwapiah, G., Campanile, L.F.: Nonlinear aeroelastic behavior of compliant airfoils. Smart Mater. Struct. **19**, 035020 (2010)
13. Wang, I., Gibbs, S.C., Dowell, E.H.: Aeroelastic model of multi segmented folding wings: theory and experiment. J. Aircr. **42**(2), 911–921 (2012)
14. Hu, H., Yang, Z., Gu, Y.: Aeroelastic study for folding wing during the morphing process. J. Sound Vib. **365**, 216–229 (2016)
15. Kim, D.K., Lee, J.S., Lee, J.Y., Han J.H.: An aeroelastic analysis of a flexible flapping wing using modified strip theory. In: SPIE 15th Annual Symposium Smart Structures and Materials, vol. 6928 (2008)
16. Nakata, T., Liu, H.: A fluid-structure interaction model of insect flight with flexible wings. J. Comput. Phys. **231**, 1822–1847 (2012)

17. Chimakurthi, S.K., Stanford, B.K., Cesnik, C.E.S., Shyy, W.: Flapping wing CFD/CSD aeroelastic formulation based on a co-rotational shell finite element. In: 50th AIAA/ASME/ASCE/AHS/ASC Structures, Structural Dynamics, and Materials Conference, AIAA Paper 2009-2412, Palm Springs, California, USA, 4–7 May 2009
18. Unger, R., Haupt, M.C., Horst, P., Radespiel, R.: Fluid-structure analysis of a flexible flapping airfoil at low Reynolds number flow. J. Fluid Struct. **28**, 72–88 (2012)
19. Ghommem, M., Hajj, M.R., Mook, D.T., Stanford, B.K., Beran, P.S., Snyder, R.D., Watson, L.T.: Global optimization of actively morphing flapping wings. J. Fluids Struct. **33**, 210–228 (2012)
20. Roccia, B.A., Preidikman, S., Massa, J.C., Mook, D.T.: A modified unsteady vortex-lattice method to study the aerodynamics of flapping wings in hover flight. AIAA J. **51**(11), 2628–2642 (2013)
21. Wie, S.Y., Lee, S., Lee, D.J.: Potential panel and time-marching free-wake coupling analysis for helicopter rotor. J. Aircr. **46**(3), 1030–1041 (2009)
22. Verstraete, M.L., Preidikman, S., Roccia, B.A., Mook, D.T.: A numerical model to study the nonlinear and unsteady aerodynamics of bioinspired morphing-wing concepts. Int. J. Micro Air Vehicles **7**(3), 327–345 (2015)
23. Preidikman, S., Mook, D.T.: Time-Domain simulations of linear and non–linear aeroelastic behavior. J. Vib. Control **6**(8), 1135–1176 (2000)
24. Preidikman, S.: Numerical Simulations of Interactions Among Aerodynamics, Structural Dynamics, and Control Systems. Ph.D. thesis, Virginia Polytechnic Institute and State University, Blacksburg (1998)
25. Kalmar-Nagy, T., Stanciulescu, I.: Can complex systems really be simulated? Appl. Math. Comput. **227**, 199–211 (2014)
26. Roccia, B.A., Preidikman, S., Balachandran, B.: Computational dynamics of flapping wings in hover flight: a co-simulation strategy. AIAA J. (2017, in press)
27. Shabana, A.A.: Dynamics of Multibody Systems, 3rd edn. Cambridge University Press, Cambridge (2010)
28. Cook, R.D., Malkus, D.S., Plesha, M.E., Witt, R.J.: Concepts and Applications of Finite Element Analysis, 4th edn. Wiley, New York (2001)
29. Beckert, A., Wendland, H.: Multivariate interpolation for fluid-structure-interaction problems using radial basis functions. Aerosp. Sci. Technol. **5**, 125–134 (2001)
30. Roccia, B.A., Preidikman, S., Verstraete, M.L., Mook, D.T.: Influence of spanwise twisting and bending on lift generation in MAV-like flapping wings. J. Aerosp. Eng. (ASCE) **30**(1), 1–17 (2016). Paper 04016079
31. Fry, S.N., Sayaman, R., Dickinson, M.H.: The aerodynamics of hovering flight in drosophila. J. Exp. Biol. **208**, 2303–2318 (2005)

ILQG Planner Applied to Dynamic Systems with Intermittent Contact

Henrique B. Garcia(✉), Leonardo S. Luna, Gustavo Jose Giardini Lahr, and Glauco A.P. Caurin

Robotics Manipulation Laboratory, Engineering School of Sao Carlos, University of Sao Paulo, Sao Carlos, SP, Brazil
henriqueborgesgarcia@gmail.com

Abstract. The usage of simulated environments for robotics tasks enables the design and preliminary analysis of trajectory planners. There are different methods that can be used to generate paths, and controllers that allow the strategy definition at a higher level are extremely useful. This study seeks to generate trajectories in a simulated environment through an optimization process in an intermittent contact task. An iLQG controller coupled with a predictive controller aims to keep a ball bouncing in the air. Using the physics engine MuJoCo, results are presented in a simulation environment. Analysis of the control action for each axis variation, the sphere position and the robot tool center point over time are presented. The utilized method has shown interesting results for applications where emergent behaviors are expected.

Keywords: Dynamic programming · iLQG · Model predictive control · Rigid bodies simulation

1 Introduction

The simulation process of both trajectory and controller of robotic systems must combine fidelity to the real world and processing capacity. That is a hard task to achieve, since the fine tuning of compensators is difficult, and numerical processing often leads to undesirable large simulation times. To overcome this problem, most software simulate mechanical structures as rigid bodies. This technique, although not an actual situation, allows good solutions in many cases, thus aiding the design of robotic systems.

There are some physical simulation engines that allow this interface. Some of the most famous engines are the PhysX [5], Havok [6], ODE (open-source) [9] and Bullet (open source) [1]. All of them are used as physics engines for games, but the latter two are mainly used in robotics projects, such as V-REP [11].

A physics engine was developed specially to help robotics design, named MuJoCo: **Mu**lti-**Jo**int dynamics with **Co**ntact [14]. It was thought to be applied in controller design, unlike its commercial competitors, who are interested in the simulation of entire environments. This physics engine has useful features for

J.C.M. Carvalho et al. (eds.), *Multibody Mechatronic Systems*,
Mechanisms and Machine Science 54, DOI 10.1007/978-3-319-67567-1_32

its target area, such as the possibility of calculations of the system dynamic without the obligation to update the simulation, which is useful for the finite difference method [14]. Also, the engine makes it possible to calculate the inverse dynamics even in the presence of contacts and equality constraints. It is possible to program in different languages, and therefore the engine works as a library with all the models and dynamics calculations embedded.

A comparative study of the physics engines was conducted by [3], analyzing the speed, accuracy and stability of algorithms using identical dynamic models. In the study were tested a model of a robotic arm with a hand to grasp a body, accounting for a total of 35 degrees of freedom (DoF), and a model of 27 capsules in free fall (162 DoF). The MuJoCo achieved better results in numerical stability in the grasp situation with robotic hand, since its integration time step could reach up to 16 ms and still perform the task with stability, while the second best result was the PhysX with a maximum step of 2 ms. The other results are shown in Table 1, with ODE and Bullet having a maximum step 64 and 512 times smaller than MuJoCo.

Table 1. Maximum integration time steps

Physics engines	Integration steps (ms)
Bullet	1/32
MuJoCo	16
ODE	1/4
PhysX	2

MuJoCo was the fastest simulator in the grasp simulation, performing 6.5 thousand evaluations per second, and the slowest one in the capsules simulation, with only 3.6 thousand evaluations, 7 times less than ODE. However, in both simulations MuJoCo had the most accurate results. Figure 1 shows the two simulated situations and the performance of each physics engine. The third column shows the accuracy of simulation for its speed in relation to reality. The data placed closer to the top right section of the plot have the highest speed and lowest discrepancy, therefore meaning a better simulator.

Being developed specially for games simulation, both Havok and PhysX do not require high positioning precision. To improve stability and speed in the calculations, they do not take into account the components of Coriolis forces, which must not be ignored in many applications in robotics. MuJoCo, for its turn, does not rule out this factor.

This paper applies MuJoCo in the simulation of a dynamic programming situation using *iterative Linear-Quadratic-Gaussian* controller (iLQG), an iterative algorithm that resembles the classic *Differential Dynamic Programming* (DDP) [7], but differs in the usage of the derivatives of the dynamics [13]. The proposed task is to hit a free body, a spherical geometry, with a paddle. The ball is released

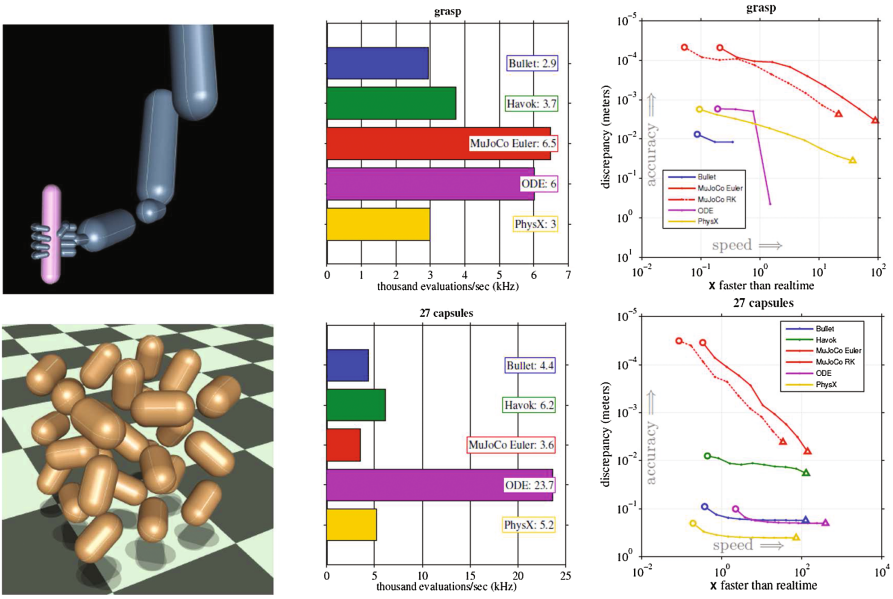

Fig. 1. Comparison between the available physics engines [3]

from an specified height, and the controller makes the TCP (Tool Center Point) in the paddle follow the sphere's XY position in space, bouncing it in the Z direction, trying to prevent its fall. The MuJoCo works as an implementation platform of the rigid body model and the controller, allowing the creation of a prototype of the real system.

2 Simulation Environment and Control Strategy

To be able to simulate with MuJoCo, two steps are required: geometric modeling (Sect. 2.1) and definition of the control strategy (Sects. 2.2 and 2.3). The iLQG is in charge of calculating the control action. The technique requires a cost function, its weights and their predefined values, which are obtained through predictive control. The sphere is approximated to a material point in space and kinematic equations are used to predict its movement.

2.1 Geometric Modelling

MuJoCo provides convex shapes for geometric modeling, as the contact recognition is based on these equations [4]. Capsules, spheres, ellipsoids, cones and boxes are some examples of shapes available to the user. If a non-convex shape is necessary, it is possible to create the geometry through the concatenation of the available forms.

All data is defined in this step: positions of actuators, reduction ratio, damping and friction in the joints and between the bodies, integration time step and many other characteristics. The type of actuator depends on which joint is implemented, among linear (slide) and rotating (hinge). Other joints may be further defined: spherical (three rotations in space) and free (three displacements and three rotations), which are represented by 4 and 7 generalized coordinates, respectively. This is defined because the engine uses quaternions to describe a rotation in space [14].

A unique feature is that the mentioned joints can compose more complex joints without the need for defining auxiliary dummy bodies [14], which is a common practice in classic rigid body softwares. The geometric model is defined by a XML document, which allows the concatenation of bodies in sequence simply nesting the file tags. Although the basic geometry types are limited to the ones mentioned, it is possible to import a mesh from a CAD file, improving the visualization of the whole system.

The proposed model corresponds to a paddle capable of moving in the three Cartesians directions: XYZ, represented by the red, green and blue directions, respectively, in Fig. 2. Therefore, the TCP is a cylinder-type rigid body with three linear joints, with a reduction ratio of 1000 for all directions. The sphere has three linear type joints, with all rotations ignored. This is justified by the fact that in the real system its rotation can be disregarded, since that with the system working properly at the time of contact, the horizontal speed of the TCP is very small. At the start of the simulation, the sphere is located in the air, distant to the TCP by 2 m in Z direction. Figure 2 shows the geometric model and its configuration at the start of the simulation.

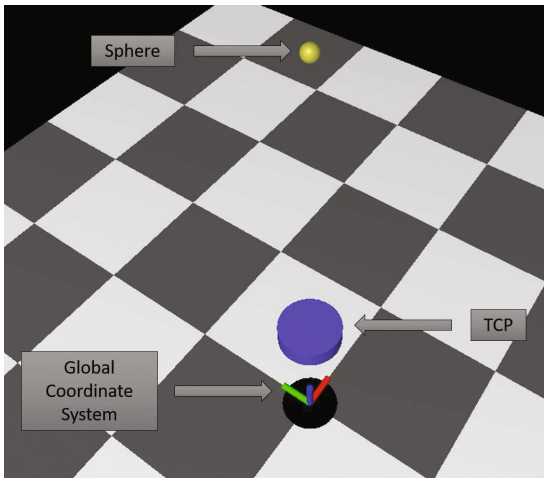

Fig. 2. Geometric model used in the simulation with sphere and TCP

2.2 iLQG Algorithm

The second step requires the implementation of the controller. In this study, it was used the algorithm known as iLQG [13], modifying the feedback gain matrix to allow the controller to work with constraints in stochastic systems. To illustrate the operation of the algorithm, an implementation was developed comprising the steps proposed by [13], shown in the flowchart, Fig. 3. The method begins with the time discretization in K steps, each with Δt s long.

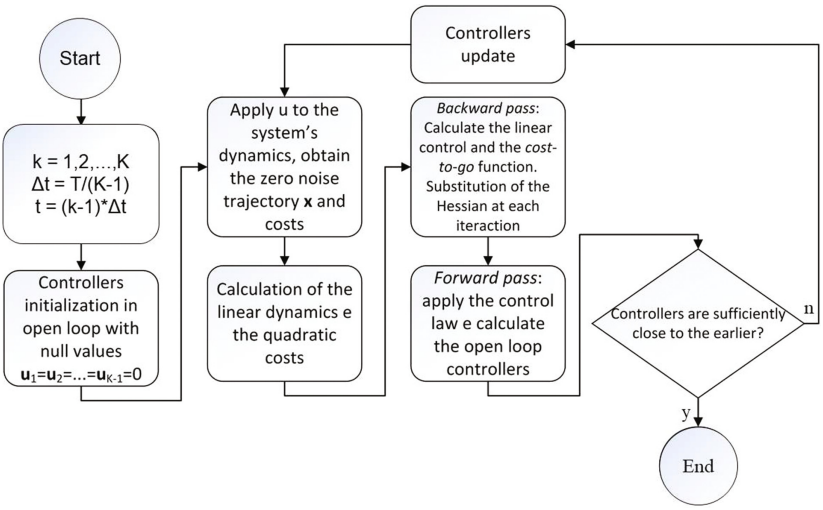

Fig. 3. Flowchart presenting the steps of iLQG algorithm

The strategy is implemented with a cost function that involves various system characteristics in question [8]. All instructions are high level if compared to traditional controller techniques, which tends to control the motors' current to achieve the desired movement. In this type of implementation the desired characteristics are defined, and then a cost function that penalizes the system, when it is not in accordance with the desired characteristics, must be created.

To transform the LQG technique into an iterative one, it was proposed by the authors a technique known as dynamic programming, which requires the division of the system in states [13]. In the initial situation, the robot finds itself at simulation start, and the end state is the desired final position, dividing the interval in auxiliary states. The dynamic programming then starts calculating the final state, which is the desired, and returns calculating the earlier stages [10], until the initial state. The control actions are the output of this method.

Equation (1) shows the cost function of the whole system, which has the term of each state ($l(x(t), \mathbf{u}(t))$), and only the last state, $h(x(T))$, is independent of the action of control, $\mathbf{u(t)}$. The Eqs. (2) and (3) present the terms to be calculated at the end.

The algorithm is responsible for finding the control action $\mathbf{u}(t)$ that minimizes the cost J_0. v_{sphere}^{after} is the actual speed of the ball right after the contact, and $\mathbf{v}_{desired}$ the desired speed after the shock. $p_{desired}$ is the wanted position in the Z coordinate of the TCP, and H is the unit step function with $\dot{b}_z$ being the velocity of the ball in Z directions right before the contact. For its turn, w_v is the weight in the sphere return speed error, w_w is the weight of the XY paddle position distance from the center of the workspace, w_z weights the error of the distance from the actual position of the TCP (p_z) with $p_{desired}$, w_p is the sphere error related with the projection in the XY plane of the TCP, and w_d weights the sphere velocity before the contact.

$$J_0 = h(x(T)) + \sum_{t=1}^{T-1} l(x(t), \mathbf{u}(t)) \tag{1}$$

$$l(x, \mathbf{u}) = \|\mathbf{u}\|^2 + w_w \|\mathbf{p}_{xy}\|^2 + w_z (p_z - p_{desired})^2 + w_p \|\mathbf{p}_{xy} - \mathbf{b}_{xy}\|^2 \tag{2}$$

$$h(x) = w_v \|v_{sphere}^{after} - \mathbf{v}_{desired}\|^2 + w_d H(\dot{b}_z) + w_p \|\mathbf{p}_{xy} - \mathbf{b}_{xy}\|^2 \tag{3}$$

2.3 Predictive Control

As the desired height that the sphere must reach is not controlled directly, but through the interaction with the TCP, it is necessary to understand what are the characteristics of the state during contact, translated to the end cost $h(x(T))$. This equation involves $v_{desired}$, which will lead to a impact related to the intended maximum height, defined by the kinematic equations of the free sphere in space. It is known that, in simulated environment, viscous dissipation of the air may be disregarded. Then, by the mechanical energy conservation law, the desired speed of the sphere leaving contact is given by Eq. (6). Using the kinematic equation of partially elastic collision between two bodies (Eq. (5)), it was defined the speed that the TCP should have at the time of the collision. Right after the contact, the sphere has the speed needed to achieve the desired height. As the velocities of the TCP and the ball in the state $x(t)$ are known and the speed of the TCP in the state $x(t + \delta t)$ is approximated by Eq. (4), it is possible to obtain v_{sphere}^{after}. The difference between v_{sphere}^{after} and $v_{desired}$ is the error of the sphere return speed, that is the related instruction to w_v.

$$v_{TCP}^{after} = v_{TCP}(T + \Delta t) = 2v_{TCP}(T) - v_{TCP}(T - \Delta t) \tag{4}$$

$$e = \frac{v_{separation}}{v_{approximation}} = \frac{v_{sphere}^{after} - v_{TCP}^{after}}{v_{sphere}^{before} - v_{TCP}^{before}} \tag{5}$$

$$v_{desired} = \sqrt{2gh} \tag{6}$$

For the parameters of the geometric modeling used, the coefficient of restitution was calculated for the defined time step as $e = 0.77$. Note that, although it is possible for the iLQG to deal with stochastic systems, which is a interesting approach to the intermittent contact between the sphere and the paddle, it was not used in the current study. Instead, the dynamic of the bodies was calculated by kinematic equations.

2.4 Simulation

Using MuJoCo as a library for the Matlab environment, a simulation was conducted using the geometric models and controller described in previous sections. The weights were estimated empirically, and each one is related to a high level instruction. The best results and their respective values are displayed at Table 2.

Table 2. Simulation weights implemented

Weight	Related instruction	Value
w_w	XY position of the paddle	10
w_z	desired height of the paddle	10
w_p	XY projection of the sphere in the paddle	50
w_v	desired sphere return speed	50
w_d	sphere speed before contact	1

The integration time step is 1 ms, the mass of the TCP was fixed at 1 kg, and the weight of the sphere, in the simulation environment, is 26.8 g.

Figure 4 shows the results about the XY positions. It was calculated the L_2 norm of the error between the center of the paddle and the sphere along XY axis, resulting in the Fig. 4a. The red line is the radius of the paddle. A qualitative examination is possible with Fig. 4b, which demonstrates that all

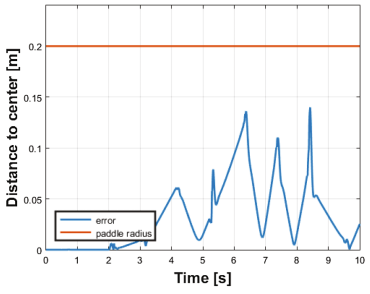

(a) Distance between the center of the paddle and the sphere

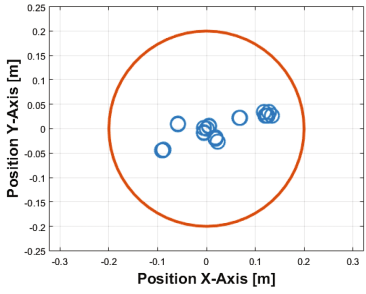

(b) Points of contact of the sphere relative to the position of the paddle

Fig. 4. Analysis of the XY positions between the two bodies: L_2 norm of the error (a) and relative position of the sphere (b)

sphere positions were inside the initial simulated position of the paddle. As it is possible to notice from the figure, the TCP was successful at keeping a planar alignment with the sphere.

The Z position of both bodies is shown in Fig. 5a, where the distance between the center of the bodies is because of the geometry size. The nonexistence of a crossing between the Z positions of both bodies show that the controller was successful to bounce the sphere during the 10 s of the simulation. Figure 5b shows the control signals in the X, Y and Z axis. The controller actions increased close to the contact with the ball, and the controller almost did not act when the ball is in the air.

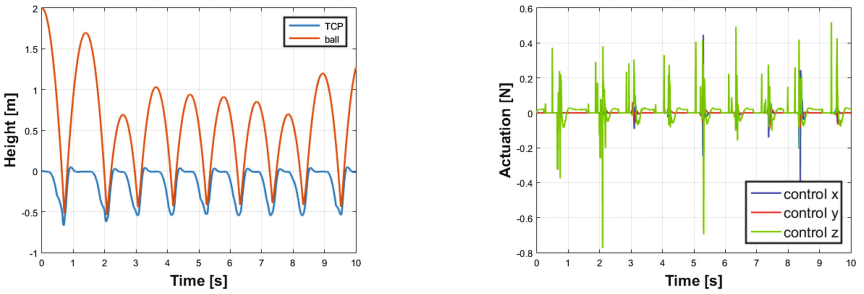

(a) Z positions

(b) Controller signals send to the TCP

Fig. 5. Z position (a) and control signals (b) versus time

However, the controller still troubles to return the sphere to the desired height. This is because of the complementary-free contact dynamics that MuJoCo uses [12], that makes difficulty to simulate the restitution coefficient of the intermittent contact.

3 Conclusion

The use of predictive control with an iterative LQG controller has been addressed in this study. To solve an intermittent contact condition was implemented a simulation that deals with the need of using algorithms that allow the insertion of high level instructions, changing the standard traditional implementations. The iLQG algorithm is a viable solution for non-trivial control systems, even nonlinear, as shown in this study.

One may improve the results by adjusting the weights of the cost function, decreasing mass of TCP (to reduce inertia) and/or changing the control signal gain. The achievement of a more realistic coefficient of restitution and its implementation in the simulation is also intended, such as a stochastic approach to the intermittent contact between the bodies. In further work, the aim is to allow the execution of an actual experiment using EEROS Delta robot [2] and a vision system.

Acknowledgements. We would like to acknowledge FAPESP (processes 2013/07276-1 and 2015/07484-9), EMBRAER (cooperation project GSI-1168-15), CNPq and CAPES.

References

1. Bullet Physics Library: Real-Time Physics Simulation (2016). http://bulletphysics.org/wordpress
2. EEROS (2016). http://eeros.org/
3. Erez, T., Tassa, Y., Todorov, E.: Simulation tools for model-based robotics: Comparison of Bullet, Havok, MuJoCo, ODE and PhysX. In: Proceedings of IEEE International Conference on Robotics and Automation, pp. 4397–4404. IEEE, June 2015. doi:10.1109/ICRA.2015.7139807
4. Featherstone, R.: Rigid Body Dynamics Algorithms, vol. 10. Springer, New York (2014). https://books.google.com/books?id=GJRGBQAAQBAJ&pgis=1
5. GeForce: PhysX (2016). http://www.geforce.com/hardware/technology/physx
6. Havok: About Havok (2016). http://www.havok.com/about-havok
7. Jacobson, D.H., Mayne, D.Q.: Differential dynamic programming (1970)
8. Kulchenko, P., Todorov, E.: First-exit model predictive control of fast discontinuous dynamics: application to ball bouncing. In: Proceedings of IEEE International Conference on Robotics and Automation, pp. 2144–2151 (2011). doi:10.1109/ICRA.2011.5980196
9. ODE-Wiki: Open Dynamics Engine (ODE) Community Wiki (2016). http://ode-wiki.org/wiki/index.php?title=Main_Page
10. Rao, S.S.: Engineering Optimization, vol. 56. Wiley, New Jersey (2009). doi:10.1080/03052150500066646
11. Robotics, C.: Features V-REP (2016)
12. Todorov, E.: Convex and analytically-invertible dynamics with contacts and constraints: theory and implementation in MuJoCo. In: 2014 IEEE International Conference on Robotics and Automation (ICRA), pp. 6054–6061. IEEE (2014). doi:10.1109/ICRA.2014.6907751. http://ieeexplore.ieee.org/lpdocs/epic03/wrapper.htm?arnumber=6907751
13. Todorov, E., Li, W.L.W.: A generalized iterative LQG method for locally-optimal feedback control of constrained nonlinear stochastic systems. In: Proceedings of the 2005 American Control Conference (2005). doi:10.1109/ACC.2005.1469949
14. Todorov, E., Erez, T., Tassa, Y.: MuJoCo: A physics engine for model-based control. In: 2012 IEEE/RSJ International Conference on Intelligent Robots and Systems, pp. 5026–5033. IEEE (2012). doi:10.1109/IROS.2012.6386109. http://ieeexplore.ieee.org/lpdocs/epic03/wrapper.htm?arnumber=6386109

Cost Effective Provisioning of Electricity in Smart Nano-grid Using GA and Optimized Heuristic Algorithm

Nabila Ahmad(✉), Rabiya Bibi, and Shoab Ahmed Khan

Computer Engineering, CEME, National University of Sciences and Technology (NUST), H-12, Islamabad, Pakistan
n.ahmad3293@gmail.com, rabiyabibi999@yahoo.com, kshoab@yahoo.com

Abstract. In the last few decades, developing countries power demand has increased which lead to several critical issues like frequent power outages and peak pricing hours. Utilization of distributed energy sources along with utility grid has helped to cope with these issues to certain level but still there are some loopholes. Novel intelligent algorithms are needed to handle such hybrid systems. In this paper, an algorithm is proposed for consistent and cost effective power supply for Grid-connected photovoltaic system which considers a set of constraints i.e. load-shedding hours, tariff hours and weather conditions. This paper proposes genetic algorithm for making optimal decision for the cost, considering all the above mentioned constraints. The research has also presented another heuristic algorithm which takes much less computation time then Genetic Algorithm and provides comparable results.

Keywords: Genetic algorithm · Best fitness value · Smart nano-grid · Heuristic algorithm

1 Introduction

According to U.S. Department of Energy (DoE) "Smart grid" commonly alludes to a class of advancements that individuals are using to bring utility power conveyance frameworks into the 21st century, making use of PC based remote control and automation. These frameworks are made conceivable by two way digital communication technologies and computer processing that has been in use for decades as a part of different ventures [1]. Despite of the fact that electricity demand has increased, there has been not sufficient investment to get the energy for transmission and supply. It also limits reliability and efficiency of the Grid. According to a survey, in developed country like United States, there have been incessant high-voltage transmission lines paths throughout the country and from 2000 to 2010; there has been only 668 additional miles interstate transmission. Therefore, framework imperative decline when blackouts and power quality issues are assessed to cost American business more than $100 billion almost each year [2].

J.C.M. Carvalho et al. (eds.), *Multibody Mechatronic Systems*,
Mechanisms and Machine Science 54, DOI 10.1007/978-3-319-67567-1_33

Distributed energy resources have become a major source of power production because of their unlimited supply and low installation cost. Solar energy is one of the attractive renewable energy sources. Although these resources are beneficial in many aspects but their irregular nature is one of the hurdles in their utilization which needs to be resolved. A grid connected solar system along with a storage unit i.e. battery can overcome this hurdle and will increase system efficiency and reliability. Innovative ideas are required to maintain a consistent flow of electricity between grid, renewable energy source and battery. The main objectives of the proposed research are:

- After the load consumption is satisfied, the remaining PV and battery is fed back to the grid resulting in net metering. One can even get profit instead of paying electricity bills
- Maximum power generation through renewable sources
- Consistent power supply to load
- Minimum use of utility grid at peak hours
- Cost effectiveness

In the proceeding sections, Sect. 2 is the literature review of the paper. Section 3 elaborates the proposed smart nano-grid algorithms and in Subsects. 3.2 and 3.3, algorithms are explained. Section 4 is the results and performance evaluation whereas in Sect. 5, conclusion and future work is analyzed. The inspiration driving this work is stable and efficient generation of electricity.

2 Literature Review

Recently, a significant amount of work has been carried out in the field of smart nano-grid. Study reveals that two primary objectives of the efforts were: to provide uninterrupted power supply to the load and minimized energy cost. The authors in [3] suggest a novel approach for optimization of total energy cost using genetic algorithm. The technique used by them is multivariable single objective genetic algorithm. Cost is analyzed for three different values of battery capacities and it is observed that electricity cost reduces as the battery storage capacity increases. Researchers used agent based modeling in [4] to propose a pre-test based model for smart grid simulation before establishing an actual smart grid. They divided the model into three layers; supply layer, demand layer and EMS layer. Supply layer is comprised of many renewable energy resources, the demand layer contains various types of loads and EMS layer ensures flow of electricity between demand and supply layer. A power management model based on object interaction is proposed in [5]. The model highlights the role of storage devices i.e. (batteries) to overcome the fluctuations caused by renewable energy resources for a stable power supply. In [6], a hybrid genetic tabu search algorithm is proposed. Many attempts have been made by various tools and heuristics to solve the job shop scheduling problem but none of the solutions were enough to resolve it. The reason for using hybrid method is to deal with the problem by combining the diversified search of GA and extensive local search of TS. To achieve better performance, multiple algorithms can be combined. In [7], Mehmet proposed genetic algorithm, Bayesian method and k-Nearest Neighbors (KNN) effective methods for machine

learning. Hybrid methods are used for classification by eliminating the data which gives better results. This approach is tested on UCI ML datasets which give successful results after investigating with the previous work. Metaxiotis and Liagkouras discuss review of Multiobjective Evolutionary Algorithms in [8]. They explain the evolution of genetic algorithm. Vector Evaluation Genetic Algorithm (VEGA) introduced in 1980's, which was the first implementation of MOEA. Then followed by Niched Pareto Genetic Algorithm (NPGA), Niched Pareto Genetic Algorithm II (NPGA-II), Non-dominated Sorting Genetic Algorithm (NSGA) and so on. With each evolution, adjustments were made to get enhanced results. Gabor el al proposed in [9] that complex optimization problems are solved well with genetic algorithm. They further proposed that GA brings novelty to the creative designs by finding the fittest of the population for survival and it is well suited for different engineering design domains.

In this research, an energy management system is suggested using two algorithms i.e. genetic algorithm and heuristic algorithm for Grid connected Photovoltaic (PV) system which manages power flow between PV, battery and Grid to provide uninterrupted and cost effective electric power supply. The illustration of the Grid connected distributed system is shown in Fig. 1.

The battery and PV can be used to feed the load i.e. providing power to the grid. Battery can be charged from the grid or from the solar panels. Similarly, system can make use of grid on cloudy days or in case of any power shortage/breakdown due to non-availability of PV and battery. The system has two way connections of electricity which makes it more stable. The whole energy flow requires an efficient approach to sense the deviation in power availability, load shedding hours, peak pricing hours, load demands in order to make optimized decision.

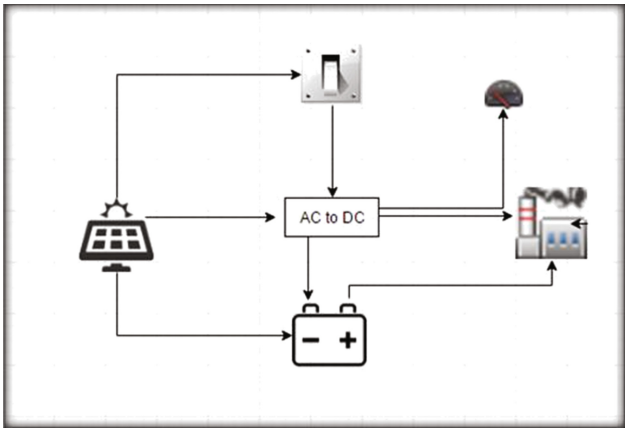

Fig. 1. A PV connected smart nano-grid system

3 Proposed Algorithms

3.1 Problem Formulation

Various scenarios are considered during implementation in MATLAB. As various resources are available for smart nano-grids, but in this paper, the resources considered have to be availed in such a manner so that there is minimum switching to the power grid for maximum natural resource utilization. One of the assumptions made for the proposed system is that battery is preferred to be charged with PV. Similarly battery has certain constraints:

$$\begin{aligned} BOC_{min} \leq BOC(t) \leq BOC_{max} \\ BOC_{min}\ \text{Is}\ 40\%\ \text{of Battery charging;} \\ BOC_{max}\ \text{Is}\ 90\%\ \text{of Battery charging;} \\ BOC(t)\ \text{Is the charging of the Battery at a particular instant;} \end{aligned} \tag{1}$$

Battery should not discharge below 40% and charge above 90%. It has to be between 40% and 90% of battery charging in order to increase battery life. If battery charging is less than 90, then battery is charged by PV or Grid.

$$\begin{aligned} 6:00:00\,pm \leq T(h) \leq 10:00:00\,pm \\ Grid\ Availability\ Pattern\ (1\ h\ outage\ after\ 3\ h) \end{aligned} \tag{2}$$

$T(h)$ is the Tariff Hours. For the following assumption, $T(h)$ Tariff hours is between 6 pm to 10 pm.

3.2 Genetic Algorithm

Genetic algorithm is well suited for problems in which objective function is nonlinear, discontinuous or stochastic as in [10]. It can solve both constraint and unconstraint problems. At each step, it selects individuals from current population and uses them as parents to produce offspring for coming generation. Successive generations lead to best solution. The basic steps for genetic algorithm are shown in Fig. 2.

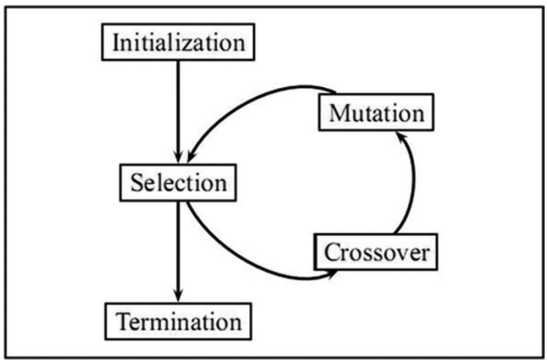

Fig. 2. The basic steps of genetic algorithm [10]

The steps involved in genetic algorithm are as follows: Initialization, Selection, Mutation, Crossover, and Termination. Detailed explanation of the steps is explained in the next Subsect. 3.2.1.

Genetic algorithms are a group of computational models motivated by advancement. These calculations encode a potential answer for a particular issue on a straightforward chromosome-like information structure, and apply recombination operators to these structures so as to save basic data. Genetic calculations are regularly seen as function analyzers, despite the fact that the scope of issues to which genetic algorithms have been applied is reasonably large.

3.2.1 Proposed Multivariable Single Objective Genetic Algorithm

The detail of multi-variable single objective Genetic Algorithm is described below:

- Initialization: A random population is created within bounds of each constraint variable. In the proposed solution [PV, Grid, and Battery] is assigned values which are Excel file input for a day. Random population is initialized for cost which is the output to be optimized.
- Evaluation: Offspring population is created and fitness is evaluated. Offspring population is given values which better fit the desired output.
- Selection: Selection allocates more copies of those solutions with higher fitness values and thus imposes the survival-of-the-fittest mechanism on the candidate solutions. Our algorithm uses Rank + Roulette wheel selection.
- Recombination: crossover parameter is set considering two parents to produce an offspring for recombination.
- Mutation: While recombination works on two or more parental chromosomes, mutation locally yet haphazardly changes a solution. Mutation was taken into account by mutation Gaussian function.
- Combined Population: Both parent and child population is combined using elitism function and then sorted based on fitness values. It is a black box through which output is acquired.
- Iterate: Repeat step 1 to 6 until convergence is achieved.

3.3 Optimized Heuristic Approach

The optimization algorithm takes into account all the above mentioned constraints and schedules them to optimize cost and generate consistent supply. There are two priority scenarios within an optimization algorithm: PV_Battery_Grid and PV_Grid_Battery. PV_Battery_Grid is valid for residential loads and PV_Grid_Battery is valid for industrial loads. The working of the algorithm for residential and industrial load is as follows.

3.3.1 Heuristics for Residential Area

The flow of Heuristics for residential area is shown in Fig. 3.

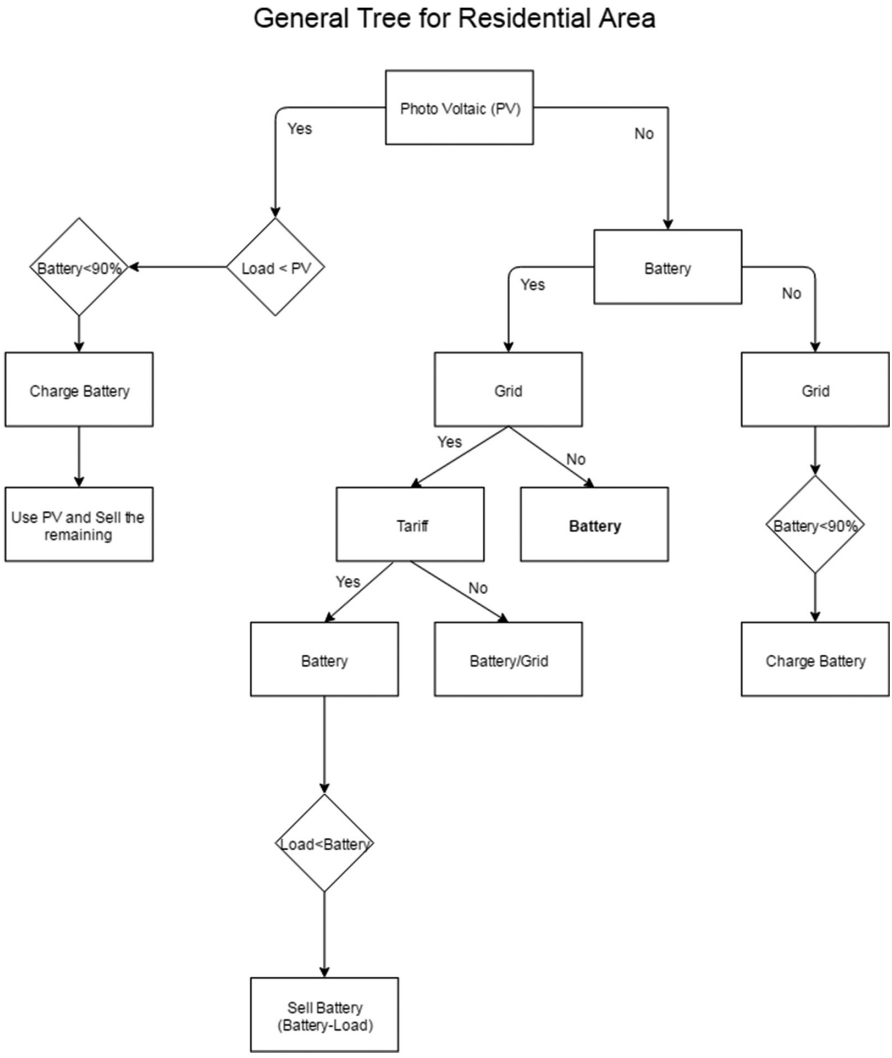

Fig. 3. Residential area heuristics

PV will be given high precedence, then Battery and then Grid. According to the 'load profiles' used, high power battery is used which will give an independent system and there is no switching to the grid as PV and Battery meet the requirement of the household profile. If the load profile reaches up to certain limit and there is a need for Grid utilization and Heuristic for residential areas do not meet the demand, then the system will switch to power grid as in Heuristics for industrial area discussed in

Sect. 3.3.2. In residential area, the load is fulfilled by PV, and battery is charged by PV. This system is of great importance because it almost reaches the stage of self sufficiency as PV and Battery are the only power supply source.

3.3.2 Heuristics for Industrial Area

In this algorithm, the precedence of PV is high as it was for residential Area heuristics. Then Grid is given priority over Battery unlike residential area heuristics. The flow chart is shown in Fig. 4. In the algorithm following steps are followed.

(1) Photovoltaic is checked, if it is available then use PV. Check Battery, if Battery charge is less than 90%, charge it and sell the remaining PV to the Grid. If PV is not available, go to step 2.

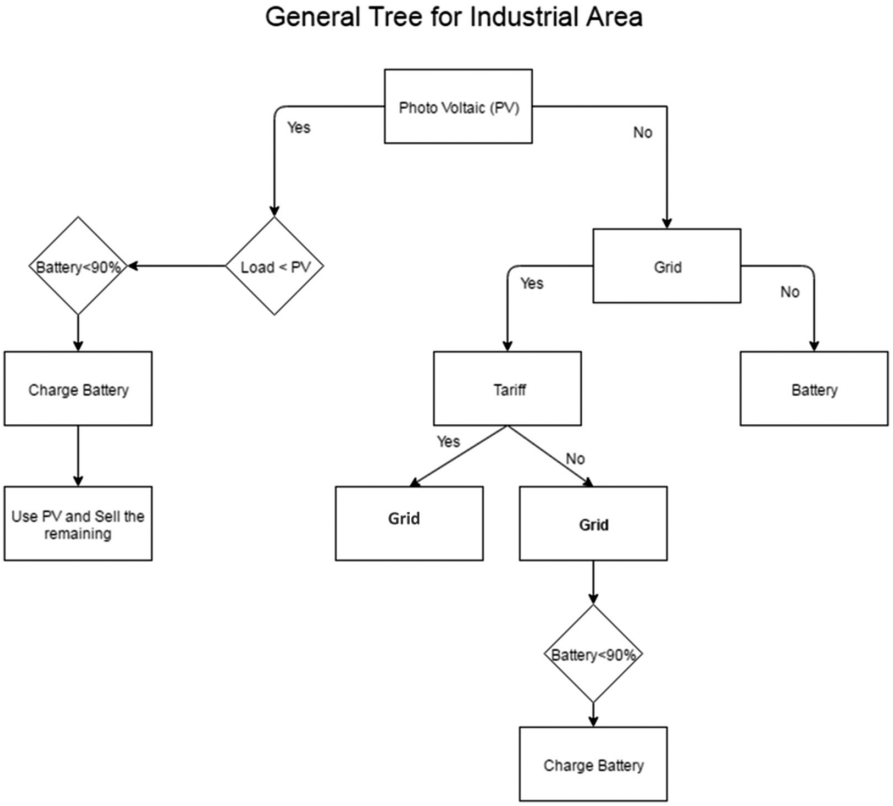

Fig. 4. Industrial area heuristics

(2) Check Grid, if Grid is available then it is time to check tariff hours. If it is high tariff hour, switch to the Battery utilization. For low tariff hours, Grid is preferred. If Battery charge is less than 90% and as PV is not available, charge the Battery from the Grid. If Grid is not available go to step 3. For residential Heuristic, if PV and Battery is not available, then the algorithm will proceed from step 2 of Industrial heuristics.
(3) Use Battery as it is charged from Grid and PV in blackouts.
(4) Go to Step 1.

3.3.2.1 User Case for Power Supply in Industrial Area

In a cloudy weather, PV is not available. Load will be shifted to grid. If neither grid nor PV is available, then battery will fulfill the load demand. After the availability of grid, battery will be charged with it. In this particular case, load will be shifted between the battery and the electric power grid.

4 Results and Performance Evaluation

In this research multi-variable, single objective algorithm is used. The algorithm is simulated using MATLAB to provide stable power at an optimized cost. Data is divided into different use cases e.g. industrial load profile and residential load profile in autumn, spring, summer and winter. One of the 24 h load profile from our dataset used for system evaluation is shown in Fig. 5.

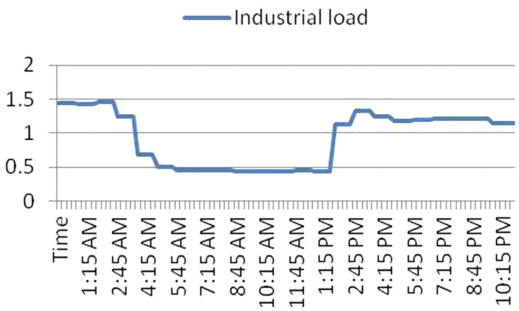

Fig. 5. 24 h load profile in spring season

Both the algorithms as described in Subsects. 3.3 and 3.4 are applied on our datasets and they produced comparable results. The grid utilization is minimized with supplying power to the grid. The graphical data in Figs. 6 and 7 indicates many negative values which is profitable for the consumer. The average electricity cost is in PKR (Pakistani Rupees) for 30 min each. A cost optimization by GA and estimated by heuristic algorithm for 24 h is shown in Figs. 6 and 7 respectively.

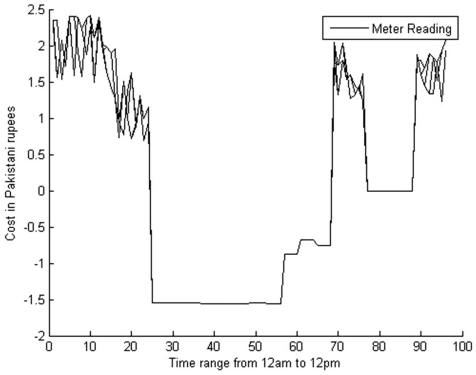

Fig. 6. Cost estimation by genetic algorithm

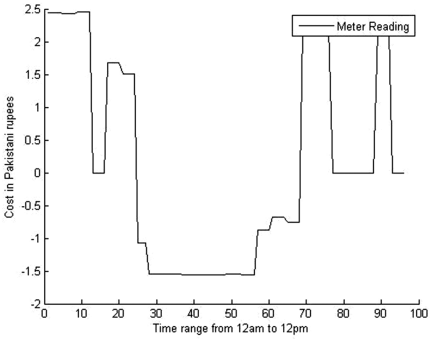

Fig. 7. Cost estimation by optimized heuristic algorithm

Figure 8 gives of utilization of PV, battery and Grid. It shows that load is mostly fed by renewable energy source and battery. Grid utilization is minimized which proves that proposed system is profitable.

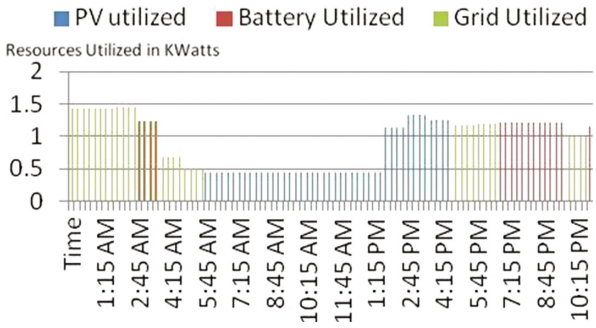

Fig. 8. A comparison of utilization of resources

A cost comparison of GA algorithm and optimized heuristic algorithm is shown in Fig. 9. The figure reveals that the cost estimated by GA is more profitable for consumer as of optimized heuristic algorithm.

The cost difference between genetic algorithm and heuristic algorithm varies approximately 8% to 10%.

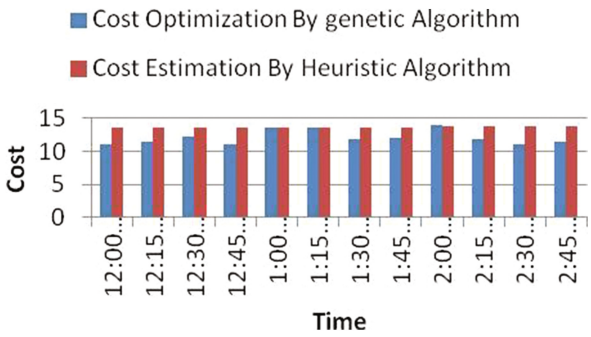

Fig. 9. Comparison of cost estimation by genetic and heuristic algorithms

5 Conclusion and Future Work

Smart nano-grid algorithms proposed in the paper are effective solution to the system. By adding further renewable resources to the system will most probably make it more efficient in the long run. Other than PV, the resources that can be added to the system are wind, rain and generators. The algorithms proposed can be implemented in the real life system resulting in opening new doors to the further research in the field of smart nano-gird. The compatibility of the algorithms with the systems is another area of research for smart nano-gird researchers. It is a wide area of research for scientists due to non-availability of legacy system. The algorithms proposed can be made intellectual property by adding them to the system and then further optimized through research and development.

References

1. Mohsenian-Rad, H.: Communications and Control in Smart Grid, Department of Electrical & Computer Engineering, Texas Tech University (2012)
2. U.S. Department of Energy by Litos Strategic Communication: Exploring the Imperative of Revitalizing America's Electric Infrastructure (2010)
3. Marry, G.A., Rajarajeswari, R.: Smart grid cost optimization using genetic algorithm. IJRET **3**(7), 282–287 (2014)
4. Jeon, G., Kim, Y.B., Park, J.: Agent based smart grid modeling. In: IEEE Winter Simulation Conference (WSC), pp. 3114–3115, December 2015

5. Worighi, I., Maach, A., Hafid, A.: Modeling a smart grid using objects interaction. In: IEEE 2015 3rd International Renewable and Sustainable Energy Conference (IRSEC), pp. 1–6 December 2015
6. Meeran, S., Morshed, M.S.: A hybrid genetic tabu search algorithm for solving job shop scheduling problems: a case study, Springer Science + Business Media, LLC (2011)
7. Aci, M., Inan, C., Avci, M.: A hybrid classification method of k nearest neighbor, bayesian methods and genetic algorithm. Expert Syst. Appl. **37**, 5061–5067 (2010)
8. Metaxiotis, K., Liagkouras, K.: Multiobjective evolutionary algorithms for portfolio management: a comprehensive literature review. Expert Syst. Appl. **39**, 11685–11698 (2012)
9. Rennera, G., Ekárt, A.: Genetic algorithms in computer aided design. Comput. Aided Des. **35**, 709–726 (2003)
10. Lin, H., Wagholikar, K., Yang, Z.: Identifying protein complexes with fuzzy machine learning model. In: IEEE International Conference on Bioinformatics and Biomedicine, October 2012

Prototypes and Experimental Validations

Mathematical Modeling and Prototype Development of a Pneumatically-Actuated Bench for Sloping Terrain Simulation

M.R.M.H. Porsch(✉), N. Kinalski, R. Goergen, A. Fiegenbaum, L.A. Rasia, and A.C. Valdiero

Regional University of Northwestern Rio Grande do Sul State, Ijuí, Brazil
marcia_porsch@hotmail.com, {nivia.kinalski,rasia, valdiero}@unijui.edu.br, betinhamtm@gmail.com, andrei.fig@hotmail.com

Abstract. This paper presents the mathematical modeling of a nonlinear system for a sloping terrain simulation bench with pneumatic actuation, as well the prototype development of the adopted dynamic system. The use of pneumatics is advantageous in agricultural machinery for its easy maintenance, its relatively low cost and good power-to-size ratio, and also for its quick action with great speed variation. However, it introduces difficulties in control due to the nonlinear characteristics of the system. The mathematical modeling of this dynamic system is important because it enables the prediction of the same oscillation conditions found in the field through simulations, the controller design and the behavior study of its variables in prototypes. Thus, a fifth-order nonlinear mathematical model was developed to describe such slope from combination of the servo valve model with the pneumatic cylinder model, and includes dead zone nonlinearity, valve orifice flow rate, pressure dynamics and piston movement with dynamic friction, and also includes rotating platform dynamics. The motivation for the development of a test bench for sloping terrain simulation is to contribute for the improvement of the experimental prototype in agricultural machines.

Keywords: Mathematical modeling · Servo pneumatic · Experimental bench · Prototype development

1 Introduction

This paper presents a study of the mathematical modeling and the prototype development of a pneumatically-actuated test bench for a sloping terrain simulation. The dynamic sloping terrain simulation bench is very useful for laboratory tests because it predicts the same oscillation conditions found in the field, simulating the lateral sloping variations of a combined self-propelled harvester.

Much has been researched on pneumatic actuators and their application in several areas, for example, Sun et al. [1] describe that silicone-based pneumatic bending

J.C.M. Carvalho et al. (eds.), *Multibody Mechatronic Systems*,
Mechanisms and Machine Science 54, DOI 10.1007/978-3-319-67567-1_34

actuators (SPAs) have been very popular because they offer solutions for many applications that require comfort and safety. Yamamoto et al. [2] describes the mechanism of a robot with one-legged pneumatic muscle actuators that can mimic the muscular and skeletal system of a human leg. In addition to control studies, in a recent study, Lin et al. [3] proposed a new approach to control the final effector of a robot using the pneumatic system.

Compressed air is widely used in machinery and equipment due to characteristics such as simple maintenance, low implementation costs, relentless operation, good power-to-size ratio of its components, great reliability, installation flexibility, as well as the fact that it is available in nearly every industrial installation [2, 4, 5].

However, difficulties occur in modeling and pneumatic actuation control due to its several nonlinear characteristics [3, 6], such as the compressibility of the air, the nonlinear behavior of the mass flow from the valve orifices [7], the nonlinearity of the valve dead zone [8], and the friction in cylinder sealing [9, 10].

Mathematical modeling may be applied in the simulation of dynamic system behavior, as well as in model-based control applications as a way of compensating for these nonlinear characteristics, and of minimizing its damaging effects, which harm system performance [3, 11].

This article proposes and describes a mathematical model for an experimental bench activated by a pneumatic actuator starting from the main nonlinear characteristics of this dynamic system. The system parameters are chosen based on experimental data on the laboratory bench prototype. The main contribution of this paper is the full mathematical modeling of bench movement with actuator and mechanism.

2 Description of the Prototype with Pneumatic Drive

The experimental bench is comprised of a system concept [11] that is composed of a fixed base and an articulated system whose function is to simulate the transversal slope (angular movements) of an agricultural machine or piece of equipment at work on undulated terrain. Actuation is performed by a pneumatic servo positioner comprising a double-acting cylinder and a simple rod, and a five-way directional servo valve. The controller is implemented through a block diagram with a dSPACE electronic board that uses integrated MatLab/Simulink and ControlDesk software as its programming means. Figure 1-(a) illustrates a schematic drawing of the experimental bench for the application of the pneumatic actuator, designed on CAD (Computer Aided Design) software, and Fig. 1-(b) shows a photograph of its prototype that was constructed at the NIMASS (Automatic Machinery and Servo Systems Innovation Center). The detailed process of the project, modeling, simulation, and the control system for the terrain slope simulation bench with a pneumatic actuator took place simultaneously with the construction of the prototype.

(a) (b)

Fig. 1. Pneumatically-actuated bench for sloping terrain simulation: (a) Schematic drawing on CAD (Computer Aided Design) software; (b) Prototype photograph.

The Fig. 2 presents the block diagram containing the scheme for the main mathematical modeling data used to represent the dynamic behavior of the pneumatically-actuated bench for the simulation of terrain sloping.

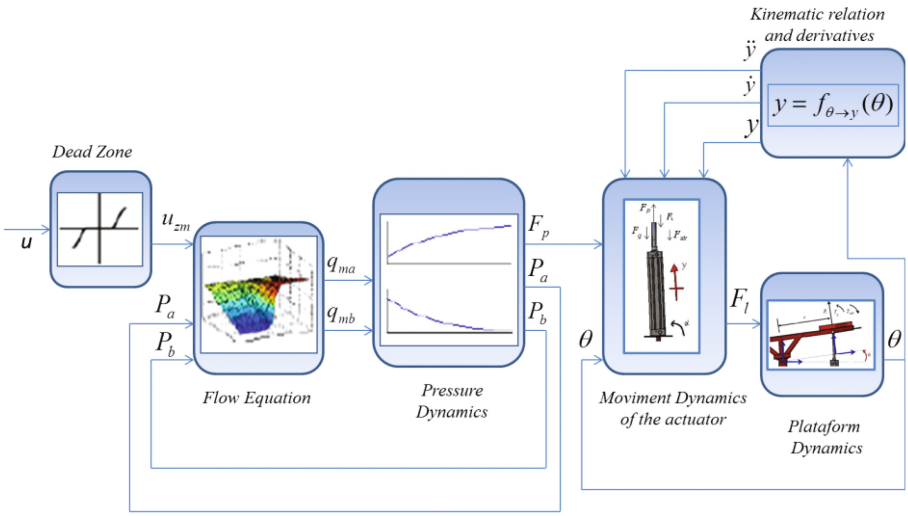

Fig. 2. Scheme for the mathematical modeling of the bench

The u signal represents the input signal of the system that characterizes an open loop control signals. The first block represents the nonlinearity of the dead zone, since the width of the spool is greater than the width of the hole where there is the passage of air under pressure in the servo valve. It also presents a block for the equation of mass flow, one for the dynamics of the pressures, another for the dynamics of the movement of the pneumatic actuator, another of the dynamics of the rotating platform of the bench and also one for the kinematic relation and its derivatives.

3 Mathematical Modeling of the System

The dead zone is a very common imperfection in pneumatic valves because the width of the spool shoulder is greater than the width of the orifice through which the air passes, in such a way that there is no air flow in a variety of positions [4]. Another important nonlinearity is the relation between flow and pressure in the orifices of the valve, which depends on the difference in pressure at the orifice and at the opening of the valve. The pressure dynamics model is obtained through the continuity equation and results in two first-order nonlinear equations, which they depend on the physical characteristics of the pneumatic cylinder [7].

Friction is the factor that most influences the movement equation, since it is hard to precisely describe and analyze it. Friction changes periodically and depends on environmental factors, such as temperature and lubrication conditions. In this paper, the friction model by the LuGre method will be described, as proposed in Canudas et al. [12] and improved by Dupont et al. [13] to include effects during stiction.

The pneumatic servo positioner used in this paper is composed of a directional servo valve and a double-acting pneumatic cylinder with a simple rod. This actuator allows placing a load at a specific point in the actuator stroke or following a variable trajectory related to time.

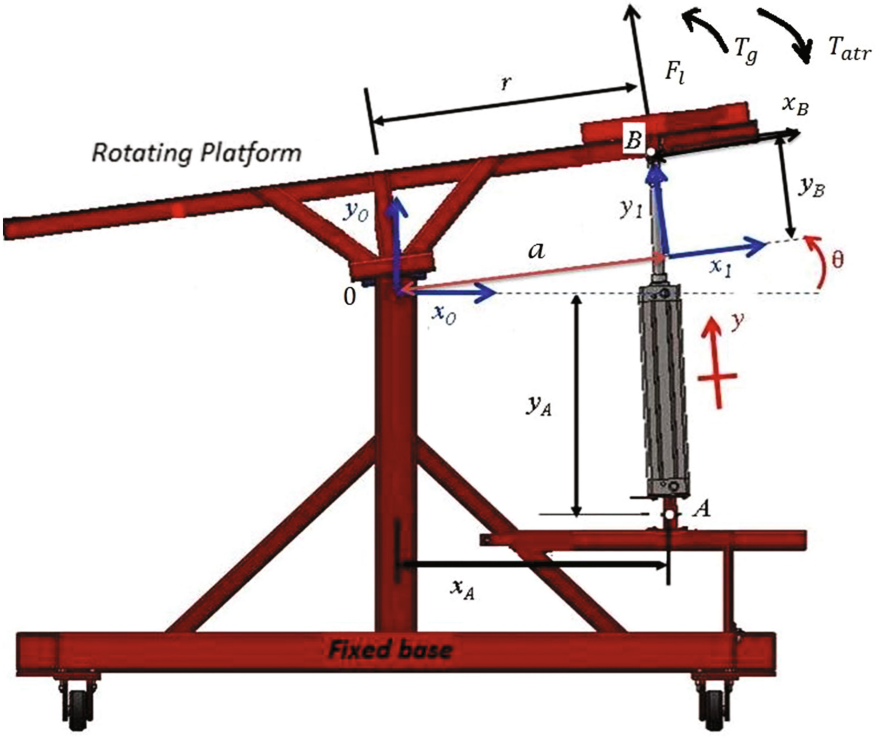

Fig. 3. Schematic drawing of the bench with the representation of the reference coordinates system and the actuating forces

The mechanical system of the workbench is shown in Fig. 3, where the main loads and parameters involved in the rotation dynamics are represented. Applying the sum of the torques ($\sum T_0$), we have Eq. (1).

$$\sum T_0 = rF_l - T_{atr} + T_g = I_0\ddot{\theta} \tag{1}$$

where F_l is the load force, T_{atr} ($= \sigma_2\dot{\theta}$) is the friction torque, where σ_2 is viscous friction and $\dot{\theta}$ is the angular velocity, T_g represents the gravity torque ($= h\,g\,m\,\sin\theta$), which is directly proportional to the height (h) of the center of gravity of the bench, to the gravitational acceleration (g), to the mass of the bench (m) and to sin (θ), I_0 is the moment of inertia of the rotating platform about the rotation axis, $\ddot{\theta}$ is the angular acceleration of the platform and r is the distance from the turning center to the point of application of the force.

In that manner, we have Eq. (2), which represents the dynamics of the rotating platform coupled with pneumatic actuator [11].

$$I_0\ddot{\theta} + T_{atr} - T_g = r\left(F_p - M\ddot{y} - F_{atr} - F_g\right) \tag{2}$$

where M is the displaced mass, $\ddot{y}$ is the cylinder piston acceleration, F_p is the pneumatic force given by Eq. (7), F_{atr} is the friction force and F_g is the component of the gravitational force in pneumatic actuator. The kinematic relation between linear movement y by the pneumatic actuator rod and the angular movement θ by the rotating platform can be obtained through the methodology proposed by Valdiero [14], and is shown in Eq. (3):

$$y(\theta) = \sqrt{L_1^2 + L_2^2 - 2|L_1||L_2|\cos(\theta - \Delta\phi)} - L_3 \tag{3}$$

where the constructive parameters L_1, L_2, and $\Delta\varphi$ are given by the following expressions:

$$L_1 = \sqrt{x_A^2 + y_A^2} \tag{4}$$

$$L_2 = \sqrt{(a + x_B)^2 + y_B^2} \tag{5}$$

$$\Delta\varphi = \varphi_1 - \varphi_2 = ar\,tan\,2\left(\frac{y_A}{x_A}\right) - ar\,tan\,2\left(\frac{y_B}{a + x_B}\right) \tag{6}$$

where (x_A, y_A) and (x_B, y_B) are the coordinates that define, respectively, the points of articulation A e B on the pneumatic actuator in relation to the reference systems x_0y_0 (on the fixed base) and x_1y_1 (on the rotating platform), a is the distance between the

origin of these reference systems, and L_3 represents the length of the actuator (segment AB) at the midpoint of the cylinder stroke ($y = 0$). Pneumatic force F_p is given by Eq. (7):

$$F_p = A_1 p_a - A_2 p_b \tag{7}$$

where A_1 and A_2 are the transversal section areas in the chambers of the pneumatic cylinder, and p_a and p_b are the respective pressures in these chambers, whose dynamics can be obtained through the application of the principle of conservation of energy and the ideal gas law, as presented in Valdiero et al. [8] and described in Eqs. (8) and (9):

$$\dot{p}_a = -\frac{A_1 \gamma \dot{y}}{A_1 y + V_{a0}} p_a + \frac{R \gamma T}{A_1 y + V_{b0}} q_{ma}(p_a, u) \tag{8}$$

$$\dot{p}_b = \frac{A_2 \gamma \dot{y}}{V_{b0} - A_2 y} p_b + \frac{R \gamma T}{V_{b0} - A_2 y} q_{mb}(p_b, u) \tag{9}$$

where q_{ma} and q_{mb} are the mass flows of the cylinder chambers, T is the supply air temperature in Kelvin, R is the universal gas constant, γ is the relation between the mass heat capacities of air, V_{a0} and V_{b0} are the cylinder chamber volumes in the position $y = 0$, u is the control signal applied to the servo valve, $y(\theta)$ and $\dot{y}(\theta)$ are, respectively, linear position and velocity of the pneumatic actuator rod, written as functions on the angular position of the rotating platform. A detailed study in [7] for the mass flow equating q_{ma} q_{mb} resulted in the Eqs. (10) and (11):

$$q_{ma}(u, p_a) = g_1(p_a, sign(u)) arctg(2u) \tag{10}$$

$$q_{mb}(u, p_b) = g_2(p_b, sign(u)) arctg(2u) \tag{11}$$

where g_1 and g_2 are functions given by Eqs. (12) and (13).

$$g_1(p_a, sign(u)) = \beta \Delta p_a = \begin{cases} (p_{\text{sup}} - p_a)\beta^{ench} & if \quad u \geq 0 \\ (p_a - p_{atm})\beta^{esv} & if \quad u < 0 \end{cases} \tag{12}$$

$$g_2(p_b, sign(u)) = \beta \Delta p_b = \begin{cases} (p_{sup} - p_b)\beta^{ench} & if \quad u < 0 \\ (p_b - p_{atm})\beta^{esv} & if \quad u \geq 0 \end{cases} \tag{13}$$

considering that p_{sup} is the supply pressure, p_{atm} is the atmospheric pressure, β^{ench} and β^{esv} are constant coefficients respectively regarded to the filling and emptying of the cylinder chambers. Critical center pneumatic servo valves (the width of the spool is larger than the passage orifice) present a nonlinear dead zone characteristic, where there is no output air mass flow for a certain value range for the control signal $u(t)$. The

mathematical model for dead zone nonlinearity can be described by [8] as shown in Eq. (14):

$$u_{zm}(t) = \begin{cases} md(u(t) - zmd) & if \quad u(t) \geq zmd \\ 0 \quad if \quad zme < u(t) < zmd \\ me(u(t) - zme) & if \quad u(t) \leq zme \end{cases} \tag{14}$$

where u is the input signal, u_{zm} is the output value, *zmd* is the right-hand limit of the dead zone, *zme* is the left-hand limit of the dead zone, *md* is the right-hand slope of the dead zone, and *me* is the left-hand slope of the dead zone.

According to the LuGre model, friction is proportional to the average elastic bristle deflection; when a tangential force is applied, the bristles deflect like springs, and if this deflection is sufficiently great, the bristles start to slip [12, 13]. This average bristle deflection is determined by the speed of a movement in steady state. This friction model is frequently used within the scientific field because it is based on the understanding of the microscopic mechanism of the friction phenomenon. The dynamic friction used is based on the understanding of the microscopic mechanism of the friction phenomenon given by:

$$F_{atr} = \sigma_0 z + \sigma_1 \dot{z} + \sigma_2 \dot{y} \tag{15}$$

where σ_0 represents the coefficient of stiffness of the microscopic deformations between the contact surfaces, z is a non-measurable internal state that represents the average deformation that occurs between the surfaces, σ_1 is the damping coefficient associated with the variation rate z, σ_2 is the coefficient for viscous friction, and $\dot{y}$ is the relative velocity between the surfaces. Thus, friction force is comprised of a portion that is proportional to the average micro deformation ($\sigma_0\, z$), a portion that is proportional to the deformation variation rate ($\sigma_1\, \dot{z}$), and the viscous friction portion ($\sigma_2\, \dot{y}$). For the dynamics of state z, Dupont et al. [13] propose the Eq. (16):

$$\frac{dz}{dt} = \dot{y}\left(1 - \alpha(z, \dot{y})\frac{\alpha_0}{g_{ss}(\dot{y})} sign(\dot{y}) z\right) \tag{16}$$

where $g_{ss}(\dot{y})$ represents a function of the friction in a steady state, and is given by:

$$g_{ss}(\dot{y}) = F_c + (F_s - F_c)e^{-\left(\frac{\dot{y}}{\dot{y}_s}\right)^2} \tag{17}$$

where F_c is the Coulomb friction force, F_s is the static friction force, $\dot{y}$ is the speed, and $\dot{y}_s$ is the *Stribeck* velocity. Using the variables at state $x_1 = \theta$ (angle described by the platform), $x_2 = \dot{\theta}$ (angular velocity), $x_3 = p_a$(pressure in chamber A), $x_4 = p_b$ (pressure in chamber B) e $x_5 = z$ (average micro deformation), it is possible to represent the dynamic system as a mathematical model through the following set of nonlinear ordinary differential equations of the fifth order:

$$\dot{x}_1 = x_2 \tag{18}$$

$$\dot{x}_2 = \frac{r}{I}(A_1 x_3 - A_2 X_4 - F_{atr}(x_5, \dot{y}) - F_g - M\ddot{y}) - \frac{1}{I}(\sigma_2 x_2 - T_g) \tag{19}$$

$$\dot{x}_3 = -\frac{A_1 \gamma\, \dot{y}(x_1)}{A_1\, y(x_1) + V_{a0}} x_3 + \frac{R\, \gamma\, T}{A_1\, y(x_1) + V_{a0}} q_{ma}(x_3, u) \tag{20}$$

$$\dot{x}_4 = \frac{A_2\, \gamma\, \dot{y}(x_1)}{V_{b0} - A_2\, y(x_1)} x_4 + \frac{R\, \gamma\, T}{V_{b0} - A_2 y(x_1)} q_{mb}(x_4, u) \tag{21}$$

$$\dot{x}_5 = \dot{y} - \alpha(x_5, \dot{y}) \frac{\sigma_0}{g_{ss}(\dot{y})} sign(\dot{y}) x_5 \tag{22}$$

Figure 4 shows the validation results of the chosen mathematical model and makes a comparison with experimental and desired signal for classical proportional control. The results show that the adopted model is adequate and allows the simulation of the sloping terrain dynamic behavior with pneumatically-actuated bench.

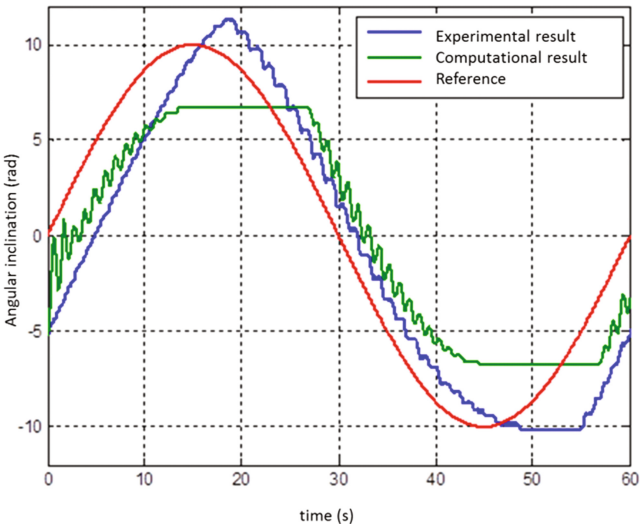

Fig. 4. Results of the simulations and real experiments with feedback control.

4 Conclusions

A non-linear mathematical model of 5th order was developed for simulation of land slope with pneumatic drive. This model shows the dynamics of the rotating platform coupled with pneumatic actuator, including the dead zone nonlinearity, the mass flow in the servo-valve orifices, pressures dynamics in cylinder chamber, the friction dynamics

considering the LuGre friction model and a kinematic relationship of angular to linear conversion. The results obtained will contribute to the elaboration of control strategies and also to the experimental prototype improvement for innovation in agricultural machines. This work is a contribution to the advancement in farm machines. As highlight it was presented a mathematical modeling strategy for pneumatically-actuated bench for sloping terrain simulation. The development model can be used for simulation on the practical application in level control in combine harvesters.

Acknowledgments. The authors would like to thank CAPES (Brazilian Federal Agency for the Support and Evaluation of Graduate Education), CNPq (National Council for Scientific and Technological Development) and Finep (Funding Authority for Studies and Projects) by financial support at the Innovation Center for Automatic Machines and Servo Systems (NIMASS) in UNIJUÍ University.

References

1. Sun, Y., Liang, X., Yap, H.K., Cao, J., Ang, M.H., Hua Yeow, R.C.: Force measurement toward the instability theory of soft pneumatic actuators. IEEE Robot. Autom. Lett. **2**(2), 985–992 (2017)
2. Yamamoto, Y., Nishi, H., Torii, Y., Takanishi, A., Lim, H.O.: Mechanism and jumping pattern of one-legged jumping robot with pneumatic actuators. In: 2016 16th International Conference on Control, Automation and Systems (ICCAS), Gyeongju, pp. 1132–1136 (2016)
3. Lin, W., Dong, W., Deng, Y., Qian, C., Qiu, J.: Contact force modelling and adaptive control of pneumatic system. In: 2016 31st Youth Academic Annual Conference of Chinese Association of Automation (YAC), Wuhan, pp. 357–362 (2016)
4. Belforte, G., Bertetto, A.M., Mazza, L., Orrù, P.F.: Analysis of wear in guide bearings for pneumatic actuators and new solutions for longer service life. In: Proceedings of MUSME 2011, the International Symposium on Multibody Systems and Mechatronics, Valencia, Spain, pp. 25–28, October 2011
5. Tao, G., Kokotovic, P.V.: Adaptive Control of Systems with Actuators and Sensors Nonlinearities. Wiley, New York (1996)
6. Tassa, Y., Tingfan, W., Movellan, J., Todorov, E.: Modeling and identification of pneumatic actuators. In: 2013 IEEE International Conference on Mechatronics and Automation (ICMA), pp. 437–443, 4–7 August 2013
7. Valdiero, A.C., Ritter, C.S., Rios, C.F., Rafikov, M.: Nonlinear mathematical modeling in pneumatic servo position applications. Math. Probl. Eng. **2011**, 1–16 (2011). Hindawi Publishing Corporation
8. Valdiero, A.C., Andrighetto, P.L., Carlotto, L.: Dynamic modeling and friction parameters estimation to pneumatic actuators. In: Proceedings of MUSME 2005, the International Symposium on Multibody Systems and Mechatronics, Uberlandia, Brazil (2005)
9. Perondi, E.A.: Controle Não-Linear em Cascata de um Servoposicionador Pneumático com Compensação de Atrito, 182f. Tese de Doutorado, Departamento de Engenharia Mecânica, Universidade Federal de Santa Catarina, Brasil (2002)
10. Ritter, C.S.: Modelagem matemática das características não lineares de atuadores pneumáti-cos. 2010. 87 f. Dissertação (Mestrado em Modelagem Matemática) – Universidade Regional do Noroeste do Estado do Rio Grande do Sul, Ijuí (2010)

11. Porsch, M.R.M.H., Mantovani, I.J., Valdiero, A.C.: Modelagem Matemática, Simulação Computacional e Validação Experimental de uma Bancada para Simulação de Aclives de Solos Agrícolas. In: XXXVI Congresso Nacional de Matemática Aplicada e Computacional, 2016, Gramado. Proceeding Series of the Brazilian Society of Computational and Applied Mathematics, vol. 5, pp. 1–7. Sociedade Brasileira de Matemática Aplicada e Computacional, São Carlos (2016)
12. De Wit, C.C., Olsson, H., Åström, K.J., Lischinsky, P.: A new model for the control of systems with friction. IEEE Trans. Autom. Control **40**(3), 419–425 (1995)
13. Dupont, P., Armstrong, B., Hayward, V.: Elasto-plastic friction model: contact compliance and stiction. In: ACC, American Control Conference, Illinois, pp. 1072–1077, March 2000
14. Valdiero, A.C.: Modelagem matemática de robôs hidráulicos, vol. 1, p. 200. Unijuí, Ijuí (2012)

An Experimental Characterization of Roll Hemming Process

Eduardo Esquivel[1,2(✉)], Giuseppe Carbone[2], Marco Ceccarelli[2], and Carlos Jáuregui[1]

[1] Universidad Autónoma de Querétaro, Santiago de Querétaro, Mexico
je.esquivel@outlook.com
[2] University of Cassino and South Latium, Cassino, Italy

Abstract. Roll hemming is analyzed for flat surface-straight edge sheets to illustrate how defects and forces behave. The analysis of defects is carried out trough illustrative models to emphasize the main variables of the process. A testing rig to investigate the process is designed and built. Experimental tests are carried out to measure how forces influence final quality part and the experimental data is analyzed and discussed to relate it with main parameters and defects.

Keywords: Roll hemming · Wrinkles · Flat surface-straight edge

1 Introduction

The roll hemming is an automotive manufacturing process for the panels of cars, such as doors, hoods and deck lids [12]. It has two main purposes, the first is to improve exterior appearance of the car and the second is to attach one metal sheet to the other (the outer panel to the inner panel). In this process, a robot moves an end-effector roller along the edge of the panel, and trough different steps, the roller bends a flange to the inside -from 90° to 0°- [10]. Usually, the roller shapes the flange thorough the first (60°), second (30°) and final step (0°).

Several authors have studied the hemming process, the classical hemming uses stamping dies to form the part and roll hemming uses an industrial serial robot through different steps, the classical hemming is applied for massive serial production where the manufacturing condition are established and do not change frequently, thus, there is no need of flexibility since the fixed production conditions allow the design of a big die where no immediate modifications are required. But in some cases (where a car is taken out of the market) the companies are obliged to supply replacements for clients who need them, in this case there is no justification for an expensive stamping die. In low batches and different pieces, flexibility and reprogramability are valuable factors, those cases are suitable for the roll hemming process, where a robot can be programmed with the trajectories desired for each different part. For example in [11], the authors analyzed classical hemming process, they carried out tests and obtained

J.C.M. Carvalho et al. (eds.), *Multibody Mechatronic Systems*,
Mechanisms and Machine Science 54, DOI 10.1007/978-3-319-67567-1_35

plots relating the starting parameters with the defects. In [13], the authors analyzed classical hemming process using a Finite Element Model of plain solid deformation in two dimensions with LS-Dyna. They used only one type of aluminum, thickness and geometry. Other authors have studied the roll hemming process, for example in [5], the authors proposed a combined hardening rule to simulate the process and they identified the combined model parameters using uni axial tension and compression tests. Results showed how fracture is affected by cyclic plastic deformation. In [10], the authors developed a finite element model based on flat surface-straight edge in aluminum alloy 6061T6 for flanging, pre-hemming and hemming. In addition, they worked out experiments to measure the roll in/out to compare with simulation results. In [6], the authors set a material model for simulation based on anisotropic elastic-plastic mixed hardening, for a curved surface-curved edge part, considering the pre-strain history of the part, wrinkles were similar in experiments and simulations. In [1], the authors analyzed final quality part in roll hemming based on different robot positions, they concluded that robot configuration affects springback of part and the stiffness of robot in the roll hemming process.

Although, the roll hemming process is widely addressed in literature, different aspects of this process deserve attention and research in order to improve the quality of the shaped parts and to reduce the appearance of defects, also when fast production and high productivity require new and flexible processes. Accordingly, the main objectives of the experimental characterization in this paper are: to analyze the main defects and force behavior, to design a testing rig to reproduce the roll hemming process without the effect of robot compliance, to measure the forces and finally, to analyze the shape in the hemmed parts.

2 Main Parameters of Roll Hemming Process

We propose different models to identify the main characteristics of the process (Fig. 1(a)), such as usual defects (on the hemmed part) and the interaction forces between roller and the part. The Fig. 1(b) illustrates the roller attached to a tool (end-effector) and a small section of the part to be hemmed. We set a reference frame in the roller $\{R\}$, and a reference frame in the part $\{P\}$, R_x and P_x are

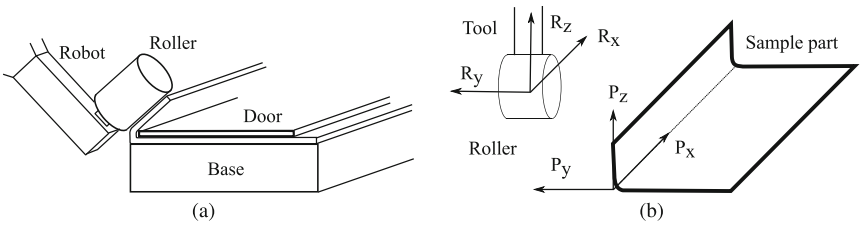

Fig. 1. A scheme of the roll hemming process. (a) A general process. (b) The frame $\{R\}$ is attached to roller and the frame $\{P\}$ is attached to the part.

oriented to the direction of motion, R_z is oriented to the robot arm and P_z is oriented to the flange. Usually, the roller starts pressing the flange and advancing over it all along the edge.

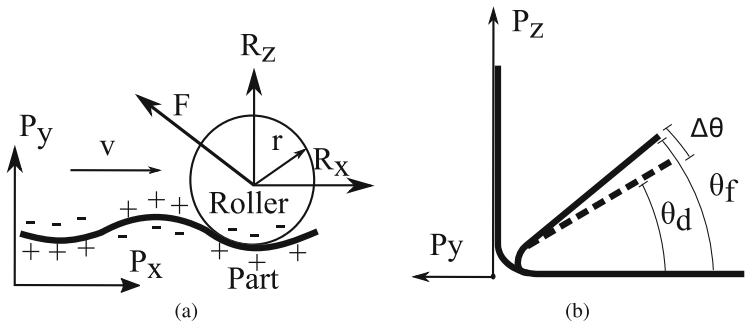

Fig. 2. Defects in roll hemming process. (a) Roller moves and generates wrinkles; F is the force applied to the center of roller, V is the speed of tool in hemming path, r is the radius of roller; the deformation of part is illustrated as tension and compression sections $(+-)$. (b) Springback, $\triangle\theta$, is the difference between θ_f and θ_d.

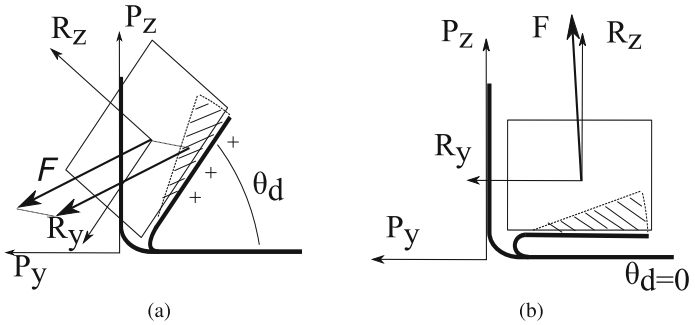

Fig. 3. Force in different hemming steps. (a) One resultant vector at the origin of $\{R\}$ frame. (b) In final hemming force, frame $\{R\}$ and $\{P\}$ have the same orientation and $\theta_d = 0$.

Usually the applied force F, the speed of the tool v, and the part deformation generate wrinkles. The classical hemming and the roll hemming are based on different technologies, the classical hemming shapes the door panels with stiff stamping machines holding dies that press the entire panel in every pre-hemming step, on the other hand, the roll hemming uses an attached roller that gradually shapes one panel section at the time starting in one corner and closing a trajectory cycle in that corner, as consequence in classical hemming a wrinkles defect appears in curved panels only -the hemming in straight panels allows uniformity

in material deformation without waves or fluctuations- but in roll hemming wrinkles defect appears in straight panels, the gradual process deforms the material section by section, generating tension and compression stages as roller moves over the edge of the panel. The consequence of wrinkles defect is no uniform surface on the final panel and no contact between the external panel and the inside panel in some critical parts. Furthermore, the sealing could be weak if adhesive is used to attached exterior and interior panels. Figure 2(a) describes how roller deals with an external force (unknown direction and magnitude) meanwhile the motion generates tension and compression effects in the flange which leads to wrinkles defects.

In roll hemming elastic and plastic deformation influence the final quality panel. Springback is the elastic deformation of the flange in the process, when the roller shapes a specific section of the panel, the flange deforms plastically taking a new shape but when the roller has passed that section the elasticity of the material recovers (not entirely) the flange. It means the final position of the shaped flange differs from the roller path based on the design of the door, thus leading to a surface defect that affects final quality part. Figure 2(b) shows a front view of a part, where the springback $\triangle\theta$, is how much the desired angle θ_d, differs from the real angle θ_f. Some works focused on prediction of springback for metalforming applications such as in [3]. Figure 3(a) illustrates the force vector F, unaligned to R_z for 1st and 2nd pre-hemming steps (60° and 30°) and Fig. 3(b) illustrates the force vector F mainly in R_z component for the final step (0°) where R and P have the same orientation and $\theta_d = 0$. Thus, the attached problem in Sect. 2 is characterized by the main parameters, the force and the final displacement of the part.

3 The Experimental Layout

To know the required force and to observe the defects, the following experiments reproduce the process without a robot by means of a designed testing rig. In [11], the authors studied most of the significant parameters for classical hemming and in [2], the authors did the same for roll hemming. The tests considered the following data: aluminum of 6000 series and steel of standard quality for sample sheets, a part thickness of 0.5 mm -other works report 0.8 mm or 1 mm [8,12] but we defined only one part thickness below the range reported to ensure the force generated by the material deformation could not overpass the force sensor range since experiment is in low scale-, a flange length of 10 mm -average in other works-, a flat surface, a straight edge (Table 1), three hemming steps (60°, 30° and 0°) as shown in Figs. 4(a), (b) and (c) and a roller radius of 20 mm. We considered the output parameters as the hemming force and the quality of the hemmed part.

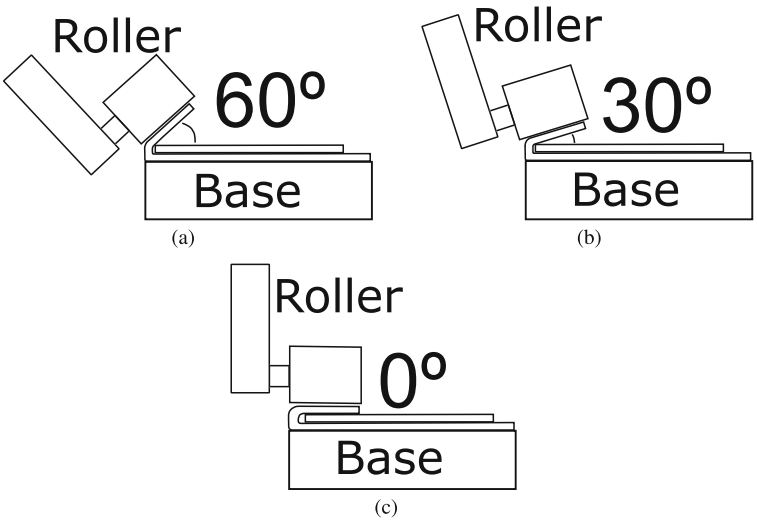

Fig. 4. The process steps: (a) The first step. (b) The second step. (c) The third step.

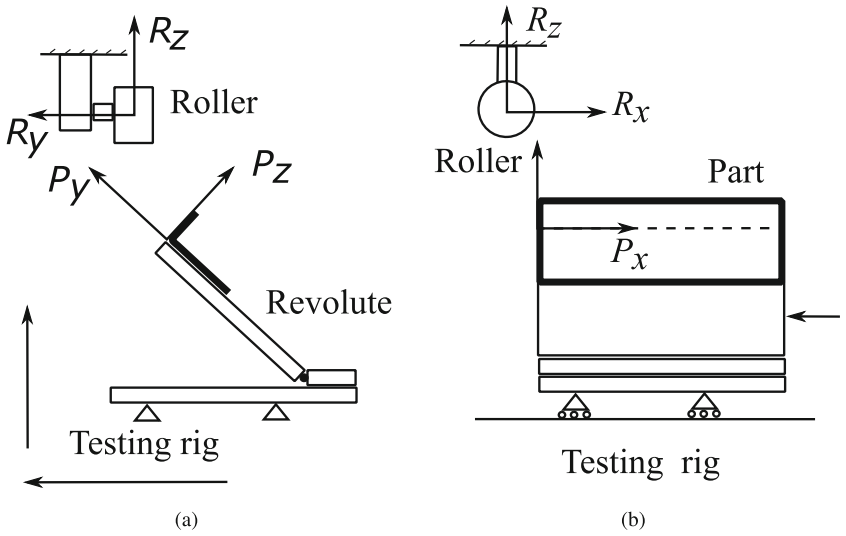

Fig. 5. A designed scheme for the layout of the proposed testing rig (a)–(b).

Figures 5(a) and (b) show the frontal and side layout of the designed rig, respectively. The rig constraints the roller in all degrees of freedom. The Figs. 6(a) and (b) show the frontal and side view of the built rig at LARM in Cassino. The Figs. 7(a) and (b) show the components of the tool (end-effector) that has been previous designed in [4] with one direction force sensor in range of 0–1 KN.

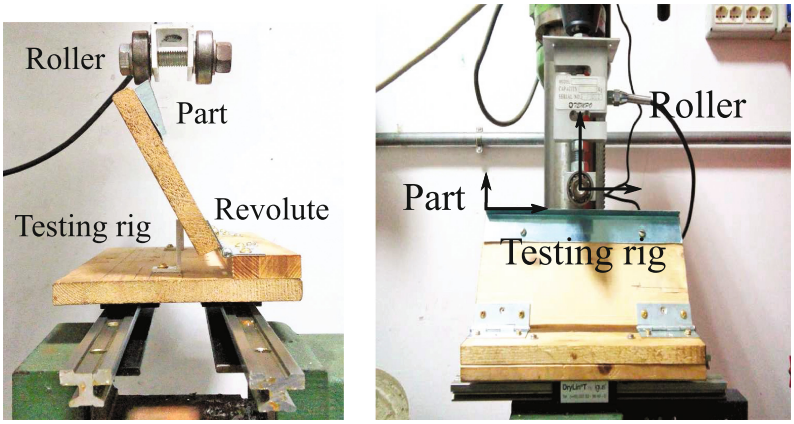

(a) (b)

Fig. 6. The built prototype of the testing rig: (a) Frontal view, (b) Lateral view.

Table 1. Main process parameters

Material	Aluminum, Steel
Thickness (t)	0.5 mm
Flange length (f_l)	10 mm
Surface part	Flat
Edge part	Straight
Hemming step (θ)	$60, 30, 0°$
Roller radius (r)	20 mm

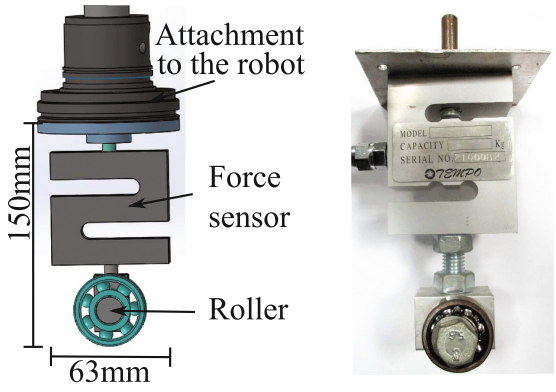

(a) (b)

Fig. 7. The designed tool: (a) The mechanical design. (b) The built prototype.

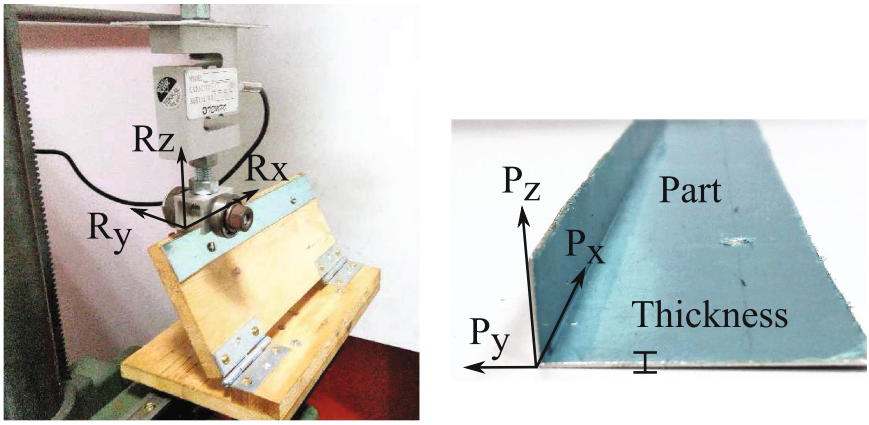

(a) (b)

Fig. 8. Coordinate frames on the testing rig and parts. (a) Coordinates in tool (end-effector). (b) Coordinates in the part.

This means, for these experiments that we measured force in R_z component only. The Figs. 8(a) and (b) show the coordinates for the roller, $\{R\}$, and the coordinates for the part, $\{P\}$.

In order to reproduce the roll hemming with a total of 6 samples the flange was bend to 90°, the part was fixed to the rig, the angle was oriented (according to the proper step), the part was positioned in R_y direction, the height was adjusted in P_z direction (until roller contacted the flange) and the platform was moved in R_x direction (until flange was hemmed). The process was repeated 18 times for every sample test for statistical purposes.

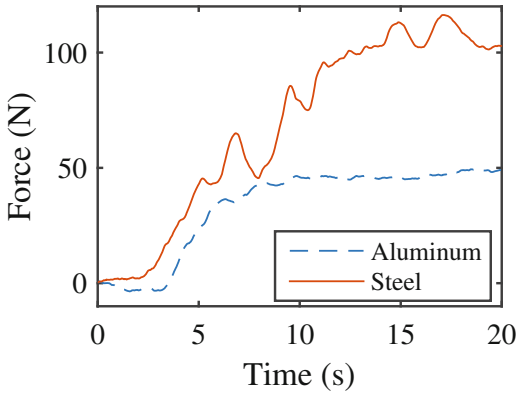

Fig. 9. Forces vs time for the first pre-hemming (60°) step for aluminum and steel.

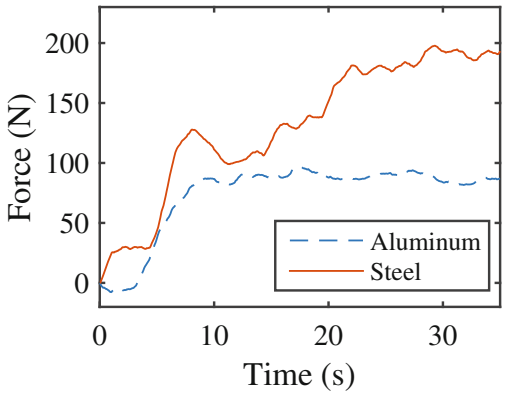

Fig. 10. Forces vs time for the second pre-hemming (30°) step for aluminum and steel.

4 Experimental Results

Figure 9 shows tests results in terms of force and time for first pre-hemming step (60°) for aluminum and steel parts: the force rises in the first 10 s and the maximum force registered 49.72 N for aluminum and 116.27 N for steel. The plot shows the first 20 s because next values remained constants. Figure 10 shows plot of force and time for second pre-hemming step (30°) for aluminum and steel parts: the force rises in the first 15 s to 20 s and the maximum force registered 97.18 N for aluminum and 197.75 N for steel. The plot shows the first 35 s because following values remained constants. Figure 11 shows plot of force and time for the final hemming step (0°) for aluminum and steel parts: the force rises in the first 5 s to 10 s; the maximum force registered 173.28 N for aluminum and 500.05 N for steel. The plot shows the first 20 s, in this case aluminum values

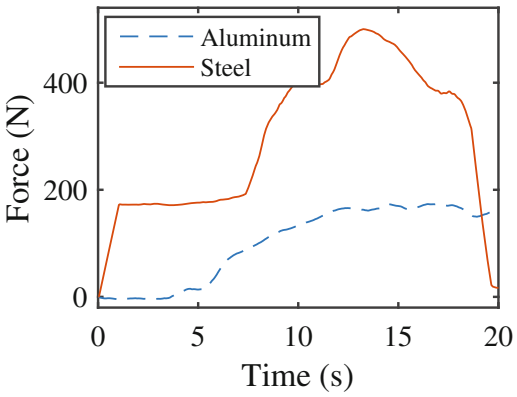

Fig. 11. Forces vs time for the final hemming (0°) step for aluminum and steel.

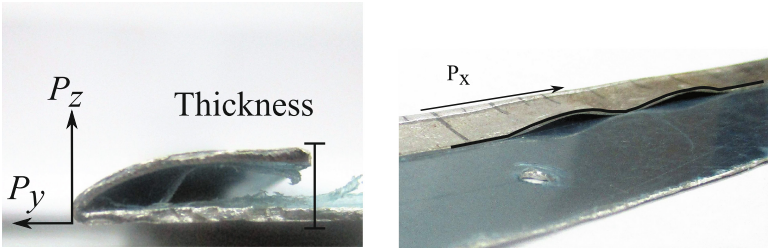

Fig. 12. Results in tested samples. (a) Thickness on hemmed parts. (b) Wrinkles defect on hemmed parts.

remained constants but for steel the platform was forced and the roller leaved the trajectory. The force increases as the hemming steps increase, so the lower the angle, the higher the force required, also each graph can be divided in two sections, the section of rising, when the roller is deforming the sheet to the desired angle and the section of constant force, where the roller is moving along the edge. Comparing the differences between aluminum and steel, the steel sheet requires higher force to be hemmed causing the process to be more complex. Comparing the results of the registered loads with other author's results we can observe lower loads. [9] reached a 50 KN in load for classical hemming. Thus in classical hemming is easier to reach higher loads. For the application in roll hemming [7] mentioned a 2500 KN which is higher and in the work of [10] the load reached in the pre-hemming steps is around 700 N and reaching 2000 N for the final hemming. So it is noticed that a higher force is required to be applied on the sheet, this can be considered for a design of a next testing rig.

When tests were finished, every sample was marked every 5 mm and the thickness in z direction was measured with a vernier caliper as shown in Fig. 12(a). Figure 12(b) shows wrinkles that were formed in an aluminum part along x direction, accordingly to [11] the wrinkles defect does not appear in flat surface-straight edge but the experiment shows that for roll hemming it does. The Fig. 13 shows plot of the thickness of a desired part -a constant line of 1 mm-, the thickness of an aluminum part and the thickness of a steel part -less deformed respect to aluminum-; the maximum thickness for aluminum and steel were 2.8 mm and 5 mm, respectively; the better shape is in the middle of the parts, this is for the designed rig. Accordingly to the results of the thickness, a stiffer machine is needed in order to ensure a better quality in the final part applying the higher load. There is a correlation between the thickness and the load applied for every sample, as the load increases the thickness is higher, thus the material needed higher force to be deformed.

The Table 2 lists the main values of previous plots; the force increases on every hemming step and maximum thickness in aluminum parts differs from that of steel parts. The Figs. 14(a) and (b) show the trajectory deviation obtained during the process experimentation. The results showed a deviation of the tool

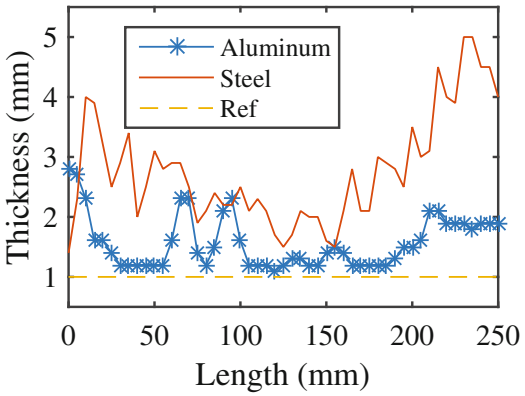

Fig. 13. Completed results from tests as thickness vs part length.

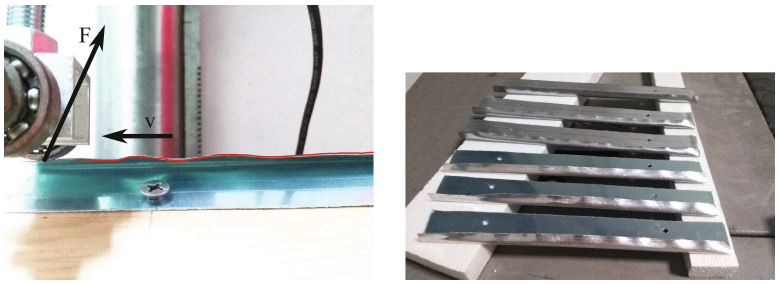

(a) (b)

Fig. 14. Trajectory deviation on hemmed parts. (a) Tool deviation while deforming the sheet. (b) Samples tested.

Table 2. Measured forces during tests.

Run	Aluminum			Steel		
	F_{max}	F_{min}	t_{max}	F_{max}	F_{min}	t_{max}
1 Step	49.72 N	−3.57 N	-	116.27 N	0.2 N	-
2 Step	97.18 N	−7.76 N	-	197.75 N	0 N	-
Final Step	173.28 N	−4.58 N	2.8 mm	500.05 N	0 N	5 mm

end-effector in the trajectory and the presence of wrinkles defect in flat surface-straight edge. The design needs to consider higher loads and it could be helpful to measure other components of force during the process. While doing this experiment, one factor not considered before emerged as result of the observation of the relaxing time of material and the process steps, this factor is the speed of the process, the speed at which each step is carried out. So for other experiments it is recommendable to consider the speed of the process. The roller geometry may

influence the results due to its interaction with the door where the roller radius defines the contact surface, for a small radius of the roller the contact surface is small -which may lead to a force concentration and increasing the deformation- and for a big radius the contact surface is big which may lead to a smooth distribution of the forces and a decreasing in the fluctuation of the material. The wrinkles defect could be related with the roller radius and a further study comparing different geometries of the roller would be valuable.

5 Conclusions

In this paper an experimental characterization is presented for the main defects in roll hemming. Descriptive models for the main parameters and defects of the process were proposed. Experiments were performed on a testing rig designed specifically to highlight forces and deformations during the process in different operation steps. It is recommended to control the speed of the process and to measure more components of the force. Future work is planned to designed a compensation strategy for the path deviations of the roll hemming end-effector.

Acknowledgements. The first author wishes to gratefully acknowledge Universidad Autónoma de Querétaro through grant scholarship of Conacyt (Consejo Nacional de Ciencia y Tecnología) no. 373760/251911, for permitting his period of research at LaRM of Cassino University in the year 2016 within a double PhD degree program.

References

1. Drossel, W.-G., Pfeifer, M., Findeisen, M., Rössinger, M., Eckert, A., Barth, D.: The influence of the robot's stiffness on roller hemming processes. In: ISR/Robotik 2014 - 45th International Symposium on Robotics, Berlin, pp. 531–538 (2014)
2. Roll, K., Eisele, U., Liewald, M.: Development of an empirical model to determine results from FEA roller hemming processes. LS-Dyna Forum, Metallumformung **I**, 1–14 (2010)
3. El Salhi, S., Coenen, F., Dixon, C., Khan, M.S.: Predicting "springback" using 3D surface representation techniques: a case study in sheet metal forming. Expert Syst. Appl. **42**(1), 79–93 (2015)
4. Esquivel, E., Carbone, G., Ceccarelli, M., Jáuregui, J.: Requirements and constraints for a robotized roll hemming solution. In: RAAD 2016, Belgrade, Serbia, pp. 244–251. Springer (2017)
5. Hu, X., Zhao, Y., Huang, S., Li, S., Lin, Z.: Numerical analysis of the roller hemming process. Int. J. Adv. Manufact. Technol. **62**(5–8), 543–550 (2011)
6. Le Maoût, N., Manach, P.Y., Thuillier, S.: Influence of prestrain on the numerical simulation of the roller hemming process. J. Mater. Process. Technol. **212**, 450–457 (2012)
7. Le Maoût, N., Thuillier, S., Manach, P.Y.: Aluminum alloy damage evolution for different strain paths - application to hemming process. Eng. Fract. Mech. **76**(9), 1202–1214 (2009)
8. Le Maoût, N., Thuillier, S., Manach, P.Y.: Classical and roll-hemming processes of pre-strained metallic sheets. Exp. Mech. **50**, 1087–1097 (2010)

9. Le Maoût, N., Thuillier, S., Manach, P.Y.: Drawing, flanging and hemming of metallic thin sheets: a multi-step process. Mater. Des. **31**(6), 2725–2736 (2010)
10. Li, S., Hu, X., Zhao, Y., Lin, Z., Nanqiao, X.: Cyclic hardening behavior of roller hemming in the case of aluminum alloy sheets. Mater. Des. **32**, 2308–2316 (2011)
11. Livatyali, H., Müderrisoglu, A., Ahmetoglu, M.A., Akgerman, N., Kinzel, G.L., Altan, T.: Improvement of hem quality by optimizing flanging and pre-hemming operations using computer aided die design. J. Mater. Process. Technol. **98**, 41–52 (2000)
12. Thuillier, S., Le Maoût, N., Manach, P.Y., Debois, D.: Numerical simulation of the roll hemming process. J. Mater. Process. Technol. **198**(1–3), 226–233 (2008)
13. Wanintradul, C., Golovashchenko, S.F., Gillard, A.J., Smith, L.M.: Hemming process with counteraction force to prevent creepage. J. Manufact. Proces. **16**, 379–390 (2014)

Experimental Characterization of a Feedforward Control for the Replication of Moving Resistances on a Chassis Dynamometer

E. Bertoti(✉), J.J. Eckert, R.Y. Yamashita, L.C.A. Silva, and F.G. Dedini

University of Campinas, Campinas, Brazil
{bertoti, javorski, ludmila, dedini}@fem.unicamp.br, rodrigo.yamashita@gmail.com

Abstract. Dynamometers are devices that for long have been employed for acquiring power and torque outputting a prime mover, such as an engine. However, with the improvements in controllability, they may as well be applied nowadays to reproduce in laboratory conditions real operational loads, increasing the replicability of the tests and the reproducibility of the results. In this regard, the main goal of the present work is to describe the first outcomes of a project being carried in the Laboratory for Integrated Systems of Unicamp whose main goal is to further develop its chassis dynamometer for emulating real driving resistances, such as inclines and aerodynamic drag, upon the driveline of the vehicle being tested. In a first attempt to improve the control platform of the device, a lookup table was created in order to control an eddy-current brake and to verify its dynamical performance under voltage inputs. Compensation for the difference in inertia between the vehicle and the dynamometer and for the aerodynamic drag was also provided during the execution of an FTP-72 drive cycle. After the inclusion of the control structure, correlation coefficients of around 0.95 have been found when comparing the torque read at the torquemeter with the expected torque with compensation.

Keywords: Chassis dynamometer · Feedforward control · Eddy-current brake

1 Introduction

Dynamometers play an important role in the field of automotive engineering since they provide reliable and controlled experimental conditions for benchmarking new technologies deployed in the energy converters or in the driveline of road vehicles. According to Figliola and Beasley [1], these devices must absorb the power output of a prime mover in order to assess its performance. Modern dynamometers, however, are capable not only to perform passive measurements but also of emulating actively the perturbations to which cars are commonly submitted when employed under real driving circumstances.

J.C.M. Carvalho et al. (eds.), *Multibody Mechatronic Systems*,
Mechanisms and Machine Science 54, DOI 10.1007/978-3-319-67567-1_36

Following this principle, the Laboratory for Integrated Systems (LabSIn) of the University of Campinas (Unicamp) intends to develop a control system for its twin roller chassis dynamometer, which must have the capacity, on the long run, to emulate a complete drive cycle with its characteristic movement resistances: aerodynamic drag, inclines and declines, rolling resistance and also inertial compensation. One step towards this goal is to analyze the performance of the power absorber unit (PAU) of the chassis dynamometer, which is composed of an eddy current (EC) brake and its current controller. In the present paper, the authors propose the application of a static feed-forward control, in order to assess, the performance of its PAU.

2 Two-Wheel Drive Vehicle Longitudinal Dynamics

The longitudinal dynamics of a road vehicle (x-axis) is governed by three main moving resistances: the rolling resistance of the tire-road contact (R_x); the aerodynamic drag (D_A); the incline resistance (W sin Θ), which depends on the weight W of the vehicle and on the gradient Θ of the road. These are the forces that must be overcome by the traction force (F_x) of the driving wheels, so that the vehicle may be able to accelerate or at least to travel in a constant cruise speed [2, 3]. For two-wheel drive vehicles, however, a fourth term must be added since the two non-driven wheels introduce another drag when the vehicle accelerates. In other words, the rotational inertia I_w of each of the two non-driving wheels must be rotationally accelerated by a torque equivalent to $T_{nd} = I_w \cdot a_x / r_w$, being r_w the radius of the wheel and a_x the longitudinal acceleration of the car. This torque must be provided by a force $F_{nd} = T_{nd}/r_w$ applied by the wheel knuckles whose reaction must be deducted from F_x. The equation of longitudinal motion of a two-wheel drive vehicle is then provided by Eq. (1), in which m stands for the total mass of the vehicle.

$$F_x - D_a - R_x - W \sin \Theta - 2F_{nd} = ma_x \tag{1}$$

The aerodynamic drag can be defined by Eq. (2) [2, 3]:

$$D_a = \frac{1}{2} \rho_{air} C_D A_f v_x^2 \tag{2}$$

In which ρ_{air} is the density of the air (1.2258 kg/m^3), C_D represents the drag coefficient of the vehicle, A_f stands for its frontal projected area and v_x is the forward speed of the vehicle. The traction force required to be delivered by the powertrain to the driving wheels of the car under real road conditions may be finally determined by employing Eq. (3).

$$F_x = \frac{1}{2} \rho_{air} C_D A_f v_x^2 + R_x + W \sin \Theta + \left(m + 2 \frac{I_w}{r_w^2} \right) a_x \tag{3}$$

On a chassis dynamometer, however, this dynamic equation may not be entirely represented, since all four described forces are either absent (aerodynamic drag and

climbing resistance) or they may behave differently from the actual road condition: the tire resistance upon twin rollers are significantly higher because of the road-tire contact [4, 5]; the equivalent linear inertia of the rollers and its appendices may be different from that of the vehicle [4]; the non-driving wheels may not rotate.

Therefore, some sort of compensation is required in a chassis dynamometer, by either inputting or absorbing power from the system, so that reliable data may be collected from the vehicle during the tests. These compensations are nowadays standard in the field and there are plenty of patents concerning this topic, such as in [6–8]. Nevertheless, as stated by [9] few works have been effectively publicized in regard to the performance of these methods, possibly due to the confidentiality of this information inside the industry.

3 Eddy-Current Brake and SPC-Controller

The eddy-current brake is one of the methods employed to absorb mechanic power from an automotive dynamometer system, either in order to perform the measurements of the overall torque outputting the vehicle under test or to emulate the resistive forces of the longitudinal dynamics [10].

The working principle of this magnetic retarder consists of inducing eddy currents on a ferromagnetic rotating disk by means of an external and fixed magnetic field placed parallel to the axis of the shaft. The disk and its free electrons form a resistive circuit, whose internal current tries to mitigate the local changes in the magnetic flux passing through the metal; by doing so, through Joule effect, the kinetic energy of the dynamometer is converted into heat [10, 11]. The stored heat contained in the warm disk can then be removed by means of forced convection and, therefore, a refrigeration system is necessary. Figure 1a shows a schema of a simple eddy current retarder.

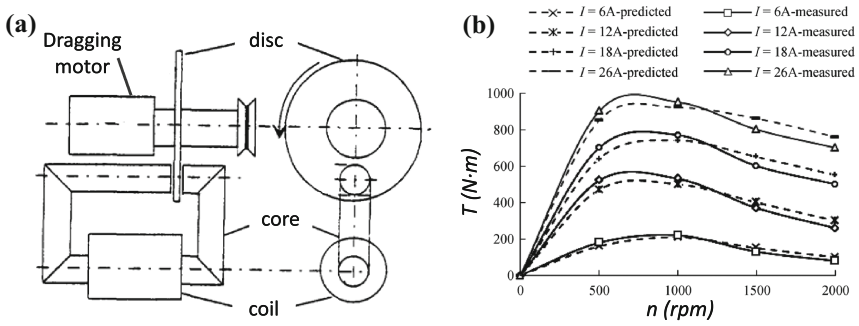

Fig. 1. (a) Schematic representation of an EC-brake (adapted from [12]); (b) Typical torque curves produced by an EC-brake according to the exciting DC current in its coils [11].

The most common way of controlling an EC-brake is to vary the DC electric current injected into the exciting coils that generate the magnetic field acting upon the surface of the rotating disk [10]. The generated torque is not, however, a linear function

of the current, being variable with both the angular speed of the disk and the applied current, as shown in Fig. 1b. According to [12], there are three main regions of operation on an eddy current torque map: (i) below critical speed, the induced magnetic field is significantly smaller than the one being applied by the coil and the overall magnetic field in the gap keeps perpendicular to the face of the disk – torque grows linearly with the speed; (ii) near the critical speed, the induced magnetic field becomes considerable, deforming the overall magnetic field in the gap – torque reaches its maximum; (iii) above the critical speed, the induced magnetic field deforms even more the one applied by the coil – the device gradually loses its braking capacity. In the limit, at very high speeds, torque may even approach zero.

Another source of nonlinearities comes from the rectified single phase controller (SPC), since the outputting current preserves the ripple of the rectifier, maintaining its oscillatory characteristic. Furthermore, the DC component is not directly proportional to the voltage input, given the fact that the 1–5 V analogic input controls the phase angle for which the signal is cut, rather than its RMS value. Considering these nonlinearities regarding the outputting torque in relation to the input voltage signal, which regulates the coil current, the control of an EC-brake may be considered a challenge for the designer and the application of linear controllers, such as PIDs, may lead to instabilities, as already detected in previous attempts performed in our laboratory.

Bearing this in mind, in order to control the EC-brake assembled into the dynamometer effectively, a reliable model of the system must be developed, so that most part of the control signal does not need to rely solely on the feedback loop.

4 Experimental Setup

In this section, a brief description of the equipment used during the tests is presented. Firstly, the chassis dynamometer along with its actuators and its acquisition system are described; a list of its inertia and resistive torques is also provided. Secondly, the inertial and aerodynamic parameters of the vehicle employed to execute the drive cycle are both characterized.

The chassis dynamometer assembled in LabSIn is a twin roller chassis dynamometer provided with: four inertia rollers of $r_R = 200$ mm radius, two for each driven wheel, for power accumulation; an alternate current (AC) 30 CV 2-poles induction machine and its WEG CFW701 frequency inverter, which are employed for the power supply; an air-refrigerated 6-poles eddy-current brake system for power absorption and its single phase power controller with rectifier. A schematic diagram of the system may be seen in Fig. 2. This figure depicts all of the power sources (boxes with horizontal lines), absorption elements (boxes with vertical lines) and accumulators (boxes with diagonal lines).

Regarding the employed sensors, the device counts on two universal torque transducers HBM-T40B – contactless torque flanges: one capable of measuring up to 500 N•m of rotating shaft torque connected to the AC-motor shaft and a second which measures torques up until 3 kN•m, acquiring the torque provided by the EC-brake system. An optic encoder with 60 pulses per revolution was also attached to the AC-motor shaft, in order to read the angular speed of the rollers.

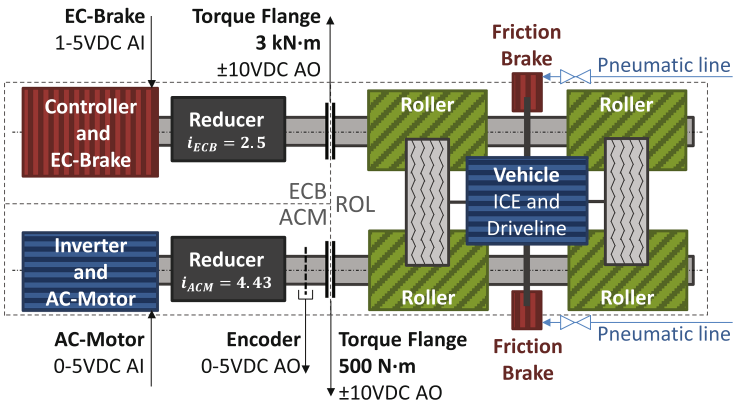

Fig. 2. Schematic representation of the twin roller chassis dynamometer of LabSIn.

For the acquisition system, a National Instrument cDAQ-9178 module was used along with two NI 9239 analog-digital converters (ADC) for ±10 V inputs (50 kS/s/ch; 24 bits) and an NI 9263 digital-analog converter (DAC) for generating ±10 V signal outputs (100 kS/s; 16 bits). The ADC was employed to gather the voltage signals coming from the encoder and from both torque flanges and digitalize them to the Labview control structure, which was developed for the control and Human-Machine Interface (HMI) of the dynamometer, as described in [4]. This program processes the signal and sends two control outputs to the DAC module, one communicating with the frequency inverter and the other with the SPC. Since the computer was not dedicated for processing purposes, being also employed also as HMI, an acquisition rate of 5 kS/s/ch was selected.

Inertia and friction parameters of the test bench, as obtained by [4], are listed in Table 1. Since the gear ratios of both reducers are constant, the moments of inertia and resistive torques are already provided as perceived from the shaft connected to the rollers, in order to simplify calculations. Friction torques are speed dependent, because of the viscous effect of the lubricants.

Table 1. Parameters for inertia and friction losses for the chassis dynamometer of LabSIn [4].

Equipment	Eq. mom. of inertia	Friction torque (v_x in km/h)
EC-brake + reducer	$I_{ECB} = 5.43$ kg·m^2	$M_{RES,ECB} = 0.134v_x + 3.67$ N·m
AC-motor + reducer	$I_{ACM} = 1.38$ kg·m^2	$M_{RES,ACM} = 0.105v_x + 3.67$ N·m
Rollers + bearings	$I_{ROL} = 28.03$ kg·m^2	$M_{RES,ROL} = 3.3968v_x^{0.1951}$ N·m

For the execution of the drive cycle, a FIAT Punto 2008 with a 1.4-liter gasoline engine was employed. All the relevant parameters necessary during the calculation of the resistive forces are listed in Table 2.

Table 2. Inertial and aerodynamic parameters of the vehicle under test [4].

Variable	Value
Mass of vehicle plus driver	$m = 1090$ kg
Moment of inertia of one wheel	$I_w = 0.7279$ kg·m^2
Tire static radius	$r_w = 0.3075$ m
Frontal area	$A_f = 2.16$ m^2
Drag coefficient	$C_D = 0.34$

5 Model Identification of the Eddy-Current Brake

As mentioned in Sect. 3, the setup of the equipment installed in LabSIn imposes some sources of nonlinearities, which cannot be easily modeled by employing analytical equations. In this sense, an experimental approach was performed in order to model the EC-brake for different static input signals.

The experiment consisted of controlling the induction motor in eighth different angular speeds selected in a manner to move the EC-Brake from 250 rpm (7.54 km/h for the vehicle) to 2000 rpm (60 km/h) in steps of 250 rpm with no vehicle on the test bed. It was not possible to acquire data for angular speeds higher than 2000 rpm since at this point the induction motor reached its top speed. The speed control was performed by the frequency inverter of the AC-machine and the torque was transferred from one shaft to another by a 1:1 roller chain transmission. At each angular speed, a voltage signal ranging from 1.0 V to 2.2 V in steps of 0.1 V was manually set in the *Labview* application and the torque obtained in the torque flange attached to the shaft of the EC-Break was read for one minute, gathering a total of around 300,000 samples. The mean value of the signal was then deduced from the resistance torque of the bearings and of the reducer attached to the shaft of the EC-brake ($M_{RES,ECB}$), divided by the gear ratio i_{ECB} and was stored. A total of 104 experiments (8 speeds $\times$ 13 voltages) were performed during this stage and the results are shown in Fig. 3a.

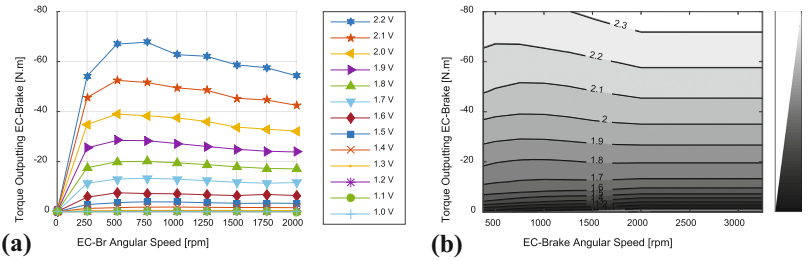

Fig. 3. (a) Acquired torque outputting the EC-brake (discounting losses in the reducer), as a function of input voltage and angular speed; (b) Inverse characterization of the EC-brake as a look-up table with linear interpolation.

It is remarkable that the behavior of the constant voltage curves are similar to that provided in the literature (Fig. 1b), despite the fact that the coils of the EC-Brake were not excited by a pure direct current but rather with the rectified AC-signal. The appearance of a characteristic speed around 500 rpm (15 km/h) for each voltage curve is also noticeable and, as it was expected, the torque outputted by the EC-brake decayed after this threshold value.

For its application in the controller, the inverse model was obtained by means of interpolation, and the voltage value was kept constant for angular speeds of the EC-brake higher than 2000 rpm. Figure 3b depicts a contour plot of the inverse model. This method was chosen in spite of extrapolation for safety reasons, i.e., in order to avoid unexpected torque-overshoots in the region that no measurements were performed.

6 Experimental Validation

As mentioned before, this work presents a preliminary study on the subject of the control of an EC-Brake for emulating real driving conditions on a chassis dynamometer. Following this idea and after noticing that a PID controller was not providing the desired controllability for the system, a simplified feedforward control was added to the control loop as shown in Fig. 4. For the examination of its performance, the feedback controller was deactivated, in other words, the system worked as open loop, during the following tests.

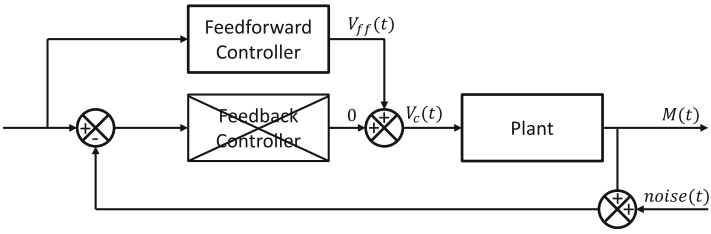

Fig. 4. Feedforward control loop (open loop system).

The required torque outputting the EC-brake (M_{req}) becomes a function of the difference between the resistance force to which the car would be submitted upon the dynamometer without compensations (F_D) and the resistance force to which the vehicle should be submitted on the road (equal to F_x). Equation (4) depicts this relationship, standing $r_R = 0.2$ m for the radius of the rollers and $i_{ECB} = 2.5$ for the transmission ratio of the reducer attached to the EC-Brake.

$$M_{req} = \min\left(\frac{(F_D - F_x)r_R}{i_{ECB}}, 0\right) \tag{4}$$

Being F_D described by Eq. (5) and R_{xD} the rolling resistance of the two driven wheels when rolling upon the four rollers:

$$F_D = R_{xD} + \frac{1}{r_R}\left(M_{RES,ECB} + M_{RES,ACM} + M_{RES,ROL} + (I_{ECB} + I_{ACM} + I_{ROL})\frac{a_x}{r_R}\right) \quad (5)$$

Since the main goal of the present work is to assess the controllability of the EC-Brake by providing more resistances to the vehicle on the dynamometer, it was assumed that $R_x = R_{xD} + 1/r_R \cdot \left(M_{RES,ECB} + M_{RES,ACM} + M_{RES,ROL}\right)$, i.e., that the rolling resistance on the road was equal to all friction forces of the test bed. This way, the usage of the electric motor is minimized and, by considering $\Theta = 0°$, M_{req} becomes:

$$M_{req} = \min\left(\frac{\left(I_{ECB} + I_{ACM} + I_{ROL} - mr_R^2 - 2I_w\left(\frac{r_R}{r_w}\right)^2\right)\frac{a_x}{r_R} - \frac{1}{2}\rho_{air}C_D A_f v_x^2 r_R}{i_{ECB}}, 0\right) \quad (6)$$

In other terms, the torque that must be delivered by the EC-Brake is a function of the speed and acceleration of the vehicle at a given time in the drive cycle. Since the brake controller has still a delay of around on second, it was opted for inputting the speed and acceleration of the drive profile with one second in advance rather than the instantaneous speed and acceleration of the vehicle on the test bench. The theoretical objective torque M_{obj} that must be read by the 3 kN·m torque flange is provided by Eq. (7).

$$M_{obj} = -M_{req}(t) \cdot i_{ECB} + M_{RES,ECB} + I_{ECB}\frac{a_x}{r_R} \quad (7)$$

In order to evaluate the performance of the presented controller, the vehicle was submitted to five runs over the FTP-72 drive cycle, being four experiments run with compensation for evaluating the reproducibility of the results and the last one executed without any control input for comparison. The torque curves read at the torque flange assembled in the EC-Brake shaft were then compared with M_{obj}; Table 3 lists the correlation coefficient obtained in each of the tests.

Table 3. Correlation between the measured torque and the expected torque at the torque flange.

Experiment	Compensation	R^2
Run 1	On	0.9560
Run 2	On	0.9572
Run 3	On	0.9503
Run 4	On	0.9543
Run 5	Off	0.8292

Figure 5 provides an overview of the difference of executing the drive cycle with and without any compensation. The shown excerpt corresponds to the second pulse of the FTP-72 when the vehicle hits a highway scenario and high braking forces are needed for compensating the absence of the aerodynamic drag at the top speed of 91.15 km/h. Besides that, this drive pulse is also characterized by strong acceleration excerpts, which must be compensated by the actuation of the EC-Brake, since the equivalent longitudinal inertia of the dynamometer is circa 21% less than that of the vehicle. This can be noticed by a torque compensation of around 160 N.m at 165 s of the execution of the drive cycle. It is remarkable that both types of compensation were not performed during the fifth run, meaning that the vehicle consumed less fuel than in a real case scenario.

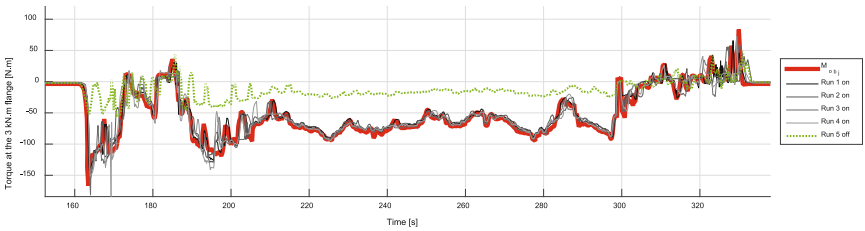

Fig. 5. Torque acquired at the 3 kN·m torque flange in five executions of the drive cycle compared to the objective torque with compensation for driving resistances.

7 Conclusions

This work presented the application of a static feedforward control for the replication of resistive forces on a twin roller chassis dynamometer by means of an Eddy-Current Brake. In order to achieve this goal, the static inverse model of the EC-Brake was determined and for evaluation of its performance, five FTP-72 drive cycles were executed on the test bench, being the first four with and the fifth run without any compensation.

As conclusions of the modeling stage, the authors stated that the EC-Brake assembled in the dynamometer of LabSIn showed a very similar behavior in comparison with the models found in the literature: it presented a characteristic angular speed for which the torque reached its maximum value with a constant control input and the outputted torque has not linearly grown with the control input, complicating the controllability of the device. Additionally, as it could be noticed from the execution of the drive cycles, significant improvements were already obtained with such a simple control approach. During the four controlled runs, a correlation coefficient of around 0.955 was achieved when comparing the torque measured at the torque flange and the expected torque at the same position. To trace a parallel, when no compensation was employed, this metric has decayed to 0.8292.

For further works, the authors perceived the necessity of performing not only a static characterization of EC-Brake model but also a frequency representation of the system. This model could help the evaluation of the robustness of the controlled

system. Furthermore, by the addition of a feedback loop for small corrections, some more improvements could also be delivered. Finally, all these analyses should be extended to the AC-motor and its frequency inverter, in order that the complete controllability of the dynamometer could be achieved.

Acknowledgments. This work was conducted during scholarships supported by the Brazilian Federal Agency for Support and Evaluation of Graduate Education (CAPES), by the National Council for Scientific and Technological Development (CNPq) and by the University of Campinas (UNICAMP).

References

1. Figliola, R.S., Beasley, D.E.: Theory and Design for Mechanical Measurements. Wiley, Hoboken (2006)
2. Gillespie, T.D.: Fundamentals of Vehicle Dynamics. Society of Automotive Engineers, Warrendale (1992)
3. Mitschke, M., Wallentowitz, H.: Dynamik der Kraftfahrzeuge. Springer, Berlin (2014)
4. Eckert, J.J.: Desenvolvimento de Bancada Dinamométrica para Validação da Influência de Estratégias de Troca de Marchas na Dinâmica Veicular Longitudinal. Doctoral thesis, Unicamp (2017)
5. Silva, L.C.A., et al.: Measurement of wheelchair contact force with a low cost bench test. Med. Eng. Phys. **38**(2), 163–170 (2016)
6. Gibson, H., Maddock, R.B.: Dynamometer control system. United States Patent n. 2,982,128. United States Patent Office (1961)
7. Susuki, M.: Chassis dynamometer control system. United States Patent n. 6,157,878. United States Patent Office (2000)
8. Carley, D.: Method of controlling a chassis dynamometer. United States Patent n. 6,360,591. United States Patent Office (2002)
9. Matthews, C., Dickinson, P.B., Shenton, A.T.: Chassis dynamometer torque control: a robust control methodology. Int. J. Passeng. Cars **2**(1), 263–270 (2009). SAE International
10. Martyr, A.J., Plint, M.A.: Engine Testing: Theory and Practice. Butterworth-Heinemann, Oxford (2007)
11. Ye, L., Yang, G., Li, D.: Analytical model and finite element computation of braking torque in electromagnetic retarder. Front. Mech. Eng. **9**(4), 367–379 (2014). Springer, Heidelberg
12. Simeu, E., Georges, D.: Modeling and control of and eddy current brake. Control Eng. Pract. **4**(1), 19–26 (1996). Elsevier Science

Experimental Setup of a Novel 4 DoF Parallel Manipulator

Marina Valles[1(✉)], Pedro Araujo-Gomez[2], Vicente Mata[3], Angel Valera[1], Miguel Diaz-Rodriguez[2], Alvaro Page[4], and Nidal M. Farhat[5]

[1] Instituto U. Automatica e Informatica Industrial, Universitat Politecnica de Valencia, UPV, Valencia, Spain
{mvalles,avalera}@ai2.upv.es
[2] Dpto. Tecnologia y Diseño, Facultad de Ingenieria, Universidad de los Andes, Merida, Venezuela
{pfaraujo,dmiguel}@ula.ve
[3] Centro de Investigación en Ingenieria Mecanica, UPV, Valencia, Spain
vmata@mcm.upv.es
[4] Dpto. Fisica Aplicada, UPV, Valencia, Spain
alvaro.page@ibv.upv.es
[5] Department of Mechanical and Mechatronics Engineering, Faculty of Engineering and Technology, Birzeit University, Birzeit, Palestine
nfarhat@birzeit.edu

Abstract. Parallel manipulators (PM) started with the introduction of architectures with 6 Degree of Freedom (DoF), but a vast of applications require less than 6 DoF. In this respect, architectures for 3 and 4 DoF PM have been proposed. With respect to the 4 DoF most of the robots that have become prototypes are the kind of three translation and one rotation (3T1R) or 3R1T, yet relatively 4 DoF manipulators of the class 2R2T have been built. In this paper the stages for designing and prototyping, including the control architecture design of a 4 DoF PM with 2R2T are put forward. The choice of the DoF is based on the necessary motion for fulfilling the tasks for diagnosis and rehabilitation of human lower-limbs. First, the robot design including the inverse and forward kinematics equation is presented. Then, the prototype is described, and the hardware and control architecture are developed. A control scheme is implemented and the result showing the tracking accuracy of the proposed controller have been included, showing accurate response in terms of position error.

Keywords: Parallel manipulator · Robot control · Mechatronics · Kinematics

The authors wish to express their gratitude to the Plan Nacional de I+D, Comisión Interministerial de Ciencia y Tecnología (FEDER-CICYT) for the partial financing of this study under the project DPI2013-44227-R.

J.C.M. Carvalho et al. (eds.), *Multibody Mechatronic Systems*,
Mechanisms and Machine Science 54, DOI 10.1007/978-3-319-67567-1_37

1 Introduction

A Parallel Manipulator (PM) is a mechanical system that uses (at least two) kinematics chains to connect a moving platform with a fixed base. The PM end-effector is fixed to the moving base, and the load is shared by the kinematics chains. This provides to the PM high accuracy and load-carrying capacity and very good stiffness [1].

Due to their advantages, PMs receive a lot of attention and it is a very active research area. Different applications based on PM can be found, like flight and motion simulations [2], food manipulators [3], medical applications [4], milling machines [5], assembly manipulators [6], robotic rehabilitation [7], etc.

Different mechanical architectures of PM can be found [1,2]. The first PMs were focused on 6 DoF mechanisms [8]. However, because many applications do not require so many DoF, PMs with less DoF being developed are increasing. Manipulators with less DoF maintain the same advantages with less total costs (development, manufacturing and operations). One example of this kind of PMs with 3 translational DoF is the well-known Deta Robot [9]. Other architectures of PMs with 3 DoF has also proposed. These manipulators combine translational and rotary motions, like 3-RPS [10] or 3-PRS [6], where R, P and S stands for the revolute, prismatic and spherical joint, respectively.

In a previous work, the authors of the current paper developed a 3 DoF PM. This manipulator consists on 3 PRS kinematics chains. This configuration was chosen because of the need to develop a low-cost manipulator with 2 DoF of angular rotation in two axes (rolling and pitching) and 1 DoF translation motion (heave). In [11] a completed description of the mechatronic development process of the PM is presented.

The current paper is the continuation of the work done with this 3 DoF robot. The main objective is to develop a new PM that can be useful for diagnosis and rehabilitation of human lower-limbs. After a review of biomechanical aspects and current devices, the PM kinematic requirements were established. For diagnosis, the required range of motion (RoM) can be established according with the Pivot Shift Test [12]. For rehabilitation requirements, the knee joint can rotate around the transverse axis and the vertical axis. Moreover, the knee can translate in the sagittal plane. Therefore, a robot with 4 DoF (2 rotational and 2 translational movements) would cover a large number of procedures applicable to an injured knee, in which the mobile platform simulates the foot trajectory during physiotherapy exercises.

This work has two main purposes: the first one is to develop, starting from scratch, the completed mechatronic design of a low-cost robot with 4 DoF. The aim is to develop a manipulator that allows two translations in the X-Z plane and two rotations: pitch and yaw angles. For the parallel robot implementation, four powerful Maxon DC motors have been used. These motors are equipped with angular position sensors and brakes. For the control of these actuators, a new power unit has been developed. It is composed by an analog to Pulse Width Modulation stage, and H-bridge gate driver and a FETs stage.

The second main purpose of this paper is to develop an open control architecture, which allows the implementation and testing different control algorithm for PM with 4 DoF. The reason for building an open architecture is that the control is a field where there is still great potential for study in order to improve their accuracy [13]. Thus, the robot developed can be used as a control scheme bench. Specially for 4 DoF manipulator, it is important to highlight that, according to the authors' point of view, lots of published works deal with kinematic motion, yet few prototypes have been built of 4 DoF.

In this work, an industrial PC has been used. The computer is equipped with industrial data acquisition cards to obtain the positions of the actuators (be means of the encoders sensors) and to supply the control actions to the power stage. The computer runs the Linux Ubuntu operating system, parched with the real-time kernel Xenomai. For programming the control algorithms, two robot middleware are used: Open Robot Control (Orocos) and Robot Operating System (ROS). The software architecture used is a component-based system that allows a modular implementation.

2 Parallel Robot Design

2.1 Presentation of the 4 DoF Parallel Robot

The choice of PKM architecture is guided by the need for developing a low-cost manipulator able to generate angular rotation in two axes and two translation (X-Z axes) movements. Different alternative design architectures were considered: 2PRS + 2PUS, 2RPU + 2SPS, 2PCUP + PRC + PPU, PRS + 3PUS, etc. After comparing the advantages and disadvantages of each one of the alternatives, the RPS + 3UPS architecture was finally selected. The proposed manipulator consists on four limbs equipped with an active prismatic joint (P). Figure 1 shows the actual PKM and its schematic representation. The limbs are located as follows: three identical 3-UPS external limbs and a central RPU limb.

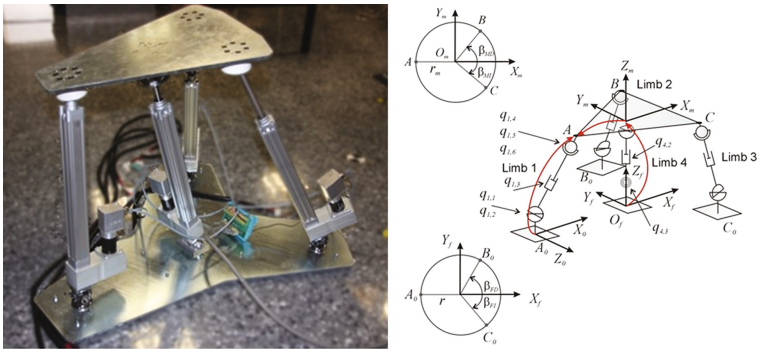

Fig. 1. Actual PKM and its localization of the coordinate systems

The external limbs are equally spaced around the central limb to a radius r. The first axis of rotation of the U-joints, located at the base, points up parallel to the axis the central R joint.

Table 1 shows the D-H parameters for the external limbs of the PKM. The subscript ij denotes the joint j on limb i. Table 1 shows the D-H parameters for the central limb. In both cases, the Paul notation [14] has been used (Table 2).

Table 1. D-H Parameter for the UPS limbs (for i = 1..3) of the 4 DoF PKM

j	α_{ij}	a_{ij}	d_{ij}	θ_{ij}
1	$-\pi/2$	0	0	q_{i1}
2	$\pi/2$	0	0	q_{i2}
3	0	0	q_{i3}	0
4	$\pi/2$	0	0	q_{i4}
5	$\pi/2$	0	0	q_{i5}
6	$\pi/2$	0	0	q_{i6}

Table 2. D-H Parameter for the RPS limb of the 4 DoF PKM

j	α_{4j}	a_{4j}	d_{4j}	θ_{4j}
1	$-\pi/2$	0	0	q_{41}
2	$\pi/2$	0	q_{42}	π
3	$\pi/2$	0	0	q_{43}
4	0	0	0	q_{44}

2.2 The 4 DoF Parallel Robot Inverse Kinematics

The inverse kinematics consist of given the rotation (pitch (β) and yaw (ψ)) angles and the translations in the X-Z plane, finding the actuators linear motion: $q_{i,3}, i = 1..3$, for the external limbs (UPS) and $q_{4,2}$ for the central limb (RPU). This problem will be divided into two parts: first, the UPS limb coordinates $q_{i,1}$,$q_{i,2}$,$q_{i,3}, i = 1..3$, and the central RPU limb coordinates $q_{4,1}$,$q_{4,2}$ are obtained. In the second part, the passive coordinates ($q_{i,4}, q_{i,5}, q_{i,6}, i = 1..3$) of the UPS limbs and $q_{4,3}$ and $q_{4,4}$ of RPU are obtained.

In order to define the orientation and translation of frame j with regard to the j-1 for the i-th limb, the next transformation matrix can be used:

$$\mathbf{^{j-1}H}_j^i = \begin{bmatrix} C_{\theta_{ij}} & -C_{\alpha_{ij}} S_{\theta_{ij}} & S_{\alpha_{ij}} S_{\theta_{ij}} & a_{ij} C_{\theta_{ij}} \\ S_{\theta_{ij}} & -C_{\alpha_{ij}} C_{\theta_{ij}} & -S_{\alpha_{ij}} C_{\theta_{ij}} & a_{ij} S_{\theta_{ij}} \\ 0 & S_{\alpha_{ij}} & C_{\alpha_{ij}} & d_{ij} \\ 0 & 0 & 0 & 1 \end{bmatrix} \quad (1)$$

where C and S stands for sine and cosine of the corresponding angle. The closure equation for the central limb will be the following (see Fig. 1):

$$\begin{bmatrix} x_m \\ y_m \\ z_m \end{bmatrix} = \left[{}^{\mathbf{f}}\mathbf{H}_0^4 \cdot {}^{\mathbf{0}}\mathbf{H}_1^4 \left(q_{4,1}\right) \cdot {}^{\mathbf{1}}\mathbf{H}_2^4 \left(q_{4,2}\right) \right]_{[4,1..3]} \tag{2}$$

for the other limbs, the closure equations can be established as follows,

$$\begin{bmatrix} x_m \\ y_m \\ z_m \end{bmatrix} + {}^f\mathbf{R}_m \cdot \begin{bmatrix} -R_m \\ 0 \\ 0 \end{bmatrix} = \left[{}^{\mathbf{f}}\mathbf{H}_0^1 \cdot {}^0\,\mathbf{H}_1^1 \left(q_{1,1}\right) \cdot {}^{\mathbf{0}}\mathbf{H}_2^1 \left(q_{1,2}\right) \cdot {}^0\,\mathbf{H}_3^1 \left(q_{1,3}\right) \right]_{[4,1..3]}$$

$$\begin{bmatrix} x_m \\ y_m \\ z_m \end{bmatrix} + {}^f\mathbf{R}_m \cdot \begin{bmatrix} R_m C_{\beta_m} \\ R_m S_{\beta_m} \\ 0 \end{bmatrix} = \left[{}^{\mathbf{f}}\mathbf{H}_0^2 \cdot {}^0\,\mathbf{H}_1^1 \left(q_{2,1}\right) \cdot {}^{\mathbf{0}}\mathbf{H}_2^2 \left(q_{2,2}\right) \cdot {}^0\,\mathbf{H}_3^2 \left(q_{2,3}\right) \right]_{[4,1..3]} \tag{3}$$

$$\begin{bmatrix} x_m \\ y_m \\ z_m \end{bmatrix} + {}^f\mathbf{R}_m \cdot \begin{bmatrix} R_m C_{\beta_m} \\ -R_m C_{\beta_m} \\ 0 \end{bmatrix} = \left[{}^{\mathbf{f}}\mathbf{H}_0^3 \cdot {}^0\,\mathbf{H}_1^3 \left(q_{3,1}\right) \cdot {}^{\mathbf{0}}\mathbf{H}_2^3 \left(q_{3,2}\right) \cdot {}^0\,\mathbf{H}_3^3 \left(q_{3,3}\right) \right]_{[4,1..3]}$$

for the points A, B and C respectively. ${}^fR_m$ is the rotation matrix among the fixed references systems $\{O_f - X_f Y_f Z_f\}$ and those, fixed also, attached to the base of the external limbs. Subscript $[4, 1..3]$ indicates that only the fourth column from rows 1 to 3 are considered in the corresponding matrix.

Developing Eq. (2), for the central limb,

$$\begin{aligned} x_m &= -S_{q_{4,1}} \cdot q_{4,2} \\ y_m &= 0 \\ z_m &= C_{q_{4,1}} \cdot q_{4,2} \end{aligned} \tag{4}$$

From those equations if trivial to obtain the active generalized coordinate $q_{4,2}$ and also the passive one, $q_{4,1}$. For the external limbs, a similar procedure can be followed in order to obtain explicit expressions for the generalized coordinates; for instance, considering limb 1, the active generalized coordinate and for the first two passive coordinates can be obtained as follows,

$$\begin{gathered} a = x_m^2 + z_m^2 + R^2 + R_m^2 + 2 \cdot R \cdot x_m + 2 \cdot R_m \cdot z_m \cdot sen\left(\theta\right) \\ -2 \cdot R_m \cdot x_m \cdot cos\left(\theta\right) \cdot cos\left(\psi\right) - 2 \cdot R \cdot x_m \cdot cos\left(\theta\right) \cdot cos\left(\psi\right) \end{gathered}$$

$$\begin{gathered} b = -x_m^2 - z_m^2 - R^2 - R_m^2 - 2 \cdot R \cdot x_m - 2 \cdot R_m \cdot z_m \cdot sen\left(\theta\right) \\ +2 \cdot R \cdot R_m \cdot cos\left(\theta\right) \cdot cos\left(\psi\right) + 2 \cdot R_m \cdot x_m \cdot cos\left(\theta\right) \cdot cos\left(\psi\right) \\ +R_m^2 \cdot cos^2\left(\theta\right) \cdot sen^2\left(\psi\right) \end{gathered} \tag{5}$$

$$q_{1,3} = \sqrt{a}$$

$$q_{1,2} = atan2\left(\sqrt{-\frac{b}{a}}, \frac{R_m \cdot cos\left(\theta\right) \cdot sen\left(\psi\right)}{\sqrt{-b}}\right) \tag{6}$$

$$q_{1,3} = atan2\left(\frac{z_m + R_m \cdot cos\left(\theta\right)}{\sqrt{-b}}, \frac{R_m \cdot cos\left(\theta\right) \cdot sen\left(\psi\right)}{\sqrt{-b}}\right) \tag{7}$$

for the second stage, the rest of the passive generalized coordinates, $q_{i,4}$, $q_{i,5}$, $q_{i,6}$, of the external limbs can be obtained from the equation,

$$ {}^{f}R_3\left(q_{i,1}, q_{i,2}, q_{i,3}\right) \cdot {}^{3}R_6\left(q_{i,4}, q_{i,5}, q_{i,6}\right) = {}^{f}R_m\left(\phi, \theta, \psi\right) \tag{8} $$

2.3 The 4 DoF Parallel Robot Direct Kinematics

For each one of the robot's limbs, the following vectorial closure equations could be established.

$$ \begin{aligned} \overrightarrow{r}_{A_0A} &= \left(q_{1,1}, q_{1,2}, q_{1,3}\right) = \begin{bmatrix} x_m \\ 0 \\ z_m \end{bmatrix} + {}^{f}R_m\left(\theta, \psi\right) \cdot \begin{bmatrix} -R \\ 0 \\ 0 \end{bmatrix} \\ \overrightarrow{r}_{B_0B} &= \left(q_{2,1}, q_{2,2}, q_{2,3}\right) = \begin{bmatrix} x_m \\ 0 \\ z_m \end{bmatrix} + {}^{f}R_m\left(\theta, \psi\right) \cdot \begin{bmatrix} R \cdot cos\left(\beta_{MD}\right) \\ R \cdot sen\left(\beta_{MD}\right) \\ 0 \end{bmatrix} \\ \overrightarrow{r}_{C_0C} &= \left(q_{3,1}, q_{3,2}, q_{3,3}\right) = \begin{bmatrix} x_m \\ 0 \\ z_m \end{bmatrix} + {}^{f}R_m\left(\theta, \psi\right) \cdot \begin{bmatrix} R \cdot cos\left(\beta_{MI}\right) \\ -R \cdot sen\left(\beta_{MI}\right) \\ 0 \end{bmatrix} \\ \overrightarrow{r}_{O_fO_m} &= \left(q_{4,1}, q_{4,2}\right) = \begin{bmatrix} x_m \\ 0 \\ z_m \end{bmatrix} \end{aligned} \tag{9} $$

from 9, a system of 11 non-trivial equations with 11 unknowns can be obtained. This system could be solved by means of Newton-Raphson (N-R) numerical algorithm. N-R converges rather quickly when the initial guess is close to the desired solution [15], so it can be used in real-time applications. However, in order to improve the calculation time and the convergence speed, the passive generalized coordinates will be eliminated from those equations, leading to a system of only four equations,

$$ \begin{aligned} \Phi_1 = q_{1,3}^2 - R^2 - 2 \cdot R \cdot x_m + 2 \cdot R \cdot R_m \cdot cos\left(\psi\right) \cdot cos\left(\theta\right) - x_m^2 \\ +2 \cdot x_m \cdot R_m \cdot cos\left(\psi\right) \cdot cos\left(\theta\right) - z_m^2 - 2 \cdot z_m \cdot R_m \cdot sen\left(\theta\right) - R_m^2 = 0 \end{aligned} \tag{10} $$

$$ \begin{aligned} \Phi_2 = q_{2,3}^2 - R^2 + 2 \cdot R \cdot R_m \cdot sen\left(\beta_{FD}\right) \cdot sen\left(\psi\right) \cdot cos\left(\theta\right) \cdot cos\left(\beta_{MD}\right) \\ +2 \cdot R \cdot R_m \cdot sen\left(\beta_{FD}\right) \cdot cos\left(\psi\right) \cdot sen\left(\beta_{MD}\right) + 2 \cdot R \cdot x_m \cdot cos\left(\beta_{FD}\right) \\ +2 \cdot R \cdot R_m \cdot cos\left(\beta_{FD}\right) \cdot cos\left(\psi\right) \cdot cos\left(\theta\right) \cdot cos\left(\beta_{MD}\right) \\ -2 \cdot R \cdot R_m \cdot cos\left(\beta_{FD}\right) \cdot sen\left(\psi\right) \cdot sen\left(\beta_{MD}\right) - x_m^2 \\ -2 \cdot x_m \cdot R_m \cdot cos\left(\psi\right) \cdot cos\left(\theta\right) \cdot cos\left(\beta_{MD}\right) \\ +2 \cdot x_m \cdot R_m \cdot sen\left(\psi\right) \cdot sen\left(\beta_{MD}\right) \\ -R_m^2 - z_m^2 + 2 \cdot z_m \cdot R_m \cdot sen\left(\theta\right) \cdot cos\left(\beta_{MD}\right) = 0 \end{aligned} \tag{11} $$

$$\begin{aligned}\Phi_3 = q_{3,3}^2 - R^2 - R_m^2 + 2 \cdot R \cdot R_m \cdot cos\,(\beta_{FI}) \cdot cos\,(\psi) \cdot cos\,(\theta) \cdot cos\,(\beta_{MI}) \\ +2 \cdot z_m \cdot R_m \cdot cos\,(\beta_{MI}) \cdot sen\,(\theta) + 2 \cdot R \cdot x_m \cdot cos\,(\beta_{FI}) \\ -2 \cdot x_m \cdot R_m \cdot sen\,(\beta_{FI})\, sin\,(\psi) \\ -2 \cdot R \cdot R_m \cdot sen\,(\beta_{FI}) \cdot sen\,(\psi) \cdot cos\,(\theta) \cdot cos\,(\beta_{MI}) \\ -z_m^2 + 2 \cdot R \cdot R_m \cdot cos\,(\beta_{FI}) \cdot sen\,(\psi) \cdot sen\,(\beta_{MI}) \\ x_m^2 - 2 \cdot x_m \cdot R_m \cdot cos\,(\psi) \cdot cos\,(\theta) \cdot cos\,(\beta_{MI}) \\ +2 \cdot R \cdot R_m \cdot sen\,(\beta_{FI}) \cdot sen\,(\beta_{MI}) \cdot cos\,(\psi) = 0\end{aligned} \tag{12}$$

$$\Phi_4 = q_{4,3}^2 - z_m^2 - x_m^2 = 0 \tag{13}$$

Thus, for each set of active generalized coordinates, the N-R algorithm converges very quickly to the solution of the direct position problem. In order to avoid some singular configurations, an asymmetrical array of the limbs is proposed, with values $R = 0.40\,\text{m}$, $R_m = 0.20\,\text{m}$, $\beta_{FD} = 50°$, $\beta_{FI} = 40°$, $\beta_{MD} = 40°$ and $\beta_{MI} = 30°$.

3 Mechatronic Robot Development

For the implementation of the 4 DoF proposed manipulator, four DC motors equipped with power amplifiers have been used. The actuators are Maxon RE40 GB 150W graphite brushes motors. The performance specifications of these Maxon's motors are 24 [V] nominal voltage, 6940 [rpm] nominal speed, 6 [A] max. continuous current and 2420 [Nm] stall torque. These actuators are equipped encoder sensors and brakes. The encoder sensor is the ENC DEDL 9149 system. It has 500 counts per turn, 3 channels and 100 kHz max. operating frequency. The brake system is Brake AB 28 system. It is a 24 [V], 0.4 [Nm] permanent magnet, single face brake for DC motors that prevents rotation of the shaft at standstill or with turned off motor power.

3.1 Hardware Control Architecture

In order to implement the control architecture for this parallel manipulator, an industrial PC and a power amplifier stage have been used. The PC is based on a high performance 4U Rackmount industrial system with 7 PCI slots and 7 ISA slots. It has a 3.10 GHz Intel®CORE I7 processor and 4 GB DDR3 1333 MHz SDRAM. The industrial PC is equipped with 2 Advantech$^{\text{TM}}$ data acquisition cards: a PCI-1720 and a PCI-1784. The PCI-1720 card has been used for supplying the control actions for each parallel robot actuator. It provides four 12-bit isolated digital-to-analog outputs for the Universal PCI 2.2 bus. It has multiple output ranges (0–5 V, 0–10 V, ±5 V, ±10 V), programmable software and an isolation protection of 2500 VDC between the outputs and the PCI bus. The PCI-1784 card is a 4-axis quadrature encoder and counter add-on card for the PCI bus. The card includes four 32-bit quadruple AB phase encoder counters, an onboard 8-bit timer with a wide range time-based selector and it is optically isolated up to 2500 V.

For the control of the Maxon's motors, an amplifier unit has been developed. It is composed by three stages: an analog to Pulse Width Modulation (PWM) stage, an H-bridge gate driver, and a FETs stage. The first stage transforms the analog voltage supplied by the PC control into a PWM. It is based on an LTC6992 silicon oscillator (TimerBlox®). The output frequency is determined by a single resistor that programs the LTC69920's internal master oscillator frequency. The PWM signal and the movement sense (provided by a digital output of the PC control) are suministrated to the H-bridge gate driver. It is based on the DRV8701 device of Texas Instruments®. It is a brushed DC motor full-bridge driver that uses four external N-channel MOSFETs targeted to drive a 12 V to 24 V bidirectional brushed DC motor. Finally, the power amplifier unit has four MOSFET in a full H-bridge configuration.

3.2 Software Control Architecture

A critical aspect for implementing a new robot system is it software architecture. In the last years, component-based software development has been increasing. This kind of software development has several advantages like modular design and structure, fully reusable code and modules, modules reconfigurable and distributed execution of the modules, improving total execution time.

Due to the modular design and structure, and because the different control schemes have common parts, these parts can be developed as several modules. After that, these modules can be reused to implement different controllers. It is as simple as inserting the necessary modules, to configure them (making connections with each other) and running them. Note that, although it can be a complicated task at first, the development of component-based software makes the programmer's job easier in the end because if a module works correctly in one particular scheme, it will certainly work correctly in another control scheme. Therefore, besides the advantages discussed above, this approach minimizes the chance of programming errors in the implementation of any of the modules.

The software architecture uses the Linux Ubuntu 12.04 operating system. Because real-time characteristics are required, Ubuntu was patched with Xenomai, a real-time kernel. Based on an industrial PC, this control architecture presents two main advantages: on the one hand, it is an open system that gives a powerful platform for developing high-level tasks. In this way, any control algorithm can be programmed and implemented, and it is possible to use external sensors, like cameras of artificial vision, force sensors, accelerometers, etc. The second advantage is related with the price of the control architecture: because the programming platform is based on free software, and because it is a PC equipped with industrial data acquisition cards, the cost of this system does not exceed $ 2000.

For the development of the different robot control algorithms, the middlewares *Open Robot Control Software* (Orocos, www.orocos.org) and *Robot Operating System* (ROS, www.ros.org) have been used. Orocos is one of the best real-time motion control frameworks available at the moment. However, it presents certain constraints when trying to achieve something other than the control

itself. One of the solutions is ROS that has been designed as a conglomeration of various tools organized in packages. Each package or "stack" may contain libraries, executables or scripts and a manifest which defines the dependencies on other packages and meta information about the package itself. A ROS package called rtt ros integration allows for Orocos components to connect to the ROS network. This way they can both publish and subscribe to all the available streamed topics, being both middlewares fully compatible.

What is important is that while ROS has many tools and functionalities that are useful in the development of robotic applications, Orocos provides a solid core for the main control scheme in real time. In other words, ROS and Orocos complement each other, broadening the range of solutions they can offer as standalone platforms.

4 Control of the 4 DoF Robot

In order to implement the PM control, different control strategies can be proposed. There are some model-based controllers that compensate the nonlinearities of the robot (such as inertial, gravity and Coriolis terms) by adding these forces to the control action. This kind of controllers has two main problems. First, they are more difficult to program and have greater computational complexity. On the other hand, model-based controllers require the model dynamic parameters, so it is needed a parameter identification process [16].

In this work, a passivity-based controller has been developed for controlling the novel 4 DoF parallel manipulator. The passivity-based approach solves the control problem by exploiting the manipulator system's physical structure, and specifically, it passivity property. The passivity controllers reshape the natural energy of the systems in such a way that the tracking control objective is achieved. The control algorithm is based on the work of [17]. The control law follows the next equation:

$$\tau_c = -K_p \cdot e - K_d \cdot v - K_i \cdot \int_o^t (e + v)\, dt \tag{14}$$

where K_p, K_d and K_i are positive definite diagonal matrices. It is a very simple controller that offers significant performance and robustness system properties. This controller has a proportional, a derivative and an integral components. The first one calculates the error between the active generalized coordinates and their references ($e = q - q_d$). The active coordinates values of the linear actuators are measured using the encoder card. The derivative component depends on the velocity of the joints. Because the proposed robot does not provide velocity sensors, for this controller the velocity measurement has been replaced by approximate differentiation:

$$v = diag\left\{\frac{b_i s}{s + a_i}\right\} q \tag{15}$$

with $a_i > 0$ and $b_i > 0$. Finally, the controller provides an integral component. It is a standard practical remedy to compensate the robot gravity term.

This control algorithm has been implemented using the open control architecture. Figure 2 shows the OROCOS diagram for the passivity-based controller proposed in Eq. (14). The *SensorPose* module provides the robot position using the encoders Advantech's PCL-1784 card. Module *Ref-Gener* calculates the movement references in the cartesian plane, and the *Kinematics* module obtains the references for the four active joints of the robot. Module *Estim-Vel* calculates the robot velocity estimation following the Eq. (15), and the calculation of the position error and integral term are implemented on modules *Pos-Error* and *Integral*. The *Combiner* module calculates the action control depending on the proportional, derivative and integral terms and it provides the inputs (control actions) to the *Actuator* modules, which are responsible for carrying out digital-analog conversions through Advantech's PCI-1720 cards. The control scheme also provides the *Supervisor* module. It monitores the correct operation of the system and it is charged with deactivating the control unit and stops the robot in the case of detecting a malfunction in the system.

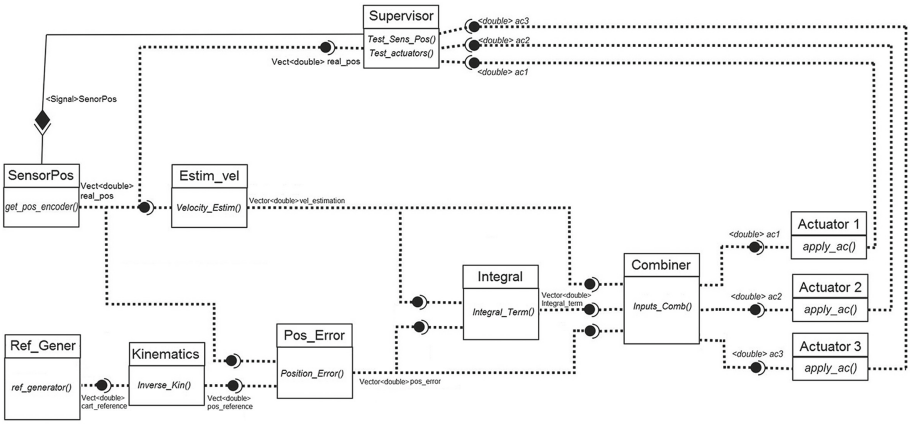

Fig. 2. Orocos scheme for the passivity-based robot controller

In order to validate the robot design and control architecture, several trajectories have been tested. Due to the lack of space, only one of them have included in this work. In this case the reference for the Z coordinate is a sinusoidal movement. The references for the rest of the robot coordinates: X , pitch (β) and yaw (ψ) are equal to 0.

Figure 3 presents the response of the four active coordinates of the parallel robot, according to the Cartesian references proposed above. These show the joint references (obtained by the inverse kinematics of the robot by Eqs. (5–8)) and the joint robot positions. They also show the control action applied. As can readily be appreciated, the manipulator follows the required trajectory. The mean errors are −1.345e−5, 3.8931e−5, 8.1243e−6 and −1.346e−5 for the q13, q23, q33 and q42 robot joints. The control algorithm implemented gives a very

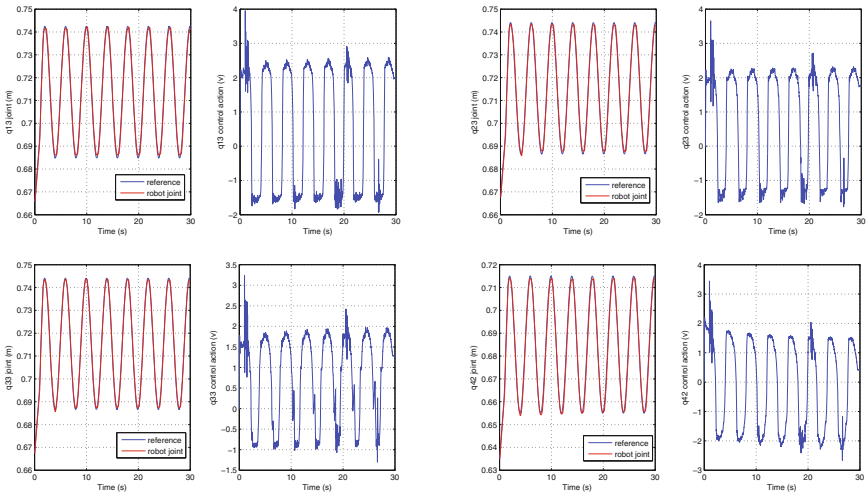

Fig. 3. Active robot coordinates and control actions.

low error, which means that the system works without problems the reference indicated.

5 Conclusions

This paper has shown a novel low-cost 4 DoF parallel manipulator. The mechatronic design, mechanical structure, electric actuators and control system has been fully developed. For the robot control, a new open control architecture has been developed. The control hardware is based on an industrial PC equipped with industrial data acquisition cards to read the positions of the robot axes and to provide the control actions to the actuator by means of the digital to analog converters. The proposed control architecture has two main advantages. On the one hand, it is an open control system, so different control algorithms can be developed. On the other hand, the price of this control system is low cost. In the control unit, both direct and inverse kinematic equations for the PM have been programmed, and a passivity-based control scheme has been developed. This control algorithm is a point-to-point controller that uses an estimation of the robot velocity and an integral action to cancel the gravitational term of the robot.

References

1. Merlet, J.P.: Parallel Robots, vol. 128. Springer Science & Business Media, Cham (2006)
2. Tsai, L.W.: Robot Analysis: The Mechanics of Serial and Parallel Manipulators. Wiley, London (1999)

3. Xu, W.L., Pap, J.S., Bronlund, J.: IEEE Trans. Industr. Electron. **55**(2), 832 (2008)
4. Li, Y., Xu, Q.: IEEE/ASME Trans. Mechatron. **12**(3), 265 (2007)
5. Pierrot, F., Company, O.: Proceedings of IEEE/ASME International Conference on Advanced Intelligent Mechatronics, 1999, pp. 508–513. IEEE (1999)
6. Chablat, D., Wenger, P.: IEEE Trans. Robot. Autom. **19**(3), 403 (2003)
7. Vallés, M., Cazalilla, J., Valera, A., Mata, V., Page, A., Díaz-Rodríguez, M.: Robotica, pp. 1–19 (2015)
8. Stewart, D.: Proc. Inst. Mech. Eng. **180**(1), 371 (1965)
9. Clavel, R.: Proceedings of International Symposium on Industrial Robots, pp. 91–100 (1988)
10. Carretero, J., Nahon, M., Podhorodeski, R.: Int. J. Robot. Autom. **15**(4), 1021 (2000)
11. Vallés, M., Díaz-Rodríguez, M., Valera, Á., Mata, V., Page, Á.: Mech Based Des. Struct. Mach. **40**(4), 434 (2012)
12. Wheeless, C.R.: Wheeless' Textbook of Orthopaedics (1996)
13. Paccot, F., Andreff, N., Martinet, P.: Int. J. Robot. Res. **28**(3), 395 (2009)
14. Paul, R.P.: Robot Manipulators: Mathematics, Programming, and Control: The Computer Control of Robot Manipulators. The MIT Press (1981). ISBN 026216082X. Massachusetts
15. De Jalón, J., Bayo, E.: Kinematic and Dynamic Simulation of Multibody Systems: The Real-Time Challenge. Springer, New York (1994)
16. Mata, V., Page, A., Valera, A., Diaz-Rodriguez, M., Farhat, N.: Dynamic Parameter Identification for Parallel Manipulators. INTECH Open Access Publisher (2008)
17. Ortega, R., Perez, J.A.L., Nicklasson, P.J., Sira-Ramirez, H.: Passivity-Based Control of Euler-Lagrange Systems. Mechanical, Electrical and Electromechanical Applications. Springer Science & Business Media, London (2013)

Behaviour Comparison Between Mechanical Epicyclic Gears and Magnetic Gears

M. Desvaux[1(✉)], B. Multon[1], H. Ben Ahmed[1], and S. Sire[2]

[1] SATIE Laboratory, ENS Rennes, Université Bretagne Loire, CNRS, Bruz, France
{melaine.desvaux, bernard.multon, hamid.benahmed}@ens-rennes.fr
[2] Université de Bretagne Occidentale, FRE CNRS 3744, IRDL, Brest, France
stephane.sire@univ-brest.fr

Abstract. This article deals with the magnetic gears with modulating ring and mechanical epicyclic gears and their operation. A power transmission analysis is done and permits to obtain an analogy of the kinematics between the two gear systems. Moreover, a transposition of the mechanical epicyclic gear arrangements to a magnetic gear arrangements can be made. Finally, a load repartition evolution description is proposed to complete the comparison between magnetic gears with modulating ring and mechanical epicyclic gears.

Keywords: Arrangements · Gear ratio · Load repartition · Magnetic gear · Mechanical epicyclic gear

1 Introduction

In many mechatronic drive chains, such as wind turbine drives [1, 2], mechanical gearbox failure and maintenance increase operating costs, particularly in offshore locations. To improve drive train reliability, one potentially attractive solution consists of replacing the mechanical gearboxes by a magnetic gear [3]. The most studied topology of magnetic gears has been proposed by Martin [4] and was the subject of different behaviour studies proposed by Atallah [3].

The magnetic gear shown in Fig. 1a includes an internal ring of permanent magnets, an external ring of permanent magnets and a ring of ferromagnetic pole pieces between the permanent magnets rings.

Different studies show that in wind turbine context, this topology of magnetic gear potentially offers high performance with a higher torque density and a higher reliability than mechanical gearboxes [5, 6]. It becomes even more attractive for high-torque applications, like a high-power wind turbine (on the order of several MN.m and several MW) [7].

The behaviour of the magnetic gear with modulating ring [3] can be compared with mechanical epicyclic gear [5] shown in Fig. 1b. Mechanical epicyclic gear is composed of a planetary carrier with its satellites, an internal ring and an external ring. Different topologies of mechanical epicyclic gear have been studied since many years [8] and four epicyclic gear simple arrangements are commonly presented as shown in Fig. 2. In wind turbine, the most attractive arrangement is the epicyclic gear with a single range

J.C.M. Carvalho et al. (eds.), *Multibody Mechatronic Systems*,
Mechanisms and Machine Science 54, DOI 10.1007/978-3-319-67567-1_38

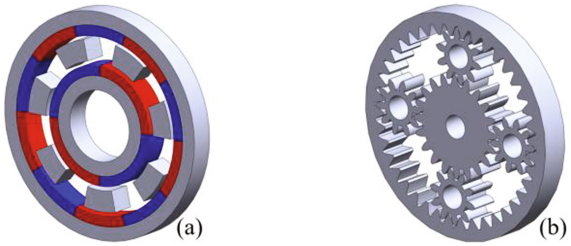

Fig. 1. (a) Magnetic gear with modulating ring [3] and (b) Mechanical epicyclic gear

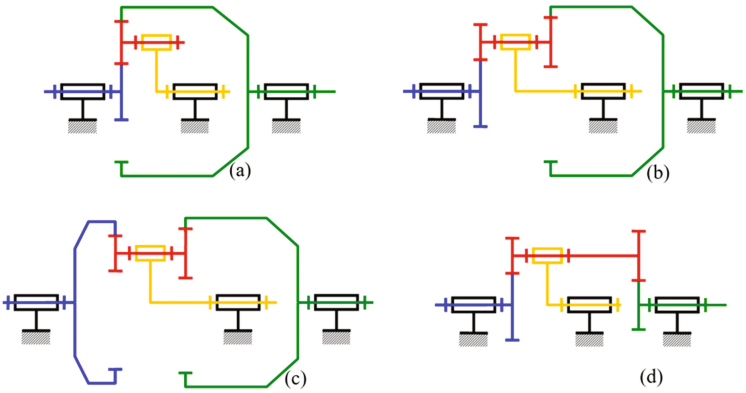

Fig. 2. Schematic epicyclic gear arrangements with (a) an internal ring, an external ring and a planetary carrier with its satellites, (b) an internal ring, an external ring and a planetary carrier with two ranges of satellites, (c) two external rings and a planetary carrier with two ranges of satellites and (d) two internal rings and a planetary carrier with two ranges of satellites.

of satellites (Fig. 2a) since the fact to have only one range of satellites increase the power density of the system.

In this article, the major contribution is the comparison between the four epicyclic gear arrangements and magnetic gear with modulating ring arrangements. It will includes an arrangement, a kinematic (with a study of the gear ratio) and a load repartition approaches.

2 Mechanical Epicyclic Gear Behaviour

To explain the power transmission performed by the mechanical epicyclic gear and compare it with the power transmission of the magnetic gear with modulating ring, the arrangement shown in Fig. 1a is studied. Moreover, it is considered that the input of the system is the ring with the high teeth number (which will be called the input ring) and the output of the system is the ring with the low teeth number (which will be called the output ring) as shown in Fig. 3.

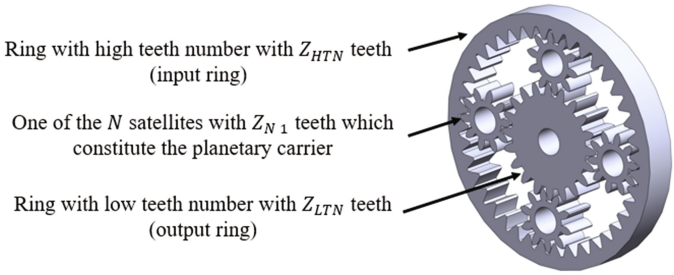

Fig. 3. Rings definition of the mechanical epicyclic gear

2.1 General Principle

All arrangements of mechanical epicyclic gears are composed of three rings:

- A ring with Z_{LTN} of teeth (with low teeth number) and a module m_{LTN},
- A ring with Z_{HTN} of teeth (with high teeth number) and a module m_{HTN},
- A planetary carrier with one or two ranges of satellites composed of N satellites with Z_{Ni} teeth and a module m_{Ni} for the range i (an example is given in Fig. 3 with: $Z_{LTN} = 20$, $Z_{HTN} = 40$, $Z_{N1} = Z_{N2} = 10$ and $N = 4$).

2.2 Power Transmission

The contact between input ring teeth and the planetary teeth generates friction and then a complex mechanical stress state on the contact point of the N satellites Eq. (1). In the case of a straight toothed gear, only the $\sigma_{r\theta}$ stress component generates tangential loads. For the N satellites, these loads $F^n_{tang}(t)$ defined in Eq. (2) are calculated from the integration of the stress component $\sigma_{r\theta}$ on the contact area $S(t)$. In the same time, the N satellites are in contact with the output ring. From the mechanical equilibrium, satellites transmit directly the tangential loads to the output ring. The mechanical torque on the output ring is then given by Eq. (3).

$$\overline{\overline{\sigma_{mech}}}(M,\,t) = \begin{pmatrix} \sigma_{rr}(t) & \sigma_{r\theta}(t) & \sigma_{rz}(t) \\ \sigma_{r\theta}(t) & \sigma_{\theta\theta}(t) & \sigma_{\theta z}(t) \\ \sigma_{rz}(t) & \sigma_{\theta z}(t) & \sigma_{zz}(t) \end{pmatrix}_{(\overrightarrow{e_r},\overrightarrow{e_\theta},\overrightarrow{e_z})} \tag{1}$$

$$F^n_{tang}(t) = \int_{S(t)} \sigma_{r\theta}(t).dS(t) \tag{2}$$

$$T_{LTN}(t) = R.\sum_{n=1}^{N} F^n_{tang}(t) \tag{3}$$

The mechanical power transmission can be performed if the average value of the mechanical torque is different to zero when the different rings are in rotation. This condition can be made by imposing a single module m defined in Eq. (4) for the

different rings and by imposing the Eq. (5) between the teeth number for the different rings (in the general case).

$$m = m_{LTN} = m_{HTN} = m_{N1} = m_{N2} \tag{4}$$

$$Z_{LTN} + Z_{N1} = Z_{HTN} + Z_{N2} \tag{5}$$

With these equations, it is possible to define the ratio λ_{mech} defined in Eq. (6) where n_{mech} corresponds to the number of rings external to the planetary carrier and the Willis relation for a mechanical epicyclic gear is given in Eq. (7). Then the gear ratio G_{mech} depends on the fixed ring as shown in Eq. (8) [9].

$$\lambda_{mech} = \frac{\omega_{LTN/0} - \omega_{PC/0}}{\omega_{HTN/0} - \omega_{PC/0}} = \frac{Z_{HPN}.Z_{N1}}{Z_{N2}.Z_{LPN}}(-1)^{n_{mech}} \tag{6}$$

$$\omega_{LTN/0} - \lambda_{mech}.\omega_{HTN/0} + (\lambda_{mech} - 1).\omega_{PC/0} = 0 \tag{7}$$

$$\begin{cases} \omega_{LTN/0} = 0 \rightarrow G_{mech} = \frac{\omega_{HTN/0}}{\omega_{PC/0}} = \frac{(\lambda_{mech}-1)}{\lambda_{mech}} \\ \omega_{PC/0} = 0 \rightarrow G_{mech} = \frac{\omega_{LTN/0}}{\omega_{HTN/0}} = \lambda_{mech} \\ \omega_{HTN/0} = 0 \rightarrow G_{mech} = \frac{\omega_{LTN/0}}{\omega_{PC/0}} = -(\lambda_{mech} - 1) \end{cases} \tag{8}$$

3 Magnetic Gear with Modulating Ring Behaviour

To explain the power transmission performed by the magnetic gear [3], it is considered that the input of the system is the low speed permanent magnet ring with the high pole number (which will be called the input permanent magnets ring) and the output of the system is the high speed permanent magnet ring with the low pole number (which will be called the output ring) as shown in Fig. 4.

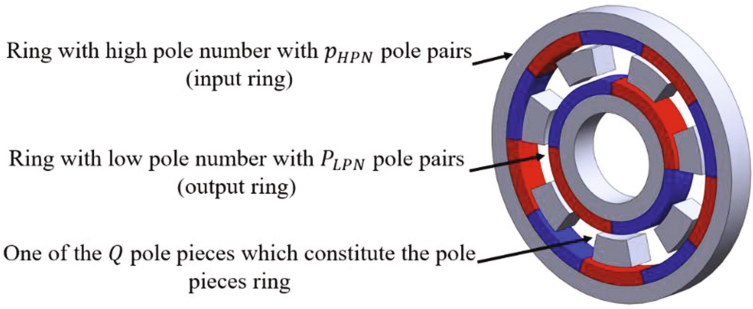

Fig. 4. Definition of the different parts of the studied magnetic gear arrangement

3.1 General Principle

The general principle of the different magnetic gear with modulating ring arrangements can be described from the magnetic gear [3] which corresponds to the magnetic gear arrangement presented in Fig. 4. All arrangements of magnetic gear with modulating ring are composed of three rings:

- A ring with p_{LPN} low pole number of pole pairs of permanent magnets and a ferromagnetic yoke,
- A ring with p_{HPN} high pole number of pole pairs of permanent magnets and a ferromagnetic yoke,
- A ring with Q ferromagnetic pole pieces (an example is given in Fig. 4 with low pole numbers, to improve readability: $p_{LPN} = 2$, $p_{HPN} = 5$ and $Q = 7$).

Contrary to the mechanical epicyclic gear, pole pieces do not rotate like the satellites on the planetary carrier.

3.2 Power Transmission

The input permanent magnets ring generates in air gaps a wave of magneto-motive force and then an induction $\overrightarrow{B_{HPN}}$ defined in Eq. (9) in the neighbouring air gap (to simplify the demonstration, only the fundamental wave of the three rings is taken into account). Ferromagnetic pole pieces module the permeance to obtain in the air gap close to the output permanent magnet ring the induction from the input permanent magnet ring $\overrightarrow{B_{mHPN}}$ defined in Eq. (10). There is also in this airgap the induction from the output permanent magnets ring $\overrightarrow{B_{LPN}}$ as shown in Eq. (11). Both inductions produce then a global induction $\overrightarrow{B_{tot}}$ defined in Eq. (12) close to the output permanent magnets ring.

$$\overrightarrow{B_{HPN}}(t) = \left(B_r^{HPN}.\overrightarrow{e_r} + B_\theta^{HPN}.\overrightarrow{e_\theta}\right)\cos(p_{HPN}.\omega_{HPN}.t) \tag{9}$$

$$\overrightarrow{B_{mHPN}}(t) = \left(B_{mr}^{HPN}.\overrightarrow{e_r} + B_{m\theta}^{HPN}.\overrightarrow{e_\theta}\right)\cos((p_{HPN} - Q).\omega_{HPN}.t) \tag{10}$$

$$\overrightarrow{B_{LPN}}(t) = B_r^{LPN}\left(B_r^{LPN}.\overrightarrow{e_r} + B_\theta^{LPN}.\overrightarrow{e_\theta}\right)\cos(p_{LPN}.\omega_{LPN}.t) \tag{11}$$

$$\overrightarrow{B_{tot}}(t) = \overrightarrow{B_{mHPN}}(t) + \overrightarrow{B_{LPN}}(t) = B_r^{tot}(t).\overrightarrow{e_r} + B_\theta^{tot}(t).\overrightarrow{e_\theta} \tag{12}$$

The global induction $\overrightarrow{B_{tot}}$ will generate a mechanical stress state which corresponds to the 2-D Maxwell tensor $\overline{\overline{\sigma_{magn}}}$ defined in Eq. (13). The instantaneous magnetic torque on the output permanent magnets ring T_{LPN} can be computed from the Eq. (14).

$$\overline{\overline{\sigma_{magn}}}(M,t) = \frac{1}{\mu_0}\begin{pmatrix} B_r^{tot}.B_\theta^{tot} - B_r^{tot2}/2 & B_r^{tot}.B_\theta^{tot} & 0 \\ B_r^{tot}.B_\theta^{tot} & B_r^{tot}.B_\theta^{tot} - B_\theta^{tot2}/2 & 0 \\ 0 & 0 & 0 \end{pmatrix}_{(\overrightarrow{e_r},\overrightarrow{e_\theta},\overrightarrow{e_z})} \tag{13}$$

$$\begin{cases} T_{LPN}(t) = R.F_t(t) \\ F_{tang}(t) = \frac{L_z}{\mu_0} \int_0^{2\pi} B_r^{tot}(t).B_\theta^{tot}(t) R\, d\theta \end{cases} \tag{14}$$

The magnetic power transmission can be performed with two conditions: the part of the magnetic energy stored in airgaps which generates magnetic torque defined in Eq. (15) must be different to zero, the average value of the magneto-mechanical torque defined in Eq. (16) must also be different to zero.

$$W_{mLPN}(t) = \frac{e.L_z}{\mu_0} \int_0^{2\pi} B_r^{tot}(t).B_\theta^{tot}(t) R\, d\theta \tag{15}$$

$$T_{LPN}(t) = -\frac{\partial W_{mLPN}(t)}{\partial \theta_{LPN}} \tag{16}$$

Considering the global induction defined in Eq. (12), the energy stored in airgaps is different to zero only if the condition defined in Eq. (17) is respected. There is then a ratio between the average magnetic torques which corresponds to the gear ratio of the system. Like mechanical epicyclic gears, it is possible to define the ratio (18) where n_{magn} corresponds to the number of rings external to the pole pieces ring. The Willis equation for a magnetic gear is given in Eq. (19). Then the gear ratio G_{magn} depends on the fixed ring as shown in Eq. (20) [10]. In these equations, the number of pole pairs and pole pieces corresponds to the number of teeth of the mechanical epicyclic gear.

$$p_{HPN} + p_{LPN} = Q \tag{17}$$

$$\lambda_{magn} = \frac{\omega_{LPN/0} - \omega_{Q/0}}{\omega_{HPN/0} - \omega_{Q/0}} = \frac{p_{HPN}}{p_{LPN}} (-1)^{n_{magn}} \tag{18}$$

$$\omega_{LPN/0} - \lambda_{magn}.\omega_{HPN/0} + \left(\lambda_{magn} - 1\right).\omega_{Q/0} = 0 \tag{19}$$

$$\begin{cases} \omega_{LPN/0} = 0 \rightarrow G_{magn} = \frac{\omega_{HPN/0}}{\omega_{Q/0}} = \frac{\left(\lambda_{magn} - 1\right)}{\lambda_{magn}} \\ \omega_{Q/0} = 0 \rightarrow G_{magn} = \frac{\omega_{LPN/0}}{\omega_{HPN/0}} = \lambda_{magn} \\ \omega_{HPN/0} = 0 \rightarrow G_{magn} = \frac{\omega_{LPN/0}}{\omega_{Q/0}} = -\left(\lambda_{magn} - 1\right) \end{cases} \tag{20}$$

4 Comparison Between Mechanical and Magnetic Gears

4.1 Transposition of Mechanical Epicyclic Gear Arrangements

To obtain a magnetic interaction between permanent magnets rings, it is not necessary to have the three concentric rings of the magnetic gear. Indeed, like the mechanical epicyclic gears presented Fig. 2, it is possible to have different arrangements with two internal permanent magnet rings or with two external permanent magnet rings as shown

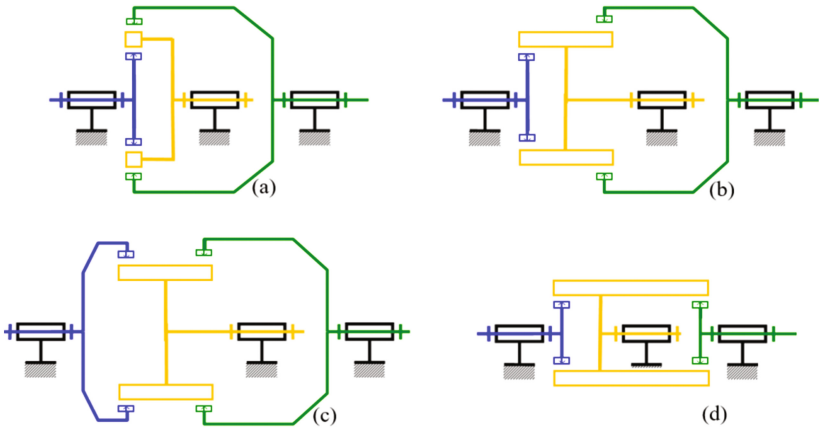

Fig. 5. Magnetic gear arrangements with (a) a concentric internal and external permanent magnets rings with a pole pieces ring, (b) a non-concentric internal and external permanent magnets ring with a pole pieces ring, (c) two external permanent magnets rings and a pole pieces ring and (d) two internal permanent magnets rings and a pole pieces ring.

in Fig. 5. The arrangement with two internal rings of permanent magnets has been studying by [11–13], unlike the arrangements shown in Fig. 5b and c which have not been studied for the moment. For the magnetic gear arrangements shown in Fig. 5b, c and d, the coupling between permanent magnet rings force to have a transverse flux in pole pieces.

4.2 Kinematics

From Eqs. (8) and (20), it is possible to compare in Table 1 the gear ratio of the mechanical and magnetic gears depending on the fixed ring and the arrangement. Table 1 shows that the kinematic behaviour in the same for the mechanical and magnetic gears for the different arrangements and depending on the fixed ring.

Table 1. Gear ratio comparison depending on the arrangement and the fixed ring

Config.	Fixed rings (mechanical and magnetic)		
	$\omega_{HPN/0} = \omega_{HTN/0} = 0$	$\omega_{LPN/0} = \omega_{LTN/0} = 0$	$\omega_{Q/0} = \omega_{PC/0} = 0$
Arrangement Figs. 2a and 5a	$G_{magn} = \frac{Q}{p_{LPN}}$ $G_{mech} = \frac{Z_{N1}}{Z_{LTN}}$	$G_{magn} = \frac{Q}{p_{HPN}}$ $G_{mech} = \frac{Z_{N2}}{Z_{HTN}}$	$G_{magn} = -\frac{p_{HPN}}{p_{LPN}}$ $G_{mech} = -\frac{Z_{HTN}}{Z_{LTN}}$
Arrangement Figs. 2b and 5b	$G_{magn} = \frac{Q}{p_{LPN}}$ $G_{mech} = \frac{Z_{N1}}{Z_{LTN}}$	$G_{magn} = \frac{Q}{p_{HPN}}$ $G_{mech} = \frac{Z_{N2}}{Z_{HTN}}$	$G_{magn} = -\frac{p_{HPN}}{p_{LPN}}$ $G_{mech} = -\frac{Z_{HTN}.Z_{N1}}{Z_{N2}.Z_{LTN}}$
Arrangement Figs. 2c and 5c	$G_{magn} = \frac{Q}{p_{LPN}}$ $G_{mech} = \frac{Z_{N1}}{Z_{LTN}}$	$G_{magn} = \frac{Q}{p_{HPN}}$ $G_{mech} = \frac{Z_{N2}}{Z_{HTN}}$	$G_{magn} = \frac{p_{HPN}}{p_{LPN}}$ $G_{mech} = \frac{Z_{HTN}.Z_{N1}}{Z_{N2}.Z_{LTN}}$
Arrangement Figs. 2d and 5d	$G_{magn} = \frac{Q}{p_{LPN}}$ $G_{mech} = \frac{Z_{N1}}{Z_{LTN}}$	$G_{magn} = \frac{Q}{p_{HPN}}$ $G_{mech} = \frac{Z_{N2}}{Z_{HTN}}$	$G_{magn} = \frac{p_{HPN}}{p_{LPN}}$ $G_{mech} = \frac{Z_{HTN}.Z_{N1}}{Z_{N2}.Z_{LTN}}$

4.3 Load Distribution Evolution

Due to the non-contact power transmission between the different rings of the magnetic gear, contrary to the mechanical epicyclic gear, the permanent magnets that correspond to the teeth of the mechanical gear can transmit continuously energy. A comparison can be made between the power transmitted by a tooth of a mechanical gear and the power transmitted by a magnet of a magnetic gear. For this, we consider that the fixed ring is the planetary carrier for the epicyclic gear and the pole pieces ring for the magnetic gear. An example is given in Fig. 6 where the power transmission is performed for the mechanical epicyclic gear configuration show in Fig. 3 ($Z_{LTN} = 20$, $Z_{HTN} = 40$, $Z_{N1} = Z_{N2} = 10$ and $N = 4$) and for the magnetic gear configuration show in Fig. 4 ($p_{LPN} = 2$, $p_{HPN} = 5$ and $Q = 7$).

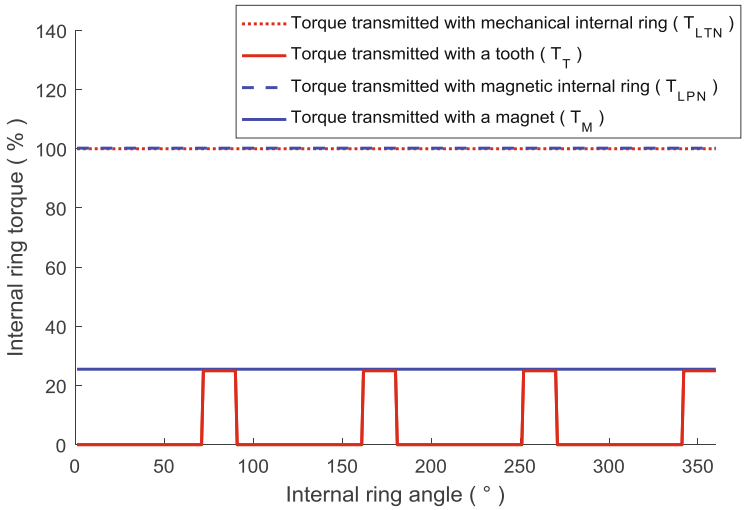

Fig. 6. Load repartition evolution in function of the internal ring angle for a mechanical gear with $Z_{LTN} = 20$, $Z_{HTN} = 40$, $Z_{N1} = Z_{N2} = 10$ and $N = 4$ and a magnetic gear with $p_{LPN} = 2$, $p_{HPN} = 5$ and $Q = 7$.

Figure 6 shows that a tooth of a ring of a mechanical epicyclic gear transmits tangential load only when the tooth is in contact with a corresponding tooth of a satellite. On the opposite, the magnets of the magnetic gear transmit tangential load at every moment since there is a non-contact power transmission. It is then possible to express the percentage of the torque transmitted by a tooth T_T or a magnet T_M according to the gear type defined in Eq. (21) where T_{LTN} and T_{LPN} are defined in Eqs. (3) and (16). It is also possible to express the utilization rate of a tooth τ_T or a magnet τ_M according to the studied gear type defined in Eq. (22).

$$\begin{cases} T_T(\%) = \frac{100}{N} \\ T_M(\%) = \frac{100}{2.p_{LPN}} \end{cases} \tag{21}$$

$$\begin{cases} \tau_T(\%) = \frac{100.N}{Z_{LTN}} \\ \tau_M(\%) = 100 \end{cases} \tag{22}$$

This result contributes to demonstrate that the power density of magnetic gear is higher than mechanical epicyclic gear power density [5]. The benefit of a magnetic gear over mechanical gearboxes is greater for high-torque application since the number of teeth or pole increases more quickly than the number of satellites. However, the permanent magnet costs slow down the development of magnetic gear industrial applications.

5 Conclusions

This article presents a comparison between magnetic gears with modulating ring and mechanical epicyclic gears. It illustrates a kinematic analogy between the two gears for different arrangements. On the other hand, this study shows that the load repartition evolution is fundamentally different since a tooth of a mechanical gear transmits the power intermittently while a magnet of a magnetic gear transmits the power continuously. Magnetic gears have a high potential for applications requiring high reliability and a high power and torque density such as offshore wind turbines.

References

1. Keller, J., Guo, Y., Sethuraman, L.: Gearbox reliability collaborative investigation of gearbox motion and high-speed-shaft loads. Technical report, TP-5000-65321. NREL (2016)
2. Teng, W., Ding, X., Zhang, X., Liu, Y., Ma, Z.: Multi-fault detection and failure analysis of wind turbine gearbox using complex wavelet transform. Renew. Energy **93**, 591–598 (2016)
3. Atallah, K., Howe, D.: A novel high-performance magnetic gear. IEEE Trans. Magn. **37**(4), 2844–2846 (2001)
4. Martin, T.B.: Magnetic transmission. Patent US3378710 (1968)
5. Gouda, E., Mezani, S., Baghli, L., Rezzoug, A.: Comparative study between mechanical and magnetic planetary gears. IEEE Trans. Magn. **47**(2), 439–450 (2011)
6. Matt, D., Jac, J., Ziegler, N.: Design of a mean power wind conversion chain with a magnetic speed multiplier. In: Advances in Wind Power, pp. 247–266 (2012). Chapter 10 of InTech book
7. Penzkofer, A., Atallah, K.: Magnetic gears for high torque applications. IEEE Trans. Magn. **50**(11), 1–4 (2014)
8. Coy, J.J., Townsend, D.P., Zaretsky, E.V.: Gearing (1985)
9. Mathis, R., Remond, Y.: Kinematic and dynamic simulation of epicyclic gear trains. Mech. Mach. Theory **44**(2), 412–424 (2009)
10. Desvaux, M., Traullé, B., Latimier, R.L.G., Sire, S., Multon, B., Ben Ahmed, H.: Computation time analysis of the magnetic gear analytical model. IEEE Trans. Magn. **53**(5), 1–10 (2017)

11. Yong, L.Y.L., Jingwei, X.J.X., Kerong, P.K.P., Yongping, L.Y.L.: Principle and simulation analysis of a novel structure magnetic gear. In: International Conference on Electric Machines and Systems, No. 1, pp. 3845–3849 (2008)
12. Li, Y., Xing, J.W., Lu, Y.P., Yin, Z.J.: Torque analysis of a novel non-contact permanent variable transmission. IEEE Trans. Magn. **47**(10), 4465–4468 (2011)
13. Bomela, W., Bird, J.Z., Acharya, V.M.: The performance of a transverse flux magnetic gear. IEEE Trans. Magn. **50**(1), 8–11 (2014)

Mechatronic Systems for Assistive Technology

Design Optimization of a Cable-Driven Parallel Robot in Upper Arm Training-Rehabilitation Processes

Eusebio Hernandez[1(✉)], S. Ivvan Valdez[2], Giuseppe Carbone[3], and Marco Ceccarelli[3]

[1] Secc. de Estudios de Posgrado e Investigacion, ESIME UP TICOMAN, IPN, Mexico City, Mexico
euhernandezm@ipn.mx

[2] Department of Computer Science, Center for Research in Mathematics, Mexico City, Mexico
ivvan@cimat.mx

[3] Laboratory of Robotics and Mechatronics, University of Cassino and Southern Lazio Meridionale, Cassino, Italy
{carbone,ceccarelli}@unicas.it

Abstract. This paper presents an optimized design of a cable driven parallel manipulator which is intended in rehabilitation or exercise of patients with shoulder problems like illness, traumatic events or for the elderly who need to exercise their limbs. Cable based parallel manipulators have characteristics that make them suitable for rehabilitation-exercise purposes like large workspace, re-configurable architecture, portability and low cost. From these purposes, upper-limb movements are analyzed and different prescribed workspaces are defined. After kinematic and wrench analysis, the Jacobian matrix of the cable driven manipulator is derived, which is used as a quantitative representation of dexterity along the workspace. An optimization model is presented to simultaneously fulfill the prescribed workspace and to improve dexterity by selecting proper length cables and other structural parameters. Numerical examples delineate effectiveness of an Estimation of Distribution Algorithm (EDA), where correlation among variables are inserted in the optimization process.

Keywords: Assistive robotics · Upper limb · Exercise and rehabilitation · Cable-based system · Optimized design

1 Introduction

Recently, the increasing need of limb rehabilitation therapies aims researches at the robotics area to propose robot aided strategies with the purpose of compensating the effects of permanent or temporal disabilities. In addition, limb exercising has attracted significant research interest due to its practical usefulness for sport training, to increase mobility of upper limb and for self rehabilitation purposes. Moreover, in order to assist disabled or elderly people, there

J.C.M. Carvalho et al. (eds.), *Multibody Mechatronic Systems*,
Mechanisms and Machine Science 54, DOI 10.1007/978-3-319-67567-1_39

are several patents which propose machines for limb exercising, or exoskeletons for human walking assistance or for rehabilitation purposes [1–3]. Some authors have also proposed the use of cable driven robots for limb exercising and physiotherapy applications. In fact, cable driven robots are a special class of parallel mechanisms, whose trusts consist of cables, [4]. This feature allows a significant reduction of inertia and a reduced risk in human robot interactions as well as reduced manufacturing costs, [4]. There are significant examples of cable driven robots for rehabilitation, for instance, NeReBot (NEuroREhabilitation robot), a three degrees of freedom (DOFs) cable driven parallel robot for post stroke upper-limb rehabilitation, [5,6]; CALOWI (Cassino Low-Cost Wire Driven), a four cable robot for limb exercising and rehabilitation, [7]; MACARM (Multi-Axis Cartesian-based Arm Rehabilitation Machine), an eight cable robot for upper limb rehabilitation, [8,9]. Besides a wide literature on the topic there are still several issues to be addressed. For example, the structural frame of a cable driven robot can be significantly larger than the usable workspace. Considering that users are often injured or disabled people, it is important that the size and shape of the structural frame facilitates the access to workspace area. Additionally, portability could allow the use of a robot in home environments with the purpose of increasing users motivation towards the training/rehabilitation process. For this purpose, this proposal addresses the optimum design of a cable driven robot proposed recently [10]. This solution is pretended to be portable while keeping a low-cost and user-friendly features. The objective of optimization process is the dimensional synthesis of the cable driven manipulator to fulfill a prescribed dexterous workspace. The rest of the paper is organized as follows: Sect. 2 analyses human shoulder joint motion for rehabilitation tasks, from these movements different kind of prescribed workspaces are defined. Section 3 introduces the cable driven parallel robot, kinematics and static analysis are described. Section 4 presents an optimization model of the cable driven parallel robot aiming at achieving the best dexterity. The optimization algorithm is formulated in Sect. 5, where correlation among variables are inserted in the optimization process in order to boost an Estimation of Distribution Algorithm. Numerical examples are presented in Sect. 6, and some remarking conclusions are summarized in Sect. 7.

2 Prescribed Workspace for Rehabilitation or Exercise Purposes

Upper-limb exercising consists in repetitive movements to activate limb muscles in various ways to keep them fit. Physical arm rehabilitation is the process of helping patients in regaining control over their limbs, there are a lot of people with shoulder problems like stroke, polio, arthritis and disaster recovery. In particular, upper-limbs rehabilitation after stroke consists mainly in physical repetitive exercises of the injured limb. Among the different robotic structures existing, the cable driven parallel robots have characteristics that make them suitable for rehabilitation purposes. The main advantage is they have a large workspace and

can be reconfigured by simply changing the attachment points or the actuators positions. These features allow the adaptation to different patients and different rehabilitation exercises. Another characteristic is their portability, they can be placed aside a wheelchair or a bed and easy to be stored after treatment. Furthermore, they are intrinsically safe for patients and therapists thanks to the use of cables instead of rigid links. Finally, the way in which the patient perceives the treatment is of great importance. Therefore, the use of cables increases the acceptability by the patient, who feels guided and not constrained by the machine, [11,12]. Movements of human upper-limb consists of several degrees of freedom, basically 3DOF just considering the shoulder joint, 2DOF in the elbow joint and 2DOF in the wrist joint. In particular, the shoulder joint has the following movements: vertical flexion-extension, Fig. 1(a), horizontal flexion-extension, Fig. 1(b), adduction-abduction, Fig. 1(c) and medial rotation. In Fig. 1(d), three prescribed workspaces derived from flexion-extension and adduction-abduction movements are defined.

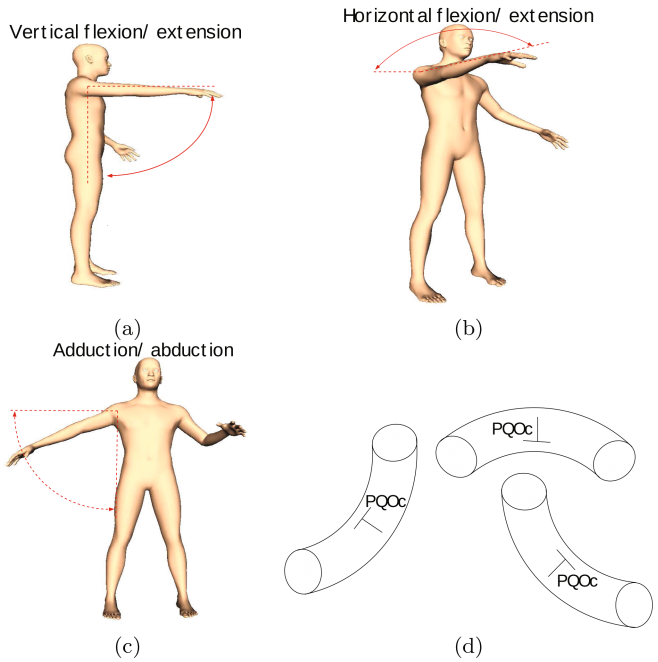

Fig. 1. Upper-limb rehabilitation movements: (a) Vertical flexion-extension, (b) Horizontal flexion-extension, (c) Adduction-abduction, (d) Defined workspaces from upper-limb rehabilitation movements.

3 The Cable-Driven Parallel Robot

Cable driven parallel robots have a particular configuration within the class of parallel manipulators, their trusts consist of cables whose lengths are adjustable trusts to control the end-effector's pose [11]. The position and orientation of the end-effector, determined by its degrees of freedom, is manipulated by actuating motors that extend or retract the cables. As it is pointed out in [11],the condition for a mobile platform with n DOFs in order to have a fully controlled motion is to have, at least $m = n + 1$ cables. This comes from, due to their nature, that cables require positive tension. They can only exert pulling action, being able to carry loads in tension but not in compression, therefore a redundant numbers of cables are required to avoid uncontrollable situations. In Fig. 2(a), the general structure of a cable driven parallel robot an its main components are presented. In Fig. 2(b) and (c) we can observe the kinematic schemes as referring to the planes $X-Y$, $X-Z$, respectively. The inverse kinematic problem (IKP) consists in finding the cable lengths as function of the end-effector degrees of freedom. As stated below, in both cases the length of each cable can be written in terms of difference of coordinates of its endpoints.

Kinematic Analysis. A kinematic model can be established for the cable driven parallel robot with the aim to express the position of the end-effector as function of the coordinates of the cable attachments to the mechanical structure and as function of the cable length. First, considering the flexion-extension movement, the kinematic scheme for cables C and D is shown in Fig. 2(b). Because of the symmetry of the structure and arm position it moves along a plane, so the IKP for this cables is simplified. The length of the cable, l_C, is defined by the points C and P, which represent the attachment points of the cable to the motor and to the upper face of the end-effector, respectively. Two reference frames have been considered: OXY is the fixed frame and GX_GY_G is the moving frame associated to the end-effector center of gravity. Parameter R indicates the distance from the center of gravity of the end-effector to the attachment point P, this is, half the height of the frame arms. θ represents the angular displacement of the arm axis and also the orientation of the moving reference frame with respect to the fixed one. It is intended one of the three DOFs to define the pose of the end-effector. The other two DOFs are related to the position of the frame arms in the plane, and could defined by the coordinates of the center of gravity or by the coordinates of point P. Finally, since the trajectory followed by point G is a circumference arc, it is interesting to write the equations in terms of the coordinates of its rotation center, O_C. Thus, the following equations can be written for the kinematics of cable C by referring to a planar motion of the end-effector within the plane shown in Fig. 2(b). Thus, the following equations can be written for the kinematics of the cable C by referring to a planar motion of the end-effector within the plane considered before.

$$l_C = ((X_{OC} - R\cos\theta + r\sin\theta - X_C)^2 + (Y_{OC} + R\sin\theta + r\cos\theta - Y_C)^2)^{\frac{1}{2}} \quad (1)$$

where X_i and Y_i are the X and Y Cartesian coordinates of the i-th point; r and R are geometrical sizes of the end-effector and θ is the angular displacement of

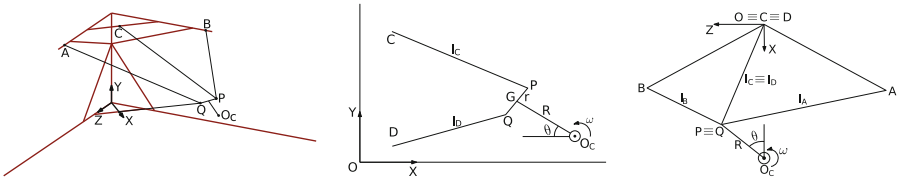

Fig. 2. Kinematic schemes of cable driven parallel robot: (a) General kinematic scheme, (a) X-Y plane (flexion-extension movements), (b) X-Z plane (adduction-abduction movements).

a limb in the X-Y plane, as shown in Figs. 2(b) and (c). Similar equations can be written for cable D. Cables A and B do not just move along the plane, but along the space in the three dimensions. However, the equations for their lengths l_A and l_B can be defined similarly to the ones of cables C and D, as difference of coordinates of their endpoints. Therefore, the equation for cable A can be written as

$$l_A = ((X_{OC} - R\cos\theta + r\sin\theta - X_A)^2 + (Y_{OC} - R\sin\theta + r\cos\theta - Y_A)^2 + (Z_P - Z_A)^2)^{\frac{1}{2}} \quad (2)$$

Wrench Analysis. A wrench analysis for cable driven parallel manipulators can be considered since all cables must remain in tension under any load. Considering this, the end-effector exerts force and moment on the external environment are transmitted by extending and retracting cables, and by ensuring the condition of pulling cables. For the condition of static equilibrium, the sum of external forces and torques exerted on the end-effector by the cables must equal the resultant external wrench that is exerted on the environment [4]. Since the cable driven manipulator is intended for rehabilitation purposes, the velocity of the system is very slow, therefore, a wrench analysis can be formulated based on a static model of forces.The static equilibrium of the cable driven parallel manipulator can be written as

$$\sum_{i=1}^{4} \mathbf{F}_i = \sum_{i=1}^{4} F_i \mathbf{l}_i = \mathbf{P} \quad (3)$$

$$\sum_{i=1}^{4} \mathbf{t}_i = \sum_{i=1}^{4} \mathbf{Qp} \times \mathbf{l}_i = \mathbf{M} \quad (4)$$

In Eqs. 3 and 4, $\mathbf{P}$ and $\mathbf{M}$ are the resultant force and torque, respectively, which considered together produce a wrench $\mathbf{W}$ in the form

$$\mathbf{J}^T\mathbf{F} = \mathbf{W} \quad (5)$$

in which vector $\mathbf{F} = [F_1 ... F_4]^T$ contains the values of the tensions of cables. $\mathbf{J}$ is the Jacobian matrix that can be expressed in the form

$$\mathbf{J} = \begin{bmatrix} \mathbf{l}_a & \mathbf{l}_b & \mathbf{l}_c & \mathbf{l}_d \\ \mathbf{Qa} \times \mathbf{l}_a & \mathbf{Qb} \times \mathbf{l}_b & \mathbf{Qc} \times \mathbf{l}_c & \mathbf{Qd} \times \mathbf{l}_d \end{bmatrix} \quad (6)$$

where **Q** is rotation matrix between fixed and moving frame, it can be expressed as

$$\mathbf{Q} = \begin{bmatrix} \cos\beta\cos\gamma & -\cos\beta\sin\gamma & \sin\beta \\ \sin\theta\sin\beta\cos\gamma + \cos\theta\sin\gamma & -\sin\theta\sin\beta\sin\gamma + \cos\theta\cos\gamma & -\sin\theta\cos\beta \\ -\cos\theta\sin\beta\cos\gamma + \sin\theta\sin\gamma & \cos\theta\sin\beta\sin\gamma + \sin\theta\cos\gamma & \cos\theta\cos\beta \end{bmatrix} \quad (7)$$

4 Optimization Model for the Cable Driven Robot

In Fig. 2(a) one can identify geometrical parameters of the cable driven parallel robot. As a first approach, in this work, an optimization model is intended for finding the position of the cables, in order to keep positive tension in cables for any point in the workspace. In particular, the selected optimization parameters for the optimization process are: $\alpha = [A, B, C, D]$. Notice how these parameters completely define the geometrical model of the manipulator, and they can be computed using three optimization parameters as it is shown in the next subsection.

Objective Function: Maximum Tension in Cables. A prescribed workspace W (as those in Fig. 1(d) derived from rehabilitation movements), possibly irregular, could be discretized by a set of points $\mathbf{X} \in \mathbf{R}^{d\times n}$. The general optimization problem is to find the positions of the manipulator for reaching all the points $\mathbf{X} \in W$ with a positive tension in cables. For this purpose, we propose a discretized workspace, defined according the following algorithm:

```
for r=1:2:5 do
    for v=(-1π/2):0.1:(1π/2) do
        for u=0:0.3:π do
            x = [x(50 + (R + r cos(u)) cos(v))];
            y = [y(50 + (R + r cos(u)) sin(v))];
            z = [z0];
        end
    end
end
```

Algorithm 1. Workspace discretization

For $R = 40$ and $r = 5$. Then, we compute the objective function in Eq. 8, according positions A, B, C, and D, where $A = [(199x_2 + 1)cos(45),\ l_{base},\ (199x_2 + 1)sin(45)]$, $B = [(199x_3 + 1)\ cos(45),\ l_{base}, -(199x_2 + 1)sin(45)]$, $C = [l_{base}/2, l_{base}, 0]$, $D = [l_{base}/2cos(45), 0, 0]$, and $l_{base} = 199x_1 + 1$. The optimization variables x_1, x_2, and x_3 are in the range [0,1]. Let us define $I(F(k) > 0.1)$, $I(F_k)$ for short, as an indicator function which equals 1 if all cable forces for the point k are greater than 0.01 N and 0 otherwise, and

$N_W(x) = \sum_{k=1}^{K} I(F_k)$ as the number of points which fullfil the requirement of positive tension in cables, in this last equation and in the following K is the total number of points in the workspace. Notice that $F(k)$ is the vector of forces in cables for the point k, $F_c(k)$ is an element of the vector associated with the c cable.

$$\max_{\cdot} \mathcal{F}(\mathbf{x}) = \begin{cases} N_W(x) & \text{if } N_W(x) < K, \\ K + N_W(x) \sum_{k=1}^{K} I(F_k) \sum_c F_c(k) & otherwise \end{cases} \tag{8}$$

The objective function returns the number of points in the workspace with positive tension in cables if not all of them have positive tension, and the sum of the forces in cables for all points in the workspace, plus the number of points, if the cables have positive tension for all points. Thus, if any point has less tension than the required the objective function value is less than K, otherwise it is greater than K. The external wrench (W) for computing cable tensions is always **gravity** with a 0 torque, it is to say -9.81 N in y direction, thus we solve the equation $F = (J^T)^{(-1)}W$, using a pseudoinverse $(J^T)^{(-1)}$. As it can be seen above the range for A, B, C, and D values is bounded between [1,200].

5 Optimization Algorithm

In the automated optimal synthesis of mechanisms, very often, the objective function is neither convex, nor it has continuous derivatives, and it has multiple local minima. In addition, very frequently, the most practical approach for solving the end-effector pose is by means of a numerical simulation rather than using a close explicit form. In this vein, evolutionary algorithms specially suited for dealing with non-convex, non-derivable problems in the context of the, so called, black-box optimization [13]. For this case study, we propose to use an Estimation of Distribution Algorithm [14], in order to take advantage of its particular way of working via the coding of correlations among variables. EDAs are a kind of evolutionary algorithms which replace the crossover and mutation operators by estimating and sampling from a probability distribution. The workflow of a standard EDA is shown in Algorithm 2, it works as follows, an initial population X^0 is sampled from a uniform probability distribution $U(x)$ inside the search limits x_{inf} and x_{sup}, then it is evaluated in the objective function f_{obj}. The generation or iteration counter is denoted as t. A selected set S^t of the best candidate solutions is chosen using a *selection method* and the objective function values, in this step we also select and store the best solution known x^t_{best}, often called as *the elite*, and its objective value f^t_{best}. Then, using the selected set the parameters ϕ^t are computed in order to define a new parametric probability distribution $Q(\phi^t, x)$, Q^t for short, which is biased to the best known solutions. Q^t is used for sampling new candidate solutions $\hat{X}^t$ which, in turn, together with the elite, integrate the new population X^{t+1}. The evaluation and selection steps are applied, and the loop is repeated until a stopping criterion is met. The most of the EDAs in continuous domains, use as *search distribution*, Q^t, the Gaussian

input : n= num. of variables, $[x_{inf}, x_{sup}]$= var. limits, f_{obj} =Objective function
1 $t = 0$; // Generation number
2 $\hat{X}^t$= Sample($U(x)$,x_{inf}, x_{sup});
3 F^0= Evaluate(f_{obj},X^0);
4 $[S^0, F_S^0, x_{best}^0, f_{best}^0]$= Selection($F^0$,$X^0$);
5 **while** *Stopping criteria is not met* **do**
6 $Q(\phi^t, x)$=EstimateParameters(S^t,F_S^t);
7 X^t= Sample($Q(\phi^t, x)$,x_{inf}, x_{sup});
8 X^{t+1}= Replace(x_{best}^t, $\hat{X}^t$);
9 t=t+1;
10 F^t= Evaluate(f_{obj},X^t);
11 $[S^t, F_S^t, x_{best}^t, f_{best}^t]$= Selection($F^t$,$X^t$);
12 **end**

Algorithm 2. Standard Estimation of Distribution Algorithm

distribution [15], in one of two fashions: univariate or multivariate models. Univariate models are simple and computationally inexpensive, while multivariate require larger computations as a payoff of integrating variable correlations in the search process. Using a search probability distribution provides of several benefits to the search process, for instance, in contrast with other evolutionary algorithms, EDAs learn or estimate the distribution parameters from the current population without needing user given parameters, such as crossover and mutation probabilities. In addition, EDAs, naturally, deal with variable correlations, most of the time, the correlations structure G_Q^t is learned from data (the selected set), and used by the probability distribution Q^t. Using G_Q^t not only could boost the performance of the algorithm, by detecting when two or more variable must be updated in a correlated (dependent) way, but also could provide of information about the physical phenomenon, by indicating these relations between physical variables. On the other hand, G_Q^t can be naturally induced in Q^t if an expert provides the information about physical correlation among optimization variables. In the context of automated synthesis of mechanisms, it is a reasonable hypothesis that the mechanical elements which are physically linked are correlated in the optimization process. In this article we propose to define the structure of the correlations among variables, and to use them in the optimization process assuming a normal search distribution, these correlations are inserted into the algorithm by means of the covariance matrix. In the subsection below we introduce in detail the algorithmic steps for the optimization process.

Introducing Physical Correlations into the Multivariate Normal EDA. A multivariate normal probability density is defined as follows:

$$q(z, \Sigma, \mu) = \frac{1}{\sqrt{(2\pi)^{n_{var}}|\Sigma|}} exp\left(-\frac{1}{2}(z-\mu)^T \Sigma^{-1}(z-\mu)\right), \tag{9}$$

where μ is the mean vector and Σ is the covariance matrix. The covariance matrix introduces physical correlations among variables. The selection step is carried out

in a similar fashion than in [16]. At the first generation the whole population is selected, and a threshold θ^t is initialized as the worst (maximum) value in the objective functions of the current population. At the second generation, the selected set are those values in the best half of the population that have an objective function value smaller or equal to θ^t, and θ^{t+1} is the maximum objective function value in the selected set.

Estimate Parameters Step. In this step we consider a variant of the empirical selection distribution of binary tournament [17]. The process is the following:

- Compute weights for each $i-th$ individual in the selected set, with size n_{sel}, using the following formulae:

$$p_i = \frac{\sum_j^{n_{sel}} I(f(z_i), f(z_j))}{\sum_i^{n_{sel}} \sum_j^{n_{sel}} I(f(z_i), f(z_j))}, \; I(a,b) = \begin{cases} 1 \; if \; a < b \\ 0 \; otherwise \end{cases} \tag{10}$$

- Compute the mean vector using the weights in Eq. (10)

$$\mu = \sum_i^{n_{sel}} p_i z_i \tag{11}$$

- Compute weights for the variance estimator.

$$\hat{p}_i = \frac{\sum_j^{n_{sel}} I(f(z_i), f(z_j))}{\sum_i^{n_{sel}} \sum_j^{n_{sel}} I(f(z_i), f(z_j))}, \; I(a,b) = \begin{cases} 1 \; if \; a > b \\ 0 \; otherwise \end{cases} \tag{12}$$

- Then, compute the covariance estimator for each position i, j in the covariance matrix. For each $i, j \in \pi_i$ for $i = 0, ..., 3$:

$$\sigma_{jk} = \sum_i^{n_{sel}} \hat{p}_i (z_{ij} - \mu_j)(z_{ik} - \mu_k) \tag{13}$$

After computing mean μ and covariance matrix Σ we can sample a new population using a multivariate normal distribution $N(\mu, \Sigma)$.

6 Results and Examples

The optimization problems are tackled using the algorithm presented in the section above. The best solution found is $x_1 = 0.10346, x_2 = 0.95762, x_3 = 0.93123$ which corresponds to $l_{base} = 21.589$ $A = [100.634, 21.589, 163.005]$, $B = [97.875, 21.589, -158.536]$, $C = [5.67047, 0.0, 0.0]$ and $D = [5.67047, 21.58854, 0.0]$ with an objective function of 3627.2. The found solution is plotted in Fig. 3.

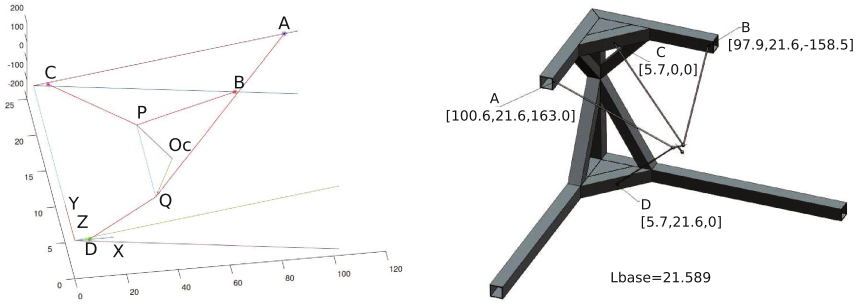

(a) (b)

Fig. 3. Optimized mechanical structure: (a) Kinematic configuration of the cable-driven structure, (b) A 3D model of the optimized mechanical structure.

7 Conclusions

This paper deals with the optimized design of a cable-driven parallel manipulator, which recently has been proposed as a device for rehabilitation and limb exercising. In particular, an optimization model is presented to simultaneously fulfill a rehabilitation-exercising task and to improve dexterity by selecting proper length cables and geometrical parameters. In this article, we proposed to *apriori* define the structure of the correlations among optimization variables, and to use them in the optimization process to boost an EDA. Numerical results show effectiveness of tested Estimation of Distribution Algorithm, where correlation among variables is inserted in the optimization process. Finally, the proposed methodology can be firstly used to optimize the cable-driven structure in terms of a more complete range for rehabilitation movements, and secondly used for other cable-driven manipulators.

Acknowledgements. First and second authors are grateful to CONACYT and SIP-IPN, for grants AEM-Conacyt 262887 and SIP20162113, and for supporting a research stay at the Laboratory of Robotics and Mechatronics, University of Cassino, Italy.

References

1. Kollet, K.W., Potash, R.L., Potash, R.J.: Exercise system for physical rehabilitation and fitness. US PATENT 20140135174A1 (2014)
2. Bhugra, K., Smith, J.: Exoskeleton for gait assistance and rehabilitation. US PATENT WO 2013019749 A (2012)
3. Scholz, J., Agrawal, S., Mao, Y.: Wearable cable-driven exoskeleton for functional arm training. US PATENT 9144528 B2 (2015)
4. Ceccarelli, M.: Fundamentals of Mechanics of Robotic Manipulation. Springer, Netherlands (2004)
5. Rosati, G., Gallina, P., Masiero, S., Rossi, A.: Design of a new 5 d.o.f. wire-based robot for rehabilitation. In: Proceedings of the 2005 IEEE 9th International Conference on Rehabilitation Robotics, Chicago, pp. 430–433 (2005)

6. Pei, Y., Kim, Y., Member, S., Obinata, G., Member, S., Hase, K., Stefanov, D., Member, S.: Trajectory planning of a robot for lower limb rehabilitation. In: 33rd Annual International Conference of the IEEE EMBS, Boston, pp. 1259–1263 (2011)
7. Ceccarelli, M.: Problems and experiences on cable-based service robots for physiother- apy applications. New Trends Med. Serv. Robots **16**(4), 27–42 (2013)
8. Mayhew, D., Bachrach, B., Rymer, W.Z., Beer, R.F.: Development of the MACARM a novel cable robot for upper limb neurorehabilitation. In: Proceedings of the 2005 IEEE 9th International Conference on Rehabilitation Robotics, Chicago, pp. 299–302 (2005)
9. John, M.R.S., Thomas, N., Sivakumar, V.P.R.: Design and development of cable driven upper limb exoskeleton for arm rehabilitation. Int. J. Sci. Eng. Res. **7**(3), 1432–1440 (2016)
10. Carbone, G., Cavero, C.A., Ceccarelli, M., Altuzarra, O.: A Study of Feasibility for a Limb Exercising Device, pp. 11–21. Springer, Cham (2017)
11. Ceccarelli, M., Romdhane, L.: Design issues for human-machine platform interface in cable-based parallel manipulators for physiotherapy applications. J. Zhejiang Univ. Sci. A **11**(4), 231–239 (2010)
12. Loureiro, R.C.V., Collin, C.F., Harwin, W.S.: Robot aided therapy: challenges ahead for upper limb stroke rehabilitation. In: Proceedings of the 5th International Conference on Disability, Virtual Reality and Associated technology, no. 1999, pp. 33–39 (2004)
13. Hernandez, E.E., Valdez, S.-I., Ceccarelli, M., Hernandez, A., Botello, S.: Design optimization of a cable-based parallel tracking system by using evolutionary algorithms. Robotica **33**(3), 599–610 (2015)
14. Zhang, Q., Mühlenbein, H.: On the convergence of a class of estimation of distribution algorithms. IEEE Trans. Evol. Comput. **8**(2), 127–136 (2004)
15. Larrañaga, P., Lozano, J.A.: Estimation of Distribution Algorithms: A New Tool for Evolutionary Computation. Kluwer Academic Publishers, Norwell (2001)
16. Valdez, S.I., Hernández, A., Botello, S.: A Boltzmann based estimation of distribution algorithm. Inf. Sci. **236**, 126–137 (2013)
17. Valdez-Peña, S.I., Hernández-Aguirre, A., Botello-Rionda, S.: Approximating the search distribution to the selection distribution in EDAs. In: Proceedings of the 11th Annual conference on Genetic and evolutionary computation, pp. 461–468. ACM (2009)

Kinematic Analysis of an Exoskeleton-Based Robot for Elbow and Wrist Rehabilitation

N. Plitea[1], B. Gherman[1(✉)], G. Carbone[2], M. Ceccarelli[2], C. Vaida[1], A. Banica[1], D. Pisla[1], and A. Pisla[1]

[1] CESTER, Technical University of Cluj-Napoca, Cluj-Napoca, Romania
{nicolae.plitea, bogdan.gherman, calin.vaida, alexandru.banica, doina.pisla}@mep.utcluj.ro
[2] LARM, University of Cassino and South Latium, Cassino, Italy
{carbone, ceccarelli}@unicas.it

Abstract. The paper presents the kinematics of an exoskeleton-based robotic system for upper limb rehabilitation of post-stroke patients. The targeted arm areas are the elbow and the wrist, while the targeted motions are flexion/extension, pronation/supination and adduction/abduction. The paper presents the (direct and inverse) kinematic analysis of the proposed solution, the generated workspace of the robot and simulations for a proposed exercise for post-stroke upper limb rehabilitation.

Keywords: Upper limb rehabilitation · Exoskeleton's kinematics · Workspace · Simulation

1 Introduction

Stroke is a leading cause of disability in the western society [20]. The European Registers of Stroke study (EROS) reveal that 40% of patients with first-ever strokes had a poor outcome in terms of the Barthel Index (which measures the extent to which somebody can function independently and has mobility in their activities of daily living (ADL) i.e. feeding, bathing, grooming, dressing, etc.) [6]. Because the results of physical therapy for restoring the activities of daily living vary greatly [11], robotic therapy research has shifted towards robotic systems that can be designed for rehabilitation especially in the form of exoskeleton-based robots. Because designing the kinematics of an exoskeleton relies on the replication of the human limb kinematics, certain advantages are observed, such as similarity of the workspaces, singularity avoidance, as described in [14] or one to-one mapping of joint force capabilities over the workspace. However, a major drawback to this paradigm is that human kinematics is impossible to be precisely replicated with a robot, because morphology drastically varies among subjects and joint kinematics is very hard to be reproduced by conventional robot joints [19]. Finding any consensual model of the human kinematics in the biomechanics literature is almost impossible, due to complex geometry of bones interacting surfaces related to human arm anatomy. In [17] an explicit model to predict and interpret constraint force creation has been developed, taking into consideration that deformation at the interface between two kinematic chains is caused by low

J.C.M. Carvalho et al. (eds.), *Multibody Mechatronic Systems*,
Mechanisms and Machine Science 54, DOI 10.1007/978-3-319-67567-1_40

stiffness of human skin and tissues surrounding the bones. Solutions to cope with this problem can be of two kinds. The first one, as described in [18], consists of making the exoskeleton highly adjustable by creating robotic segments with adjustable length and by adding pneumatic components to introduce elasticity in the robot fixations. The second approach consists of adding passive degrees of freedom to connect the 2 kinematic chains. This was proposed in [10, 13] or [3] among others. There are several commercially available rehabilitation devices for upper limbs, such as the exoskeletons: the Armeopower, the ArmeoSpring and the ArmeoBoom sling suspension system designed by Armeo (Hocoma AG, Switzerland). Other commercial devices are the mPower arm brace (Myomo Inc., Cambridge, MA), a 1 DOF portable arm brace which uses electromyogram (EMG) signals measured from the bicep and triceps muscles to generate assistive torques for elbow flexion/extension, albeit features the disadvantage of flexibility, having just 1 degree of freedom. Other exoskeleton designs having 7 DOF's are the CADEN-7 and the PERCRO arm [5], that utilize two nonanthropomorphic joints to represent motion of the wrist and fingertips, which greatly improves the replication of human kinematics and movement, but are rather complicated. Other state-of-the-art arms lack one or more of the following aspects: low-backlash gearing [7], back drivable transmissions [8], low-inertia links [1], high stiffness transmissions [2], open mHMIs or physiological ROMs.

Regarding the human rehabilitation of upper limbs, in this paper the authors have proposed a conceptual solution for a medical rehabilitation robotic system that is based on exoskeleton architecture (ReExRob). The ReExRob intends to rehabilitate the upper limb, aiming especially at the achievement of the following motions: the flexion/extension of the elbow, the supination/pronation of the forearm and the extension/flexion and adduction/abduction of the wrist.

2 Kinematic Modelling of a New Robotic Structure

The motion study is extremely important in designing a robotic system for rehabilitation due to the efficiency and safety that such a system targets. The ReExRob [15] conceptual solution is based on an exoskeleton architecture, that is designed for the rehabilitation of the upper limb, especially the mobilization of the elbow and the wrist (the forearm). The targeted motions by the ReExRob are presented in Fig. 1 and they refer to flexion/extension of the elbow, the pronation/supination and adduction/abduction and flexion/extension of the wrist. Figure 1 presents the motions amplitude, indicating the maximum mean ranges for each targeted motion of the upper limb (the patients group age has not been considered), [12]. Regarding the mobilization of the limbs, a series of anchor points have been defined. Figure 2 presents the major anchor points for each motion, where the dotted line represents the active anchor area (which performs the motion) and the continuous line represents the passive anchor area (which remains fixed). It is to note that the active anchor area for the flexion/extension of the elbow becomes the passive anchor area for the wrist motions (flexion/extension and adduction/abduction).

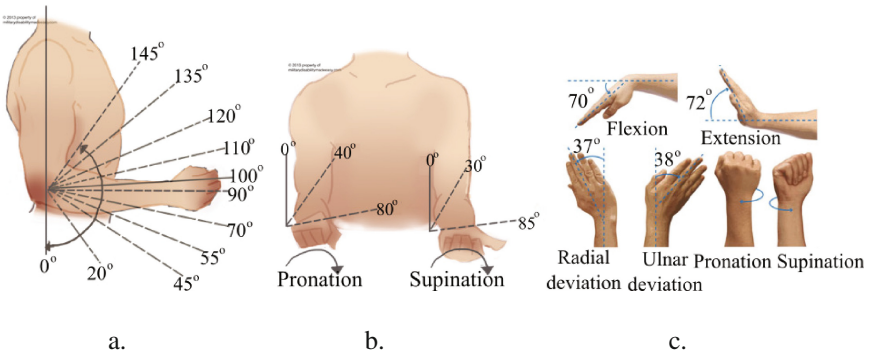

Fig. 1. Motion intervals of the shoulder during flexion/extension (a), pronation/supination (b) and wrist motions (c) [16]

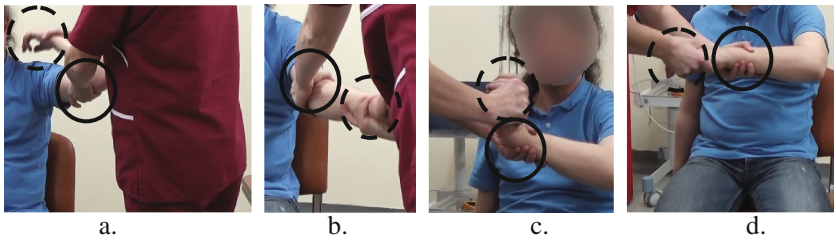

Fig. 2. Motion anchor points for elbow and wrist mobilization: (a) flexion/extension; (b) pronation/supination; (c) wrist flexion/extension; (d) adduction/abduction.

Considering the above aspects, the authors propose the ReExRob robotic system, whose kinematic design is presented in Fig. 3. The 4R robot is built as based on an anthropomorphic structure, having only active rotation joints, each one performing a certain rehabilitation motion (i.e. q_1 performs elbow flexion/extension, q_2 pronation/supination, q_3 the wrist flexion/extension and q_4 the wrist adduction/abduction). To simplify the mathematical model, at this stage, the fixed coordinate system *OXYZ* has been placed in the middle of the R_1 joint. The size parameters of the robot are: l_1, l_2, l_3, l_4, l_5. Figure 4 presents the ReExRob 3D model design. Its key features include: the fixing elements, the three anchors: the passive one and the active anchors (2 – for supination/pronation and 3 for the wrist motions). The pronation/supination motion is designed using a spur gear mechanism actuated by Motor 2.

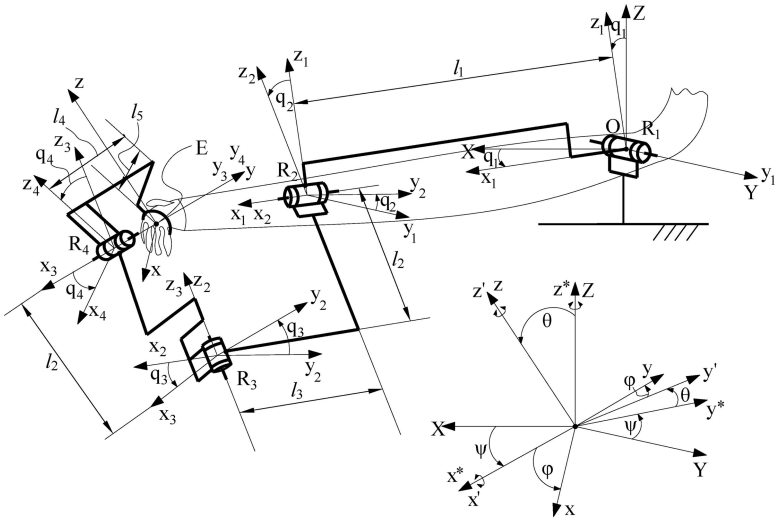

Fig. 3. A kinematic design of the ReExRob robotic system for elbow and wrist mobilization

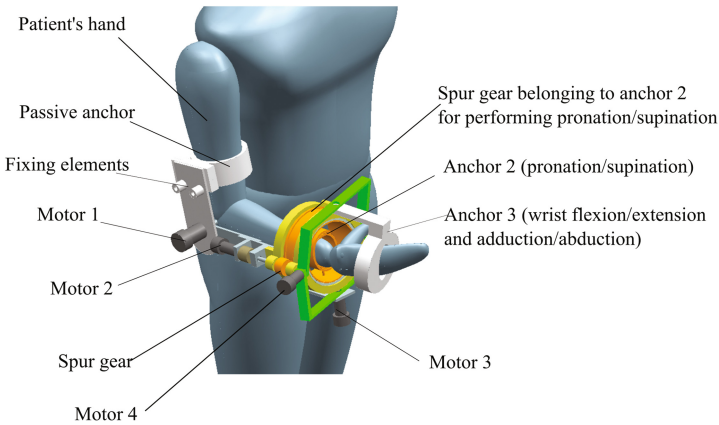

Fig. 4. ReExRob robotic system kinematic scheme for elbow and wrist mobilization

2.1 Direct Kinematics

The direct kinematics of the ReExRob takes as input data the values of the active joints q_1, q_2, q_3, q_4 when l_1, l_2, l_3, l_4, l_5 are given and the target is to determine the end-effector coordinates (X_E, Y_E, Z_E) and the Euler angles ψ, θ and ϕ, Fig. 1. Kinematic model is summarized in Table 1 to give the expressions from manipulator analysis [4]. Matrix transformations in (1) are used for kinematics analysis.

$$[\,X_E \quad Y_E \quad Z_E \quad 1\,]^T = [T]_0^1 \cdot [T]_1^2 \cdot [T]_2^3 \cdot [T]_3^4 \cdot [T]_4^5; \tag{1}$$

to

$$\begin{cases} X_E = (l_1 + l_3)\cos(q_1) + l_5\cos(q_4)\cos(q_1)\cos(q_3) \\ \quad + l_5 \cdot (\sin(q_1)\sin(q_2)\sin(q_3) - \cos(q_2)\sin(q_1)\sin(q_4)); \\ Y_E = l_5(\sin(q_2)\sin(q_4) + \cos(q_2)\cos(q_4)\sin(q_3)); \\ Z_E = (l_1 + l_3)\sin(q_1) - l_5\cos(q_4)(\sin(q_1)\cos(q_3) - \cos(q_1)\sin(q_2)\sin(q_3)) \\ \quad + l_5\cos(q_2)\cos(q_1)\sin(q_4); \end{cases} \tag{2}$$

with

$$\cos(\theta) = \cos(q_4)\cos(q_1)\cos(q_2) - \sin(q_4)(\sin(q_1)\cos(q_3) - \cos(q_1)\sin(q_2)\sin(q_3)) \tag{3}$$

$$\cos(\psi) = -(\sin(q_4)\cos(q_2)\sin(q_3) - \cos(q_4)\sin(q_2))/\sin(\theta) \tag{4}$$

$$\cos(\phi) = -(\sin(q_1)\sin(q_3) + \cos(q_1)\cos(q_3)\sin(q_2))/\sin(\theta) \tag{5}$$

Table 1. The transformation matrices of ReExRob

Rotation matrix	Actuation
$[T]_0^1 = \begin{bmatrix} \cos(q_1) & 0 & \sin(q_1) & 0 \\ 0 & 1 & 0 & 0 \\ -\sin(q_1) & 0 & \cos(q_1) & 0 \\ 0 & 0 & 0 & 1 \end{bmatrix}$	Rotation around OY axis with q_1
$[T]_1^2 = \begin{bmatrix} 1 & 0 & 0 & l_1 \\ 0 & \cos(q_2) & -\sin(q_2) & 0 \\ 0 & \sin(q_2) & \cos(q_2) & 0 \\ 0 & 0 & 0 & 1 \end{bmatrix}$	Translation along O_1x_1 with l_1 followed by a rotation around Ox_2 axis with q_2
$[T]_2^3 = \begin{bmatrix} \cos(q_3) & -\sin(q_3) & 0 & l_3 \\ \sin(q_3) & \cos(q_3) & 0 & 0 \\ 0 & 0 & 1 & -l_2 \\ 0 & 0 & 0 & 1 \end{bmatrix}$	Translations along O_2x_2 with l_3 and along O_2z_2 with $-l_2$ followed by a rotation around Oz_3 axis with q_3
$[T]_3^4 = \begin{bmatrix} \cos(q_4) & 0 & \sin(q_4) & 0 \\ 0 & 1 & 0 & -l_4 \\ -\sin(q_4) & 0 & \cos(q_4) & l_2 \\ 0 & 0 & 0 & 1 \end{bmatrix}$	Translations along O_3x_3 with $-l_4$ and along O_3z_3 with l_2 followed by a rotation around Oy_4 axis with q_4
$[T]_4^5 = \begin{bmatrix} l_5 \\ l_4 \\ 0 \\ 1 \end{bmatrix}$	Geometric parametric translations along O_4x_4 with l_5 and along O_4y_4 with l_4

The coordinates of E, are obtained using (1) and the closed form of these coordinates are shown in (2). The Euler angles ψ, θ and ϕ can be computed using (3)–(5), after applying atan2.

2.2 Inverse Kinematics

The inverse kinematics consists in determining the joint variables q_1, q_2, q_3, q_4, when the coordinates X_E, Y_E, Z_E and orientation of the end-effector are given. Usually, for serial robots, this could lead to multiple solutions. Several methods have been used to solve the inverse kinematics of serial robots, like Jacobian pseudoinverse, Jacobian transpose, Jacobian damping and filtering, damped least-squares, gradient projection, task priority, each one with their advantages and disadvantages [9]. For ReExRob, the Jacobian pseudoinverse algorithm has been used and implemented in a numerical procedure to find a solution for the inverse kinematics. In pseudo-code, the algorithm can be described by the expressions:

$$\begin{aligned} dXe &= \mathrm{X_E}(q_{1\_start}, q_{2\_start}, q_{3\_start}, q_{4\_start}) \\ dYe &= \mathrm{Y_E}(q_{2\_start}, q_{3\_start}, q_{4\_start}) \\ dZe &= \mathrm{Z_E}(q_{1\_start}, q_{2\_start}, q_{3\_start}, q_{4\_start}) \end{aligned}$$

with the following steps:

$$\begin{aligned} &\text{while } \sqrt{(dXe - X_{e\_in})^2 + (dYe - Y_{e\_in})^2 + (dZe - Z_{e\_in})^2} < c \\ &\quad \{\bullet \text{ compute Jacobian J} \\ &\quad \bullet \text{ compute the Jacobian pseudoinverse } \mathrm{J}^+ \\ &\quad \bullet \text{ compute active joint values } \mathrm{dQ} = \mathrm{J}^+ \cdot [\, dXe \quad dYe \quad dZe \,]^T \\ &\quad \bullet Q = Q + \alpha \cdot dQ \text{ (yielding } \mathrm{q_1, q_2, q_3, q_4}) \\ &\quad \bullet dXe = X_E(q_1, q_2, q_3, q_4);\ dYe = Y_E(q_2, q_3, q_4);\ dZe = Z_E(q_1, q_2, q_3, q_4)\} \end{aligned}$$

where $q_{i\_start} = 0, i = \overline{1,4}$, dXe, dYe, dZe represents the end-effector current position, α is a small increment (in this case $\alpha = 1°$), c is an satisfactory chosen error (whose size is related to human arm precision, as for example arm tremor) and $dX_{e\_in}, dY_{e\_in}, dZ_{e\_in}$ is the desired end-effector position. The goal is to determine a convergence to a feasible solution.

3 ReExRob Workspace Analysis

One of the main requirements for ReExRob is to provide a suitable workspace for the elbow and wrist rehabilitation. Figure 5a shows the maximum workspace of the robot in the XZ plane, corresponding to the extension/flexion motion of the elbow. The plot represents the area that can be covered by the patient's hand during exercising this kind of motion. In a similar way, the workspace that can be provided for the wrist motions is determined and plotted in Figs. 5b and 6a. Figure 5b presents the robot workspace as

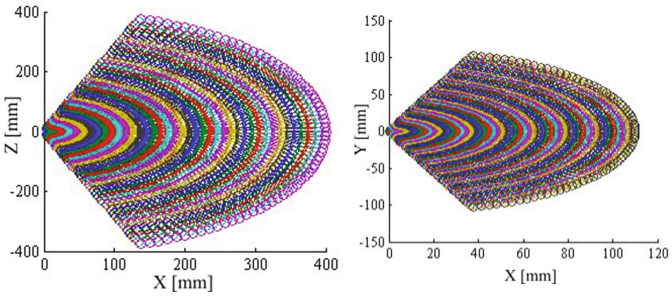

Fig. 5. ReExRob workspace for the flexion/extension of the elbow (a) and wrist (b)

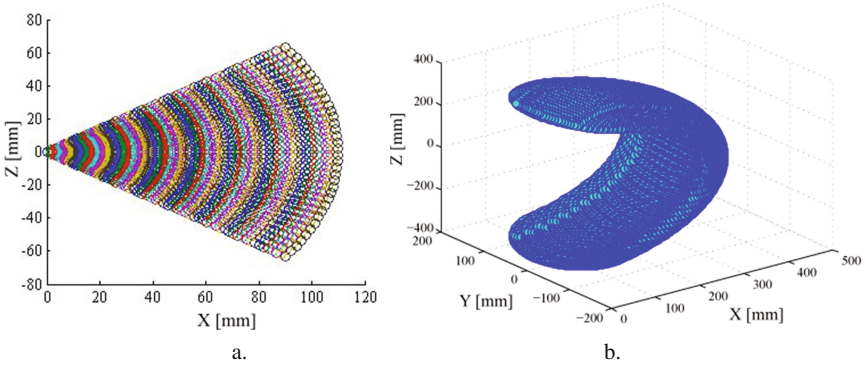

Fig. 6. ReExRob workspace for the adduction/abduction motion (a) and the total workspace (b)

generated by a motion due to the q_3 active joint when the q_2 active joint, remains fixed, the wrist motion being in the XY plane (the flexion/extension of the wrist).

Figure 6a shows the amplitude motion for the adduction/abduction motions of the wrist, as obtained for a motion of the q_4 active joint, when q_3 is kept fixed. Figure 6b shows the isometric view of the whole workspace of the robot, for the full amplitude of each type of motion. The presented workspaces have been generated using the following values for the size parameters: $l_1 = 258.3\,\text{mm}, l_2 = 83\,\text{mm}, l_3 = 35.36\,\text{mm}, l_4 = 104.72\,\text{mm}, l_5 = 110\,\text{mm}$, for an average-size human arm [12].

4 Motion Simulations

In the first phase (or the acute phase) of a post-stroke survivor, rehabilitation is achieved by mobilizing the affected limb, to avoid muscles atrophiation with time and the mobility loss of the joints. ReExRob system has been designed to be used from the very beginning as a rehabilitation tool immediately after stroke. As already mentioned, ReExRob system addresses four types of motions (elbow flexion/extension, pronation/

supination, wrist flexion/extensions and adduction/abduction), but some of these motions can be grouped together to increase the efficiency, in a combination of joint motions like: $q_1 + q_2$, $q_1 + q_3$, $q_2 + q_3$, $q_1 + q_4$, usually without any risk for the patient, if the workspace limits are acknowledged. Based on a study in [12], the maximum values for motion parameters can be assumed as $v_{max} = 6.5°/s$ and $\varepsilon_{max} = 6°/s^2$. The proposed formulation of kinematic analysis can be used in optimal design procedures and operation simulation to characterize the feasibility of the proposed exoskeleton design. Thus Fig. 6 shows a simulation for the coupled motion of the joints q_1 and q_2: the patient's motion starts from the 0 position (for all joints, when the elbow is in the horizontal plane); the patient's elbow starts a flexion motion upwards (q_1 has negative values), up to -45^o and simultaneously a supination motion (using q_2, which has positive values, up to 81^o) is achieved (see the time history diagrams for q_1 and q_2, while $q_3 = q_4 = 0$); after reaching the imposed position, the elbow starts an extension motion up to $+83^o$ (yielding a total angle of 128^o for q_1), while simultaneously executing a pronation motion using q_2. The two generated motions using q_1 and q_2 have been correlated, so that when q_1 reaches to -45^o, q_2 completely performs the supination motion and when q_1 reaches $+83^o$, q_2 completely performs the pronation motion. Figure 8 presents the time history diagrams of the end-effector coordinates, based on the imposed motion, including velocities and accelerations. As it is a planar motion, the Y_E coordinate is constant (zero) (Fig. 7).

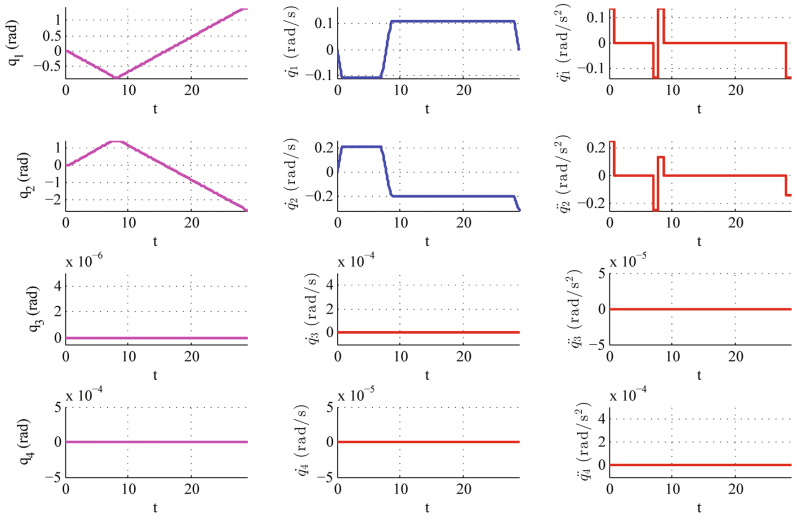

Fig. 7. Computed joint motions of ReExRob for elbow flexion/extension and pronation/supination motion: positions, velocities and accelerations of the active joints

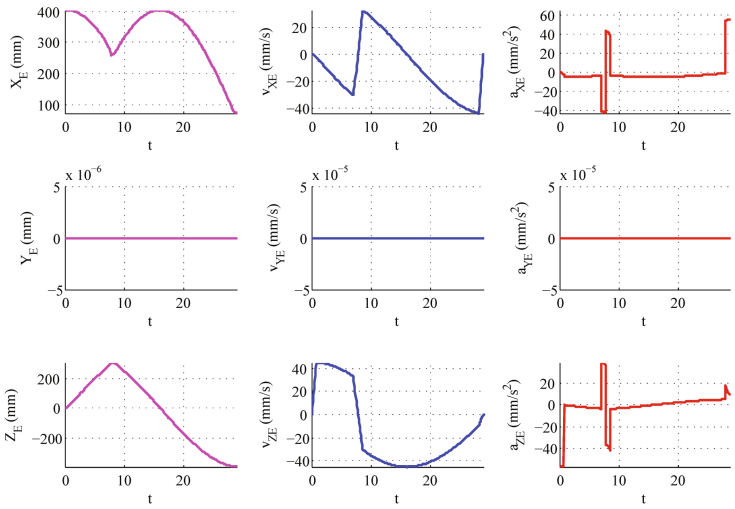

Fig. 8. The time history diagrams of the end-effector (coordinates X_E, Y_E, Z_E), velocities and accelerations for a simulated rehabilitation exercise

5 Conclusions

The paper presents the design and kinematics of an exoskeleton-based robotic structure. The presented kinematics is useful for operation purposes in rehabilitation motions of post-stroke human arms. The inverse kinematics provides a solution for the joint variables, but since the final configuration is unknown, it will not be used in the robot control. The computed workspace, fulfills the needed range of motion to perform the upper limb rehabilitation. The presented motion simulations have been developed as an example of rehabilitation exercises. As future work, the authors plan to build a prototype for testing and practical implementation.

Acknowledgments. The paper presents results from the research activities of the project ID 37_215, MySMIS code 103415 "Innovative approaches regarding the rehabilitation and assistive robotics for healthy ageing" co-financed by the European Regional Development Fund through the Competitiveness Operational Programme 2014-2020, Priority Axis 1, Action 1.1.4, through the financing contract 20/01.09.2016, between the Technical University of Cluj-Napoca and ANCSI as Intermediary Organism in the name and for the Ministry of European Funds.

References

1. Bergamasco, M., Allotta, B., Bosio, L., Ferretti, L., Parrini, G., Prisco, G.M., Salsedo, F., Sartini, G.: An arm exoskeleton system for teleoperation and virtual environments applications. In: Proceedings of the IEEE International Conference on Robotics Automation, vol. 2, pp. 1449–1454 (1994)

2. Caldwell, D.G., Kocak, O., Andersen, U.: Multi-armed dexterous manipulator operation using glove/exoskeleton control and sensory feedback. In: Proceedings of the IEEE/RSJ International Conference on Intelligent Robots and Systems 1995. Human Robot Interaction Cooperative Robots, vol. 2, pp. 567–572 (1995)
3. Carbone, G., Aróstegui, C., Ceccarelli, M., Altuzarra, O.: A study of feasibility for a limb exercising device. In: Advances in Italian Mechanism Science, pp. 11–21 (2016)
4. Ceccarelli, M.: Fundamentals of Mechanics of Robotic Manipulation. Springer, New York (2004)
5. Frisoli, A., Rocchi, F., Marcheschi, S., Dettori, A., Salsedo, F., Bergamasco, M.: A new force-feedback arm exoskeleton for haptic interaction in virtual environments. In: Proceedings of the 1st Joint Eurohaptics Conference and Symposium on Haptic Interfaces for Virtual Environment and Teleoperator Systems, pp. 195–201 (2005)
6. Heuschmann, P.U., Wiedmann, S., Wellwood, I., Rudd, A., Di, C.A., Bejot, Y., et al.: Three-month stroke outcome: the European Registers of Stroke (EROS) investigators. Neurology **76**, 159–165 (2011)
7. Jau, B.M.: Anthropomorphic exoskeleton dual arm/hand telerobot controller. In: Proceedings of the IEEE International Workshop on Intelligent Robots, pp. 715–718 (1988)
8. Kazerooni, H.: The human amplifier technology at the University of California, Berkeley. Robot. Auton. Syst. **19**, 179–187 (1996)
9. Kumar, S., Sukavanam, N., Balasubramanian, R.: An optimization approach to solve the inverse kinematics of redundant manipulator. Int. J. Inf. Syst. Sci. **7**(2–3), 204–213 (2011)
10. Lamoreux, L.W.: Kinematic measurements in the study of human walking. Bull. Prosthet Res. **10**(15), 3–84 (1971). PMID: 5131748
11. Langhorne, P., Bernhardt, J., Kwakkel, G.: Stroke rehabilitation. Lancet **377**, 1693–1702 (2011)
12. Major, K.A., Major, Z.Z., Carbone, G., Pîslă, A., Vaida, C., Gherman, B., Pîslă, D.: Ranges of motion as basis for robot-assisted post-stroke rehabilitation. Int. J. Bioflux Soc. Hum. Vet. Med. **8**(4), 192–196 (2016)
13. Markolf, K.L., Mensch, J.S., Amstutz, H.C.: Stiffness and laxity of the knee–the contributions of the supporting structures. A quantitative in vitro study. J. Bone Jt. Surg. Am. **58**(5), 583–594 (1976)
14. Mihelj, M., Nef, T., Riener, R.: Armin ii - 7 DoF rehabilitation robot: mechanics and kinematics. In: 2007 IEEE International Conference on Robotics and Automation, pp. 4120–4125, 10–14 April 2007
15. Gherman, B., Pisla, D., Plitea, N., Vaida, C., Carbone, G., Pisla, A., Banica. A.: Family of robots for upper limb rehabilitation, Patent pending no. A00375/14.06.2017
16. Report on upper limb disability. http://www.militarydisabilitymadeeasy.com/elbowandforearm.html. Accessed Mar 2017
17. Schiele, A.: An explicit model to predict and interpret constraint force creation in pHRI with exoskeletons. In: 2008 IEEE International Conference on Robotics and Automation, ICRA 2008, pp. 1324–1330, 19–23 May 2008
18. Schiele, A., Van der Helm, F.C.T.: Kinematic design to improve ergonomics in human machine interaction. Neural Syst. Rehabil. Eng. **14**(4), 456–469 (2006)
19. Scott, S.H., Winter, D.A.: Biomechanical model of the human foot: kinematics and kinetics during the stance phase of walking. J. Biomech. **26**(9), 1091–1104 (1993)
20. Wardlaw, J.M., Sandercock, P.A., Murray, V.: Should more patients with acute ischaemic stroke receive thrombolytic treatment? (2009). doi:10.1136/bmj.b4584

Experimental Evaluation of Artificial Human Ribs

L.A. Aguilar[1,2(✉)], M. Ceccarelli[1], Ch.R. Torres-San-Miguel[2], G. Urriolagoitia-Sosa[2], and G. Urriolagoitia-Calderón[2]

[1] Laboratory of Robotics and Mechatronic, Department of Civil Engineering and Mechanics, University of Cassino and South Latium, Via Di Biasio 43, 03043 Cassino, Frosinone, Italy
laguilarp0600@egresado.ipn.mx, ceccarelli@unicas.it

[2] Instituto Politécnico Nacional, Escuela Superior de Ingeniería Mecánica y Eléctrica Sección de Estudios de Posgrado e Investigación, Unidad Profesional "Adolfo López Mateos" Zacatenco, Col. Lindavista, 07738 México D.F., Mexico
laguilarpe@gmail.com, ctorress@ipn.mx

Abstract. The paper presents a testing machine and its operation for evaluating key features of artificial ribs on an anteroposterior biological compression. A model of artificial ribs is elaborated out to build a testing sample. Design for a new machine is developed for an experimental layout in laboratory testing. The results of experimental tests show the efficiency of the designed testing machine and a characterization of artificial ribs with human-like behavior.

Keywords: Biomechanics · Thorax · Experimental test · Cam

1 Introduction

The biomechanical response of an impact event on human thorax is characterized by the risk of the damage caused in the biological tissues. One way to express the probability of causing the death is by using injuries criterion [5]. An injury criterion represents a combination of statistical data that relates the likelihood of injury the body due to the action of physical variables like accelerations, compressions or even loads applied on certain areas. In order to formulate an injury criterion, physical variables must be measured under the close real impact conditions. The closest way to reconstruct a real impact event can be planned by using Live Humans Subjects (LHS). During the tests, the effects on the body must be analyzed to guarantee that the people will not be harmed lethally. The Declaration of Helsinki by the World Medical Association has established ethical principles on researches using this kind of test subjects.

On the other side, anthropomorphic test devices (ATD) have the capability of reproducing the human-like biomechanical response with accurate values [2]. Thus, the stiffness of a ribcage modifies the properties of the rib bone. On this way, it has less resistance in elements working on tension than those working on compression. For this reason, the fracture starts on the side working in tension and going to the surface in compression. Based on these considerations, commonly is determined the mechanical

J.C.M. Carvalho et al. (eds.), *Multibody Mechatronic Systems*,
Mechanisms and Machine Science 54, DOI 10.1007/978-3-319-67567-1_41

properties of the bone by using uniaxial tests. Equally, important tests for bone by using flexion in 3 or 4 points. Kemper et al. [7] have proposed a specific procedure to analyze rib bone under dynamics loads. In his work describes how to reproduce a compression in the rib similar to the produced by the 35-mph automotive crash. Analogous to that procedure, Charpail et al. [8] characterized the behavior of a rib under dynamical conditions. They define an experiment where the rib is hit by a pendulum of controlled mass. They draw our attention to the importance of the curvature of an edge in the rib and their influence on the load distribution. Thus, the open problem is correlated to the reproduction of the dynamic behavior of the ribs by artificial elements.

The purpose to study the dynamic behavior of an artificial is to present the design and test considerations of a dynamic test machine for artificial ribs. The design of the proposed artificial ribs used in the testing was developed in [1]. The anteroposterior compression proposed was numerically studied in this work. Exploiting this condition, the standard of cardiopulmonary resuscitation procedure (CPR) establishes similar compression load applied over the thorax. On this way is proposed the design of a machine that reproduces those similar conditions. The proposed machine uses a cam-follower mechanism to simulate that dynamic input as a frontal impact. The obtained results are presented in three plots. The objective of the first plot is to show the load reaction against the velocity of impact. The aim of the second plot is to show the displacement against the velocity of impact. A third plot is obtained by comparing the load reaction against a displacement. The third graphic allows to observe the complete duty cycle of load and unload of the rib. A duty cycle is defined as a representation of one compression of the CPR procedure generated by the cam-follower mechanism.

2 The Model of an Artificial Rib

Commonly, the ATD are used to develop injury criteria. They are designed by using mechanical parts with similar behavior to biological elements. In order to test individual components, a dynamic test is made under well-controlled variables. As regards the thorax, this is defined in a section between the diaphragm and the neck. It is named as ribcage all the bone elements under this volume. The main function of the ribcage is to absorb forces that can be applied in an opposed way to the natural movement of the chest, protecting the internal elements of any damage. All the bone elements are joined in the center to the breastbone by cartilage. Figure 1 shows the bones that shape a ribcage. It is important to mention that the largest element on it are the ribs.

Taking advantage of this condition is important to point out that the rib properties influence the ribcage stiffness. Thus, the anthropometric parameters of human ribs can be adjusted to design an artificial human rib. This will allow to study the response of artificial human ribs in ATD easily, in order to reproduce a proper human-like response. Using the mathematical model described in [1], the morphology of a rib can be reproduced and manufactured in a properly way by using a 3D printing technology for low-cost samples. The ribcage behavior is analyzed by assuming the same morphology between the seven pairs of true ribs (ribs that are directly connected to the breastbone), just by considering size differences through scaled parameters.

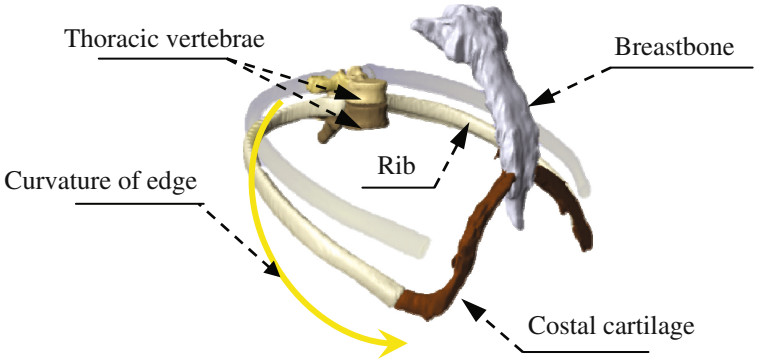

Fig. 1. A model of the human ribcage as a reconstruction obtained from a tomography

Figure 2a shows the kinematic design of the artificial human rib. The shape of the rib is designed as an elliptical shape with the depth of the thorax named as A and the width of the thorax defined as B. By defining a plane of symmetry where the payload *P* is applied, the cross section along the rib can be considered constant as an elliptical disk. The load reaction of the rib is represented by *Pr*. The variable $Dmax_{in}$ represents the major axis of the internal ellipse and the $Dmax_{out}$ represents the major axis of the external ellipse. The variable $Dmin_{in}$ represents the minor axis of the internal ellipse and the $Dmin_{out}$ represents the minor axis of the external ellipse. The *P* load component represents the axial compression of the rib. Figure 2b shows the physical construction of the prototype of artificial human rib. Table 1 lists the values for the construction of the sample prototype of artificial human rib in Fig. 2b.

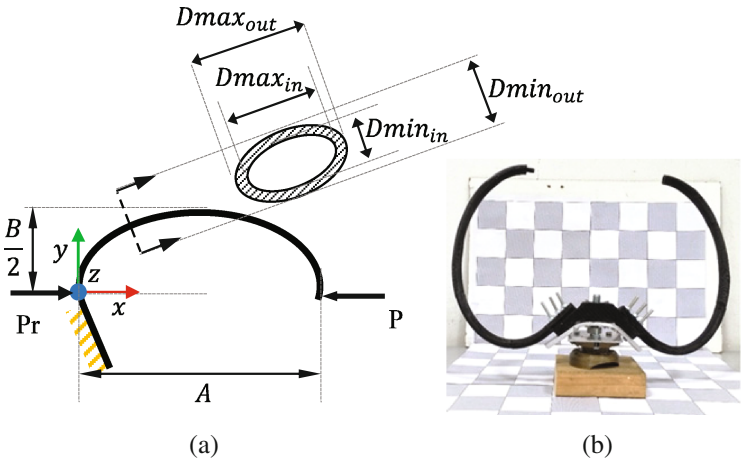

Fig. 2. A model of human rib: (a) Kinematic scheme whit its design parameters; (b) A sample prototype of artificial human rib

Table 1. Parameter values of the built prototype of artificial rib in Fig. 2b

	$D_{min_{out}}$ (mm)	$D_{min_{in}}$ (mm)	$D_{max_{out}}$ (mm)	$D_{max_{in}}$ (mm)	A (mm)	B (mm)	Young's module (GPa)
Rib 7th	16.20	10.48	11.02	4.88	226.93	152.00	11.50

3 Experimental Layout with a Testing Machine

The conceptual design of the Test Machine for Artificial Ribs (TEMARI), is divided into three areas of development, namely control of movement and its measuring, the design of law of movement and fixation of the artificial human rib on the machine. Integrating those areas in a block diagram, Fig. 3 shows the conceptual design of the TEMARI machine proposed in this work.

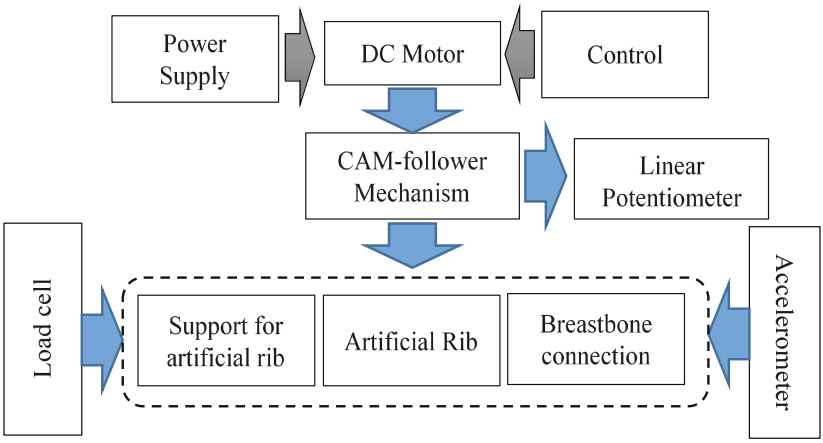

Fig. 3. A block diagram of the layout structure of TEMARI machine

The TEMARI machine is controlled by open loop because the parameters of behavior are not dependent on the response obtained by the rib. The main variable to control is the velocity of the motors. The test variables are load reaction, acceleration, position, and velocity. For the input, movement is used a DC motor with a gearbox and encoder with a theoretical maximum velocity of 89.7 rpm, the nominal voltage of 12 V, and a maximum torque of 4.5 Nm. The law of movement was designed to apply a pattern of displacement on the rib similar to the CPR compression pattern. In reference [4] a procedure is reported to determine the laws of movement in different sections of the body due to a crash test. Based on this procedure, a law of movement is defined to identify injury criteria in the thorax under dynamic conditions. The law of movement for the profile of the cam used in TEMARI machine is synthesized by the function generator reported in Ref. [3]. A linear potentiometer measures the movement

of the shaft on the mechanism. The design of the supports for the artificial ribs are a function of the impact event. A fundamental problem about this issue is solved by defining the boundary conditions of the analysis. On this case, it will be used the boundary conditions defined by a frontal impact with a restraint on the back. The posterior end of the rib is fixed to a load cell to measure the load reaction. The frontal end of the rib is fixed partially, allowing the displacement only in one direction. On this end, an accelerometer is attached to agreement to the standard ISO 2631. This sensor will measure the mechanical vibration and shock applied on the artificial human rib by the cam-follower mechanism.

The proposed kinematic design of TEMARI is shown in Fig. 4a, where K_{rc} represents the stiffness of the ribcage, K_s means the structural stiffness of the spring element that maintains the contact between the follower and the roller; K_t perform the torsional stiffness of the cam element. In addition, the m_{ch} assume the role of the mass of the chest, m_f is the mass of the follower; m_c is the mass of the cam. The variable τ act as the input torque applied by the motor; F_c is the force of contact between the cam and the follower. The angle θ correspond to the angle of contact between the cam and the follower; X_c appear as the coordinates of the cam in the general frame of the machine. The variable X_f represents the coordinates of the follower in the general frame of the machine. The variable X_{rc} perform the coordinates of the breastbone in the general frame of the machine. The variable X_g act as the gap between the breastbone connection and the follower in the general frame of the machine. To manufacture the TEMARI machine, a CAD design was elaborated as in Fig. 4b. The CAD design shows an artificial vertebra support attached to the loadcell. This artificial vertebra-like support was manufactured by using a 3D printing and metal supports. The breastbone function is replicated by using a linear bearing. That restriction allows only linear displacement.

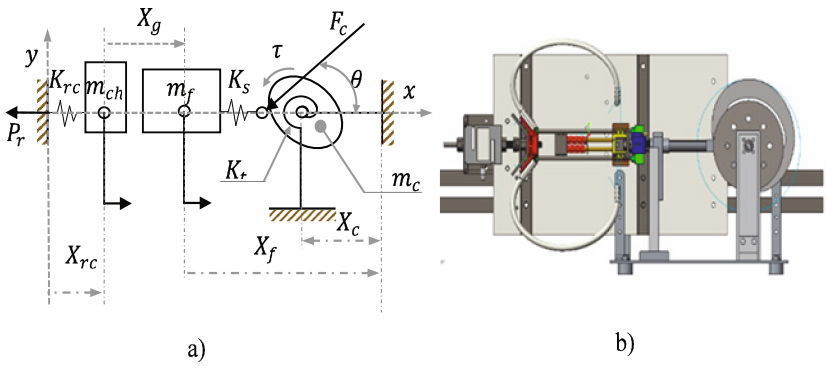

Fig. 4. Conceptual design of TEMARI; (a) A kinematic model; (b) A CAD design of elements

A prototype of the testing machine TEMARI for artificial ribs is shown in Fig. 5. The load measures are done by a load cell type S; the linear displacement is measured by a linear potentiometer of 10 kΩ; a chip ADXL345 measures the acceleration of the

impact. The load cell, the potentiometer, and the encoder are used together with a DAQ USB 6009 of National Instruments. To control the velocity of the motor is used a circuit based on the MOSFET IRF3205. The law of movement was designed to be like the cardiopulmonary assistance procedure with a maximum displacement of the stroke as 40 mm. The duty cycle is reached in a period of 1 s. A duty cycle is defined as a load and unloads cycle applied on the rib. It is assumed that the maximum stroke is reached at 0.667 s and the returning of the mechanism is on 0.333 s. The built prototype of the testing machine is shown in Fig. 5.

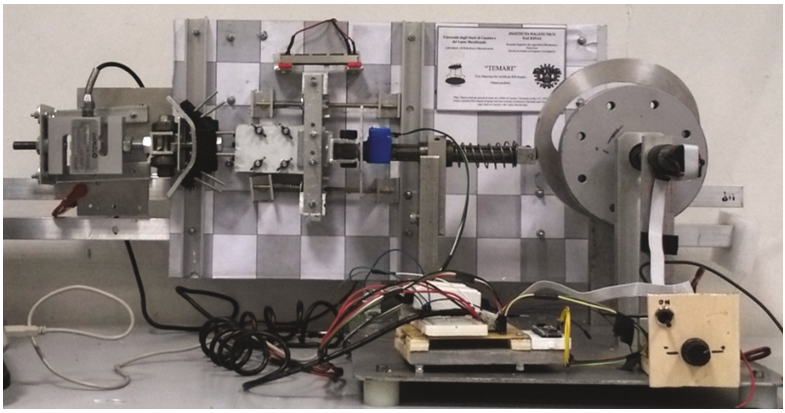

Fig. 5. The experimental Layout for the testing machine TEMARI at LARM (Laboratory of Mechatronics and Robotics)

4 Experiment Planning

The TEMARI machine is designed to test different sizes of artificial human ribs. Figure 6 shows a block diagram for the preliminary planning in the TEMARI machine. On this way, the first step is to verify the initial conditions of the test. The given initial conditions of the trial are the width, named as "A" on the artificial human rib parameters, the number "N" of impacts applied on the rib and the velocity "V" of the cam-follower mechanism. After that, the artificial human rib is fixed on the machine supports. The posterior end of the rib is attached to an artificial vertebra, and the frontal end is attached to the artificial breastbone. After that, a calibration of TEMARI is performed by looking at values of the sensors and setting the zero set-point on the data acquisition software. The used data acquisition system is allowed to read samples at 10 kHz. Once TEMARI is calibrated, a test can be started with a prescribed motion for impact simulation.

During the test, the times that the cam-follower mechanism hits the rib is recorded. If the rib sample is broken on the condition $i < N$ times, the test is stopped, and the artificial rib is replaced. This condition causes a new test and the previous process of testing being repeated. On the other way, if the rib sample is not broken before N times,

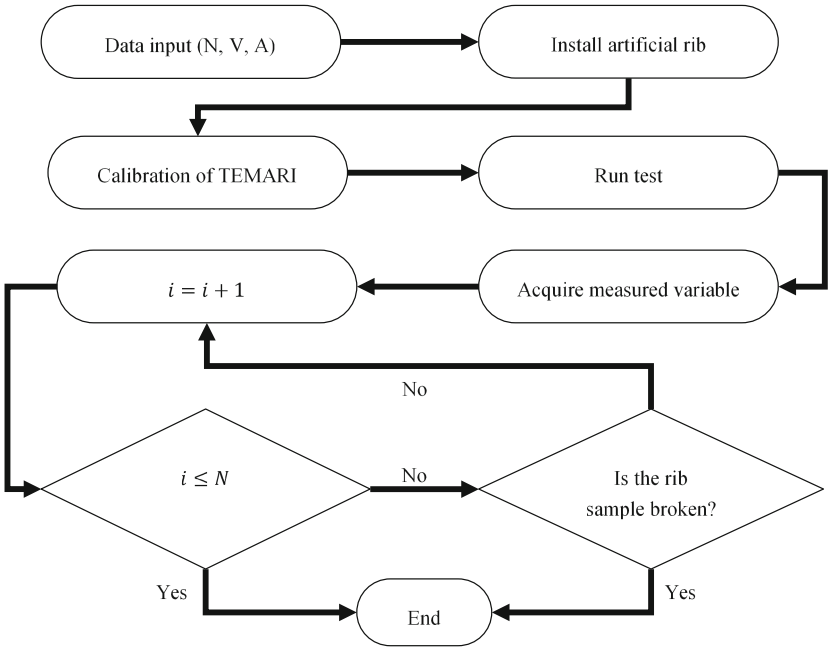

Fig. 6. A block diagram for the experimental planning in machine TEMARI at LARM

the test is ended. The described process for testing the artificial rib can be applied for different velocities of the cam-follower. The objective of this condition is to analyze the dynamic behavior of the artificial human rib.

5 Test Results and Design Considerations

Test with samples of artificial human ribs were carried out by using the TEMATRI machine, Fig. 7. 3D printing manufactured the used samples of artificial human ribs.

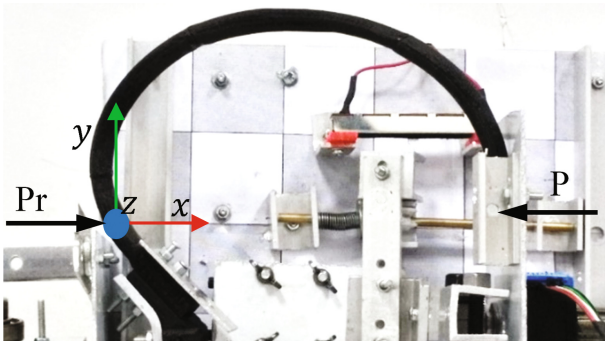

Fig. 7. A sample of artificial rib for testing with TEMARI at LARM

The dynamic response of the artificial human rib obtained by the TEMARI machine is characterized by three parameters, payload reaction, acceleration, and displacement. The first parameter characterizes the common load response. This behavior characterizes the law of movement. The second value characterizes the impact behavior of the artificial rib. Finally, the third parameter is used to analyze the simple harmonic behavior of the rib in a duty cycle. This behavior is characterized by the overlapping of the two simple harmonic reactions plotted in perpendicular directions in a duty cycle. By using the Lissajous curves, it is possible to obtain the gap between the input displacement and the output load reaction in the rib [6]. In order to show the behavior of the results achieved by the TEMARI machine, it was run a test on low velocity. The rib was hit 20 times during 45.16 s.

Figure 8 shows the computed results for the test evaluated. In Fig. 8a is shown the measures of load reaction for a cycle of 10 hits on the artificial rib. The average load reaction is 59.61 mN. The load reaction measured shows an oscillating behavior, that is quite similar to the computed values obtained in reference [1]. This behavior can be attributed to the spring-like behavior of the material. On the other side, the Fig. 8b shows a characteristic hit during one second. Due the load-cell is used for quasi-static loads, the equipment did not record the values obtained under 1 s. The plot is useful to show the load reaction that is applied on the artificial vertebra. The possibility of rib damage is predicted by the load oscillation This load represents the largest component to be considered in a fracture on an anterior-compression load situation. In Fig. 8c is shown the measures of the impact acceleration measured on the artificial rib for one hit.

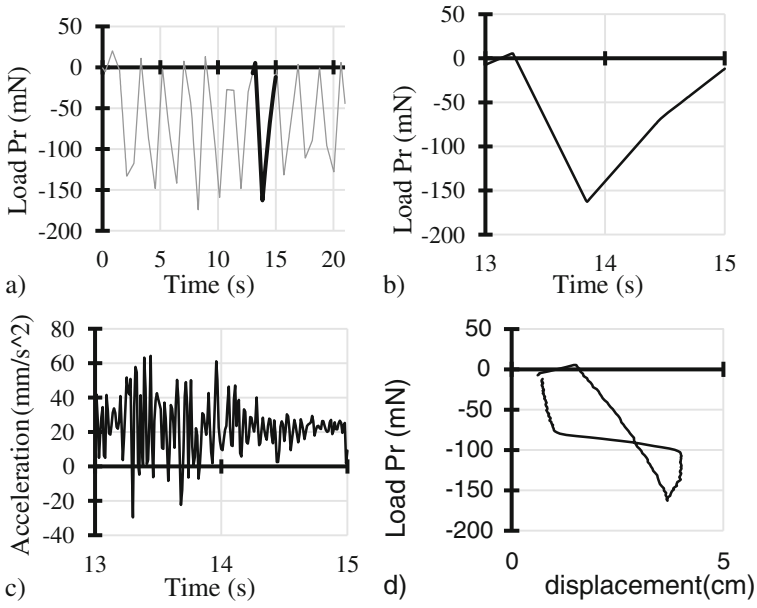

Fig. 8. Results of a test with a sample of artificial rib by using TEMARI, Fig. 6: (a) measured Pr during ten hits; (b) measured Pr during one characteristic hit; (c) measured acceleration during one characteristic hit; (d) response Pr displacement during one characteristic hit.

The oscillation on the impact is modified by the spring-like behavior of the rib as is reported in [1]. Finally, Fig. 8d shows the displacement measured versus the load reaction Pr. This Figure represents the simple harmonic behavior of the rib in the entire duty cycle. By using the Lissajous curves in this particular case, it is possible to approximate the gap between the input displacement and the output load reaction as the $\pi/4$ phase of difference [6].

6 Conclusions

Testing requirements on artificial ribs have suggested a novel design of a testing machine with suitable sensorisation. The TEMARI machine (test machine for artificial ribs) design is presented as result of a necessity to design and to test artificial human ribs under dynamic conditions. The characteristics of design for the TEMARI machine are used to carry out tests on artificial ribs whose results characterize the response of the investigate samples that have been built with low-cost manufacturing by 3D printing. Acquired measures of test parameters show both the efficiency of TEMARI testing machines and the feasibility of the designed human artificial ribs.

Acknowledgments. The first author wishes to gratefully acknowledge Consejo Nacional de Ciencia y Tecnologia (CONACyT) and Instituto Politécnico Nacional through scholarship "Beca mixta para estancias de investigación en el extranjero" for allowing his period of study at LARM of Cassino University in the A.Y. 2016–17 within a double Ph.D. degree program and the International Federation for the Promotion of Mechanism and Machine Science (IFToMM) for support the diffusion of this work.

References

1. Aguilar, P.L.A., Cecarrelli, M., Torres-San-Miguel, C.R., Urriolagoitia-Sosa, G., Urriolagoitia-Calderón, G.: Analysis of the rib properties as modifier of the ribcage stiffness. J. Braz. Soc. Mech. Sci. Eng., 1–10 (2017)
2. Alén, C.C., Carbone, G., Cecarrelli, M., Echávarri, J., Luis, M.J.: Experimental tests in human-robot collision evaluation and characterization of a new safety index for robot operation. Mech. Mach. Theor. **80**, 184–199 (2014)
3. Cecarrelli, M., Lanni, C., Carbone, G.: Numerical and experimental analysis of cam profiles with circular-arcs. In: IX International Conference on the Theory of Machines and Mechanisms, Liberec, Czech Republic, pp. 189–207 (2004)
4. Cortes, V.O., Torres-San-Miguel, C.R., Urriolagoitia-Sosa, G., Cruz, J.I.L., Aguilar, P.L.A., Martinez, S.L., Urriolagoitia-Calderón, G.: Numerical simulation of run over scenarios to adult pedestrian with vehicle type sedan in Mexico City. DYNA New Technol. **4**, 1–17 (2016)
5. Duma, S.M., Kemper, A.R., Stitzel, J.D., McNally, C., Kennedy, E.A., Matsuoka, F.: Rib fracture timing in dynamic belt tests with human cadavers. Clin. Anat. **24**, 327–338 (2011)
6. Al-Khazali, H.A.H., Askari, M.R.: Geometrical and graphical representations analysis of Lissajous figures in rotor dynamic system. IOSR J. Eng. **2**, 971–978 (2012)

7. Kemper, A.R., McNally, C., Wyatt, C.L., Duma, S.M.: Controlling boundary conditions and specimen preparation for testing human ribs: effects of periosteum, hydration, and strain gages. In: Injury Biomechanics Research, Proceedings of the Thirty-Fourth International Workshop, United States. Washington, D.C., pp. 63–78 (2006)
8. Sandoz, B., Laporte, S., Charpail, E., Trosseille, X., Lavaste, F.: Influence of velocity in human ribs response. J. Biomech., 1 (2007)

Kinetostatic Model of the Human Knee for Preoperative Planning: Part A
Method and Validation

D. Ponce[1(✉)], L. Mejia[1], E. Ponce[3], D. Martins[4], C.R.M. Roesler[4], and J.F. Golin[2]

[1] Federal University of Santa Catarina - UFSC, Rua Pomerode, 710, Blumenau, SC 89065-300, Brazil
{daniel.alejandro,leonardo.mejia.rincon}@ufsc.br
[2] Federal Institute of Santa Catarina (IFSC), A. Mauro Ramos, 950, Florianopolis, SC 88020-300, Brazil
julio.golin@ifsc.edu.br
[3] Universidad de Tarapaca (UTA), 18 de Septiembre 2222 Casilla 6-D., 1000000 Arica, Chile
eponce@uta.cl
[4] Federal University of Santa Catarina (UFSC), Florianopolis, SC 88040-900, Brazil
daniel.martins@ufsc.br, rroesler@hu.ufsc.br

Abstract. The main objective of this work is to develop a static and spatial model of the human knee, based on mechanism theory, to provide orthopedic surgeons information that relates forces at the anterior cruciate ligament graft (ACL) with its fixing position. This fixing position must be defined at the preoperative planning phase of the ligament replacement surgery. The best position for the graft insertion is taken as the one where the force developed at the graft is similar to the forces seen in an intact ligament during the knee flexion movement. The methodology for the static model is based on reimplementing a pure kinematic knee model available in the literature. In particular, this kinematic model is redefined using Davies' method to obtain a static model that yields the forces at ligaments and condyles. The current kinematic model is able to satisfactorily reproduce the passive movement of the knee. We believe that any theoretical improvement in modeling and simulation of the forces at ligaments and grafts is an important contribution to the preoperative planning and improve the medical decision making capacity.

Keywords: Knee modelling · Preoperative planning · Kinetostatics · Screw theory · Davies method

1 Introduction

When anterior cruciate ligament (ACL) surgery is indicated, preoperative planning is a critical step in defining the procedure's parameters. During this planning phase, surgeons must define the insertion position for the replacement graft

J.C.M. Carvalho et al. (eds.), *Multibody Mechatronic Systems*,
Mechanisms and Machine Science 54, DOI 10.1007/978-3-319-67567-1_42

that best matches the functionality of an intact ACL. Particularly complex cases arise when the ACL graft cannot be positioned in its natural insertion area, which may occur when the area is too small for a surgical procedure. In such cases, adjacent areas are chosen. However, if such insertion area is not satisfactorily chosen, the knee's natural kinetostatics may be harmfully impacted.

The objective of this work is to devise a spatial static model of the knee, based on mechanism design theory, on Davies' Method [1,2] and on a kinematic knee model previously proposed by [3,4]. Our current model presents a tridimensional analysis of the forces arising in the knee's anatomical elements, improving upon previously presented bidimensional static models [5–7] and also upon purely kinematic spatial models. The implementation of this methodology targets personalized knee models, in order to provide information for preoperative planning for ACL replacement procedures. In *Part A* of this work, the proposed method is presented, along with its validation and results. In *Part B*, a clinic application of the method is presented through simulation and validation of a case study.

2 Proposed Method

Knee models based on mechanism design theory focus on position kinematics. The forces in the model are not provided by these approaches, requiring additional analyses to be obtained. This is of special relevance due to the complexity of the problem, since the functionality of the ligaments vary depending on the knee's flexion angle. Although dynamic models with more complex anatomical representations exist [8,11–13], they are computationally demanding [3,4], lose restriction functions of anatomical structures and produce results that are difficult to interpret by surgeons and prosthetists.

The kinetostatic modeling proposed in this work (Fig. 1b) aims at improving the kinematic model presented by [3,4] through an additional static implementation of Davies' method [1,2]. Davies' method provides an unique and systematized approach to the static analysis of the knee's mechanical model, offering a solution for the calculation of the forces involved in each position. This enables an analysis with low computational demands of the function performed by each anatomical structure.

Particularly, the proposed static modeling (Fig. 1b) enables the analysis of the *in situ* force of the ACL (or graft) as a function of an external force applied on the knee. This analysis can provide valuable data for preoperative planning of ligament reconstruction. The method encompasses modeling and simulation of the experimental procedure implemented by [9] (Fig. 1a) to evaluate the *in situ* force on the ACL. The *in situ* force is the force acting upon the ligament (or graft) as the result of a load applied to the knee. The experimental *in situ* force serves as validation for the proposed model.

The experimental procedure consists in the application – with the aid of a robotic system – of a force $F_x = 110\,\mathrm{N}$ directed along the anterior tibial direction and a moment M_z around the lateral medial z axis, so that the articular structures are purely subject to the force F_x. The force F_x and the moment M_z,

applied on the tibia, are transmitted through ligaments and condyles to the femur in the form of a reaction force F_{xr} and a reaction torque M_{zr}, drawn in blue (Fig. 1a). These loads were applied to reproduce the drawer test (useful for clinical evaluation of the ACL), subjecting the ACL to tension.

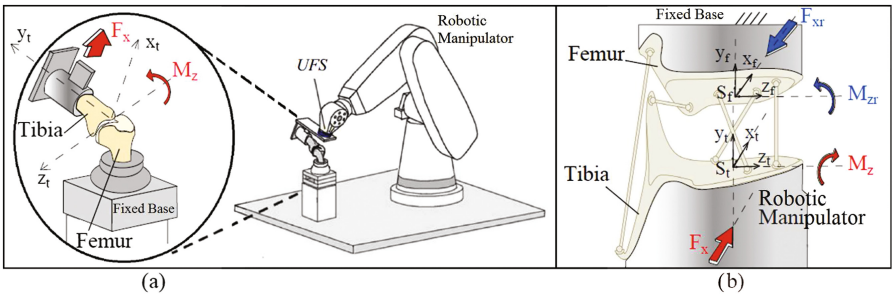

Fig. 1. (a) Experimental procedure [9], (b) Static modeling of the experimental procedure.

The proposed static modeling consists of five main steps: (a) Kinematic modeling and identification of the successive positions of anatomical elements, (b) topological characterization of the mechanism, (c) static characterization of the mechanism's couplings, (d) formulation and solution of the static equations system and (e) results and validation.

2.1 Step a: Kinematic Modeling and Identification of the Successive Positions of Anatomical Elements

The kinematic model of the knee as proposed by [3,4] is presented in Fig. 2a. This model, composed by two rigid links connected via spherical joints, has been capable of satisfactorily reproducing the knee's passive motion. As Fig. 2a presents a schematic (topological) drawing of the model, an equivalent model with a more anatomically representative geometry is adopted in this work – as shown in Fig. 2b. Figure 2c represents the human knee's anatomy, where PCL = posterior cruciate ligament, MCL = medial collateral ligament, and LCL = lateral collateral ligament.

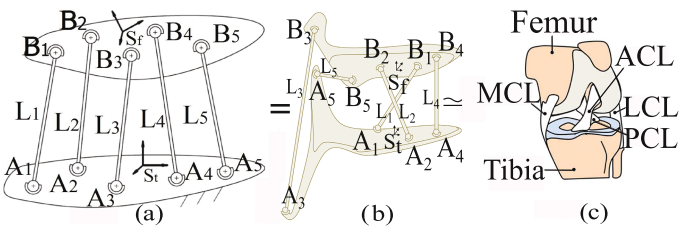

Fig. 2. (a) Kinematic model of the knee, as proposed by [3,4]. (b) Adopted model, topologically equivalent to [3,4]. (c) Human knee and its anatomical elements.

The kinematic model has 1 spatial degree of freedom (DOF), that is, for each imposed flexion angle, the position and orientation of the upper platform in respect to the lower one can be unequivocally determined. In this model, the tibia is represented by the lower platform, with its anatomical center located at S_t. The femur is in turn represented by the upper platform, with the anatomical center at S_f. The identification of the ligaments and condyles adopted in Fig. 2a and b are detailed as follows:

- A_1, A_2 and A_3: spatial positions of the ACL, PCL and MCL tibial insertion points, respectively.
- B_1, B_2 and B_3: spatial positions of the ACL, PCL and MCL femoral insertion points, respectively.
- A_4 and A_5: spatial positions of the medial and lateral tibial condyles' centroids, respectively.
- B_4 and A_5: spatial positions of the medial and lateral femoral condyles' centroids, respectively.
- $L1$, $L2$ and $L3$: ACL, PCL and MCL lengths, respectively.
- L_4 and L_5: distances between the medial and lateral condyles' centroids, respectively.

Spherical joints were modeled on coordinates A_i and B_i, $(i = 1, \ldots, 5)$, while L_i, $(i = 1, \ldots, 5)$ were modeled as rigid links. The positions A_i and B_i and the lengths L_i are known as geometric parameters, or *GP*.

Motion data from S_f on S_t, the lengths L_i and the initial positions for A_i and B_i (when the flexion angle $\alpha = 0°$) are obtained from [3,4]. In this current work, the motion of each anatomical element A_i and B_i, during the displacement from S_f on S_t, was obtained via inverse kinematics.

Since this modeling process employs the Davies' method, from now on the *GP* A_i and B_i will be represented by an appropriate notation. Thus: $A_i = \boldsymbol{S}_{0A_i}$ and $B_i = \boldsymbol{S}_{0B_i}$, $(i = 1, \ldots, 5)$.

Regarding the experimental procedure (Fig. 1a), the knee's motion occurs with a fixed femur. Therefore, the kinematics inversion presented in (Eq. 1) – formulated in terms of screw theory – is adopted, allowing one to obtain $\boldsymbol{S}_{0A_i}$ on S_f,

$$^{f}\boldsymbol{S}_{0A_i} = -\mathbf{p} + {}^{B}R_A \boldsymbol{S}_{0A_i}, \quad {}_{(i=1,\ldots,5)} \tag{1}$$

where:

- $^{f}\boldsymbol{S}_{0A_i}$ is the point $\boldsymbol{S}_{0A_i}$ measured in relation to S_f;
- $^{B}R_A = [^{A}R_B]^{-1}$ is the matrix describing the rotation of S_t in relation to S_f;
- $\mathbf{p}$ is the vector describing the position (x, y, z) of S_t in relation to S_f.

Similarly, the positions $\boldsymbol{S}_{0B_i}$ are fixed and measured in relation to S_f (Eq. 2), and therefore $\boldsymbol{S}_{0B_i}$ can be directly obtained from the *GP* in [3].

$$^{f}\boldsymbol{S}_{0B_i} = \boldsymbol{S}_{0B_i}, \quad {}_{(i=1,\ldots,5)} \tag{2}$$

2.2 Step b: Topological Characterization of the Mechanism

In this step, the mechanism's *coupling network* and *coupling graph* are established [2].

The *coupling network* is a representation of the proposed mechanical model's topology. In the *coupling network*, the mechanism's couplings are represented by vertices labeled by letters A_i and B_i, $(i = 1, \ldots, 5)$. Each body in the *coupling network* represents a link in the mechanism, and is labeled by a number.

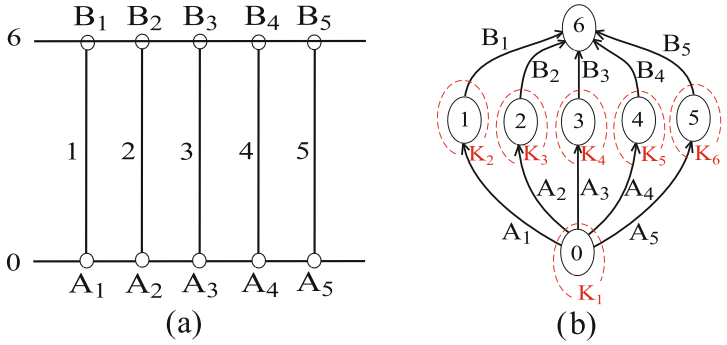

Fig. 3. (a) Model's coupling network. (b) Coupling graph G_C.

In the *coupling graph*, each body in the *coupling network* is represented by a node and each coupling is represented by a edge, as shown in Fig. 3b, where the edges of G_C are oriented from smaller to larger nodes.

In order to determine the cuts in the G_C graph, it must be considered that each one of the $k = 6$ cuts must split the G_C graph into 2 different graphs [2]. Each k-th cut is thus represented with a dashed red line in (Fig. 3a).

2.3 Step c: Static Characterization of the Mechanism's Couplings

In this step the external loads must be determined, modeled and internalized, gathering all coupling's characteristics required in the formation of the wrenches and in the construction of the *action graph* G_A. This step thus comprises 4 sub-steps, detailed as follows:

Sub-step c.1: Modeling the load conditions. In this step, the external loads applied on the knee are modeled based upon the experimental procedure performed in [9] – shown in (Fig. 1a). For such modeling, the cut-set law defined by [1,2] is employed. The experimental procedure consists in exerting a force $F_x = 110\,\mathrm{N}$ on the knee specimen – with the aid of a robotic system – directed along the anterior tibial direction, and a moment M_z around the lateral medial z axis. The force F_x and the moment M_z are applied on the tibia, while the femur remains fixed. The moment M_z locks the flexion motion imposed by the

force F_x. The force F_x and the moment M_z, applied on the tibia, are transmitted through ligaments and condyles to the femur in the form of a reaction force F_{xr} and a reaction torque M_{zr}, drawn in blue in (Fig. 1a). These loads are applied for various flexion angles (0°, 15°, 30°, 60° and 90°), also via a robotic system. The robot's Universal Force Sensor (UFS), attached to the tibia, provides an indirect measure of the *in situ* forces of the ACL through the inverse Jacobian [10], defining a vector of forces and moments for the anatomical coordinate system of the femur, labeled ${}^{Anat}F$ (Eq. 3).

$$ {}^{Anat}F = [f_x, f_y, f_z, m_x, m_y, m_z]^T \tag{3} $$

Sub-step c.2: Internalization of external loads. Here, the mechanism must be restricted in order to prevent any motion [1,2]. The reactions – or active actions – F_{xr} and M_{zr}, must be internalized in the couplings as passive actions R_{Aix}, R_{Aiy}, R_{Aiz}, R_{Bix}, R_{Biy} e R_{Biz}, $(i = 1, \ldots, 5)$ (Fig. 4a).

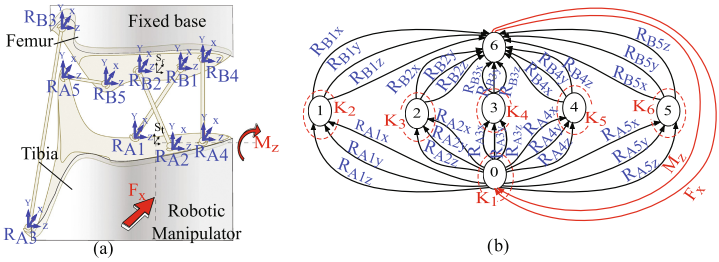

Fig. 4. (a) Internalized actions on couplings. (b) Action Graph and k cuts (dashed lines).

In order to form the wrenches, three unit direction vectors $\boldsymbol{S}$, subscripted x, y and z, are attached to each spherical pair A_i and B_i of the mechanism (Fig. 4a).

$$ \boldsymbol{S}_x = \begin{pmatrix} 1 \\ 0 \\ 0 \end{pmatrix}; \boldsymbol{S}_y = \begin{pmatrix} 0 \\ 1 \\ 0 \end{pmatrix}; \boldsymbol{S}_z = \begin{pmatrix} 0 \\ 0 \\ 1 \end{pmatrix} \tag{4} $$

Sub-step c.3: Representation of the *action graph* G_A. The *action graph* G_A is created [2] (Fig. 4b), in which: each vertex represents a link in the mechanism; 30 dark edges represent the passive actions, 2 red edges represent the active actions F_x and M_z, and $k = 6$ cuts from the *coupling network* (Fig. 3b) are substituted as red dashed lines. The number of variables C in the system corresponds to the total amount of edges in the *action graph* G_A ($C = 32$).

Sub-step c.4: $ wrench construction. The results of the passive actions and of F_x are pure force states, therefore, its wrenches are (Eq. 5):

$$\$ = \begin{pmatrix} \boldsymbol{S}_0 \times \boldsymbol{R} \\ \boldsymbol{R} \end{pmatrix} = \begin{pmatrix} \boldsymbol{S}_0 \times \boldsymbol{S} \\ \boldsymbol{S} \end{pmatrix} \boldsymbol{R} \tag{5}$$

Furthermore, M_z is a pure torque state ($\boldsymbol{T}$), equivalent to the wrench in (Eq. 6).

$$\$ = \begin{pmatrix} \boldsymbol{T} \\ \boldsymbol{0} \end{pmatrix} = \begin{pmatrix} \boldsymbol{S} \\ \boldsymbol{0} \end{pmatrix} \boldsymbol{T} \tag{6}$$

Considering (Eqs. 1, 2, 4, 5 and 6), the following wrenches are obtained for each active load and for each coupling in the proposed static model:

$$\begin{gathered} \$_{M_z} = \begin{pmatrix} \boldsymbol{M_z} \\ \boldsymbol{0} \end{pmatrix}; \$_{A_{ix}} = \begin{pmatrix} {}^f\boldsymbol{S}_{0Aix} \times \boldsymbol{R}_{A_{ix}} \\ \boldsymbol{R}_{A_{ix}} \end{pmatrix}; \$_{A_{iy}} = \begin{pmatrix} {}^f\boldsymbol{S}_{0Aiy} \times \boldsymbol{R}_{A_{iy}} \\ \boldsymbol{R}_{A_{iy}} \end{pmatrix}; \\ \$_{F_x} = \begin{pmatrix} {}^f\boldsymbol{S}_{0Fx} \times \boldsymbol{Fx} \\ \boldsymbol{Fx} \end{pmatrix}; \$_{A_{iz}} = \begin{pmatrix} {}^f\boldsymbol{S}_{0Aiz} \times \boldsymbol{R}_{A_{iz}} \\ \boldsymbol{R}_{A_{iz}} \end{pmatrix}; \$_{B_{ix}} = \begin{pmatrix} {}^f\boldsymbol{S}_{0Bix} \times \boldsymbol{R}_{B_{ix}} \\ \boldsymbol{R}_{B_{ix}} \end{pmatrix}; \\ \$_{B_{iy}} = \begin{pmatrix} {}^f\boldsymbol{S}_{0Biy} \times \boldsymbol{R}_{B_{iy}} \\ \boldsymbol{R}_{B_{iy}} \end{pmatrix}; \$_{B_{iz}} = \begin{pmatrix} {}^f\boldsymbol{S}_{0Biz} \times \boldsymbol{R}_{B_{iz}} \\ \boldsymbol{R}_{B_{iz}} \end{pmatrix} \end{gathered} \tag{7}$$

where ${}^f\boldsymbol{S}_{0Fx}$ represents the point where the force F_x is applied on the tibia, measured in relation to S_f.

2.4 Step d: Formulation and Solution of the Static Equations System

For a restricted chain with internalized actions, with k cuts in the λ space, one can write λk equations, expressing conditions that must be satisfied by C variables. In the following, the steps required to formulate the static equations system defined by Davies' *cut-set law* are carried out. The solution to the system yields the forces actuating on each link of the proposed static model.

Sub-step d.1: Defining the unitary actions matrix. Davies' *cut-set law* [2] defines that the algebraic sum of the $ wrenches belonging to a same cut is zero. To apply this law, one must first construct the *Unit Network Action Matrix* $[\hat{A_N}]_{\lambda.k \times C}$. The rows in this matrix correspond to the $ wrenches (edges in G_A) intercepted by the k cuts, while the columns respectively represent the normalized wrenches $\hat{\$}_{A_1}$, $\hat{\$}_{A_2}$, $\hat{\$}_{A_3}$, $\hat{\$}_{A_4}$, $\hat{\$}_{A_5}$, $\hat{\$}_{B_1}$, $\hat{\$}_{B_2}$, $\hat{\$}_{B_3}$, $\hat{\$}_{B_4}$, $\hat{\$}_{B_5}$, $\hat{\$}_{M_z}$, $\hat{\$}_{F_X}$, where it must be considered that: $\$\hat{A}_i = [\$\hat{A}_{ix}; \$\hat{A}_{iy}, \$\hat{A}_{iz}]_{6\times3}$; $\$\hat{B}_i = [\$\hat{B}_{ix}, \$\hat{B}_{iy}, \$\hat{B}_{iz}]_{6\times3}$, $(i = 1, .., 5)$; $\$M_z = [\$M_z]_{6\times1}$; $\$F_x = [\$F_x]_{6\times1}$. The vector representing the magnitudes of the wrenches is known as the magnitude action vector $\{\boldsymbol{\Psi}\}_{C\times1}$. To define this vector, it must be considered that: $R_{Ai} = [R_{A_{ix}}; R_{A_{iy}}; R_{A_{iz}}]^T_{1\times3}$; $R_{Bi} = [R_{B_{ix}}; R_{B_{iy}}; R_{B_{iz}}]^T_{1\times3}$, $(i = 1, .., 5)$; $M_z = [M_z]_{1\times1}$; $F_x = [F_x]_{1\times1}$.

Sub-step d.2: Construction and solution of the static equations system. Applying the *cut-set law* [2] to the static model, the following system is obtained:

$$[\hat{A}_N]_{36\times32}\ \{\mathbf{\Psi}\}_{32\times1} = \{\mathbf{0}\}_{36\times1} \tag{8}$$

The consistency of the equation system depends on the rank a of the matrix $[\hat{A}_N]_{36\times32}$, where the rank a corresponds to the amount of linearly independent lines (that is, equations).

By reducing the matrix $[\hat{A}_N]_{36\times32}$ to its echelon form, the matrix $[\hat{A}_{N_{ESC}}]_{31\times32}$ is obtained, with a corresponding rank $a = 31$ of linearly independent lines. The *cut-set law* in the echelon form is presented in Eq. 9:

$$[\hat{A}_{N_{ESC}}]_{31\times32}\ \{\mathbf{\Psi}\}_{32\times1} = \{\mathbf{0}\}_{31\times1} \tag{9}$$

Since $C = 32$ and $a = 31$, the number of independent variables is $C_N = 1$, and therefore 1 variable must be imposed in order to enable the computation of a solution for the system. Independent variables are labeled with the sub-index P, and dependent variables are sub-indexed with S:

$$\left[[\hat{A}_{NS}]_{31\times31} \vdots [\hat{A}_{NP}]_{31\times1}\right]\left[[\mathbf{\Psi}_S]_{31\times1} \vdots [\mathbf{\Psi}_P]_{1\times1}\right]^T = \{\mathbf{0}\}_{31\times1} \tag{10}$$

The last step is isolating the vector of unknowns $\{\Psi_S\}_{31\times1} = [R_{A_1}\ R_{A_2}\ R_{A_3}\ R_{A_4}\ R_{A_5}\ R_{B_1}\ R_{B_2}\ R_{B_3}\ R_{B_4}\ R_{B_5}\ M_z]^T$, which yields the static solution

$$\{\mathbf{\Psi}_S\}_{31\times1} = -[\hat{A}_{NS}]^{-1}_{31\times31}[\hat{A}_{NP}]_{31\times1}\{\mathbf{\Psi}_P\}_{1\times1} \tag{11}$$

By attributing a value to the primary static variable $\mathbf{\Psi}_P = \boldsymbol{F}_x$, it is possible to obtain the static solution $\{\mathbf{\Psi}_S\}_{31\times1}$ for Eq. 11.

3 Results and Validation

Results: The static solution $\{\Psi_S\}_{31\times1} = [R_{A_1}\ R_{A_2}\ R_{A_3}\ R_{A_4}\ R_{A_5}\ R_{B_1}\ R_{B_2}\ R_{B_3}\ R_{B_4}\ R_{B_5}\ M_z]^T$ is obtained by imposing $\mathbf{\Psi}_P = \boldsymbol{F}_x = 110\,\text{N}$ (Eq. 11) over the entire flexion trajectory of the knee. The *in situ* forces on the ACL (F_{ACL}), PCL (F_{PCL}) and MCL (F_{MCL}) are computed via the norm of the actions occurring on the couplings A_1, A_2 and A_3 respectively, and are represented in Fig. 5 as FLCA, FLCP and FLCM. The compression forces on the medial and lateral condyles (MC and LC, respectively), are calculated via the norm of the forces occurring in the couplings A_4 and A_5 respectively, and are represented in Fig. 5 as FCM and FCL.

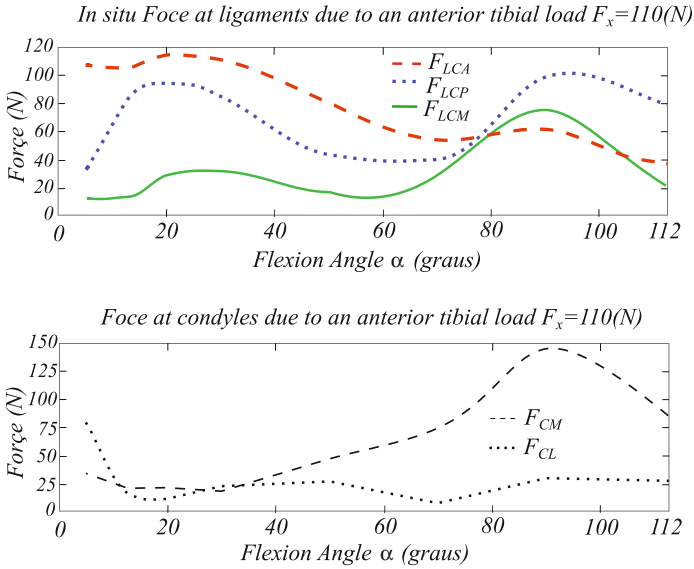

Fig. 5. Simulation results: forces on the anatomical elements of the model due to an anterior tibial load of $\boldsymbol{F}_x = 100\,\mathrm{N}$ over the course of the knee's flexion motion.

Validation: In order to validate the results, the *in situ* forces on the ACL obtained through the static model are compared with the results obtained in the experimental procedure proposed by [9]. The comparison between both results is shown in Fig. 6. Experimental data are represented by a continuous black line, with vertical bars representing the standard deviation. Data obtained from the proposed static model are represented with a dotted blue line, which finds itself inside the standard deviation specified by the experimental data.

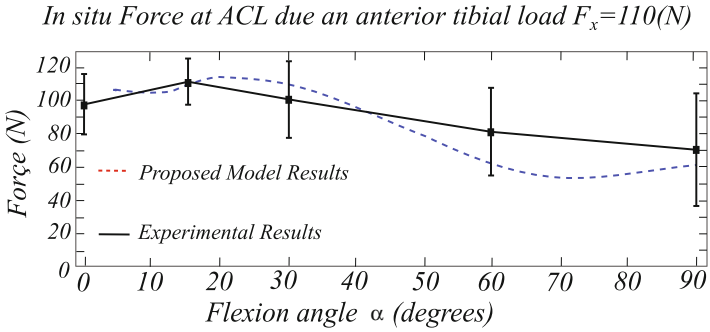

Fig. 6. Validation of the results for the *in situ* force on the ACL.

4 Conclusions

A kinetostatic modeling of the knee was presented, which enables the determination of the *in situ* forces of the ligaments and the compression forces on the condyles when subjected to an external load. This model emerges from the reimplementation of the statics on an existing kinematic model [3,4], capable of adequately reproducing the knee's passive motion. Considering the satisfactory validation of the obtained results, the present model may contribute in supporting preoperative planning for human knee operation procedures, as well as in ACL substitution procedures. Also, the implementation of the present model allowed to improve previously presented results, in which the two-dimensional static modeling [5–7] had limitations in some aspects. Based on the results, the proposed work stands as an evidence that modeling based upon mechanism theory, screw theory and Davies' method enables simulations with results similar to physiological ones, and can be considered a validated tool for the modeling of biomechanical systems.

References

1. Davies, T.: Circuit actions attributable to active couplings. Mech. Mach. Theor. **30**(7), 1001–1012 (1995)
2. Davies, T.: Freedom and constraint in coupling networks. Proc. Inst. Mech. Eng. Part C J. Mech. Eng. Sci. **220**(7), 989–1010 (2006)
3. Parenti-Castelli, V., Sancisi, N.: Synthesis of spatial mechanisms to model human joints. In: 21st Century Kinematics, pp. 49–84. Springer, Heidelberg (2013)
4. Sancisi, N., Parenti-Castelli, V.: A 1 DoF parallel spherical wrist for the modelling of the knee passive motion. Mech. Mach. Theor. **45**(3), 658–665 (2010)
5. Ponce, D., Martins, D., de Mello-Roesler, C.R., Teixeira-Pinto, O., Fancello, E.A.: Relevance of the hyperelastic behavior of cruciate ligaments in the modeling of the human knee joint in sagittal plane, Revista Facultad de Ingeniera Universidad de Antioquia, vol. 76, pp. 123–133 (2015)
6. Ponce, D., Martins, D., Roesler, C.R.M., Rosa, F., More, A.: Modeling of human knee joint in sagittal plane considering elastic behavior of cruciate ligaments. In: 22nd International Congress of Mechanical Engineering - COBEM 2013, Ribeirao Preto, Sao Paulo. Proceedings of the 22nd International Congress of Mechanical Engineering [S.l.:s.n.] (2013)
7. Ponce, D., de Mello-Roesler, C.R., Martins, D.: A human knee joint model based on screw theory and its relevance for preoperative planning. In: Mecanica Computacional. Computational Modeling in Bioengineering and Biomedical Systems (B), vol. XXXI, no. 24, pp. 3847–3871 (2013)
8. Olanlokun, K., Wills, D.: A spatial model of the knee for the preoperative planning of knee surgery. Proc. Inst. Mech. Eng. Part H J. Eng. Med. **216**(1), 63 (2002). Sage Publications
9. Woo, S., Fox, R., Sakane, M., Livesay, G., Rudy, T., Fu, F.: Biomechanics of the ACL: measurements of in situ force in the ACL and knee kinematics. The Knee **5**(4), 267–288 (1998). Elsevier
10. Fujie, H., Livesay, G.A., Fujita, M., Woo, S.L.: Forces and moments in six-DOF at the human knee joint: mathematical description for control. J. Biomech. **29**(12), 1577–1585 (1996). Elsevier

11. Andriacchi, T., Mikosz, R., Hampton, S., Galante, J.: Model studies of the stiffness characteristics of the human knee joint. J. Biomech. **16**(1), 23–29 (1983). Elsevier
12. Abdel-Rahman, E., Hefzy, M.S.: A two-dimensional dynamic anatomical model of the human knee joint. J. Biomech. Eng. **115**(4A), 357–365 (1993). American Society of Mechanical Engineers
13. Wismans, J., Veldpaus, F., Janssen, J., Huson, A., Struben, P.: A three-dimensional mathematical model of the knee-joint. J. Biomech. **13**(8), 677–685 (1980). Elsevier

Kinetostatic Model of the Human Knee for Preoperative Planning: Part B

Clinical Application for Medical Decision Making

D. Ponce[1(✉)], J.F. Golin[2], E. Ponce[3], D. Martins[4], C.R.M. Roesler[4], and L. Mejia[1]

[1] Federal University of Santa Catarina (UFSC), Rua Pomerode, 710, Blumenau, SC 89065-300, Brazil
{daniel.alejandro,leonardo.mejia.rincon}@ufsc.br
[2] Federal Institute of Santa Catarina (IFSC), A. Mauro Ramos, 950, Florianopolis, SC 88020-300, Brazil
julio.golin@ifsc.edu.br
[3] Universidad de Tarapaca (UTA), 18 de Septiembre 2222 Casilla 6-D, Arica 1000000, Chile
eponce@uta.cl
[4] Federal University of Santa Catarina (UFSC), Florianopolis, SC 88040-900, Brazil
daniel.martins@ufsc.br, rroesler@hu.ufsc.br

Abstract. In anterior cruciate ligament (ACL) graft surgeries, the location of the insertion point is a critical definition for the functional success of the surgery and patient health. This location is determined during preoperative planning and can be defined according to some criteria such that the biomechanical function is preserved in its best. In this work, simulations based on the method previously presented in part A are presented, taking experimental data available in the literature. Here, this clinical application uses the *in situ* force of the ACL at selected insertion points as criteria. This aims to determine the graft insertion points, at femur, that best leads to the natural response of an intact knee. Results show the applicability of the method as a support tool for medical decision making in the preoperative planning period.

Keywords: Knee modelling · Preoperative planning · Kinetostatics · ACL replacement graft · Davies method

1 Introduction

In part A of this work, a static model of the human knee was implemented on an existing kinematic model. This implementation resulted in a new kinetostatic model. Based on the results and validation presented in part A, it can be established that the model can simulate results similar to the physiological ones, and can be considered as a tool for modeling biomechanical functions of the knee.

In this manuscript a practical application of the model, proposed in part A, is performed. The clinical application presented here intends to show the usability

J.C.M. Carvalho et al. (eds.), *Multibody Mechatronic Systems*,
Mechanisms and Machine Science 54, DOI 10.1007/978-3-319-67567-1_43

of the model as support to the preoperative planning of the ligament substitution procedure.

In particular, we aim to define the best insertion point for the ACL graft, in the femur, that leads to an in-situ force similar to those found in an intact ACL.

For validation purposes, we considered an experimental procedure that found the best insertion point for the ACL graft, by use of the slip-ratio, where the best insertion point produces a similar slip-ratio to that found in an intact knee. The simulation results are compared with experimental ones, and both analysis obtain the same best point of insertion of the ACL graft.

Based on the obtained results, it can be concluded that the proposed kineto-static model can be useful as a support tool in the medical decision making and in the preoperative planning of the human knee.

For a better understanding of the clinical problem, the first section of this paper explain the factors that affect the outcome of ACL surgery.

2 Factors Affecting the Outcome of the ACL Reconstruction

Some of the factors that can alter the outcome of an ACL reconstruction are the graft selection, the tunnel location, the initial tension (or pre-tension) of the graft and the graft fixation type [4]. Details of each of these factors are presented below.

2.1 Graft Selection

During the last years a variety of autograft and allograft have been used in ACL reconstruction. Synthetic grafts have are being reported, but still with unsatisfactory results. For the e autograft, the *Bone patellar tendon bone* (BPTB) and the *semitendinosus and gracilis tendon grafts* (QSTG) are the most common. Although some surgeons also use the quadriceps tendon, at the time the autografts BPTB are being proclamed as the *gold standard* in ACL reconstruction.

2.2 Femoral and Tibial Tunnel Locations

The best location of the femoral tunnel is still a controversial subject, and has a profound effect on knee kinematics. Recently, many surgeons decided to change the position of the femoral tunnel to the zone corresponding to the 11 o'clock position, viewed from the sagittal plane of the right knee flexed to 90°, as seen in Fig. 1). However, biomechanical studies indicate that such location of the femoral tunnel might not provide a rotational stability of the knee, whereas a location closer to the 10 o'clock position would provide better results [5]. Besides that, it should be taken in account the sagittal plane of the tunnel [6], since in a review of ACL reconstruction surgeries, it has been found that a large percentage of tunnels were performed incorrectly in this plane [7]. It should also be noted that

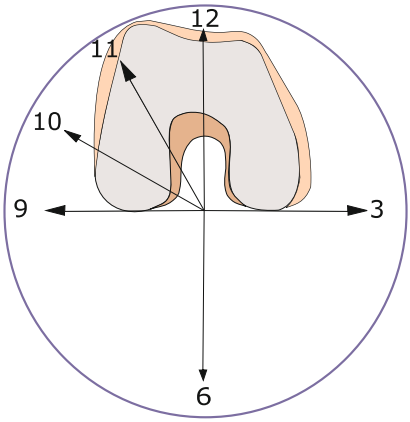

Fig. 1. Positions from 10 and 11 o'clock to the femoral tunnel in the right knee.

there is not a unique location of the tunnel the tunnel that produces a rotational stability of the knee close to that of an intact knee [5].

The position of the tibial tunnel is located in the native area of the LCA insertion. To assist in the positioning and orientation of the tunnel a device called the *Acuflex director* [8] is used, as shown in Fig. 2. This device has a guide tip, a horizontal arm and a guide pin where the drill enters.

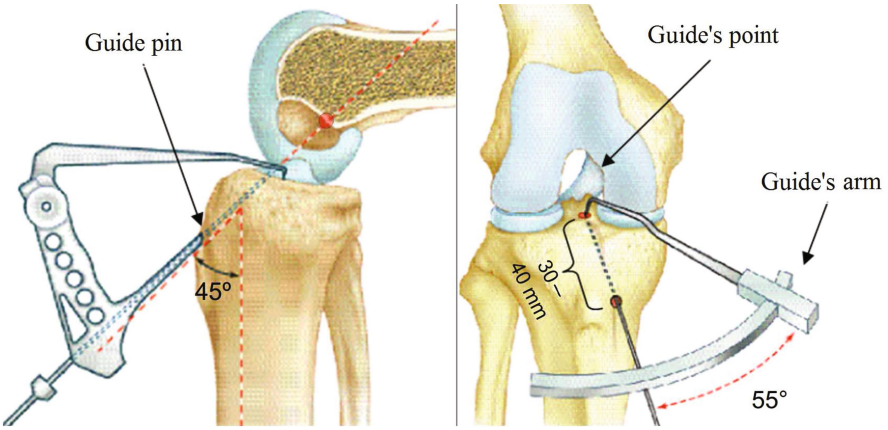

Fig. 2. Determination of position and orientation of the tibial tunnel using the *Acuflex director* instrument. Modified from [8]. (Color figure online)

The cannula guide pin is applied at a point between 30 to 40 mm below the lateral-medial axis of the joint, as shown in Fig. 2 (right), passing through the medial tibial tuberosity. The tip of the guide engages the posterior fibers of the

LCA insertion in the tibia. The tip of the guide should be located between 20 and 30 mm in the anterior direction, in relation to the earlier of the LCP fibers. The guide pin should be sagitally, oriented 45° relative to the longitudinal axis of the tibia as shown in Fig. 2 (left); and in the transverse plane it must care that the angle between the tibial tunnel and the horizontal arm of the guide is 55° [8] as shown in Fig. 2 (left).

If desired, the drilling operation for the femoral tunnel can be guided by the use of the tibial tunnel. The guide pin can be projected a few inches inside the joint with the purpose of marking the entry point of the femoral tunnel. An inspection by arthroscopy checks whether the tip of the guide pin is positioned correctly on the femur (red circle in Fig. 2 (left)). The tibial tunnel is made using a special milling cutter whose diameter must match the diameter of the graft.

2.3 Pretension of the Graft

Laboratory research has found that a graft pretension force of 88 N results in knees with movement restrictions, while a low pretension force equivalent of 44 N could be more convenient [9]. Studies related to tissue viscoelasticity reveal that the graft pretension decreases to a maximum 50% within a short time after fixation, due to the relaxation stress of internal tissue stresses [10]. Other surveys [11] evaluated pretension in the range of 20, 40, and 80 N, finding that the highest equivalent to 80 N produces great knee stability. Thus, the literature is still unclear in this subject, with the controversy remaining in the subject of graft pretension.

2.4 Type of Graft Fixation

In order to improve the functionality of the knee, and thus a rapid return to daily or sports activities, the resistance of implant fixation has increased, and a wide variety of devices are available for this purpose. In biomechanical terms, for grafts tendons with bone at one or both ends (quadriceps tendon, Achilles tendon, and BPTB), interference-type implants (Fig. 3) have been highly successful [12].

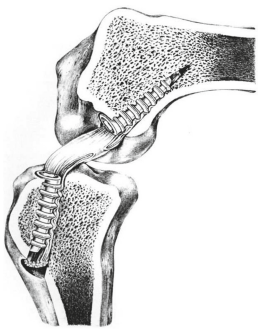

Fig. 3. Interference screws at knee joint [13].

Also available are the bioabsorbable screws, which according to Walton [14] have magnitudes of stiffness and maximum resistance comparable to the metal screws ones. The advantage of these bioabsorvable screws is that they do not need to be removed in case of revision or arthroplasty, nor for magnetic resonance imaging. Disadvantages include possible ruptures during the insertion process, inflammatory response of the patient, or inadequate fixation due to rapid degradation of the implant prior to incorporation of the graft into the femoral tunnel [4].

Another type of fixation is the so-called button fixation (Fig. 4), to attach the graft to the lateral femoral cortex (surface). Honl et al. [16] indicates that the rigidity of this type of fixation supports a force limit of 572 ± 105 N. The cross-pin technique (Fig. 5) is another fixation method that supports a 934 ± 296 threshold force [17].

In addition to considering this variety of fixation devices, it is very important to take into account the flexion angle of the knee at the time of fixation of the graft. It has been shown that full extension fixation of the knee helps to increase knee movement, while a fixation at 30 degrees of flexion, increases knee stability [19].

Other factors that may affect the outcome of ACL reconstruction are the movement of the graft in the tunnel and the healing of the graft and the tunnel [4].

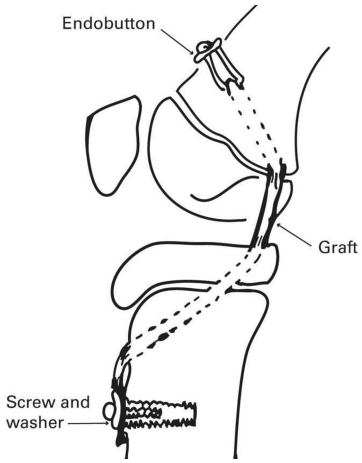

Fig. 4. Button fixation for anterior cruciate ligament reconstruction: *Endobutton* [15].

Considering the various factors that influence ACL surgery, it may be useful for orthopedists and surgeons to have a simulation tool that helps to know the best position of the ACL graft in the sagitall plane of the femur, subject still controversial.

In the sequence a clinical application of the knee model, presented in part A of this work, is developed. The model, simulations and results aiming to support the medical decision in the selection of the best insertion point of the ACL graft in the sagittal plane of the femur.

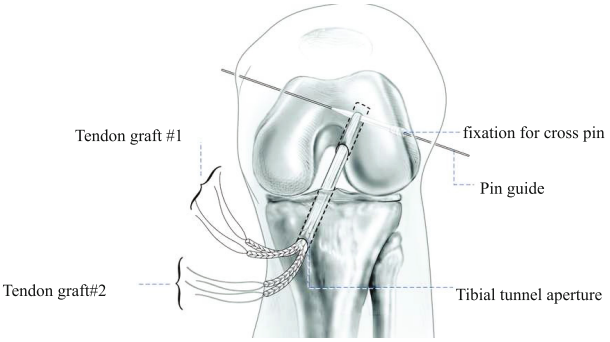

Fig. 5. Cross-pin fixation. Adapted from [18]

3 Method

The precise location of the insertion point of the graft is very important in the ACL reconstruction. The authors [1,3] presents an experimental procedure where the effects of small deviations in defining the insertion point is considered. In particular, the slip ratio was determined for eight different insertion points at the femur. Slip ratio is defined as the ratio between rolling and sliding movements when the femur is moving over the tibia along the knee flexion (Fig. 6).

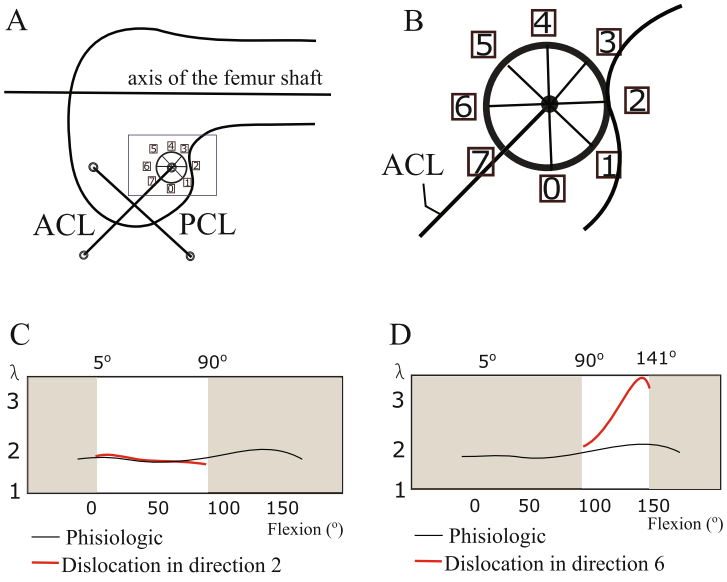

Fig. 6. ACL reconstruction geometry (panels A and B) and slip ratios for positions 2 and 4 (panels C and D) [1,3]. Positioning the graft in point 6 leads to severe injuries in tibia.

Repositioning the ACL graft into point 2 makes the obtained slip ratio similar to the physiological one. When the graft is repositioned to point 6, the slip ratio varies significantly and differs from the physiological.

If a surgery procedure is adjusted to point 6, the slip of the femur would be much larger than its slipping on/over the tibia, and therefore different parts of the femoral condyle would contact the same part of the tibial surface. This would lead to injuries to the tibia, and consequently, a need to repositioning the femur graft to point 2 in order to obtain a slip ratio much closer to the physiological one.

As an application of the method proposed at part A of this work, the *in situ* force for grafts settled at points 2 and 6 were analyzed and simulated taking the load conditions proposed in [2]. A radius r of 3 mm was considered, equivalent to one tenth of the total length of the modeled ACL. The insertion point (to be set at point 2 and 6) is described by the vector $\mathbf{s_{0A_i}}$, so the variation of its coordinates is equivalent to repositioning the insertion point (Eq. 1).

$$ {}^{f}\mathbf{S}_{0A_i} = -\mathbf{p} + {}^{B}R_A \mathbf{S}_{0A_i}, \quad (i = 1,\ldots,5) \tag{1} $$

where:

- ${}^{f}\mathbf{S}_{0A_i}$ is the point $\mathbf{S}_{0A_i}$ measured in relation to S_f;
- ${}^{B}R_A = [{}^{A}R_B]^{-1}$ is the matrix that describes the rotation of S_t relative to S_f;
- $\mathbf{p}$ is the position vector of (x, y, z) de S_t in relation to S_f.

4 Results

The results for the *in situ* force in the LCA due to anterior tibial load are showed at Fig. 7. There, the continue black line corresponds to the experimental *in situ* force obtained from an intact ligament fixed at natural insertion point [2].

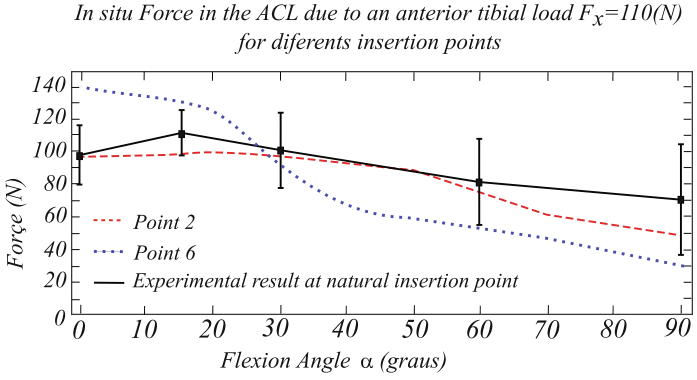

Fig. 7. *In situ* forces at the ACL graft relative to insertion points 2 and 6. The continuous line corresponds to experimental data of an intact ACL [2].

The segmented lines are the simulated results obtained in this work. The red segmented line is the simulated result of the *in situ* force from an ACL graft fixed at point 2 of the femur. The blue pointed line is the simulated result of the *in situ* force from an ACL graft settled at point 6 of the femur.

5 Conclusion

From the proposed method, the best achieved insertion point for the graft is point 2. This is in accordance to [1,3]. It is also shown that the obtained *in situ* force is closer to the response when the graft is repositioned to point 2 (dashed line in Fig. 5.30). It is also shown that this force diverges from the physiological one when the insertion point is located at point 6 (dotted line in Fig. 5.30). The continuous line corresponds to an intact ACL knee obtained by [2]. Important to note that [1,3] obtained its results based on the slip ratio criteria. The presented methodology achieved the same best insertion point based in the *in situ* ACL force.

References

1. Zatsiorsky, V.: Kinematics of human motion. In: Human Kinetics, pp. 244–246 (1998)
2. Woo, S., Fox, R., Sakane, M., Livesay, G., Rudy, T., Fu, F.: Biomechanics of the ACL: measurements of in situ force in the ACL and knee kinematics. The Knee **5**(4), 267–288 (1998). Elsevier
3. Thoma, W., Jaguer, A., Schreiber, S.: Kinematic analyses of the knee joint with regard to the load transfer on the cartilage. In: Clinical Biomechanics and Related Research, pp. 96–102. Springer, Tokyo (1994)
4. Woo, S.L.Y., Wu, C., Dede, O., Vercillo, F., Noorani, S.: Biomechanics and anterior cruciate ligament reconstruction. J. Orthop. Surg. Res. 1–9 (2006)
5. Loh, J., Fukuda, Y., Tsuda, E., Steadman, R., Fu, F., Woo, S.: Knee stability and graft function following anterior cruciate ligament reconstruction: comparison between 11 o'clock and 10 o'clock femoral tunnel placement. Arthroscopy J. Arthroscopic Relat. Surg **19**(3), 297–304 (2003). Elsevier
6. Bernard, M., Hertel, P., Hornung, H., Cierpinski, T.: Femoral insertion of the ACL. Radiographic quadrant method. Am. J. Knee Surg. **10**(1), 14–21 (1997)
7. Sommer, C., Friederich, N., Muller, W.: Improperly placed anterior cruciate ligament grafts: correlation between radiological parameters and clinical results. Knee Surg. Sports Traumatol. Arthroscopy **8**(4), 207–213 (2000). Springer
8. Plaweski, S.: Technique of anterior cruciate ligament reconstruction using pes anserinus tendons. Maitrice orthopedique. n. 95 (2009). http://www.maitrise-orthopedique.com/articles/technique-de-reconstruction-du-ligament-croise-anterieur-par-les-tendons-de-la-patte-doie-345. Accessed 06 June 2017
9. Mae, T., Shino, K., Miyama, T., Shinjo, H., Ochi, T., Yoshikawa, H., Fujie, H.: Single-versus two-femoral socket anterior cruciate ligament reconstruction technique. Arthroscopy J. Arthroscopic Relat. Surg. **17**(7), 708–716 (2001). Elsevier

10. Boylan, D., Greis, P., West, J., Bachus, K., Burks, R.: Effects of initial graft tension on knee stability after anterior cruciate ligament reconstruction using hamstring tendons: a cadaver study. Arthroscopy J. Arthroscopic Relat. Surg. **19**(7), 700–705 (2003). Elsevier
11. Yasuda, K., Tsujino, J., Tanabe, Y., Kaneda, K.: Effects of initial graft tension on clinical outcome after anterior cruciate ligament reconstruction. Am. J. Sports Med. Am. Orthopaed. Soc. Sports Med. **25**(1), 99–106 (1997)
12. Lambert, K.: Vascularized patellar tendon graft with rigid internal fixation for anterior cruciate ligament insufficiency. Clin. Orthop. Relat. Res. **172**, 85–89 (1983)
13. Weiler, A., Peine, R., Pashmineh-Azar, A., Abel, C., Sudkamp, N.P., Hoffmann, R.F.: Tendon healing in a bone tunnel. Part I: biomechanical results after biodegradable interference fit fixation in a model of anterior cruciate ligament reconstruction in sheep. Arthroscopy J. Arthroscopic Relat. Surg. **18**(2), 113–123 (2002)
14. Walton, M.: Absorbable and metal interference screws: comparison of graft security during healing. Arthroscopy J. Arthroscopic Relat. Surg. **15**(8), 818–826 (1999). Elsevier
15. Liddle, A.D., Imbuldeniya, A.M., Hunt, D.M.: Transphyseal reconstruction of the anterior cruciate ligament in prepubescent children. Bone Joint J. **90**(10), 1317–1322 (2008)
16. Honl, M., Carrero, V., Hille, E., Schneider, E., Morlock, M.: Bone-patellar tendon-bone grafts for anterior cruciate ligament reconstruction an in vitro comparison of mechanical behavior under failure tensile loading and cyclic submaximal tensile loading. Am. J. Sports Med. **30**(4), 549–557 (2002)
17. Brown, C.H., Wilson, D.R., Hecker, A.T., Ferragamo, M.: Graft-bone motion and tensile properties of hamstring and patellar tendon anterior cruciate ligament femoral graft fixation under cyclic loading. Arthroscopy J. Arthroscopic Relat. Surg. **20**(9), 922–935 (2004)
18. Williams, R.J., Hyman, J., Petrigliano, F., Rozental, T., Wickiewicz, T.: Anterior cruciate ligament reconstruction with a four-strand hamstring tendon autograft. J. Bone Joint Surg. (Am.) **86**(2), 51–66 (2005)
19. Asahina, S., Muneta, T., Ishibashi, T., Yamamoto, H.: Effects of knee flexion angle at graft fixation on the outcome of anterior cruciate ligament reconstruction. Arthroscopy J. Arthroscopic Relat. Surg. **12**(1), 70–75 (1996). Elsevier

On the Kinematics of an Innovative Spherical Parallel Robot for Shoulder Rehabilitation

N. Plitea[1(✉)], C. Vaida[1], G. Carbone[2], A. Pisla[1], I. Ulinici[1], and D. Pisla[1]

[1] CESTER, Technical University of Cluj-Napoca, Cluj-Napoca, Romania
{Nicolae.Plitea, Calin.Vaida, Ionut.Ulinici, Doina.Pisla}@mep.utcluj.ro, adrian.pisla@muri.utcluj.ro
[2] University of Cassino and South Latium, Cassino, Italy
carbone@unicas.it

Abstract. Robotic rehabilitation for post-stroke patients is an on-growing field of research aiming to provide personalized care with maximum therapeutic effects. This paper presents a simple but effective solution for shoulder rehabilitation. It is based on the design of a novel spherical parallel robot, whose name is ASPIRE. Kinematics and workspace are analysed as well as motion simulations are thoroughly presented to show the feasibility and effectiveness of the proposed solution.

Keywords: Kinematics · Spherical parallel robot · Workspace · Post-stroke rehabilitation

1 Introduction

Surviving patients that have suffered from an ischemic stroke can undergo lengthy and rigorous rehabilitation procedures to help them reintegrate into society. Nowadays, due to the continuous grows of the ageing population the stroke incidents increase each year to numbers that are impossible to manage with the existing physical therapists [8]. In the past decade, researchers have been proposing to improve post-stroke rehabilitation by using specific robotic devices. Robotic devices provide some major advantages when compared to human specialists, robots do not get tired as opposed to their human counterparts. Also they have the advantage of repeating the same motion a countless number of times with the same precision, and they allow therapists to work with more patients at a time.

An important aspect to be taken into consideration in the development of a robotic rehabilitation device is the alignment of the human and robotic joints (mostly in the form of rotation joints). A spherical parallel mechanism (SPM) seems to represent an easy to adapt architecture for the purpose as it uses only rotational joints which are characterized by the intersection of the joint axes in a single point. Several devices that use the SPM structure are already in development. A device intended for the rehabilitation of the human ankle joint, based on the Agile Eye [7] (intended for the motion of lightweight cameras), the PKAnkle [9] prototype is currently being developed by CNR-ITIA.

J.C.M. Carvalho et al. (eds.), *Multibody Mechatronic Systems*,
Mechanisms and Machine Science 54, DOI 10.1007/978-3-319-67567-1_44

Typical disadvantages for parallel robots come in the form of a reduced and anisotropic workspace, a more complex kinematic calibration, and matters related to the management of the controller, and all of this can be traced to the elevated nonlinearity of the kinematic problem solution [2]. When it comes to performance indices for parallel manipulators, several have been defined. A manipulability index based on the Jacobian matrix was developed by Yoshikawa [14], as kinematic accuracy, a dexterity index was presented by Salisbury and Craig [11], where dexterity was defined as the condition number of the Jacobian matrix of the robot, this was in turn distributed in the whole workspace resulting in the GCI (Global Conditioning index) developed by Gosselin [7], furthermore a kinematic sensitivity index was presented by Cardou [5]. Thus kinematic optimization can provide the largest workspace, fewest singularities, and highest stiffness [8]. Stiffness aspects are also addressed in [4].

The aim of the paper is to present a simple yet efficient solution for the rehabilitation of the shoulder which is suitable for a wide variety of Human-robot interactions: active, passive, passive mirrored, resistive and path guidance. The modular design enables the addition of supplementary modules which can be used for the other joints of the upper limb. The kinematic model, workspace analysis and some simulations illustrate the motions capability of the proposed innovative solution.

2 Key Facts on Robotic Rehabilitation

An overview of existing robotic solutions for rehabilitation of the upper limb has pointed out some general recommendations for new robotic devices [1, 13]:

- from a medical standpoint, to recuperate a stroke affected limb, attention must be headed towards both proximal and distal joints, in order to obtain a real improvement of the patients' movement functions, in regard to his daily activities (activities of daily living- ADL);
- the robotic system must integrate in its structure the human and a multiple entrances for the command system. Thereby, the first correlation refers to the coordinate systems. A human coordinate system is presented in Fig. 1(a), generated by the intersection of 3 orthogonal planes. The robot coordinate system (Fig. 2(b)) should refer to the human plane system, in order to establish a link between the human subject and the robot. Thereby, for an easy modeling of the kinematic equations, a simple solution is to maintain the axes parallel to each other, which means that the transformation is requiring only translation components.

2.1 Shoulder Rehabilitation

Regarding the motions, the shoulder flexion/extension and abduction/adduction are necessary during the rehabilitation process, as illustrated in Fig. 2, where the amplitude measurements have been taken on a number of 21 patients with ages ranging between 43 and 83 years old [9]. These measurements have been taken on relatively healthy subjects, therefore to adapt the system to a patient that would have reduced sensory and

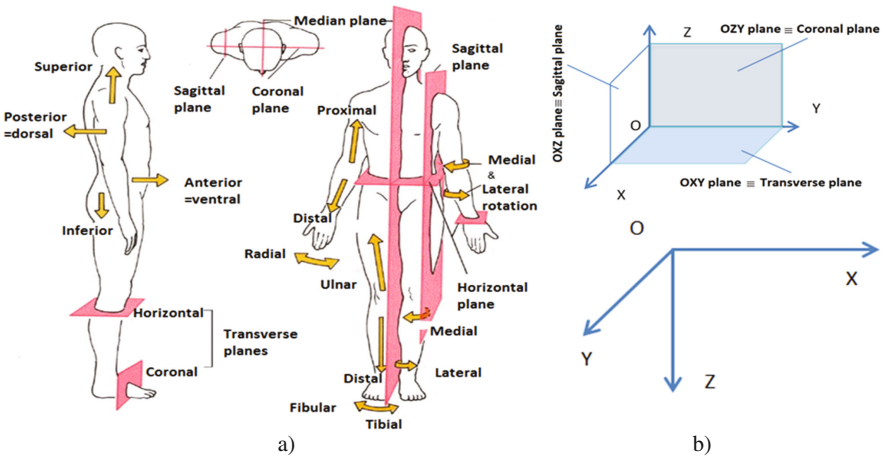

Fig. 1. (a) Reference planes of the human body, detailed representation [6], (b) Possible coordinate systems of the robotic device and the correspondence to the human planes

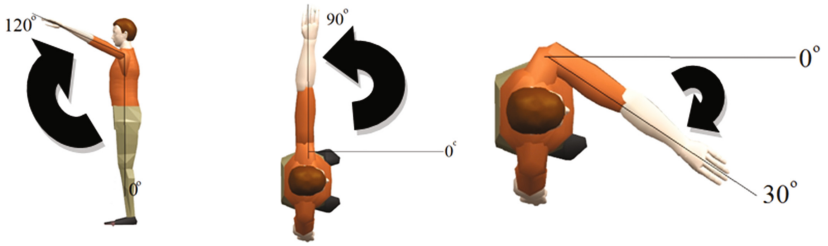

Fig. 2. Shoulder motions reproduced on a human model [3].

motor capabilities in the upper limb, the maximum angular amplitudes that the robot system has to achieve were adapted accordingly.

Figure 3 illustrates the main motions at the level of the shoulder, in a detailed way, where it can be seen that the upper limb motion at the level of the shoulder joint can be easily associated with a spherical motion. Referring to the main motions that have to be achieved, a simple way to describe them illustrate that flexion/extension is a motion performed in a horizontal plane, while abduction/adduction is performed in a vertical plane. Thus, a simple way to replicate these two motions can be to develop a spherical mechanism which uses as center of rotation the shoulder joint and allows the simple generation of the two motions of interest. Furthermore, as shown in [1] more advanced training stages, where the patient has already gained some control of the arm, impose the generation of complex motions that would replicate upper limb motions that are used in ADL, where a spherical device would have basically no limitations in fulfilling these requirements.

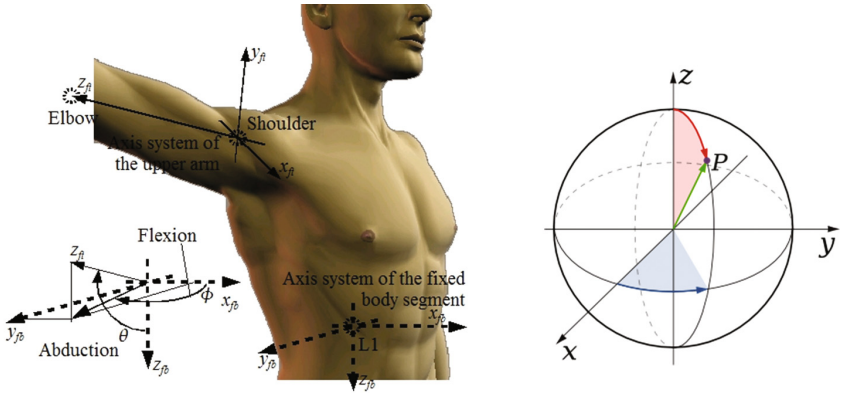

Fig. 3. Shoulder joint and the main motions

3 A Spherical Parallel Robot for Shoulder Rehabilitation

With respect to the general motion requirements presented in Sect. 2.1, a simple but very effective concept mechanism is proposed as a robotic device for the shoulder rehabilitation, whose name is ASPIRE is illustrated in Fig. 4 [10].

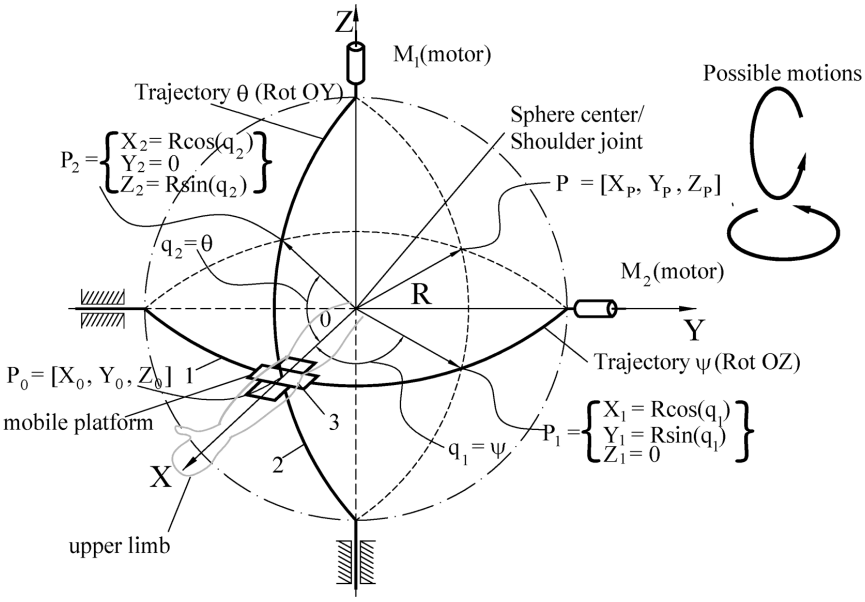

Fig. 4. Kinematic scheme of the spherical mechanism for shoulder rehabilitation.

According to its structure, the mechanism allows a generalized movement on the sphere surface, which enlarges the universality degree of the solution and enables the

definition of a wide range of exercises, having various amplitudes within a unconstrained working volume, including both simple and combined movements, which increase the shoulder mobility through interactive trajectories. The main advantages of this structure are the simple concept, wide range of motions, modular design which allows the addition of other modules and simple attachment to the patient shoulder. As drawback one can mention the size of the spherical guides but this has no effect on the medical task completion.

The spherical mechanism, ASPIRE, with radius R has two spherical guides, 1 and 2, actuated by the M1 and M2 motors that determine the position of the mobile platform, the arm guiding element, 3, which moves along the two guides. This mechanism has 3 mobile elements and 4 rotation joints, two of which belong to the mobile element. The two guides determine the basic motions of the element 3: trajectory ψ – a rotation around the OZ axis that defines the basic horizontal motion and trajectory θ – a rotation around the OY axis that defines the basic vertical motion. The ASPIRE mobility degree is calculated using the formula defined by Plitea, derived from Grubler's criterion [12]:

$$M = (6 - F) \cdot N - \sum_{i=1\ldots5} (i - F) \cdot C_i \tag{1}$$

Where: M – represent the parallel mechanism' degree of mobility; F – represents the family of the mechanism; N – represents the number of mobile elements; C_i – the number of class "i" joints, where "i" represents the number of suppressed degrees of freedom.

The family of the mechanism is defined as: the number of imposed restrictions for a degree of liberty common to all the elements of the mechanism. For the spherical mechanism, the analysis of the possible restrictions and movements for each element of the mechanism show that F = 4. The number of mobile elements, N = 3 and the number of class 5 joints is $C_5 = 4$ Using Eq. (1), it results:

$$M = (6 - 4) \cdot 3 - (5 - 4) \cdot C_5 = 6 - 4 = 2 \tag{2}$$

Based on the kinematic scheme from Fig. 4, for the inverse kinematics of the spherical robot, the input data is represented by the two angles, ψ and θ. In addition, the robot has one important geometric parameter, the radius of the sphere (R) which, based on the anthropometric data of the human body was established at R = 350 mm which fits persons with a height between 165 cm and 185 cm. Depending on the patient data several radius values will be used to fit variable anthropometric data, that will be determined through experimental measurements.

The robot motion can be described using two rotation matrices, R1 – rotation around OZ axis with the angle ψ and R2 – rotation around the OY axis with the angle θ. Defining also the geometric coordinates of the sphere center O (0, 0, 0) and the initial position of the human arm:

$$P_0 = [R \quad 0 \quad 0] \tag{3}$$

The generalized coordinates of a point P on the sphere, is calculated as follows:

$$\begin{bmatrix} X_P \\ Y_P \\ Z_P \end{bmatrix} = \begin{bmatrix} \cos(\psi) & -\sin(\psi) & 0 \\ \sin(\psi) & \cos(\psi) & 0 \\ 0 & 0 & 1 \end{bmatrix} \cdot \begin{bmatrix} \cos(\theta) & 0 & \sin(\theta) \\ 0 & 1 & 0 \\ -\sin(\theta) & 0 & \cos(\theta) \end{bmatrix} \cdot \begin{bmatrix} R \\ 0 \\ 0 \end{bmatrix} \tag{4}$$

Thus, the coordinates of point P, are:

$$\begin{cases} X_P = R \cdot \cos(\psi) \cdot \cos(\theta) \\ Y_P = R \cdot \cos(\theta) \cdot \sin(\psi) \\ Z_P = -R \cdot \sin(\theta) \end{cases} \tag{5}$$

which respect, of course, the condition:

$$X_P^2 + Y_P^2 + Z_P^2 = R^2 \tag{6}$$

Using the coordinates of the point P the active joints q_1(flexion-extension) and q_2(abduction-adduction) are:

$$\begin{cases} q_1 = \text{atan2}(Y_P, X_P) \\ q_2 = \text{atan2}\left(-Z_P, \frac{X_P}{\cos(q_1)}\right) \end{cases} \tag{7}$$

The Eq. (7), expressed in spherical coordinates will lead, to the trivial expressions:

$$\begin{cases} q_1 = \psi \\ q_2 = \theta \end{cases} \tag{8}$$

Based on the Eq. (8) the closure equations can be written in a simple form leading to very simplex expressions of the Jacobi matrices, which point out the direct correspondence between the angles which define the basic motions of the human arm around the shoulder wrist (ψ – horizontal rotation, θ – vertical rotation):

$$\begin{cases} f_1 : q_1 - \psi = 0 \\ f_2 : q_2 - \theta = 0 \end{cases} \Rightarrow A = \begin{bmatrix} -1 & 0 \\ 0 & -1 \end{bmatrix};\ B = \begin{bmatrix} 1 & 0 \\ 0 & 1 \end{bmatrix} \tag{9}$$

Analyzing Eq. (9) it can be easily seen that the mechanism has no singularities and that the identities are preserved for both speeds and accelerations:

$$\begin{cases} q_1 = \psi,\ \dot{q}_1 = \dot{\psi}, \ddot{q}_1 = \ddot{\psi} \\ q_2 = \theta, \dot{q}_2 = \dot{\theta}, \ddot{q}_2 = \ddot{\theta} \end{cases} \tag{10}$$

The analytical workspace of the robot is presented in Fig. 5, where the range of motions for the angles ψ and θ are:

$$\begin{cases} \psi \in (-80^\circ : 80^\circ) \\ \theta \in (-80^\circ : 80^\circ) \end{cases} \tag{11}$$

These values have been selected to describe the maximum range of motions that the mechanism can develop. Also, due to the construction of the mechanism, each simple motion can be performed for different fixed values of the opposite angle (Fig. 5a). By varying in the same the both angles the total workspace of the ASPIRE spherical robot is obtained (Fig. 5b).

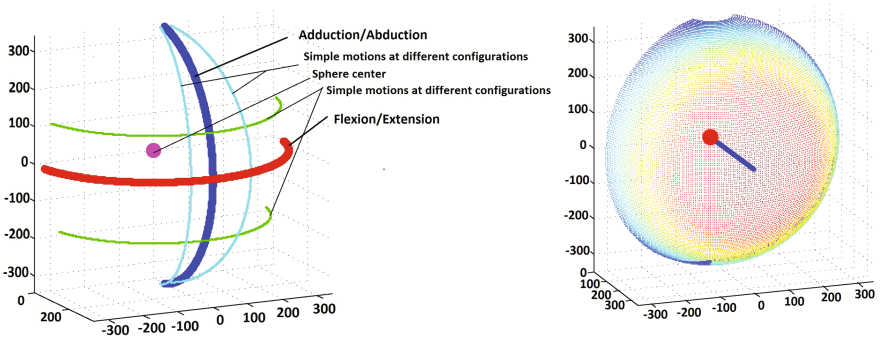

a) sample motion path b) full robot workspace

Fig. 5. The analytic workspace of ASPIRE spherical robot

4 Kinematic Motion Simulations

Having the kinematic model of the ASPIRE robot, some motion simulations have been achieved. The particularity of the motion for this robot is the fact that the point P is constrained to move on a sphere. In the example a general motion is considered with variation at the level of both angles ψ and θ chosen randomly within robot workspace constrictions. Thus, the initial and final values for the two angles are defined as

$$\begin{cases} \psi_i = -15^\circ \\ \theta_i = 0^\circ \end{cases}; \begin{cases} \psi_f = 40^\circ \\ \theta_f = -30^\circ \end{cases} \tag{12}$$

The angular speed and acceleration at the level of upper limb are:

$$\omega = 10^\circ/\mathrm{s}; \quad \varepsilon = 5^\circ/\mathrm{s}^2 \tag{13}$$

In order to compute the angle and the arc length on the sphere, the following relations are defined as

$$\begin{cases} DX = \cos(\theta_f) \cdot \cos(\psi_f) - \cos(\theta_i) \cdot \cos(\psi_i) \\ DY = \cos(\theta_f) \cdot \sin(\psi_f) - \cos(\theta_i) \cdot \sin(\psi_i) \\ DZ = \sin(\theta_f) - \sin(\theta_0) \end{cases} \tag{14}$$

Using Eq. (14) the central angle on the sphere and its length can be computed as

$$\begin{cases} \alpha = 2 \cdot \operatorname{asin}\left(\frac{\sqrt{DX^2 + DY^2 + DZ^2}}{2}\right) \\ l_\alpha = R \cdot \alpha \end{cases} \tag{15}$$

The motion time is computed based on the angle and imposed maximum speed and acceleration. Imposing a trapezoidal profile for the speed, the motion times are (t1 – acceleration time, t2 – motion time until deceleration, t3 – full motion):

$$t_1 = \frac{\omega}{\varepsilon}; \quad t_2 = \frac{|\alpha|}{\omega}; \quad t_3 = \frac{|\alpha|}{\omega} + \frac{\omega}{\varepsilon} \tag{16}$$

Using Eq. (14) the individual angular accelerations can be computed as

$$\varepsilon_\psi = \frac{2 \cdot (\psi_f - \psi_i)}{2 \cdot t_1 \cdot t_3 - t_1^2 - (t_3 - t_2)^2}; \quad \varepsilon_\theta = \frac{2 \cdot (\theta_f - \theta_i)}{2 \cdot t_1 \cdot t_3 - t_1^2 - (t_3 - t_2)^2} \tag{17}$$

Having this data, the simulation results are presented in Fig. 6.

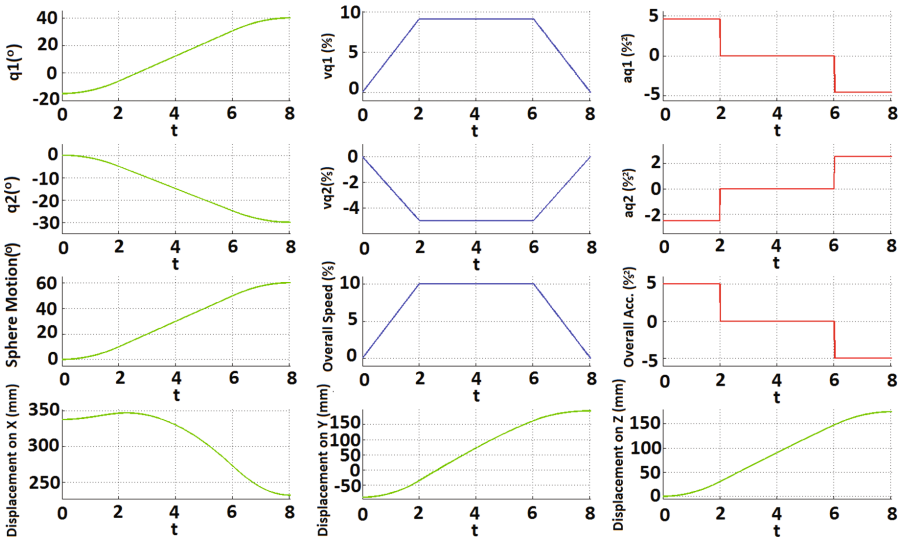

Fig. 6. Motion simulation of the ASPIRE robot

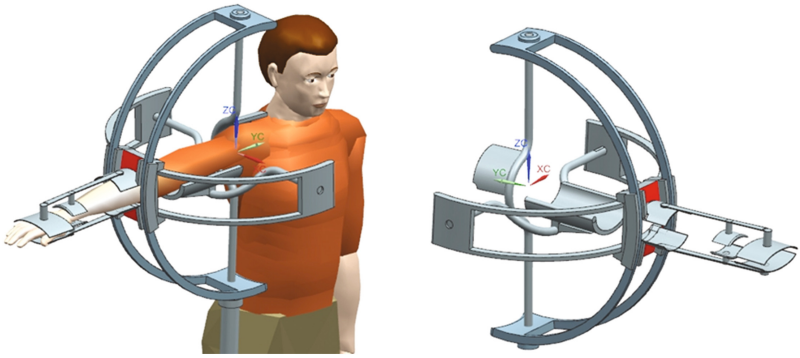

Fig. 7. 3D CAD model of the ASPIRE robot

The initial design of ASPIRE robot, where an anatomically correct human body has also been used is presented in Fig. 7. The robot introduces the following motion particularities (Fig. 7):

- the center of the sphere is positioned in the shoulder articulation;
- the mechanism utilizes a set of spherical guides, which have the rotation center in the sphere center;
- the two guiding platforms have spherical and cylindrical contact surfaces;
- similarly, the platform has spherical movement surfaces and cylindrical guiding elements.

5 Conclusions

Robotic assisted rehabilitation is a field of research which is becoming unavoidable due to the demographic changes in average life expectancy. Accordingly, this paper proposes a robotic shoulder rehabilitation device as based on a novel spherical robotic system called ASPIRE. It combines a simple kinematic architecture with a large motion range for a shoulder joint. The robot workspace analysis and a motion simulation illustrate the robot performance for shoulder rehabilitation. As future work, a detailed design analysis will be performed, to identify the interactions of the spherical joints with the human body as well as dynamic effects also from experimental viewpoint.

Acknowledgments. The paper presents results from the research activities of the project ID 37_215, MySMIS code 103415 "Innovative approaches regarding the rehabilitation and assistive robotics for healthy ageing" cofinanced by the European Regional Development Fund through the Competitiveness' Operational Programme 2014–2020, Priority Axis 1, Action 1.1.4, through the financing contract 20/01.09.2016, between the Technical University of Cluj-Napoca and ANCSI as Intermediary Organism in the name and for the Ministry of European Funds.

References

1. Basteris, A., et al.: Training modalities in robot-mediated upper limb rehabilitation in stroke: a framework for classification based on a systematic review. J. NeuroEng. Rehab. **11**(111), 15 (2014)
2. Cappa, P., Jackson, J.L., Fabrizio, P.: Moment measurement accuracy of a parallel spherical robot for dynamic posturography. IEEE Trans. Biomed. Eng. **57**(5), 1198–1208 (2010)
3. Carbone, G., Marco, C., Gherman, B., Ulinici, I., Vaida, C., Pisla, D.: Design issues for an inherently safe robotic rehabilitation device. In: Robotics in Alpe Andria Danube Region, RAAD 2017 (in print)
4. Carbone, G.: Stiffness analysis and experimental validation of robotic systems. Front. Mech. Eng. **6**(2), 182–196 (2011)
5. Cardou, P., Bouchard, S., Gosselin, C.: Kinematic-sensitivity indices for dimensionally on homogenous Jacobian matrices. IEEE Trans. Robot. **26**(1), 166–173 (2010)
6. Free diagrams of the human body (2014). https://ro.pinterest.com/pin/324400597929092O9/
7. Gosselin, C., Pierre, E.S., Gagne, M.: On the development of the agile eye. Rob. Aut. Mag. **3** (4), 29–37 (1996). IEEE
8. Kucuka, S., Bingul, Z.: Comparative study of performance indices for fundamental robot manipulators. Robot. Auton. Syst. **54**, 567–573 (2006)
9. Major, K.A., Major, Z.Z., Carbone, G., Pisla, A., Vaida, C., Gherman, B., Pisla, D.L.: Ranges of motion as basis for robot-assisted post-stroke rehabilitation. HVM Bioflux **8**(4), 192–196 (2016)
10. Vaida, C., Plitea, N., Pisla, D., Carbone, G., Gherman, B., Ulinici, I.: Spherical mechanism for upper limb proximal segments rehabilitation, Patent application N.A00374/14.06.2017
11. Salisbury, J.K., Craig, J.J.: Articulated hands: force control and kinematic issues. Int. J. Robot. Res. **1**(1), 4–17 (1982)
12. Tsai, L.W.: Robot Analysis: the Mechanics of Serial and Parallel Manipulators. Wiley, Hoboken (1999)
13. Vaida, C., et al.: On human robot interaction modalities in the upper limb rehabilitation after stroke. Acta Tehnica Napocensis **60**(1) (2017)
14. Yoshikawa, T.: Manipulability of robotic Mechanisms. Int. J. Robot. Res. **4**(2), 3–9 (1985)

Automatic Elevation System of a Wheelchair

Sergio Yoshinobu Araki[1(✉)], Pâmela Florentino[1], Eduardo Bock[1], Michele Saito[1], Mariana Hernandes[1], Luciano Fuentes[1], Isac Fujita[1], Rodrigo Stoeterau[2], Daniel Martins[3], and Antônio Celso Fonseca de Arruda[4]

[1] Laboratory of Biomaterials and Bioengineering, Federal Institute of Technology of Sao Paulo, IFSP, Sao Paulo, Brazil
araki.sergio@yahoo.com.br, pamela-florentino@hotmail.com, eduardo_bock@gmail.com, saito.mi@hotmail.com, marianahernandes@gmail.com, lucianofleo@ig.com.br, ikfujita@gmail.com

[2] Laboratory of Surface Phenomena, Sao Paulo University, USP, Sao Paulo, Brazil
rodrigo.stoeterau@usp.br

[3] Federal University of Santa Catarina, UFSC, Florianopolis, Brazil
daniel.martins@ufsc.br

[4] Faculty of Mechanical Engineering, Campinas State University, UNICAMP, Campinas, Brazil
celso@fem.unicamp.br

Abstract. Assistive Technology is an area of knowledge, with an interdisciplinary characteristic that encompasses products, resources, methodologies, strategies, practices and services that aim to promote functionality related to the activity and participation of people with disabilities, disabilities or reduced mobility, independence, quality of life and social inclusion. The wheelchair faces a number of obstacles along its journey and a variety of mobility restrictions, such as a wheelchair that allows the user to access objects that are outside their specific range The vertical position with greater ease, also provide greater comfort during a dialogue with other people and also facilitate their placement and removal of the chair with the help of relatives or nurses in their residence or hospitals. This work aims to adapt a common wheelchair, with an automatic vertical lift system in its seat, which allows the user to have a height equivalent to the average human height, standing in a vertical position (standing position). Simple mechanism with electric control, which is easy to maintain and low cost, making it accessible to all social classes.

Keywords: Wheelchair lift · Low cost · Ease · Comfort

1 Introduction

In order to increase the quality of life of disabled people, several research fields, therapies, products and new technologies have been created and promoted [1–6].

J.C.M. Carvalho et al. (eds.), *Multibody Mechatronic Systems*,
Mechanisms and Machine Science 54, DOI 10.1007/978-3-319-67567-1_45

Multiple campaigns have been developed in many parts of the world, seeking to draw attention to the minimum accessibility that affects greatly how people who use wheelchairs [2].

Other efforts have been continually developed and need to be supported at all times. The wheelchair consists of a chair that has wheels in place of the legs. It was invented in order to help people who have some kind of disability that prevents them from getting around [3].

Even with all technological innovations, there are limitations and needs that have not yet been met, such as helping the user reach objects in higher places. With an attempt to solve this, they created an orthostatic wheelchair (Fig. 1). This has a system in which the seat and the backrest move in alignment, placing the user in an upright position, as if standing. However, the use of this benefit is cumbersome and uncomfortable, since it requires the user to use two safety items: the support for the knees and the belt or chest, and has a restriction: the disabled with the legs amputated could not use it [4].

Fig. 1. Orthostatic Chair

A chair with gyroscopic technology has also been developed, Fig. 2, which allows the chair to swing and run on only two of its four wheels, thus raising the user to a height comparable to an upright person. It also incorporates features of climbing ladders and maneuvers on all four wheels. However, they are limited to certain types of users, not covered by most insurance plans, and are very costly [5, 6].

Fig. 2. Gyroscopic Chair

However, the seat elevation system is more comfortable, it does not need to adapt any type of safety item, it still allows the use by people who have legs amputated and is very affordable financially speaking.

Several researches are carried out in order to increase the quality of life of disabled people. This created the wheelchairs, a chair mounted on wheels that can be moved manually or electrically by the occupant or pushed by someone. A basic wheelchair has a seat and a backrest; two small (caster) front wheels and two large wheels, one on each side and a foot rest.

The wheelchair with lifting system is formed by a "mechanical Car Jack", coupled to the seat of the chair, and driven by an electric motor that moves vertically the same. The purpose of this system is to allow the wheelchair user to access objects that are beyond their vertical range with greater ease and provide greater comfort when talking to other people, behind the counter or any other obstacle that makes it difficult the visual contact between them, making them more independent.

1.1 Percentage of Physical Deficient Research

On October 11, the Day of the Disabled is celebrated. This is an important date for nine million Brazilian citizens, their families, friends and society. On this day, the Association for Assistance to the Disabled Child (AACD) warns about the need to prevent diseases and accidents that cause paraplegia and tetraplegia and stresses the importance of social inclusion [7].

Specialized in the treatment and recovery of people with physical disabilities for more than 62 years, the AACD says that prevention can contribute to reduce the percentage of paraplegic or quadriplegic Brazilians, or with some type of paralysis. Prevention is twofold: avoiding accidents (from cars, with guns, falls and dips) that cause traumatic injuries, and diseases that can lead to disability, such as myelomeningocele, which can be prevented by taking folic acid. In this regard, AACD is commemorating the fact that it has succeeded in approving the law, already in force, making it compulsory to add the product to all flours produced and marketed in the country.

As for the traumatic accidents, the data are more worrisome. According to a survey by the AACD's Bone Marrow Clinic, 77.4% of the disabled treated by the institution acquired the problem due to car accidents, firearms and falls. The AACD Spinal Cord Injury Clinic also reveals that 43.6% of its patients suffered injuries due to firearms accidents. Statistical data from the last three years also show that 83.5% of the patients are male and 68.3% are paraplegic.

According to data from the last National Health Survey (PNS) [7], there are in Brazil about 12.4 million people with disabilities (PPD). In this scenario, the PNS estimates that 1.3% of the Brazilian population has some type of physical disability; 0.3% of the population was born with physical disability, while 1.0% acquired as a result of illness or accident.

The disability question is the only one that, by law, has to be included in the census questionnaire. The subject was included in the 1991 Census questionnaire by virtue of Law 7,853 of 1989, after pressure from entities representing persons with disabilities [8–12].

2 Methodology and Materials

2.1 Mechanical Design Development

In the following, step-by-step photos of changing the basic wheelchair to an automatic lift system are presented in Fig. 3 showing design of the proposed design for the wheelchair lift system.

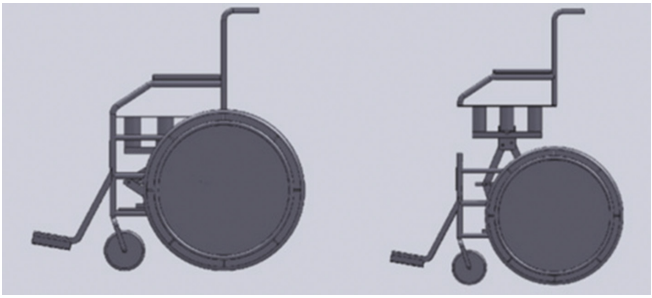

Fig. 3. Positions of wheelchair

Initially the cut of the structure of the simple wheelchair was made, to begin the automation project [9, 12].

2.2 Description of the Lifting System

The design consists of a tubular wheelchair, according to Fig. 4, by a DC electric motor, according to Fig. 5, by the lifting system "known as a Car Jack" and Micro Swift up and down controllers [10, 12].

Fig. 4. Simple Wheelchair Tubular

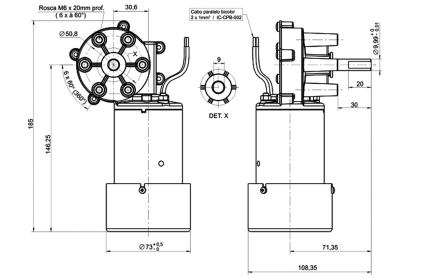

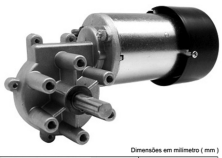

Controladores recomendados: CVE 2002 ou CVE 8701 — Dimensões em milímetro (mm)

MODEL	VOLTS	S / CARGA		Maximum Efficiency					Torque Locked
	V	RPM	A	RPM	A	TORQUE kgf cm	POTENCIA W/ CONSUMO	POTENCIA W/ ENTREGA	
MR 110 VE / VER - 25	24	25	0,4	15	0,8	30	19	5	100
MR 110 VE / VER - 45	24	45	0,6	30	1,6	42	38	13	130
MR 110 VE / VER - 60	24	60	0,89	45	2,2	41	53	18	182
MR 110 VE / VER - 120	24	120	1,5	105	4,2	28	100	30	197
MR 110 VE / VER - 240	24	240	1,5	210	4,2	14	100	30	88

Fig. 5. Lift Motor

The Car Jack system that was purchased has a lifting load of 800 kg, much higher than the load to be driven, which was calculated as an average of 100 kg. Hoisting Car Jack for the wheelchair lift system, according to Fig. 6.

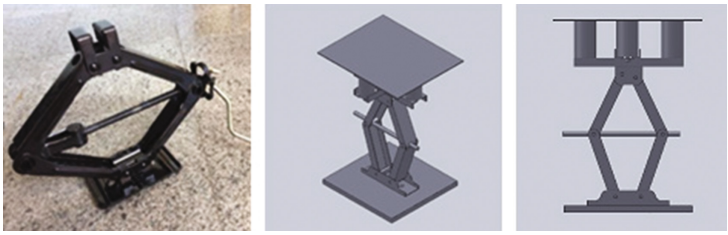

Fig. 6. Lift System Car Jack

Micro Switch to control the maximum and minimum displacement of the Car Jack in the lifting system, according to Fig. 7.

Fig. 7. Micro Switch Up and Down Controller

2.3 Components and Materials

Selections were based on the identified list of criteria. Wheelchairs considered manual, have a great variation of prices, depending on the material to be made and its finish, its variation can occur from US$110 to the simplest of folding steel, reaching US$645 of aluminum with backrest and seat base with leather and cushion.

Motorized wheelchairs also have a large variation of their price, depending on the accessories that accompany their price, ranging from US$2300 to US$3900.

The sport wheelchairs, are specific by the modality that the wheelchair will practice, its price ranges from US$900 to US$1650 [12].

2.4 Cost Analysis

The price of a wheelchair Orthostatic is in approximately US$2200 to US$2600.

The price of a Gyroscopic wheelchair is approximately US$3900.

The costs involved in the project for its preparation are in the items listed below:

(A) 01 wheelchair US$120
(B) 01 mechanical Car Jack US$32
(C) 01 step motor US$100
(D) 01 battery US$65
(E) 01 lifting system US$60
(F) 01 set of tubes and support plates US$60

The price of the assembled set is approximately US$437.
Note: No labor figures were computed [12].

2.5 Testing and Validation

A prototype was assembled and had its performance tested for validation of mechanical design criteria listed above. Functional tests were performed with 100 kg user in daily routine of up and down elevation until battery run out (approximately 60 cycles).

The tubular wheelchair was purchased to be adapted in up and down movements with an approximate displacement of 30 cm, in order to cause the user to reach a height that allows access in environments that have balconies or even for a conversation with friends at a suitable time in their conditions.

The tubular wheelchair when in its normal size the user is seated at a height of 0.57 m in relation to the ground, which after the system actuated in the raised position it will be up to 0,81 m of height in relation to the Soil [12].

3 Results

The following results show how the tubular structure was modified Fig. 8, how the automation was performed and, therefore, it presents the analyzed behavior during the elevation task [12].

Fig. 8. Photo of structure cut

In the photos below, it's observed the assembly of the structure of the base to support the Car Jack. Attachment planning with lifting motor, according Fig. 9.

Fig. 9. Mounting and fixing the Car Jack, raising and lowering the engine position

Mounting the seat frame and locking the wheelchair closing movement, and wheelchairs mounted with frame to receive automatic lifting system, according to Fig. 10.

Fig. 10. Picture of seat basis structure and wheelchair assembled

Assembly of the frame in the Car Jack (angle brackets and polypropylene), for the system of lifting and lowering the wheelchair seat, according Fig. 11.

Fig. 11. Photo of detail of fixing of the structure of lifting and lowering system.

Assembling of the seat lifting and lowering frame with the engine attachment, according Fig. 12.

Fig. 12. Photo of engine fixing on Car Jack

Details of fixing the polypropylene rods on the wheelchair seat, according Fig. 13.

Fig. 13. Photo of the detail of seat fixing in the lifting and lowering system

Tests using the motor to perform the movement of raising and lowering the wheelchair seat, according Fig. 14.

Fig. 14. Photo of front and rear elevation movement.

Details of the wheelchair seat elevation and lowering system, according Fig. 15.

Fig. 15. Photo of elevation movement

Seat lifting and lowering system coupled to the wheelchair driven, according Fig. 16.

Fig. 16. Picture of the raised lifting and lowering system

Details of the wheelchair seat raising and lowering system actuated, according Fig. 17.

Fig. 17. Picture of details of lifting and lowering system

Details of the battery securing system and end of travel system, ascent and descent, according Fig. 18.

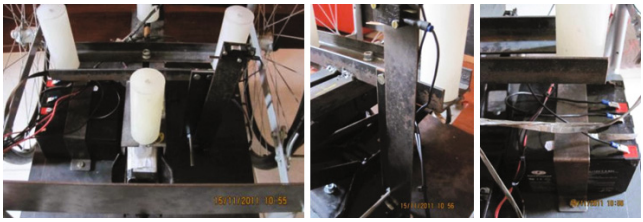

Fig. 18. Detail photo of battery fixing and end of stroke system

4 Conclusions

The design of the lifting system was great learning and rewarding, as it really became a project aimed at people with mobility disabilities. Through this system of vertical movement of the seat, the wheelchair can communicate/dialogue at the same height of sight. During the implementation of this project, from its conception until its realization, it was necessary to put into practice technical and scientific knowledge of the mechanical and electrical areas.

It can be stated, through the results of the tests carried out, that the lifting system is very viable. In future works, to change the design of the lifting mechanism because it was an unstable climb; include a battery level meter, which will show the user the limit of use thus avoiding a stop during the ascent and descent course. In this way, the wheelchair with lifting system can still be enhanced before scale production.

References

1. Demers, L., Weiss-Lambrou, R., Ska, B.: Development of the Quebec user evaluation of satisfaction with assistive technology (QUEST). Assist. Tecnhol. **8**, 3–13 (1996)

2. Chugo, D., Shioatni, K., Sakaida, Y., Yokota, S., Hashimoto, H.: An automatic adjustable backrest for a posture coordination of a seated patient on a wheelchair. In: Proccedings of 6th International Conference on Human System Interactions (HSI) (2013). doi:10.1109/HSI.2013.6577808
3. Carrino, F., Dumoulin, J., Mugellini, E., Khaled, O., Ingold, R.: A self-paced BCI system to control an electric wheelchair: evaluation of a commercial, low-cost EEG device. In: Biosignals and Biorobotics Conference (2012). doi:10.1109/BRC.2012.6222185
4. Chugo, D., Shioatni, K., Sakaida, Y., Yokota, S., Hashimoto, H.: A review of assistive devices for arm balancing. In: Proceedings of 6th International Conference on Human System Interactions (HSI) (2013). doi:10.1109/HSI.2013.6577808
5. Ahmad, S., Tokhi, M.O.: Fuzzy logic control of a wheelchair on two wheels. In: Modelling, Identification, and Control, p. 596 (2008)
6. Chakrabarti, D.: Indian Anthropometric Dimensions for Ergonomic Design Practice. National Institute of Design, Ahmedabad (1997)
7. PNS: National Health Survey 2013, IBGE (2015)
8. Sanders, M.S., McCormick, E.J.: Human Factors in Engineering Design. McGraw Hill, New York (1992)
9. Matsumoto, H., Ueki, M., Uehara, K., Noma, H., Nozawa, N., Osaki, M., Hagino, H.: Comparison of healthcare workers transferring patients using either conventional or robotic wheelchairs: kinematic, electromyographic, and electrocardiographic analyses. J. Healthc. Eng. **2016**, 7 (2016). Article ID 5963432
10. Blay, N., Duffield, C.M., Gallagher, R., Roche, M.: A systematic review of time studies to assess the impact of patient transfers on nurse workload. Int. J. Nurs. Pract. **20**(6), 662–673 (2014)
11. Wang, H., Tsai, C., Jeannis, H., et al.: Stability analysis of electrical powered wheelchair-mounted robotic-assisted transfer device. J. Rehabil. Res. Dev. **51**(5), 761–774 (2014)
12. Araki, S., Grandinetti, F.: Automatic lifting system of a wheelchair type vehicle. Rev. Sinerg. **12**(3), 267–274 (2011)

An Initial Assessment of Mechanisms for the Development of New Hospital Beds

R.L.P. Barreto(✉), R. Simoni, and D. Martins

Universidade Federal de Santa Catarina, Florianópolis, Brazil
rlpbarreto@hotmail.com,
{roberto.simoni,daniel.martins}@ufsc.br

Abstract. Adjustments available in hospital beds are performed by different mechanisms. This paper presents an initial assessment of mechanisms for the development of new hospital beds focused on assistive technology. First it is presented a review on a mechanism design methodology, following by an evaluation of a commercial hospital bed. This reverse engineering is used to identify the project requirements. The commercial bed is divided into three mechanisms for further analysis. The design requirements are mapped to guarantee that the new mechanisms will perform the motions similarly to the existing one. Later, the potential development of new mechanisms are evaluated for each of the three sections of the hospital bed. Finally, a new concept and a mock-up of a novel hospital bed is provided.

Keywords: Hospital bed · Mechanism design methodology · Mechanisms synthesis · Assistive technology

1 Introduction

Assistive technology is an important branch of engineering as it involves improving the daily lives of people. The improvement and development of new hospital bed is interesting in assistive technology for health and economical factors. In Brazil, around 6% of the population stayed in a hospital for at least a day in 2013 [6], while in the United States expenditures for treating pressure ulcers in bedridden patients have been estimated at $11 billion per year [4].

The US National Pressure Ulcer Advisory Panel defines pressure ulcers as: "localized injury to the skin and/or underlying tissue usually over a bony prominence, as a result of pressure, or pressure in combination with shear" [13]. Langemo et al. [7] lists some factors that increase the risk of the development of pressure ulcers, such as advanced age, protein-calorie malnutrition, friction and shear, exposure to moisture and immobility. The development of new mechanisms for hospital beds aims to decrease the incidence of pressure ulcers due to immobility.

There are several papers regarding the development of new mechanisms for hospital beds. Hua et al. [5] developed a hospital bed device seeking to reduce the physical strain of hospital nurses and improving the recuperation of the patients. The objective was to provide a bed with lying and sitting positions, as well as assisting nurses to rotate patients and transfer them to another bed. This mechanisms has 3-DOF in a

J.C.M. Carvalho et al. (eds.), *Multibody Mechatronic Systems*,
Mechanisms and Machine Science 54, DOI 10.1007/978-3-319-67567-1_46

planar workspace, seven inner loops, nineteen links and twenty five joints. Peng et al. [15] disclose the mechanism design and control for a multifunctional hospital bed. That project contains two beds, the main patient support and an auxiliary bed for transportation, the same concept presented in the previous work. The main bed has 6-DOF in a planar workspace, four inner loops, fifteen links and eighteen joints. Pavlovic et al. [14] presented an automated multifunctional hospital bed. In that work, the authors show the development of the mechanisms for the backrest elevation and the knee and lower leg elevation. The bed developed by these authors has 5-DOF in a planar workspace, five inner loops, sixteen links and twenty joints. That mechanism is interesting due to the possibility of adjusting the position of only one leg while maintaining the position of the other. Many other authors focuses on hospital bed designs such as [1, 2, 11, 12].

The objective of this work is to evaluate the potential for innovation for new hospital beds mechanisms. This work is part of the project entitled "Reconfigurable Platform of Assistive Technology for Bedridden Patients", an ongoing project in the Professor Raul Güenther Robotics Laboratory of the Universidade Federal de Santa Catarina (UFSC) in partnership with the Instituto Federal de Educação, Ciência e Tecnologia de São Paulo (IFSP) and Universidade do Estado de Santa Catarina (UDESC), funded by the Coordenação de Aperfeiçoamento de Pessoal de Nível Superior (CAPES).

The remaining of this paper is organized as follows. Section 2 presents the mechanism design methodology applied to design novel hospital bed mechanisms. Section 3 presents the structural representation and the kinematic chain of a commercial hospital bed. Section 4 presents the design requirements and Sect. 5 presents the potential for innovation in mechanisms for hospital beds.

2 Mechanism Design Methodology

The mechanism methodology used in this work was proposed by Yan [17] and is based on the study of existing mechanisms to propose new concepts upon modification on the original mechanism. This methodology also aims to generate all possible topological concepts possible for the proposed problem. Yan's methodology can be summarized in the following six steps:

- Review of the state of the art to identify existing designs, with the purpose of defining topological characteristics relevant to the project.
- Select an existing mechanism and generalize it into an equivalent kinematic chain.
- Generate all feasible mechanisms with the same characteristics of the analyzed concept. This step is known as the number synthesis.
- Assign types of members and joints to the generalized kinematic chain. This is the type synthesis step of the design process.
- Particularize every mechanism developed in the previous step into a mechanical device.
- Review all the existing designs and create an atlas of new concepts.

The methodology is further explained in Fig. 1.

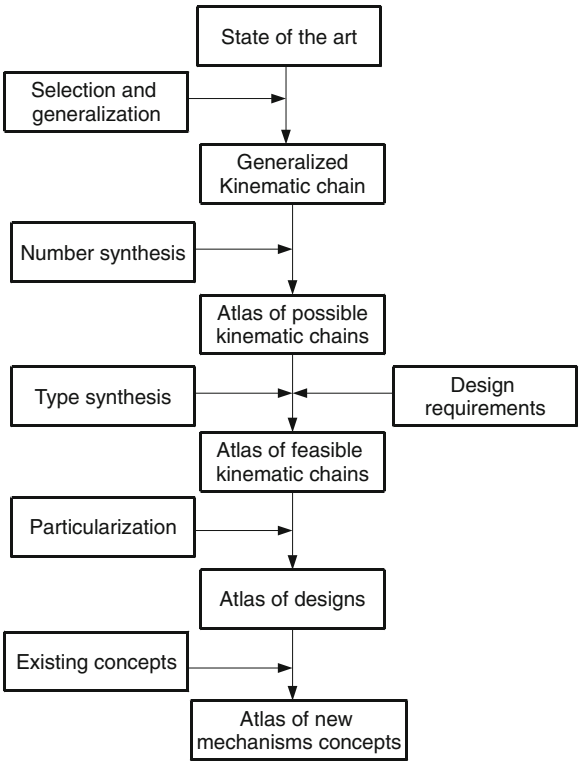

Fig. 1. Yan's mechanism design methodology

After reviewing the existing designs, the generalizations consist in replacing the specific joints by generalized revolute joints. From the generalized kinematic chains, characteristics such as number of joints and links are ascertained. This paper focuses on generating all the feasible kinematic chains as well as performing the type synthesis.

3 Kinematic Chain of the Linet Bed

The Linet bed model Eleganza 3C [8] was chosen as the benchmark for the initial assessment of the project due to the availability of the device in the Hospital Universitário of the Universidade Federal de Santa Catarina. By analyzing the bed in operation, a schematic drawing of the bed was developed, shown in Fig. 2(a).

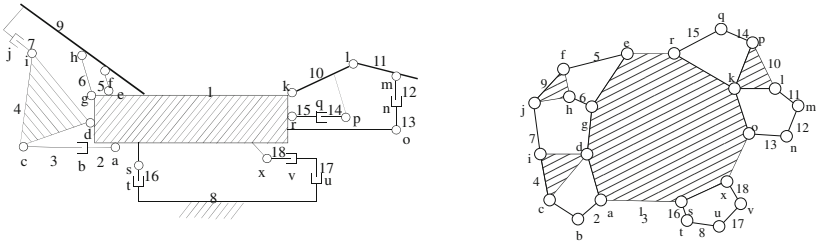

(a) Structural representation (b) Kinematic chain

Fig. 2. Structural representation and kinematic chain of the Linet bed

After the schematic drawing, it is possible to develop the kinematic chain that represents the hospital bed mechanism. The kinematic chain is shown in Fig. 2(b). The kinematic chain presented in this figure is a planar kinematic chain with mobility equals to five, with six independent loops, eighteen links and twenty-three joints, i.e., $M = 5$, $v = 6$, $n = 18$, $j = 20$ and $\lambda = 3$. It is important to notice that the Linet bed mechanism is fractionated, divided in three sections: back support, leg support and height and angle adjustment. More details on fractionation of kinematic chains, consult [10]. The first section has $M = 1$, $v = 3$, $n = 8$, $j = 10$. The leg support section has $M = 2$, $v = 2$, $n = 7$, $j = 8$. The last section has $M = 2$, $v = 1$, $n = 5$, $j = 5$.

4 Design Requirements for Hospital Beds

One of the most important steps in mechanism design is to identify the design requirements. In order to define the design requirements, several papers were considered. Maletz et al. [9] reviewed the exiting positions enabled by current hospital beds, and how often each of those are found in commercial products. Defloor [3] reviewed many bed positions, such as the semi-Fowler and several angles of supine, in order to evaluate the pressure on the patients skin. Pavlovic et al. [14] analyzed several hospital bed patents and listed the most important bed functions: height adjustment, Trendelenburg and reverse-Trendelenburg, lateral bed tilting, backrest elevation, knee and lower leg lifting. Taking these works into considerations and asserting the Linet bed mechanism and the different positions provided by the available hospital beds, it was decided that the mechanism should provide the same positions and movements of the Linet bed.

Considering the importance of the profiling hospital bed in the prevention of pressure sores, the relative motion between support bases should not interfere with or worsen the sores. If two subsequent support bases have a relative motion that is, for example, rotation and displacement, the skin of person lying in the bed will suffer friction and shear, both factors that increase the incidence of pressure sores. In order to do so, the design should guarantee that every section of the mattress support platform has only rotation to each of the subsequent sections.

The Linet bed mechanism analysis found a fractionable mechanism that can be divided into three parts. Considering this, the development of each part will be done

separately. Also, all of the actuators are required to be prismatic, as they can easily perform the desired movements. Finally, in the type synthesis the fixed link will the defined as the highest order link.

5 Potential for Innovation of New Mechanisms for Hospital Beds

According Yan's Methodology [17], a random mechanism should be picked to be analyzed. As the Linet bed was available in the Hospital Universitário, this was the mechanism chosen. The kinematic chain shown in Sect. 3 has $M = 5$, $v = 6$, $n = 18$, $j = 20$ and $\lambda = 3$ as well as three independent sections, therefore three independent analysis are done for the mechanism. This means the fractionated mechanism is separated into three non-fractionated mechanism.

5.1 Generation of Atlas of Generalized Kinematic Chains

The third step of Yan's methodology is to generate all kinematic chains with the same characteristics of the analyzed concept. The height and angle adjustment in Fig. 1 is a five-link mechanism, which has only one possible kinematic chain available. The leg support mechanism shown in Fig. 2 has seven joints and eight links, therefore there are three existing kinematic chains with the same characteristics [16]. According to Tsai [16] there are sixteen possible kinematic chains available for eight-links and ten joints mechanisms. All of the kinematic chains are presented in Fig. 3.

The kinematic chains of the Linet bed, both in Fig. 3(b) and (c) are the first chain on the left. Assembling the sixteen kinematic chains shown in Fig. 3(c) and the three shown in Fig. 3(b), there are forty-eight possible kinematic chains combinations for a new bed mechanism.

5.2 Generation of Atlas of Feasible Mechanisms

At this stage, the types of kinematic pairs are chosen to replace the generalized revolute joint. The analysis will follow the sequence of the previous section and will start by the height and angle adjustment mechanism, which was previously presented in Fig. 3(a).

As defined by the design requirements, the two actuated joints are prismatic. Therefore two of the five joints have to be prismatic joints. Considering this constraint, there are four possible combinations PPRRR, PPPRR, PPPPR and PPPPP. The last two combinations are not interesting since there are only one or none revolute joints, so both of them are excluded of posterior analysis. Defining the fixed link as link 1, there are 20 different possible mechanisms.

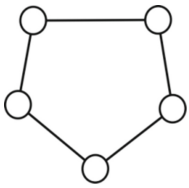

(a) Planar kinematic chain with M = 2 and $v = 1$

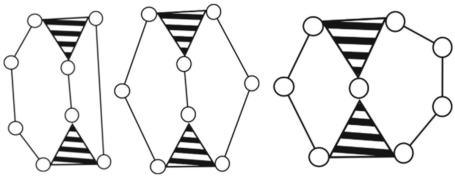

(b) Planar kinematic chain with M = 2 and $v = 2$

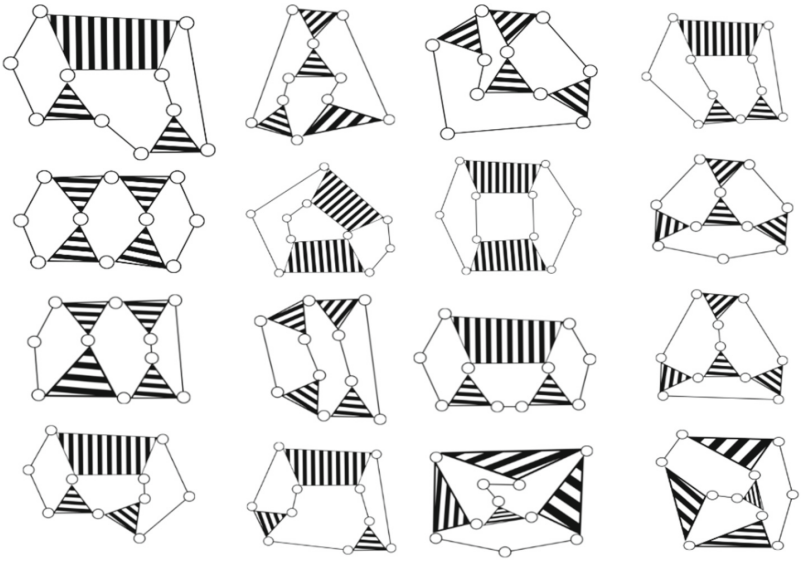

(c) Planar kinematic chain with M = 1 and $v = 3$

Fig. 3. Potential kinematic chains for new hospital bed mechanisms

The leg support mechanism has nine joints. Using the requirement of the actuation done by prismatic joints, two of those nine joints need to be prismatic joints. Some additional requirements are created for this mechanism to guarantee the new mechanism performs similar function to the benchmark device:

- One of the ternary links is defined as the base.
- The upper leg movement should have degree of control equal to 1.
- The lower leg lift movement should have degree of control equal to 2.

The first analyzed kinematic chain is presented in Fig. 4(a).

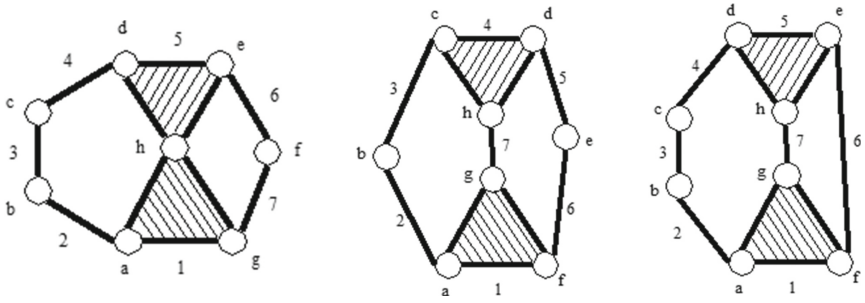

(a) Kinematic chain 1 (b) Kinematic chain 2 (c) Kinematic chain 3

Fig. 4. Kinematic chains for the leg support

The link 1 is defined as the base of the mechanism. Remembering the design requirements, the upper and lower leg support should be connected to each other by a revolute joint. Using this requirement and the new ones created for the leg support, the upper leg support can only be place in link five, and therefore the lower leg support can only be placed in the link 4. The joints h and d, respectively between the links 1 and 5 and between 4 and 5, are required to be revolute joints. Remembering that the design requirements dictates that the two actuated joints should be prismatic, there are six joints to be defined. Due to the force transmission, the prismatic actuator works better if placed between revolute joints. Accordingly, the joint f is defined as a prismatic joint and joints e and g are defined as revolute. This results in only two joint types yet to be defined, and alongside these, the position of the second prismatic joint is not yet established. The total possible different mechanisms with these conditions is seven.

The second kinematic chain is shown in Fig. 4(b). To begin, the link 1 is chosen as the fixed link. With this decision, the links 2, 6 and 7 are possible choices for the upper leg support. However, due to the requirements set, the only choice available is link 7. After defining links 1 and 7, link 4 must be defined as the lower leg support. Therefore, joints g and h are required to be revolute joints. This mechanism enables two RPR legs for the actuations, so by choosing this characteristic, every joint of the mechanism is defined and there is only one possible mechanism choice.

The third and last kinematic chain in presented in Fig. 4(c). The link 1 is defined as the fixed link. By the requirements set for this mechanism, the upper leg support needs to be one of the links 2, 6 or 7, but with the restriction to the lower leg support, the only viable link are the 6 and 7. These links are symmetrical, so only one of them is relevant, and for this analysis link 6 is chosen. After defining the upper leg support as the link 6, the lower leg support has to be the link 5. Between the links 1 and 6 and between 5 and 6, the joints f and e need to be defined as revolute joints. Therefore, there are six joints still to be defined, remembering two of them are required to be prismatic joints for the actuators. This results in 64 different mechanisms. The difference of results of this kinematic chain and the first analyzed, with seven results, is due to the restriction

imposed by the revolute joint h in the first kinematic chain, and the possibility of using a RPR leg to improve force transmission. The remaining joins will most likely be revolute joints, the amount of possible combinations will decrease considerably.

For the backrest support, as there are sixteen kinematic chains, one was randomly chosen for further study. This kinematic chain is shown in Fig. 5.

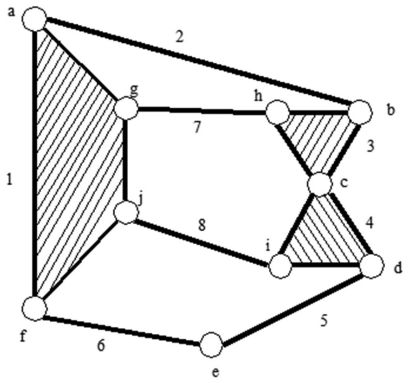

Fig. 5. Randomly chosen kinematic chain

In this case, it is interesting to define link 1 as the base. Due to the design requirement, the upper body support could be placed in links 2, 6, 7 or 8. Links 2 and 7 are symmetrical, so one of them is excluded, remaining links 2, 6 and 8. Applying here the RPR leg for the actuation of the backrest elevation mechanism in links 5 and 6, on the joints d, e and f, the back support may only be placed on links 2 and 8. The joint between the back support and the base is required to be revolute. Out of ten joint, six are still to be defined, which results in sixty four possible mechanism for each of the back supports possibilities, adding up to 128 different mechanisms for the backrest elevation mechanism.

Using the results found for the height adjustment (20 possibilities), the leg support mechanism (72 possibilities), the backrest adjustment (128 possibilities) and combinatorial analysis it is possible to calculate the total number of different mechanisms possible for a hospital bed according to the methodology by Yan [17]. The total result is 184320 different possible mechanisms. It is unlikely that a designer will go through all these results, so more design requirements are needed. One such requirement is the limitation of the number of prismatic joints.

5.3 Particularization

In this section, all the mechanisms found in the previous step are particularized and dimensioned. As an example, a mechanism was randomly chosen from the previous analysis to be demonstrated. First, in Fig. 6, it is presented the kinematic chain relative to the chosen mechanism.

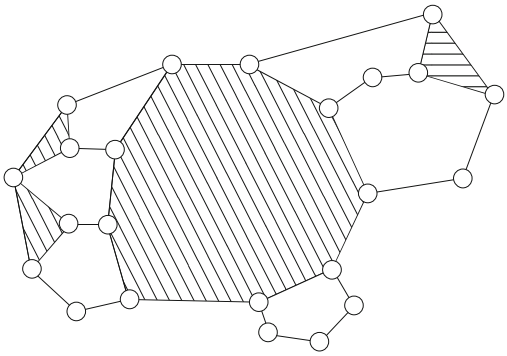

Fig. 6. New bed kinematic chain example

From this kinematic chain, a new concept of a mechanism was created, and is shown in Fig. 7(a) and a mock-up, provided by a 3d printer, is shown in Fig. 7(b).

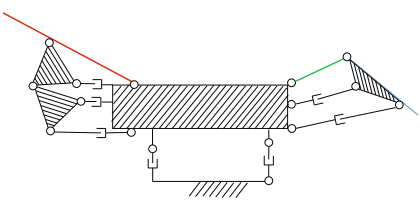

(a) Structural representation

(b) Mock-up

Fig. 7. New bed mechanism concept

The mechanism shown in Fig. 7 was not dimensioned or optimized. This mechanism holds the same number of links and joints as the original mechanism from the Linet bed, including the same degrees of freedom and basic characteristics of the movements and positions.

6 Conclusions

This paper presented the number and type synthesis of mechanisms for hospital beds. The concepts presented in the paper were originated by Yan's mechanism design methodology. Dividing the bed into three independent sections, there were found over one hundred thousand possible combinations for new mechanisms. One such mechanism was chosen for structural representation and development of a mock-up.

Further work includes the assessment of more design requirements to filter the number of possible mechanisms and means to compare and evaluate the developed mechanisms with the existing devices aiming to find the advantages and disadvantages of each mechanism.

Acknowledgments. This work is funded by the CAPES under the project PGPTA nº59/2014.

References

1. Abdullah, F., Yaacob, S., Basah, S.N.: Novel 3-DOF parallel mechanism for bedridden repositioning system: a kinematics analysis. J. Med. Bioeng. **4**(3), 235–238 (2015)
2. Andhare, A., Onker, A., Padole, P.: Design of bed for bedridden patients: analysis and synthesis of mechanisms. In: 15th National Conference on Machines and Mechanisms (2011)
3. Defloor, T.: The Effect of Position and Mattress on Interface Pressure. Appl. Nurs. Res. **13**(1), 2–11 (2000)
4. HILL-ROM: Hill-Rom. http://www.hill-rom.com/usa/. Accessed June 2016
5. Hua, W.C., Chun, T.T., Chich, H.S., Chun, C.W., Ming, C.Y.: Hospital bed with auxiliary functions of lateral positioning and transferring for immobilized patients. In: The 33rd Annual Conference of the IEEE Industrial Electronics Society (IECON) (2007)
6. IBGE. Instituto Brasileiro de Geografia e Estatística. Pesquisa Nacional de Saúde 2013: Acesso e utilização dos serviços de saúde, acidentes e violência, Rio de Janeiro (2015)
7. Langemo, D.K., Black, J.: NPUAP. Pressure ulcers in individuals receiving palliative care: a National Pressure Ulcer Advisory Panel White Paper. Advances in Skin and Wound Care (2010)
8. Linet. Linet do Brasil. http://www.linetbrasil.com/pt-BR/. Accessed June 2016
9. Maletz, E.R., Barreto, R.L.P., Martins, D.: Revisão do estado da arte de camas hospitalares: análise de mercado e pesquisa de patentes. I Congresso Brasileiro de Pesquisa e Desenvolvimento em Tecnologia Assistiva, Curitiba (2016)
10. Martins, D., Simoni, R., Carboni, A.P.: Fractionation in planar kinematic chains: reconciling enumeration contradictions. Mech. Mach. Theor. **45**(11), 1628–1641 (2010)
11. Mascaro, S., Spano, J., Asada, H.: A reconfigurable holonomic omnidirectional mobile bed with unified seating (RHOMBUS) for bedridden patients. In: Proceedings, 1997 IEEE International Conference on Robotics and Automation. IEEE (1997)
12. Mohammed, M.N., Khrit, N.G., Abdelgnei, M.A., Abubaker, E.S., Muftah, A.F., Omar, M. Z., Salleh, M.S.: A new design of multi-functional portable patient bed. JurnalTeknologi **59**, 61–66 (2012)
13. NPUAP. National Pressure Ulcer Advisory Panel: Pressure Ulcer Prevention and Treatment Clinical Practice Guideline (2009)
14. Pavlovic, N.D., Milosevic, M., Pavlovic, N.T.: Development of mechanisms for adjusting positions of a multifunctional bed. In: 13th World Congress in Mechanism and Machine Science, Guanajuato, México (2011)
15. Peng, S.W., Lian, F.L., Fu, L.C.: Mechanism design and mechatronic control of a multifunctional test bed for bedridden healthcare. IEEE/ASME Trans. Mechatron. **15**(2), 234–241 (2010)
16. Tsai, L.: Mechanism Design: Enumeration of Kinematic Structures According to Function. Mechanical Engineering Series. CRC Press, Boca Raton (2001)
17. Yan, H.S.: Creative Design of Mechanical Devices. Springer, Singapore (1998)

Vehicle Dynamics

Rollover of Long Combination Vehicles: Effect of Overweight

Gonzalo Moreno[1(✉)], Vangelo Manenti[2], Lauro Nicolazzi[2], Rodrigo Vieira[2], and Daniel Martins[2]

[1] Department of Mechanical Engineering, University of Pamplona, Pamplona 543050, Colombia
gmoren@hotmail.com

[2] Department of Mechanical Engineering, Federal University of Santa Catarina, Florianópolis 88040-900, Brazil
vangelomanenti@gmail.com, {lauro,rvieira}@grante.ufsc.br, daniel.martins@ufsc.br

Abstract. The stability of long combination vehicles (*LCV's*) has been the focus of research efforts in recent decades. Several characteristics of the vehicles have been analyzed to determine their influence on the vehicle stability calculation; however, the overweight is rarely analyzed. To conduct this research, the Davies method is used to obtain the static of the mechanism that represent the last trailer of the vehicle. Finally, a numerical case study is showed and the overweight, the longitudinal, lateral and vertical displacements of the gravity center are investigated. This study demonstrates that the overweight has important role on the static rollover threshold (SRT) calculation.

Keywords: Overweight · Static Rollover Threshold (SRT) · Long combinations vehicles · Road safety · Davies method

1 Introduction

The static rollover threshold (SRT) is one of the most important parameters used to define the stability of vehicles. This factor is highly dependent on the location of the vehicle center of gravity (CG), and it represents the maximum lateral acceleration - a_y (expressed in terms of gravity acceleration - g) in a quasi-static situation immediately before one tyre of the vehicle model loses contact with the ground [8,9,27].

Several researchers have considered the influence of the suspension, tyres, chassis, and fifth-wheel on the lateral, vertical, and longitudinal CG location, which affects the vehicle behavior [2,3,5,8–10].

Additionally, Rill [23] and Winkler [28] reported that the chassis has a significant torsional compliance, which would allow that its front and rear parts roll almost independently. In this regard, Kamnik et al. [14] reported that the lateral load transfer (LLT) is different for the front and the rear axles of the trailer.

J.C.M. Carvalho et al. (eds.), *Multibody Mechatronic Systems*,
Mechanisms and Machine Science 54, DOI 10.1007/978-3-319-67567-1_47

On the other hand, an improperly loaded trailer can result in a poor trailer stability, overweight on axles, tyres deterioration, and damage of the pavement [22,25].

In a previous research [18,19], we analyzed the last trailer of *LCV's*, and reported that the SRT factor represents a three-dimensional phenomenon, and that longitudinal parameters and lateral load transfer play important roles in relation to the SRT factor calculation.

Following the methodology developed in a previous work [20], we developed a three-dimensional simplified model that considers different characteristics of trailers, such as: the suspension, tyres, fifth-wheel, chassis and trailer/trailer angle, to calculate the three-dimensional SRT factor for a trailer.

The paper is organized as follows. Section 2 introduces the mechanism of the three-dimensional trailer model with the characteristics mentioned above; Sect. 3 presents the static analysis of the proposed model; the results presented in Sect. 3 are analyzed and discussed within a case study in Sect. 4; and finally, conclusions are drawn in Sect. 5.

2 Trailer Model

According to Jindra [13], Melo [16] and Rempel [24] the last unit (trailer) of *LCV's* is subjected to a high lateral acceleration compared to the tractor unit, this acceleration is caused by the phenomenon known as rearward amplification (*RA*), impacting the rollover threshold of the last unit and the vehicle.

For this reason, the last trailer of the *LCV's* is the critical unit and it is prone to rollover; taking into account this aspect, a simplified trailer model (Fig. 1) is modeled and analyzed to calculate the SRT factor for *LCV's*.

More details concerning the developed model are contained in the technical report to this paper, which includes the modelling and analysis of the trailer model [21].

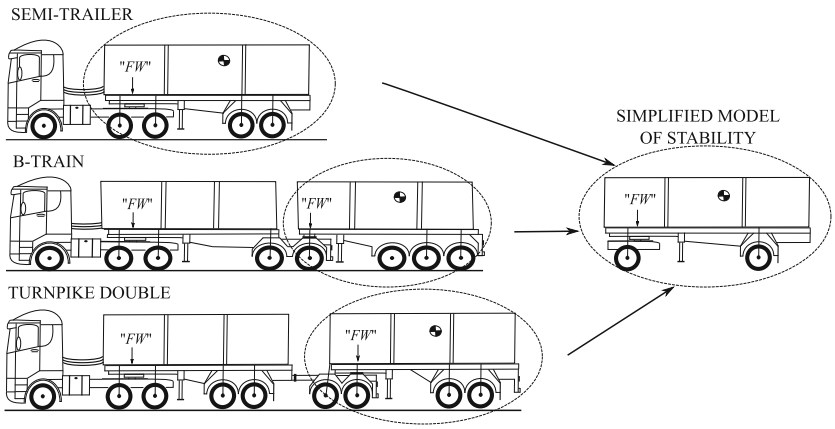

Fig. 1. Simplified trailer model.

Mechanical systems can be represented by kinematic chains composed of links and joints, which facilitates their modeling and analysis [4,15,26]. Using mechanism theory, the three-dimensional model that represents the last trailer of *LCV's* is proposed (Fig. 2).

The model is composed of three mechanisms:

- the first mechanism is located at the front of the trailer, and it is composed of sub-mechanisms that represent the tyres (tyres system), the suspension (rigid suspension system), and the fifth wheel (fifth-wheel system),
- the second mechanism is located at the rear of the trailer, and it is composed of sub-mechanisms that represent the tyres (tyres system), and the suspension (rigid suspension system), and
- the third mechanism represents the trailer body (chassis), and it links the front and rear trailer mechanisms.

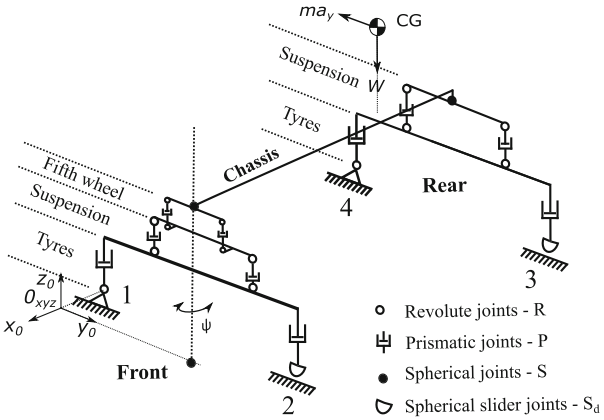

Fig. 2. Trailer model.

Tyres, suspension, fifth-wheel and chassis are directly responsible for the *CG* movements; these movements are dependent on the forces acting on the center of gravity (*CG*) of the trailer, such as the trailer weight (*W*), disturbances forces imposed by the ground and the lateral inertial force (ma_y) when the vehicle makes a turn or evasive maneuvers.

The kinematic chain of the trailer model (Fig. 2) is composed of twenty-eight joints ($j = 28$; *14* - revolute joints "R", *10* - prismatic joints "P" *2* spherical joints "S", *2* spherical slider joints "S_d"), and twenty-three links (n = 23).

3 Static Analysis of the Mechanism

Several methodologies allow us to obtain a complete static analysis of a mechanism. In this study, the formalism presented by Davies [6] was used as the primary mathematical tool to analyze the mechanisms statically.

The Davies method provides a systematic way to relate the joint forces and moments in closed kinematic chains [1]. This method is based on graph theory, screw theory and the Kirchhoff cut-set law and it can be used to obtain the statics of a mechanism as a matrix expression.

Applying Davies method to the analysis of the trailer stability, and considering the chassis flexibility, fifth-wheel, suspension, tyres, and the trailer/trailer angle, when a trailer model makes a horizontal curve, the model is subjected to an increasing lateral load (inertial force) until it reaches the rollover threshold. During the turning, the rear inner tyre is normally (tyre *3* - Fig. 2) prone to loses contact with the ground. For this condition ($F_{z3} = 0$), then the static rollover threshold (SRT) for the trailer is defined by the Eq. 1. More details of the trailer model can be consulted in [21].

$$SRT_{3D_\psi} = \frac{a_y}{g} = \frac{h_1}{h_2}\left(1 - \frac{t_1 F_{z2}\cos\psi + P_1(F_{z4} - W)}{W h_1}\right) \tag{1}$$

where SRT_{3D_ψ} factor is the three-dimensional static rollover threshold for a trailer model with trailer/trailer angle (ψ), P_1 is a system variable ($P_1 = (2l_{13}\sin\psi + t_2(\cos\psi - 1))/2$), h_1 is the instantaneous lateral distance between the zero-reference frame and the center of gravity, and h_2 is the instantaneous CG height, l_{13} is the distance between the fifth-wheel and the front axle, t_1 is the front track width of the trailer, t_2 is the front axle width of the trailer.

4 Case Study - B-train

In this study, a three-dimensional trailer model of a Semi-train with two axles on front and three axles on rear is analyzed. In this model a suspension system with a tandem axle is used and the suspension parameters are dependent on the construction materials. Harwood et al. [11] reported that the range of values for the stiffness of the suspension per axle is $k_{Ls} = 1500 - 2400\,\mathrm{kN.m^{-1}}$. Figure 3 and Table 1 show the parameters of the trailer used in this analysis [7].

The SRT factor calculation was conducted using the steady state circular test [12], the load conditions include a load laterally centered, load with CG displacement and overweight with CG displacement.

The simulation model was applied using MATLAB®. To calculate the SRT factor, the inertial force was increased until the lateral load transfer on the rear axle become complete (the entire load is transferred from the rear inner tyre to the rear outer tyre when the trailer makes a turn).

Taking into account that the overweight on the front axle induces the understeer of the vehicle, and the overweight on the rear axle induces the oversteer of the vehicle. The SRT factor calculation was conducted using 5% and 10% of overweight, load laterally centered, and load with CG displacement.

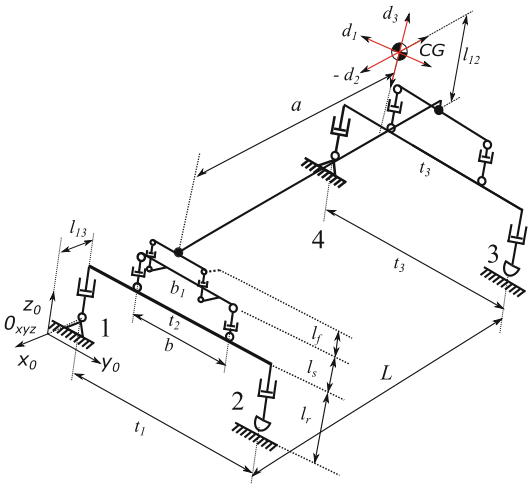

Fig. 3. Parameters of the trailer model.

Table 1. Parameters of the trailer model - B-train.

Parameter	Value	Units
Trailer weight - W	355.22	kN
Front and rear track widths - $t_{1,3}$	1.86	m
Front and rear axle widths - $t_{2,4}$	1.86	m
Stiffness of the suspension per axle - k_{Ls} [11]	1800	kN/m
Number of axles at the front (trailer) (4 tyres per axle)	2	
Number of axles at the rear (trailer) (4 tyres per axle)	3	
Vertical stiffness per tyre - k_T [11]	840	kN/m
Initial suspension height - $l_s = l_{3,4,9,10}$	0.205	m
Initial dynamic rolling radius - $l_r = l_{1,2,7,8}$ [17]	0.499	m
Initial height of the fifth wheel - l_f	0.1	m
Lateral separation between the springs - b	0.95	m
Fifth-wheel width - b_1	0.6	m
CG height above the chassis - l_{12}	1.346	m
Distance between the fifth wheel and the front axle - l_{13}	0.15	m
Wheelbase of the trailer - L	4.26	m
Distance from the front axle to the center of gravity - a	3	m
Lateral CG displacement, offset of the cargo d_1	± 0.1	m
	± 0.2	
Longitudinal CG displacement d_2	± 0.5	m
	± 1	
	± 1.5	
Vertical CG displacement d_3	± 0.1	m
	± 0.2	
Trailer/trailer angle (ψ)	0	^{0}

The example shows a sensibility analysis of a trailer with relatively low stability that under the action of the suspension, tyres and the chassis, the SRT_{3D_ψ} factor is 0.3272 g (normal load and no displacement). Figures 4(a) and (b) show the influence of the overweight on the SRT factor calculation; this overweight affects the CG height (h_2) and the trailer roll angle (θ), 1% of overweight corresponds to a loss of stability of around 0.2%.

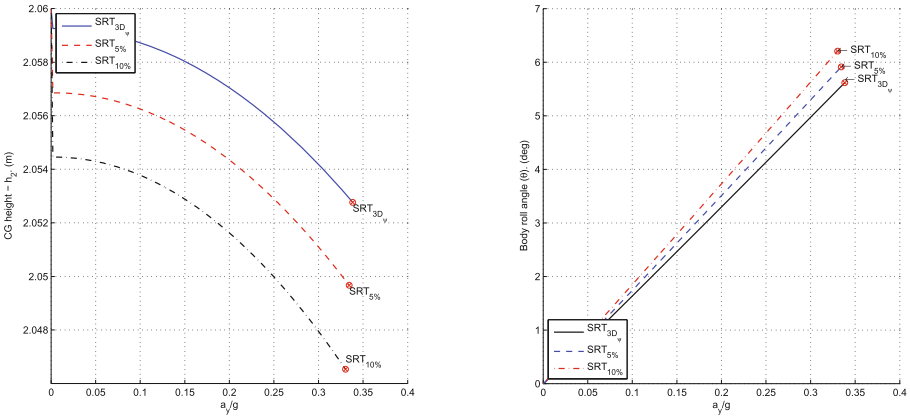

Fig. 4. (a) CG height - Overweight - SRT factor - B-train. (b) Total roll angle (θ_{all}) - Overweight - SRT factor - B-train.

Figure 5 shows the influence of lateral CG displacement (d_1) and the overweight on the SRT factor calculation and the trailer roll angle: on the average, 2 cm of lateral CG displacement and 1% of overweight corresponds to a loss of stability of around 0.0106 g.

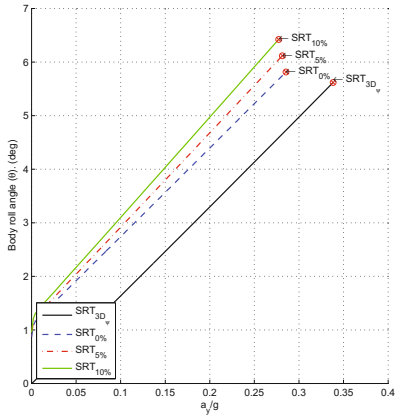

Fig. 5. Lateral CG movement - Overweight - SRT factor - B-train.

Figures 6(a) and (b) show the influence of vertical CG displacement (d_3) and the overweight on the SRT factor calculation and the trailer roll angle: Fig. 6(a) shows that on the average: 4 cm of vertical increase of the CG location and 1% of overweight corresponds to a loss of stability of around 0.0106 g; and Fig. 6(b) shows that on the average: 4 cm of vertical decrease of the CG location corresponds to an increase of stability of around 0.01 g, and 1% of overweight corresponds to a loss of stability of around 0.0006 g.

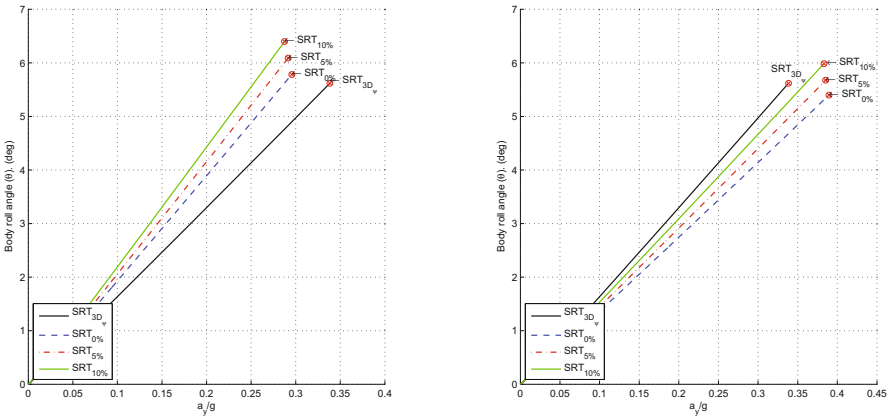

Fig. 6. (a) Vertical CG movement - Overweight - SRT factor - B-train. (b) Vertical CG movement - Overweight - SRT factor - B-train.

For the longitudinal CG displacement (d_2), the overweight on the front or the rear axle enable an increase of the SRT factor; but, the overweight on the front axle induces the understeer of the vehicle, and the overweight on the rear axle induces the oversteer of the vehicle

5 Conclusion

The results of this study demonstrate that the overweight and the load distribution have an important role on the SRT factor calculation of $LCV's$. The case study shows that:

- the overweight and the lateral CG displacement can reduce the SRT factor,
- the overweight and the vertical CG displacement can reduce or increase the SRT factor, and
- the longitudinal CG displacement of the trailer enables an increase of the SRT factor; but the overweight on the front axle produces understeer of the vehicle, and the overweight on the rear axle produces the oversteer of the vehicle.

The SRT factor increase is important, as it allows to set new road speed limits, which contributes with road safety and decreases vehicle stability related to accidents, which are very high nowadays.

Acknowledge. This research was supported by the Brazilian governmental agencies Coordenação de Aperfeiçoamento de Pessoal de Nível Superior (CAPES) and Conselho Nacional de Desenvolvimento Científico e Tecnológico (CNPq). The authors declare that there is no conflict of interest regarding the publication of this paper.

References

1. Cazangi, H.R.: Aplicação do método de Davies para análise cinemática e estática de mecanismos com múltiplos graus de liberdade. Master's thesis, Federal University of Santa Catarina, Florianópolis, Brazil (2008)
2. Cheng, C., Cebon, D.: Parameter and state estimation for articulated heavy vehicles. Veh. Syst. Dyn. **49**(1–2), 399–418 (2011)
3. Cole, D., Cebon, D.: Truck suspension design to minimize road damage. Proc. Inst. Mech. Eng. Part D J. Autom. Eng. **210**(2), 95–107 (1996)
4. Crossley, F.R.E.: A contribution to Grübler theory in number synthesis of plane mechanisms. ASME J. Eng. Ind. B **86**(2), 1–8 (1964)
5. Dahlberg, E., Wideberg, J.: Influence of the fifth-wheel location on heavy articulated vehicle handling. In: 8th International Symposium on Heavy Vehicle Weights and Dimensions, Johannesburg, South Africa (2004)
6. Davies, T.H.: Mechanical networks-III Wrenches on circuit screws. Mech. Mach. Theor. **18**(2), 107–112 (1983a)
7. Ervin, R.D., Guy, Y.: The influence of weights and dimensions on the stability and control of heavy duty trucks in Canada. UMTRI - The University of Michigan Transportation Research Institute, Report UMTRI-86-35/III, USA (1986)
8. Gillespie, T.D.: Fundamentals of Vehicle Dynamics, 7th edn., pp. 309–327. SAE International, Warrendale (1992)
9. Hac, A.: Rollover stability index including effects of suspension design. In: SAE 2002 World Congress, Detroit, 4–7 March 2002, Paper no. 2002-01-0965
10. Hac, A., Fulk, D., Chen, H.: Stability and control considerations of vehicle-trailer combination. SAE Int. J. Passeng. Cars Mech. Syst. **1**(2008-01-1228), 925–937 (2008)
11. Harwood, D.W., Torbic, D.J., Richard, K.R., Glauz, W., Elefteriadou, L.: Review of Truck Characteristics as Factors in Roadway Design, pp. 40–60. Transportation Research Board, Washington (2003)
12. ISO-14792: Heavy commercial vehicles and buses - steady state circular tests. International Organization for Starndardization, Geneva, Switzerland (2011)
13. Jindra, F.: Handling characteristic of tractor-trailer combinations. SAE International. SAE Paper No. 650720 (1996)
14. Kamnik, R., Boettiger, F., Hunt, H.: Roll dynamics and lateral load transfer estimation in articulated heavy freight vehicles. Proc. Inst. Mech. Eng. Part D J. Automobile Eng. **217**(11), 985–997 (2003)
15. Kutzbach, K.: Mechanische Leitungsverzweigung, ihre Gesetze und Anwendungen. Maschinenbau. Betrieb. **8**(8), 710–716 (1929)
16. Melo, R.P.: Avaliação da Estabilidade Lateral de CVCs. Masters thesis, Pontifícia Universidade Católica do Paraná - Brazil (2004)

17. Michelin LTA: Michelin XZA Tire. Michelin North America, Inc., Greenville (2013)
18. Moreno, G.G., Nicolazzi, L., Vieira, R.S., Martins, D.: Three-dimensional analysis of the rollover risk of heavy vehicles using Davies method. In: 14th World Congress in Mechanical and Machine Science (IFToMM2015), Taipei, Taiwan, vol. 6567 (2015)
19. Moreno, G., Barreto, R.L.P., Nicolazzi, L., Vieira, R.S., Martins, D.: Cap. Three-dimensional analysis of vehicles stability using graph theory. In: Graph-Based Modelling in Engineering, pp. 117–129. Springer, Cham (2016a)
20. Moreno, G.G., Nicolazzi, L., Vieira, R.S., Martins, D.: Rollover of heavy truck using Davies method. In: RS5C 2016 - 17th International Conference Road Safety on Five Continents, Ro de Janeiro, Brasil (2016b)
21. Moreno, G.G., Nicolazzi, L., Vieira, R.S., Martins, D.: Modeling and analysis of the trailer model Davies method. Technical report. https://www.researchgate.net/publication/313472027_Modeling_and_analysis_of_a_trailer_vehicle_using_Davies_Method (2016). Accessed 19 Jan 2017
22. Ray, J.J.: A web-based spatial decision support system optimizes routes for oversize/overweight vehicles in Delaware. J. Decis. Support Syst. **43**, 1171–1185 (2005). 2015
23. Rill, G.: Road Vehicle Dynamics: Fundamentals and Modeling, pp. 276–287. CRC Press, Graz (2011)
24. Rempel, M.R.: Improving the dynamic performance of multiply-articulated vehicles. Master thesis - The University of British Columbia, Vancouver, Canada (2001)
25. Sadeghi, J., Fathali, M.: Deterioration analysis of flexible pavements under overweight vehicles. J. Transp. Eng. **133**(11), 625–633 (2007)
26. Tsai, L.-W.: Mechanism Design: Enumeration of Kinematic Structures According to Function. CRC Press, Boca Raton (2001)
27. Winkler, C.: Experimental determination of the rollover threshold of four tractor-semitrailer combination vehicles, 79 p., Final Report to Sandia Labs, Report No. UMTRI-87-43, July 1987
28. Winkler, C.: Rollover of Heavy Commercial Vehicles, p. 74. Society of Automotive Engineers, Warrendale (2000)

Development of a Robust Integrated Control System to Improve the Stability of Road Vehicles

Abel Castro[1(✉)], Georg Rill[2], and Hans I. Weber[1]

[1] PUC-Rio, Rua Marquês de São Vicente, Rio de Janeiro, RJ 22451-900, Brazil
abel.arrieta@aluno.puc-rio.br, hans@puc-rio.br
[2] OTH Regensburg, Galgenbergstr. 30,
93053 Regensburg, Germany
georg.rill@oth-regensburg.de

Abstract. Nowadays, new technologies are pushing the road vehicle limits further. Promising applications, e.g., self-driving cars, require a suitable control system that can maintain the vehicle's stability in critical scenarios. In most of current cars, the control systems actuates independently, meaning there is not a coordination or data sharing between them. This approach can produce a conflict between these standalone controllers and thus, no improvements on the vehicle's stability are achieved or even a worse scenario can be generated. In order to overcome these problems, an integrated approach is developed in this work. This integration, defined in this work as Integrated Control (IC), is done by an intelligence coordination of all standalone controllers inside the vehicle, i.e., Anti-Lock Braking System (ABS), Electronic Stability Program (ESP) and Four-Wheel Steering System (4WS). The ABS model was built using Fuzzy logic, for which only three rules were necessary to get a good performance. To design the ESP and the 4WS, the simple handling vehicle model was used as a reference behavior. The IC was designed using the hierarchical approach with two layers, i.e., the upper and lower layer. The upper one, observes the side slip angle and depends of its value the upper layer triggers the ESP or the 4WS. Finally, in order to prove the improvements of the IC system over the non-integrated approach, a full-size vehicle model was used to perform simulation in run-off-road and μ-split scenarios.

Keywords: Integrated control · ABS · ESP · 4WS · Run-off-Road scenarios

1 Introduction

Safety and comfort are the most important aspects that automakers take into account when developing road vehicles. Therefore, for the automotive industry and engineers, it is of high priority to reduce road fatalities by applying new technologies. In reality, for many countries, e.g., countries in Europe, Japan, the USA.

J.C.M. Carvalho et al. (eds.), *Multibody Mechatronic Systems*,
Mechanisms and Machine Science 54, DOI 10.1007/978-3-319-67567-1_48

and Brazil the use of Anti-Lock Braking System (ABS) is mandatory. The Electronic Stability Program (ESP) is capable of reducing by 49% the number of SVA [1]. Other types of controllers, like the Four-Wheel Steering System (4WS), can improve the vehicle's response in normal driving situation [2], that means when the roll angle of the vehicle is relative small (no roll-over situations). If these controllers, i.e., the ABS, ESP and 4WS actuate over the vehicle at the same time, this may lead to a conflict that becomes a worse scenario to the driver. Therefore, it is important to develop a methodology to integrate them in order to improve the vehicle performance on those scenarios. In [3], a integration of the Active Front Steering System (AFS) and the ESP was performed. The results shown that this integration improve the vehicle lateral stability. Moreover, in [4], an integration of the 4WS, ESP and ABS was done using a simple switch control law between the 4WS and ESP for run-off-road scenarios. Simulation performed shown an improvement of the vehicle's lateral stability in different road conditions. This study also concluded that, the benefits of the 4WS in combination with the ESP and ABS is a good options to improve the overall dynamic response of modern cars.

2 Vehicle and Tire Modeling

2.1 Fully Non-linear Vehicle Model

The mathematical model of the vehicle is built applying the multi-body approach. Using this method, it is possible to modeling the vehicle by subsystems as presented in [5,7]. In this work, nine rigid bodies are used, i.e., 4 knuckles, 4 wheel-tire sets and 1 chassis, see Fig. 1. The equations of motion are obtained using the Jourdain's Principle and derived respect to the vehicle-fixed axis system $\boldsymbol{F}$ (located in the middle of the front axle). Finally, the vehicle dynamics is characterized by a set of non-linear first order differential equations as follows:

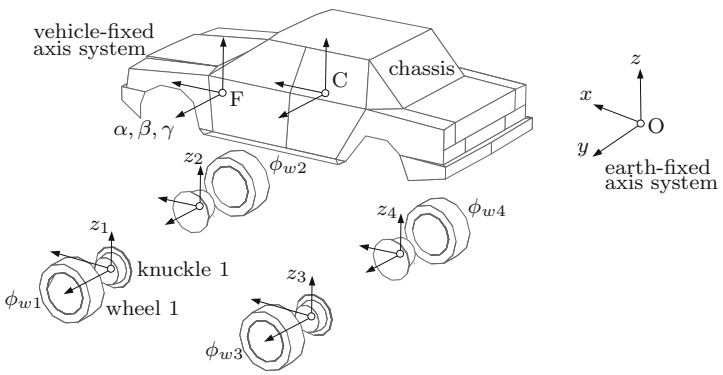

Fig. 1. Multi-body vehicle model (14 dof).

$$K(y)\,\dot{y} = z, \quad M(y)\,\dot{z} = q(y,z,s,u), \quad \dot{s} = f(y,z,s,u),$$
$$y = [x, y, z, \alpha, \beta, \gamma, z_1, z_2, z_3, z_4, \phi_{w1}, \phi_{w2}, \phi_{w3}, \phi_{w4}] \tag{1}$$

where y is a vector that collects the generalized coordinates of the vehicle. K is the kinematic matrix used to define an appropriate vector of generalized velocities z. The mass matrix of the multi-body vehicle model is denoted by M. The vector of generalized forces q is function of the input u and the additional states s. Furthermore, the vector s collects the internal states of the dynamic force elements and tire deflections respectively.

2.2 Simple Handling Model

For control design purposes, the desired response of the vehicle to driver's input is necessary. Generally, the simple handling model is used as a reference, see Fig. 2. According to the assumptions in the right side of Fig. 2, the equation of motion of the handling model are defined as follows:

$$m\left(v\omega + |v|\dot{\beta}\right) = F_{yf} + F_{yr} \qquad \text{and} \qquad \Theta\dot{\omega} = a_1 F_{yf} - a_2 F_{yr}, \tag{2}$$

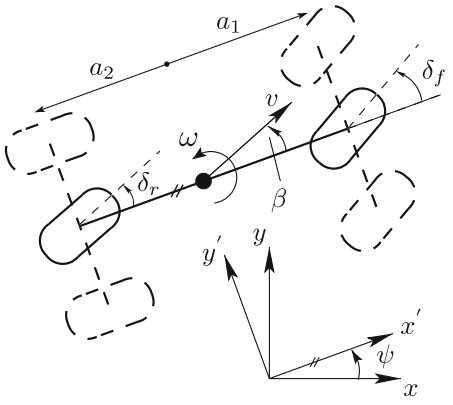

- tires operates in the linear region.
- only planar motion.
- no driving or braking is applied i.e, $\dot{v} = 0$.
- δ_f represents the mean of the front steering angles.
- δ_r represents the mean of the rear steering angles.
- δ_f, δ_r and β are assumed to be small.

Fig. 2. Simple handling vehicle model and assumptions.

where the inertia properties of the handling model are represented by its mass m, the moment of inertia around the z axis Θ and the distances, a_1 and a_2, from its center of gravity to the front and rear axle respectively. In addition, the tire lateral forces F_{yi} are described as a function of the cornering stiffness c_{si} and the lateral slips s_{yi} $(i = f, r)$ as follows:

$$F_{yi} = c_{si} s_{yi}, \qquad s_{yf} = -\beta - \frac{a_1}{|v|}\omega + \frac{v}{|v|}\delta_f, \qquad s_{yr} = -\beta + \frac{a_2}{|v|}\omega + \frac{v}{|v|}\delta_r. \tag{3}$$

Finally, rearranging and simplifying (2) and (3), the linear state equation is obtained as:

$$\underbrace{\begin{bmatrix}\dot{\beta}\\ \dot{\omega}\end{bmatrix}}_{\dot{x}} = \underbrace{\begin{bmatrix} -\frac{c_{sf}+c_{sr}}{m|v|} & \frac{a_2c_{sr}-a_1c_{sf}}{m|v||v|}-\frac{v}{|v|} \\ \frac{a_2c_{sr}-a_1c_{sf}}{\Theta} & -\frac{a_1^2c_{sf}+a_2^2c_{sr}}{\Theta|v|}\end{bmatrix}}_{A}\underbrace{\begin{bmatrix}\beta\\ \omega\end{bmatrix}}_{x} + \underbrace{\begin{bmatrix} \frac{v}{|v|}\frac{c_{sf}}{m|v|} & \frac{v}{|v|}\frac{c_{sr}}{m|v|} \\ \frac{v}{|v|}\frac{a_1c_{sf}}{\Theta} & -\frac{v}{|v|}\frac{a_2c_{sr}}{\Theta}\end{bmatrix}}_{B}\underbrace{\begin{bmatrix}\delta_f\\ \delta_r\end{bmatrix}}_{u}, \tag{4}$$

where the time derivative of the yaw angular velocity ω and the vehicle side slip angle β are the output states of the model. The cornering stiffness of the front and rear axle are represented by c_{sf} and c_{sr} respectively. Lastly, the vehicle velocity v, δ_f and δ_r are inputs of this model.

2.3 TMeasy Tire Model

TMeasy [6], is a semi-empirical tire model that uses a small number of parameters to characterize the tire-road contact forces. In normal driving maneuvers, e.g., the acceleration or deceleration in a curve, the longitudinal slip s_x and lateral slip s_y occur at the same time. Therefore, the combination of slips and forces should be handled by the tire model. TMeasy perform this combination process as follows:

$$s = \sqrt{\left(\frac{s_x}{\hat{s}_x}\right)^2 + \left(\frac{s_y}{\hat{s}_y}\right)^2} = \sqrt{\left(s_x^N\right)^2 + \left(s_y^N\right)^2}, \tag{5}$$

where s_x^N and s_y^N are the normalized slips. Furthermore, the normalizing factor $\hat{s}_x$ and $\hat{s}_y$ take into account the longitudinal and lateral force characteristics and are defined as follows:

$$\hat{s}_i = \frac{s_i^M}{s_x^M + s_y^M} + \frac{F_i^M/dF_i^0}{F_x^M/dF_x^0 + F_y^M/dF_y^0}, \quad \text{where: } i = \{x, y\}. \tag{6}$$

Similar to the curve of longitudinal and lateral forces, the combined force $F = F(s)$ can be defined by their characteristic parameters dF^0, s^M, F^M, s^S, and F^S. These parameters are defined as:

$$\begin{aligned} dF^0 &= \sqrt{(dF_x^0\hat{s}_x\cos\phi)^2 + (dF_y^0\hat{s}_y\sin\phi)^2} \\ s^M &= \sqrt{\left(\tfrac{s_x^M}{\hat{s}_x}\cos\phi\right)^2 + \left(\tfrac{s_y^M}{\hat{s}_y}\sin\phi\right)^2} \qquad F^M = \sqrt{\left(F_x^M\cos\phi\right)^2 + \left(F_y^M\sin\phi\right)^2} \\ s^S &= \sqrt{\left(\tfrac{s_x^S}{\hat{s}_x}\cos\phi\right)^2 + \left(\tfrac{s_y^S}{\hat{s}_y}\sin\phi\right)^2} \qquad F^S = \sqrt{\left(F_x^S\cos\phi\right)^2 + \left(F_y^S\sin\phi\right)^2} \end{aligned} \tag{7}$$

The angular function ϕ grant a smooth transition from the longitudinal and lateral force to the combined force as follows:

$$F_x = F\cos(\phi),\ F_y = F\sin(\phi) \quad \text{and} \quad \cos(\phi) = \frac{s_x^N}{s},\ \sin(\phi) = \frac{s_y^N}{s}. \tag{8}$$

Figure 3 shows the tire friction limits computed using TMeasy and a set of parameters that represent a commercial passenger tire.

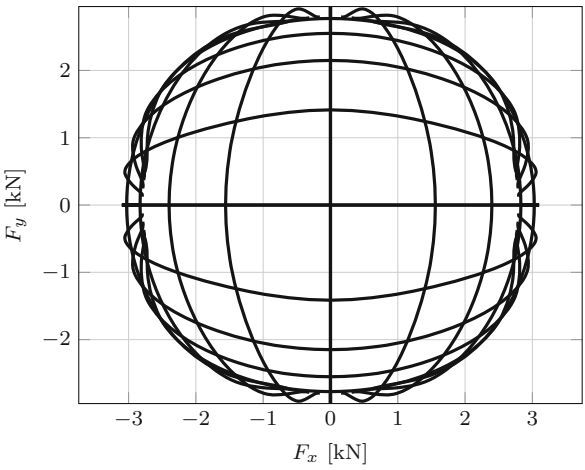

Fig. 3. Tire friction limits for commercial passenger car (tire code: P265/40 R18).

3 Standalone Controllers

For all the simulations presented in this section, a full-size car with characteristic parameters defined in Table 1 is used. The road and off-road scenarios are characterized by friction coefficients of 1.0 and 0.4 respectively. In addition, the road surface is located 5 cm above the off-road surface and an obstacle is placed at 150 m in front of the vehicle. The virtual test driver, based on fuzzy logic, try to avoid the obstacle and then, force the vehicle to go off-road. For the driver model the cross track error and the vehicle's orientation are used as inputs to maintain the vehicle in the road's center line.

3.1 Anti-lock Braking System - ABS

For this ABS model, the friction coefficient μ is assumed to be unknown and therefore, the longitudinal slip s_x was taken as control variable. It is defined as:

$$s_x = -\frac{(v_x - \Omega r_D)}{|\Omega| r_D + v_N}, \tag{9}$$

Table 1. Full-size vehicle parameters

Parameter	Value	Units
Velocity	90	km/h
Chassis mass	1927.8	kg
Chassis inertia	$I_{xx} = 452$, $I_{yy} = 2645.3$, $I_{zz} = 2813.5$	kg$\times$ m^2
Suspension	Double wishbone (front and rear)	-
Tires	P265/40 R18	-
Wheel base	2.9	m
Track front	1.53	m
Track rear	1.52	m

where v_x is the vehicle velocity, Ω is the wheel angular velocity, r_D is the tire dynamic radius and v_N is a fictitious velocity, introduced to avoid numerical problems.

The ABS model is based on Fuzzy Logic because this strategy can handle non-linearities better than linear control strategies. The proposed ABS model works with a set of rules defined in Table 2.

Table 2. Fuzzy control rules for the proposed ABS model.

Longitudinal slip [-]	Braking torque [N.m]
Low	High
Medium	Medium
High	Small

In order to prove the effectiveness of the ABS model, two scenarios were simulated. In the first one, a straight line braking maneuver is used. With the ABS off, all wheels are locking instantly as we can see in the left upper plot (dashed lines) of Fig. 4. In the other hand, with the ABS on, the wheels are still rolling and then, it results in a smaller slip $(0.1 - 0.2)$, left upper plot (solid lines) of Fig. 4. In addition, with the ABS on, the vehicle is reaching decelerations up to $\frac{\dot{v}}{g} = 1.0$, left bottom plot (solid line) of Fig. 4, which is the limit imposed by the friction coefficient ($\mu = 1.0$). The last scenario is built in order to test the gain in stability using the ABS model. In this simulation, the vehicle is driving in a straight line and at $t = 3.6\,\text{s}$ the steering wheel is applied and then at $t = 4.0\,\text{s}$, the brakes are triggered. With the ABS off, the wheels are locked by the braking torque. Therefore, the vehicle follows a straight trajectory because the front wheels are not capable to generate neither lateral or longitudinal forces. In the case of ABS on, the vehicle follows the driver's intentions because the front wheels can generate lateral forces. These results are shown in the right multi-frame shots of the trajectories in Fig. 4.

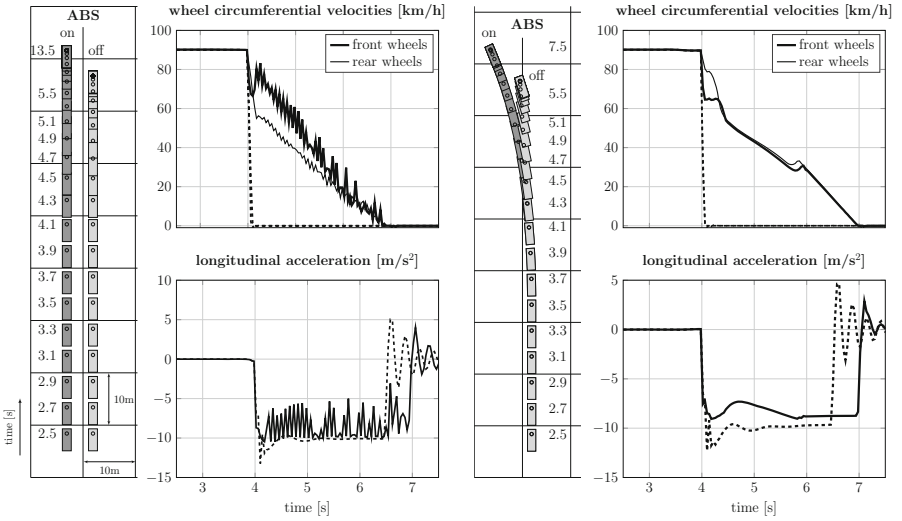

Fig. 4. Left: braking in a straight line. Right: braking in a turn (— ABS on, - - - ABS off)

3.2 Electronic Stability Program - ESP

The main objective of this system is to assist the driver in a critical driving situations, e.g. to avoid an unexpected obstacle on the road, and also compensate the disturbance produced by the driver in this critical scenario and thus prevent loss of vehicle stability. The ESP analyze the current states of the vehicle using two variables: direction of the driving steering and direction in which the vehicle is moving. For that, ESP uses the simple handling vehicle model as a reference. The difference between the actual yaw rate ω and the reference (Eq. 2) ω_d, gives to ESP the necessary information to respond in critical scenarios, see Fig. 5. Finally, ESP triggers the ABS in order to apply the correct brake torque to the selected wheel and then, a compensatory yaw moment T is generated.

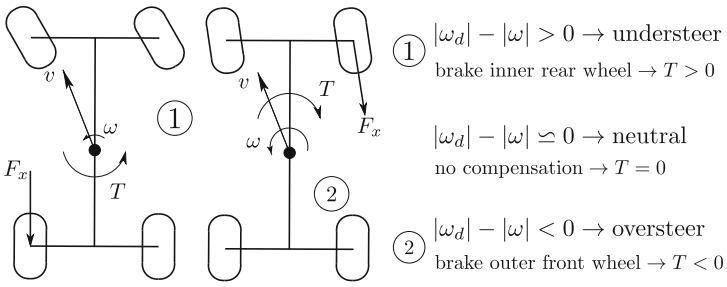

Fig. 5. ESP control law.

In Fig. 6, two simulations are compared. The solid line indicates the results of an avoidance maneuver with ESP on, the dashed one considers the same maneuver with ESP off. It is possible to distinguished that, the torque frequency applied by ESP to the outer front wheel is high when the vehicle is on off-road $t = 5.75 \rightarrow 8\,\text{s}$. This is because, there is a μ-split condition when the vehicle goes off-road and come back to the road again, and this requires a torque compensation to maintain the vehicle stability. In this period, the yaw angular velocity (left upper plot), lateral acceleration (right upper plot) and total the overall yaw moment (left bottom plot) are maintained in a safe range for the ESP. Finally, ESP assisted the driver to maintain the desired path as indicated by the multi-frame shot at the very left of Fig. 6.

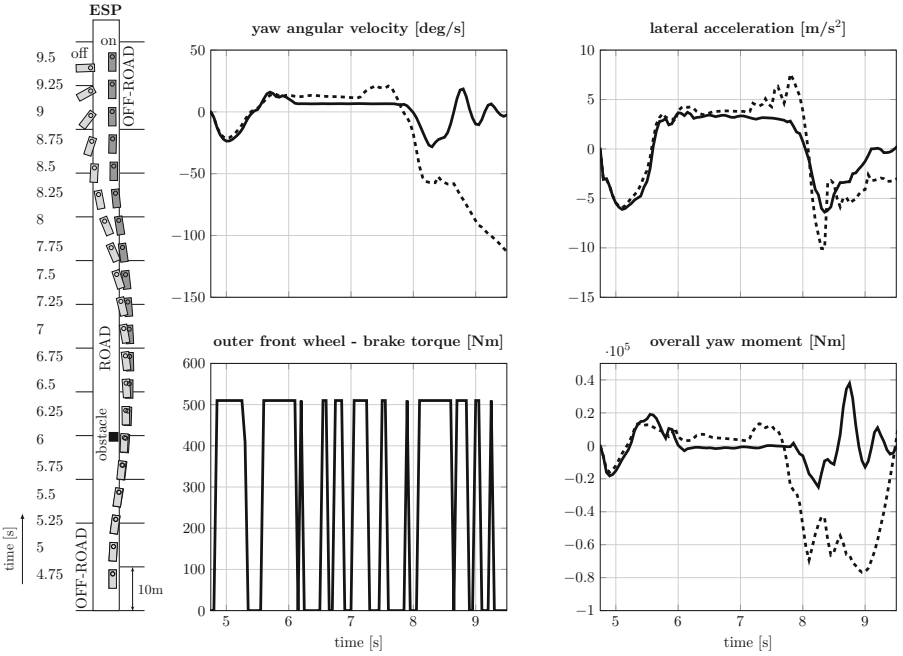

Fig. 6. Trajectory and main states of the vehicle: — ESP on, - - - ESP off.

3.3 Four-Wheel Steering System - 4WS

The 4WS was introduced by Nissan in its model R31 Skyline in the late of 1985. The main advantages of this system are: improve the maneuverability at low velocities and the lateral stability at high velocities. In [2], it is concluded that a simple feed-forward control can improve the vehicle lateral stability. In this work the controller monitors the front steering angle and depending of this value a rear wheel angle is imposed, see Fig. 7.

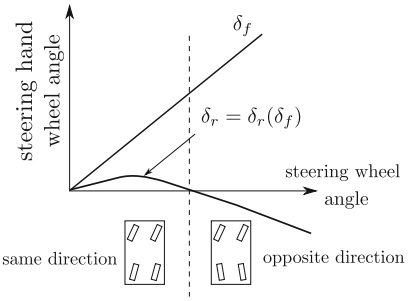

Fig. 7. Proposed feed-forward control law.

In Fig. 8 can be distinguished some benefits of the 4WS system. From $t \approx 5\,\text{s}$ to 7 s, there is a slight improvement of the 4WS system on the vehicle stability. A large enhancement can be noticed between $t \approx 7\,\text{s}$ to 9.5 s. In this interval, the yaw angular velocity, lateral acceleration and the overall yaw moment are maintained in a safe range due to the 4WS.

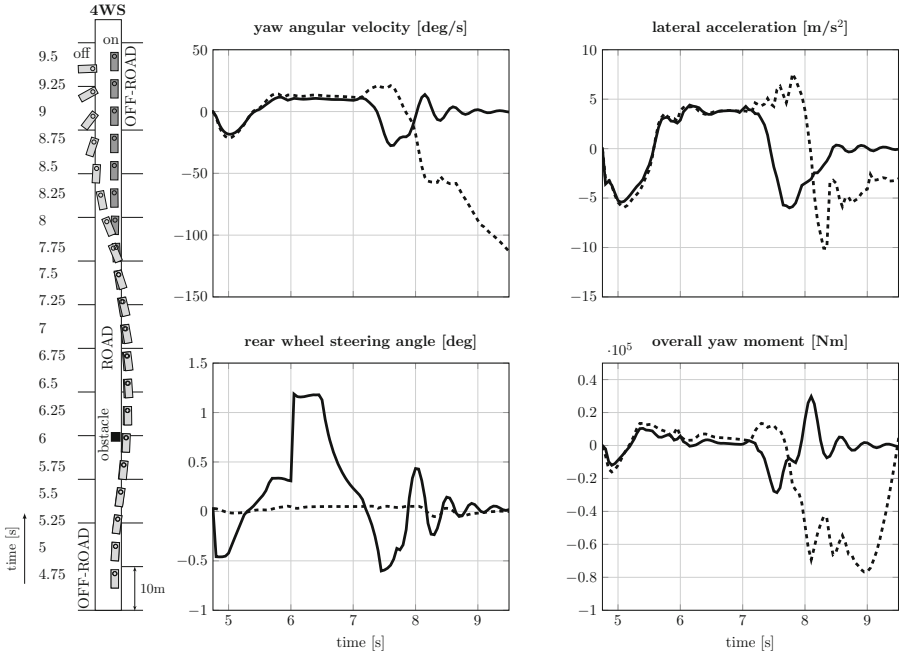

Fig. 8. Trajectory and main states of the vehicle: — 4WS on, - - - 4WS off.

4 Integrated Approach

For the integrated system, a hierarchical approach with two layers is employed, i.e., the upper and the lower layer. The upper one uses the side slip angle as a control variable to trigger the standalone controllers (lower layer), i.e., the ESP and the 4WS. Therefore, the IC will use the 4WS when smaller front steering wheel angles are imposed for the driver, and will use the ESP otherwise. To trigger the correct standalone controller, a boundary for the side slip angle is defined as follows:

$$IC = \begin{cases} \textbf{4WS: on} \ \& \ \textbf{ESP: off}, & \text{if } |\beta| \leq \beta_U \\ \textbf{4WS: off} \ \& \ \textbf{ESP: on}, & \text{otherwise} \end{cases} \tag{10}$$

where β represent the side slip angle of the vehicle and $\beta_U = 3°$ is the upper bound value for β.

In Fig. 9, simulations of a vehicle with the ESP and 4WS with (IC) and without integration is shown. In the multi-frame shots we can realize a smaller lateral error of the vehicle using the IC system. In addition, the vehicle with IC system use properly the brake torque on the outer front wheel as presented in the bottom-right plot of Fig. 9.

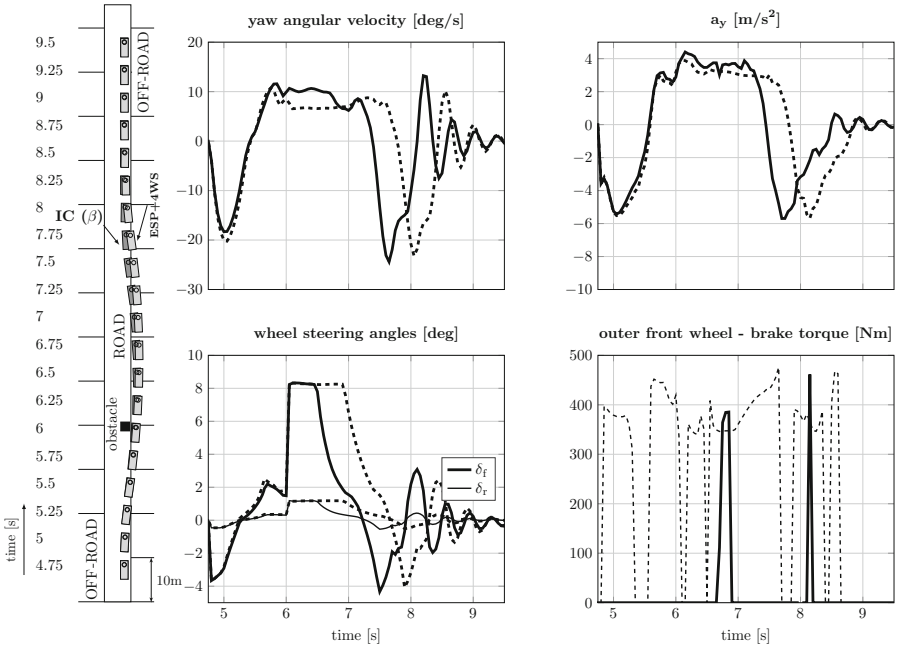

Fig. 9. Trajectory and main states of the vehicle: — 4WS on, - - - 4WS off.

5 Conclusions

An integration system, called IC, of the ABS, ESP and 4WS was presented. The approach used for the IC system is based on a hierarchical architecture. The upper layer triggers the standalone controllers (lower layer) using the side slip angle of the vehicle as a control variable. Simulations on a run-off-road scenario shown an improvement on the vehicle's lateral stability using the IC system. Finally, an improvement of the overall vehicle dynamics of the integrated approach against the non-integrated one can be concluded.

References

1. Erker, A.: Effects of electronic stability control (ESC) on accidents: a review of empirical evidence. Accid. Anal. Prev. **40**, 167–173 (2008)
2. Furukawa, Y., et al.: A review of four-wheel steering studies from the viewpoint of vehicle dynamics and control. Veh. Syst. Dyn. **18**, 151–186 (1989)
3. Castro, A., Rill, G., Weber, H.I.: Designing an integrated control based on a hierarchical architecture to improve the performance of ground vehicles. In: 23rd ABCM International Congress of Mechanical Engineering (2015)
4. Castro, A., Basilio, R., Rill, G., Weber, H.I.: Use of integrated control to enhance the safety of vehicles in run-off-road scenarios. In: XVII International Symposium on Dynamic Problems of Mechanics (2017)
5. Rill, G.: Road Vehicle Dynamics: Fundamentals and Modeling. CRC Press, Boca Raton (2011)
6. Rill, G.: TMeasy - a handling tire model based on a three-dimensional slip approach. In: XXIII International Symposium on Dynamic of Vehicles on Roads and on Tracks - IAVSD (2013)
7. Rill, G.: Simulation von Kraftfahrzeugen. Vieweg, Braunschweig (1994)

Powertrain Optimization to Improve Vehicle Performance and Fuel Consumption

Jony J. Eckert(✉), Fernanda C. Corrêa, Elvis Bertoti, Rodrigo Y. Yamashita, Ludmila C.A. Silva, and Franco G. Dedini

University of Campinas - UNICAMP, Campinas, SP 13083-970, Brazil
javorski@fem.unicamp.br

Abstract. The available gearbox transmission ratios associated with gear shifting strategies influence the vehicle performance and fuel consumption because it changes the powertrain inertia and the engine operation point. However, the best configuration for the vehicle powertrain, according to a specific driving condition, is difficult to be determined. Therefore, this paper presents an Interactive Adaptive-Weight Genetic Algorithm to optimize the vehicle powertrain gear ratios and the gear shifting strategies to allow the vehicle to operate in the best compromise among fuel consumption and performance in the urban driving scenario provided by the FTP-72 cycle. The optimization process results in a fuel saving of 10.61% and 50.12% improvement in the vehicle performance when using the best-compromised configuration.

Keywords: Genetic Algorithm Optimization · Powertrain · Gear shifting · Fuel consumption · Vehicular performance

1 Introduction

Vehicles propelled by internal combustion engines (ICE) are one of the most prominent fossil fuel consumers around the world [1]. Optimized layouts for the vehicle powertrain could save fuel, specially when the gear change is made at the right moment, as in the case of an automated manual transmission (AMT) or with the help of a driving assistance equipment. Gear shifting strategies for fuel economy usually anticipate the upshift processes in order to force the ICE to operate at a lower speed and higher torque condition. However, focusing solely on fuel economy may lead to poor performance, since in case of a torque demand increase the ICE would not be able to supply the required force, without performing a downshift.

Several studies propose optimization techniques to improve the vehicle performance and fuel consumption. In the paper presented by [2], a 6 gear AMT vehicle propelled by a 2.2 L ICE presents 4.6% fuel saving with the optimization of the gear shifting strategy on the New European Driving Cycle (NEDC) and an improvement of 9.1% for the Wuhan city driving cycle. In another study, despite employing a large tolerance for the resultant velocity profile, [3] achieved

J.C.M. Carvalho et al. (eds.), *Multibody Mechatronic Systems*,
Mechanisms and Machine Science 54, DOI 10.1007/978-3-319-67567-1_49

34% fuel economy by optimizing the gear shifting strategy for fuel consumption (eco-driving) in a 1.5 L vehicle with 5 gear ratios and considering variables associated with traffic condition. According to [4], the eco-driving technique consists in keeping the engine running at lower speed and performing the upshift with the ICE operating inside the range of 2000–2500 rpm (according to the vehicle design).

As mentioned before, powertrain setups that aim only at fuel saving usually are associated with poor acceleration performance. In this concern, [5] optimizes the gear shifting strategies to minimize fuel consumption, attending to the power demand required by the driver. The optimized gear shifting strategies result in 25.4% for the Federal Test Procedure cycle (FTP).

In a previous work [6] analyses powertrains with 5 to 7 gear ratios designed by the progressive and geometric gearboxes approaches, as proposed by [7]. This study also carries out a gear shifting strategy optimization for each developed powertrain configuration. The optimization presents 25.07% fuel saving for a 5 speed geometric gearbox as a best result over the FTP-72 cycle. In this paper an Genetic Algorithm optimization is presented to define the vehicle powertrain gear ratios and associated gear shifting strategy to improve the vehicle performance and save fuel in the FTP-72 urban driving cycle.

2 Simulation Model

This paper focuses on the vehicle longitudinal dynamics simulation based on the equations proposed by [8]. The simulation is performed in the Simulink interface and starts by defining the required torque at the ICE T_{req} [Nm] Eq. (1), in which: D_A [N] represents the aerodynamic drag, R_x [N], the tires rolling resistance; M [kg], the vehicle mass; I_e [kgm^2], engine moment of inertia; N_t and I_t [kgm^2], the gearbox transmission ratio an inertia; N_d and I_d [kgm^2], the differential gear ratio and inertia; I_w [kgm^2], wheels inertia; r [m], tire radius (disregarding the wheels rotation dynamics effects); η_{td} is the powertrain mechanical efficiency. The required acceleration a_{req} [m/s^2] is defined by the difference between the current vehicle speed and the drive cycle objective speed V_c [m/s] one time step Δ_t [s] ahead of the current simulation time.

$$T_{req} = \frac{(Ma_{req} + R_x + D_A)\, r + \left((I_e + I_t)(N_t N_d)^2 + I_d N_d^2 + I_w\right) \frac{a_{req}}{r}}{N_t N_d \eta_{td}} \tag{1}$$

$$a_{req} = \frac{V_c - V}{\Delta_t} \tag{2}$$

The aerodynamic drag D_A [N] and the tires rolling resistance R_x [N] are estimated by equations dependent on the vehicle speed V [m/s]. Where g [m/s^2] is the gravitational acceleration, C_D is the drag coefficient and A [m^2] represents the vehicle frontal projected area.

$$D_A = \frac{1}{2}\rho V^2 C_D A \tag{3}$$

$$R_x = 0.01Mg\left(1 + \frac{2.24V}{100}\right) \tag{4}$$

Once the ICE required torque T_{req} is defined, it is compared to the engine maximum torque curve (100% throttle) provided by the Fig. 1a. If the required torque exceeds the ICE maximum limit, the clutch input torque is capped by the 100% throttle curve. During the gear shifting process, the gearbox input torque T_t [Nm] will be limited by the clutch transmissible torque T_{cl} [Nm], defined in function of the inner R_i [m] and external R_o [m] radii of the clutch disks, the number of discs n, the friction coefficient μ_{cl}, and the normal force F_n [N] applied by the clutch spring, as proposed by [9]. The F_n force is defined by a graphic method according to the clutch pedal position during the shift process, as proposed in [10].

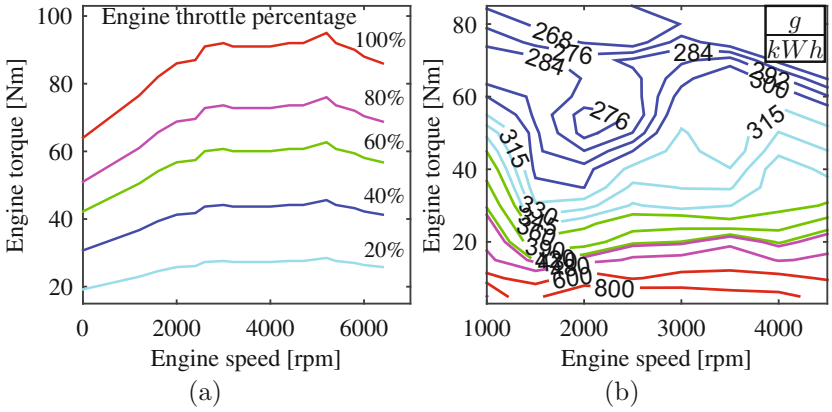

Fig. 1. Engine torque and specific fuel consumption maps [11,12]

$$T_{cl} = \frac{2}{3}\mu_{cl}F_n n\frac{R_o^3 - R_i^3}{R_o^2 - R_i^2} \tag{5}$$

If the engine output torque is superior to the transmissible torque T_{cl}, the gearbox input must be equal to the transmissible torque ($T_t = T_{cl}$). Therefore, the available traction force F_x [N] is calculated by Eq. (6) as a function of the vehicle current acceleration a_x [m/s^2].

$$F_x = \frac{T_t N_t N_d \eta_{td}}{r} - ((I_e + I_t)(N_t N_d)^2 + I_d\ N_d^2 + I_w)\frac{a_x}{r^2} \tag{6}$$

However, in some cases, the available traction force is restricted by the traction limit of the tire-ground contact F_{max} [N] given by Eq. (7), in function of the tire-ground peak friction coefficient μ, the vehicle wheelbase L [m], the height of the gravity center h [m], and the longitudinal distance between the vehicle rear axle and the gravity center c [m], as proposed by [7].

$$F_{max} = \mu \left(\frac{Mg\ c}{2L} - \frac{Mh\ a_x}{2L} \right) \tag{7}$$

The vehicle acceleration a_x [m/s^2] is calculated by Eq. (8), depending on the traction force F_t [N], which equals either the transmissible force if $F_x \geq F_{max} \therefore F_t = F_{max}$, or becomes equal to the available traction force if $F_x < F_{max} \therefore F_t = F_x$.

$$a_x = \frac{F_t - R_x - D_A}{M} \tag{8}$$

Due to the fact that Eqs. (6) and (7) depend on the resultant acceleration a_x provided by the Eq. (8), the estimated initial condition that considers $a_x = a_{req}$ may generate inaccurate results. Therefore, an iterative process among the Eqs. (6), (7) and (8) must be performed until the convergence of F_t and a_x happens. The vehicle acceleration is integrated by ODE45 to define the current vehicle speed V. The engine real output torque T_e [Nm] used to calculate the fuel consumption is defined by Eq. (9):

Table 1. Vehicle parameters [11]

Components	Units	Speed				
		1^{st}	2^{nd}	3^{rd}	4^{th}	5^{th}
Gearbox ratio (N_t)	-	4.27	2.35	1.48	1.05	0.8
Gearbox inertia (I_t)	kgm^2	0.0017	0.0022	0.0029	0.0039	0.0054
Engine inertia (I_e)	kgm^2			0.1367		
Differential inertia (I_d)	kgm^2			9.22E−04		
Wheels + tires inertia (I_w)	kgm^2			2		
Differential ratio (N_d)	-			4.87		
Powertrain efficiency (η_{td})	-			0.9		
Total vehicle mass (M)	kg			980		
Vehicle frontal area (A)	m^2			1.8		
Drag coefficient (C_d)	-			0.33		
Tires 175/70 R13 radii (r)	m			0.2876		
Tire peak friction coefficient (μ)	-			0.9		
Wheelbase (L)	m			2.443		
Gravity center height (h)	m			0.53		
Rear axle to gravity center (c)	m			1.460		
Clutch friction coefficient (μ_{cl})	-			0.27		
Clutch external disk radius (R_o)	mm			95		
Clutch internal disk radius (R_i)	mm			67		
Clutch faces (n)	-			2		

$$T_e = \frac{F_t r}{N_t N_d \eta_{td}} + ((I_e + I_t)(N_t N_d)^2 + I_d\ N_d^2 + I_w)\frac{a_x}{r} \tag{9}$$

The engine speed ω_e [rad/s] is provided by Eq. (10). The fuel consumption C_l [l] is calculated by Eq. (11), according to the ICE fuel consumption map $C_e(dt)$ [g/kWh] (Fig. 1b).

$$\omega_e = \frac{V N_d N_t}{r} \tag{10}$$

$$C_l = \int_0^{t_c} \frac{C_e(dt) T_e \omega_e}{3600 \rho_c} \tag{11}$$

Where t_c [s] represents the cycle duration, and ρ_c [kg/m^3] is the fuel density. Table 1 shows the original parameters for the simulated vehicle.

3 Optimization Problem

The optimization problem is formulated by two optimization criteria. The first one is to minimize the ICE fuel consumption C_l resultant from the simulation process. The second one aims to improve the vehicle performance compared to the FTP-72 driving cycle. The vehicle performance is measured by the correlation coefficient R [11] as given by Eq. (12), in which V_{ci} represents the FTP-72 speed, V_i is the simulated vehicle speed and $\bar{V}_c$ and $\bar{V}$ are the mean values of the standardized profile and the simulated cycle, respectively:

$$R = \sqrt{\frac{\left(\sum \left(V_{ci} - \bar{V}_c\right)\left(V_i - \bar{V}\right)\right)^2}{\sum \left(V_{ci} - \bar{V}_c\right)^2 \sum \left(V_i - \bar{V}\right)^2}} \tag{12}$$

The fact that the perfect correlation between the simulated speed profile and the driving cycle results would happen at $R = 1$, the goal of the optimization is to minimize the difference $1 - R$ for improving the vehicle performance.

Therefore the optimization criteria are:

$$\min f_1(X) = 1 - R(X) \tag{13}$$

$$\min f_2(X) = C_l(X) \tag{14}$$

Where X represents the chromosome that contains the design variables, such as the vehicle gearbox available gear ratios N_t and differential transmission ratio N_d. The chromosome X also defines the upshift speeds V_{un} [m/s] $(1 \leq n \leq 4)$ that indicates the speed limit where the driver/AMT must change the gearbox transmission ratio $V = V_{un} \therefore N_{tn} \longrightarrow N_{t(n+1)}$.

The downshift speed V_{dn} [m/s] must be lower than the upshift speed to avoid instabilities [13]. Therefore, this difference is calculated by Eq. (16) according to the variable D_s [m/s] (also a design variable to be optimized) that is subtracted for the upshift speed V_{un}.

$$[X] = [N_{t1}\ N_{t2}\ N_{t3}\ N_{t4}\ N_{t5}\ N_d\ V_{u1}\ V_{u2}\ V_{u3}\ V_{u4}\ D_s] \tag{15}$$

$$V_{dn} = V_{un} - D_s \tag{16}$$

In all cases the proposed gear ratios and gear shifting speeds must respect the ICE maximum and minimum speeds, $\omega_{max} = 471\,\text{rad/s}$ (4500 rpm) and ω_{min} (idle speed) $= 89\,\text{rad/s}$ (850 rpm) respectively. The problem constraints C are listed in Eq. 17.

$$C = \begin{cases} V_{un} < V_{u(n+1)} \\ V_{dn} > V_{d(n+1)} \\ N_{tn} \geq N_{t(n+1)} + 0.1 \\ N_{t1} \leq 6 \\ N_{t5} \geq 0.6 \\ 4 \leq N_d \leq 7 \\ \omega_{min} \leq \omega_e \leq \omega_{max} \\ 0.3 \leq D_s \leq 3 \\ (1 - R) \leq 4.1 \times 10^{-4} \end{cases} \tag{17}$$

Also, an acceptable performance limit ($(1 - R) \leq 4.1 \times 10^{-4}$) was stipulated, which corresponds to the standard vehicle setup (Table 1) under the gear shifting strategy proposed by [14] for a vehicle similar to the one simulated in this work.

For the new configurations, the values for the powertrain inertia I_d and I_{tn} are interpolated among the new gear ratios from the chromosome X and the gear ratios and moments of inertia shown in Table 1, as proposed in [6].

3.1 Interactive Adaptive-Weight Genetic Algorithm

The optimization process starts with 50 individuals generated with random design variables for the chromosomes X (respecting the constraints C). These results are stored in a database called population that is classified according to the fitness value $Ft(X)$ defined by the interactive adaptive-weight fitness approach proposed by [15]. The fitness value is calculated by Eq. (18) in function of the maximum and minimum values for each optimization criterion presented in the population. This technique also considers a $P_p = 1$ value to the non-dominated solutions that correspond to the Pareto frontier. The results that are fully dominated in the two optimization criteria receive a penalty value $P_p = 0$, which decreases the selection probability.

$$Ft(X) = \frac{f_1^{max} - f_1(X)}{f_1^{max} - f_1^{min}} + \frac{f_2^{max} - f_2(X)}{f_2^{max} - f_2^{min}} + P_p(X) \tag{18}$$

To combine the design variables of the chromosomes and generate new individuals in the population, the roulette wheel technique [16] is used to select two members (M_1 and M_2) of the population randomly. The solutions that present higher fitness values $Ft(X)$ have the selection probability $S_P(X)$ increased. The Eq. (19) defines the selection probability for N members of the population ($1 \leq X \leq N$).

$$S_P(X) = \frac{Ft(X)}{\sum_{X=1}^{N} Ft(X)} \tag{19}$$

The design variables of the selected members M_1 and M_2 are randomly combined by the crossover operator ($0 \leq Cr \leq 1$). If $Cr \leq 0.5$ the design variable from M_1 is selected for the new chromosome. On the other hand, if $Cr > 0.5$ a design variable coming from M_2 is added to X. If all design variables respect the constraints C, the crossover chromosome is simulated and the achieved result added to the population. If the crossover chromosome does not comply with the constraints, the combination process is repeated until an adequate chromosome is found.

To provide variability in the design variables values, the mutation operator ($0 \leq \ Mt \ \leq 1$) changes randomly some parameters of the crossover chromosome. If $Mt < 0.5$ the mutated chromosome keeps the design variable value from the crossover output. If $Mt \geq 0.5$, the design variable is modified according to $-2 \leq V_{mut} \leq 2$ for the speeds V_{un} and D_s, or $-0.1 \leq N_{mut} \leq 0.1$ for the gear ratios N_{tn} and N_d. The mutation parameters V_{mut} and N_{mut} are then added to their respective design variables at the crossover chromosome. As for the crossover process, the mutation operator runs until it finds a mutated chromosome that respects the constraints C, and then this chromosome is simulated and included in the population.

Furthermore, the population size tends to increase through the evolutionary process. When the population reaches the limit of $P_{lim} = 100$, the last Pareto ranking individuals (worst results) are removed in order to control the population size. To avoid the elimination of non-dominated solutions (Pareto rank = 1), the population limit increases ($P_{lim} = P_{lim} + 50$) when the solutions of the Pareto frontier become higher than P_{lim}.

The optimization algorithm ends if the Pareto frontier is repeated along 100 consecutive generations (crossover and mutation). When the algorithm reaches the convergence criterion, the results that compose the Pareto frontier of the non-dominated solutions are considered as optimized configurations.

4 Optimization Results

By running the presented algorithm and after its convergence, the results shown in Fig. 2 were found. This figure also shows the initial population and, for comparison, the fuel consumption and performance obtained with the standard setup of the vehicle. Among the optimized solutions three results were selected: Minimum f_1, which represents the best performance solution; Minimum f_2, which corresponds to the fuel economy configuration; Maximum Ft, which is the best-compromised solution between the optimization criteria. Table 2 compares the results of the optimized solutions with the standard configuration; their respective design variables are listed in Table 3.

According to the powertrain configurations of the selected optimized solutions, the vehicle runs the ICE in different regimes. Figure 3 compares the ICE operation histogram according to the different set of gear ratios and shifting strategies. The minimum f_1 solution improves the vehicle performance by keeping the ICE running at higher speeds and by deploying more overall transmission

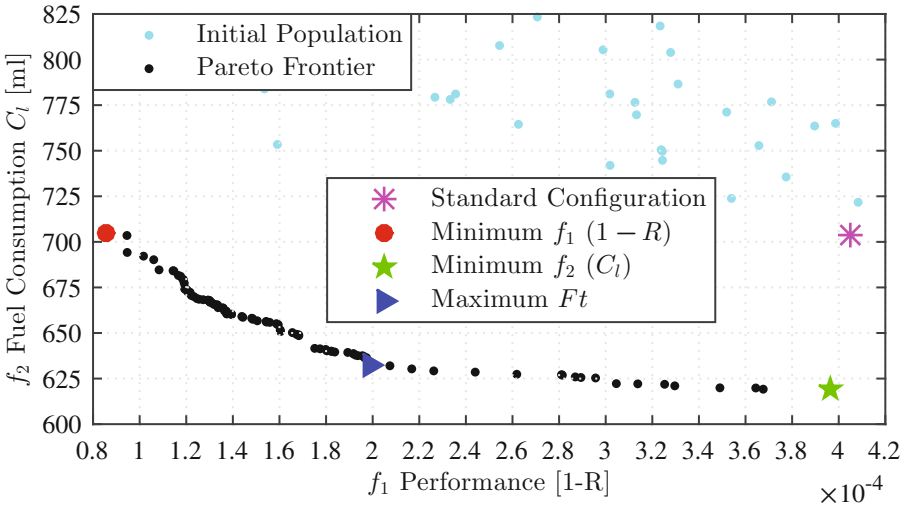

Fig. 2. Pareto frontier of non-dominated solutions along with initial population

Table 2. Optimized solution results compared to the standard configuration

Solutions	f_1 Performance $(1-R)$	f_2 Fuel consumption (C_l)	Fitness Ft
Standard	0.000405	703.84 ml	- - -
Min. f_1	0.000086	704.71 ml	2.1543
Min. f_2	0.000397	619.12 ml	2.0000
Max Ft	0.000202	632.31 ml	2.5051

Table 3. Optimized design variables compared to the standard configuration

Solutions	N_{t1}	N_{t2}	N_{t3}	N_{t4}	N_{t5}	N_d	V_{u1}	V_{u2}	V_{u3}	V_{u4}	D_s
Standard	4.27	2.35	1.48	1.05	0.80	4.87	4.17	8.33	13.88	20.00	0.83
Min. f1	4.40	4.24	2.02	1.11	0.71	6.60	3.50	4.57	5.02	15.99	2.38
Min. f2	4.45	4.06	1.47	1.03	0.61	5.11	2.27	4.91	9.53	20.02	2.23
Max Ft	4.39	4.24	1.40	1.03	0.61	5.24	2.84	5.33	10.22	20.23	2.56

ratios ($N_t N_d$) that amplify torque. It decreases the ICE output torque, minimizing the clutch losses during the gearshifts. On the other hand, the minimum f_2 solution aims at fuel economy, anticipating the upshift, especially at V_{u1}, in order to make the ICE operate at lower speed and higher torque conditions. It represents a more efficient region of the engine map.

The maximum Ft design presents the best compromised solution between performance and fuel consumption, with a powertrain configuration close to the one presented by the fuel economy solution (considering the total gear

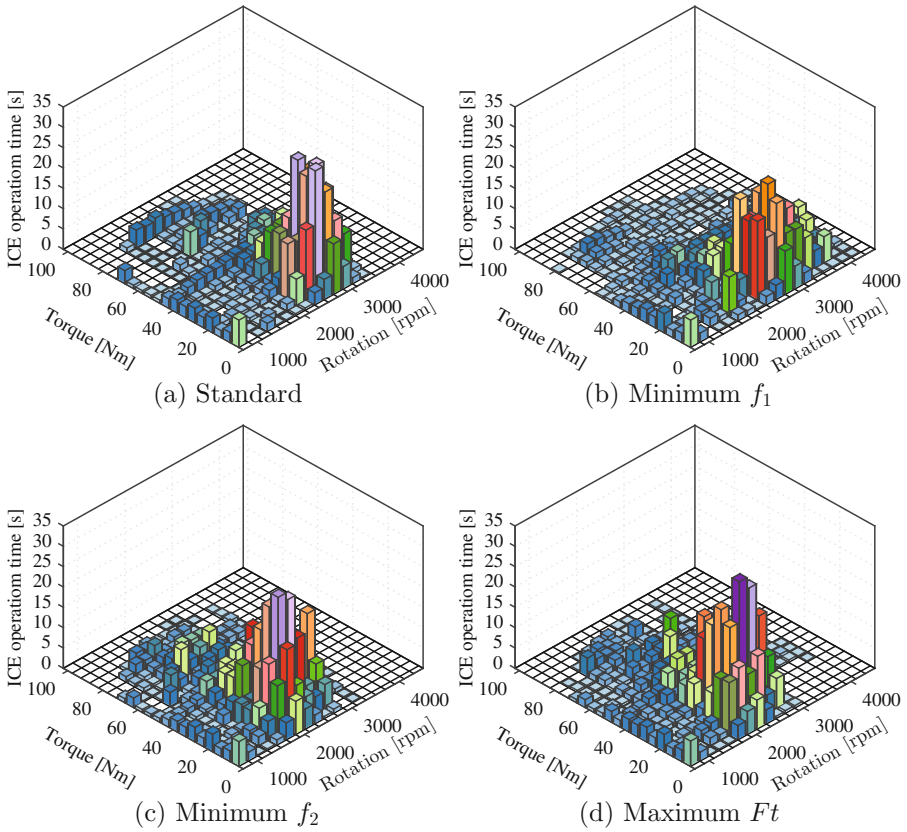

Fig. 3. Frequency histograms for the ICE operation

ratio $N_t N_d$). However, this compromised setup presented higher V_{un} values, which postponed the upshifts, improving this way the overall performance of the vehicle as compared to the minimum f_2 solution. Furthermore, the compromised setup prevented the ICE to operate close to its maximum speed (ω_{max}), ensuring fuel savings in contrast with the minimum f_1 configuration.

5 Conclusion

In this paper a multiobjective optimization problem was formulated to simultaneously optimize the performance and fuel consumption of a vehicle by changing the powertrain transmission ratios and the gear shifting strategy.

The optimization delivered a set of optimum solutions, from which three main layouts were selected. The first configuration presented the best performance metric ($1 - R$), with 78.76% improvement when compared with the standard setup and by only increasing by 0.12% the fuel consumption. The second solution provided by the algorithm presented the best fuel economy, with 12.04%

decrease in consumption when compared with the standard configuration along with 1.97% improvement in performance. The last selected configuration is the best compromised solution, which outputted the maximum fitness value with 50.12% performance improvement associated with 10.16% improvement in fuel saving as compared to the standard layout.

However, the powertrain configurations achieved by this study do not consider constructive issues of the gearbox and of the differential components. Therefore, an improved optimization algorithm should be developed in order to reach a feasible assembly setup, with transmission ratios as close as possible to the theoretical values achieved with the process described in this paper.

Furthermore, this work focused only upon an urban cycle. Therefore, different driving patterns like highways and profiles with higher power demands (high acceleration) should be included in the simulations. This would ensure a more reliable powertrain configuration capable of delivering not only good performance, but also better fuel consumption at all possible driving scenarios.

Acknowledgements. This work was conducted during scholarships supported by the Brazilian Federal Agency for Support and Evaluation of Graduate Education (CAPES), National Council for Scientific and Technological Development (CNPq), Federal University of Technology - Paraná (UTFPR) and the University of Campinas (UNICAMP).

References

1. Delkhosh, M., Foumani, M.S., Boroushaki, M.: Geometrical optimization of parallel infinitely variable transmission to decrease vehicle fuel consumption. Mech. Based Des. Struct. Mach. **42**(4), 483 (2014)
2. Chen, W., Li, R., Xiao, X., Ding, J., Jia, J., Peng, Y., Yu, Z.: Proceedings of SAE-China Congress 2015: Selected Papers, pp. 609–619. Springer (2016)
3. Mensing, F., Bideaux, E., Trigui, R., Tattegrain, H.: Trajectory optimization for eco-driving taking into account traffic constraints. Transp. Res. Part D Transp. Environ. **18**, 55 (2013)
4. Thijssen, R., Hofman, T., Ham, J.: Ecodriving acceptance: an experimental study on anticipation behavior of truck drivers. Transp. Res. Part F Traffic Psychol. Behav. **22**, 249 (2014)
5. Ngo, V.D., Colin Navarrete, J.A., Hofman, T., Steinbuch, M., Serrarens, A.: Optimal gear shift strategies for fuel economy and driveability. Proc. Inst. Mech. Eng. Part D J. Automobile Eng. **227**(10), 1398 (2013)
6. Eckert, J.J., Santiciolli, F.M., Costa, E.S., Silva, L.C.A., Dionísio, H.J., Corrêa, F.C., Dedini, F.G.: Fuel consumption reduction based on the optimization of the vehicle gear shifting strategy considering new gear ratios. SAE Technical Paper (2015)
7. Jazar, R.N.: Vehicle Dynamics. Springer, New York (2008)
8. Gillespie, T.D.: Fundamentals of Vehicle Dynamics. SAE, Warrendale (1992)
9. Kulkarni, M., Shim, T., Zhang, Y.: Shift dynamics and control of dual-clutch transmissions. Mech. Mach. Theor. **42**(2), 168 (2007)
10. Eckert, J.J., Santiciolli, F.M., Bertoti, E., Costa, E.S., Corrêa, F.C., Silva, L.C.A., Dedini, F.G.: Gear shifting multi-objective optimization to improve vehicle performance, fuel consumption and engine emissions. Mech. Based Des. Struct. Mach. doi:10.1080/15397734.2017.1330156. Accessed 19 May 2017

11. Eckert, J.J., Corrêa, F.C., Santiciolli, F.M., Costa, E.S., Dionísio, H.J., Dedini, F.G.: Vehicle gear shifting strategy optimization with respect to performance and fuel consumption. Mech. Based Des. Struct. Mach. **44**(1–2), 123 (2016)
12. Costa, E.S., Eckert, J.J., Santiciolli, F.M., Silva, L.A., Corrêa, F.C., Dedini, F.G.: Economic and energy analysis of hybridized vehicle by means of experimental mapping. SAE Technical Paper (2016)
13. Xi, L., Xiangyang, X., Yanfang, L.: WRI World Congress on Software Engineering, WCSE 2009, vol. 2, pp. 476–480. IEEE (2009)
14. General Motors, Owner Manual Chevrolet Celta 2013. General Motors Brazil Ltda (2013)
15. Gen, M., Cheng, R., Lin, L.: Network Models and Optimization: Multiobjective Genetic Algorithm Approach. Springer, London (2008)
16. Sastry, K., Goldberg, D., Kendall, G.: Search Methodologies, p. 93. Springer, New York (2005)

Design and Analysis of a Wheel with Flexible Spokes

Shuaisong Hou[1], Jing-Shan Zhao[1(✉)], and Misyurin Sergey Yurevich[2]

[1] Department of Mechanical Engineering, Tsinghua University, Room A1033, Lee Shau Kee Science and Technology Building, Beijing 100084, China
houssl4@mails.tsinghua.edu.cn, jingshanzhao@mail.tsinghua.edu.cn
[2] Institute of Cyber Intelligence Systems, National Research Nuclear University MEPhI, 31, Kashirskoe shosse, 115409 Moscow, Russia
ssmmrr@mail.ru

Abstract. Wheel is an important component for the whole bicycle. Wheels are not only loading and moving parts but also shock absorbing components. The traditional bicycle wheels rely on tire to absorb shock from rough roads as their spokes are rigid. In this paper, we propose a new type of bicycle wheel. This wheel is wider than the traditional ones and it has two columns of spokes. We replace the rigid spokes with soft strings of some elastic materials to increase the radial deformations while keeping sufficient lateral stiffness. Through establishing objective function of optimization, we select the best connection configuration of spokes. Then, we analyze its mechanical properties. Compared with the traditional bicycle wheels, this new wheel has better riding and shock absorbing characteristics.

Keywords: Bicycle wheel · Flexible spoke · Shock absorbing · Optimization analysis

1 Introduction

Bicycle is a fundamental vehicle in people's daily life. The bicycle has been invented more than 100 years. Due to environmental protection and traffic congestion problem, bicycles once again become the favorite traffic and fitness tools of all people, especially the residents in developed countries. In recent years, the global climate problem is becoming more and more serious. So people pay more attention to green travels. Bicycle travel is a good choice. Bicycles are becoming an entertainment tools for sports, leisure and fitness. So people attach great importance to the safety and comfort of bicycle.

Traditional bicycle wheels rely heavily on the tire to absorb shock from rough roads. The damping effect is relatively limited. In order to increase the comfort of a bicycle, people have accomplished some design and research on bicycle structure. For example, people use various sensors and other methods to measure the speed signal,

J.C.M. Carvalho et al. (eds.), *Multibody Mechatronic Systems*, Mechanisms and Machine Science 54, DOI 10.1007/978-3-319-67567-1_50

acceleration signal and vibration of bicycle under different road conditions [1–3]. Besides, people have conducted some research on the structure of bicycle. Auxiliary modes are designed to analyze the relationship between the radial stiffness and spoke load distribution [4, 5]. Some new materials are also used to the structure design of bicycle [6]. Some people did experiments to assess the relative contribution of bicycle components on the vibration induced to the bicyclist [7, 8].

Mechanical property is a key indicator of bicycle comfort. In order to improve the mechanical property of bicycle, people also investigated the spokes' pre-stress [9] and the relationship between sportsman's status and bicycle performance [10, 11]. Besides, people accomplished some research on the influence of wheel radius on bicycle properties [12].

The comfort and security are two important indicators of a bicycle. A lot of research has been finished to improve the bicycle comfort. Some people proposed a test protocol evaluating the comfort of bicycles using in-situ measurements [13]. The cyclist's weight and posture have an effect on riding comfort [14]. While studying the comfort of bicycle, security cannot be ignored. A large number of children are injured by bicycle wheels when they ride bicycles [15, 16]. So we should pay more attention to the security of bicycles.

The aim of this paper is to propose a design scheme that improves the comfort and security of a bicycle. Through optimization analysis, we select the best connection configuration of spokes. Then we analyze the load and stiffness of the wheel. Some materials with low elastic modulus can be used to replace the steel spokes. For example, we can use high elastic rubber to connect rim and hub. The flexible spokes will not only improve the comfort of bicycle, but also keep the security of bicycle.

2 Design of Bicycle Wheel with Flexible Spokes

The wheel model is shown in Fig. 1. The spokes are made of soft material. The configuration of spokes determines the stiffness of the wheel. We will discuss the configuration of spokes in this section.

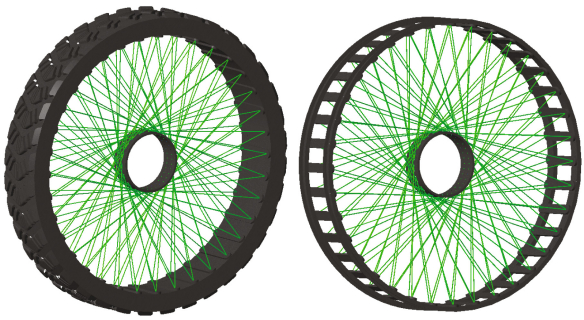

Fig. 1. Soft spoke concept model of a wheel

2.1 The Connection Configuration of Wheel Spokes

The configuration of spokes attached to a row on the hub is shown in Fig. 2.

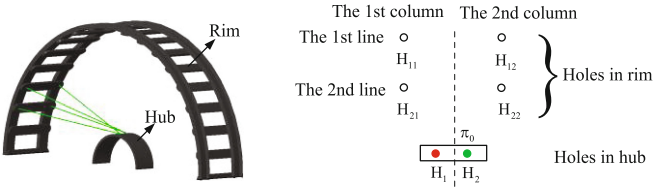

Fig. 2. Configuration of spokes and the number of holes

The relative position relationship of holes in rim and holes in hub is shown in Fig. 2, where π_0 is the central plane of wheel. The two holes in the hub are marked with H_1 and H_2. The holes in rim are marked with H_{ij} (i = 1, 2; j = 1, 2). The configuration rule is that every hole in the hub is connected to arbitrary two holes in the rim, but the holes in rim is only connected to one hole in the hub. The initial lengths of all spokes are approximately identical. Then we calculate the total number of configurations according to the permutation and combination:

$$C_4^2 C_2^2 = 6 \tag{1}$$

These six configurations are exhaustively illustrated in Fig. 3.

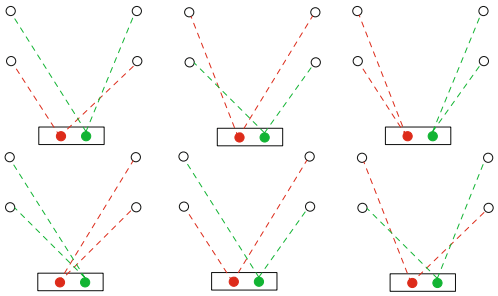

Fig. 3. The six configurations

Further, the two holes in rim connected with H_1 and the two holes in rim connected with H_2 are symmetrical about plane π_0. Then we get the following four different connection configurations (Fig. 4).

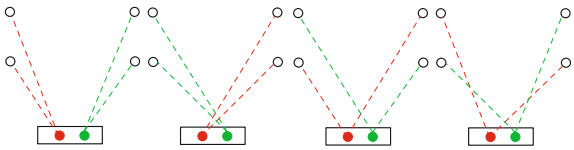

Fig. 4. The symmetrical four configurations

2.2 Optimal Selection of the Four Different Connection Configurations

The four connection configurations are listed in Table 1.

Table 1. Connection configurations of spokes

Configuration	H_1	H_2
1	H_{11} H_{21}	H_{12} H_{22}
2	H_{12} H_{22}	H_{11} H_{21}
3	H_{12} H_{21}	H_{11} H_{22}
4	H_{11} H_{22}	H_{12} H_{21}

The length of spoke which connects hole H_1 and the ith line hole in rim is $l_{1i}(i = 1, 2)$. So the lengths are l_{11} and l_{12}. The length of spoke which connects hole H_2 and the ith line hole in rim is $l_{2i}(j = 1, 2)$. So the lengths are l_{21} and l_{22}. The optimization goal is that the lengths of all spokes are as similar as possible. According to the symmetry of wheel, we propose the objective function of $f(l)$.

$$f(l) = \frac{1}{2}\sum_{i=1}^{2}(l_{1i} - l_0)^2 \tag{2}$$

where l_0 is the mean value and $l_0 = (l_{11} + l_{12})/2$.

The length of the spoke that connects hole H_1 and hole H_{11} is $l_{H_1H_{11}}$, the length of the spoke that connects hole H_1 and hole H_{12} is $l_{H_1H_{12}}$, and the length of spoke which connects hole H_2 and hole H_{22} is $l_{H_2H_{22}}$.

Then we get

$$f(l) = \left[(l_{11} - l_0)^2 + (l_{12} - l_0)^2\right]/2 \tag{3}$$

where $l_{11} \in \{l_{H_1H_{11}}, l_{H_1H_{12}}\}$, $l_{12} \in \{l_{H_1H_{21}}, l_{H_1H_{22}}\}$.

According to the three-dimensional model of a wheel, we get the length of every spoke, listed in Table 2.

Table 2. The length of every spoke (mm)

Hole	H_{11}	H_{12}	H_{21}	H_{22}
H_1	268.64	272.16	280.44	283.82
H_2	272.14	268.65	283.80	280.45

Then we calculate the objective function of the four connection configurations. The spokes' length of four connection configurations are shown in Table 3.

Table 3. The spokes' length of four configurations (mm)

Configuration	l_{11}	l_{12}	l_{21}	l_{22}
1	268.64	280.44	268.65	280.45
2	272.16	283.82	272.14	283.80
3	272.16	280.44	272.14	280.45
4	268.64	283.82	268.65	283.80

Then we get the objective functions $f(l)$ of the four connection configurations according to formula (2), listed in Table 4.

Table 4. The objective functions of four configuration

Configuration	1	2	3	4
$f(l)$	34.81	33.99	17.14	57.61

According to Table 4, we know that the least $f(l)$ is $f_3(l)$. The smaller the objective function is, the better the mechanical property of wheel will be. So connection configuration 3 is the best connection which is shown in Fig. 5.

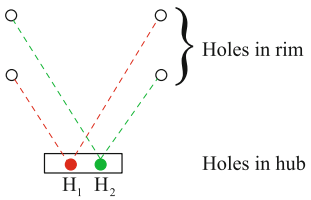

Fig. 5. Connection configuration three

3 Force Analysis of the Wheel Spokes

3.1 Vertical and Longitudinal Loads

The vertical load P is shown in Fig. 6.

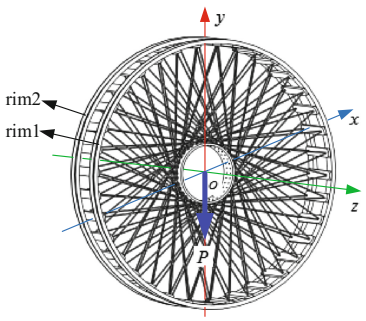

Fig. 6. Vertical load P along *y-axis*

Firstly, we analyze the forces of spokes connecting hole H_1 which is shown in Fig. 7. Hole H_1 is linked with two spokes.

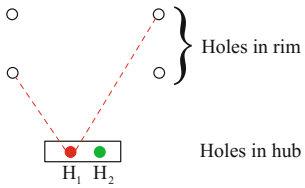

Fig. 7. Spokes linked with H_1

The hub has 36 holes in every column, so there are 36 spokes which connect the hub's first column hole and rim's first column hole. We call them spoke H_1R_1. Suppose that the number of spoke H_1R_1 is an even integer denoted with n, the subtended angle between any two adjacent spokes is $\theta = 2\pi/n$ which is illustrated in Fig. 8.

Assume that the wheel is in the position shown in Fig. 8, two spokes are in the horizontal line (x-axis) and two spokes are in a vertical line (y-axis). Then we establish the static equilibrium equation in the y-direction

$$P_{11} = \sum_{i=1}^{n} N_i \cos \alpha_i \tag{4}$$

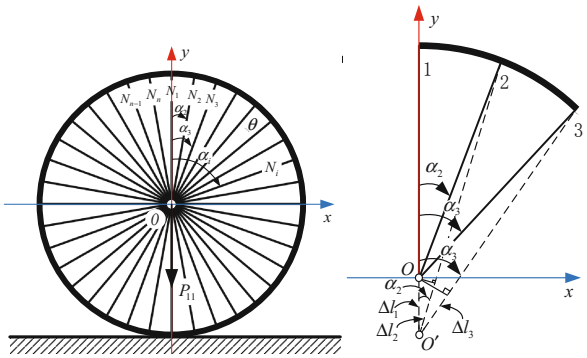

Fig. 8. The force and deformation geometry of spoke H_1R_1

where $\alpha_i = (i-1)\theta$ is the subtended angle between the ith spoke and the first one, N_i is the tensile force of the ith spoke, P_{11} is the load acting on spoke that connects hub's hole in the first column and first rim.

As shown in Fig. 8, we get compatibility equation of deformation according to the structure geometry of spokes.

The original length of spokes is l. Assume that $\Delta l_i (i = 1, 2, 3 \cdots n)$ is the deformation of the ith spoke, and α_1 equals zero. We immediately get the following equation according to the geometry relationship shown in Fig. 8:

$$\Delta l_i = \Delta l_1 \cos \alpha_i \tag{5}$$

According to Hooke's law, $\Delta l = Fl/EA$ where F is the tensile load, l is the initial length of a spoke, E is the elastic modulus of the material and A is the cross-sectional area of the spoke. We then obtain $\Delta l_i = N_i l/EA$.

Associating the compatibility equation of deformation and Hooke's law, we get the equation about tensile force of the ith spoke.

$$N_i = N_1 \cos \alpha_i \tag{6}$$

Substituting Eq. (6) into the equilibrium Eq. (4), we gain that $P_{11} = \sum_{i=1}^{n} N_1 \cos^2 \alpha_i$.

According to the trigonometric identity $\cos^2 \alpha = (1 + \cos 2\alpha)/2$, we immediately have:

$$P_{11} = \frac{1}{2}\left(n + \sum_{i=1}^{n} \cos 2\alpha_i\right) N_1 \tag{7}$$

where $\alpha_i = (i-1)2\pi/n$ is an angle between 0–2π, and it's arithmetic progression satisfies that $\sum_{i=1}^{n} \cos 2\alpha_i = 0$. Then we gain $N_1 = 2P_{11}/n$, and

$$N_i = \frac{2P_{11}}{n}\cos\frac{2\pi(i-1)}{n} \tag{8}$$

Therefore, the inner tensile force of every spoke is changing between 0 and $2P_{11}/n$. Practically, the spokes don't pass through the center of a wheel, and the angle between a spoke and the vertical line is φ_{11} which is shown in Fig. 10. Considering the influence of angle φ_{11}, we have

$$N_i = \frac{2P_{11}}{n\cos\varphi_{11}}\cos\frac{2\pi(i-1)}{n} \tag{9}$$

Then we calculate angle φ_{11} according to the geometrical relationship in Fig. 9.

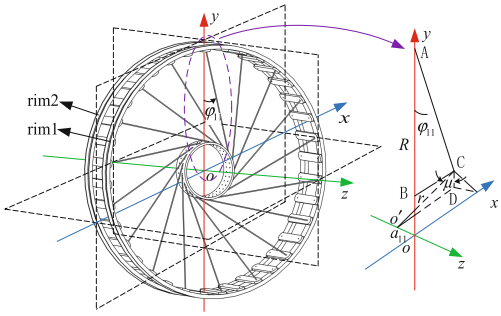

Fig. 9. Schematic sketch angle between a spoke and the vertical line

In Fig. 9, o is the origin of coordinate system o-xyz. o' is the center of the first column in hub. R is the radius of wheel and r is the radius of hub. a_{11} is the distance between point o and o'. oA equals R. $o'C$ equals r and μ is the angle between $o'C$ and CD. μ equals $16\pi/\mathrm{n}$. The number of holes in clockwise direction is $n/2$. There are four holes between connection point in rim and connection point in hub. So the angle $\mu = \frac{2\pi}{n/2} \cdot 4 = 16\pi/\mathrm{n}$. According to the geometrical relationship in triangle ABC, we have

$$\cos\varphi_{11} = \frac{AB}{AC} = \frac{R - r\cos\mu}{\sqrt{R^2 + r^2 + a_{11}^2 - 2Rr\cos\mu}} \tag{10}$$

Namely,

$$N_i = \frac{2P_{11}\sqrt{R^2 + r^2 + a_{11}^2 - 2Rr\cos\mu}}{n(R - r\cos\mu)}\cos\frac{2\pi(i-1)}{n} \tag{11}$$

According to the above calculation, we get the force of every spoke. Supposing that the force of a spoke that connects the hub's hole in the kth and rim j is $N_{i(kj)}(k = 1, 2; j = 1, 2)$, we get

$$N_{i(kj)} = \frac{2P_{kj}\sqrt{R^2 + r^2 + a_{kj}^2 - 2Rr\cos\mu}}{n(R - r\cos\mu)}\cos\frac{2\pi(i-1)}{n} \tag{12}$$

where a_{kj} is the distance between plane of hole in the hub's kth column and plane of rim j, P_{kj} is the load acting on the spoke that connects the hole in hub's kth column and rim j. The wheel is symmetric about x-axis and y-axis simultaneously, so we get the force of every spoke under the longitudinal load in the x-direction.

$$N_{i(kj)} = \frac{2P_{kj}\sqrt{R^2 + r^2 + a_{kj}^2 - 2Rr\cos\mu}}{n(R - r\cos\mu)}\cos\frac{2\pi(i-1)}{n} \tag{13}$$

3.2 Lateral Load Along z-direction

The simplified model under the load in z-direction is illustrated in Fig. 10.

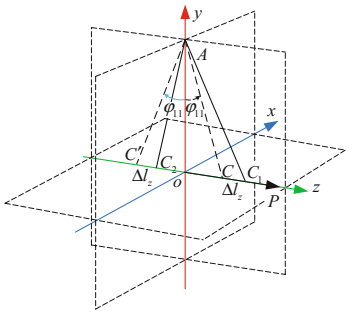

Fig. 10. Simplified model under *z-axis* direction load

In Fig. 10, AC and AC' are the original length of a spoke, AC_1 and AC_2 are the spoke lengths after deformation, Δl_z is the displacement in the axial direction.

3.2.1 When the Displacement Is an Infinitesimal

As Δl_z is an infinitesimal, we get $\Delta l_{11} = \Delta l_z \sin\varphi_{11}$, where Δl_{11} is the deformation of spoke. According to Hooke's law, we know that $\Delta l_{11} = F_{11}l_{11}/EA$, and then we get the tensile force of the spoke

$$F_{11} = \frac{\Delta l_{11}}{l_{11}} EA = \frac{\Delta l_z \sin\varphi_{11}}{l_{11}} EA \tag{14}$$

Then we get the force of every spoke $F_{kj}(k = 1, 2; j = 1, 2)$

$$F_{kj} = \frac{\Delta l_{kj}}{l_{kj}} EA = \frac{\Delta l_z \sin\varphi_{kj}}{l_{kj}} EA \tag{15}$$

where F_{kj} is the force of the spoke that connects the hub's hole in the kth column and rim j. l_{kj} is the original length of the spoke that connects the hub's hole in the kth column and rim j. Δl_{kj} is the deformation of spoke l_{kj}. φ_{kj} is the angle between spoke l_{kj} and perpendicular bisector.

3.2.2 When the Displacement Is not Infinitesimal

According to the geometric relationship, we get the lengths of AC_1 and AC_2.

$$AC_1 = \sqrt{l_{11}^2 + \Delta l_z^2 + 2\Delta l_z a_{11}},\ AC_2 = \sqrt{l_{11}^2 + \Delta l_z^2 - 2\Delta l_z a_{11}}$$

Then we get the deformations of AC and AC'.

$$\begin{aligned} \Delta l_{AC} &= AC_1 - l_{11} = \sqrt{l_{11}^2 + \Delta l_z^2 + 2\Delta l_z a_{11}} - l_{11}, \Delta l_{AC'} = l_{11} - AC_2 \\ &= l_{11} - \sqrt{l_{11}^2 + \Delta l_z^2 - 2\Delta l_z a_{11}} \end{aligned} \tag{16}$$

According to Hooke's law, we have $\Delta l = Fl/EA$. Then we get the tensile force of every spoke which is longer than the length before deformation $F'_{kj}(k = 1, 2; j = 1, 2)$.

$$F'_{kj} = \frac{\Delta l_{kj}}{l_{kj}} EA = \frac{\sqrt{l_{kj}^2 + \Delta l_z^2 + 2\Delta l_z a_{kj}} - l_{kj}}{l_{kj}} EA \tag{17}$$

We also get the tensile force of every spoke that is shorter than the length before deformation $F''_{kj}(k = 1, 2; j = 1, 2)$.

$$F''_{kj} = \frac{\Delta l_{kj}}{l_{kj}} EA = \frac{l_{kj} - \sqrt{l_{kj}^2 + \Delta l_z^2 - 2\Delta l_z a_{kj}}}{l_{kj}} EA \tag{18}$$

3.3 Torques Around *x*- and *y*-directions

The schematic diagram of deformation is shown in Fig. 11.

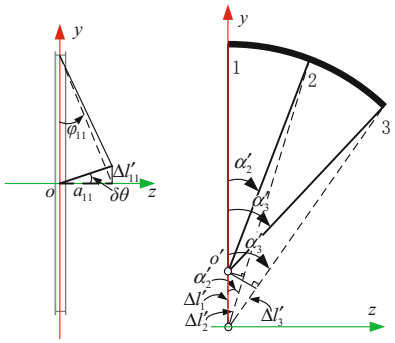

Fig. 11. Schematic diagram under torque T around *x-axis*

$$\Delta l'_{11} = a_{11}\delta\theta \tag{19}$$

In Fig. 11, $\delta\theta$ is a tiny torsional angle under the action of torque T exerting on the wheel, and $\Delta l'_{11}$ is the displacement of a spoke, α'_1 is zero, and $\Delta l'_1 = \Delta l'_{11}$. Assume that $\Delta l'_1 (i = 1, 2, 3 \cdots n)$ is the deformation of the ith spoke. We immediately get the following equation according to the geometry relationship $\Delta l'_i = \Delta l'_1 \cos\alpha'_i = \Delta l'_{11} \cos\alpha'_i$. According to Hooke's law, we obtain that $\Delta l'_i = N'_i l_{11}/EA$ where N'_i is the tensile force of the ith spoke. Then we get the equation of the tensile force of the ith spoke $N'_i = N'_1 \cos\alpha'_i$. The angle between a spoke and the vertical line is φ_{11}, so we get the relationship between the torque T_{11} acting on spoke H_1R_1 and the tensile force N'_i.

$$T_{11} = \sum_{i=1}^{n} N'_i \cos\alpha'_i a_{11} \cos\varphi_{11} = \frac{n a_{11} N'_1 \cos\varphi_{11}}{2} + \frac{a_{11} N'_1 \cos\varphi_{11}}{2} \sum_{i=1}^{n} cos2\alpha'_i \tag{20}$$

where $\alpha'_i = (i-1)2\pi/n$ is an angle between 0–2π, and it's arithmetic progression satisfies that $\sum_{i=1}^{n} \cos 2\alpha'_i = 0$. Then we get $T_{11} = n a_{11} N'_1 \cos\varphi_{11}/2$.

According to Hooke's law, we know that $N'_1 = \Delta l'_1 EA/l_{11} = a_{11}\delta\theta EA/l_{11}$. Then we have

$$T_{11} = n a_{11}^2 EA \cos\varphi_{11}\delta\theta/2l_{11} \tag{21}$$

We have the tensile force of the ith spoke N'_i.

$$N'_i = \frac{a_{11}\delta\theta EA}{l_{11}} \cos(i-1)\frac{2\pi}{n} \tag{22}$$

Then we get the tensile force of every spoke $N'_{i(kj)}$.

$$N'_{i(kj)} = \frac{a_{kj}\delta\theta EA}{l_{kj}}\cos(i-1)\frac{2\pi}{n} \tag{23}$$

The wheel is symmetric about x-axis and y-axis, so we get the force of every spoke resulting from the torque around y-direction.

$$N'_{i(kj)} = \frac{a_{kj}\delta\theta EA}{l_{kj}}\cos(i-1)\frac{2\pi}{n} \tag{24}$$

3.4 Torque Around z-direction

The deformation under the action of torque T around z-axis is shown in Fig. 12.

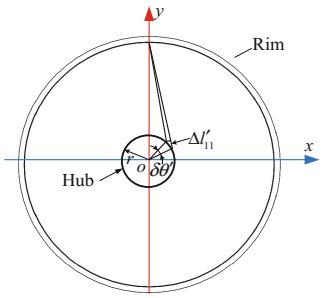

Fig. 12. Deformation geometry of spoke under torque T around *z-axis*

In Fig. 12, $\Delta l'_{11}$ is the deformation of a spoke. $\delta\theta'$ is the torsional angle under the torque T around z-axis.

$$\delta\theta' = T/C_z \tag{25}$$

where C_z is the torsional stiffness around z-axis.

So the deformation is $\Delta l'_{11} = \delta\theta' r$. According to Hooke's law, we get the tensile force of every spoke.

$$N'_i = \Delta l'_{11} EA/l_{11} = rEA\delta\theta'/l_{11} \tag{26}$$

Then we get the tensile force of every spoke $N'_{i(kj)} = rEA\delta\theta'/l_{kj}$. The moment of a force $\boldsymbol{F}$ contributed to the axis of hub exerting at point $\boldsymbol{r}$ is $\boldsymbol{M} = \boldsymbol{r} \times \boldsymbol{F}$. Supposing that

$\boldsymbol{M} = (M_x, M_y, M_z)$, $\boldsymbol{r} = (x, y, z)$, and $\boldsymbol{F} = (F_x, F_y, F_z)$, we get the torque about the axes x, y and z expressed with the following equation.

$$\begin{bmatrix} M_x \\ M_y \\ M_z \end{bmatrix} = \begin{bmatrix} 0 & -z & y \\ z & 0 & -x \\ -y & x & 0 \end{bmatrix} \begin{bmatrix} F_x \\ F_y \\ F_z \end{bmatrix} \tag{27}$$

The vector $\boldsymbol{N}_i$ and $\boldsymbol{r}_i$ are represented in Fig. 13, where β_i is the angle between y-axis and oB.

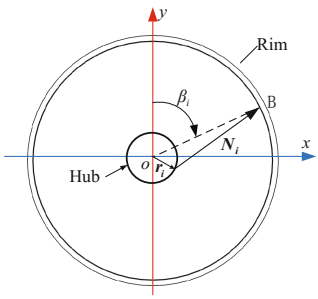

Fig. 13. Vectors of $\boldsymbol{N}_i$ and $\boldsymbol{r}_i$

According to the geometry relationship in space shown in Fig. 11, we get the vector $\boldsymbol{N}_i$ and the corresponding position vector $\boldsymbol{r}_i$:

$$\boldsymbol{N}_i = \begin{bmatrix} N_x \cos\beta_i + N_y \sin\beta_i \\ N_y \cos\beta_i - N_x \sin\beta_i \\ N_z \end{bmatrix} \quad \boldsymbol{r}_i = \begin{bmatrix} r_x \cos\beta_i + r_y \sin\beta_i \\ r_y \cos\beta_i - r_x \sin\beta_i \\ a_{11} \end{bmatrix}$$

where $r_x = r\sin\mu$, $r_y = r\cos\mu$ $N_x = \dfrac{r\sin\mu\cos\varphi_{11}}{R - r\cos\mu}\left(\dfrac{rEA\delta\theta'}{l_{11}}\right)$, $N_y = \dfrac{rEA\delta\theta'}{l_{11}}\cos\varphi_{11}$, and $N_z = \dfrac{a_{11}\cos\varphi_{11}}{R - r\cos\mu}\left(\dfrac{rEA\delta\theta'}{l_{11}}\right)$.

Then we gain that

$$\begin{bmatrix} M_x \\ M_y \\ M_z \end{bmatrix}_i = \begin{bmatrix} 0 & -a_{11} & r_y\cos\beta_i - r_x\sin\beta_i \\ a_{11} & 0 & -r_x\cos\beta_i - r_y\sin\beta_i \\ r_x\sin\beta_i - r_y\cos\beta_i & r_x\cos\beta_i + r_y\sin\beta_i & 0 \end{bmatrix} \begin{bmatrix} N_x\cos\beta_i + N_y\sin\beta_i \\ N_y\cos\beta_i - N_x\sin\beta_i \\ N_z \end{bmatrix}.$$

We get the resultant torque about the axes x, y and z

$$M_x = \sum_{i=1}^{n} M_{xi} = \frac{a_{11}\cos\varphi_{11}(2r\cos\mu - R)}{R - r\cos\mu}\left(\frac{rEA\delta\theta'}{l_{11}}\right)\sum_{i=1}^{n}\cos\beta_i$$

$$M_y = \sum_{i=1}^{n} M_{yi} = \frac{a_{11}\cos\varphi_{11}(R - 2r\cos\mu)}{R - r\cos\mu}\left(\frac{rEA\delta\theta'}{l_{11}}\right)\sum_{i=1}^{n}\sin\beta_i$$

$$M_z = \sum_{i=1}^{n} M_{zi} = \frac{nrR\sin\mu\cos\varphi_{11}}{R - r\cos\mu}\left(\frac{rEA\delta\theta'}{l_{11}}\right) \tag{28}$$

where β_i is an angle between 0–2π, and its arithmetic progression satisfies $\sum_{i=1}^{n}\cos\beta_i = 0$.

Then we immediately gain that $M_x = 0$, $M_y = 0$. So we get the torque $\boldsymbol{T}'_{11}$ that acts on spoke which connects the hub's hole in the first column and rim 1.

$$\boldsymbol{T}'_{11} = \left[0 \quad 0 \quad \frac{nrR\sin\mu\cos\varphi_{11}}{R - r\cos\mu}\left(\frac{rEA\delta\theta'}{l_{11}}\right)\right]^{\mathrm{T}} \tag{29}$$

Then we get $T'_{11} = \dfrac{nrRsin\mu cos\varphi_{11}}{R - rcos\mu}\left(\dfrac{rEA\delta\theta'}{l_{11}}\right)$. The torque T_{kj} that acts on the spoke which connects the hub's kth column hole and rim j can be expressed as

$$T_{kj} = \frac{nrR\sin\mu\cos\varphi_{\mathrm{kj}}}{R - r\cos\mu}\left(\frac{rEA\delta\theta'}{l_{\mathrm{kj}}}\right) \tag{30}$$

Then we get the torque T around the z-axis.

$$T = \sum_{\mathrm{k}=1}^{2}\sum_{\mathrm{j}=1}^{2} T_{kj} = \frac{r^2 nREA\delta\theta'\sin\mu}{R - r\cos\mu}\sum_{\mathrm{k}=1}^{2}\sum_{\mathrm{j}=1}^{2}\frac{\cos\varphi_{\mathrm{kj}}}{l_{\mathrm{kj}}} \tag{31}$$

4 The Six-Directional Stiffnesses of a Wheel

4.1 The Stiffnesses of a Wheel in Vertical and Longitudinal Directions

Assume that the deformation in y-axis is Δl_y, then we get the relationship between the deformation and load. Figure 14 represents the spoke H_1R_1 that connects the hub's hole in the first column and rim 1.

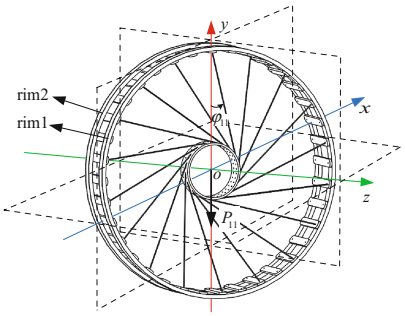

Fig. 14. The wheel under load P_{11}

The load P_{11} acts on the spoke H_1R_1. According to Eq. (9), we get $N_1 = 2P_{11}/n\cos\varphi_{11}$. According to Hooke's law, we get $\Delta l_{11} = 2l_{11}P_{11}/nEA\cos\varphi_{11}$, where l_{11} is the original length of spoke H_1R_1 and Δl_{11} is the deformation of spoke H_1R_1. According to the geometrical relationship shown in Fig. 9. We get $\Delta l_y = \Delta l_{11}\cos\varphi_{11}$. Then, we get

$$\Delta l_y = 2l_{11}P_{11}/nEA \tag{32}$$

Similarly, we get the equation about deformation Δl_y and load P_{12}.

$$\Delta l_y = 2l_{12}P_{12}/nEA \tag{33}$$

According to the above calculation and the symmetry of a wheel, we get the load about y-axis.

$$\mathrm{P} = 2(\mathrm{P}_{11} + \mathrm{P}_{12}) \tag{34}$$

Substituting Eqs. (32) and (33) into Eq. (34), we get

$$\Delta l_y = \frac{P}{nEA}\frac{l_{11}l_{12}}{l_{11}+l_{12}} \tag{35}$$

According to the calculation in Fig. 9, we obtain the original length of spoke $l_{kj} = (R - r\cos\mu)/\cos\varphi_{kj}$, where $l_{kj}(k = 1; j = 1, 2)$ is the original length of the spoke that connects hub's hole in the kth column and rim j. The wheel's deformation along y-direction is

$$\Delta l_y = \frac{P(R - r\cos\mu)}{nEA}\sum_{j=1}^{2}\frac{1}{\cos\varphi_{1j}} \tag{36}$$

According to the deformation Δl_y, we get the stiffness in y-direction k_y.

$$k_y = \frac{P}{\Delta l_y} = \frac{nEA}{R - r\cos\mu}\sum_{j=1}^{2}\cos\varphi_{1j} \tag{37}$$

According to the symmetry of a wheel, the stiffnesses in the x- and y-directions must be the same. The stiffness along the x-axis is

$$k_x = \frac{P}{\Delta l_x} = \frac{nEA}{R - r\cos\mu}\sum_{j=1}^{2}\cos\varphi_{1j} \tag{38}$$

4.2 The Stiffness of Wheel Along z-axis

4.2.1 When the Displacement Is an Infinitesimal

According to the equation $F_{kj} = \Delta l_{kj}/EAl_{kj} = \Delta l_z \sin\varphi_{kj}/EAl_{kj}$, we get the load P_{kj} that acts on the spoke which connects hub's hole in the kth column and rim j.

$$P_{kj} = nF_{kj}\sin\varphi_{kj} = nEA\sin^2\varphi_{kj}\Delta l_z/l_{kj} \tag{39}$$

So we get the load P along z-direction.

$$P = \sum_{k=1}^{2}\sum_{j=1}^{2} nF_{kj}\sin\varphi_{kj} = \frac{n\Delta l_z EA}{R - r\cos\mu}\sum_{k=1}^{2}\sum_{j=1}^{2}\sin^2\varphi_{kj}\cos\varphi_{kj} \tag{40}$$

So the stiffness along the z-axis is

$$k_z = \frac{P}{\Delta l_z} = \frac{nEA}{R - r\cos\mu}\sum_{k=1}^{2}\sum_{j=1}^{2}\sin^2\varphi_{kj}\cos\varphi_{kj} \tag{41}$$

4.2.2 When the Displacement Is not Infinitesimal

According to $F'_{kj} = \dfrac{EA\Delta l_{kj}}{l_{kj}} = \dfrac{\sqrt{l_{kj}^2 + \Delta l_z^2 + 2\Delta l_z a_{kj}} - l_{kj}}{l_{kj}}EA$ and $F''_{kj} = \dfrac{EA\Delta l_{kj}}{l_{kj}} = \dfrac{l_{kj} - \sqrt{l_{kj}^2 + \Delta l_z^2 - 2\Delta l_z a_{kj}}}{l_{kj}}EA$, we get the load P_{kj} that acts on the spoke which connects hub's hole in the kth column and rim j.

$$P'_{kj} = nF'_{kj}\frac{\Delta l_z + a_{kj}}{\sqrt{l_{kj}^2 + \Delta l_z^2 + 2\Delta l_z a_{kj}}}, P''_{kj} = nF''_{kj}\frac{a_{kj} - \Delta l_z}{\sqrt{l_{kj}^2 + \Delta l_z^2 - 2\Delta l_z a_{kj}}} \tag{42}$$

where P'_{kj} is the load acting on the spoke that are longer than the length before deformation, P''_{kj} is the load acting on the spoke that are shorter than the length before deformation. Then we get the load P along the z-direction.

$$P = \sum_{j=1}^{2} \left(P'_{1j} + P''_{2j} \right) \tag{43}$$

So the stiffness along the z-axis is

$$k_z = \frac{P}{\Delta l_z} = nEA \sum_{j=1}^{2} \left[\frac{\left(\sqrt{l_{1j}^2 + \Delta l_z^2 + 2\Delta l_z a_{1j}} - l_{1j} \right) (\Delta l_z + a_{1j})}{\Delta l_z l_{1j} \sqrt{l_{1j}^2 + \Delta l_z^2 + 2\Delta l_z a_{1j}}} + \frac{\left(l_{2j} - \sqrt{l_{2j}^2 + \Delta l_z^2 - 2\Delta l_z a_{2j}} \right) (a_{2j} - \Delta l_z)}{\Delta l_z l_{2j} \sqrt{l_{2j}^2 + \Delta l_z^2 - 2\Delta l_z a_{2j}}} \right] \tag{44}$$

4.3 Torsional Stiffness Around the *x*-axis

According to the above calculation, we know that $T_{11} = na_{11}^2 EA \cos \varphi_{11} / 2\delta\theta l_{11}$. Then we immediately get $T_{kj} (k = 1, 2; j = 1, 2)$ which acts on the spoke that connects the hub's hole in the kth column and rim j.

$$T_{kj} = na_{kj}^2 EA \cos \varphi_{kj} / 2l_{kj} \delta\theta \tag{45}$$

So we get the torque T around x-axis.

$$T = \sum_{k=1}^{2} \sum_{j=1}^{2} T_{kj} = \frac{nEA\delta\theta}{2} \sum_{k=1}^{2} \sum_{j=1}^{2} \frac{a_{kj}^2 \cos \varphi_{kj}}{l_{kj}}$$

So the torsional stiffness around the x-axis is:

$$C_x = \frac{T}{\delta\theta} = \frac{nEA}{2(R - r\cos\mu)} \sum_{k=1}^{2} \sum_{j=1}^{2} a_{kj}^2 \cos^2 \varphi_{kj} \tag{46}$$

4.4 Torsional Stiffness Around the *y*-axis

According to the symmetry of a wheel, the torsional stiffness around x-axis and y-axis must be the same. The torsional stiffness around the y-axis is

$$C_y = \frac{nEA}{2(R - r\cos\mu)} \sum_{k=1}^{2} \sum_{j=1}^{2} a_{kj}^2 \cos^2 \varphi_{kj} \tag{47}$$

4.5 Torsional Stiffness Around the z-axis

The torsional stiffness around the z-axis can be expressed by the following equation.

$$C_z = T/\delta\theta' \tag{48}$$

where T is the torque around z-axis and $\delta\theta'$ is the torsional angle under the torque T.

We know that the torque T around the z-axis is $T = \dfrac{r^2 nREA\delta\theta' \sin\mu}{R - r\cos\mu} \sum_{k=1}^{2} \sum_{j=1}^{2} \dfrac{\cos\varphi_{kj}}{l_{kj}}$.

Then we get the torsional stiffness, C_z:

$$C_z = \frac{T}{\delta\theta'} = \frac{r^2 nREA\sin\mu}{(R - r\cos\mu)^2} \sum_{k=1}^{2} \sum_{j=1}^{2} \cos^2\varphi_{kj} \tag{49}$$

5 Case Analysis

The parameters of wheel are as follows. Suppose that the width of a wheel is 100 mm, the distance of the hole in the hub is 200 mm, the radius of wheel rim is 300 mm, and the radius of wheel hub is 70 mm. When we select a spoke the radius of which is 1 mm and the number of spokes, n, is 36, we get the angle φ_{kj} and the distance a_{kj}, listed in Table 5.

Table 5. The angle φ_{kj} and the distance a_{kj}

a_{11}	a_{12}	a_{21}	a_{22}	$\cos\varphi_{11}$	$\cos\varphi_{12}$	$\cos\varphi_{21}$	$\cos\varphi_{22}$
400 mm	600 mm	600 mm	400 mm	0.73	0.72	0.72	0.73

According to the above data, we get the six directional stiffness which is listed in Table 6.

Table 6. The six directional stiffness

k_x(N/mm)	k_y(N/mm)	k_z(N/mm)	C_x(N · m/°)	C_y(N · m/°)	C_z(N · m/°)
0.57E	0.57E	0.54E	0.019E	0.019E	0.073E

In Table 6, E is elastic modulus and its unit is MPa.

The ordinary steel's elastic modulus is about 2.06×10^5MPa. So we can select some materials with lower elastic modulus. For example, we select the material with elastic modulus 1000 MPa. Then we get the six directional stiffness, listed in Table 7.

Table 7. The six directional stiffness of material with elastic modulus 1000 MPa

k_x	k_y	k_z	C_x	C_y	C_z
570 N/mm	570 N/mm	540 N/mm	19 N · m/°	19 N · m/°	73 N · m/°

With the parameters in Table 7, we calculate the deformation of wheel simply. Suppose that the total weight of bicycle is 100 kg. The vertical load on one wheel is 50 kg, so the vertical deformation is 0.86 mm. The lateral load on one wheel is $0.4 \cdot 50$ kg = 20 kg, so the lateral deformation is 0.36 mm. The length of hub is 200 mm. When the load acts on one end of hub, the torque around x-axis or y-axis is maximum. The maximum torque is $(0.1 \text{ m}) \cdot (50 \cdot 9.8 \text{ N}) = 49 \text{ N} \cdot \text{m}$. So the rotational deformation around x-axis or y-axis is 2.58°. Suppose that the acceleration of bicycle is 2 m/s^2. We obtain the rotational deformation around z-axis is 6.85°. We can control the deformation through selecting different materials compared to the traditional wheel.

Obviously, the six directional stiffnesses meet the requirements of a bicycle. The above calculations show the relationship between stiffness and elastic modulus, so we can select different elastic moduli according to different road conditions and different riding conditions.

Then we modify a bicycle with two columns of spokes. We replace the steel spokes with flexible ones. In this experiment, we replace the steel spokes with tennis racket line. The tennis racket line is fiber resin synthetic materials. It has good elasticity and tensile strength. The modification result is shown in Fig. 15.

Fig. 15. The modification result

Then we apply impact load to the wheel with flexible spokes, shown in Fig. 16.

Fig. 16. Impact load

When we ride the flexible spokes bicycle through obstacles, we can feel the good flexibility from the flexible spokes. Meanwhile, the experiment proves that the wheel with flexible spokes is reliable in structure and safe on the cycling.

6 Conclusions

This paper explored the connection configuration and calculation of tensile forces of soft spokes in the bicycle wheels. We obtained the best connection configuration of spokes through optimization analysis and calculation. This optimization analysis method can be expended to the design of all wheels with multi-row flexible spokes. The calculation of tensile forces and stiffness shows accurate mechanical performance of bicycle wheels. We get the relationship between the stiffness and elastic modulus. It is available to choose different materials to connect the hub and rim of a bicycle wheel. On the premise of ensuring the lateral stiffness, we can select some materials with low elastic modulus. The wheel with low elastic modulus material will greatly improve the comfort of a bicycle. Meanwhile, the security of bicycle will also be improved greatly.

References

1. Lépine, J., Champoux, Y., Drouet, J.-M.: A laboratory excitation technique to test road bike vibration transmission. Exp. Tech. **40**, 227–234 (2013)
2. Giubilato, F., Petrone, N.: A method for evaluating the vibrational response of racing bicycles wheels under road roughness excitation. Procedia Eng. **34**, 409–414 (2012)
3. Pogni, M., Petrone, N.: Comparison of the aerodynamic performance of five racing bicycle wheels by means of CFD calculations. Procedia Eng. **147**, 74–80 (2016)
4. Mínguez, J.M., Vogwell, J.: An analytical model to study the radial stiffness and spoke load distribution in a modern racing bicycle wheel. Part C J. Mech. Eng. Sci. **222**, 563–576 (2008)
5. Petrone, N., Giubilato, F.: Methods for evaluating the radial structural behavior of racing bicycle wheels. Procedia Eng. **13**, 88–93 (2011)
6. Hong, H.-T., Chun, H.-J., Choi, H.-S.: Optimal strength design of composite bicycle wheels. Int. J. Precis. Eng. Manuf. **15**, 1609–1613 (2014)
7. Lépine, J., Champoux, Y., Drouet, J.-M.: The relative contribution of road bicycle components on vibration induced to the cyclist. Sports Eng. **18**, 79–91 (2015)
8. Lépine, J., Champoux, Y., Drouet, J.-M.: Road bike comfort: on the measurement of vibrations induced to cyclist. Sports Eng. **17**, 113–122 (2014)
9. Burgoyne, C.J., Dilmaghanian, R.: Bicycle wheel as prestressed structure. J. Eng. Mech. **119**, 439–455 (1993)
10. Kadomura, A., Ichioka, Y., Tsukada, K., Rekimoto, J., Siio, I.: AwareCycle: application for sports visualization using an afterimage display attached to the wheel of a bicycle. In: Human-Computer Interaction, pp. 256–264 (2014)
11. Stone, C., Hull, M.L.: The effect of rider weight on rider-induced loads during common cycling situations. J. Biomech. **28**, 365–375 (1995)
12. Steiner, T., Müller, B., Maier, T., Wehrlin, J.P.: Performance differences when using 26- and 29-inch-wheel bikes in Swiss National Team Cross Country Mountain Bikers. J. Sports Sci. **34**, 1438–1444 (2015)
13. Lépine, J., Champoux, Y., Drouet, J.-M.: Test protocol for in-situ bicycle wheel dynamic comfort comparison. Sports Eng. **147**, 568–572 (2016)

14. Lépine, J., Champoux, Y., Drouet, J.-M.: Influence of test conditions on comfort ranking of road bicycle wheels. Spec. Top. Struct. Dyn. **6**, 77–82 (2013)
15. Mak, C.Y., Chang, J.H.T., Lui, T.H., Ngai, W.K.: Bicycle and motorcycle wheel spoke injury in children. J. Orthop. Surg. **23**, 56–58 (2015)
16. Agarwal, A., Pruthi, M.: Bicycle-spoke injuries of the foot in children. J. Orthop. Surg. **18**, 338–341 (2010)

Multibody Model of a Small Tire Test Bench

Fabio Mazzariol Santiciolli(✉), Ludmila Corrêa de Alkmin e Silva, Elvis Bertoti, Jony Javorski Eckert, Rodrigo Yassuda Yamashita, and Franco Giuseppe Dedini

University of Campinas, Campinas, Brazil
{fabio, ludmila, bertoti, javorski, dedini}@fem.unicamp.br, rodrigo.yamashita@gmail.com

Abstract. In despite of the necessity to control the mobile robots, it is possible to observe the absence of tire models and experimental parameterization regarding small tires. This paper aims to collaborate with part of the fulfilment of this gap in the literature by proposing some updates to a test bench that focus on the parameterization of small tires. The multibody dynamics model including the updates of the test bench was executed in ADAMS/View in order to indicate whether these updates are feasible and whether the data acquired by the virtual load cells is correlated with the virtual tire contact loads. The resulting virtual tire contact loads are compared with the ones calculated directly by ADAMS/Tire routine and by Pacejka equations, demonstrating a good correlation.

Keywords: Mobile robot tires · Pacejka tire models · Parameterization · Multibody test bench

1 Introduction

The mobile robots applications have increased over the years. Concerning the indoor environment autonomous wheelchairs, healthcare assistant, vacuum cleaner and self-organizing chairs are examples of mobile robots for sale or in final stage of development. Following the guidelines of the Industry 4.0, the use of automated guided vehicles in industrial plants and warehouses will become intensive in the next years. In an outdoor environment, some kinds of harvesting mobile robots have already been patented; autonomous vehicles have been used for public and private transportation and are fundamental in the context of the smart cities.

From the machine architecture approach, regardless the application, every kind of terrestrial mobile robot require elements to perform the contact between itself and the driving surface. In general, there are three types of such element: tires, treads, and omnidirectional wheels. The present paper focuses on some issues regarding modelling and parametrization of the robotic tires. They were chosen among the other contact elements because they have the widest spectra of applications considering the diverse types of robots, tasks and driving surfaces nowadays.

The automotive industry and the academy have already developed well-established tire models, e.g. CDTIRE, TMEASY, SWIFT, FTIRE, TreadSim [13, 18]. These models are normally commercialized as plug-ins or toolboxes integrated with

J.C.M. Carvalho et al. (eds.), *Multibody Mechatronic Systems*,
Mechanisms and Machine Science 54, DOI 10.1007/978-3-319-67567-1_51

multibody dynamic software or numerical computing environments. Less popular models have also been developed by the academy and the industry.

It is possible to classify the tire models in function of the complexity. From the simpler to the most complex the classification is “Empirical Models”, “Semiempirical Models”, “Simple Physical-Theoretical Models” and “Complex Physical-Theoretical Models”. The computational effort required by each kind of model also increases with the complexity [5]. Thus, it is common that the commercial tire models move on the degree of complexity, increasing or reducing the complexity according to the scope of the simulation.

The Empirical Models emulate with good quality the forces and torques acting on the tire in simple handling scenarios, i.e. steady or slow changes on the tire states up on flat and rigid floor. On the other hand, the Complex Physical-Theoretical Models are able to model local loads and deformations (in some cases including stress and strain) of tires and rims facing rough (in some cases non-rigid) driving surface in a context of NVH (noise, vibration, and harshness). It is possible to notice how the problem solved by the Empirical Models can be considered simple; however this fact makes them real-time tire models and prone for the embedded control of mobile robots in a handling scenario.

These are the reasons why the Empirical Models are predominant in Robotics. It is possible to notice in the literature that part of the Empirical Model applied to Robotics are based on the Pacejka Equations [1, 6, 7, 17] and part consist in other kinds of abstraction [4, 10–12]. A caveat should be made regarding the use of Pacejka Equations in robotics, some authors claim that there is a shortage of robotic tire parametrization methods, which takes them away from this method and leads them to simpler abstractions. Some of the ones that use the Pacejka Equations do not expose how the parameters were obtained or use generic automotive parameters.

In despite of being described as “simple” in relation to the majority of tire models, the Pacejka Equations demand batch tests on specialized machines to be parameterized. This paper aims to help to fulfill the gap in the parameterization of robotic tires by continuing the researches proposed by [15, 16] regarding a test bench for the parameterization of the Pacejka Equations of small tires. This paper contributes with the multibody simulation of a new version of the test bench including a new load cell that enables the acquisition of the tire contact loads regarding the 6 degrees of freedom; focusing on the evaluation whether this new load cell is effective.

To accomplish this objective, in Sect. 2 the Pacejka Equations are reviewed as well as the previous methods for acquisition of experimental data of small tires. In Sect. 3 the new load cell is proposed, the multibody model of the new load cell is demonstrated, and the sensitivity matrix of the resulting test bench is derived. In Sect. 4 some virtual tests of the updated test bench with an automotive PAC89 Adams Tire Model are performed considering vertical loads compatible with small tires, and the virtual experimental data are compared with the expected PAC89 curves. The paper is concluded in Sect. 5.

2 Pacejka Equations

After years of experience on measurements regarding tire dynamics, the group of engineers and researches lead by Hans Bastiaan Pacejka derived a tire model based on an equation that could fit very well the experimental data. It is important to notice that this equation does not have a direct correlation with the tire and road physical properties but it aims to fit experimental data acquired in a discrete domain and infer about the forces acting on the tire in a continuous domain. Thus, it was named as Magic Formula (MF) with a little of academic sense of humor. This name is widely used by the interested community; Pacejka also adopts it in his documents. The most recent version of the MF was launched in 2002 [14] while the pioneer versions were launched in the end of the decade of 1980 [2, 3].

Before introducing the MF itself, it is time to set the forces and torques that the road imposes on the tire, and the quantities of side slip angle, longitudinal slip, and camber angle. Looking at Fig. 1 (left) it is possible to observe the orientation of Longitudinal Force (F_x), Lateral Force (F_y), Vertical Force (F_z), Overturning Moment (M_x), Rolling Resistance (M_y), and Self-align Torque (M_z). An important remark is that the forces and moments follow the right hand rule, excepting F_z that was established in the opposite direction (note the opposite orientation of F_z in relation to z axis).

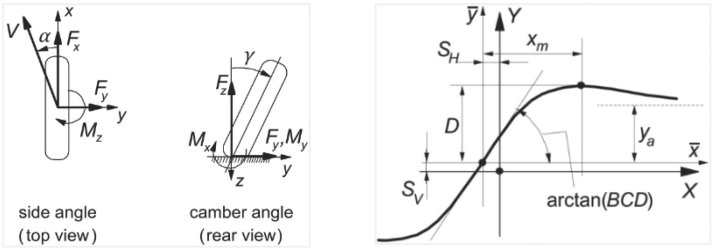

Fig. 1. Orientation of the forces, torques, side slip and camber angle in the MF and a typical MF curve (adapted from [14])

The side slip angle (α) is defined between the direction of the tire travel velocity (V) and the tire heading direction (note that the reference system xyz follows the tire heading direction, keeping it parallel to x axis). The camber angle (γ) is the angle that the tire tips around the x axis; it is measured in relation to z axis (note that the reference system xyz does not rotate in x according to the camber angle, keeping the plane xy parallel to the road plane). Finally the longitudinal slip (κ), is the ratio that takes into account the actual tire angular velocity (Ω), the tire effective radius (r_e) and the tire longitudinal velocity ($V_x = V * \cos(\alpha)$) [14]:

$$\kappa = -\frac{V_x - r_e\Omega}{V_x} \tag{1}$$

The MF is composed of a core equation, an input equation, and an output equation. These equations are described by Eqs. (2), (3) and (4), respectively [14].

$$\bar{y}(\bar{x}) = D\sin(C\arctan(B\bar{x} - E(B\bar{x} - \arctan(B\bar{x})))) \tag{2}$$

$$\bar{x} = X + S_h \tag{3}$$

$$Y(X) = \bar{y}(\bar{x}) + S_v \tag{4}$$

The output term $Y(X)$ is a general term that can represent F_x, F_y or M_z. One dedicated MF must be implemented and parameterized for each of these physical quantities. The input term X refers to α when the output term $Y(X)$ corresponds to F_y or M_z, but X refers to κ when $Y(X)$ outputs F_x. The parameters that modulate the MF are B (stiffness factor), C (shape factor), D (peak factor), E (curvature factor), S_h (horizontal shift) and S_v (vertical shift). The typical behavior of the MF can be observed in Fig. 1 (right).

The Eq. (2) is an antisymmetric function defined in the Cartesian plane $\bar{x}\bar{y}$. The parameter D determines the peak of Eq. (2). The parameter C limits the size of the argument the sine function of Eq. (2), determining its shape. The product BCD controls the slope of Eq. (2) at $\bar{x}$ equal to zero; however, C and D already define other characteristics of curve. Thus, the parameter B will be the main responsible for modulating the slope. The parameter E is able to stretch or compress the curve without changing its slope at $\bar{x} = 0$ and its peak. Finally, Eq. (2) tends to y_a when $\bar{x}$ tends to ∞; on the other hand its peak value occurs at $\bar{x} = x_m$.

If the tire structure is ideal, the Cartesian planes $\bar{x}\bar{y}$ and XY are coincident. However, in real life $\bar{x}\bar{y}$ is shifted away from XY. This is the use of the parameters S_h and S_v in the input and in the output equations (Eqs. 3 and 4); they relocate the core function (Eq. 2) in relation to the plane XY in order to make the MF meaningful, correlating it with the data acquired from the tire. The camber angle also modifies the value of S_h and S_v.

All these parameters can be modulated and scaled by other subparameters, but they are far from the scope of the present paper. This section is meant to come up with a general review of the MF behavior.

The Pacejka model launched in 1989 includes only this MF described here, thus it calculates only the Longitudinal Force, the Lateral Force and the Self-align Torque. However the most recent one also contains other equations for the Overturning Moment and Rolling Resistance, as well as it includes an extended amount of subparameters to modulate and scale the main parameters. For the sake of simplicity, we decided to focus on the 1989 model, but in a future stage of the research it is planned to incorporate the 2002 model.

In the automotive industry there are several ways of obtaining experimental data for the parameterization of the MF of a given tire specimen. Normally actuators are used to set the vertical load, the slip angle, the camber angle and the longitudinal slip of the tire, which slips and rolls on a dummy road. This dummy road can be an inner drum, an outer drum, a large belt that connects two drums or a flat plank. In the majority of the cases, the dummy road moves; the tire just rolls and slips but does not translate.

Considering non-automotive tires there are just a few relevant works. Doria et al. [8] proposed a test bench to measure forces and moments on bicycle and motorcycle tires. In this case the dummy road is a disc (3 m in diameter) that turns around the vertical axis and is equipped with a high adhesion surface. The tire specimen rolls and slips held by an apparatus that sets the camber and slip angle and measures the lateral force and self-aligning moment by means of load cells. Dressel and Rahman [9] used a similar apparatus, but now the road is straight and a cart translates the specimen and the measuring devices.

The present research is the continuation of the researches proposed by [15, 16]. Here in, the tire is driven on a flat table. Camber angle, slip angle and longitudinal slip are set previously. A load cell composed of strain gauges acquires torques on the wheel carrier. The flat table is not a trivial table. I contains hinges and ball joints that allow the acquisition of loads that act on the lateral and longitudinal directions. The next section introduces further details about this test bench explains how it is possible to correlate the loads acquired by the load cells with the forces and moments that act on the tire specimen.

3 Proposed Test Bench

It is possible to observe the multibody model of the proposed test bench in Fig. 2. It contains some parts identical to the test bench that has already been physically assembled and resulted in the articles [15, 16], and some updated parts (still in a virtual viability study) that are explained here.

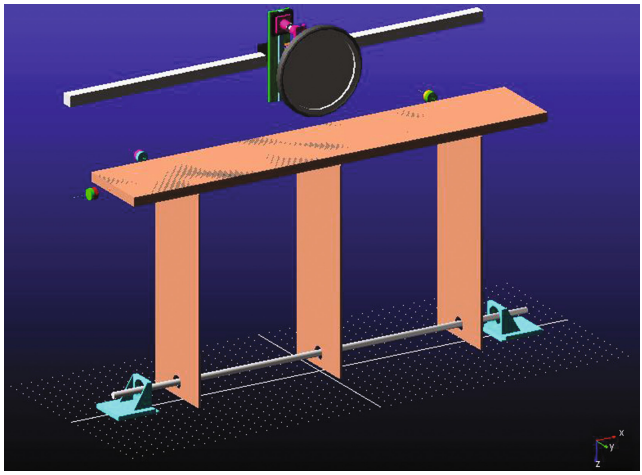

Fig. 2. Multi body model of the test bench executed in ADAMS/View.

The test bench can be divided into two parts: the table and the wheel carrier. Starting from the table, it is possible to notice that it does not have trivial legs; in the

bottom they are supported by ball joints, aligned by a round bar. This round bar hangs over the floor held by two supports in such a way that the table legs are far from touching and interfering with the floor. The connections between the legs and the plank are made by means of hinges, thus the table is able to tip around x and fold around y. However, two lateral load cells hold the tip movement and one longitudinal load cell holds the fold movement, lasting just the virtual movements according to the strains of the load cells. The force signals provided by these load cells are named F_{l1}, F_{l2} and F_{long}, respectively. This part of the virtual test bench has not received any update in this paper. The updates are concentered in the wheel carrier.

The wheel carrier is translated horizontally and vertically by means of horizontal and vertical guides. A stepper motor and a horizontal fuse promote the horizontal translation. The first update is the inclusion of a pneumatic cylinder that is responsible for the application of the vertical force and also executes the vertical translation aided by a vertical slider. In the original version of the test bench these functions were executed by a four bar mechanism. Another update is a load cell installed in the end of the pneumatic cylinder stem to acquire data about the vertical force. The force signal of this load cell is named F_p. In the original test bench this function was executed by weights. In the virtual test bench the pneumatic cylinder and this load cell are represented as an ideal vertical guide and a vertical force applied to the vertical slider.

In Fig. 3 it is possible to observe other updates in the wheel carrier. It is composed of tree hinge joints, one responsible for setting the slip angle, one responsible for the camber angle and one responsible for spinning the wheel. The previous version of the test bench performed the angle adjustment by means of a constrained ball joint. Although it works, it is difficult to manipulate and to set both angles in one single joint. Thus, it was decided to split it into two new joints.

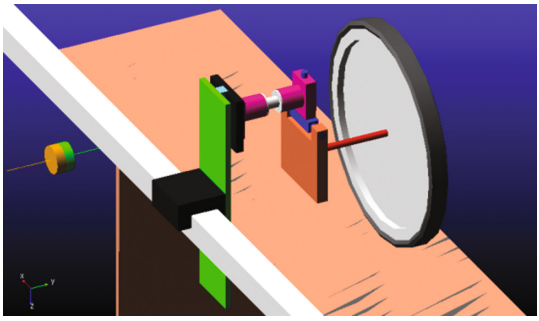

Fig. 3. Detail of the updates on the wheel carrier and its load cell

The last update is the new load cell in the wheel carrier; it is the gray part between the magenta parts. In this updated virtual test bench this load cell is able to acquire torques in x, y and z. In the previous physical test bench, it was able to acquire torques in z. The necessity for acquiring the other torques comes from the fact that the torques in x stimulates the lateral load cells of the table, and the torques in y are related to the Rolling Resistance.

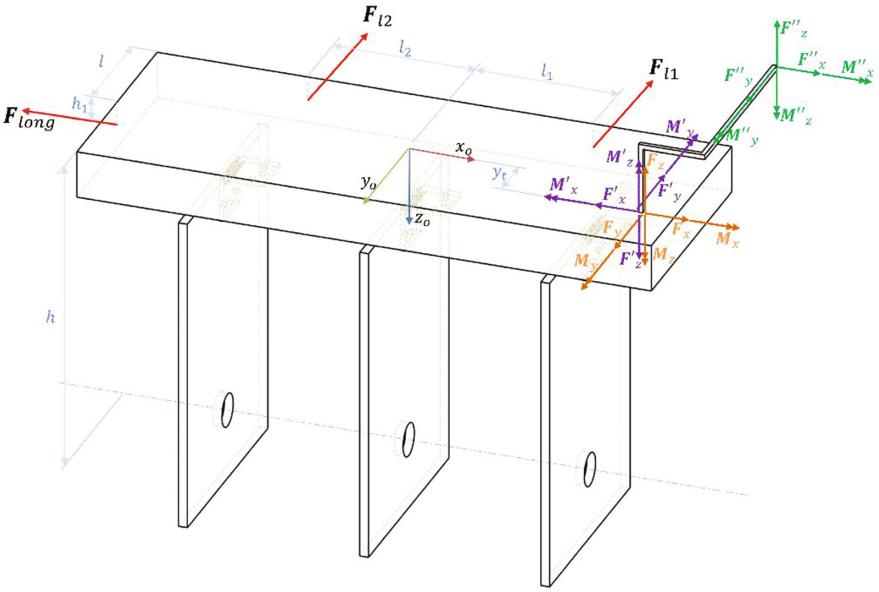

Fig. 4. Didactic approach of the virtual test bench (Color figure online)

To derive the system of equations of this new virtual test bench, it is necessary to set some of its dimensions as well as the direction of forces and moments acting on the tire, on the table and on the wheel carrier. As the tire angular speed is imposed by a motor, the tire and the wheel carrier behave like a portico. These forces and dimensions can be observed in Figs. 4 and 5. They have been distorted to show some details in a didactic manner. In Fig. 4 in red, one can find the forces acting on the table executed by the table load cells. In orange, it is possible to find the forces acting on the tire executed by the table, as well as its reaction on the table can be found in purple. Finally, in green, it is possible to observe the forces and moments performed by the wheel carrier load cell in the wheel carrier.

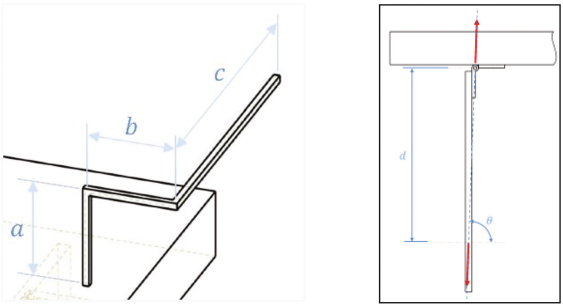

Fig. 5. Detail of the portico like wheel plus carrier (left) and the forces between the table joints (right)

In Fig. 5 (right) it is possible to observe the small misalignment (describing a θ angle) between the ball joints (bottom) and hinges (top) that hold the table legs. It causes a longitudinal resultant in the table plank when any vertical force is applied, exciting F_{long}.

Finally, according to the Newton Laws, it is possible to correlate the signal acquired by the load cells and the forces acting on the tire according to the following system of equations:

$$\begin{Bmatrix} F_{long} \\ F_{l1}+F_{l2} \\ F_p \\ M_x'' \\ M_y'' \\ M_z'' \end{Bmatrix} = \begin{bmatrix} -1 & 0 & d\frac{\sin(\theta)}{\cos(\theta)} & 0 & 0 & 0 \\ 0 & \frac{-h}{h-h_1} & \frac{y_t}{h-h_1} & \frac{-1}{h-h_1} & 0 & 0 \\ 0 & 0 & 1 & 0 & 0 & 0 \\ 0 & -a & -c & 1 & 0 & 0 \\ a & 0 & -b & 0 & 1 & 0 \\ -c & -b & 0 & 0 & 0 & 1 \end{bmatrix} \begin{Bmatrix} F_x \\ F_y \\ F_z \\ M_x \\ M_y \\ M_z \end{Bmatrix} + \begin{Bmatrix} 0 \\ 0 \\ -m_t * g \\ 0 \\ 0 \\ 0 \end{Bmatrix} \quad (5)$$

In this system of equations, m_t is the total mass of the bodies that are supported by the vertical actuator (including the wheel and tire) and g is the gravity. To obtain the forces acting on the tire executed by the floor, one must solve this system for $\{F_x \quad F_y \quad F_z \quad M_x \quad M_y \quad M_z\}^T$. To get the tire forces in the referential of Fig. 1 (left) one must apply a rotation matrix around z considering the angle α

4 Results

Finally, simulations were performed in ADAMS/View. The tire applied to the virtual test bench is automotive and its parameters are contained in the file mdi_tire01.tir available at ADAMS/Tire library. However, the vertical forces applied are compatible with mobile robots (200 N;400 N and 600 N), thus it is an attempt to deal with forces as close as possible to the ones performed by robot tires but using a generic tire parameterization. The slip angle and the longitudinal slip were varied in ranges between −100% and 100%, and −20° and 20°, respectively.

The results can be observed in Fig. 6. It is possible to compare the forces and moment obtained from Eqs. (2), (3) and (4) (in continuous line), the ones outputted by ADAMS/View (in crosses), and the ones calculated by means of Eq. (5) (in circles). The results demonstrated a good correlation.

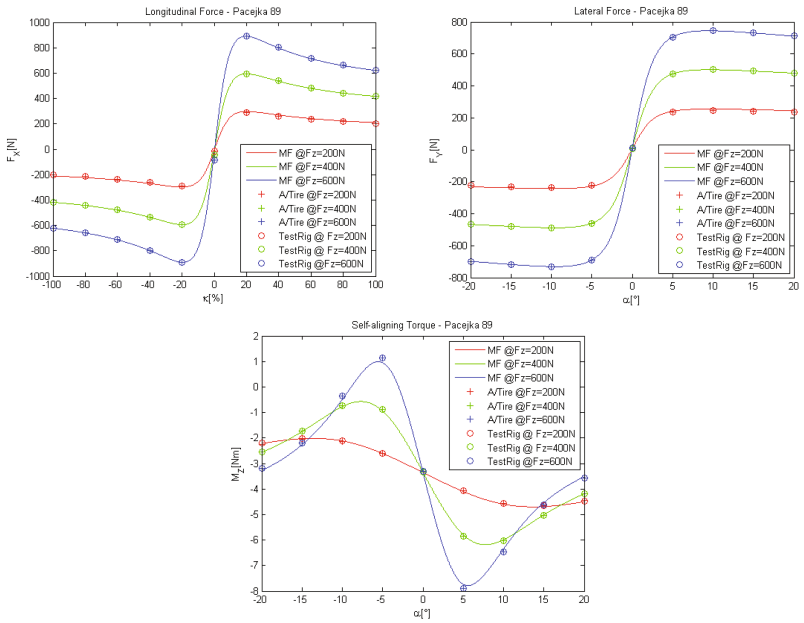

Fig. 6. Results for Lateral Force, Longitudinal Force and Self-align Torque

5 Conclusions

Facing the absence of robot tire parameterization processes, this paper proposes the update of a test bench for the parameterization of small tires. This research is in the stage of viability study, thus the updates have been simulated in ADAMS/View using rigid bodies and automotive tire parameters in order to check whether the planed updates are consistent.

A system of equations was created to correlate the signal of the virtual load cells with the forces and moments in the contact between the tire and the floor. The results coming from this system of equations in the virtual experiment were consistent with the values calculated using the MF and with the results output directly from the ADAMS/Tire routine. The results encourage the authors to optimize and physically implement the proposed updates by means of flex bodies introduced into the virtual model of the test bench in ADAMS/View.

Acknowledgments. The authors want to acknowledge the support received from CAPES and CNPq.

References

1. Aliseichik, A.P., Pavlovsky, V.E.: The model and dynamic estimates for the controllability and comfortability of a multiwheel mobile robot motion. Autom. Remote Control **76**(4), 675–688 (2015)
2. Bakker, E., Nyborg, L., Pacejka, H.B.: Tyre modelling for use in vehicle dynamics studies. SAE Technical Paper (1987)
3. Bakker, E., Pacejka, H.B., Lidner, L.: A new tire model with an application in vehicle dynamics studies. SAE Technical Paper (1989)
4. Bayar, G., Koku, A.B., Konukseven, E.I.: Dynamic modeling and parameter estimation for traction, rolling, and lateral wheel forces to enhance mobile robot trajectory tracking. Robotica **33**(10), 2204–2220 (2015)
5. Castellví, M.C.: Benchmark of Tyre Models for Mechatronic Application. University of Cranfield, Cranfield (2011)
6. Dąbek, P., Trojnacki, M.: Requirements for tire models of the lightweight wheeled mobile robots. In: Mechatronics: Ideas, Challenges, Solutions and Applications, pp. 33–51. Springer International Publishing (2016)
7. Dąbek, P., Trojnacki, M.: Tire models for studies of wheeled mobile robot dynamics on rigid grounds–a quantitative analysis for longitudinal motion. In: International Conference on Systems, Control and Information Technologies, pp. 409–424 Springer International Publishing (2016)
8. Doria, A., Tognazzo, M., Cusimano, G., Bulsink, V., Cooke, A., Koopman, B.: Identification of the mechanical properties of bicycle tyres for modelling of bicycle dynamics. Veh. Syst. Dyn. **51**(3), 405–420 (2013)
9. Dressel, A., Rahman, A.: Measuring sideslip and camber characteristics of bicycle tyres. Veh. Syst. Dyn. **50**(8), 1365–1378 (2012)
10. Ghasemi, M., Nersesov, S.G., Clayton, G.: Finite-time tracking using sliding mode control. J. Franklin Inst. **351**(5), 2966–2990 (2014)
11. Khan, H., et al.: Longitudinal and lateral slip control of autonomous wheeled mobile robot for trajectory tracking. Front. Inf. Technol. Electron. Eng. **16**(2), 166–172 (2015)
12. Lucet, E., Lenain, R., Grand, C.: Dynamic path tracking control of a vehicle on slippery terrain. Control Eng. Pract. **42**, 60–73 (2015)
13. Mohammadi, F.: Tire characteristics sensitivity study, Chalmers University (2012)
14. Pacejka, H.: Tire and Vehicle Dynamics. Elsevier, New York (2012)
15. Silva, L.C.A., Corrêa, F.C., Eckert, J.J., Santiciolli, F.M., Dedini, F.G.: A lateral dynamics of a wheelchair: identification and analysis of tire parameters. Comput. Meth. Biomech. Biomed. Eng. **20**(3), 332–341 (2017)
16. Silva, L.C.A., et al.: Measurement of wheelchair contact force with a low cost bench test. Med. Eng. Phys. **38**(2), 163–170 (2016)
17. Tian, Yu., Sarkar, Nilanjan: Control of a mobile robot subject to wheel slip. J. Intell. Rob. Syst. **74**(3–4), 915–929 (2014)
18. Uil, R.T.: Tyre Models for Steady-State Vehicle Handling Analysis. Eindhoven University of Technology, Eindhoven (2007)

Maneuverability Study of a Vehicle with Rear Wheel Steering

Silva Jhino(✉), Vargas Lincol, Liberato Josue, Quispe Junior, and Munares Carlos

National University of Engineering, Lima, Peru
jsilvan@uni.pe

Abstract. Steering of current vehicles, forward steering, has remained quasi-constant along years. Hence, few times a vehicle with steering different, as rear wheel steering, was put under analysis. The kinematic study that happens when changing the steer to the rear position will be develop in the following paragraphs, as well as some simulations of maneuverability of a vehicle with these features. The purpose is to give to know that a vehicle with rear wheel steering has kinematic features that are advantageous against another vehicles with front wheel steering.

Keywords: Rear wheel steering · Front wheel steering · Ackermann steering geometry · Turning radius

1 Introduction

From ancient civilizations man has always used means of transportation such as horses, carriages and chariots, these latter are horse-drawn carts. Over time steam vehicles were created, then these vehicles gave way to internal combustion vehicle and hybrid vehicles that currently exist [1]. All these vehicles have something in common, they have the steering on the front, with the passing of history always cars had been built in this way, so the aim is to analyze a vehicle with a rear wheel steering.

There are car designs that propose a steering for each of the four tires [2, 3], the difficult maneuverability of these vehicles is their biggest disadvantage against ordinary cars. At present there are already vehicles using the rear wheel steering called forklifts, but these are used indoors, there are also designs to rear wheel steering cars so we propose the study of these same [4].

For several people is difficult to park a car correctly with front wheel steering because they have to use the reverse gear to do it, in the case of a car with rear wheel steering this would be a much more manageable task. This is due to the geometry and kinematics that the car adopts when changing steering position to the back, like this advantage there are several important points to be analyzed in a car with rear wheel

Munares Carlos—Assessor, National University of Engineering, Lima, Peru, e-mail: cmunarest@gmail.com.

J.C.M. Carvalho et al. (eds.), *Multibody Mechatronic Systems*,
Mechanisms and Machine Science 54, DOI 10.1007/978-3-319-67567-1_52

steering, so we need a study model specific. This paper will develop succinctly the kinematic and geometric analysis for demonstrating the advantages it has over conventional models.

2 Front Wheel Steering

There are several kinematic models when talking about land vehicles, one of the most used and present in cars with front wheel steering is the Ackerman model [5].

The principle of Ackerman geometry is based on that to have a correct steering is required of perpendicular axes of the vehicle wheels from the center thereof to the instantaneous center of rotation of the vehicle, which position consist of the intersection of all these projected axes [6].

Having located the instantaneous center of rotation, the total vehicle behaves as a rigid body so that his movement will consist of a turn around this center of rotation forming different turning radius for each wheel of the vehicle. Being the smallest turning radius of the left rear wheel and the largest of the front right.

As shown in Fig. 1 there are two angles of steering in the front wheels, is angle difference is called toe angle [7] and it is necessary for the Ackerman geometry can be met; however, in today's vehicles there is an error in the angles that does not allow a Ackerman geometry exact.

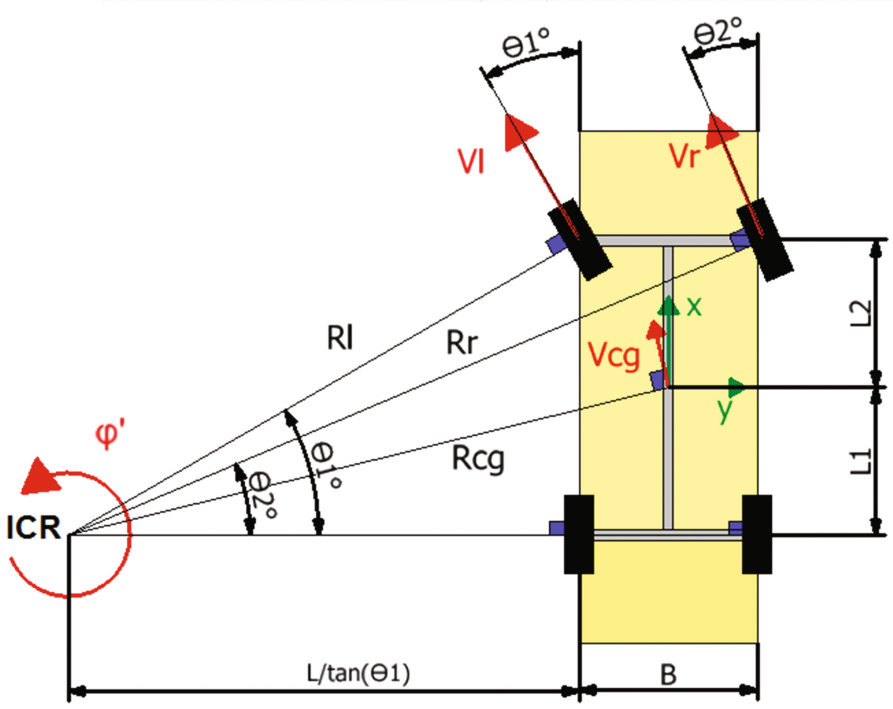

Fig. 1. Front wheel steering.

In Fig. 1 it can better appreciated how to rotate a front wheel steering system. To analyze the speed using equations it has named some variables shown as the angular velocity $\dot{\varphi}$, the steering angles θ_1 and θ_2, the angle of the center of gravity speed α, the speed of the left wheel $\vec{V}_l$, the speed of the right wheel $\vec{V}_r$ and the center of gravity $\vec{V}_{CG}$. In addition to these direction magnitudes there are the distances and point's position as the instantaneous center of rotation ICR, distance from center of gravity to the front L_2, distance from the center of gravity to the rear L_1, the base of the car B and their radius of rotation of each wheel R_l R_r and R_{CG}. Then it will be performing the calculations of the speed equations.

Given the speed position in the center of gravity can be decomposed by its angle as shown in Eqs. (1) and (2).

$$V_x = \left|\vec{V}_{CG}\right|\cos\alpha \tag{1}$$

$$V_y = \left|\vec{V}_{CG}\right|\sin\alpha \tag{2}$$

Then decomposing in the cartesian plane the speeds of each wheel, similar to Eqs. (1) and (2) it was obtained Eqs. (3) and (4).

$$\vec{V}_r = \left|\vec{V}_r\right|\cos(\theta_2)\hat{i} + \left|\vec{V}_r\right|\sin(\theta_2)\hat{j} \tag{3}$$

$$\vec{V}_l = \left|\vec{V}_l\right|\cos(\theta_1)\hat{i} + \left|\vec{V}_l\right|\sin(\theta_1)\hat{j} \tag{4}$$

The speed of center of gravity can be deduced vectorially taking relative velocity between one speed of the two wheels and using the distances and the angular velocity. Equal shown in the following Eq. (5).

$$\vec{V}_{CG} = \vec{V}_r + (-\dot{\varphi}\hat{k}) \times \left(-L_2\hat{i} - \frac{B}{2}\hat{j}\right) \tag{5}$$

Replacing $\vec{V}_r$ obtained above in Eq. (3) into Eq. (5), subsequently carrying out the vector product and gathering the equations are obtained (6), (7) and (8).

$$\vec{V}_{CG} = \left[\left|\vec{V}_r\right|\cos(\theta_2) - \frac{B}{2}\dot{\varphi}\right]\hat{i} + \left[\left|\vec{V}_r\right|\sin(\theta_2) + L_2\dot{\varphi}\right]\hat{j} \tag{6}$$

$$V_x = \left|\vec{V}_r\right|\cos(\theta_2) - \frac{B}{2}\dot{\varphi} \tag{7}$$

$$V_y = \left|\vec{V}_r\right|\sin(\theta_2) + L_2\dot{\varphi} \tag{8}$$

Finally it is obtained the module of $\vec{V}_{CG}$ using Eq. (9) and its vector can be obtained using the Eqs. (1) and (2). Also note that the steering angles have a geometric relationship in the figure shown in Eqs. (10) and (11).

$$\left|\vec{V}_{CG}\right|^2 = V_x^2 + V_y^2 \tag{9}$$

$$\sin\theta_1 = \frac{L_1 + L_2}{R_l} \tag{10}$$

$$\sin\theta_2 = \frac{L_1 + L_2}{R_r} \tag{11}$$

3 Rear Wheel Steering

In the development of a vehicle with rear wheel steering is applied the same Ackerman geometry than in a vehicle with front wheel steering due to its translation capability after locate its instantaneous center of rotation.

In a rear wheel steering vehicle with Ackerman geometry can be seen the change in the lengths of the turning radius of each wheel, as well as its translation will be modified. For example Fig. 2 shows that the smallest turning radius belongs to the front left wheel while the largest turning radius belongs to the back right wheel.

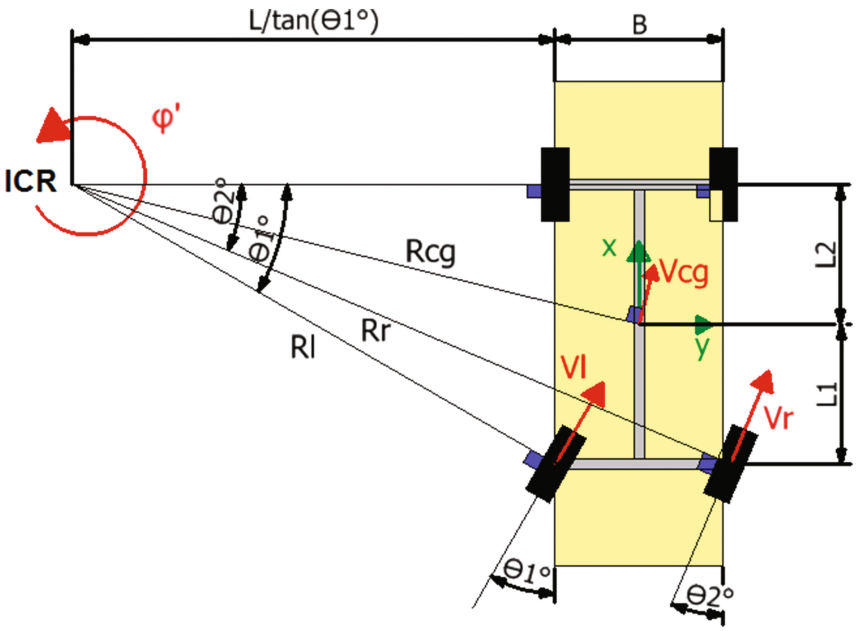

Fig. 2. Rear steering wheel.

Given the kinematic study of the previous section, it can be obtained in the same way the equations for a rear wheel steering. Now the velocities in the wheels and their

decomposition can be obtained from the same manner as the previous study which are shown in Eqs. (1), (2), (3) and (4). The difference in the Eq. (5) would be the distances and directions affecting the vector product with the angular velocity so you would get a new Eq. (12).

$$\vec{V}_{CG} = \vec{V}_r + (-\dot{\varphi}\hat{k}) \times (L_1\hat{i} - \frac{B}{2}\hat{j}) \tag{12}$$

Subsequently, as well as done in Eqs. (6), (7) and (8). $\vec{V}_r$ is replaced in Eqs. (3) and (12), then effecting the vector product and gathering the Eqs. (13), (14) and (15) are been obtained.

$$\vec{V}_{CG} = \left[|\vec{V}_r|\cos(\theta_2) - \frac{B}{2}\dot{\varphi}\right]\hat{i} + \left[|\vec{V}_r|\sin(\theta_2) - L_1\,\dot{\varphi}\right]\hat{j} \tag{13}$$

$$V_x = |\vec{V}_r|\cos(\theta_2) - \frac{B}{2}\dot{\varphi} \tag{14}$$

$$V_y = |\vec{V}_r|\sin(\theta_2) - L_1\,\dot{\varphi} \tag{15}$$

Once obtained this can be replaced in Eq. (9) and use the relationships shown in Eqs. (10) and (11).

4 Maneuverability Comparison

This chapter will be analyzed, through mathematical simulations in MATLAB software, in different cases where the study and comparison between a vehicle with front steering and other with rear wheel steering can be done. These simulations can analyze the different characteristics that occur when using each kind of steering. To obtain a simulation proximately close to the reality, a modeled vehicle with Ackerman geometry and measurements of a wirelessly controlled scale car was plotted.

In order to study the differences that occur when changing the position of the steering, two specific cases were chosen to be analyzed. First, it will be analyzed the case of parking, in this case it will be verified which steering is easiest for a driver to park in a parallel parking lot. And second, it will be analyzed the case where the vehicle has to turn on a corner of 90°. The ease of maneuverability, the space occupied, and which vehicle is most susceptible to invade the pedestrians' berm will be seen.

4.1 Parking

In this first section it will be analyzed the case of parking a vehicle based on simulations for each case of steering.

Figure 3 shows the parking process of a vehicle with front steering. As a first detail to note in this configuration is that for proper parking, this vehicle should do it backwards which brings complications first instance for the driver because driving in

reverse direction is much more complicated than driving in forward direction. This is how noted that in the second vignette the car starts to turn with a turning radius that is at the same height of a front obstacle. This vehicle continues back toward the halfway point where it reverses its steering angles so that the third vignette can be observed as can be placed within the allotted space. This assigned parking space is based on the rule of Peruvian construction [8].

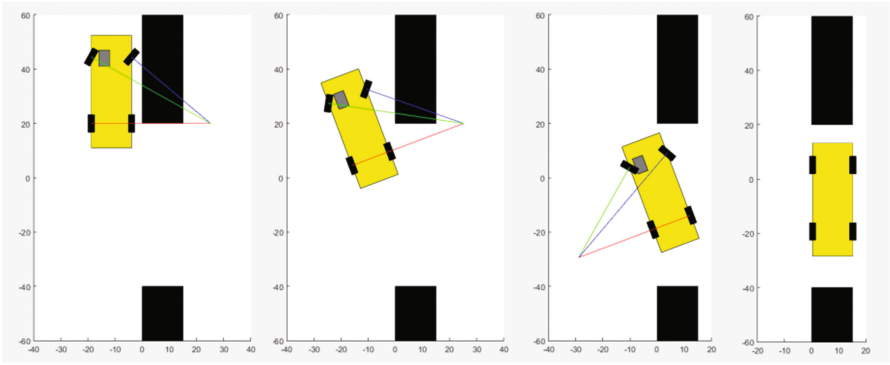

Fig. 3. Front wheel steering parking.

In the other hand, in Fig. 4 it will be observed the parking process of a vehicle with rear wheel steering. A feature in the parking of this vehicle is the facility and comfort that rear steering brings to people that learn to drive. In both cases is shown an appropriate parking to each kind of steering.

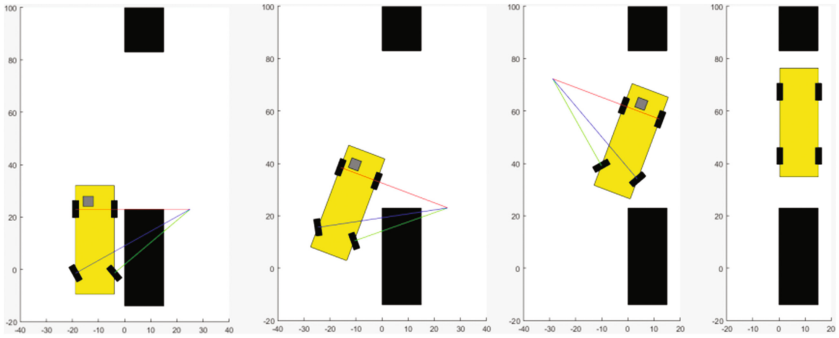

Fig. 4. Rear wheel steering parking.

4.2 Corner Turn

As it was observed in the parking section, the advantage that own a vehicle with rear wheel steering versus other with front wheel steering is the space occupied when

turning, then it will be observed the behavior of both types of steering for the case of turning a 90° corner.

In Fig. 5 it will be analyzed this case to a vehicle with front wheel direction in which is observed if the vehicle has a correct corner turn. To achieve this correct turn, the vehicle must exceed the corner with a large length since because of its instantaneous center of rotation, the radius of the lower right wheel is small dimension causing a high probability that the vehicle goes up to the berm invading the pedestrian space. Given this and the geometry of the vehicle, the driver must be able to calculate the length at which you have to turn the wheels to turn the corner without problems.

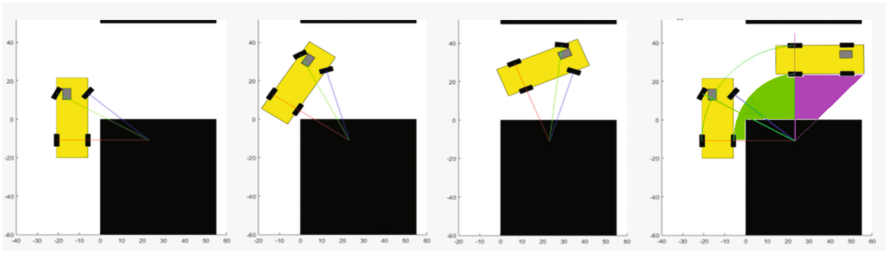

Fig. 5. Front wheel steering corner turn. (Color figure online)

In the other hand, in Fig. 6 a vehicle with rear wheel steering turn around the corner easier is seen. Unlike the front wheel steering, a vehicle with rear wheel steering can overcome this case without problems due to the fact that its instantaneous center of rotation the vehicle does not need to surpass the corner to bend it but only to be at the same height.

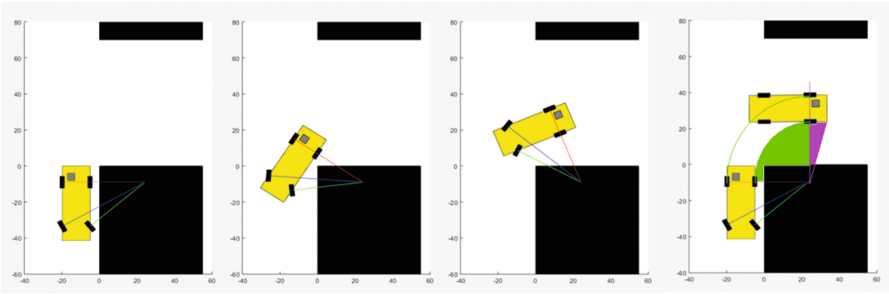

Fig. 6. Rear wheel steering corner turn. (Color figure online)

Table 1 shows the sweeping area that the vehicle employs to turn a corner, these areas (green and purple area) are plotted in the last images of Figs. 5 and 6. The green area is the area employed by the wheel without steering, the right static wheel, having the vehicle's ICR as its center; the purple area is the triangular area that forms when reaching the horizontal position of the vehicle having as an opposite point the vehicle's ICR.

Table 1. Area employed by a car to turn a corner

	Area green [cm^2]	Area purple [cm^2]	Total area [cm^2]
Forward steering	456,858	405	861,858
Rear steering	456,858	105	561,858

5 Graphics and Results

The main relationship obtained in the simulation of vehicle rear wheel steering was the function in which the radius of rotation of each wheel varies depending on the turning angle of the steering wheels.

Next, in Fig. 7, the graphs found in the simulation are shown with a range of angle of turn from 10 to 50 sexagesimal degrees. In the upper graphs it is seen the shape that adapts this relationship between the rotation angle and the turning radii, noting that the smaller the turn angle, the greater the radius of rotation and vice versa. Due to this particularity it is can also be observed that there are two asymptotes in the turn angle 0 and in the radius of rotation 0. The asymptotic of turn angle 0 occurs because very small angles would cause infinite turn radii, it which is not adapted reality; likewise it is impossible for there to be a turn radius 0.

In the lower graphs it is seen a magnifying to the turning angles in which the measurements for the turn radius are detailed, proving in this way that at each turn angle the greater radius will be, the lower left wheel (R21) and the smaller one, the upper right wheel (R12).

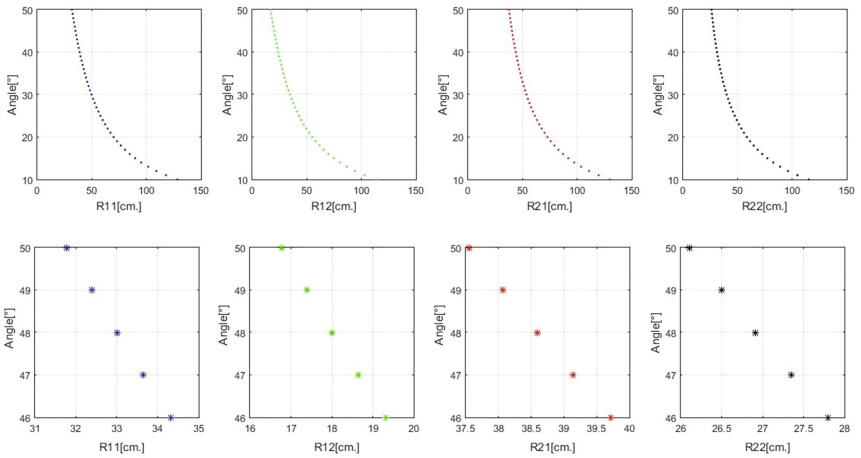

Fig. 7. Graphs of the turning radius. R11 Left Front Wheel, R12 Right Front Wheel, R21 Left Back Wheel, R22 Right Back Wheel.

6 Conclusions

Driving cars is more comfortable with rear wheel steering as could be seen in the simulations of Sects. 4.1 and 4.2. In the case of corner turn, rear steering improves turning on the corner reducing the possibility of mounting on the corner; as well as maneuverability of parking is easier due to the fact of not using the reverse gear that can bring complications to the drivers. However, it can be seen in the graphs obtained in Fig. 6 that a vehicle with rear wheel steering can invade rails that it doesn't use, causing problems and even accidents with other drivers. Also, it can been seen in Figs. 5 and 6 that the front wheel steering employs more area than rear wheel steering when is necessary to turn a corner.

Due to this last point mentioned, more studies should be carried out on cars with rear wheel steering since there are also other advantages such as the reduction of inertia at the time of braking, causing as a result less tire wear; wear that is also produced to a greater extent on the rear tires due to the location of the steering in conventional vehicles; these mentioned points are studies for a dynamic analysis that will be developed in a future work.

References

1. Eckermann, E.: World History of the Automobile. Society of Automotive Engineers, Warrendale (2001)
2. Bean, A.J., Blumberg, M.J., Livdahl, R.J., Mellott, L.A.: Vehicle offset with extendible axles and four-wheel independent steering control. US, 6827176B2. (B62D7/1509, B60B35/003, B60B35/1054, B60B35/109, B60K17/30, B60K17/356, B60K7/0015, B60Y2200/416, Y10S180/906), 07 December 2004 (Appl. 10337385, 07 Jan 2003)
3. Singh, A., Kumar, A., Chaudhary, R., Singh, R.C.: Study of 4 wheel steering systems to reduce turning radius and increase stability. In: International Conference of Advance Research and Innovation (ICARI-2014) (2014)
4. Onaya, H., Takashi, Y., Sasaki, H.: Rear wheel steering vehicle. US9145167B2 (cl B62D7/15; B62D7/14, B62D7/159, B62D7/148), 29 September 2015 (Appl. 12/921685, 30 Jan 2009)
5. Abe, M.: Vehicle Handling Dynamics: Theory and Application, pp. 139–142. Butterworth-Heinemann, Oxford (2009)
6. Zhao, J.S., Liu, X., Feng, Z.J., Dai, J.S.: Design of an Ackermann-type steering mechanism. Proc. Inst. Mech. Eng. Part C J. Mech. Eng. Sci. **227**(11), 2549–2562 (2013)
7. Lipták, T., Kelemen, M., Gmiterko, A., Virgala, I., Miková, L., Hroncová, D.: Comparison of Different Approaches of Mathematical Modelling of Ackerman Steered Car-like System. J. Autom. Control **4**(2), 15–21 (2016)
8. National Building Regulations, Peru: Architecture (Title III.1) Standard A.010, Parking (Chapter XI), Article 65, 8 June 2006